frontiers | Research Topics

New insights in microbial stress tolerance mechanisms

Edited by
Z. Petek Cakar, Hector Alex Saka and Jose Echenique

Published in
Frontiers in Microbiology

ISSN 1664-8714
ISBN 978-2-8325-5821-8
DOI 10.3389/978-2-8325-5821-8

About Frontiers

Frontiers is more than just an open access publisher of scholarly articles: it is a pioneering approach to the world of academia, radically improving the way scholarly research is managed. The grand vision of Frontiers is a world where all people have an equal opportunity to seek, share and generate knowledge. Frontiers provides immediate and permanent online open access to all its publications, but this alone is not enough to realize our grand goals.

Frontiers journal series

The Frontiers journal series is a multi-tier and interdisciplinary set of open-access, online journals, promising a paradigm shift from the current review, selection and dissemination processes in academic publishing. All Frontiers journals are driven by researchers for researchers; therefore, they constitute a service to the scholarly community. At the same time, the *Frontiers journal series* operates on a revolutionary invention, the tiered publishing system, initially addressing specific communities of scholars, and gradually climbing up to broader public understanding, thus serving the interests of the lay society, too.

Dedication to quality

Each Frontiers article is a landmark of the highest quality, thanks to genuinely collaborative interactions between authors and review editors, who include some of the world's best academicians. Research must be certified by peers before entering a stream of knowledge that may eventually reach the public - and shape society; therefore, Frontiers only applies the most rigorous and unbiased reviews. Frontiers revolutionizes research publishing by freely delivering the most outstanding research, evaluated with no bias from both the academic and social point of view. By applying the most advanced information technologies, Frontiers is catapulting scholarly publishing into a new generation.

What are Frontiers Research Topics?

Frontiers Research Topics are very popular trademarks of the *Frontiers journals series*: they are collections of at least ten articles, all centered on a particular subject. With their unique mix of varied contributions from Original Research to Review Articles, Frontiers Research Topics unify the most influential researchers, the latest key findings and historical advances in a hot research area.

Find out more on how to host your own Frontiers Research Topic or contribute to one as an author by contacting the Frontiers editorial office: frontiersin.org/about/contact

New insights in microbial stress tolerance mechanisms

Topic editors

Z. Petek Cakar — Istanbul Technical University, Türkiye

Hector Alex Saka — Centro de Investigaciones en Bioquímica Clínica e Inmunología (CIBICI), CONICET, Argentina

Jose Echenique — National University of Cordoba, Argentina

Citation

Cakar, Z. P., Saka, H. A., Echenique, J., eds. (2024). *New insights in microbial stress tolerance mechanisms*. Lausanne: Frontiers Media SA.

doi: 10.3389/978-2-8325-5821-8

Table of contents

frontiers | Frontiers in Microbiology

TYPE Editorial
PUBLISHED 10 December 2024
DOI 10.3389/fmicb.2024.1513485

OPEN ACCESS

EDITED AND REVIEWED BY
Biswarup Mukhopadhyay,
Virginia Tech, United States

*CORRESPONDENCE
Zeynep Petek Çakar
✉ cakarp@itu.edu.tr
Hector Alex Saka
✉ alex.saka@unc.edu.ar
Jose Echenique
✉ jechenique@unc.edu.ar

†These authors have contributed equally to this work and share last authorship

RECEIVED 18 October 2024
ACCEPTED 26 November 2024
PUBLISHED 10 December 2024

CITATION
Çakar ZP, Saka HA and Echenique J (2024) Editorial: New insights in microbial stress tolerance mechanisms.
Front. Microbiol. 15:1513485.
doi: 10.3389/fmicb.2024.1513485

Editorial: New insights in microbial stress tolerance mechanisms

Zeynep Petek Çakar[1,2*†], Hector Alex Saka[3,4*†] and Jose Echenique[3,4*†]

[1]Department of Molecular Biology and Genetics, Faculty of Science and Letters, Istanbul Technical University, Istanbul, Türkiye, [2]Dr. Orhan Ocalgiray Molecular Biology, Biotechnology and Genetics Research Center (ITU-MOBGAM), Istanbul Technical University, Istanbul, Türkiye, [3]Centro de Investigaciones en Bioquímica Clínica e Inmunología (CIBICI)-Consejo Nacional de Investigaciones Científicas y Técnicas (CONICET), Córdoba, Argentina, [4]Departamento de Bioquímica Clínica, Facultad de Ciencias Químicas, Universidad Nacional de Córdoba, Córdoba, Argentina

KEYWORDS

bacteria, oxidative stress, metal stress, influenza A virus, adaptive laboratory evolution, fungi, salt stress, microbial stress response

Editorial on the Research Topic
New insights in microbial stress tolerance mechanisms

In nature, microorganisms must survive a variety of stressors, including toxic metals, oxidative environments, pH changes, nutrient deprivation, antimicrobial agents, and host immune responses. This Research Topic comprises 14 manuscripts that explore different aspects of microbial stress tolerance mechanisms, with a particular emphasis on responses to metal, acidic, and oxidative stress, including studies on bacteria and filamentous fungi relevant for human health and also for biotechnological applications.

Heavy metal pollution is a major health and environmental issue. Chen et al. investigated the effects of chromium on the gut microbiota of silkworm and their metabolome. They identified a complex network emphasizing the interrelation between diverse bacterial species, their metabolic byproducts and functional significance during chromium stress. The authors suggested that this innovative approach, which combines metagenomic sequencing coupled with non-targeted metabolomics, can enhance our understanding of gut microbiota-metabolite interactions under chromium stress. This methodology may be useful for future investigations related to heavy metal-induced ecological disruption.

Metal(loid)s are toxic to microbial cells by generating reactive oxygen species (ROS). Through proteomic analysis and a genome-wide screening deletion collection of *Escherichia coli*, Cornejo et al. showed that certain metal(loid)s induce bacterial death by promoting the aggregation of specific proteins in a ROS-independent manner. The aggregated proteins were associated with several essential processes, including amino acid biosynthesis as enzymes. The authors proposed that metal(loid) toxicity is a multifactorial phenomenon that could lead to cell death.

Vibrio cholerae is an aquatic bacterium and the cause of cholera pandemics. Little is known about its response to stresses induced by heavy metals. Zhang B. et al. explored how *V. cholerae* responds to stress triggered by metals and found that Cd^{2+}, Pb^{2+}, and Zn^{2+} decreased bacterial cell membrane fluidity, while that of Ni^{2+} increased it. Surprisingly, these stressing stimuli increased the production of proteins related to adhesion, invasion,

cell-damage and virulence, raising intriguing questions about their impact on *V. cholerae*-host interactions.

With their high metabolic versatility, *Rhodobacter* species are used to study photosynthesis, hydrogen production, bioremediation and biosensing. Atay et al. developed a robust and highly cobalt-stress-resistant *Rhodobacter sphaeroides* strain using adaptive laboratory evolution. The evolved strain was also resistant to other metal ions and salt stress, and could hold Co^{2+} ions, indicating its bioremediation potential. Genomic analyses revealed mutations in genes related to transcriptional regulators, NifB-family-FeMo-cofactor biosynthesis, putative virulence factors, TRAP-T family transporter, sodium/proton antiporter (NhaD), and genes with unknown functions that may be important in cobalt-stress-resistance.

Zamal et al. investigated the photosynthetic apparatus of a *Rhodobacter alkalitolerans* strain newly isolated from an alkaline pond, under high light intensity and alkalinity stress conditions. Although increased light intensity led to a decrease in the stability of the photosystem complexes at normal pH, acclimation to increased light intensity was observed in *R. alkalitolerans* at alkaline conditions, manifested as photoprotection at high pH. Based on increased expression of the antiporter NhaD, they suggested that it may be crucial in maintaining homeostatic balance in alkaline conditions.

Streptococcus pneumoniae, a bacterial human pathogen, must overcome different conditions to survive during infection, such as nutrient depletion, acidic, and oxidative stress. Zhang C. et al. described that methionine semi-starvation resulted in intracellular acidification and a subsequent bacterial growth retardation. Curiously, the addition of glutamine restored optimal intracellular pH and promoted pneumococcal growth, a correction attributed to glutamine deamination. The authors proposed that this novel adaptation mechanism for nutrient deficiency could provide new drug targets for inhibiting pneumococcal infections.

S. pneumoniae produces high levels of H_2O_2 to eliminate other microorganisms from the respiratory tract microbiota. Hernandez-Morfa, Olivero et al. provide a comprehensive analysis of the various strategies employed by this pathogen to counteract oxidative stress generated both by itself and by host cells, including the use of H_2O_2 scavengers. This review also focused on the relevance of metal homeostasis in the oxidative stress response regulation. In addition, a particular focus was given to the role of the oxidative stress response during the transient intracellular life of *S. pneumoniae*.

Hernandez-Morfa, Reinoso-Vizcaino et al. elucidated the impact of influenza A coinfection on the induction of fluoroquinolone persistence in *S. pneumoniae*. Viral infection increases the intracellular ROS production in host cells, which contributes to increased fluoroquinolone persistence. This enhancement is partially attributable to ROS because this phenotype manifests only in autophagy-proficient cells. The authors propose a novel mechanism by which viral infection promotes antibiotic persistence of *S. pneumoniae* within host cells, generating concern for the fluoroquinolone treatment of pneumococcal infections in patients with influenza.

Intracellular oxidative stress from H_2O_2/superoxide has been thought to potentially result in the oxidation of cysteine residues of cytoplasmic proteins. *E. coli* responds to H_2O_2 by inducing glutaredoxin-1 and thioredoxin-2, which seems to support that view. Eben and Imlay tested the abilities of different oxygen species to oxidize either model thiols or protein cysteine residues *in vitro*. They showed that chemical cysteine oxidations were rare events and cellular glutaredoxin and thioredoxin may have undiscovered roles under other growth conditions than those employed in their study.

Pseudomonas aeruginosa is a ubiquitous bacterium in soil and aquatic environments and a recognized antibiotic multi-resistant pathogen, especially within hospital settings. Sodium hypochlorite (NaOCl) is among the most effective disinfectants due to its potent oxidizing properties. da Cruz Nizer et al. investigated novel mechanisms employed by *P. aeruginosa* to combat NaOCl oxidative stress. Using transposon mutagenesis, they identified mutants with heightened susceptibility to NaOCl. Unexpectedly, this study revealed that *P. aeruginosa* leverages HCN production to mitigate NaOCl toxicity.

Haemophilus influenzae, a human bacterial pathogen, is able to survive in the presence of hypochlorite (OCl^-) generated by immune cells. Nasreen et al. reported that the expression of the DmsABC S-/N-oxide reductase is induced by OCl^- and it is essential for bacterial survival during infection. They proposed that MsrAB methionine sulfoxide reductase is necessary for physical resistance to HOCl, DmsABC is essential for intracellular colonization, and MtsZ S-oxide reductase contributes to resistance against N-chlorotaurine. This study underscores the significance of these enzymes in bacterial virulence.

Trichoderma harzianum is a soil fungus used in agriculture as a biocontrol agent. However, its efficacy is limited by soil salinization and excessive pesticide use. Yang et al. carried out a detailed analysis of the transcriptional responses of *T. harzianum* to NaCl-induced stress revealing that genes involved in cellular detoxification, glutathione metabolism and active oxygen clearance were differentially expressed. Overall, this study provides significant insights into *T. harzianum*'s adaptation to salt stress, potentially improving biocontrol strategies.

Aspergillus species are fungi with biotechnological and ecological importance, and pathogenicity. As their genome structure and function are highly conserved, Jorge et al. tested if they also have conserved stress regulators. They integrated transcriptome signatures of different *Aspergillus* species to various organic compounds and identified a single gene, *AN9181*, assigned as NmrB, that showed the same response across different datasets. Comparison of the single deletion mutant Δ*AN9181* with the wild-type strain revealed that NmrB negatively regulates *Aspergillus nidulans* metabolism under oxidative stress condition.

Listeria monocytogenes, a foodborne pathogen that causes listeriosis in humans, is able to survive in different stressful environments. Ładziak et al. demonstrated that Lmo0946 is an SOS response interfering factor essential for normal growth in both stress-free and multi-stress conditions. In addition, Lmo0946 contributes to biofilm formation, susceptibility to β-lactam antibiotics, and virulence. The *lmo0946* mutation resulted in the induction of the SOS response, the mobilization of genetic elements, and the downregulation of genes related to bacterial general stress response and virulence.

In conclusion, this Research Topic provides novel insights into the molecular, biochemical, and physiological aspects of microbial stress response and tolerance strategies to survive in diverse environments, including soil, water, and host tissues. The diversity and complexity of stress response and tolerance mechanisms, particularly against heavy metal and oxidative stress, highlights the need for further investigations, using powerful strategies including adaptive laboratory evolution, omics analysis, and reverse engineering. Future research should delve deeper into the molecular mechanisms of protein aggregation and metal(loid)s-induced bacterial and fungal death. In addition, exploring strategies of pathogenic bacteria for survival within host cells and the impact of co-infection on microbial persistence and drug resistance could provide valuable therapeutic targets. Finally, elucidating the genetic and biochemical mechanisms regulating microbial response and tolerance to heavy metals, oxidative stress, antimicrobial drugs, and host immunity remains crucial for future advancements and innovative solutions in bioremediation and infectious disease control.

Author contributions

ZÇ: Conceptualization, Writing – original draft, Writing – review & editing. HS: Conceptualization, Writing – original draft, Writing – review & editing. JE: Conceptualization, Writing – original draft, Writing – review & editing.

Conflict of interest

The authors declare that the research was conducted in the absence of any commercial or financial relationships that could be construed as a potential conflict of interest.

The author(s) declared that they were an editorial board member of Frontiers, at the time of submission. This had no impact on the peer review process and the final decision.

Publisher's note

All claims expressed in this article are solely those of the authors and do not necessarily represent those of their affiliated organizations, or those of the publisher, the editors and the reviewers. Any product that may be evaluated in this article, or claim that may be made by its manufacturer, is not guaranteed or endorsed by the publisher.

frontiers | Frontiers in Microbiology

TYPE Review
PUBLISHED 13 September 2023
DOI 10.3389/fmicb.2023.1269843

OPEN ACCESS

EDITED BY
Haike Antelmann,
Freie Universität Berlin, Germany

REVIEWED BY
Jan-Ulrik Dahl,
Illinois State University, United States
Stephanie Neville,
The University of Melbourne, Australia
Claudia Trappetti,
University of Adelaide, Australia

*CORRESPONDENCE
Jose Echenique
✉ jechenique@unc.edu.ar

†These authors have contributed equally to this work and the order of these authors is arbitrary

‡PRESENT ADDRESSES
German E. Piñas,
State of Utah, Department of Health, Salt Lake City, UT, United States
Nicolas M. Reinoso-Vizcaino,
Department of Molecular Genetics and Microbiology, Duke Center for Virology, Duke University School of Medicine, Durham, NC, United States
Melina B. Cian,
Health Sciences Center, University of Oklahoma, Norman, OK, United States

RECEIVED 30 July 2023
ACCEPTED 28 August 2023
PUBLISHED 13 September 2023

CITATION
Hernandez-Morfa M, Olivero NB, Zappia VE, Piñas GE, Reinoso-Vizcaino NM, Cian MB, Nuñez-Fernandez M, Cortes PR and Echenique J (2023) The oxidative stress response of *Streptococcus pneumoniae*: its contribution to both extracellular and intracellular survival.
Front. Microbiol. 14:1269843.
doi: 10.3389/fmicb.2023.1269843

The oxidative stress response of *Streptococcus pneumoniae*: its contribution to both extracellular and intracellular survival

Mirelys Hernandez-Morfa[1,2†], Nadia B. Olivero[1,2†], Victoria E. Zappia[1,2†], German E. Piñas[1,2‡], Nicolas M. Reinoso-Vizcaino[1,2‡], Melina B. Cian[1,2‡], Mariana Nuñez-Fernandez[3], Paulo R. Cortes[1,2] and Jose Echenique[1,2*]

[1]Centro de Investigaciones en Bioquímica Clínica e Inmunología (CIBICI-CONICET), Facultad de Ciencias Químicas, Universidad Nacional de Córdoba, Córdoba, Argentina, [2]Departamento de Bioquímica Clínica, Facultad de Ciencias Químicas, Universidad Nacional de Córdoba, Córdoba, Argentina, [3]Centro de Química Aplicada, Facultad de Ciencias Químicas, Universidad Nacional de Córdoba, Córdoba, Argentina

Streptococcus pneumoniae is a gram-positive, aerotolerant bacterium that naturally colonizes the human nasopharynx, but also causes invasive infections and is a major cause of morbidity and mortality worldwide. This pathogen produces high levels of H_2O_2 to eliminate other microorganisms that belong to the microbiota of the respiratory tract. However, it also induces an oxidative stress response to survive under this stressful condition. Furthermore, this self-defense mechanism is advantageous in tolerating oxidative stress imposed by the host's immune response. This review provides a comprehensive overview of the strategies employed by the pneumococcus to survive oxidative stress. These strategies encompass the utilization of H_2O_2 scavengers and thioredoxins, the adaptive response to antimicrobial host oxidants, the regulation of manganese and iron homeostasis, and the intricate regulatory networks that control the stress response. Here, we have also summarized less explored aspects such as the involvement of reparation systems and polyamine metabolism. A particular emphasis is put on the role of the oxidative stress response during the transient intracellular life of *Streptococcus pneumoniae*, including coinfection with influenza A and the induction of antibiotic persistence in host cells.

KEYWORDS

***Streptococcus pneumoniae*, oxidative stress, two-component systems, intracellular survival, immune cells, influenza A, persistence, fluoroquinolones**

Introduction

Streptococcus pneumoniae (or the pneumococcus) is an aerotolerant pathogen that colonizes the human nasopharynx. In fact, it is part of the commensal microbiota found in the human upper respiratory tract (Bogaert et al., 2004), where this pathogen can be isolated from 5–90% of healthy individuals, depending on the range age of the population (Gierke et al., 2021). This asymptomatic transitory phase can lead to various pneumococcal diseases when bacteria migrate to the lower respiratory tract (Subramanian et al., 2019). *Streptococcus pneumoniae* can

cause both minor infections, such as otitis and sinusitis, and severe invasive infections, such as community-acquired pneumonia and meningitis. It has been reported that around 10% of patients with invasive pneumococcal disease die from their illness (CDC, 2012). Regardless of the availability of antibiotics and vaccines, pneumococcal diseases remain the leading cause of death among vaccine-preventable diseases worldwide. According to the World Health Organization (WHO), these diseases cause over 1 million deaths annually.[1]

Streptococcus pneumoniae employs various adaptive mechanisms to survive in the mucosa of the respiratory tract and cause disease. It can tolerate different levels of oxygen in aerobic conditions. In the nasopharynx and lungs, the pneumococcus is exposed to a partial pressure of oxygen that is similar to that of the atmosphere and thrives in micro-aerophilic conditions in the lower respiratory tract or middle ear. However, during more severe infections like bacteremia and meningitis, it must also be able to survive in anaerobic conditions.

In addition to naturally stressful environments, the pneumococcus is also subjected to oxidative conditions imposed by the host's immune response. In response to a bacterial infection, the body's first line of defense involves the migration of leukocytes and the generation of chemokines and cytokines. In this context, polymorphonuclear leukocytes produce hydrogen peroxide (H_2O_2), superoxide anion radicals (O_2−•), and nitric oxide (NO•). Importantly, superoxide anion radicals and nitric oxide can combine to form peroxynitrite (ONOO), a potent oxidant with cytotoxic effects (Barichello et al., 2013).

In this review, we will summarize how the exceptional endogenous production of H_2O_2 affects the oxidative stress response (OSR) of this pathogen. We will also review the molecular defense mechanisms that *S. pneumoniae* has developed to protect itself against oxidative stress induced by human tissues. Furthermore, we will outline the impact of metal transport and signal transduction systems on the development of oxidative stress response. Finally, we focus on the relevance of the pneumococcal OSR during the transient intracellular life in host cells, as well as the emergence of an antibiotic persistence induced by oxidative conditions, and the risk to generate antibiotic resistance, a scenario that complicates the antimicrobial therapy of pneumococcal diseases.

Generation of endogenous H_2O_2

Streptococcus pneumoniae exhibits the ability to tolerate and metabolize oxygen, producing high levels of H_2O_2 as a byproduct that can accumulate to millimolar concentrations, providing it with a competitive edge over other commensal and pathogenic bacteria in the upper respiratory tract (Pericone et al., 2000). Moreover, the H_2O_2 exposure induces toxic DNA double-strand breaks that precede apoptosis in alveolar cells. These genotoxic and cytotoxic effects are directly implicated in the pathogenesis of host cellular injury in pneumococcal pneumonia (Duane et al., 1993; Rai et al., 2015).

Endogenously generated H_2O_2 by the pneumococcus can rapidly diffuse through cell membranes, accumulate in the extracellular milieu, and eliminate other microorganisms, thereby promoting colonization and worsening virulence (Pericone et al., 2000). The hyperproduction of H_2O_2 is approximately 10^3 times higher than the level that inhibits the growth of *Escherichia coli* cells that lack the ability to scavenge H_2O_2 (Seaver and Imlay, 2001). Concentrations between 0.1 and 1.0 mM H_2O_2 are capable to kill or inhibit *in vitro* other respiratory tract pathogens, such as *Moraxella catarrhalis*, *Haemophilus influenzae*, and *Neisseria meningitidis*. Despite producing catalase, an important metabolic enzyme used to eliminate H_2O_2, these bacterial species were found to be sensitive to H_2O_2 concentrations produced by *S. pneumoniae* (Pericone et al., 2000).

One of the metabolic pathways utilized by pneumococci to process O_2 involves the production of H_2O_2. The SpxB pyruvate oxidase is responsible for over 80% of endogenous H_2O_2 synthesis, which is generated by converting pyruvate to acetyl phosphate and releasing H_2O_2 (Pericone et al., 2000; Lisher et al., 2017). Because the SpxB reaction generates ATP, it was reported that the susceptibility of the *spxB* mutant to external 20 mM H_2O_2 was due to a rapid depletion of ATP that affected pneumococcal viability (Pericone et al., 2003). Furthermore, lactate oxidase (LctO) complements this oxidative reaction through the generation of pyruvate from lactate, consuming O_2 and releasing H_2O_2. The biosynthesis of pyruvate by LctO facilitates the production of H_2O_2 through the SpxB pathway (Lisher et al., 2017; Figure 1).

The induction of apoptosis-like death during the stationary phase of *S. pneumoniae* is attributed to the presence of H_2O_2, which is mainly generated by SpxB, and confers a selective advantage in nasopharyngeal colonization. It seems that the *spxB* mutant strain is unable to thrive in this environment, unlike the wild-type strain (Regev-Yochay et al., 2007). In this sense, the *spxB* mutant exhibited impaired virulence in animal models for sepsis, pneumonia, and nasopharyngeal colonization, indicating that SpxB is a crucial factor in determining the virulence of *S. pneumoniae* (Spellerberg et al., 1996).

It has been suggested that the activity of pyruvate oxidase plays a crucial role in the response of *S. pneumoniae* to fluctuations in oxygen levels, regardless of exposure to external H_2O_2 (Carvalho et al., 2013). This specific activity is believed to regulate capsule production, which is controlled by the bacterium to adapt to its environment. The absence of SpxB results in various metabolic changes, including an upregulation of the *cps* operon, leading to excessive production of the capsule. These findings were confirmed in a mutant strain lacking *spxB* that exhibited lower levels of acetyl-CoA, an intermediary metabolite involved in capsule biosynthesis. This effect was observed only in certain serotypes that produce acetylated sugars. It was proposed that the reduced availability of acetyl-CoA is responsible for the decreased capsule production (Echlin et al., 2016).

It has been reported that *S. pneumoniae* has the capability to modulate the flow of pyruvate metabolism based on the specific type of carbohydrate present in its environment. In the presence of galactose, there is a shift in pyruvate metabolism toward the production of acetyl-CoA. Notably, the majority of acetyl-CoA produced by the enzymes SpxB and the pyruvate dehydrogenase complex is primarily utilized for the biosynthesis of the bacterial capsule. Conversely, the acetyl-CoA produced by pyruvate formate lyase serves the purpose of regenerating NAD+ (Echlin et al., 2020). These variations in capsule production have been found to have significant implications in assays *in vivo*, as they play a critical role in the pathogenesis of pneumococcal infections (Kim and Weiser, 1998).

1 https://www.cdc.gov/pneumococcal/global.html

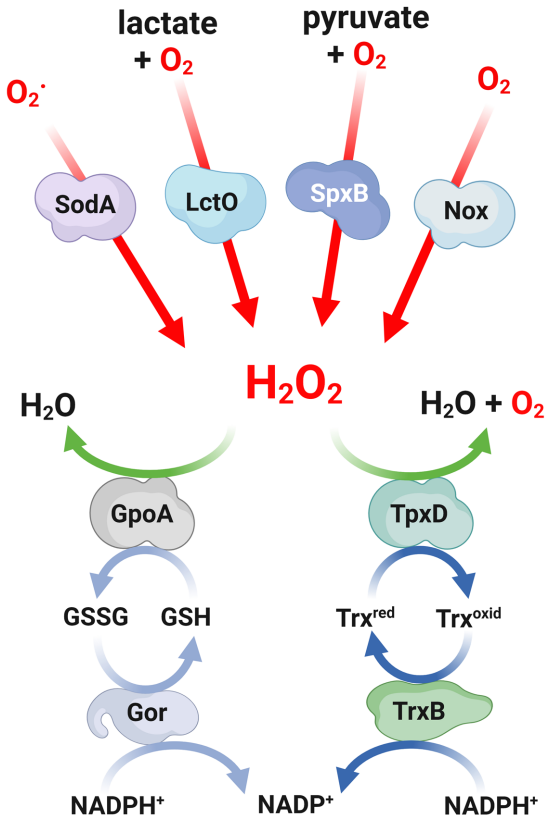

FIGURE 1
Mechanisms involved in both production and defense against H_2O_2 in *Streptococcus pneumoniae*. Scheme of the mechanisms involved in both the production and defense against H_2O_2 in *S. pneumoniae*. Red lines indicate the enzymatic reactions involved in the production of H_2O_2, while green lines represent the pathways for detoxifying H_2O_2. The light blue and blue lines show the redox reactions that involve glutathione and peroxiredoxins, respectively. H_2O_2, hydrogen peroxide; O_2, superoxides; SodA, superoxide dismutase; LctO, lactate oxidase; SpxB, pyruvate oxidase; Nox, NADH oxidase; GpoA, glutathione peroxidase; Gor, glutathione reductase; TpxD, thiol peroxidase; TrxB, thioredoxin reductase.

Detoxifying mechanisms of reactive oxygen species

Reactive oxygen species (ROS) are chemical entities that arise from oxygen metabolism, including peroxides and superoxides, which have a role in different cellular processes, such as cell signaling and homeostasis, and produce cellular damage. The generation of H_2O_2 is a crucial virulence determinant for *S. pneumoniae*. The production and discharge of high levels of H_2O_2 are capable of eliminating other bacterial pathogens and causing damage to human tissues during infection. Nevertheless, apart from the endogenous H_2O_2 production that serves as a metabolic weapon, the pneumococcal cells necessitate a potent stress response to endure oxidative conditions. Several oxidative gene mutants that have been examined thus far have demonstrated susceptibility to exogenous H_2O_2, implying their involvement in the OSR mechanism of *S. pneumoniae*. The first enzyme involved in H_2O_2 tolerance was SpxB, which is responsible for endogenous H_2O_2 generation. Clearly, SpxB has no a role as a detoxification mechanism, however, it is probable that SpxB-mediated H_2O_2 production facilitates the induction of OSR in *S. pneumoniae*.

The oxygen metabolism generates ROS, and these harmful compounds require the presence of catalases and peroxidases, as well as superoxide dismutases and reductases, for the detoxification of bacterial ROS (Mishra and Imlay, 2012). NADPH peroxidase and catalases are the most common H_2O_2 detoxifying enzymes in bacteria. However, the corresponding encoding genes have not been found in the genomes of streptococci, enterococci, and leuconostoc (Mishra and Imlay, 2012). Instead, *S. pneumoniae* expresses many other H_2O_2 scavengers, as reported in other bacterial genera, although the underlying reason for this enzymatic diversity remains unknown.

As described for peroxides, the control of superoxide levels is also relevant for bacterial survival and it is considered one of the major defense mechanisms against oxidative stress (McCord and Fridovich, 1968). In prokaryotes, superoxides are converted to peroxides by the action of superoxide dismutases. Metals can be used as cofactors for various enzymes that react with superoxides to produce H_2O_2, a less reactive compound that should be metabolized by other enzymes. To date, six types of bacterial superoxide dismutases have been characterized. This classification depends on the metal cofactor, such as SodA (MnSOD), SodB (FeSOD), SodC (CuSOD) (McCord and Fridovich, 1968), CuSOD (Steinman, 1985), Cu/Zn-SOD (Langford et al., 1996; Desideri and Falconi, 2003) and NiSOD (Wuerges et al., 2004).

In *S. pneumoniae*, two superoxide dismutases, namely SodA and SodB, have been identified. However, it has been observed that only SodA is involved in the response to oxidative stress (Yesilkaya et al., 2000). The expression of SodA was found to be upregulated in aerobic cultures, and a mutant lacking this enzyme exhibited reduced growth and increased susceptibility to paraquat, a compound that generates superoxide upon reacting with oxygen. These findings suggest that the primary function of SodA is to scavenge superoxide radicals (Figure 1). Furthermore, in a mouse model of intranasal infection, the *sodA* mutant displayed a slower multiplication rate in the lungs within the first 24 h and a delayed appearance in the bloodstream, indicating the contribution of SodA to the virulence of pneumococcal infections (Yesilkaya et al., 2000). The *sodA* gene exhibited a significant increase in expression levels, exceeding 10-fold, in the lung and brain tissues compared to the blood, suggesting its significance in the context of infection (Oggioni et al., 2006). Through the utilization of microarrays and virulence assays, genes that were expressed during mouse infection were identified, and it was proposed that SodA plays a crucial role in the colonization process of *S. pneumoniae* (Mahdi et al., 2015).

In addition to SodA, which serves as the primary defense against superoxide anions, *S. pneumoniae* also utilizes other enzymatic systems to combat ROS, such as the thioredoxin and glutathione systems. Within the thioredoxin family, the thiol peroxidase (or peroxiredoxin) TpxD plays a significant role in regulating H_2O_2 levels by facilitating its reduction (Figure 1). It has been observed that the expression of the *tpxD* gene is upregulated in the presence of exogenous H_2O_2. Consistently, the absence of the *tpxD* gene has been found to negatively impact the survival and growth of *S. pneumoniae* under these conditions (Hajaj et al., 2012, 2017). The regulatory network that controls the expression of the *tpxD* gene will be commented in the "Gene Regulation mechanisms" section.

In the presence of oxidative conditions, one of the most prevalent biochemical reactions that occurs within cells is the reversible oxidation of cysteine thiols. This particular reaction can serve as a

signal transduction pathway for cells (Lo Conte and Carroll, 2013), making it the most significant posttranslational modification that arises from exposure to H_2O_2. The sulfenylation (or S-hydroxylation) of thiols by H_2O_2 is particularly relevant due to the oxidative burst induced by neutrophils. It has been demonstrated the essential role of TpxD and glutathione in protecting against proteome sulfenylation. As a consequence of exposure to H_2O_2, more than 50 proteins in the pneumococcus become sulfenylated (Lisher et al., 2017).

In general, the efficient removal of peroxides by peroxiredoxins is facilitated by appropriate reductants. For this purpose, the most commonly utilized system is the thioredoxin (Trx) system, which consists of a Trx, a Trx reductase, and NADPH as the electron source (de Oliveira et al., 2021; Figure 1). In *S. pneumoniae*, it has been demonstrated that the recombinant TpxD thioredoxin is functional using a Trx system derived from *Escherichia coli* (Hajaj et al., 2012). The pneumococcal genome encodes multiple thioredoxins and a Trx reductase similar to the one found in *Streptococcus mutans* (Marco et al., 2013). Although the pneumococcal TrxB enzyme has not been yet characterized, it is hypothesized that this enzyme likely plays a role in facilitating efficient catalysis by the thiol peroxidase TpxD.

The tripeptide glutathione, which is composed of γ-L-glutamyl-L-cysteinyl-glycine, is the most abundant non-protein thiol found in living organisms. It serves as a powerful intracellular antioxidant and is present in eukaryotes, proteobacteria, and a limited number of Gram-positive bacteria (Ku and Gan, 2019). In certain bacteria, the synthesis of glutathione is facilitated by enzymes such as γ-glutamylcysteine and glutathione synthetase. Glutathione is primarily utilized for various cellular processes, particularly in defense against ROS attacks. In this context, the reduced form of glutathione (GSH) is converted into a disulfide-bonded form (GSSG), and the balance between these two compounds is regulated by a GSH reductase named Gor, which employs NADPH as a reducing agent. The detoxification of ROS through glutathione can occur either through direct interaction with GSH or through the action of a GSH peroxidase that utilizes GSH to reduce H_2O_2 (Arenas et al., 2010; Figure 1).

S. pneumoniae, like other bacteria, lacks GSH biosynthetic enzymes. However, this pathogen does expresses GshT, an ABC transporter that allows the uptake of extracellular glutathione (Potter et al., 2012). The disruption of the *gshT* gene resulted in increased sensitivity to external H_2O_2, indicating its involvement in the oxidative stress response of *S. pneumoniae*. Furthermore, these genes have been found to play a role in pneumococcal pathogenesis, as mutants lacking these genes exhibited reduced virulence in a mouse model of infection (Potter et al., 2012).

An alternative strategy to counteract oxidative stress involves the direct reduction of oxygen levels within cells. Despite lacking heme proteins and cytochromes, *S. pneumoniae* utilizes NADH oxidase to detoxify oxygen. This enzyme catalyze its reduction of oxygen through NADH, resulting in the production of either H_2O or H_2O_2, depending on the cellular redox state (Higuchi, 1992; Figure 1). A soluble form of NADH oxidase (Nox) has been identified and characterized in *S. pneumoniae*. Disruption of the *nox* gene, which encodes for NAD oxidase, has been found to abolish NADH oxidase activity, impair virulence and affect competence development in *S. pneumoniae*, while not compromising bacterial growth in aerobic conditions (Auzat et al., 1999; Echenique and Trombe, 2001). Indeed, other authors showed that the *nox* mutant, while displaying normal growth under limited aeration conditions, is incapable of growing exponentially in highly aerated conditions. This highlights the importance of NADH oxidase activity in enabling *S. pneumoniae* to cope with oxidative stress (Yu et al., 2001).

In eukaryotic organisms, there are transmembrane NADPH oxidases that share similar biochemical properties with NADH oxidases, but have a higher affinity for NADPH instead of NADH (Rotrosen et al., 1992). In the case of *S. pneumoniae*, it was reported for the first time as a bacterial NADPH oxidase. A recombinant form of this oxidase, also named Nox (or Nox2, to distinguish from the NADH oxidase), exhibited several biochemical characteristics that resembled those of human NOX2, which is considered the standard model for NOX enzymes. These similarities were observed in terms of oxygen consumption and the production of superoxide (Hajjar et al., 2017). NOX enzymes are commonly related to multicellularity functions that are characteristic of eukaryotic cells, but the physiological role of this NADPH oxidase in bacteria, particularly in the oxidative stress response, remains to be elucidated.

Defense mechanism against antimicrobial oxidants

The heme peroxidases present in immune cells, particularly neutrophils, play a vital role in facilitating the reaction between H_2O_2 and pseudohalide (SCN^-) or halide ions (Br^- or Cl^-) in various bodily fluids, including plasma, the oral cavity, and the digestive and respiratory tracts in humans. This reaction takes place during the oxidative burst of leukocytes and generates potent oxidizing agents such as hypochlorous acid (HOCl) and hypothiocyanous acid (HOSCN), which possess both bacteriostatic and bactericidal properties. These highly reactive compounds effectively eradicate bacteria, thereby playing a critical role in the antibacterial function of the innate immune system (Day, 2019; Arnhold and Malle, 2022).

Among the heme peroxidases responsible for the synthesis of antimicrobial oxidants, it is worth noting that myeloperoxidase (MPO) stands out as the sole enzyme capable of producing hypochlorous acid (HOCl) when released into autophagosomes during neutrophil phagocytosis (Paumann-Page et al., 2017). On the other hand, lactoperoxidase (LPO) is predominantly found in tears, breast milk, and saliva of mammals, and is recognized as the primary source of hypothiocyanous acid (HOSCN) (Ashby et al., 2009; Arnhold and Malle, 2022; Figure 2). Consequently, the LPO/H_2O_2/SCN-system, which generates HOSCN, is important for controlling the oral microbiome through the production of oxidants (Barrett and Hawkins, 2012; Courtois, 2021). In addition to the synthesis of antioxidants within cells, both myeloperoxidase (MPO) and lactoperoxidase (LPO) can be released from dying leukocytes into the extracellular space during inflammation (Winterbourn et al., 2016; Ramirez et al., 2018). In the presence of SCN^-, these heme peroxidases may selectively produce HOSCN (Arnhold and Malle, 2022). Alternatively, eosinophil peroxidase (EPO) is directly released into extracellular environments due to its enzymatic function, which is involved in eliminating parasites that cannot be phagocytized. EPO reacts with halides, but it exhibits a preference for SCN-in order to synthesize HOSCN (Ramirez et al., 2018; Arnhold and Malle, 2022; Figure 2).

S. pneumoniae possesses the capacity to produce substantial quantities of H_2O_2 in order to eliminate other microorganisms found

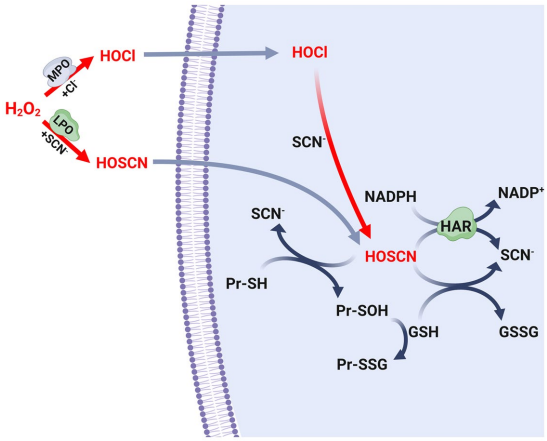

FIGURE 2
Biosynthesis and metabolism of antimicrobial oxidants. Scheme of the biosynthetic pathways of the hypochlorous acid (HOCl) and hypothiocyanous acid (HOSCN), as well as the defense mechanism of *S. pneumoniae* leaded by glutathione and the Har protein. SCN-, thiocyanate; MPO, myeloperoxidase; LPO, lactoperoxidase; GSH, reduced glutathione; GSSG, oxidized glutathione; Pr-SH, reduced protein thiols; Pr-SOH, sulfenic acid-modified proteins; Pr-SSG, glutathionylated proteins. GSSG formed in this scheme is reduced to GSH by glutathione reductase (Gor) using NADPH, as described in Figure 1.

in the respiratory tract. However, the presence of SCN-plays a significant role in reducing the levels of H_2O_2 generated by both host and bacterial cells. Specifically, the enzymes LPO and MPO, which are present in the respiratory mucosa, convert SCN-to HOSCN (Figure 2). In an environment rich in chloride, *S. pneumoniae* has been observed to be susceptible to HOCl produced by MPO. Nevertheless, the pneumococcus develops resistance due to the presence of SCN^-, which facilitates the conversion of HOCl to HOSCN (Figure 2; Shearer et al., 2022a). *In vitro* assays showed that the LPO/H_2O_2/SCN-system generated a lethal concentration of HOSCN for the pneumococcal strains TIGR4 (serotype 4) and EF3030 (serotype 19F) (Gingerich et al., 2020). In contrast, strains D39 (serotype 2) and SP264 (serotype 23) survived in cultures with a 20-fold higher concentration of HOSCN compared to those obtained with the LPO/H_2O_2/SCN-system. This discrepancy in survival can be attributed to the incubation time and the pneumococcal strains used. It is noteworthy that the pneumococcus exhibits inherent resistance to a concentration of HOSCN that is effective in eliminating other bacterial species, thereby giving it a clear advantage in evading host tissue defenses (Shearer et al., 2022a).

In *S. pneumoniae*, a strategy to reduce the levels of HOSCN involves the oxidation of GSH. HOSCN can directly oxidize the reduced thiol groups of proteins (Pr-SH) within the cell, forming sulfenic acids, while GSH is converted to GSSG. Accordingly, the sulfenic acid-modified proteins (Pr-SOH) can subsequently react with GSH to produce glutathionylated proteins (Pr-SSG) (Figure 2). In bacteria, it is important to note that both S-sulfenylation and S-glutathionylation are reversible post-translational modifications. However, the specific redoxins responsible for catalyzing these reverse reactions have yet to be identified and characterized in *S. pneumoniae*.

The role of the GSH transporter GshT and the GSH reductase Gor in the resistance mechanism of *S. pneumoniae* against HOSCN has also been investigated. Mutants lacking the *gshT* and *gor* genes have been found to exhibit increased sensitivity to exogenous HOSCN generated by the LPO/H_2O_2/SCN-system, indicating the crucial role of GSH in the HOSCN resistance mechanism of *S. pneumoniae* (Shearer et al., 2022c).

Furthermore, the identification and characterization of a flavoprotein disulfide reductase named Har (*h*ypothiocyanous *a*cid *r*eductase), which exhibits HOSCN reductase activity, has contributed significantly to the understanding of this mechanism. *In vitro* assays have shown that this enzyme utilizes NAD(P)H to reduce HOSCN to SCN-through a reaction similar to that described for thioredoxin reductases (Shearer et al., 2022b; Figure 2). The *har* mutant, when exposed to the LPO/H_2O_2/SCN-system, has shown that the HOSCN reductase is essential for pneumococcal viability in the presence of HOSCN. Nevertheless, the enzymatic activity of Har is complemented by the action of GSH as described earlier. The *har gshT* and *har gor* double mutants exhibited higher growth inhibition compared to the *har* single mutant (Shearer et al., 2022b).

Manganese transport systems

Prokaryotic cells lack internal compartments and regulate metal cation flux across the cytoplasmic membrane to maintain metal homeostasis (Jakubovics and Jenkinson, 2001). Mn^{2+} is an essential cation for bacterial physiology and plays a central role in various cellular processes, including amino acid metabolism, glycolysis, nucleic acid degradation, protein cleavage, transformation, germination, and sporulation. Its primary function, however, lies in the oxidative stress response, where it assists in the detoxification of ROS as a critical cofactor for SodA (or MnSOD). This defense mechanism is likely to be widespread among bacteria and may also contribute to their virulence (Jakubovics and Jenkinson, 2001).

In *S. pneumoniae*, the uptake of Mn^{2+} is controlled by an ATP-binding cassette (ABC) cation permease consisting of three proteins: pneumococcal surface antigen A (PsaA), which acts as the Mn^{2+}-specific solute binding component, and PsaB and PsaC. These proteins are encoded by the *psaBCAD* operon, with *psaD* (or *tpxD*) encoding for the TpxD thiol peroxidase. It is worth noting that the enzymatic activity of TpxD is not influenced by the concentration of Mn^{2+}. The *psaD/tpxD* gene is transcribed separately from the other genes in the operon (Novak et al., 1998).

When the *psa* genes are inactivated, *S. pneumoniae* becomes completely dependent on externally added Mn^{2+} for normal growth (Dintilhac et al., 1997) and shows increased sensitivity to exogenous H_2O_2 (Tseng et al., 2002; McAllister et al., 2004). Additionally, the mutants lacking *psaA* and *psaD/tpxD* exhibited elevated expression of SodA and Nox, suggesting that PsaA and PsaD/TpxD may have important roles in regulating redox homeostasis in *S. pneumoniae* (Tseng et al., 2002). The regulation of the manganese transport genes will be discussed in the "Gene Regulation Mechanisms" section.

Furthermore, it has been documented that a deficiency in Mn^{2+} leads to a reduction in the transcription of *sodA*, suggesting that the expression of this gene is controlled through an unidentified pathway that responds to Mn^{2+} levels (Eijkelkamp et al., 2014). The *psaA* mutant showed a loss of virulence in otitis media, respiratory tract, sepsis and nasopharyngeal colonization in animal models, underscoring the importance of a functional Mn^{2+} transporter in the

pathogenicity of the organism (Berry and Paton, 1996; Marra et al., 2002; McAllister et al., 2004).

In contrast to the Mn^{+2} uptake system, *S. pneumoniae* also has an Mn^{+2} exporter, named MntE, which is utilized by this pathogen to control possible high toxic levels of Mn^{2+} in the bacterial cytoplasm. The *mntE* mutant displayed heightened susceptibility to Mn^{2+} stress due to Mn^{2+} accumulation within the cell. Interestingly, this mutant strain also demonstrated increased resistance to oxidative stress, which was hypothesized to be a result of enhanced activity of Mn^{2+}-dependent superoxide dismutase. The significance of the Mn^{2+} exporter in pneumococcal pathogenesis was determined through the observation of reduced virulence in the *mntE* mutant strain in a murine model of infection (Rosch et al., 2009). To prevent Mn^{2+} toxicity in the presence of elevated cytoplasmic Mn^{2+} levels, *S. pneumoniae* expresses another Mn^{2+} exporter known as MgtA, which belongs to the PII-type ATPase family of proteins. The expression of the *mgtA* gene is upregulated in response to Mn^{2+} stress, and this regulation is dependent on a Mn^{2+}-sensing riboswitch belonging to the *yybP-ykoY* family (Martin et al., 2019).

Mn^{2+} is a vital trace element that is present in very low concentrations in the human body. In the context of bacterial pathogenesis, Mn^{2+} is found to be 1,000 times more concentrated in secretions compared to internal body sites. This significant difference in concentration may serve as a signal for bacterial cells to detect the transition from the mucosal surface to deeper tissues. It primarily circulates in the bloodstream bound to transferrin, with a smaller portion bound to albumin (Scheuhammer and Cherian, 1985).

Due to its importance in metabolism, the sequestration of Mn^{2+} has been found to impede bacterial growth. This process is a part of the host's immune response to pathogens and is facilitated by the S100A8/S100A9 heterodimer calprotectin (CP), which has the ability to bind to Mn^{2+} and Zn^{2+} ions (Damo et al., 2013). In addition to its chemotactic and proinflammatory properties, CP exhibits antimicrobial characteristics. CP is prominently expressed by neutrophils, monocytes, and epithelial cells, and it is released into the sites of inflammation caused by bacterial infections (Striz and Trebichavsky, 2004). Notably, a significant release of CP has been observed during the course of pneumococcal infections (Raquil et al., 2008). In an infection model involving mice lacking S100A9, it was observed that pneumococcal pneumonia worsened (Ostermann et al., 2023). The sequestration of Mn^{2+} by CP plays a crucial role in the defense against infection and is a vital component of the innate immune response to bacterial pathogens.

Zn^{2+} is another essential element for bacterial metabolism, and pathogens rely on acquiring this metal from host tissues in order to thrive, establish colonization, and cause disease. Similar to the mechanism observed for Mn^{+2}, the mammalian host employs a strategy of sequestering these cations to impede bacterial growth. This is achieved through the action of proteins belonging to the S100 family, such as CP and calgranulin, which are part of an innate immune response that withholds metals from invading bacteria (Hood and Skaar, 2012). On the contrary, mammalian hosts employ another antimicrobial tactic called metal intoxication, wherein high levels of Zn^{2+} are released into phagosomes to impair internalized bacteria (Sheldon and Skaar, 2019).

Regarding the metal homeostasis in *S. pneumoniae*, there exists an interplay between the metabolisms of Mn^{2+} and Zn^{2+}. Elevated levels of Zn^{2+} have been found to inhibit growth, increase susceptibility to oxidative stress, and diminish virulence (Jacobsen et al., 2011; McDevitt et al., 2011; Eijkelkamp et al., 2014). The proposed mechanism involves the displacement of Mn^{2+} by Zn^{2+} in the PsaA protein, thereby hindering the uptake of Mn^{2+} and resulting in a deficiency of this cation within the cytoplasm (Jacobsen et al., 2011; Counago et al., 2014). Nevertheless, throughout the course of pneumococcal infection, both CP (Rosen et al., 2022) and calgranulin (Rosen and Nolan, 2022) have the ability to sequester Zn^{2+} from PsaA, facilitating the binding of Mn^{2+} to this protein and subsequent uptake of Mn^{2+}. Interestingly, these proteins, which are employed by host cells as antimicrobial agents, paradoxically promote bacterial pathogenesis in this particular context.

Iron metabolism

Iron is another key metal involved in bacterial oxidative stress. It is found in human tissues at low levels and is primarily transported in plasma by transferrin. Within immune cells, the reaction between Fe^{2+} and H_2O_2 leads to the formation of ROS through the Fenton reaction. These compounds cause DNA damage and exhibits high toxicity, ultimately resulting in the death of bacterial cells (Haschka et al., 2021).

In *S. pneumoniae*, it has been reported that three ABC transporters, namely PiuBCDA, PiaABCD, and PitADBC, play a role in regulating the intracellular iron levels (Brown et al., 2001a,b, 2002). On the other hand, the endogenous production of H_2O_2 facilitates the Fenton reaction (Pericone et al., 2003).

In the context of H_2O_2 production by the wild-type strain under aerobic conditions, a microarray analysis of *S. pneumoniae* revealed the upregulation of the *piuB/piuD* and *spxB* genes, results that were compared to the wild-type strain cultured under anaerobic conditions. This resulted in an elevation of Fe^{2+} and pyruvate oxidase levels in aerobic cultures, which subsequently stimulated the synthesis of endogenous H_2O_2. In consequence, the control of intracellular Fe^{2+} levels are essential for the OSR (Lisher et al., 2017). The regulation of the iron transport genes will be discussed in the "Gene Regulation Mechanisms" section.

Lipoproteins commonly serve as substrate-binding proteins for ABC transporters of many substrates, including sugars, cations, minerals, oligopeptides, amino acids, and polyamines, which are implicated in bacterial virulence. In *S. pneumoniae*, Lgt is indirectly involved in the uptake of metals, such as Fe^{2+}, Mn^{2+}, Zn^{2+} Ni^{2+}, and Cu^{2+}. The *lgt* mutant showed impaired ABC transport functions. For example, the use of paraquat revealed that this mutant is more susceptible to oxidative stress, and this phenotype is due to a decrease in cations such as Fe^{2+} and Mn^{2+}. These cations contribute to the production of ROS and the OSR, respectively, as mentioned. This mutant also exhibited a significant impairment in nasopharyngeal colonization, sepsis, and pneumonia in mouse infection models, confirming the association between OSR and pathogenesis (Chimalapati et al., 2012).

In relation to iron metabolism, Dpr is a nonheme iron-containing ferritin that confers resistance to H_2O_2. It functions as a chelating protein that diminishes the free iron levels within the cell, thereby protecting pneumococcal cells from ROS generation by inhibiting the Fenton reaction. In a mouse model, the *dpr* mutant exhibited impaired virulence, specifically a deficiency in colonization (Hua et al., 2014).

Among the metal chelating systems cited to prevent intracellular ROS production, *S. pneumoniae* also possesses a flavin reductase,

named FlaR, originally reported as PsipB (pneumococcal surface immunogenic protein B) (Ling et al., 2004). This enzyme not only has NADP reductase activity but also binds Fe^{2+} to protect the pneumococcus from oxidative stress through the reduction of free iron concentrations within the cytoplasm. Due to its surface localization, FlaR also has the capacity to act as a pneumococcal adhesin (Morozov et al., 2018).

Repair systems

Bacteria not only require mechanisms to detoxify H_2O_2, but also repair systems to fix damaged molecules that are crucial for their survival under such stressful conditions. In the case of *S. pneumoniae*, a chaperone/protease known as HtrA (*h*igh-*t*emperature *r*equirement *A*) has been extensively studied. Initially identified as a heat shock protein, HtrA plays a vital role in the pathogenesis of *S. pneumoniae* (Gasc et al., 1998; Sebert et al., 2002). Through a signature-tagged mutagenesis screen, HtrA was identified as a virulence factor for *S. pneumoniae* (Hava and Camilli, 2002). This finding was further supported by studying an *htrA* mutant, which showed reduced virulence in a mouse model. However, in bacterial culture, this mutant exhibited slower growth at 42°C and increased sensitivity to oxidative stress, highlighting the importance of this chaperone in the OSR (Ibrahim et al., 2004).

In response to stressful conditions, certain bacteria employ a proteasome-like system that employs the ClpP protease to ensure their survival (Kahne and Darwin, 2021). This protease is coupled with hexameric ATPases, which facilitate ATP hydrolysis during the proteolysis process (Mahmoud and Chien, 2018). In *S. pneumoniae*, ClpP has been identified as a heat-shock protein that is crucial for survival during thermal and oxidative stress, as well as playing a significant role in virulence. Nevertheless, further studies are needed to understand the putative relationship between the ClpP function and OSR (Robertson et al., 2002). Analyzing a cellular infection model, it was observed that the *clpP* mutant exhibited heightened sensitivity to oxidative stress in macrophages (Park et al., 2010). In Gram-positive bacteria, ClpL is an ATPase that works in conjunction with ClpP to degrade proteins (Choi et al., 1999). The pneumococcal ClpL is a unique member of the Hsp100 family that is dependent on Mn^{2+} and exhibits chaperone activity without requiring co-chaperones (Park et al., 2015). Similar to ClpP, ClpL has also been classified as a heat-shock protein (Choi et al., 1999; Kwon et al., 2003).

In our lab we found that the *clpL* and *psaB* genes, which encodes for the ClpL chaperone and the subunit B of the Mn^{2+} transporter, PsaB, respectively, are regulated by SirR (Reinoso-Vizcaino et al., 2020), and this will be commented in the "Gene Regulation Mechanisms" section. The *clpL* mutant showed greater susceptibility to external exposure to H_2O_2, which is a similar finding to that observed in the *psaB* mutant (McCluskey et al., 2004). It is known that the presence of Mn^{2+} enhances the hydrolase and chaperone activities of ClpL, and this feature has not been reported for other proteins in the HSP100 family (Park et al., 2015). We propose that the deficiency in Mn^{2+} uptake observed in the *psaB* mutants is responsible for altering the enzymatic activity of SodA and ClpL. These enzymes are dependent on intracellular Mn^{2+} levels and are essential for the pneumococcal OSR (Reinoso-Vizcaino et al., 2020).

One potential consequence of exposure to ROS is the oxidation of methionine residues to methionine sulfoxide, which must be repaired in order for bacterial survival to occur (Saleh et al., 2013). Thioredoxins, in addition to their role in scavenging H_2O_2, are widely distributed oxidoreductases that contribute to repair systems by providing reducing equivalents to methionine sulfoxide reductases (Msr). These enzymes reduce oxidized methionines (Ezraty et al., 2005) or directly repair oxidized methionines (Collet and Messens, 2010). In *S. pneumoniae*, the TrxA and MsrAB1 thioredoxins have been identified, but a linking with OSR has not yet been determined (Kim et al., 2009). TlpA, also known as Etrx1, is an enzyme belonging to the thiol-specific antioxidant (TlpA/TSA) family (Marchler-Bauer et al., 2017) that has thioredoxin properties. The *tlpA* mutant exhibited increased susceptibility to external H_2O_2, which correlates with the observed thioredoxin activity displayed by the recombinant TlpA protein. In terms of pneumococcal pathogenesis, the *tlpA* mutation had more detrimental effects on later stages of infection compared to the initial stages in a mouse model (Andisi et al., 2012). The operon containing the *tlpA* (or *etxR1*) gene exhibited increased transcriptional activity in response to oxidative stress. This operon also facilitates the expression of genes encoding the cytochrome C-type biogenesis protein, CcdA1, and the methionine sulfoxide reductase, MsrAB2. These proteins, collectively referred to as CTM (an abbreviation for CcdA, TlpA, and MsrAB), play a vital role in the cellular response to oxidative stress. The MsrAB2 enzyme is particularly important in protecting against oxidative stress by converting methionine sulfoxide residues back to methionine. This conversion process is facilitated by the presence of thioredoxins. In a different region of the pneumococcal genome, a group of genes was identified that includes paralogues of CcdA1 and Etrx1, named CcdA2 and Etrx2. The authors of the study demonstrated that both Etrx1 and Etrx2 thioredoxins, which are exposed on the cell surface, along with their corresponding redox partners, CcdA1, CcdA2, and MsrAB2, are important for defending against exposure to ROS outside the cell and for the development of *S. pneumoniae* infections (Gennaris and Collet, 2013; Saleh et al., 2013; Ribes et al., 2016).

Polyamine metabolism

Among all the diverse factors that impact the OSR, bacterial metabolism is probably one of the most unexplored aspects. Polyamines, for example, are essential for regulating many cellular processes in bacteria. During its biosynthetic process, the enzyme lysine decarboxylase CadA contributes to the conversion of lysine to cadaverine (Nakamya et al., 2018). In *S. pneumoniae*, a metabolomics analysis of the *cadA* mutant revealed that altered polyamine levels indirectly led to reduced expression of the trehalose phosphotransferase system (Ayoola et al., 2019). Trehalose is a disaccharide that has been shown to scavenge free radicals and provide protection against oxidative stress in yeast (Jiang et al., 2019) as well as in pathogenic mycobacteria (Kalscheuer and Koliwer-Brandl, 2014). Based on these findings, it is hypothesized that CadA-mediated trehalose metabolism is crucial for the oxidative stress response (Ayoola et al., 2019) and for virulence in *S. pneumoniae* (Shah et al., 2011).

PotABCD is a transporter responsible for the uptake of putrescine and spermidine implicated in polyamine metabolism. The *potABCD* mutant exhibits heightened vulnerability to oxidative stress, akin to the *cadA* mutant, due to a notable decline in polyamine and trehalose

levels, which serve as antioxidants. Metabolomics analysis further elucidated that the *potABCD* mutant displays diminished glutathione levels, providing additional evidence to support its observed phenotype (Nakamya et al., 2021).

In the pathway of polyamine synthesis, the enzyme SpeA, which is an arginine decarboxylase, contributes in the production of agmatine (Ayoola et al., 2020). Similar to the observed effects of deletions in *cadA* and *potABCD*, the null mutant of *speA* has been found to increase susceptibility to oxidative stress. Transcriptomic and proteomic analysis determined that this mutation negatively affects the expression of various genes known to be essential for OSR, including *tpxD* and *htrA*. Additionally, the authors propose that SpeA not only regulates the synthesis of glutathione but also influences the endogenous production of H_2O_2 (Nakamya et al., 2021). The *speA* mutation also leads to an increase in carbon flow through the pentose phosphate pathway (PPP), which is considered a cellular response to oxidative stress. This metabolic route helps maintain the balance of NADH/NADPH redox and generates ribose-5-phosphate, thereby enhancing nucleotide synthesis and preventing DNA damage caused by ROS (Stincone et al., 2015). These findings highlight the significance of maintaining polyamine homeostasis in the physiology of bacterial pathogens. Furthermore, it is central to understand the relationship between specific metabolic pathways and the OSR in *S. pneumoniae*.

Gene regulation mechanisms

The pneumococcal OSR is mediated by a diverse array of proteins, suggesting that their expression is controlled by various regulatory systems to ensure the survival of this pathogen (Figure 3). Bacterial gene expression is tightly regulated by proteins that detect changes in the environment and initiate a physiological response. The pneumococcal genome displayed the presence of numerous individual regulators, as well as two-component systems (TCS), which are a common mechanism for signal transduction in bacteria (Gomez-Mejia et al., 2018). In *S. pneumoniae*, there have been 13 reported TCS, each consisting of a response regulator and its corresponding histidine kinase. The only exception is RitR, which is an orphan response regulator (Paterson et al., 2006; Gomez-Mejia et al., 2018). Notably, seven of these regulatory systems are involved in regulating oxidative stress adaptation, in addition to individual regulators. This highlights the importance of gene regulation in this adaptive mechanism of *S. pneumoniae* (Figure 3).

In the presence of a high level of Fe^{2+}, the transcription of the *piuBCDA* genes is repressed by RitR (*r*epressor of *i*ron *t*ransport) (Ulijasz et al., 2004; Ong et al., 2013). This particular orphan regulator undergoes phosphorylation by the serine–threonine kinase StkP (Figure 3). Additionally, it interacts with PhpP, which acts as a dephosphorylating agent for StkP and this interaction indirectly affects the activation state of RitR (Echenique et al., 2004; Ulijasz et al., 2009). It has been demonstrated that RitR phosphorylation promotes the expression of the *piu* genes (Ulijasz et al., 2009). Notably, a *ritR* mutant exhibited increased susceptibility to H_2O_2, which was found to be correlated with a higher intracellular concentration of free iron. This observation was attributed to the derepression of the *piu* operon, which may be responsible for the heightened toxicity resulting from ROS hyperproduction through the Fenton reaction (Ulijasz et al., 2004).

RitR has been found to have an additional regulatory role in sensing high levels of H_2O_2 through a single cysteine. When ROS levels are low, RitR in its reduced monomeric form weakly binds to the *piuBCDA* promoter, thereby facilitating the expression of this operon. However, under high ROS levels, the Cys^{128} residue of RitR undergoes oxidation, leading to the dimerization of RitR and its subsequent binding to the *piuBCDA* promoter. This results in the repression of transcription of the *piu* operon, thereby preventing iron transport and protecting pneumococci from the toxic effects of the Fenton reaction (Glanville et al., 2018). Contrary to the repressor effect showed on the expression of *piuBCDA*, RitR activates the transcription of *dpr*. In both cases, this regulator is essential to decrease the levels of free iron (Ulijasz et al., 2004; Figure 3).

In the realm of individual regulators, a transcriptional repressor belonging to the Rrf2 family has been identified and studied in *S. pneumoniae*. Even in the presence of endogenous H_2O_2, this repressor, known as SifR (streptococcal IscT-like family transcriptional repressor), is capable of detecting quinones. This ability enables *S. pneumoniae* to effectively utilize Fe^{2+}/catecholamine complexes derived from the host, which are acquired through the iron transporter PiuBCDA. Under low Fe^{2+} levels, SifR interacts with free catechol-derived quinones and disengages from the DNA promoter region, resulting in the activation of the SifR regulon. This regulon includes *piuBCDA*, among other genes, thereby facilitating an increase in iron uptake. These findings demonstrate that SifR is part of a complex regulatory system that controls the OSR in *S. pneumoniae* (Zhang et al., 2022; Figure 3).

CodY is a regulatory protein that controls many cellular processes and metabolic pathways. Its ability to bind to DNA is influenced by changes in the levels of branched-chain amino acids (Brinsmade et al., 2010). It was also reported that CodY, a regulator previously associated with nutritional gene regulation in *S. pneumoniae* (Kloosterman et al., 2006; Hendriksen et al., 2008), is capable of activating the expression of *tpxD*, which encodes the TpxD thiol peroxidase. In response to H_2O_2, CodY is activated through the oxidation of two cysteines that trigger a conformational change in this regulator, enhancing DNA binding and activating the expression of *tpxD* (Hajaj et al., 2017). In addition, CodY activates the expression of the *dpr* gene, which encodes a protein involved in iron storage and peroxide resistance, while repressing the *fat (or piu)* genes, which encode proteins responsible for iron transport (Hendriksen et al., 2008; Figure 3).

The *codY* gene has been found to be essential for the survival of *S. pneumoniae*. The *codY* mutant was only obtained by suppressing mutations that inactivated the genes encoding FatC (or PiuC) and AmiC. These genes are involved in iron and oligopeptide transport, respectively, and their expression is repressed by CodY (Caymaris et al., 2010; Johnston et al., 2015). It has been proposed that the unviability of the *codY* mutant may be attributed to iron toxicity. This is because the *codY* mutation leads to the derepression of *fat (or piu)* genes and the inhibition of *dpr* expression, resulting in increased iron levels and subsequent oxidative stress through the Fenton reaction (Hendriksen et al., 2008; Caymaris et al., 2010; Figure 3).

In *S. pneumoniae*, the NmlR regulator was reported to activate the expression of the *adhC* gene, which encodes the alcohol dehydrogenase AdhC, when bacteria were exposed to formaldehyde and methylglyoxal. The *nmlR* mutant displayed resistance to high levels of oxygen in cultures, a phenotype that was attributed to lower

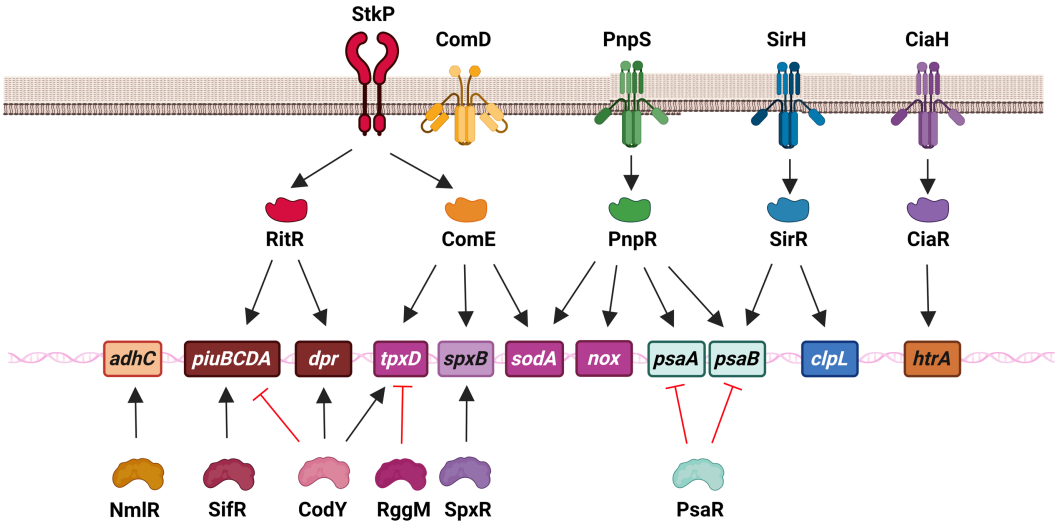

FIGURE 3
Regulatory systems that control genes involved in the oxidative stress response of *S. pneumoniae* in both extracellular and intracellular survival. This network is constituted by the serine–threonine protein kinase StkP, three two-component systems, including SirRH (TCS01), PnpSR (TCS04), and CiaRH (TCS05), as well as individual regulators, such as ComE (without its cognate kinase ComD) and RitR that belong to the family of response regulators, and NmlR, SifR, CodY, RggM, and SpxR. In the scheme, these regulatory systems control different genes that encode enzymes that contribute to iron transport (*piuBCDA* and *dpr*), manganese transport (*psaAB*), ROS detoxification (*sodA* and *tpxD*), H_2O_2 production (*spxB*), alcohol dehydrogenase (*adhC*) and repair mechanisms (*clpL* and *htrA*).

production of H_2O_2, although the mechanism remained unclear (Potter et al., 2010; Figure 3).

In relation to the detrimental effects of antimicrobial oxidants, the amino acids cysteine and methionine are most commonly oxidized by HOCl in proteins, resulting in protein unfolding and bacterial death (Ulfig and Leichert, 2021). A comprehensive analysis of the bacterial cells treated with sublethal concentrations of HOCl was conducted using RNA-seq transcriptome analysis. This analysis demonstrated that the oxidant significantly stimulated the expression of various regulons associated with diverse functions, including OSR (NmlR, SifR, CTM operon), proteostasis (CtsR, HrcA), and metal stress response (SczA, CopY), among others. Conversely, other regulons linked to OSR, such as CiaR, RitR, and CodY were found to be downregulated (Fritsch et al., 2023), and their implications are discussed in this section. It is worth noting that the CTM operon encompasses the genes responsible for encoding CcdA, EtrxA1, and MsrAB2, while the CtsR operon governs the expression of the genes encoding ClpL and ClpP. The functions of all these proteins have been discussed in the "Repair Systems" section. These findings underscore the intricate nature of the response to HOCl and offer valuable insights into the cellular damage inflicted by this potent oxidant.

In light of the significant score achieved in the RNA-seq transcriptome analysis, the NlmR transcriptional regulator was selected for further investigation as a potential candidate for detecting the presence of HOCl. Subsequently, it has been experimentally proven that NmlR possesses the ability to sense HOCl by means of the oxidation of Cys^{52}. This oxidative reaction activates the transcription of the *nmlR-adhC* operon *in vivo*. It is evident that NmlR plays an important role in the OSR, enabling *S. pneumoniae* to survive during macrophage infections. Apparently, AdhC is a metabolic enzyme whose expression is controlled by NmlR under oxidative conditions. This enzyme provides resistance to HOCl and ROS stress, however, the specific role of AdhC in ROS detoxification has not yet been elucidated (Fritsch et al., 2023; Figure 3).

As previously stated, the SpxB pyruvate oxidase is a significant virulence factor that primarily synthesizes endogenous H_2O_2 and plays a crucial role in the OSR of the pneumococcus (Pericone et al., 2003). Through a screening of morphological mutants, it was discovered that point mutations in a specific gene led to reduced H_2O_2 production in *S. pneumoniae*, resulting in alterations in the pneumococcal capsule. This gene, subsequently named *spxR* (pyruvate oxidase regulator), encodes a regulator capable of activating the expression of *spxB* and, consequently, the endogenous production of H_2O_2 in response to the metabolic state (Ramos-Montanez et al., 2008; Figure 3).

RggM (or Rgg1952) is a transcriptional regulator that belongs to the Rgg family and controls the regulation of *tpxD* gene expression in *S. pneumoniae* (Bortoni et al., 2009). In the presence of oxygen, a mutant lacking the *rggM* gene did not exhibit susceptibility to H_2O_2, and the expression of *tpxD* was higher in the *rggM* mutant compared to wild-type cells. TpxD is an important enzyme involved in detoxification, and the overexpression of *tpxD* in the *rggM* mutant is responsible for its phenotype under oxidative conditions. This suggests that RggM negatively regulates the expression of *tpxD* (Bortoni et al., 2009; Figure 3).

In our laboratory, we have characterized a new signaling pathway consisting of the serine–threonine kinase StkP (Echenique et al., 2004) and the response regulator ComE, which belongs to ComDE (TCS12) (Claverys et al., 2006). This transcription factor is typically activated through phosphorylation at an Asp^{59} residue by its cognate histidine kinase ComD. ComD is the natural receptor of CSP (competence-specific peptide) and is activated when CSP accumulates in the extracellular space through a quorum sensing mechanism (Claverys et al., 2006). Under acidic conditions, ComE is activated through

phosphorylation of the Thr^{128} residue by a crosstalk event with StkP. This activation allows ComE to control the expression of over 100 genes, indicating that the StkP/ComE pathway induces global changes in response to stress. Through transcriptomic and qPCR assays, it was revealed that the StkP/ComE pathway activates the expression of the *spxB*, *tpxD*, and *sodA* genes. The non-phosphorylatable $comE^{T128A}$ mutant, as well as the *comE* and *stkP* mutants, exhibited an impaired oxidative stress response. It was proposed that this phenotype was due to reduced expression of the *tpxD*, *sodA*, and *spxB* genes (Pinas et al., 2018). Previous studies had reported that a mutant lacking the *stkP* gene displayed decreased *tpxD* expression, but the underlying mechanism was not elucidated (Echenique et al., 2004; Nováková et al., 2005; Sasková et al., 2007). In this sense, we propose that StkP/ComE represents an alternative pathway for activating *tpxD* expression (Pinas et al., 2018; Figure 3).

Regarding the regulation of OSR mediated by TCSs, the expression of the *htrA* gene that encodes for the chaperone HtrA is regulated by CiaRH (Sebert et al., 2002; Mascher et al., 2003; Halfmann et al., 2007). Indeed, the deletion of *ciaR* mutant lead to a reduced HtrA expression and, consequently, to an increased susceptibility to external H_2O_2 similar to that of the *htrA* mutant. However, when HtrA was overexpressed, this phenotype was restored (Ibrahim et al., 2004; Figure 3).

Through a systematic screening of mutants defective in TCS, and a subsequent comparative RNAseq analysis, we found that TCS01, also known as SirRH (stress-induced response), regulates the expression of *clpL* and *psaB*, as discussed in the "Repair Systems" section. These genes are responsible for encoding the ClpL chaperone and the PsaB Mn^{2+} transporter, respectively. The *sirR*, *clpL*, and *psaB* mutants exhibited the same phenotypes as the *comE* and *stkP* strains. This is due to the absence of ClpL chaperone function or a decrease in Mn^{2+} levels, which negatively affects both SodA and ClpL since their enzymatic activities rely on Mn^{+2} levels (Reinoso-Vizcaino et al., 2020; Figure 3).

In relation to the regulation of Mn^{2+} homeostasis, TCS04 has been identified as a key regulator that activate the transcription of the *psaBCA* operon. This was evidenced by microarray assays comparing the *rr04* mutant, which lack the response regulator of this TCS, with the wild-type strain. TCS04 showed to be related to OSR due to the diminished oxidative stress response observed in the *rr04* mutant (McCluskey et al., 2004). The same phenotype was displayed by mutants in the *tcs09* genes, which encode TCS09. The probable mechanism by which TCS09 is involved in resistance against oxidative stress is mediating the regulation of carbohydrate metabolism, cell wall integrity and amount of capsular polysaccharide (Hirschmann et al., 2021; Figure 3).

In *S. pneumoniae*, the metal-dependent regulator PsaR has been observed to inhibit the transcription of the *psaBCA* operon in the presence of excess Mn^{2+} ions (Lisher et al., 2013). Microarray assays conducted using a *psaR* mutant strain demonstrated the upregulation of the *psaBCA* operon (Hendriksen et al., 2009). Notably, the *psaR* mutant exhibited reduced virulence in pulmonary infections in a mouse model, suggesting that Mn^{2+} ions serve as a signal for the expression of virulence factors in different host environments (Johnston et al., 2006). This study highlights the involvement of several transcriptional regulators in the gene regulation of OSR. PsaR belongs to a group of regulators that indirectly influence OSR by regulating the uptake of Mn^{2+} ions through the *psaBCA* genes, which are also regulated by TCS04 (McCluskey et al., 2004). This regulatory network underscores the significance of maintaining Mn^{2+} homeostasis in the OSR of *S. pneumoniae* (Figure 3).

Intracellular survival mechanism

It has been reported that *S. pneumoniae* can be internalized into host cells through various mechanisms, including clathrin- (Radin et al., 2005) and caveolin-dependent endocytosis (Gradstedt et al., 2013; Asmat et al., 2014) and dynamin-independent endocytosis (Agarwal et al., 2010). The presence of *S. pneumoniae* within vesicles that are labeled with classical endocytic markers, such as early, late, and recycling markers, as well as lysosomal markers, suggests that the bacteria are degraded through the endocytic pathway (Radin et al., 2005; Agarwal et al., 2010). On the other hand, it has been provided evidence that the autophagic pathway can also be effective in killing *S. pneumoniae* (Li et al., 2015; Ogawa et al., 2018).

For decades, *S. pneumoniae* has been considered as a prototypical extracellular pathogen. Nevertheless, recent research has revealed that this particular bacterium has the ability to survive within the host cells, despite the mechanisms that host cells employ to protect themselves against it. For instance, pneumococci have been observed within the vacuoles of intact A549 pneumocytes, as well as freely in the cytoplasm of damaged cells (Talbot et al., 1996). Similarly, when pneumococci invade brain microvascular endothelial cells, the vesicles containing the bacteria are recycled to the apical surface and can also migrate to the basolateral cell surface, enabling viable pneumococci to cross epithelial and endothelial cells (Ring et al., 1998). In these same type of cells, *S. pneumoniae* has been found to survive for extended periods of time. This survival is enhanced by the inhibition of lysosomal activity, suggesting that the majority of intracellular pneumococci are killed within vesicles that fuse with lysosomes (Gradstedt et al., 2013). When pneumococci are internalized by macrophages and dendritic cells, they are enclosed in vacuoles that are coated with MRC-1, a mannose receptor. These vacuoles do not merge with lysosomal compartments, allowing *S. pneumoniae* to survive within the host cells. This intracellular survival enables the bacteria to use macrophages and dendritic cells as Trojan horses to spread the infection (Subramanian et al., 2019). A similar phenotype was reported by other authors, who described that *S. pneumoniae* survive entrapped in autophagosomes (Ogawa et al., 2018), while this pathogen showed to be able to replicate in murine splenic macrophages (Ercoli et al., 2018). In HL-1 cardiomyocytes, *S. pneumoniae* was also found in vacuoles and it was confirmed that this pathogen replicates intracellularly, indicating that this survival mechanism is essential for the early events during cardiomyocyte invasion. Furthermore, it was shown that pneumolysin and SpxB-derived H_2O_2 production were necessary for cardiomyocyte killing (Brissac et al., 2018).

To ensure their survival within host cells, particularly immune cells, bacteria must possess the ability to withstand challenging conditions, including oxidative stress. The pneumococcal capsule is widely recognized as a crucial virulence factor that aids pneumococci in evading phagocytosis by immune cells (Feldman and Anderson, 2020). However, once internalized, this capsule assumes an antioxidant role, safeguarding the bacteria against intracellular destruction caused by the host's production of ROS. Additionally, the capsule has been found to enhance the efficiency of translocation across vascular endothelial cells (Brissac et al., 2021).

In our laboratory, we conducted experiments that revealed the ability of *S. pneumoniae* to survive for extended periods within cell lines such as human A549 pneumocytes and murine RAW 264.7 macrophages. This survival mechanism was dependent on the CiaR and ComE response regulators (Pinas et al., 2008; Cortes et al., 2015). Further, we have also investigated the StkP/ComE signaling transduction system and its role in response to acidic stress and oxidative genes (Figure 3). We found that this system controls the expression of *tpxD*, *sodA*, *spxB*, and *murN*, which are involved in various cellular processes such as cell wall biosynthesis and autolysis. Activation of the StkP/ComE pathway leads to the upregulation of these genes, and a disbalance on MurN provokes alterations in the cell membrane biosynthesis and consequent autolysis. We observed that mutants lacking *comE* and *stkP* showed increased survival within A549 pneumocytes, possibly due to the inhibition of autolysis and H_2O_2 production. This is likely caused by low expression levels of *murN* and *spxB*, respectively. Furthermore, we propose that the StkP/ComE pathway is crucial for *S. pneumoniae* to survive acidic and oxidative stress within host cells (Pinas et al., 2018). Interestingly, it was also discovered that SpxB-mediated H_2O_2 production enhances the intracellular survival of *S. pneumoniae* by inactivating lysosomal cysteine cathepsins, which affects the degradative capacity of lysosomal vesicles in brain microvascular endothelial cells. This process facilitates the movement of pneumococci across cellular compartments (Anil et al., 2021).

Synergism between influenza A and *Streptococcus pneumoniae*

Another factor that contributes to the development of pneumococcal infections is the combined effect that occurs when patients are infected with both influenza A and *S. pneumoniae*. It is well-known that individuals previously infected with influenza often suffer additional bacterial infections that complicate their treatment, and *S. pneumoniae* is one of the most commonly found bacterial pathogens in these cases (Sender et al., 2021). To gain a better understanding of this synergistic mechanism, we conducted a study to examine how influenza A infection affects the ability of *S. pneumoniae* to survive inside lung cells. We focused on the M2 protein of influenza A virus (IAV), which has been shown to inhibit the fusion of autophagosomes with lysosomes (Gannage et al., 2009). Our hypothesis was that this characteristic promotes the survival of *S. pneumoniae* within autophagosomes (Reinoso-Vizcaino et al., 2020).

Influenza A infection is associated with an elevation in ROS levels within infected cells. This increment is produced by an upregulation of the transcripts that encodes for the NADH oxidase 4 (NOX4), with a consequent overexpression of this enzyme (Amatore et al., 2015), and by the interaction of the viral M2 protein with MAVS (mitochondrial antiviral signaling protein) on mitochondria, causing overproduction of ROS (Wang et al., 2019). The overproduction of ROS can lead to lung tissue damage and the activation of inflammatory cells. The imbalance of the redox environment facilitates the transmission of the influenza virus between cells by making host epithelial cells more susceptible (Liu et al., 2017). To survive under these conditions in pneumocytes, *S. pneumoniae* must induce an oxidative stress response, and we have confirmed that influenza infection increases ROS production in pneumocytes. In this viral-bacterial synergy, we have discovered that *S. pneumoniae* senses, either directly or indirectly, cellular changes induced by IAV through a TCS named SirRH. This system regulates the expression of more than 170 genes. In particular, we analyzed the *clpL* and *psaB* genes, which encode a protein chaperone and an Mn^{+2} transporter, respectively, as mentioned above. The *sirR*, *clpL*, and *psaB* showed increased susceptibility to oxidative stress and did not exhibit any improvement in intracellular survival when pneumocyte cells were infected with IAV. These results suggest that the SirRH two-component system is capable of sensing stress conditions induced by IAV and controlling adaptive responses that enable the survival of *S. pneumoniae* in IAV-infected pneumocytes (Reinoso-Vizcaino et al., 2020).

In a mouse coinfection model, it has been observed that the growth of *S. pneumoniae* under oxidative stress conditions induced by influenza is dependent on the expression of the protease/chaperone HtrA (Sender et al., 2020). This requirement is mediated by the presence of CiaR, a response regulator that governs the expression of the *htrA* gene (Sebert et al., 2002). At present, only SirRH and CiaR have been described as direct players implicated in this synergistic mechanism. However, considering the intricate nature of regulating the OSR, it is probable that other signal transduction systems are involved in this regulatory network.

Antibiotic persistence

The endogenous synthesis of H_2O_2, facilitated by the enzyme SpxB, is also implicated in the mechanism of action of fluoroquinolones (FQs), a class of antibiotics commonly used to treat pneumococcal infections. In addition to their ability to inhibit DNA gyrase, FQs also induce metabolic changes that lead to an increase in pyruvate levels. Subsequently, SpxB converts this pyruvate, resulting in a concentration of H_2O_2 that is more than 20 times higher. Concurrently, FQs also stimulate the expression of genes involved in iron transport, which are encoded in the *piuBCDA* operon, leading to elevated levels of cytoplasmic iron. The combination of increased iron and H_2O_2 levels conducts to a significant rise in hydroxyl radical production through the Fenton reaction (Figure 3). This can cause damage to proteins, lipids, and DNA. Consequently, it has been postulated that ROS contribute to the bactericidal effect of FQs on *S. pneumoniae* (Ferrandiz et al., 2016).

During pneumococcal infections, immune cells generate inflammatory foci that produce oxidative environments. In our study, we have investigated the potential influence of these stressful conditions on the mechanism of action of fluoroquinolone antibiotics (FQs). It is well-established that bacteria can develop mechanisms to tolerate lethal concentrations of bactericidal antibiotics, under stressful conditions. When this phenomenon occurs in a bacterial subpopulation that shows a different killing rate that the rest of cells, the persisters cannot replicate in the presence of antibiotics, this capacity is not inherited, and it is induced by stress conditions, this mechanism is named "triggered persistence" (Michiels et al., 2016; Balaban et al., 2019). Different stress conditions have been identified as capable of triggering persistence, with starvation being the most commonly observed among them (Nguyen et al., 2011). Additionally, oxidative stress has been found to be another environmental factor that can induce antibiotic persistence in bacterial (Hong et al., 2012; Vega et al., 2012; Wu et al., 2012).

Our findings revealed that oxidative stress induces a state of persistence in *S. pneumoniae* when exposed to FQs. This phenomenon was observed not only in bacterial cultures but also during the temporary intracellular existence of pneumococci within pneumocytes, macrophages, or neutrophils. To our knowledge, this is the first reported mechanism of antibiotic persistence in *S. pneumoniae* (Hernandez-Morfa et al., 2022). Exposure to oxidative stress was found to upregulate the expression of two enzymes, SodA and TpxD, which provide protection against ROS induced by FQs and enhance the intracellular survival of *S. pneumoniae* (Figure 4). Importantly, other authors have validated our research outcomes using clinical strains of *S. pneumoniae*. They found persistence to multiple antibiotics, including fluoroquinolones, although the underlying mechanisms were not elucidated (Geerts et al., 2022).

Based on our findings, we propose that persistence may have implications for the effectiveness of antibiotic treatment and could be a component of a multi-step process in the development of fluoroquinolone resistance (Hernandez-Morfa et al., 2022).

Conclusion

Throughout the process of evolution, both aerobic and facultative aerobic/anaerobic bacteria have developed mechanisms to tolerate ROS. This adaptation is crucial for protecting themselves from oxidative stress-induced cellular damage. Bacterial pathogens, specifically those capable of surviving within host cells, have also developed protective systems to counteract the ROS released by immune cells in the extracellular space of infected tissues.

S. pneumoniae is known for its exceptional ability to produce H_2O_2, and this capacity allows pneumococci to be part of the human nasopharynx microbiota. This bacterium utilizes this metabolic weapon to eliminate other microorganisms that cannot survive in such oxidative conditions (Pericone et al., 2000). However, if the production of H_2O_2 is not properly controlled, it can lead to a significant imbalance of oxidative stress, ultimately causing detrimental effects on the physiology of *S. pneumoniae*. In consequence, *S. pneumoniae* has evolved various protective systems that enable its survival under oxidative stress conditions. Overcoming this initial hurdle of oxidative stress is essential for *S. pneumoniae* to successfully establish an infection.

We have underscored the intricate nature of the stress response mechanisms employed by *S. pneumoniae* for self-defense. The presence of multiple systems suggests that these mechanisms may be utilized independently or in conjunction with one another. However, it remains unclear whether this adaptability serves as a redundant safeguard to ensure an appropriate response, functions as a sequential step in a cascade of reactions, or represents a specific reaction to a particular oxidative environment. The OSR in *S. pneumoniae* is a multifaceted process that involves various regulatory mechanisms, such as two-component systems and individual regulators. These mechanisms are capable of sensing changes in redox state and initiating a physiological response to mitigate the detrimental effects of ROS on cellular components.

The majority of these investigations were conducted either *in vitro* or in animal models. Additionally, we have carried out studies that elucidate the OSR during the intracellular life cycle of *S. pneumoniae*, as well as the significance of this mechanism in the observed synergistic effect during coinfection. It is our belief that the

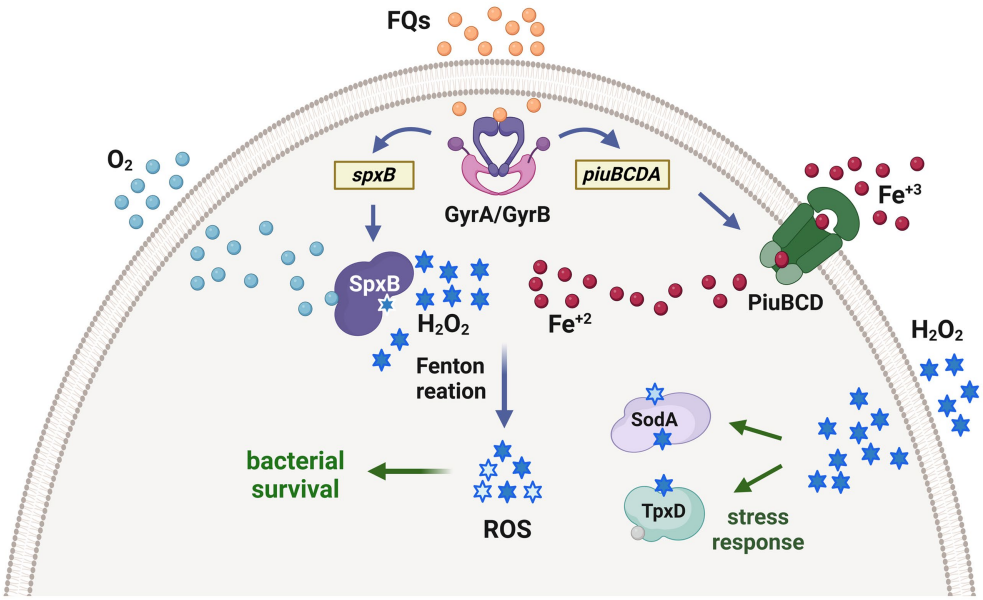

FIGURE 4
Proposed mechanism of fluoroquinolone persistence induced by oxidative stress in *S. pneumoniae*. Fluoroquinolones inhibit the topoisomerases in the bacteria, leading to the upregulation of the *piuBCDA* genes. These genes are responsible for enhancing iron uptake, which subsequently increases the levels of intracellular Fe^{+2}. Additionally, the SpxB pyruvate oxidase synthesizes endogenous H_2O_2. The interaction between Fe^{+2} and H_2O_2 through the Fenton reaction generates ROS, which cause oxidative damage to DNA, proteins, and lipids. This cellular impairment contributes to bacterial death caused by fluoroquinolones. Interestingly, prior exposure of pneumococci to H_2O_2 within host cells triggers the expression of enzymes that detoxify ROS, such as the thiol peroxidase TpxD and the superoxide dismutase SodA. These enzymes are part of an adaptive response that protects pneumococci from oxidative damage induced by fluoroquinolones and facilitates the generation of fluoroquinolone persisters, which are capable of surviving in the presence of these antibiotics [adapted from Ferrandiz et al. (2016)].

development of novel methodological approaches is imperative in order to comprehend how this pathogen regulates the intracellular attack of ROS, particularly within immune cells.

From a therapeutic standpoint, one of the most crucial discoveries pertaining to oxidative stress is its capacity to induce persistence to fluoroquinolones in host cells. In this context, the transient intracellular existence of *S. pneumoniae* may potentially create a favorable environment for the emergence of fluoroquinolone resistance, as has been suggested for other bacterial pathogens (Klugman, 2003; Dalhoff, 2012).

Finally, this revision not only underlines the complexity of the oxidative stress response and its relevance for the pneumococcal pathogenesis, but also unveils specific areas that require further investigation in the future. For example, there is a need to explore the regulatory mechanism of the oxidative stress response when the bacteria are present within immune cells. Moreover, it is crucial to examine the potential consequences of H_2O_2-induced FQ persistence on the effectiveness of antimicrobial treatment for pneumococcal infectious diseases. Further investigation is necessary to ascertain whether this persistence mechanism is an essential step in the evolution of antibiotic resistance.

Author contributions

MH-M: Conceptualization, Writing – review & editing. NO: Conceptualization, Writing – review & editing. VZ: Conceptualization, Writing – review & editing. GP: Conceptualization, Writing – review & editing. NR-V: Conceptualization, Writing – review & editing. MC: Conceptualization, Writing – review & editing. MN-F: Conceptualization, Writing – review & editing. PC: Conceptualization, Writing – review & editing. JE: Conceptualization, Writing – review & editing, Funding acquisition, Writing – original draft.

Funding

The author(s) declare financial support was received for the research, authorship, and/or publication of this article. This work was supported by the National Agency of Scientific and Technological Promotion (ANPCYT; IP-COVID-19 240; FONCYT-PICT-2016-#0805; FONCYT-PICT 2018-#2046-Prestamo BID, to JE), and the National University of Cordoba (SECYT-UNC-2020, to JE). JE is a member of the Research Career of the CONICET. MH-M and NO are recipients of CONICET PhD fellowships, and VZ is the recipient of a ANPCYT PhD fellowship.

Acknowledgments

We thank Gabriela Furlan, Noelia Maldonado, Luciana Reyna, Laura Gatica, Paula Abadie, Pilar Crespo, Alejandra Romero (CIBICI-CONICET) for helpful discussion. We apologize to authors whose work was either not referenced or not discussed. We are grateful for support mentioned above from the National Agency of Scientific and Technological Promotion, CONICET and National University of Cordoba. JE is a member of the Research Career of the CONICET. MH-M and NO are recipients of CONICET PhD fellowships, and VZ is the recipient of a ANPCYT PhD fellowship. Cartoons in Figures 1–4 were created with BioRender.com.

Conflict of interest

The authors declare that the research was conducted in the absence of any commercial or financial relationships that could be construed as a potential conflict of interest.

Publisher's note

References

Agarwal, V., Asmat, T. M., Dierdorf, N. I., Hauck, C. R., and Hammerschmidt, S. (2010). Polymeric immunoglobulin receptor-mediated invasion of *Streptococcus pneumoniae* into host cells requires a coordinate signaling of SRC family of protein-tyrosine kinases, ERK, and c-Jun N-terminal kinase. *J. Biol. Chem.* 285, 35615–35623. doi: 10.1074/jbc.M110.172999

Amatore, D., Sgarbanti, R., Aquilano, K., Baldelli, S., Limongi, D., Civitelli, L., et al. (2015). Influenza virus replication in lung epithelial cells depends on redox-sensitive pathways activated by NOX4-derived ROS. *Cell. Microbiol.* 17, 131–145. doi: 10.1111/cmi.12343

Andisi, V. F., Hinojosa, C. A., de Jong, A., Kuipers, O. P., Orihuela, C. J., and Bijlsma, J. J. (2012). Pneumococcal gene complex involved in resistance to extracellular oxidative stress. *Infect. Immun.* 80, 1037–1049. doi: 10.1128/IAI.05563-11

Anil, A., Apte, S., Joseph, J., Parthasarathy, A., Madhavan, S., and Banerjee, A. (2021). Pyruvate oxidase as a key determinant of pneumococcal viability during transcytosis across brain endothelium. *J. Bacteriol.* 203:e0043921. doi: 10.1128/JB.00439-21

Arenas, F. A., Diaz, W. A., Leal, C. A., Perez-Donoso, J. M., Imlay, J. A., and Vasquez, C. C. (2010). The *Escherichia coli* btuE gene, encodes a glutathione peroxidase that is induced under oxidative stress conditions. *Biochem. Biophys. Res. Commun.* 398, 690–694. doi: 10.1016/j.bbrc.2010.07.002

Arnhold, J., and Malle, E. (2022). Halogenation activity of mammalian Heme peroxidases. *Antioxidants (Basel)* 11:890. doi: 10.3390/antiox11050890

Ashby, M. T., Kreth, J., Soundarajan, M., and Sivuilu, L. S. (2009). Influence of a model human defensive peroxidase system on oral streptococcal antagonism. *Microbiology (Reading)* 155, 3691–3700. doi: 10.1099/mic.0.031310-0

Asmat, T. M., Agarwal, V., Saleh, M., and Hammerschmidt, S. (2014). Endocytosis of *Streptococcus pneumoniae* via the polymeric immunoglobulin receptor of epithelial cells relies on clathrin and caveolin dependent mechanisms. *Int. J. Med. Microbiol.* 304, 1233–1246. doi: 10.1016/j.ijmm.2014.10.001

Auzat, I., Chapuy-Regaud, S., Le Bras, G., Dos Santos, D., Ogunniyi, A. D., Le Thomas, I., et al. (1999). The NADH oxidase of *Streptococcus pneumoniae*: its involvement in competence and virulence. *Mol. Microbiol.* 34, 1018–1028. doi: 10.1046/j.1365-2958.1999.01663.x

Ayoola, M. B., Nakamya, M. F., Shack, L. A., Park, S., Lim, J., Lee, J. H., et al. (2020). SP_0916 is an arginine decarboxylase that catalyzes the synthesis of Agmatine, which is critical for capsule biosynthesis in *Streptococcus pneumoniae*. *Front. Microbiol.* 11:578533. doi: 10.3389/fmicb.2020.578533

Ayoola, M. B., Shack, L. A., Nakamya, M. F., Thornton, J. A., Swiatlo, E., and Nanduri, B. (2019). Polyamine synthesis effects capsule expression by reduction of

precursors in *Streptococcus pneumoniae*. *Front. Microbiol.* 10:1996. doi: 10.3389/fmicb.2019.01996

Balaban, N. Q., Helaine, S., Lewis, K., Ackermann, M., Aldridge, B., Andersson, D. I., et al. (2019). Definitions and guidelines for research on antibiotic persistence. *Nat. Rev. Microbiol.* 17, 441–448. doi: 10.1038/s41579-019-0196-3

Barichello, T., Generoso, J. S., Simoes, L. R., Elias, S. G., and Quevedo, J. (2013). Role of oxidative stress in the pathophysiology of pneumococcal meningitis. *Oxidative Med. Cell. Longev.* 2013:371465. doi: 10.1155/2013/371465

Barrett, T. J., and Hawkins, C. L. (2012). Hypothiocyanous acid: benign or deadly? *Chem. Res. Toxicol.* 25, 263–273. doi: 10.1021/tx200219s

Berry, A. M., and Paton, J. C. (1996). Sequence heterogeneity of PsaA, a 37-kilodalton putative adhesin essential for virulence of *Streptococcus pneumoniae*. *Infect. Immun.* 64, 5255–5262. doi: 10.1128/iai.64.12.5255-5262.1996

Bogaert, D., van Belkum, A., Sluijter, M., Luijendijk, A., de Groot, R., Rumke, H. C., et al. (2004). Colonisation by *Streptococcus pneumoniae* and *Staphylococcus aureus* in healthy children. *Lancet* 363, 1871–1872. doi: 10.1016/S0140-6736(04)16357-5

Bortoni, M. E., Terra, V. S., Hinds, J., Andrew, P. W., and Yesilkaya, H. (2009). The pneumococcal response to oxidative stress includes a role for Rgg. *Microbiology (Reading)* 155, 4123–4134. doi: 10.1099/mic.0.028282-0

Brinsmade, S. R., Kleijn, R. J., Sauer, U., and Sonenshein, A. L. (2010). Regulation of CodY activity through modulation of intracellular branched-chain amino acid pools. *J. Bacteriol.* 192, 6357–6368. doi: 10.1128/JB.00937-10

Brissac, T., Martinez, E., Kruckow, K. L., Riegler, A. N., Ganaie, F., Im, H., et al. (2021). Capsule promotes intracellular survival and vascular endothelial cell translocation during invasive pneumococcal disease. *MBio* 12:e0251621. doi: 10.1128/mBio.02516-21

Brissac, T., Shenoy, A. T., Patterson, L. A., and Orihuela, C. J. (2018). Cell invasion and pyruvate oxidase-derived H(2)O(2) are critical for *Streptococcus pneumoniae*-mediated cardiomyocyte killing. *Infect. Immun.* 86:569. doi: 10.1128/IAI.00569-17

Brown, J. S., Gilliland, S. M., and Holden, D. W. (2001a). A *Streptococcus pneumoniae* pathogenicity island encoding an ABC transporter involved in iron uptake and virulence. *Mol. Microbiol.* 40, 572–585. doi: 10.1046/j.1365-2958.2001.02414.x

Brown, J. S., Gilliland, S. M., Ruiz-Albert, J., and Holden, D. W. (2002). Characterization of pit, a *Streptococcus pneumoniae* iron uptake ABC transporter. *Infect. Immun.* 70, 4389–4398. doi: 10.1128/IAI.70.8.4389-4398.2002

Brown, J. S., Ogunniyi, A. D., Woodrow, M. C., Holden, D. W., and Paton, J. C. (2001b). Immunization with components of two iron uptake ABC transporters protects mice against systemic *Streptococcus pneumoniae* infection. *Infect. Immun.* 69, 6702–6706. doi: 10.1128/IAI.69.11.6702-6706.2001

Carvalho, S. M., Farshchi Andisi, V., Gradstedt, H., Neef, J., Kuipers, O. P., Neves, A. R., et al. (2013). Pyruvate oxidase influences the sugar utilization pattern and capsule production in *Streptococcus pneumoniae*. *PLoS One* 8:e68277. doi: 10.1371/journal.pone.0068277

Caymaris, S., Bootsma, H. J., Martin, B., Hermans, P. W., Prudhomme, M., and Claverys, J. P. (2010). The global nutritional regulator CodY is an essential protein in the human pathogen *Streptococcus pneumoniae*. *Mol. Microbiol.* 78, 344–360. doi: 10.1111/j.1365-2958.2010.07339.x

CDC (2012). Emerging infections program, network *Streptococcus pneumoniae*, 2010. Centers for Disease Control and Prevention. *Active Bacterial Core Surveillance (ABCs) Report*.

Chimalapati, S., Cohen, J. M., Camberlein, E., MacDonald, N., Durmort, C., Vernet, T., et al. (2012). Effects of deletion of the *Streptococcus pneumoniae* lipoprotein diacylglyceryl transferase gene lgt on ABC transporter function and on growth in vivo. *PLoS One* 7:e41393. doi: 10.1371/journal.pone.0041393

Choi, I. H., Shim, J. H., Kim, S. W., Kim, S. N., Pyo, S. N., and Rhee, D. K. (1999). Limited stress response in *Streptococcus pneumoniae*. *Microbiol. Immunol.* 43, 807–812. doi: 10.1111/j.1348-0421.1999.tb02474.x

Claverys, J. P., Prudhomme, M., and Martin, B. (2006). Induction of competence regulons as a general response to stress in gram-positive bacteria. *Annu. Rev. Microbiol.* 60, 451–475. doi: 10.1146/annurev.micro.60.080805.142139

Collet, J. F., and Messens, J. (2010). Structure, function, and mechanism of thioredoxin proteins. *Antioxid. Redox Signal.* 13, 1205–1216. doi: 10.1089/ars.2010.3114

Cortes, P. R., Pinas, G. E., Cian, M. B., Yandar, N., and Echenique, J. (2015). Stress-triggered signaling affecting survival or suicide of *Streptococcus pneumoniae*. *Int. J. Med. Microbiol.* 305, 157–169. doi: 10.1016/j.ijmm.2014.12.002

Counago, R. M., Ween, M. P., Begg, S. L., Bajaj, M., Zuegg, J., O'Mara, M. L., et al. (2014). Imperfect coordination chemistry facilitates metal ion release in the Psa permease. *Nat. Chem. Biol.* 10, 35–41. doi: 10.1038/nchembio.1382

Courtois, P. (2021). Oral peroxidases: from antimicrobial agents to ecological actors (review). *Mol. Med. Rep.* 24:12139. doi: 10.3892/mmr.2021.12139

Dalhoff, A. (2012). Global fluoroquinolone resistance epidemiology and implictions for clinical use. *Interdiscip. Perspect. Infect. Dis.* 2012:976273. doi: 10.1155/2012/976273

Damo, S. M., Kehl-Fie, T. E., Sugitani, N., Holt, M. E., Rathi, S., Murphy, W. J., et al. (2013). Molecular basis for manganese sequestration by calprotectin and roles in the innate immune response to invading bacterial pathogens. *Proc. Natl. Acad. Sci. U. S. A.* 110, 3841–3846. doi: 10.1073/pnas.1220341110

Day, B. J. (2019). The science of licking your wounds: function of oxidants in the innate immune system. *Biochem. Pharmacol.* 163, 451–457. doi: 10.1016/j.bcp.2019.03.013

de Oliveira, M. A., Tairum, C. A., Netto, L. E. S., de Oliveira, A. L. P., Aleixo-Silva, R. L., Cabrera, V. I. M., et al. (2021). Relevance of peroxiredoxins in pathogenic microorganisms. *Appl. Microbiol. Biotechnol.* 105, 5701–5717. doi: 10.1007/s00253-021-11360-5

Desideri, A., and Falconi, M. (2003). Prokaryotic Cu, Zn superoxide dismutases. *Biochem. Soc. Trans.* 31, 1322–1325. doi: 10.1042/bst0311322

Dintilhac, A., Alloing, G., Granadel, C., and Claverys, J. P. (1997). Competence and virulence of *Streptococcus pneumoniae*: Adc and PsaA mutants exhibit a requirement for Zn and Mn resulting from inactivation of putative ABC metal permeases. *Mol. Microbiol.* 25, 727–739. doi: 10.1046/j.1365-2958.1997.5111879.x

Duane, P. G., Rubins, J. B., Weisel, H. R., and Janoff, E. N. (1993). Identification of hydrogen peroxide as a *Streptococcus pneumoniae* toxin for rat alveolar epithelial cells. *Infect. Immun.* 61, 4392–4397. doi: 10.1128/iai.61.10.4392-4397.1993

Echenique, J., Kadioglu, A., Romao, S., Andrew, P. W., and Trombe, M. C. (2004). Protein serine/threonine kinase StkP positively controls virulence and competence in *Streptococcus pneumoniae*. *Infect. Immun.* 72, 2434–2437. doi: 10.1128/IAI.72.4.2434-2437.2004

Echenique, J. R., and Trombe, M. C. (2001). Competence modulation by the NADH oxidase of *Streptococcus pneumoniae* involves signal transduction. *J. Bacteriol.* 183, 768–772. doi: 10.1128/JB.183.2.768-772.2001

Echlin, H., Frank, M., Rock, C., and Rosch, J. W. (2020). Role of the pyruvate metabolic network on carbohydrate metabolism and virulence in *Streptococcus pneumoniae*. *Mol. Microbiol.* 114, 536–552. doi: 10.1111/mmi.14557

Echlin, H., Frank, M. W., Iverson, A., Chang, T. C., Johnson, M. D., Rock, C. O., et al. (2016). Pyruvate oxidase as a critical link between metabolism and capsule biosynthesis in *Streptococcus pneumoniae*. *PLoS Pathog.* 12:e1005951. doi: 10.1371/journal.ppat.1005951

Eijkelkamp, B. A., Morey, J. R., Ween, M. P., Ong, C. L., McEwan, A. G., Paton, J. C., et al. (2014). Extracellular zinc competitively inhibits manganese uptake and compromises oxidative stress management in *Streptococcus pneumoniae*. *PLoS One* 9:e89427. doi: 10.1371/journal.pone.0089427

Ercoli, G., Fernandes, V. E., Chung, W. Y., Wanford, J. J., Thomson, S., Bayliss, C. D., et al. (2018). Intracellular replication of *Streptococcus pneumoniae* inside splenic macrophages serves as a reservoir for septicaemia. *Nat. Microbiol.* 3, 600–610. doi: 10.1038/s41564-018-0147-1

Ezraty, B., Aussel, L., and Barras, F. (2005). Methionine sulfoxide reductases in prokaryotes. *Biochim. Biophys. Acta* 1703, 221–229. doi: 10.1016/j.bbapap.2004.08.017

Feldman, C., and Anderson, R. (2020). Pneumococcal virulence factors in community-acquired pneumonia. *Curr. Opin. Pulm. Med.* 26, 222–231. doi: 10.1097/MCP.0000000000000674

Ferrandiz, M. J., Martin-Galiano, A. J., Arnanz, C., Zimmerman, T., and de la Campa, A. G. (2016). Reactive oxygen species contribute to the bactericidal effects of the fluoroquinolone moxifloxacin in *Streptococcus pneumoniae*. *Antimicrob. Agents Chemother.* 60, 409–417. doi: 10.1128/AAC.02299-15

Fritsch, V. N., Linzner, N., Busche, T., Said, N., Weise, C., Kalinowski, J., et al. (2023). The MerR-family regulator NmlR is involved in the defense against oxidative stress in *Streptococcus pneumoniae*. *Mol. Microbiol.* 119, 191–207. doi: 10.1111/mmi.14999

Gannage, M., Dormann, D., Albrecht, R., Dengjel, J., Torossi, T., Ramer, P. C., et al. (2009). Matrix protein 2 of influenza A virus blocks autophagosome fusion with lysosomes. *Cell Host Microbe* 6, 367–380. doi: 10.1016/j.chom.2009.09.005

Gasc, A. M., Giammarinaro, P., Richter, S., and Sicard, M. (1998). Organization around the dnaA gene of *Streptococcus pneumoniae*. *Microbiology (Reading)* 144, 433–439. doi: 10.1099/00221287-144-2-433

Geerts, N., De Vooght, L., Passaris, I., Delputte, P., Van den Bergh, B., and Cos, P. (2022). Antibiotic tolerance indicative of persistence is pervasive among clinical *Streptococcus pneumoniae* isolates and shows strong condition dependence. *Microbiol. Spectr.* 10:e0270122. doi: 10.1128/spectrum.02701-22

Gennaris, A., and Collet, J. F. (2013). The 'captain of the men of death', *Streptococcus pneumoniae*, fights oxidative stress outside the 'city wall'. *EMBO Mol. Med.* 5, 1798–1800. doi: 10.1002/emmm.201303482

Gierke, R., Wodi, P., and Kobayashi, M. (2021). "Pneumococcal disease" in *Epidemiology and Prevention of Vaccine-Preventable Diseases -14th edition*. (Atlanta, GA: Centers for Disease Control and Prevention press), 1–15.

Gingerich, A. D., Doja, F., Thomason, R., Toth, E., Bradshaw, J. L., Douglass, M. V., et al. (2020). Oxidative killing of encapsulated and nonencapsulated *Streptococcus pneumoniae* by lactoperoxidase-generated hypothiocyanite. *PLoS One* 15:e0236389. doi: 10.1371/journal.pone.0236389

Glanville, D. G., Han, L., Maule, A. F., Woodacre, A., Thanki, D., Abdullah, I. T., et al. (2018). RitR is an archetype for a novel family of redox sensors in the streptococci that has evolved from two-component response regulators and is required for pneumococcal colonization. *PLoS Pathog.* 14:e1007052. doi: 10.1371/journal.ppat.1007052

Gomez-Mejia, A., Gamez, G., and Hammerschmidt, S. (2018). *Streptococcus pneumoniae* two-component regulatory systems: the interplay of the pneumococcus

with its environment. *Int. J. Med. Microbiol.* 308, 722–737. doi: 10.1016/j.ijmm.2017.11.012

Gradstedt, H., Iovino, F., and Bijlsma, J. J. (2013). *Streptococcus pneumoniae* invades endothelial host cells via multiple pathways and is killed in a lysosome dependent manner. *PLoS One* 8:e65626. doi: 10.1371/journal.pone.0065626

Hajaj, B., Yesilkaya, H., Benisty, R., David, M., Andrew, P. W., and Porat, N. (2012). Thiol peroxidase is an important component of *Streptococcus pneumoniae* in oxygenated environments. *Infect. Immun.* 80, 4333–4343. doi: 10.1128/IAI.00126-12

Hajaj, B., Yesilkaya, H., Shafeeq, S., Zhi, X., Benisty, R., Tchalah, S., et al. (2017). CodY regulates thiol peroxidase expression as part of the pneumococcal defense mechanism against H(2)O(2) stress. *Front. Cell. Infect. Microbiol.* 7:210. doi: 10.3389/fcimb.2017.00210

Hajjar, C., Cherrier, M. V., Dias Mirandela, G., Petit-Hartlein, I., Stasia, M. J., Fontecilla-Camps, J. C., et al. (2017). The NOX Family of proteins is also present in Bacteria. *MBio* 8:1487. doi: 10.1128/mBio.01487-17

Halfmann, A., Kovacs, M., Hakenbeck, R., and Bruckner, R. (2007). Identification of the genes directly controlled by the response regulator CiaR in *Streptococcus pneumoniae*: five out of 15 promoters drive expression of small non-coding RNAs. *Mol. Microbiol.* 66, 110–126. doi: 10.1111/j.1365-2958.2007.05900.x

Haschka, D., Hoffmann, A., and Weiss, G. (2021). Iron in immune cell function and host defense. *Semin. Cell Dev. Biol.* 115, 27–36. doi: 10.1016/j.semcdb.2020.12.005

Hava, D. L., and Camilli, A. (2002). Large-scale identification of serotype 4 *Streptococcus pneumoniae* virulence factors. *Mol. Microbiol.* 45, 1389–1406. doi: 10.1046/j.1365-2958.2002.03106.x

Hendriksen, W. T., Bootsma, H. J., Estevao, S., Hoogenboezem, T., de Jong, A., de Groot, R., et al. (2008). CodY of *Streptococcus pneumoniae*: link between nutritional gene regulation and colonization. *J. Bacteriol.* 190, 590–601. doi: 10.1128/JB.00917-07

Hendriksen, W. T., Bootsma, H. J., van Diepen, A., Estevao, S., Kuipers, O. P., de Groot, R., et al. (2009). Strain-specific impact of PsaR of *Streptococcus pneumoniae* on global gene expression and virulence. *Microbiology (Reading)* 155, 1569–1579. doi: 10.1099/mic.0.025072-0

Hernandez-Morfa, M., Reinoso-Vizcaino, N. M., Olivero, N. B., Zappia, V. E., Cortes, P. R., Jaime, A., et al. (2022). Host cell oxidative stress promotes intracellular fluoroquinolone Persisters of *Streptococcus pneumoniae*. *Microbiol. Spectr.* 10:e0436422. doi: 10.1128/spectrum.04364-22

Higuchi, M. (1992). Reduced nicotinamide adenine dinucleotide oxidase involvement in defense against oxygen toxicity of *Streptococcus mutans*. *Oral Microbiol. Immunol.* 7, 309–314. doi: 10.1111/j.1399-302X.1992.tb00594.x

Hirschmann, S., Gomez-Mejia, A., Kohler, T. P., Voss, F., Rohde, M., Brendel, M., et al. (2021). The two-component system 09 of *Streptococcus pneumoniae* is important for metabolic fitness and resistance during dissemination in the host. *Microorganisms* 9:1365. doi: 10.3390/microorganisms9071365

Hong, S. H., Wang, X., O'Connor, H. F., Benedik, M. J., and Wood, T. K. (2012). Bacterial persistence increases as environmental fitness decreases. *Microb. Biotechnol.* 5, 509–522. doi: 10.1111/j.1751-7915.2011.00327.x

Hood, M. I., and Skaar, E. P. (2012). Nutritional immunity: transition metals at the pathogen-host interface. *Nat. Rev. Microbiol.* 10, 525–537. doi: 10.1038/nrmicro2836

Hua, C. Z., Howard, A., Malley, R., and Lu, Y. J. (2014). Effect of nonheme iron-containing ferritin Dpr in the stress response and virulence of pneumococci. *Infect. Immun.* 82, 3939–3947. doi: 10.1128/IAI.01829-14

Ibrahim, Y. M., Kerr, A. R., McCluskey, J., and Mitchell, T. J. (2004). Control of virulence by the two-component system CiaR/H is mediated via HtrA, a major virulence factor of *Streptococcus pneumoniae*. *J. Bacteriol.* 186, 5258–5266. doi: 10.1128/JB.186.16.5258-5266.2004

Jacobsen, F. E., Kazmierczak, K. M., Lisher, J. P., Winkler, M. E., and Giedroc, D. P. (2011). Interplay between manganese and zinc homeostasis in the human pathogen *Streptococcus pneumoniae*. *Metallomics* 3, 38–41. doi: 10.1039/C0MT00050G

Jakubovics, N. S., and Jenkinson, H. F. (2001). Out of the iron age: new insights into the critical role of manganese homeostasis in bacteria. *Microbiology (Reading)* 147, 1709–1718. doi: 10.1099/00221287-147-7-1709

Jiang, H., Wang, H., Zou, W., Hu, Y., Chen, C., and Wang, C. (2019). Sufentanil impairs autophagic degradation and inhibits cell migration in NCI-H460 *in vitro*. *Oncol. Lett.* 18, 6829–6835. doi: 10.3892/ol.2019.10997

Johnston, C., Bootsma, H. J., Aldridge, C., Manuse, S., Gisch, N., Schwudke, D., et al. (2015). Co-inactivation of GlnR and CodY regulators impacts pneumococcal Cell Wall physiology. *PLoS One* 10:e0123702. doi: 10.1371/journal.pone.0123702

Johnston, J. W., Briles, D. E., Myers, L. E., and Hollingshead, S. K. (2006). Mn2+−dependent regulation of multiple genes in *Streptococcus pneumoniae* through PsaR and the resultant impact on virulence. *Infect. Immun.* 74, 1171–1180. doi: 10.1128/IAI.74.2.1171-1180.2006

Kahne, S. C., and Darwin, K. H. (2021). Structural determinants of regulated proteolysis in pathogenic bacteria by ClpP and the proteasome. *Curr. Opin. Struct. Biol.* 67, 120–126. doi: 10.1016/j.sbi.2020.09.012

Kalscheuer, R., and Koliwer-Brandl, H. (2014). Genetics of mycobacterial Trehalose metabolism. *Microbiol. Spectr.* 2:2013. doi: 10.1128/microbiolspec.MGM2-0002-2013

Kim, J. O., and Weiser, J. N. (1998). Association of intrastrain phase variation in quantity of capsular polysaccharide and teichoic acid with the virulence of *Streptococcus pneumoniae*. *J. Infect. Dis.* 177, 368–377. doi: 10.1086/514205

Kim, Y. K., Shin, Y. J., Lee, W. H., Kim, H. Y., and Hwang, K. Y. (2009). Structural and kinetic analysis of an MsrA-MsrB fusion protein from *Streptococcus pneumoniae*. *Mol. Microbiol.* 72, 699–709. doi: 10.1111/j.1365-2958.2009.06680.x

Kloosterman, T. G., Hendriksen, W. T., Bijlsma, J. J., Bootsma, H. J., van Hijum, S. A., Kok, J., et al. (2006). Regulation of glutamine and glutamate metabolism by GlnR and GlnA in *Streptococcus pneumoniae*. *J. Biol. Chem.* 281, 25097–25109. doi: 10.1074/jbc.M601661200

Klugman, K. P. (2003). The role of clonality in the global spread of fluoroquinolone-resistant bacteria. *Clin. Infect. Dis.* 36, 783–785. doi: 10.1086/367935

Ku, J. W., and Gan, Y. H. (2019). Modulation of bacterial virulence and fitness by host glutathione. *Curr. Opin. Microbiol.* 47, 8–13. doi: 10.1016/j.mib.2018.10.004

Kwon, H. Y., Kim, S. W., Choi, M. H., Ogunniyi, A. D., Paton, J. C., Park, S. H., et al. (2003). Effect of heat shock and mutations in ClpL and ClpP on virulence gene expression in *Streptococcus pneumoniae*. *Infect. Immun.* 71, 3757–3765. doi: 10.1128/IAI.71.7.3757-3765.2003

Langford, P. R., Loynds, B. M., and Kroll, J. S. (1996). Cloning and molecular characterization of cu,Zn superoxide dismutase from *Actinobacillus pleuropneumoniae*. *Infect. Immun.* 64, 5035–5041. doi: 10.1128/iai.64.12.5035-5041.1996

Ling, E., Feldman, G., Portnoi, M., Dagan, R., Overweg, K., Mulholland, F., et al. (2004). Glycolytic enzymes associated with the cell surface of *Streptococcus pneumoniae* are antigenic in humans and elicit protective immune responses in the mouse. *Clin. Exp. Immunol.* 138, 290–298. doi: 10.1111/j.1365-2249.2004.02628.x

Li, P., Shi, J., He, Q., Hu, Q., Wang, Y. Y., Zhang, L. J., et al. (2015). *Streptococcus pneumoniae* induces autophagy through the inhibition of the PI3K-I/Akt/mTOR pathway and ROS hypergeneration in A549 cells. *PLoS One* 10:e0122753. doi: 10.1371/journal.pone.0122753

Lisher, J. P., Higgins, K. A., Maroney, M. J., and Giedroc, D. P. (2013). Physical characterization of the manganese-sensing pneumococcal surface antigen repressor from *Streptococcus pneumoniae*. *Biochemistry* 52, 7689–7701. doi: 10.1021/bi401132w

Lisher, J. P., Tsui, H. T., Ramos-Montanez, S., Hentchel, K. L., Martin, J. E., Trinidad, J. C., et al. (2017). Biological and chemical adaptation to endogenous hydrogen peroxide production in *Streptococcus pneumoniae* D39. *mSphere* 2:291. doi: 10.1128/mSphere.00291-16

Liu, M., Chen, F., Liu, T., Chen, F., Liu, S., and Yang, J. (2017). The role of oxidative stress in influenza virus infection. *Microbes Infect.* 19, 580–586. doi: 10.1016/j.micinf.2017.08.008

Lo Conte, M., and Carroll, K. S. (2013). The redox biochemistry of protein sulfenylation and sulfinylation. *J. Biol. Chem.* 288, 26480–26488. doi: 10.1074/jbc.R113.467738

Mahdi, L. K., Van der Hoek, M. B., Ebrahimie, E., Paton, J. C., and Ogunniyi, A. D. (2015). Characterization of pneumococcal genes involved in bloodstream invasion in a mouse model. *PLoS One* 10:e0141816. doi: 10.1371/journal.pone.0141816

Mahmoud, S. A., and Chien, P. (2018). Regulated proteolysis in Bacteria. *Annu. Rev. Biochem.* 87, 677–696. doi: 10.1146/annurev-biochem-062917-012848

Marchler-Bauer, A., Bo, Y., Han, L., He, J., Lanczycki, C. J., Lu, S., et al. (2017). CDD/SPARCLE: functional classification of proteins via subfamily domain architectures. *Nucleic Acids Res.* 45, D200–D203. doi: 10.1093/nar/gkw1129

Marco, S., Rullo, R., Albino, A., Masullo, M., De Vendittis, E., and Amato, M. (2013). The thioredoxin system in the dental caries pathogen Streptococcus mutans and the food-industry bacterium *Streptococcus thermophilus*. *Biochimie* 95, 2145–2156. doi: 10.1016/j.biochi.2013.08.008

Marra, A., Lawson, S., Asundi, J. S., Brigham, D., and Hromockyj, A. E. (2002). In vivo characterization of the psa genes from *Streptococcus pneumoniae* in multiple models of infection. *Microbiology (Reading)* 148, 1483–1491. doi: 10.1099/00221287-148-5-1483

Martin, J. E., Le, M. T., Bhattarai, N., Capdevila, D. A., Shen, J., Winkler, M. E., et al. (2019). A Mn-sensing riboswitch activates expression of a Mn2+/Ca2+ ATPase transporter in Streptococcus. *Nucleic Acids Res.* 47, 6885–6899. doi: 10.1093/nar/gkz494

Mascher, T., Zahner, D., Merai, M., Balmelle, N., de Saizieu, A. B., and Hakenbeck, R. (2003). The *Streptococcus pneumoniae* cia regulon: CiaR target sites and transcription profile analysis. *J. Bacteriol.* 185, 60–70. doi: 10.1128/JB.185.1.60-70.2003

McAllister, L. J., Tseng, H. J., Ogunniyi, A. D., Jennings, M. P., McEwan, A. G., and Paton, J. C. (2004). Molecular analysis of the psa permease complex of *Streptococcus pneumoniae*. *Mol. Microbiol.* 53, 889–901. doi: 10.1111/j.1365-2958.2004.04164.x

McCluskey, J., Hinds, J., Husain, S., Witney, A., and Mitchell, T. J. (2004). A two-component system that controls the expression of pneumococcal surface antigen a (PsaA) and regulates virulence and resistance to oxidative stress in *Streptococcus pneumoniae*. *Mol. Microbiol.* 51, 1661–1675. doi: 10.1111/j.1365-2958.2003.03917.x

McCord, J. M., and Fridovich, I. (1968). The reduction of cytochrome c by milk xanthine oxidase. *J. Biol. Chem.* 243, 5753–5760. doi: 10.1016/S0021-9258(18)91929-0

McDevitt, C. A., Ogunniyi, A. D., Valkov, E., Lawrence, M. C., Kobe, B., McEwan, A. G., et al. (2011). A molecular mechanism for bacterial susceptibility to zinc. *PLoS Pathog.* 7:e1002357. doi: 10.1371/journal.ppat.1002357

Michiels, J. E., Van den Bergh, B., Verstraeten, N., and Michiels, J. (2016). Molecular mechanisms and clinical implications of bacterial persistence. *Drug Resist. Updat.* 29, 76–89. doi: 10.1016/j.drup.2016.10.002

Mishra, S., and Imlay, J. (2012). Why do bacteria use so many enzymes to scavenge hydrogen peroxide? *Arch. Biochem. Biophys.* 525, 145–160. doi: 10.1016/j.abb.2012.04.014

Morozov, G. I., Porat, N., Kushnir, T., Najmuldeen, H., Adawi, A., Chalifa-Caspi, V., et al. (2018). Flavin reductase contributes to pneumococcal virulence by protecting from oxidative stress and mediating adhesion and elicits protection against pneumococcal challenge. *Sci. Rep.* 8:314. doi: 10.1038/s41598-017-18645-8

Nakamya, M. F., Ayoola, M. B., Park, S., Shack, L. A., Swiatlo, E., and Nanduri, B. (2018). The role of Cadaverine synthesis on pneumococcal capsule and protein expression. *Med Sci (Basel)* 6:10008. doi: 10.3390/medsci6010008

Nakamya, M. F., Ayoola, M. B., Shack, L. A., Swiatlo, E., and Nanduri, B. (2021). The effect of impaired polyamine transport on pneumococcal transcriptome. *Pathogens* 10:1322. doi: 10.3390/pathogens10101322

Nguyen, D., Joshi-Datar, A., Lepine, F., Bauerle, E., Olakanmi, O., Beer, K., et al. (2011). Active starvation responses mediate antibiotic tolerance in biofilms and nutrient-limited bacteria. *Science* 334, 982–986. doi: 10.1126/science.1211037

Nováková, L., Sasková, L., Pallová, P., Janecek, J., Novotná, J., and Echenique, J. (2005). Characterization of a eukaryotic type serine/threonine protein kinase and protein phosphatase of Streptococcus pneumoniae and identification of kinase substrates. *FEBS J.* 72, 1243–1254. doi: 10.1111/j.1742-4658.2005.04560.x

Novak, R., Braun, J. S., Charpentier, E., and Tuomanen, E. (1998). Penicillin tolerance genes of *Streptococcus pneumoniae*: the ABC-type manganese permease complex Psa. *Mol. Microbiol.* 29, 1285–1296. doi: 10.1046/j.1365-2958.1998.01016.x

Ogawa, M., Matsuda, R., Takada, N., Tomokiyo, M., Yamamoto, S., Shizukuishi, S., et al. (2018). Molecular mechanisms of *Streptococcus pneumoniae*-targeted autophagy via pneumolysin, Golgi-resident Rab41, and Nedd4-1-mediated K63-linked ubiquitination. *Cell. Microbiol.* 20:e12846. doi: 10.1111/cmi.12846

Oggioni, M. R., Trappetti, C., Kadioglu, A., Cassone, M., Iannelli, F., Ricci, S., et al. (2006). Switch from planktonic to sessile life: a major event in pneumococcal pathogenesis. *Mol. Microbiol.* 61, 1196–1210. doi: 10.1111/j.1365-2958.2006.05310.x

Ong, C. L., Potter, A. J., Trappetti, C., Walker, M. J., Jennings, M. P., Paton, J. C., et al. (2013). Interplay between manganese and iron in pneumococcal pathogenesis: role of the orphan response regulator RitR. *Infect. Immun.* 81, 421–429. doi: 10.1128/IAI.00805-12

Ostermann, L., Seeliger, B., David, S., Flasche, C., Maus, R., Reinboth, M. S., et al. (2023). S100A9 is indispensable for survival of pneumococcal pneumonia in mice. *PLoS Pathog.* 19:e1011493. doi: 10.1371/journal.ppat.1011493

Park, C. Y., Kim, E. H., Choi, S. Y., Tran, T. D., Kim, I. H., Kim, S. N., et al. (2010). Virulence attenuation of *Streptococcus pneumoniae* clpP mutant by sensitivity to oxidative stress in macrophages via an NO-mediated pathway. *J. Microbiol.* 48, 229–235. doi: 10.1007/s12275-010-9300-0

Park, S. S., Kwon, H. Y., Tran, T. D., Choi, M. H., Jung, S. H., Lee, S., et al. (2015). ClpL is a chaperone without auxiliary factors. *FEBS J.* 282, 1352–1367. doi: 10.1111/febs.13228

Paterson, G. K., Blue, C. E., and Mitchell, T. J. (2006). An operon in *Streptococcus pneumoniae* containing a putative alkylhydroperoxidase D homologue contributes to virulence and the response to oxidative stress. *Microb. Pathog.* 40, 152–160. doi: 10.1016/j.micpath.2005.12.003

Paumann-Page, M., Katz, R. S., Bellei, M., Schwartz, I., Edenhofer, E., Sevcnikar, B., et al. (2017). Pre-steady-state kinetics reveal the substrate specificity and mechanism of halide oxidation of truncated human Peroxidasin 1. *J. Biol. Chem.* 292, 4583–4592. doi: 10.1074/jbc.M117.775213

Pericone, C. D., Overweg, K., Hermans, P. W., and Weiser, J. N. (2000). Inhibitory and bactericidal effects of hydrogen peroxide production by *Streptococcus pneumoniae* on other inhabitants of the upper respiratory tract. *Infect. Immun.* 68, 3990–3997. doi: 10.1128/IAI.68.7.3990-3997.2000

Pericone, C. D., Park, S., Imlay, J. A., and Weiser, J. N. (2003). Factors contributing to hydrogen peroxide resistance in *Streptococcus pneumoniae* include pyruvate oxidase (SpxB) and avoidance of the toxic effects of the Fenton reaction. *J. Bacteriol.* 185, 6815–6825. doi: 10.1128/JB.185.23.6815-6825.2003

Pinas, G. E., Cortes, P. R., Orio, A. G. A., and Echenique, J. (2008). Acidic stress induces autolysis by a CSP-independent ComE pathway in *Streptococcus pneumoniae*. *Microbiology (Reading)* 154, 1300–1308. doi: 10.1099/mic.0.2007/015925-0

Pinas, G. E., Reinoso-Vizcaino, N. M., Yandar Barahona, N. Y., Cortes, P. R., Duran, R., Badapanda, C., et al. (2018). Crosstalk between the serine/threonine kinase StkP and the response regulator ComE controls the stress response and intracellular survival of *Streptococcus pneumoniae*. *PLoS Pathog.* 14:e1007118. doi: 10.1371/journal.ppat.1007118

Potter, A. J., Kidd, S. P., McEwan, A. G., and Paton, J. C. (2010). The MerR/NmlR family transcription factor of *Streptococcus pneumoniae* responds to carbonyl stress and modulates hydrogen peroxide production. *J. Bacteriol.* 192, 4063–4066. doi: 10.1128/JB.00383-10

Potter, A. J., Trappetti, C., and Paton, J. C. (2012). *Streptococcus pneumoniae* uses glutathione to defend against oxidative stress and metal ion toxicity. *J. Bacteriol.* 194, 6248–6254. doi: 10.1128/JB.01393-12

Radin, J. N., Orihuela, C. J., Murti, G., Guglielmo, C., Murray, P. J., and Tuomanen, E. I. (2005). beta-Arrestin 1 participates in platelet-activating factor receptor-mediated endocytosis of *Streptococcus pneumoniae*. *Infect. Immun.* 73, 7827–7835. doi: 10.1128/IAI.73.12.7827-7835.2005

Rai, P., Parrish, M., Tay, I. J., Li, N., Ackerman, S., He, F., et al. (2015). *Streptococcus pneumoniae* secretes hydrogen peroxide leading to DNA damage and apoptosis in lung cells. *Proc. Natl. Acad. Sci. U. S. A.* 112, E3421–E3430. doi: 10.1073/pnas.1424144112

Ramirez, G. A., Yacoub, M. R., Ripa, M., Mannina, D., Cariddi, A., Saporiti, N., et al. (2018). Eosinophils from physiology to disease: a comprehensive review. *Biomed. Res. Int.* 2018, 9095275–9095228. doi: 10.1155/2018/9095275

Ramos-Montanez, S., Tsui, H. C., Wayne, K. J., Morris, J. L., Peters, L. E., Zhang, F., et al. (2008). Polymorphism and regulation of the spxB (pyruvate oxidase) virulence factor gene by a CBS-HotDog domain protein (SpxR) in serotype 2 *Streptococcus pneumoniae*. *Mol. Microbiol.* 67, 729–746. doi: 10.1111/j.1365-2958.2007.06082.x

Raquil, M. A., Anceriz, N., Rouleau, P., and Tessier, P. A. (2008). Blockade of antimicrobial proteins S100A8 and S100A9 inhibits phagocyte migration to the alveoli in streptococcal pneumonia. *J. Immunol.* 180, 3366–3374. doi: 10.4049/jimmunol.180.5.3366

Regev-Yochay, G., Trzcinski, K., Thompson, C. M., Lipsitch, M., and Malley, R. (2007). SpxB is a suicide gene of *Streptococcus pneumoniae* and confers a selective advantage in an in vivo competitive colonization model. *J. Bacteriol.* 189, 6532–6539. doi: 10.1128/JB.00813-07

Reinoso-Vizcaino, N. M., Cian, M. B., Cortes, P. R., Olivero, N. B., Hernandez-Morfa, M., Pinas, G. E., et al. (2020). The pneumococcal two-component system SirRH is linked to enhanced intracellular survival of *Streptococcus pneumoniae* in influenza-infected pulmonary cells. *PLoS Pathog.* 16:e1008761. doi: 10.1371/journal.ppat.1008761

Ribes, S., Abdullah, M. R., Saleh, M., Hanisch, U. K., Nau, R., and Hammerschmidt, S. (2016). Thioredoxins and methionine sulfoxide reductases in the pathophysiology of pneumococcal meningitis. *J. Infect. Dis.* 214, 953–961. doi: 10.1093/infdis/jiw268

Ring, A., Weiser, J. N., and Tuomanen, E. I. (1998). Pneumococcal trafficking across the blood-brain barrier. Molecular analysis of a novel bidirectional pathway. *J. Clin. Invest.* 102, 347–360. doi: 10.1172/JCI2406

Robertson, G. T., Ng, W. L., Foley, J., Gilmour, R., and Winkler, M. E. (2002). Global transcriptional analysis of clpP mutations of type 2 *Streptococcus pneumoniae* and their effects on physiology and virulence. *J. Bacteriol.* 184, 3508–3520. doi: 10.1128/JB.184.13.3508-3520.2002

Rosch, J. W., Gao, G., Ridout, G., Wang, Y. D., and Tuomanen, E. I. (2009). Role of the manganese efflux system mntE for signalling and pathogenesis in *Streptococcus pneumoniae*. *Mol. Microbiol.* 72, 12–25. doi: 10.1111/j.1365-2958.2009.06638.x

Rosen, T., Hadley, R. C., Bozzi, A. T., Ocampo, D., Shearer, J., and Nolan, E. M. (2022). Zinc sequestration by human calprotectin facilitates manganese binding to the bacterial solute-binding proteins PsaA and MntC. *Metallomics* 14:mfac001. doi: 10.1093/mtomcs/mfac001

Rosen, T., and Nolan, E. M. (2022). S100A12 promotes Mn(II) binding to pneumococcal PsaA and staphylococcal MntC by Zn(II) sequestration. *J. Inorg. Biochem.* 233:111862. doi: 10.1016/j.jinorgbio.2022.111862

Rotrosen, D., Yeung, C. L., Leto, T. L., Malech, H. L., and Kwong, C. H. (1992). Cytochrome b558: the flavin-binding component of the phagocyte NADPH oxidase. *Science* 256, 1459–1462. doi: 10.1126/science.1318579

Saleh, M., Bartual, S. G., Abdullah, M. R., Jensch, I., Asmat, T. M., Petruschka, L., et al. (2013). Molecular architecture of *Streptococcus pneumoniae* surface thioredoxin-fold lipoproteins crucial for extracellular oxidative stress resistance and maintenance of virulence. *EMBO Mol. Med.* 5, 1852–1870. doi: 10.1002/emmm.201202435

Sasková, L., Nováková, L., Basler, M., and Branny, P. (2007). Eukaryotic-type serine/threonine protein kinase StkP is a global regulator of gene expression in Streptococcus pneumoniae. *J. Bacteriol.* 189, 4168–4179. doi: 10.1128/JB.01616-06

Scheuhammer, A. M., and Cherian, M. G. (1985). Binding of manganese in human and rat plasma. *Biochim. Biophys. Acta* 840, 163–169. doi: 10.1016/0304-4165(85)90115-1

Seaver, L. C., and Imlay, J. A. (2001). Alkyl hydroperoxide reductase is the primary scavenger of endogenous hydrogen peroxide in *Escherichia coli*. *J. Bacteriol.* 183, 7173–7181. doi: 10.1128/JB.183.24.7173-7181.2001

Sebert, M. E., Palmer, L. M., Rosenberg, M., and Weiser, J. N. (2002). Microarray-based identification of htrA, a *Streptococcus pneumoniae* gene that is regulated by the CiaRH two-component system and contributes to nasopharyngeal colonization. *Infect. Immun.* 70, 4059–4067. doi: 10.1128/IAI.70.8.4059-4067.2002

Sender, V., Hentrich, K., and Henriques-Normark, B. (2021). Virus-induced changes of the respiratory tract environment promote secondary infections with *Streptococcus pneumoniae*. *Front. Cell. Infect. Microbiol.* 11:643326. doi: 10.3389/fcimb.2021.643326

Sender, V., Hentrich, K., Pathak, A., Tan Qian Ler, A., Embaie, B. T., Lundstrom, S. L., et al. (2020). Capillary leakage provides nutrients and antioxidants for rapid pneumococcal proliferation in influenza-infected lower airways. *Proc. Natl. Acad. Sci. U. S. A.* 117, 31386–31397. doi: 10.1073/pnas.2012265117

Shah, P., Nanduri, B., Swiatlo, E., Ma, Y., and Pendarvis, K. (2011). Polyamine biosynthesis and transport mechanisms are crucial for fitness and pathogenesis of *Streptococcus pneumoniae*. *Microbiology (Reading)* 157, 504–515. doi: 10.1099/mic.0.042564-0

Shearer, H. L., Kaldor, C. D., Hua, H., Kettle, A. J., Parker, H. A., and Hampton, M. B. (2022a). Resistance of *Streptococcus pneumoniae* to Hypothiocyanous acid generated by host peroxidases. *Infect. Immun.* 90:e0053021. doi: 10.1128/IAI.00530-21

Shearer, H. L., Pace, P. E., Paton, J. C., Hampton, M. B., and Dickerhof, N. (2022b). A newly identified flavoprotein disulfide reductase Har protects *Streptococcus pneumoniae* against hypothiocyanous acid. *J. Biol. Chem.* 298:102359. doi: 10.1016/j.jbc.2022.102359

Shearer, H. L., Paton, J. C., Hampton, M. B., and Dickerhof, N. (2022c). Glutathione utilization protects *Streptococcus pneumoniae* against lactoperoxidase-derived hypothiocyanous acid. *Free Radic. Biol. Med.* 179, 24–33. doi: 10.1016/j.freeradbiomed.2021.12.261

Sheldon, J. R., and Skaar, E. P. (2019). Metals as phagocyte antimicrobial effectors. *Curr. Opin. Immunol.* 60, 1–9. doi: 10.1016/j.coi.2019.04.002

Spellerberg, B., Cundell, D. R., Sandros, J., Pearce, B. J., Idanpaan-Heikkila, I., Rosenow, C., et al. (1996). Pyruvate oxidase, as a determinant of virulence in *Streptococcus pneumoniae*. *Mol. Microbiol.* 19, 803–813. doi: 10.1046/j.1365-2958.1996.425954.x

Steinman, H. M. (1985). Bacteriocuprein superoxide dismutases in pseudomonads. *J. Bacteriol.* 162, 1255–1260. doi: 10.1128/jb.162.3.1255-1260.1985

Stincone, A., Prigione, A., Cramer, T., Wamelink, M. M., Campbell, K., Cheung, E., et al. (2015). The return of metabolism: biochemistry and physiology of the pentose phosphate pathway. *Biol. Rev. Camb. Philos. Soc.* 90, 927–963. doi: 10.1111/brv.12140

Striz, I., and Trebichavsky, I. (2004). Calprotectin – a pleiotropic molecule in acute and chronic inflammation. *Physiol. Res.* 53, 245–253.

Subramanian, K., Henriques-Normark, B., and Normark, S. (2019). Emerging concepts in the pathogenesis of the *Streptococcus pneumoniae*: from nasopharyngeal colonizer to intracellular pathogen. *Cell. Microbiol.* 21:e13077. doi: 10.1111/cmi.13077

Talbot, U. M., Paton, A. W., and Paton, J. C. (1996). Uptake of *Streptococcus pneumoniae* by respiratory epithelial cells. *Infect. Immun.* 64, 3772–3777. doi: 10.1128/iai.64.9.3772-3777.1996

Tseng, H. J., McEwan, A. G., Paton, J. C., and Jennings, M. P. (2002). Virulence of *Streptococcus pneumoniae*: PsaA mutants are hypersensitive to oxidative stress. *Infect. Immun.* 70, 1635–1639. doi: 10.1128/IAI.70.3.1635-1639.2002

Ulfig, A., and Leichert, L. I. (2021). The effects of neutrophil-generated hypochlorous acid and other hypohalous acids on host and pathogens. *Cell. Mol. Life Sci.* 78, 385–414. doi: 10.1007/s00018-020-03591-y

Ulijasz, A. T., Andes, D. R., Glasner, J. D., and Weisblum, B. (2004). Regulation of iron transport in *Streptococcus pneumoniae* by RitR, an orphan response regulator. *J. Bacteriol.* 186, 8123–8136. doi: 10.1128/JB.186.23.8123-8136.2004

Ulijasz, A. T., Falk, S. P., and Weisblum, B. (2009). Phosphorylation of the RitR DNA-binding domain by a Ser-Thr phosphokinase: implications for global gene regulation in the streptococci. *Mol. Microbiol.* 71, 382–390. doi: 10.1111/j.1365-2958.2008.06532.x

Vega, N. M., Allison, K. R., Khalil, A. S., and Collins, J. J. (2012). Signaling-mediated bacterial persister formation. *Nat. Chem. Biol.* 8, 431–433. doi: 10.1038/nchembio.915

Wang, R., Zhu, Y., Lin, X., Ren, C., Zhao, J., Wang, F., et al. (2019). Influenza M2 protein regulates MAVS-mediated signaling pathway through interacting with MAVS and increasing ROS production. *Autophagy* 15, 1163–1181. doi: 10.1080/15548627.2019.1580089

Winterbourn, C. C., Kettle, A. J., and Hampton, M. B. (2016). Reactive oxygen species and neutrophil function. *Annu. Rev. Biochem.* 85, 765–792. doi: 10.1146/annurev-biochem-060815-014442

Wuerges, J., Lee, J. W., Yim, Y. I., Yim, H. S., Kang, S. O., and Djinovic Carugo, K. (2004). Crystal structure of nickel-containing superoxide dismutase reveals another type of active site. *Proc. Natl. Acad. Sci. U. S. A.* 101, 8569–8574. doi: 10.1073/pnas.0308514101

Wu, Y., Vulic, M., Keren, I., and Lewis, K. (2012). Role of oxidative stress in persister tolerance. *Antimicrob. Agents Chemother.* 56, 4922–4926. doi: 10.1128/AAC.00921-12

Yesilkaya, H., Kadioglu, A., Gingles, N., Alexander, J. E., Mitchell, T. J., and Andrew, P. W. (2000). Role of manganese-containing superoxide dismutase in oxidative stress and virulence of *Streptococcus pneumoniae*. *Infect. Immun.* 68, 2819–2826. doi: 10.1128/IAI.68.5.2819-2826.2000

Yu, J., Bryant, A. P., Marra, A., Lonetto, M. A., Ingraham, K. A., Chalker, A. F., et al. (2001). Characterization of the *Streptococcus pneumoniae* NADH oxidase that is required for infection. *Microbiology (Reading)* 147, 431–438. doi: 10.1099/00221287-147-2-431

Zhang, Y., Martin, J. E., Edmonds, K. A., Winkler, M. E., and Giedroc, D. P. (2022). SifR is an Rrf2-family quinone sensor associated with catechol iron uptake in *Streptococcus pneumoniae* D39. *J. Biol. Chem.* 298:102046. doi: 10.1016/j.jbc.2022.102046

frontiers | Frontiers in Microbiology

TYPE Original Research
PUBLISHED 25 October 2023
DOI 10.3389/fmicb.2023.1278271

OPEN ACCESS

EDITED BY
Z. Petek Cakar,
Istanbul Technical University, Türkiye

REVIEWED BY
Pinidphon Prombutara,
Chulalongkorn University, Thailand
Berna Sariyar Akbulut,
Marmara University, Türkiye

*CORRESPONDENCE
Xiao-Dong Li
✉ lxdong_627@163.com
De-Long Guan
✉ 2023660006@hcnu.edu.cn

†These authors have contributed equally to this work and share first authorship

RECEIVED 16 August 2023
ACCEPTED 27 September 2023
PUBLISHED 25 October 2023

CITATION
Chen Y-Z, Rong W-T, Qin Y-C, Lu L-Y, Liu J, Li M-J, Xin L, Li X-D and Guan D-L (2023) Integrative analysis of microbiota and metabolomics in chromium-exposed silkworm (*Bombyx mori*) midguts based on 16S rDNA sequencing and LC/MS metabolomics. *Front. Microbiol.* 14:1278271. doi: 10.3389/fmicb.2023.1278271

Integrative analysis of microbiota and metabolomics in chromium-exposed silkworm (*Bombyx mori*) midguts based on 16S rDNA sequencing and LC/MS metabolomics

Ya-Zhen Chen[1,2†], Wan-Tao Rong[1,2†], Ying-Can Qin[1,2], Lin-Yuan Lu[1,2], Jing Liu[1,2], Ming-Jie Li[1,2], Lei Xin[1,2], Xiao-Dong Li[1,2*] and De-Long Guan[1,2*]

[1]Guangxi Key Laboratory of Sericulture Ecology and Applied Intelligent Technology, Hechi University, Hechi, China, [2]Guangxi Collaborative Innovation Center of Modern Sericulture and Silk, Hechi University, Hechi, China

The gut microbiota, a complex ecosystem integral to host wellbeing, is modulated by environmental triggers, including exposure to heavy metals such as chromium. This study aims to comprehensively explore chromium-induced gut microbiota and metabolomic shifts in the quintessential lepidopteran model organism, the silkworm (*Bombyx mori*). The research deployed 16S rDNA sequence analysis and LC/MS metabolomics in its experimental design, encompassing a control group alongside low (12 g/kg) and high (24 g/kg) feeding chromium dosing regimens. Considerable heterogeneity in microbial diversity resulted between groups. *Weissella* emerged as potentially resilient to chromium stress, while elevated Propionibacterium was noted in the high chromium treatment group. Differential analysis tools LEfSe and random forest estimation identified key species like like *Cupriavidus* and *unspecified Myxococcales*, offering potential avenues for bioremediation. An examination of gut functionality revealed alterations in the KEGG pathways correlated with biosynthesis and degradation, suggesting an adaptive metabolic response to chromium-mediated stress. Further results indicated consequential fallout in the context of metabolomic alterations. These included an uptick in histidine and dihydropyrimidine levels under moderate-dose exposure and a surge of gentisic acid with high-dose chromium exposure. These are critical players in diverse biological processes ranging from energy metabolism and stress response to immune regulation and antioxidative mechanisms. Correlative analyses between bacterial abundance and metabolites mapped noteworthy relationships between marker bacterial species, such as *Weissella* and *Pelomonas*, and specific metabolites, emphasizing their roles in enzyme regulation, synaptic processes, and lipid metabolism. Probiotic bacteria showed robust correlations with metabolites implicated in stress response, lipid metabolism, and antioxidant processes. Our study reaffirms the intricate ties between gut microbiota and metabolite profiles and decodes some systemic adaptations under heavy-metal stress. It provides valuable insights into ecological and toxicological aspects of chromium exposure that can potentially influence silkworm resilience.

KEYWORDS

chromium exposure, silkworms, gut microbiota, metabolomics, multi-omics

Introduction

The silkworm (*Bombyx mori*), treasured for its capacity to produce versatile silk, upholds an integral place in various sectors, notably the textile industry (Huang W. et al., 2018; Bucciarelli and Motta, 2022). Places like Guangxi, China, see their local economy deeply intertwined with this economically critical insect, reflecting the living standards of farmers and workers involved with silk (Liang et al., 2013; Chen et al., 2022; Zhao et al., 2022). Intending to enhance farming efficacy, economic value, and quality of life for these communities, diligent scientific research and productive rearing practices constitute an indispensable step. However, heavy metal toxicity is a perilous interruption to silkworm farming, particularly in industry-dense regions such as Guangxi (Li et al., 2021; Xu et al., 2022). Heavy metals such as cadmium, chromium, and Arsenic harm the silkworm's average growth and silk production lifeline, often leading to death and indenting substantial economic loss (Du et al., 2021; Li et al., 2021; Zang et al., 2023). Recent scientific reviews culminated in supporting these concerns, outlining that heavy metal toxicity disturbs essential biological processes pivotal for the silkworm's lifecycle and silk production (Wan et al., 2017; Marzoli et al., 2022; Gao et al., 2023).

Chromium, a heavy metal ubiquitous in the environment, poses remarkable threats to the environment and life systems due to its widespread use in various industrial activities. Previous works on chromium's biological toxicity extend the spectrum of affected organisms, encompassing humans, animals, model organisms, and insects (Mishra and Bharagava, 2016; Rahman and Singh, 2019; Kapoor et al., 2022). Established research highlights adverse effects such as DNA damage, oxidative stress, and the induction of apoptosis (Balali-Mood et al., 2021; Chakraborty et al., 2022; Teschke, 2022). Mainly, apoptosis, a programmed cellular death, occurs consequent to a cascade of intracellular events activated under stressful conditions (Chiu et al., 2010; Balali-Mood et al., 2021; Renu et al., 2021). This potent mechanism, generally a protective action against teratogenesis, under excessive exposure can bring about damage, disease, or even organismal death.

Focusing on the silkworm milieu, chromium toxicity brings with it a profound hindrance to average growth, development, and silk production. However, this forms only part of our understanding, and the breadth of its results remains under-researched. The implications of chromium in non-tissue microenvironments such as the gut or silk glands have been less frequently analyzed (Muhammad et al., 2022; Chen et al., 2023). The silkworm gut microbiota, an indispensable entity within the silkworm physiology, plays a fundamental role in contributing to the worm's health and life activity. In the face of chromium toxicity, these microbial communities are expected to undergo dynamic shifts, potentially embodying a secondary environmental stressor for silkworms. This biotic focus on gut ecology assumes great relevance, considering its critical role in disease prevention, digestion, nutrient absorption, and apt synthesis of silk (Li et al., 2021; Li C. et al., 2022; Xu et al., 2022).

While growing scientific capabilities, novel methodologies have emerged at the intersection of microbiology and genomics; incorporating metagenomic sequencing and non-targeted metabolomics is one such leap (Dong et al., 2019; Debnath et al., 2021; Jia et al., 2021; Coker et al., 2022). In our investigation, we deploy robust 16S rDNA microbial metagenomic sequencing to gain a comprehensive image of gut microbiota composition. We couple this with LC/MS non-targeted metabolomics, aimed at widening the understanding of functionally significant metabolites in the gut. Together, these cutting-edge techniques promise powerful, high-resolution insights, allowing us to traverse both biodiversity and functional aspects within the microbiome.

Our outlined course of inquiry, exploring the impacts of chromium on the intricate gut ecology of silkworms at a diet exposure concentration of 12 g/kg and 24 g/kg, poses a monumental stride in grasping the broad scope of chromium toxicity. This investigation brings promise in elaborately resolving how chromium shapes the gut microbiota and metabolome, bridging existing knowledge gaps and directing future focus. Most meaningfully, this study could potentially reform the understanding of heavy metal toxicity, underpin a reasoned approach toward heavy metal pollution mitigation and propel sustainable practices in silkworm farming. With its far-reaching implications, we hope to inspire further research endeavors, setting the stage for application-driven initiatives to bolster the health and productivity of economically significant organisms, like silkworms, in at-risk ecological niches, thereby supporting the resilience and livelihood of human communities largely dependent on them.

Materials and methods

Sample collection

The silkworm samples utilized in this research were collected from the Gui Can No.5 string. This strain has been under long-term cultivation in the laboratory of Hechi University. Three groups were established for this experiment. Each group consists of six samples, each comprising at least 10 individuals. The control group (ACB) was fed a regular non-chromium-added artificial diet. Two experimental groups consisted of the middle group and the high group, which received feed containing Chromium chloride at concentrations of 12 g/kg (group B2B, 50% half-lethal dose at 5 days) and 24 g/kg (group C4B, half-lethal dose at 5 days), respectively. After 120 h (5 days) at stage five larval stage, entire midgut tissues were collected from 10 randomly selected live individuals from each experimental group. The tissue samples were dissected on ice and then stored at −80°C in preparation for subsequent 16s rDNA extraction and sequencing analysis.

16S rDNA gene sequencing

The total genomic DNA was extracted employing the hexadecyl trimethyl ammonium bromide (CTAB)/sodium dodecyl sulphate (SDS) method (Ramimoghadam et al., 2012; Xia et al., 2019). DNA quantification and purity were monitored using 1% agarose gel electrophoresis. The DNA samples were diluted to 1 ng/μl using sterile distilled water. Amplification of the 16S rDNA gene was carried out with primers specific for 515F – 806R (V3-V4) regions (Parada et al., 2016; Wurm et al., 2023). The PCR products were quantified and visualized by performing 2% agarose gel electrophoresis with 1× loading buffer containing SYBR Green. A sequencing library was prepared using the NEB Next Ultra DNA Library Prep Kit (Illumina; NEB, USA). Index codes were added, and quality checks were completed using a Qubit 2.0 Fluorometer (Thermo Scientific, USA)

and an Agilent BioAnalyzer 2,100 system (Agilent Technologies, Palo Alto, CA). Finally, the Illumina MiSeq platform (Illumina, NEB, USA) was used for sequencing, producing 300 bp paired-end reads.

16S rDNA statistical analysis

Paired raw reads of all 18 samples were filtered using Trimmomatic v0.38 (Bolger et al., 2014) to remove low-quality reads, including those containing adapters and contaminants. Using a custom-made script, We further excluded reads with a Phred quality score below 20 (Q20 < 90) and a total length of fewer than 50 base pairs. With the high-quality reads secured, we conducted further statistical analysis in the software environment of QIIME II (version 2.01) (Hall and Beiko, 2018; Fung et al., 2021). The DADA2 method was applied for primer trimming, quality filtering, denoising, merging, and chimera removal in the study (Callahan et al., 2016). Initially, the QIIME cut-adapt trim-paired tool removed the primer sequences and discarded the unmatched sequences. Subsequently, DADA2 was employed using the QIIME DADA2 denoise-paired command to perform quality control, denoising, merging, and chimera removal. These steps were performed separately for each library. After denoising all libraries, the ASVs' (amplicon sequence variants) feature sequences and ASV table were merged, and singleton ASVs (ASVs with only one sequence in the entire set of samples) were removed by default. The distribution of sequence lengths was calculated using an R script, considering the high-quality sequences in all samples. The ASVs generated after DADA2 quality control are currently highly recommended by QIIME2. ACB, B2B and C4B group names were assigned to the control, moderate concentrate treatment group of 12 g/kg, and high concentrate group of 24 g/kg, respectively. Each group comprise six independent samples.

We employed various ecological diversity indices to thoroughly examine the alpha diversity of the microbial communities in our samples (Hall and Beiko, 2018; Fung et al., 2021). To determine community richness, the Chao1 and Observed Species indices were used. The Shannon and Simpson indices were employed in quantifying community diversity. We used Faith's Phylogenetic Diversity (PD) index to express evolutionary diversity. Pielou's evenness index was calculated to estimate community evenness, and Good's coverage index was used to assess the coverage of our survey. The statistics for alpha diversity indices are provided in Supplementary File S1.

Downstream analyses included principal component analysis, random forest estimation, UPGMA clustering, and Venn diagram generation, performed using the PersonalBio online platform.[1] PCoA (Principal Coordinate Analysis) analysis was performed using the rarefied ASV table. The "qiime diversity core-metrics-phylogenetic" command was used to calculate four distance matrices: Jaccard, Bray-Curtis, unweighted UniFrac, and weighted UniFrac. These distance matrices were then transformed into sample distances and projected onto a two-dimensional plot. The PCoA results were evaluated based on the explained variance, and the top two components (PCoA1 and PCoA2) with the highest proportion of variation were selected. This study chose the weighted UniFrac distance matrix as it explained the highest proportion of variation. Functional capabilities of the microbiota were evaluated using the PICRUSt2 software (Douglas et al., 2020) to predict the Kyoto Encyclopedia of Genes and Genomes (KEGG) metabolic pathway annotations. Statistical significance (p-values) and false discovery rates (FDRs) were calculated using R-based scripts. The statistical tables of microbial taxa abundance at the genus level, principal component analysis sample scores, random forest analysis feature importance, taxonomical KEGG secondary functional statistics, and different KEGG pathways were shown in Supplementary Files S2–S6.

Non-targeted metabolomics sample preparation and analysis

The same experimental design was adopted for the non-targeted metabolomics, where 18 gut samples under the same chromium treatment were collected and named accordingly using ACB, B2B and C4B. A total of 100 μL of thawed tissue samples were treated with 400 μL of precooled methanol-acetonitrile solution (1:1, v/v), vortexed for 60 s, precipitated for one h at −20°C, and centrifuged at 14,000 g and 4°C for 20 min. Then, the supernatant was freeze-dried before storage at −80°C for further testing (Johnson et al., 2016; Schrimpe-Rutledge et al., 2016; Bauermeister et al., 2022).

UHPLC-QTOF/MS statistical analysis

Utilizing ProteoWizard (version 3.0.4146) (Kessner et al., 2008; Holman et al., 2014), original data was converted into an mzXML format, following which the XCMS software was adopted for peak alignment, retention time correction, and peak area extraction (Mahieu et al., 2016; Domingo-Almenara and Siuzdak, 2020). Multivariate analyses such as Pareto-scaled PCA and orthogonal partial least squares discriminant analysis (OPLS-DA) were carried out using the software SIMCA – P (version 14.1) (Wheelock and Wheelock, 2013; Wu et al., 2019). Metabolites with variable importance in projection (VIP) value greater than one were subjected to a two-sample Student's t-test to determine their significance. The statistical tables of metabolites number at the superclass level, the qualitative collation summary for positive and negative ions, differential metabolites, and enriched KEGG pathways for differential metabolites were shown in Supplementary Files S7–S10.

Omics association analysis

The principal component analysis (PCA) and Co-Inertia Analysis (CIA) were employed to validate the congruence between microbiome and metabolome profiles. Differentially abundant metabolites were subjected to correlation analysis using Spearman correlation. The associations between bacterial taxa and metabolites were identified using 16S rDNA sequencing data. The R language (Kellogg et al., 2020) and Mothur (Chappidi et al., 2019) software were combined to analyze previously mentioned PCA and CIA analyses, draw the matrix heat map, hierarchical clustering, association network, and related parameters. The final correlation between the final differential

1 https://www.genescloud.cn/

microbiota and metabolites was obtained through multiple rounds of screening and calculations.

Results

Alpha and beta – diversity

Through comparison and analysis of alpha diversity parameters across different chromium stress treatments in silkworms' gut microbiota, we can observe the impact of chromium on the gut microbiota of these organisms (Figure 1). First of all, Goods_coverage, a measure of sequence coverage represents how well the true diversity of each sample, maintained a consistency close to 1 across all groups which mean each group was well determined and characterized. According to the data, the ACB group displayed an overall higher Chao1, Faith_pd, Observed_species, and Shannon, suggesting a more diverse gut microbiota than the chromium-exposed groups (B2B and C4B). With increasing chromium concentration (from B2B to C4B), there was a decline in diversity indices, such as Chao1, Faith_pd, Observed_species, and Shannon index, implying a negative impact of chromium stress on the richness and evenness of gut microbiota (Supplementary File S1). Although the B2B group had a decline in diversity metrics compared to ACB, it showed more pronounced diversity than C4B, pointing to a dose-dependent reduction of microbiota diversity under chromium stress. The Pielou_e and Simpson also revealed decreased evenness and dominance in the gut microbiota due to chromium stress. Thus, it can be inferred that chromium disrupts the gut microbiota composition, potentially affecting the abiotic stress response of silkworms.

Beta diversity indexes focus on the differences among samples. Principal coordinates analysis (PCoA), a classical method of non-metric multidimensional scaling analysis that considers the overall distance of samples, is well-suited to the characteristics of ecological data and was thus utilized as the primary analysis tool in this study. The PCoA distance matrix generated from the UniFrac distance matrix explained the highest variation proportion, revealing distinct microbial community profiles among the ACB, B2B, and C4B (Supplementary File S2). Intriguingly, more remarkable dissimilarities were observed between ACB and B2B/C4B, suggesting chromium stress alters silkworms' intestinal microbiota. Specifically, as the chromium concentration increased, silkworms' gut microbiota underwent noticeable shifts, as depicted by the pairwise distances (Figure 2). This implies the substantial impact of heavy metal stress on the stability of gut microbiota, potentially leading to the dysbiosis of the bacterial community. The reproducibility of beta diversity within each group (ACB, B2B, C4B) indicates the robustness of biological conclusions derived from these data. Additionally, an increasing trend in PCoA distances in response to chromium concentration suggests a potential dose-dependent impact of chromium on silkworm gut microbiota. Nevertheless, this observation needs further corroboration through statistically rigorous analyses.

In a multidimensional comparison among groups ACB, B2B, and C4B, according to data drawn from permutation tests represented as distances of samples, there are evident differences to note between each. A diversified Interquartile range typically reflects increased differentiation between individual categories (Figure 3). Group ACB provided a baseline indicative of normal intestinal microbiota functioning in silkworms without chromium intervention. In contrast, groups B2B and C4B show evidence of a significant shift in intestinal microbiota under chromium stress, as gleaned from permutation analysis with Q-values (adjusted *p*-values) at 0.003 for ACB vs. B2B, ACB vs. C4B, and B2B vs. C4B. Since the Q-values are less than 0.05, these differences are statistically significant, demonstrating chromium's substantial impact on the silkworm gut microbiome. Moreover, it is observable that as the chromium pressure increases from B2B to C4B, the interquartile range narrows within each group while the median values elevate culminating at a striking over 0.9 in both the B2B and C4B groups (Figure 3). Implying that a tremendous variation occurs between the moderate and high chromium-stressed groups, it can be deduced that chromium exposure potentially has a dose-responsive influence on silkworm gut microbiota. Such a biological trend, if further affirmed, could have profound implications for understanding chromium intervention effects on other similar biological systems.

Structural diversity of silkworms' midgut microbiota

Upon treating silkworms with varying concentrations of chromium, we observed variations in the taxonomic distribution of gut bacteria among three different groups (Figure 4). The ACB group, which serves as the control group, displays a diverse microbial community, including *Thermus*, *Geobacillus*, *Dietzia*, and *Propionibacterium* as primary constituents. *Weissella's* occurrence in this group stays remarkably low. In contrast, the B2B group subjected to medium chromium concentration presents a dominance of *Weissella*, with an evident decline in Thermus and nearly no presence of *Geobacillus* and *Dietzia*, illustrating a prominent shift in the microbial community structure that can be attributed to the chromium stress. The notable company of *Methylobacterium* and *Micrococcus* also marks this group. The C4B group, subjected to high chromium concentration, shows an interesting adaptive microbial response. While a minor percentage still includes *Weissella*, the dominating species becomes unclassified ("Others") – a factor that suggests a potential emergence of chromium-resistant, uncategorized microorganisms under high mental stress (Figure 4). Propionibacterium exhibits a solid presence alongside elevated levels of *Blautia*. The noted microbiome alterations under varying chromium concentrations could indicate varying degrees of metal tolerance among different microbes, pointing toward adaptive survival strategies under stress. One of the key factors influencing the shift in bacterial diversity may be the variability in biochemical transformations that different strains can activate in the presence of chromium (Supplementary File S3). The predominance of certain species, like *Weissella* in B2B and unclassified organisms in C4B, might be due to their potential chromium-reducing capacities.

Gut microbiota changes and identification of icon species

This study aimed at understanding the distinct microbial taxa that account for the observed disparities among various groups and

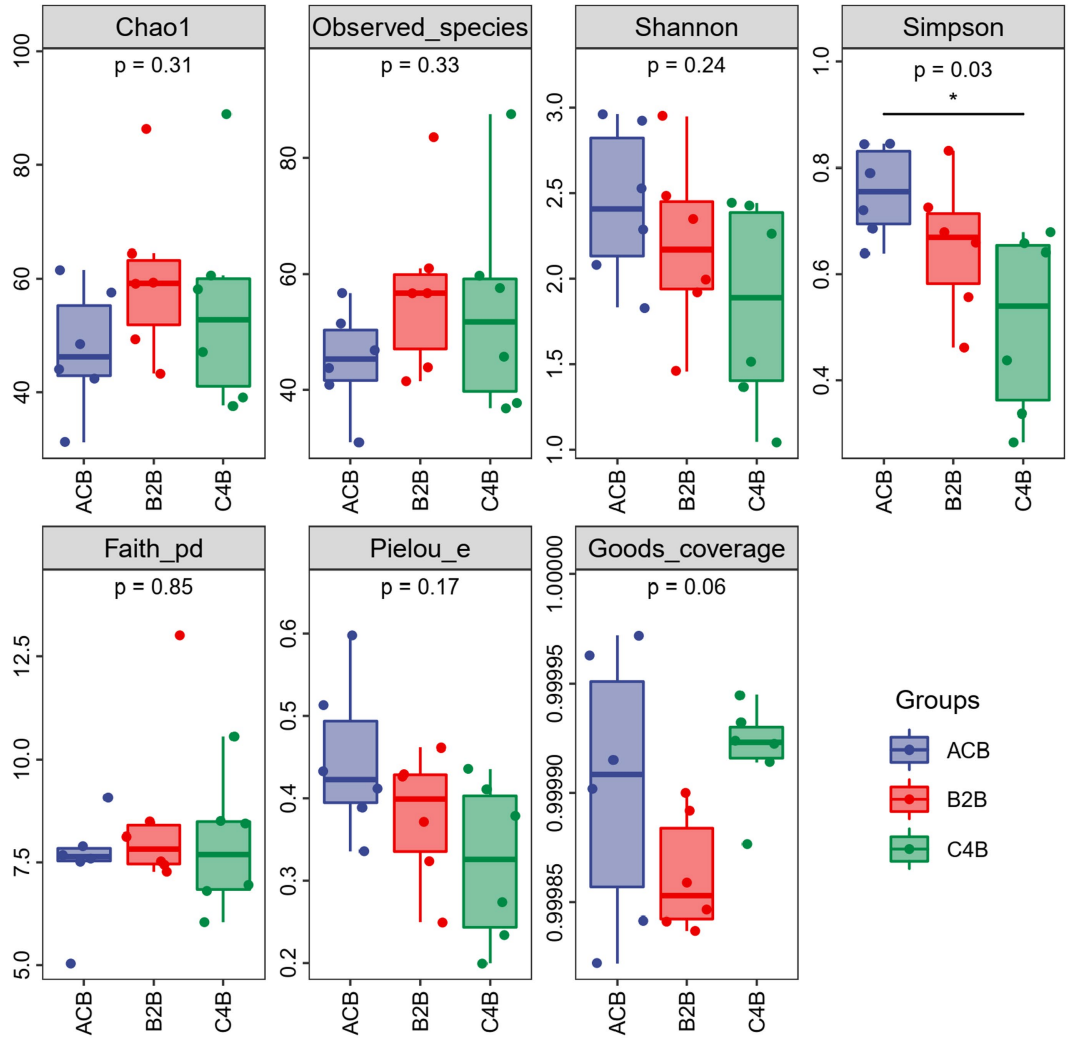

FIGURE 1
Box plot of alpha diversity indices among different treatment groups.

clarifying the mechanisms that shape gut microbiota structure. We utilized a comprehensive analytical approach, leveraging supervised and unsupervised learning methodologies. This enabled us to classify microbial communities effectively, pinpoint key taxa responsible for observed variations, and explore the mechanisms structuring gut microbiota across different groups. For example, we employed PCA, an unsupervised learning method, to condense our data and simplify the representation of intricate microbial communities, discerning primary trends and patterns. We also used Random Forests, a supervised learning method, to create predictive models based on microbial composition patterns. RFs adeptly handled high-dimensional, multicollinearity data, thereby identifying essential microbial taxa that essentially explained group disparities. Finally, we used Linear discriminant analysis Effect Size (LEfSe) to combine statistical significance with biological relevance. This approach aided us in identifying microbial taxa that could act as biomarkers for different groups.

The observed heatmap underscores the integral role that chromium plays in molding the bacterial assembly within the gut microbiota inhabiting silkworms (Figure 5). As depicted in Figure 4; the heatmap provides a clear visual representation of the composition and relative abundance of different microbial taxa within each group. The consistency of microbial taxa across multiple samples and the microbial compositions within each group were accessed through cluster analysis of columns and rows. Within the dimensions of the ACB group, the genera *Thermus*, *Geobacillus* and *Bacillus* assert dominance among the battery of taxonomic clusters, insinuating their substantial role in maintaining the unperturbed physiological state of silkworms under conditions devoid of environmental stressors. Concurrently, the onset of moderate chromium stress in the B2B group triggers a remarkable amplification in the population density of *Weissella*, accompanied by a concurrent diminution in the prevalence of *Thermus*. This raises the potential hypothesis of chromium resistance or detoxifying capability vested within the *Weissella* genus. In stark contrast, within the high chromium exposure group C4B, the relative abundance of *Propionibacterium* displays a marked increase, parallel to a simultaneous dwindling of *Weissella* (Figure 5). Such differential microbial responses propound potential adaptive modifications under diverse chromium concentrations. Intriguingly, the emergence of specific icon bacterial groups, such as *Weissella* and

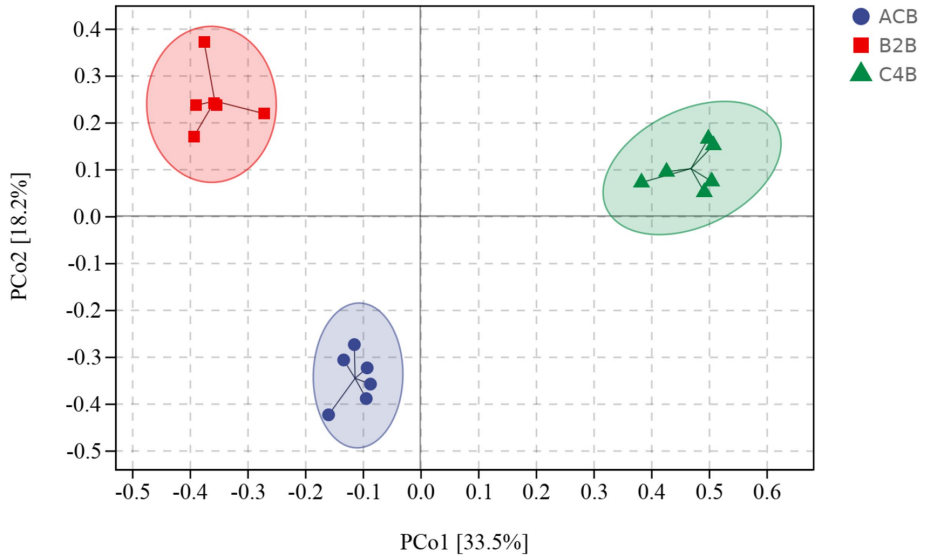

FIGURE 2
PCoA plot denotes the distance between samples integral. Sample distances were derived from a weighted UniFrac distance matrix.

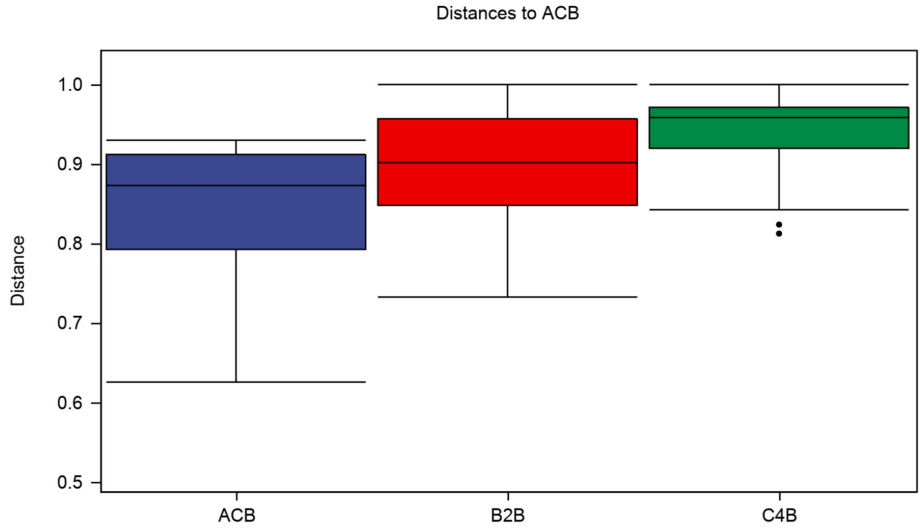

FIGURE 3
Box plot illustrates the distributions of intra-group and inter-group distances between the sample within each particular group and the samples within the rest of the groups. The top and bottom lines of the box denote the upper and lower quartiles (Interquartile range); the median line signifies the median of the sample groups, the edge lines above and below the box detect the maximum and minimum values; any data points outside these edge-lines are considered as outliers.

Cupriavidus, associated with robust heavy metal affinity portends a prospective biochemical remediation tactic employed by the gut microbiota.

Subsequently, our comparative analysis elucidates the complex interplay between microbial representatives and varying chromium stress conditions, as mapped in the context of Random Forest feature importance (Supplementary File S4). The centerpiece of our findings lies in the significant cardinal shifts in microbial populations across these groups. The markedly heightened prevalence of *Weissella paramesenteroides* in both chromium-stressed groups, B2B and C4B, when contrasted with the control group, underpins a plausible endurance or functional adaptation in the face of chromium stress (Figure 6). Contrarily, *Enterococcus casseliflavus*, conspicuous in its presence within the control environment, is wholly absent in chromium-stressed groups — hinting at a possible vulnerability to chromium stress. As we delve deeper, an intriguing narrative unfolds around *Propionibacterium acnes*; its numbers surge within the C4B group while maintaining constancy in the B2B group (Figure 6). Catching one's attention is the high prevalence of this bacteria under control conditions, which, unfortunately, meets with a dramatic decline in B2B; the trend, however, sees a relative recovery within the C4B group.

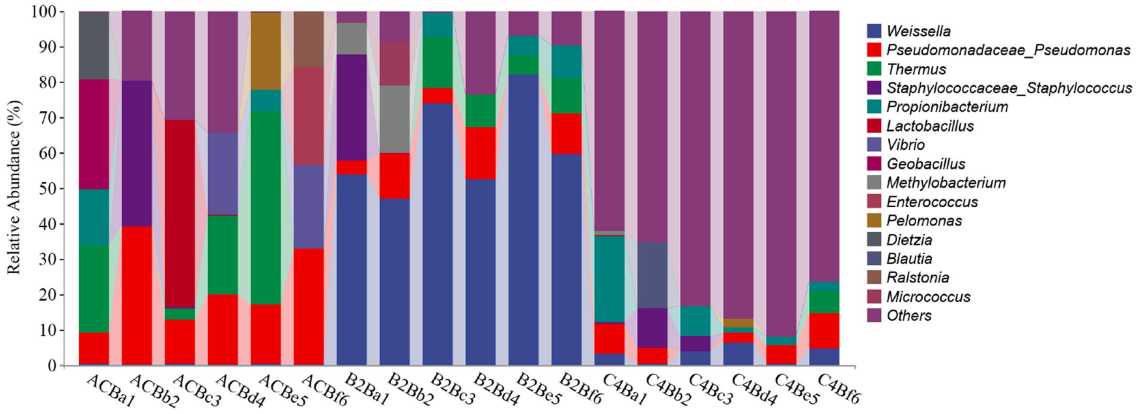

FIGURE 4
Bar plot presented delineates the taxonomic distribution of bacteria across three different groups treated with varying concentrations of chromium.

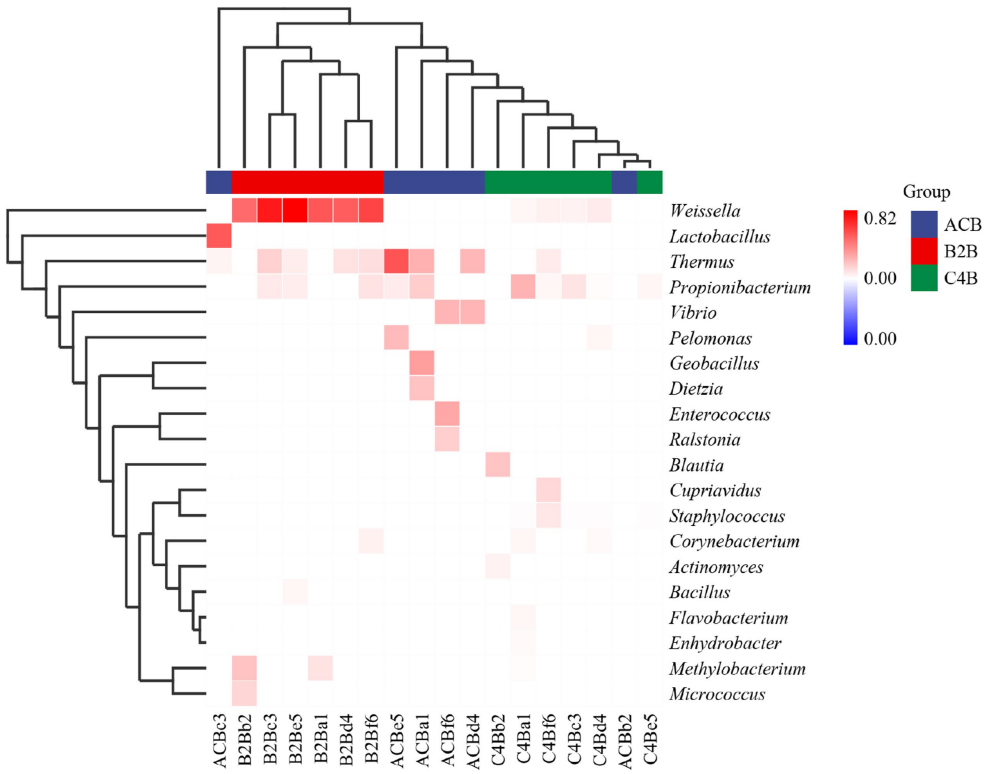

FIGURE 5
Heatmap cluster map shows the chart of microbiome abundance. The single cluster method was used for both the rows and columns.

Meanwhile, we employed Linear Discriminant Analysis Effect Size (LEfSe) analysis to discern the critical discriminatory species between different groups robustly, often referred to as our biomarker icon species. Distinct taxa abundance shifts were observed in ACB, B2B and C4B chromium-stressed silkworm gut microbiota. In the control group ACB, *Gammaproteobacteria,* especially *Pseudomonadales*, was more abundant, hinting at their foundational role in an unstressed silkworm gut environment. Conversely, in the chromium-treated groups (B2B and C4B), a decline in *Proteobacteria* abundance was accompanied by a marked rise in *Firmicutes*, notably *Bacilli* of *Weissella* and *Bacillales*. *Weissella paramesenteroides*, a species known to exhibit probiotic properties, showed significance in the B2B group, suggesting an adaptive response (Figure 7). Its presence is an indicator species for chromium stress response, which could offer a mitigation strategy against cytotoxicity induced by metals. In the C4B group, the variety of *Firmicutes* increased to include *Staphylococcus saprophyticus*. Such bacteria, well-suited to endure high osmotic stress and pH extremities, underscores the intensified stress environment in C4B. Moreover, *Actinobacteria* (ACK_M1), known

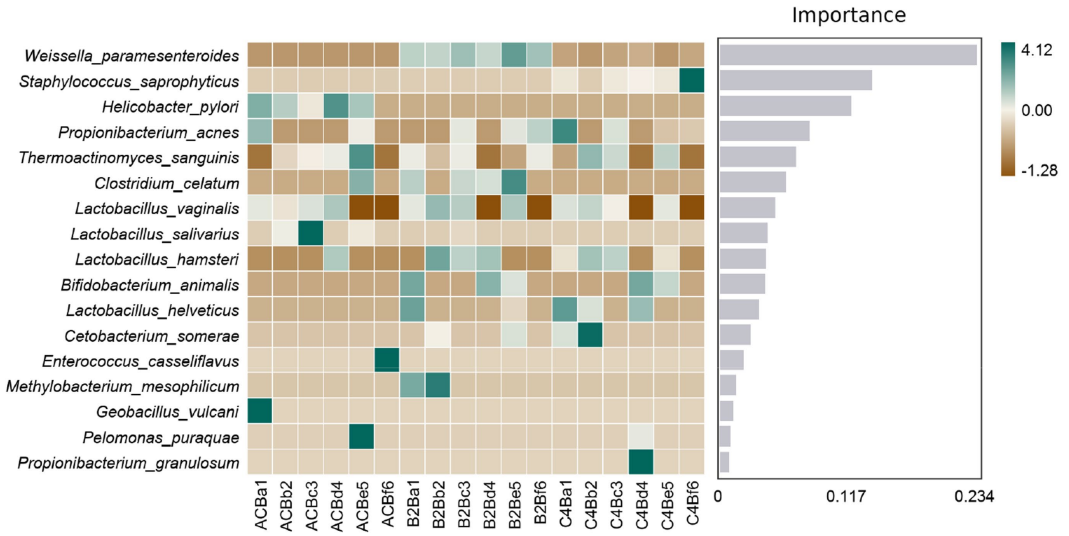

FIGURE 6
Heatmap illustrating the abundance distribution of species across different samples/groups. Species are ranked from top to bottom based on their importance to the model, with the significance diminishing progressively.

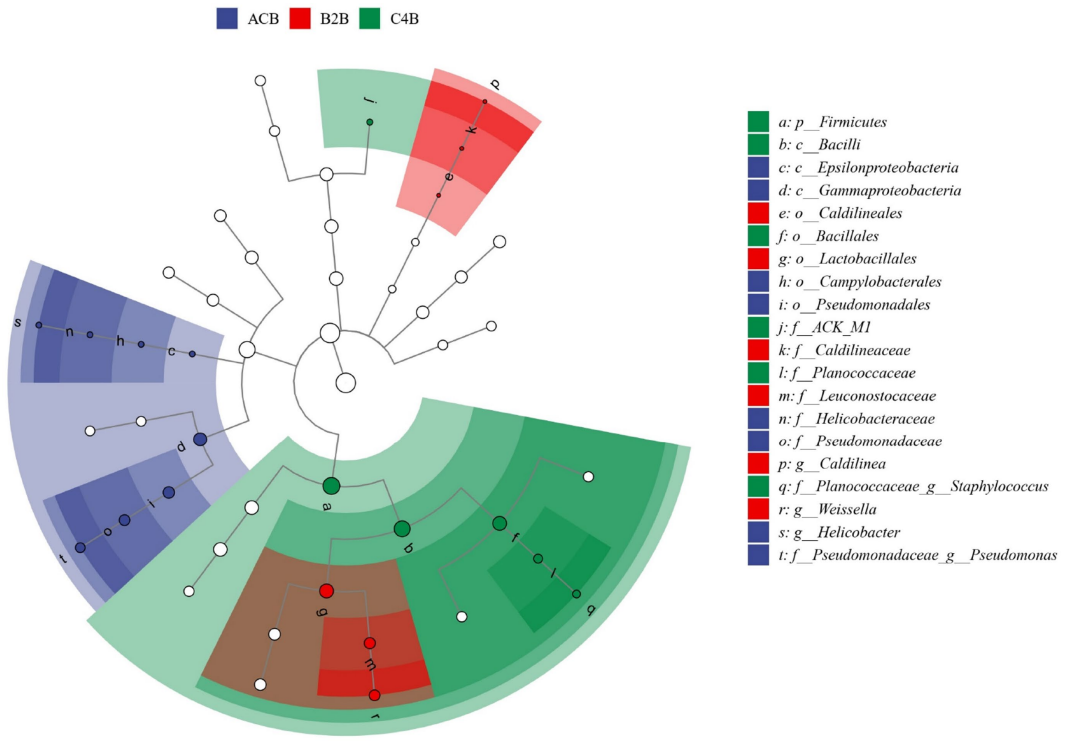

FIGURE 7
The LEfSe dendrogram represents the hierarchical organization of central taxonomic units from phylum to genus (from inner to outer circles) present within the community samples. The size of the nodes correlates with the average relative abundance of the respective taxonomic unit. Hollow nodes represent taxonomic units with non-significant (p value > 0.05) intergroup differences, whereas other colored nodes signify the taxa presenting significant (p value <0.05) group disparities. Alphabet labels denote the names of taxonomic units with significant (p value <0.05) intergroup variation.

for their role in recalcitrant compound breakdown in C4B, might reflect an attempt to detoxify chromium compounds.

Then, we sought to delve deeply into the range of biological impacts. Based on the functional annotation table retrieved through Picrust2 analysis, we applied a Wilcoxon rank-sum test to draw out variations in the stimulation of diverse KEGG biochemical routes within these three groups (Supplementary Files S5, S6). Among the key findings, the impact on microbiota functionality, particularly on biosynthetic and

degradation activities, demonstrated significant changes (p value <0.01) in response to chromium stress. The B2B group correlated with a broad suppression of most biosynthetic pathways, particularly those responsible for carbohydrates, cell structure, cofactors, prosthetic groups, electron carriers, and vitamins. Such shifts suggest a scenario of biological unrest, marked by increasing dependence on exogenous resources and dwindling endogenous biosynthetic capacities.

Conversely, the C4B group, which endured the maximum chromium concentration, showed a relative boost in all degradation categories, barring aromatic compound degradation. This trend potentially mirrors a stress-triggered metabolic upshift to ensure survival. Chromium exposure fundamentally reshaped fermentation, TCA cycle, and electron transfer processes to counter chromium-induced stress. Chromium impedes normal metabolic activities, with more significant concentrations amplifying these disturbances. A notable rise in antibiotic resistance represented a defensive countermeasure, suggesting an innate protective strategy to maintain microbiota equilibrium amidst the chromium-triggered environmental upheaval. These alterations have substantial implications for the ecological balance of gut microbiota and, consequently, the physiological performance, stress resilience, and potential biological toxicity of *B. mori*.

However, although our study identified several metabolic pathways from various samples, owing to limited sample size and the presence of outliers, no meaningful differences were observed in most of these pathways. We conducted species composition analysis of KEGG pathways using a stratified sample metabolic pathway abundance table. Among these, only the allantoin degradation IV (anaerobic) pathway was significantly upregulated ($p < 0.05$) in the C4B group as compared to both B2B and ACB groups. The observed upregulation of the allantoin degradation IV pathway in the C4B group sheds light on the notable metabolic changes this group is undergoing. This group potentially resorts to anaerobic allantoin degradation due to changing microenvironmental conditions. Allantoin degradation, primarily known for its role in nitrogen metabolism under anaerobic conditions, may indicate an alternative metabolic adaptation of the organisms within the C4B group. While we determined the composition of this pathway, a substantial amplification of the unclassified_*Bacillales* was detected (Figure 8). This observation could suggest that these bacteria have developed a survival strategy in conditions marked by increasing chromium concentrations, as inferred from their scarceness or complete absence within groups ACB and B2B. Similarly, the noticeable propagation of *Weissella* within both B2B and C4B cohorts was found repetitively, which once again denotes a probable role for this bacterium in responding to chromium-induced perturbations. Additionally, some bacterial strains, such as *Cupriavidus* and unidentified_*Myxococcales*, appear to be exclusive residents of the C4B group, potentially indicating their detoxification functionality within high-chromium environments.

Non-targeted metabolomics characterization and comparative analysis

Another pivotal cornerstone supporting our study is underpinned by comprehensive metabolomics analysis, illuminating the interplay

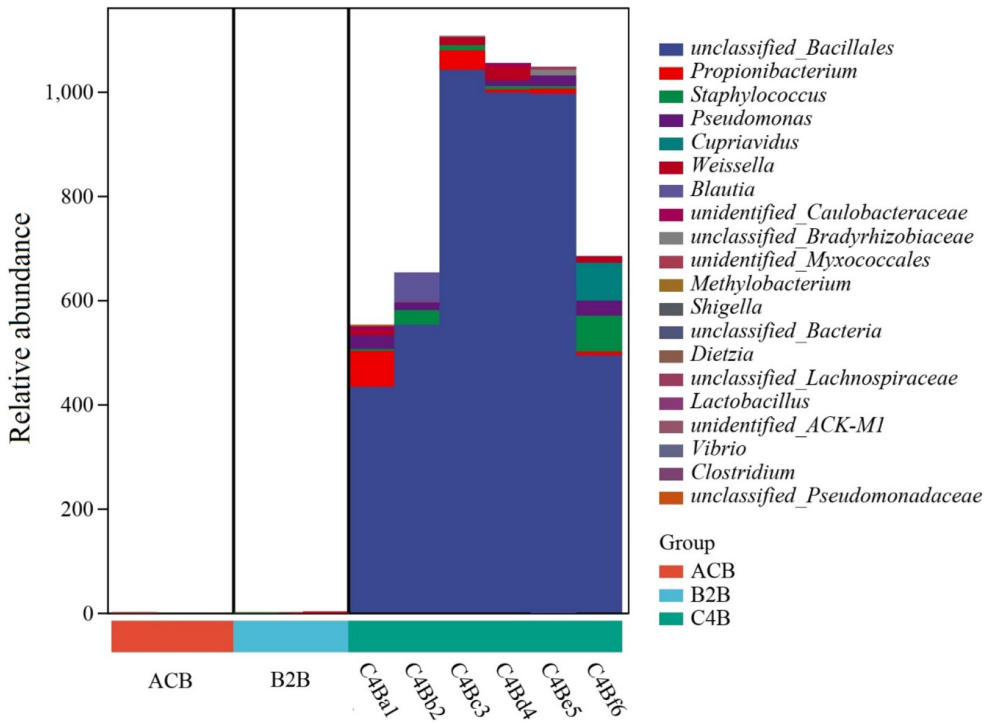

FIGURE 8
Statistical composition of species contributions to the allantoin degradation IV (anaerobic) pathway. The *x*-axis represents the sample labels, identified by different colors according to their group membership; the *y*-axis displays the relative abundance of the associated allantoin degradation IV (anaerobic) pathway. Contributions to the pathway from various taxonomic units at the taxa level are visualized as layered stacks in varying color gradients.

between the host and its microbiome and delineating the contribution of these interactions to the studied physiological phenomena. The overall metabolomic profile highlights various superclasses of metabolites identified in the intestinal microbiota following exposure to chromium. The three most dominant metabolite superclasses are "Organic acids and derivatives" (634 metabolites), "Lipids and lipid-like molecules" (546 metabolites), and an undefined category (277 metabolites) (Figure 9; Supplementary File S7). The copious diversity and quantities of "Organic acids and derivatives" suggest a high metabolic turnover involving carboxylic acids, esters and carbonyl groups, potentially related to energy production, detoxification, and chromium resistance. "Lipids and lipid-like molecules" superclass, being second abundant, might imply modifications of structural constituents of cell membranes and signaling molecules, which could be instrumental in perpetuating the chemical defences against chromium-induced stress. Perhaps signaling cascades initiated under chromium exposure might be regulated by lipid-mediated pathways, an area worth exploring. The least represented categories, such as "Lignans, neolignans and related compounds" and "Organosulfur compounds," might hint at their less significant roles in managing chromium-related disturbances. However, their relatively low abundance must not be mistaken as lacking biological significance, considering they might possess specialized functions rather than broad-spectrum activity.

Then, our study delineates the wide-ranging ramifications on the metabolome, examined across three experimental tiers. We undertook a comparative analysis of distinctions in Variable Importance in the Projection (VIP) and fold change (FC) within the ACB, B2B, and C4B clusters about metabolite fluctuations. The VIP score delineates the significance of a metabolite in discriminating between groupings, while fold change illuminates the extent of alteration in metabolite concentrations between two groups. Noteworthy divergences in VIP scores and fold changes associated with specific metabolites could elucidate chromium's biological implications on the silkworms' gut metabolism, encapsulating functional, physiological, and ecological facets, stress resistance, and physical toxicity. The ACB collective served as a reference, whereas the B2B and C4B factions represent moderate and high chromium exposure, respectively (Supplementary File S8).

A collection of metabolites demonstrated elevated VIP scores and fold changes within the B2B cohort in contrast to the ACB group, including D-mannitol 1-phosphate, L-iditol, glutamine, Glutaraldehyde, asparagine, urocanic acid, glutamic acid, Histidine, dihydropyrimidine, and L-gulono-1,4-lactone. These disparities in metabolite concentrations intimate that chromium exposure governs the metabolism of carbohydrates, amino acids, and organic acids in the silkmoth gut. The implicated metabolites partake in many physiological undertakings, such as energy metabolism, antioxidant defence, protein biosynthesis, and signal transduction. Amplified levels of Histidine and dihydropyrimidine might enlighten the mobilization of stress response mechanisms within the B2B configuration (Supplementary File S8).

Upon juxtaposition of C4B and ACB, several metabolites showcased remarkable adjustments in VIP scores and fold changes, including phenol, urocanic acid, D-galactarate, N-fructosyl pyroglutamate, 17,20-dimethylprostaglandin F1.alpha., and gentisic acid. These perturbations emphasize the influence of intensified chromium exposure on gut metabolism. Phenol, urocanic acid, and D-galactarate are linked with oxidative stress and inflammation; N-fructosyl pyroglutamate and 17,20-dimethyl prostaglandin F1.alpha. Possibly contributes to regulating gut barrier function and immune response, and gentisic acid is associated with detoxification routes and antioxidant processes. A comparison between B2B and C4B cohorts unraveled additional metabolites with significant shifts ($p < 0.01$) in VIP scores and fold changes, encompassing a range of amino acids, organic acids, and carbohydrates. These metabolites comprise glutamine, dihydrouracil, 4-ketopimelic acid, Lpc 18:2, Histidine, and L-pipecolic acid. Glutamine, dihydrouracil, and L-pipecolic acid correlate with stress response, while 4-keto pimelic acid and Lpc 18:2 might engage in lipid metabolism. Histidine is crucial in antioxidant defence, immune modulation, and protein synthesis. The differential metabolite profiles discerned from this

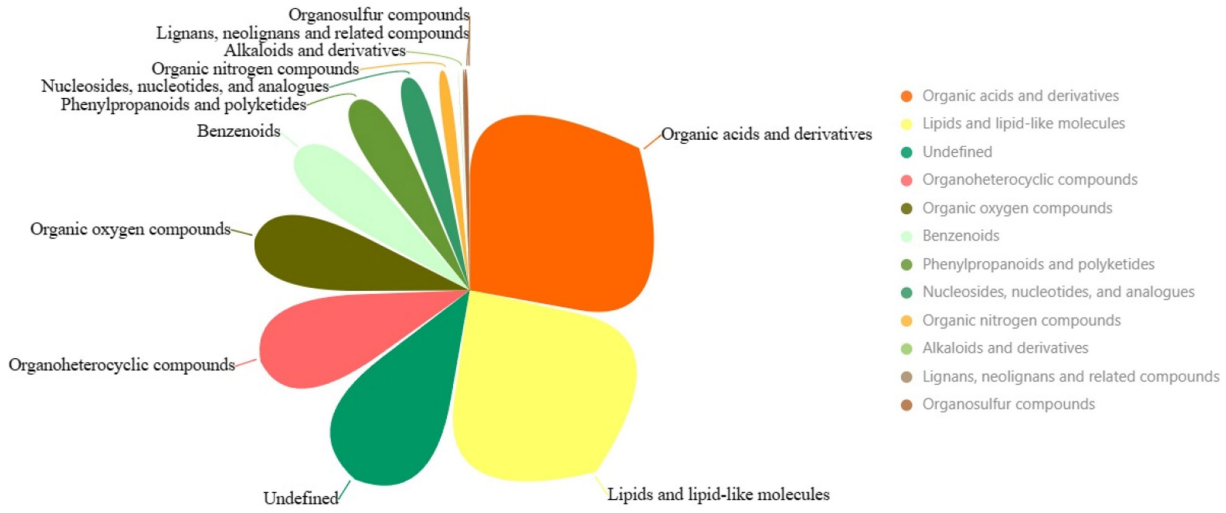

FIGURE 9
The pie chart illustrates the superclasses of metabolites. Larger areas represent more dominant categories.

study indicate that chromium exposure interferes with diverse aspects of silkworm gut metabolism. The identified metabolites participate in various biological functions, incorporating energy metabolism, stress response, immune regulation, and antioxidant events. Fluctuations in metabolite concentrations responsive to chromium exposure suggest potential adaptations within the silkworms' gut to chromium-induced stress (Supplementary File S9).

Moreover, while we assign the KEGG functional annotations to these differential metabolites, the same pattern with the gut microbiota is observed where B2B and C4B groups manifest significant deviations in an array of metabolic trajectories when contrasted against ACB, accentuating the biological relevance of metabolite inconsistencies. A prominent observation is stress-induced dysregulation. Essential pathways instrumental for amino acid biosynthesis, particularly the 'Arginine biosynthesis' and 'Valine, leucine, and isoleucine biosynthesis', underwent substantial perturbations, indicative of a pivotal regulation and redistribution of amino acid metabolism in response to chromium. Analogously, 'ABC transporters', 'Protein digestion and absorption', and 'Biosynthesis of amino acids were significantly enriched (p value <0.05), signifying a potential physiological adaptation aimed at attenuating the biomechanical hazards (Figure 10A). Moreover, the metabolic machinery regulating sugar metabolism displayed tangible transformation, signaled by alterations in pathways like the 'Pentose Phosphate Pathway', 'Fructose and Mannose Metabolism', and 'Pentose and glucuronate interconversions, providing evidence of metabolic reconfiguration for energy homeostasis under duress. A marked upregulation in detoxifying and oxidative stress-responsive networks, such as 'Ascorbate and aldarate metabolism' and 'Flavone and Flavonol biosynthesis', paints a vivid portrayal of the orchestrated defensive measures (Figure 10B). Continuing our comparative analysis between C4B and B2B, an escalating trend in these metabolic distortions is apparent as chromium dosage surges, with newer, hitherto insignificant pathways like the 'Phosphotransferase system (PTS)', 'Glyoxylate and dicarboxylate metabolism', and 'Neuroactive ligand-receptor interaction' claiming prominence (Figure 10C; Supplementary File S10).

Subsequently, after dual validation of our metabolomics data against microbial abundance through PCA and CIA analyses (Supplementary Figures S1, S2), we computed the Spearman rank correlation coefficients between these two sets. The correlation matrix results initially show a pervasive association between the two types of omics data, projecting a multiplex relationship between bacterial species and metabolic products, with numerous significant correlations ($p < 0.05$) present (Supplementary File S11). With a meticulous inspection, we identified our previously pointed out marker of differential bacterial species, such as *Weissella*, *Thermus*, *Geobacillus*, etc., as they had substantial connections with various types of differential metabolic products. These species are considered to have a crucial functional impact.

A comprehensive analysis of the presented data reveals a complex interplay between different bacterial species and metabolites, shedding light on its biological significance in the silkworm gut microbiota under chromium stress. Notably, *Weissella* and *Pelomonas* represented the marker species with distinct patterns of association with various metabolites. *Weissella* exhibited a positive correlation with metabolites

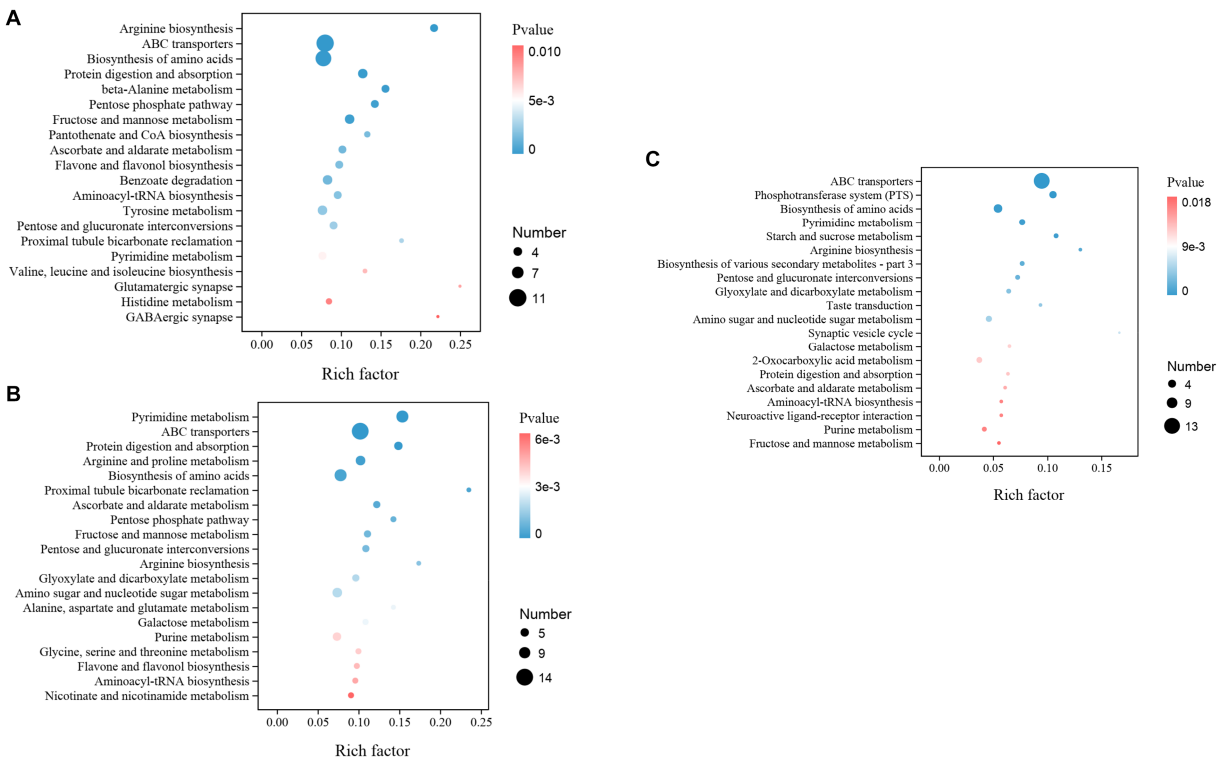

FIGURE 10
The KEGG enrichment map illustrated the top different metabolic functions among groups. **(A)** B2B vs. ACB; **(B)** C4B vs. ACB; **(C)** C4B vs. B2B. The number of genes and p-values are shown.

such as Glutaraldehyde (0.5418), 4-keto pimelic acid (0.5501), and N-epsilon-formyl-l-lysine (0.3209), while negatively correlating with N-.alpha.-(tert-butoxycarbonyl)-l-histidine (−0.4262) and Histidine (−0.3870) (Figure 11; Supplementary File S11). These patterns suggest a potential role of *Weissella* in enzyme regulation and synaptic processes that are critical under chromium exposure. Conversely, *Pelomonas*, though demonstrating relatively weaker correlations, showed a possible involvement in lipid metabolism, such as its positive relationship with Isobutyryl-l-carnitine (0.0113) and a negative one with Lpc 18:2 (−0.2910). The function of *Pelomonas* in lipid metabolism may underscore its potential in maintaining homeostasis and chromium toxicity resistance. Beneficial bacteria such as *Weissella*, *Propionibacterium*, *Methylobacterium*, *Cupriavidus*, and *Bifidobacterium* displayed notably strong correlations with metabolites like Glutaraldehyde, 4-ketopimelic acid, N-epsilon-formyl-l-lysine, and N-.alpha.-(tert-butoxycarbonyl)-l-histidine. These correlations suggest that these metabolites might modulate gut microbiota under chromium stress. Notably, *Weissella* showed a strong association with Isobutyryl-l-carnitine and Lpc 18:3 metabolites. *Propionibacterium* had a tightly coupled relationship with N-epsilon-formyl-l-lysine and 1-oleoyl-2-linoleoyl-rac-glycerol. *Methylobacterium* exhibited notable correlations with Glutaraldehyde and 4-ketopimelic acid. *Cupriavidus* was highly associated with Glutaraldehyde, 4-ketopimelic acid, and N-. Alpha. -acetyl-l-ornithine metabolites and *Bifidobacterium* revealed connections with N-epsilon-formyl-l-lysine and Isobutyryl-l-carnitine. The potential implications of these associations are speculated to indicate the biological function of chromium within the silkworm gut environment (Figure 11). The association of aromatic metabolites such as Glutaraldehyde with *Methylobacterium* may suggest the biotransformation capability and metabolic versatility of this bacterium upon chromium exposure. Likewise, the changes associated with isobutyryl carnitine and *Weissella* might underscore an elevated stress response and potential toxicity. Additionally, the dialog between *Cupriavidus* and Glutaraldehyde, or *Bifidobacterium* with acetyl-l-ornithine, might profoundly influence gut homeostasis, proving beneficial in chromium resistance.

Discussion

Gut microbiota plays a crucial role in influencing the health and wellbeing of the host organism (Ceja-Navarro et al., 2015; Aksoy, 2018; Wang et al., 2020). In this study, we investigated the changes in gut microbiota composition in response to varying levels of chromium stress in *B. mori*. Our findings provide valuable insights into the mechanisms underlying gut microbiota structure in different groups and shed light on the potential adaptations of gut microbiota to chromium stress.

We analyzed the abundance chart of the microbiome to identify substantial variations in microbial diversity across different experimental groups. The results highlighted the integral role of chromium in shaping the bacterial community within the gut of

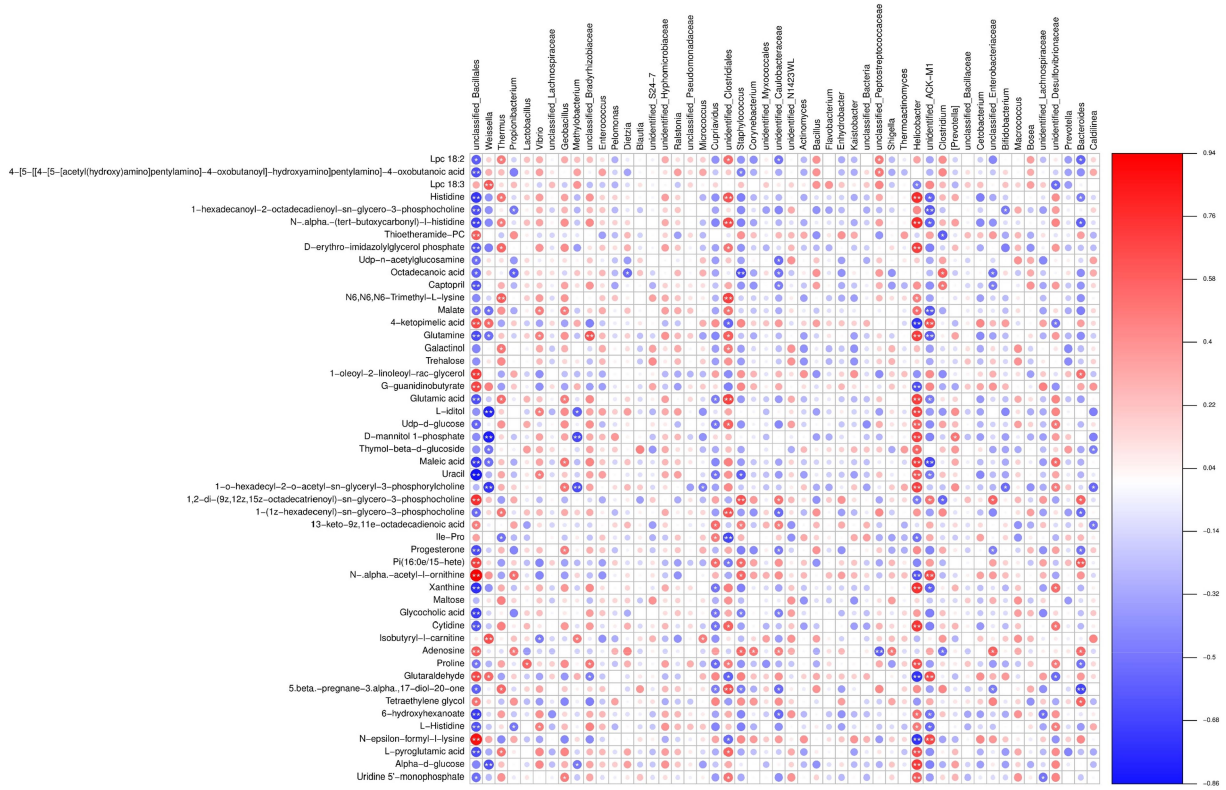

FIGURE 11
Heatmap illustrating the correlation between microbial species and metabolomic profiles. A positive correlation is depicted in red, while a negative correlation is shown in blue. The color intensity represents the strength of correlation. The pairs of "microbiota–metabolite" demonstrating significant association ($p < 0.05$) are indicated by asterisks.

silkworms. The control group (ACB) exhibited dominance of specific microbial taxa, such as *Thermus*, *Geobacillus*, and *Bacillus*, which are likely involved in maintaining the normal physiological state of silkworms under unstressed conditions. In the groups subjected to chromium stress (B2B and C4B), we observed alterations in the prevalence of specific taxa. The abundance of *Weissella* increased in the B2B group, while the prevalence of *Thermus* decreased, suggesting a potential chromium resistance or detoxification capability in *Weissella*. Similarly, in the C4B group with high chromium exposure, *Propionibacterium* showed a marked increase, while *Weissella* decreased. These shifts in microbial populations indicate potential adaptive modifications to cope with varying levels of chromium stress (Cava et al., 2009; Teixeira et al., 2021; Ahmed et al., 2022).

We employed Linear Discriminant Analysis Effect Size (LEfSe) analysis further to dissect the key discriminatory species between different groups. This analysis revealed distinct shifts in the abundance of taxa among the ACB, B2B, and C4B groups. In the control group ACB, we observed a higher quantity of *Gammaproteobacteria*, particularly *Pseudomonadales*, which may contribute to the healthy gut profile of silkworms in the absence of stress (Keller-Costa et al., 2014; Lin et al., 2016). In contrast, the chromium-treated groups (B2B and C4B) showed a decline in Proteobacteria abundance alongside an increase in Firmicutes, specifically *Weissella* (Fusco et al., 2015; Teixeira et al., 2021) and *Bacillales* (Santana et al., 2016; Daquila et al., 2021). *Weissella paramesenteroides*, a species known for its probiotic properties (Libonatti et al., 2019; Prado et al., 2020), displayed significance in the B2B group, suggesting an adaptive response to chromium stress. In the C4B group, the abundance of Firmicutes expanded to include *Staphylococcus saprophyticus* (Golledge, 1988; Ehlers and Merrill, 2023), indicating a more intense stress environment. Actinobacteria (ACK_M1) in the C4B group suggests an attempt to detoxify chromium compounds. These findings highlight the importance of specific microbial taxa in responding to chromium stress and potentially contributing to the protection and adaptation of the host organism.

Furthermore, we investigated the functional impact of chromium stress on gut microbiota by analyzing the stimulation of diverse KEGG biochemical pathways using Picrust2 analysis. The results revealed substantial changes in biosynthetic and degradation activities in response to chromium stress, consistent with previous acknowledgements (Vincent and Lukaski, 2018; Vincent, 2019; Li Y. et al., 2022). The B2B group showed suppression of most biosynthetic pathways, indicating an increased reliance on external resources and reduced endogenous biosynthetic capacities. On the other hand, the C4B group, exposed to high chromium concentrations, exhibited a relative boost in degradation pathways, excluding aromatic compound degradation. This shift suggests a metabolic upshift to ensure survival under stressful conditions. Chromium exposure also reshaped fermentation, TCA cycle, and electron transfer processes, likely as a response to counteract chromium-induced stress. Notably, an increase in antibiotic resistance was observed, potentially serving as a defensive countermeasure to maintain microbiota equilibrium in the presence of chromium stress. These alterations have significant implications for the ecological balance of gut microbiota and the physiological performance, stress resilience, and potential biological toxicity of silkworms.

Although we identified several metabolic pathways, limitations such as small sample size and the presence of outliers prevented crucial differences in most of these pathways. However, the allantoin degradation IV (anaerobic) pathway was notably upregulated in the C4B group compared to the B2B and ACB groups, indicating metabolic adaptations to changing microenvironmental conditions. The amplification of *unclassified_Bacillales* in the C4B group suggests a survival strategy in states with increasing chromium concentrations. Comprehending the relationship between allantoin degradation and *Bacillales*, an order of Gram-positive bacteria offers fresh insights into their metabolic versatility and resilience in hostile environments (Martínez-Gómez et al., 2014). The latest investigations have shown that several *Bacillales* members harbor exceptional enzymatic machinery enabling them to degrade allantoin, a nitrogen-rich compound produced from purine metabolism (Martínez-Gómez et al., 2014; Ma et al., 2016; Li et al., 2017). One pivotal gene locus, the UreD cluster, reportedly catalyzes allantoin degradation. Using *Bacillus subtilis* as a representative of *Bacillales*, researchers have empirically identified the presence of this gene cluster. Its possession confers an adaptive advantage to the bacterium, particularly in nitrogen-deficient settings, enabling allantoin to serve as an alternative nitrogen source (Li et al., 2017). A dedicated biological examination of *Bacillus subtilis* implicates that this bacterium selectively metabolizes allantoin during nutrient deprivation, as manifested by the amplified expression of associated enzymes, such as Allantoicase and Uricase (Ma et al., 2016). The fundamental mechanism underscoring this is the detoxification process, which sees the decomposition of allantoin into simpler, non-toxic compounds, thereby minimizing potential oxidative stress that can harm bacterial cells. Through such allantoin detoxifying pathways, *Bacillales* present metabolic flexibility, capable of withstanding nitrogen scarcity by switching their nitrogen source. This breakthrough understanding unravels a part of the survival strategy of bacteria in hostile conditions, proving potentially beneficial in understanding the role of microorganisms in biogeochemical nitrogen cycles. The repeated propagation of *Weissella* in both B2B and C4B groups suggests its potential role in response to chromium-induced perturbations. Additionally, specific bacterial strains such as *Cupriavidus* and *unidentified_Myxococcales* (Schäberle et al., 2014; Cao et al., 2019) were exclusively found in the C4B group, potentially indicating their detoxification functionality in high-chromium environments.

In response to the escalating problem of non-biodegradable heavy-metal contamination, bioremediation via biological agents, particularly *Bacillales*, has emerged as a potentially effective alternative to traditional physicochemical decontamination methods (Wróbel et al., 2023). Studies reveal that *Bacillales* bear exceptional heavy-metal detoxifying properties, enabling their practical use in remediating contaminated environments. Research demonstrates *Bacillales*' ability to facilitate heavy-metal ion adsorption by forming biofilms and biosorption mechanisms—experiences with *Bacillus* sp. *GH-s29* and *Bacillus* spp. *CPB4* strain provides proof of concept, each successfully removing heavy-metal ions from water systems (Maity et al., 2023). The heavy-metal resistance genes present in species like *Bacillus oceanisediminis* 2,691 underline the genetic basis for this detoxification (Kim et al., 2007; Maity et al., 2023). Moreover, *Bacillus cereus RC-1* has been shown to bioaccumulate heavy metals while releasing cations, potentially benefiting plant growth in contaminated soils. This phenomenon was observed in an experiment with Pakchoi plants, which showed increased biomass and reduced Cd and Pb uptake when grown with heavy metal-immobilizing bacteria (Jung et al., 2016; Huang F. et al., 2018; Han et al., 2020). These findings

highlight *Bacillales*' significant potential for developing bioremediation solutions for heavy-metal contamination. However, current studies are predominantly laboratory-scale, necessitating field-based, long-term studies on their practical efficacy. Further research into specific detoxifying mechanisms of *Bacillales* to enhance their functions, coupled with developing technologies for their selective growth and application, could significantly elevate our ability to manage heavy-metal contamination and mitigate associated risks.

Nevertheless, we employed non-targeted metabolomic characterization to cope with the microbiota analyses, devising an insightful perspective on the metabolic landscape amidst varied chromium exposure. The metabolites portraying differential concentrations paint a compelling picture of energy metabolism, stress response, immune regulation, and antioxidant processes, embodying the multifaceted nature of their response. Prominently, metabolites such as D-mannitol 1-phosphate, L-iditol and glutamine demonstrated by VIP scores and fold changes were under the B2B group. These metabolites hold a pivotal role in carbohydrate and amino acid metabolism, antioxidant defence, and protein biosynthesis (Mancera et al., 2002; Oosaka, 2009; Cruzat et al., 2018; Coqueiro et al., 2019; Nguyen et al., 2019), thus attesting to the metabolic flexibility of silkworms. Under the C4B group, we observed significant shifts in metabolite concentrations, underscoring increased oxidative stress, inflammation, and an enhanced detoxification and antioxidant response. Moreover, we noticed a direct correlation between the increased chromium dosage and the degree of metabolic distortions, inferring adaptive changes in the metabolic landscape. Importantly, functional annotation via the KEGG highlighted the considerable impact on metabolic pathways, mirroring the transformations ignited by chromium stress.

Exploring the association of bacterial abundance and metabolic alteration, we identified an intricate network underlining the interrelation between diverse bacterial species and their metabolic byproducts, emphasizing their functional significance during chromium exposure. Certain bacterial species, namely *Weissella*, *Pelomonas*, *Propionibacterium*, *Methylobacterium*, *Cupriavidus* and *Bifidobacterium*, exhibited strong correlations with differential metabolites, hinting at their potential contribution in chromium detoxification, enzyme regulation, lipid metabolism, antioxidants production, stress response and homeostasis maintenance (Cava et al., 2009; Keller-Costa et al., 2014; Lin et al., 2016; Dong et al., 2019; Prado et al., 2020; Daquila et al., 2021; Wurm et al., 2023).

In conclusion, our study constitutes a pioneering attempt to decipher gut microbiota-metabolite interactions under chromium stress, shaping the blueprint for an integrated understanding of heavy metal-induced ecological disruption. Our findings offer new insights into the dynamic and evolving association between the gut microbiome and metabolic changes under chromium stress in silkworms.

Data availability statement

The data presented in the study are deposited in the GSA (Genome Sequence Archive) repository, accession number PRJCA019204.

Ethics statement

Ethical approval was not required for the study involving animals in accordance with the local legislation and institutional requirements because silkworms is a common insect, and it is also a model species in scientific research.

Author contributions

Y-ZC: Data curation, Writing – original draft. W-TR: Investigation, Validation, Writing – review & editing. Y-CQ: Data curation, Investigation, Writing – original draft. L-YL: Data curation, Investigation, Writing – original draft. JL: Data curation, Investigation, Writing – original draft. M-JL: Data curation, Investigation, Writing – original draft. LX: Formal analysis, Investigation, Resources, Writing – original draft. X-DL: Writing – original draft, Writing – review & editing, Funding acquisition, Project administration, Supervision. D-LG: Conceptualization, Writing – original draft, Writing – review & editing.

Funding

The author(s) declare financial support was received for the research, authorship, and/or publication of this article. This research was funded by the Special Project of Guangxi Collaborative Innovation Center of Modern Sericulture and Silk (2022GXCSSC03, 2022GXCSSC04, 2022GXCSSC09), Guangxi University Young and Middle-aged Teachers' Basic Research Ability Improvement Project 2023KY0638.

Conflict of interest

The authors declare that the research was conducted in the absence of any commercial or financial relationships that could be construed as a potential conflict of interest.

Publisher's note

Supplementary material

The Supplementary material for this article can be found online at: https://www.frontiersin.org/articles/10.3389/fmicb.2023.1278271/full#supplementary-material

References

Ahmed, S., Singh, S., Singh, V., Roberts, K. D., Zaidi, A., and Rodriguez-Palacios, A. (2022). The Weissella genus: clinically treatable Bacteria with antimicrobial/probiotic effects on inflammation and Cancer. *Microorganisms* 10:2427. doi: 10.3390/microorganisms10122427

Aksoy, S. (2018). Insect gut microbiota: accessories to the bite. *Cell Host Microbe* 23, 8–9. doi: 10.1016/j.chom.2017.12.016

Balali-Mood, M., Naseri, K., Tahergorabi, Z., Khazdair, M. R., and Sadeghi, M. (2021). Toxic mechanisms of five heavy metals: mercury, Lead, Chromium, cadmium, and arsenic. *Front. Pharmacol.* 12:643972. doi: 10.3389/fphar.2021.643972

Bauermeister, A., Mannochio-Russo, H., Costa-Lotufo, L. V., Jarmusch, A. K., and Dorrestein, P. C. (2022). Mass spectrometry-based metabolomics in microbiome investigations. *Nat. Rev. Microbiol.* 20, 143–160. doi: 10.1038/s41579-021-00621-9

Bolger, A. M., Lohse, M., and Usadel, B. (2014). Trimmomatic: a flexible trimmer for Illumina sequence data. *Bioinformatics (Oxford, England)* 30, 2114–2120. doi: 10.1093/bioinformatics/btu170

Bucciarelli, A., and Motta, A. (2022). Use of *Bombyx mori* silk fibroin in tissue engineering: from cocoons to medical devices, challenges, and future perspectives. *Biomat. Adv.* 139:212982. doi: 10.1016/j.bioadv.2022.212982

Callahan, B. J., McMurdie, P. J., Rosen, M. J., Han, A. W., Johnson, A. J., and Holmes, S. P. (2016). DADA2: high-resolution sample inference from Illumina amplicon data. *Nat. Methods* 13, 581–583. doi: 10.1038/nmeth.3869

Cao, P., Wei, X., Awal, R. P., Müller, R., and Wall, D. (2019). A highly polymorphic receptor governs many distinct self-recognition types within the Myxococcales order. *MBio* 10:2751. doi: 10.1128/mBio.02751-18

Cava, F., Hidalgo, A., and Berenguer, J. (2009). *Thermus thermophilus* as biological model. *Extremophiles* 13, 213–231. doi: 10.1007/s00792-009-0226-6

Ceja-Navarro, J. A., Vega, F. E., Karaoz, U., Hao, Z., Jenkins, S., Lim, H. C., et al. (2015). Gut microbiota mediate caffeine detoxification in the primary insect pest of coffee. *Nat. Commun.* 6:7618. doi: 10.1038/ncomms8618

Chakraborty, R., Renu, K., Eladl, M. A., El-Sherbiny, M., Elsherbini, D. M. A., Mirza, A. K., et al. (2022). Mechanism of chromium-induced toxicity in lungs, liver, and kidney and their ameliorative agents. *Biomed. Pharmacother.* 151:113119. doi: 10.1016/j.biopha.2022.113119

Chappidi, S., Villa, E. C., and Cantarel, B. L. (2019). Using Mothur to determine bacterial community composition and structure in 16S ribosomal RNA datasets. *Curr. Protoc. Bioinformatics* 67:e83. doi: 10.1002/cpbi.83

Chen, Y., Liu, G., Ali, M. R., Zhang, M., Zhou, G., Sun, Q., et al. (2023). Regulation of gut bacteria in silkworm (*Bombyx mori*) after exposure to endogenous cadmium-polluted mulberry leaves. *Ecotoxicol. Environ. Saf.* 256:114853. doi: 10.1016/j.ecoenv.2023.114853

Chen, X., Wang, Y., Wang, Y., Li, Q., Liang, X., Wang, G., et al. (2022). Ectopic expression of sericin enables efficient production of ancient silk with structural changes in silkworm. *Nat. Commun.* 13:6295. doi: 10.1038/s41467-022-34128-5

Chiu, A., Shi, X. L., Lee, W. K., Hill, R., Wakeman, T. P., Katz, A., et al. (2010). Review of chromium (VI) apoptosis, cell-cycle-arrest, and carcinogenesis. *J. Environ. Sci. Health C Environ. Carcinog. Ecotoxicol. Rev.* 28, 188–230. doi: 10.1080/10590501.2010.504980

Coker, O. O., Liu, C., Wu, W. K. K., Wong, S. H., Jia, W., Sung, J. J. Y., et al. (2022). Altered gut metabolites and microbiota interactions are implicated in colorectal carcinogenesis and can be non-invasive diagnostic biomarkers. *Microbiome* 10:35. doi: 10.1186/s40168-021-01208-5

Coqueiro, A. Y., Rogero, M. M., and Tirapegui, J. (2019). Glutamine as an anti-fatigue amino acid in sports nutrition. *Nutrients* 11:863. doi: 10.3390/nu11040863

Cruzat, V., Macedo Rogero, M., Noel Keane, K., Curi, R., and Newsholme, P. (2018). Glutamine: metabolism and immune function, supplementation and clinical translation. *Nutrients* 10:1564. doi: 10.3390/nu10111564

Daquila, B. V., Dossi, F. C., Moi, D. A., Moreira, D. R., Caleffe, R. R., Pamphile, J. A., et al. (2021). Bioactivity of *Bacillus thuringiensis* (Bacillales: Bacillaceae) on Diatraea saccharalis (Lepidoptera: Crambidae) eggs. *Pest Manag. Sci.* 77, 2019–2028. doi: 10.1002/ps.6230

Debnath, N., Kumar, R., Kumar, A., Mehta, P. K., and Yadav, A. K. (2021). Gut-microbiota derived bioactive metabolites and their functions in host physiology. *Biotechnol. Genet. Eng. Rev.* 37, 105–153. doi: 10.1080/02648725.2021.1989847

Domingo-Almenara, X., and Siuzdak, G. (2020). Metabolomics data processing using XCMS. *Methods Mol. Biol.* 2104, 11–24. doi: 10.1007/978-1-0716-0239-3_2

Dong, L. N., Wang, M., Guo, J., and Wang, J. P. (2019). Role of intestinal microbiota and metabolites in inflammatory bowel disease. *Chin. Med. J.* 132, 1610–1614. doi: 10.1097/CM9.0000000000000290

Douglas, G. M., Maffei, V. J., Zaneveld, J. R., Yurgel, S. N., Brown, J. R., Taylor, C. M., et al. (2020). PICRUSt2 for prediction of metagenome functions. *Nat. Biotechnol.* 38, 685–688. doi: 10.1038/s41587-020-0548-6

Du, Q., Guo, P., Shi, Y., Zhang, J., Zheng, D., Li, Y., et al. (2021). Genome-wide identification of copper stress-regulated and novel MicroRNAs in mulberry leaf. *Biochem. Genet.* 59, 589–603. doi: 10.1007/s10528-020-10021-y

Ehlers, S., and Merrill, S. A., *Staphylococcus saprophyticus infection*. StatPearls Publishing LLC: Treasure Island, FL. (2023).

Fung, C., Rusling, M., Lampeter, T., Love, C., Karim, A., Bongiorno, C., et al. (2021). Automation of QIIME2 metagenomic analysis platform. *Curr. Protocols* 1:e254. doi: 10.1002/cpz1.254

Fusco, V., Quero, G. M., Cho, G. S., Kabisch, J., Meske, D., Neve, H., et al. (2015). The genus Weissella: taxonomy, ecology and biotechnological potential. *Front. Microbiol.* 6:155. doi: 10.3389/fmicb.2015.00155

Gao, Z., Wang, Y., Wang, H., Li, X., Xu, Y., and Qiu, J. (2023). Recent aptamer-based biosensors for cd(2+) detection. *Biosensors* 13:612. doi: 10.3390/bios13060612

Golledge, C. L. (1988). *Staphylococcus saprophyticus* bacteremia. *J. Infect. Dis.* 157:215. doi: 10.1093/infdis/157.1.215

Hall, M., and Beiko, R. G. (2018). 16S rRNA gene analysis with QIIME2. *Methods Mol. Biol.* 1849, 113–129. doi: 10.1007/978-1-4939-8728-3_8

Han, H., Cai, H., Wang, X., Hu, X., Chen, Z., and Yao, L. (2020). Heavy metal-immobilizing bacteria increase the biomass and reduce the cd and Pb uptake by pakchoi (*Brassica chinensis* L.) in heavy metal-contaminated soil. *Ecotoxicol. Environ. Saf.* 195:110375. doi: 10.1016/j.ecoenv.2020.110375

Holman, J. D., Tabb, D. L., and Mallick, P. (2014). Employing ProteoWizard to convert raw mass spectrometry data. *Curr. Protoc. Bioinformatics* 46:13.24.1-13.24.9. doi: 10.1002/0471250953.bi1324s46

Huang, W., Ling, S., Li, C., Omenetto, F. G., and Kaplan, D. L. (2018). Silkworm silk-based materials and devices generated using bio-nanotechnology. *Chem. Soc. Rev.* 47, 6486–6504. doi: 10.1039/C8CS00187A

Huang, F., Wang, Z. H., Cai, Y. X., Chen, S. H., Tian, J. H., and Cai, K. Z. (2018). Heavy metal bioaccumulation and cation release by growing *Bacillus cereus* RC-1 under culture conditions. *Ecotoxicol. Environ. Saf.* 157, 216–226. doi: 10.1016/j.ecoenv.2018.03.077

Jia, X., Xu, W., Zhang, L., Li, X., Wang, R., and Wu, S. (2021). Impact of gut microbiota and microbiota-related metabolites on hyperlipidemia. *Front. Cell. Infect. Microbiol.* 11:634780. doi: 10.3389/fcimb.2021.634780

Johnson, C. H., Ivanisevic, J., and Siuzdak, G. (2016). Metabolomics: beyond biomarkers and towards mechanisms. *Nat. Rev. Mol. Cell Biol.* 17, 451–459. doi: 10.1038/nrm.2016.25

Jung, J., Jeong, H., Kim, H. J., Lee, D. W., and Lee, S. J. (2016). Complete genome sequence of Bacillus oceanisediminis 2691, a reservoir of heavy-metal resistance genes. *Mar. Genomics* 30, 73–76. doi: 10.1016/j.margen.2016.07.002

Kapoor, R. T., Bani Mfarrej, M. F., Alam, P., Rinklebe, J., and Ahmad, P. (2022). Accumulation of chromium in plants and its repercussion in animals and humans. *Environ. Pollut.* 301:119044. doi: 10.1016/j.envpol.2022.119044

Keller-Costa, T., Jousset, A., van Overbeek, L., van Elsas, J. D., and Costa, R. (2014). The freshwater sponge *Ephydatia fluviatilis* harbours diverse Pseudomonas species (Gammaproteobacteria, Pseudomonadales) with broad-spectrum antimicrobial activity. *PLoS One* 9:e88429. doi: 10.1371/journal.pone.0088429

Kellogg, J. J., Kvalheim, O. M., and Cech, N. B. (2020). Composite score analysis for unsupervised comparison and network visualization of metabolomics data. *Anal. Chim. Acta* 1095, 38–47. doi: 10.1016/j.aca.2019.10.029

Kessner, D., Chambers, M., Burke, R., Agus, D., and Mallick, P. (2008). ProteoWizard: open source software for rapid proteomics tools development. *Bioinformatics (Oxford, England)* 24, 2534–2536. doi: 10.1093/bioinformatics/btn323

Kim, S. U., Cheong, Y. H., Seo, D. C., Hur, J. S., Heo, J. S., and Cho, J. S. (2007). Characterisation of heavy metal tolerance and biosorption capacity of bacterium strain CPB4 (Bacillus spp.). *Water Sci. Technol.* 55, 105–111. doi: 10.2166/wst.2007.007

Li, Y., Huang, Y., Li, Z., Tang, X., Liu, X., and Hughes, S. S. (2022). Mechanisms of chromium isotope fractionation and the applications in the environment. *Ecotoxicol. Environ. Saf.* 242:113948. doi: 10.1016/j.ecoenv.2022.113948

Li, C., Xu, S., Xiang, C., Xu, S., Zhou, Q., and Zhang, J. (2022). The gut microbiota of silkworm are altered by antibiotic exposure. *FEBS Open Bio* 12, 2203–2212. doi: 10.1002/2211-5463.13502

Li, W., Xu, S., Zhang, B., Zhu, Y., Hua, Y., Kong, X., et al. (2017). Directed evolution to improve the catalytic efficiency of urate oxidase from *Bacillus subtilis*. *PLoS One* 12:e0177877. doi: 10.1371/journal.pone.0177877

Li, T., Zhou, H., Zhang, J., Zhang, Z., Yu, Y., Wei, Y., et al. (2021). Effects of silkworm excrement and water management on the accumulation of cd and as in different varieties of rice and an assessment of their health risk. *Ecotoxicol. Environ. Saf.* 228:112974. doi: 10.1016/j.ecoenv.2021.112974

Liang, X., Lu, Z. L., Wei, B. X., Feng, J. L., Qu, D., and Luo, T. R. (2013). Phylogenetic analysis of *Bombyx mori* nucleopolyhedrovirus polyhedrin and p10 genes in wild isolates from Guangxi Zhuang autonomous region, China. *Virus Genes* 46, 140–151. doi: 10.1007/s11262-012-0820-z

Libonatti, C., Agüeria, D., García, C., and Basualdo, M. (2019). *Weissella paramesenteroides* encapsulation and its application in the use of fish waste. *Revista Argentina Microbiologia* 51, 81–83. doi: 10.1016/j.ram.2018.03.001

Lin, J. Y., Hobson, W. J., and Wertz, J. T. (2016). Ventosimonas gracilis gen. Nov., sp. nov., a member of the Gammaproteobacteria isolated from *Cephalotes varians* ant guts representing a new family, Ventosimonadaceae fam. Nov., within the order 'Pseudomonadales'. *Int. J. Syst. Evol. Microbiol.* 66, 2869–2875. doi: 10.1099/ijsem.0.001068

Ma, P., Patching, S. G., Ivanova, E., Baldwin, J. M., Sharples, D., Baldwin, S. A., et al. (2016). Allantoin transport protein, PucI, from *Bacillus subtilis*: evolutionary relationships, amplified expression, activity and specificity. *Microbiology* 162, 823–836. doi: 10.1099/mic.0.000266

Mahieu, N. G., Genenbacher, J. L., and Patti, G. J. (2016). A roadmap for the XCMS family of software solutions in metabolomics. *Curr. Opin. Chem. Biol.* 30, 87–93. doi: 10.1016/j.cbpa.2015.11.009

Maity, S., Sarkar, D., Poddar, K., Patil, P., and Sarkar, A. (2023). Biofilm-mediated heavy metal removal from aqueous system by multi-metal-resistant bacterial strain Bacillus sp. GH-s29. *Appl. Biochem. Biotechnol.* 195, 4832–4850. doi: 10.1007/s12010-022-04288-7

Mancera, M., Roffé, I., Rivas, M., Silva, C., and Galbis, J. A. (2002). Synthesis of D-mannitol and L-iditol derivatives as monomers for the preparation of new regioregular AABB-type polyamides. *Carbohydr. Res.* 337, 607–611. doi: 10.1016/S0008-6215(02)00040-X

Martínez-Gómez, A. I., Soriano-Maldonado, P., Andújar-Sánchez, M., Clemente-Jiménez, J. M., Rodríguez-Vico, F., Neira, J. L., et al. (2014). Biochemical and mutational studies of allantoinase from *Bacillus licheniformis* CECT 20T. *Biochimie* 99, 178–188. doi: 10.1016/j.biochi.2013.12.002

Marzoli, F., Antonelli, P., Saviane, A., Tassoni, L., Cappellozza, S., and Belluco, S. (2022). *Bombyx mori* from a food safety perspective: a systematic review. *Food Res. Int.* 160:111679. doi: 10.1016/j.foodres.2022.111679

Mishra, S., and Bharagava, R. N. (2016). Toxic and genotoxic effects of hexavalent chromium in environment and its bioremediation strategies. *J. Environ. Sci. Health C Environ. Carcinog. Ecotoxicol. Rev.* 34, 1–32. doi: 10.1080/10590501.2015.1096883

Muhammad, A., He, J., Yu, T., Sun, C., Shi, D., Jiang, Y., et al. (2022). Dietary exposure of copper and zinc oxides nanoparticles affect the fitness, enzyme activity, and microbial community of the model insect, silkworm *Bombyx mori*. *Sci. Total Environ.* 813:152608. doi: 10.1016/j.scitotenv.2021.152608

Nguyen, T., Kim, T., Ta, H. M., Yeo, W. S., Choi, J., Mizar, P., et al. (2019). Targeting mannitol metabolism as an alternative antimicrobial strategy based on the structure-function study of Mannitol-1-phosphate dehydrogenase in *Staphylococcus aureus*. *MBio* 10:2660. doi: 10.1128/mBio.02660-18

Oosaka, K. (2009). Possibility as monosaccharide laxative of rare sugar alcohols. *Yakugaku Zasshi* 129, 575–580. doi: 10.1248/yakushi.129.575

Parada, A. E., Needham, D. M., and Fuhrman, J. A. (2016). Every base matters: assessing small subunit rRNA primers for marine microbiomes with mock communities, time series and global field samples. *Environ. Microbiol.* 18, 1403–1414. doi: 10.1111/1462-2920.13023

Prado, G. K. S., Torrinha, K. C., Cruz, R. E., Gonçalves, A. B. B., Silva, C. A. V., Oliveira, F. M. S., et al. (2020). *Weissella paramesenteroides* WpK4 ameliorate the experimental amoebic colitis by increasing the expression of MUC-2 and the intestinal epithelial regeneration. *J. Appl. Microbiol.* 129, 1706–1719. doi: 10.1111/jam.14671

Rahman, Z., and Singh, V. P. (2019). The relative impact of toxic heavy metals (THMs) (arsenic (as), cadmium (cd), chromium (Cr)(VI), mercury (hg), and lead (Pb)) on the total environment: an overview. *Environ. Monit. Assess.* 191:419. doi: 10.1007/s10661-019-7528-7

Ramimoghadam, D., Hussein, M. Z., and Taufiq-Yap, Y. H. (2012). The effect of sodium dodecyl sulfate (SDS) and cetyltrimethylammonium bromide (CTAB) on the properties of ZnO synthesized by hydrothermal method. *Int. J. Mol. Sci.* 13, 13275–13293. doi: 10.3390/ijms131013275

Renu, K., Chakraborty, R., Myakala, H., Koti, R., Famurewa, A. C., Madhyastha, H., et al. (2021). Molecular mechanism of heavy metals (Lead, Chromium, arsenic, mercury, nickel and cadmium) – induced hepatotoxicity – a review. *Chemosphere* 271:129735. doi: 10.1016/j.chemosphere.2021.129735

Santana, M. M., Gonzalez, J. M., and Clara, M. I. (2016). Inferring pathways leading to organic-sulfur mineralization in the Bacillales. *Crit. Rev. Microbiol.* 42, 31–45. doi: 10.3109/1040841X.2013.877869

Schäberle, T. F., Lohr, F., Schmitz, A., and König, G. M. (2014). Antibiotics from myxobacteria. *Nat. Prod. Rep.* 31, 953–972. doi: 10.1039/c4np00011k

Schrimpe-Rutledge, A. C., Codreanu, S. G., Sherrod, S. D., and McLean, J. A. (2016). Untargeted metabolomics strategies-challenges and emerging directions. *J. Am. Soc. Mass Spectrom.* 27, 1897–1905. doi: 10.1007/s13361-016-1469-y

Teixeira, C. G., Fusieger, A., Milião, G. L., Martins, E., Drider, D., Nero, L. A., et al. (2021). Weissella: an emerging bacterium with promising health benefits. *Probiotics Antimicrob. Prot.* 13, 915–925. doi: 10.1007/s12602-021-09751-1

Teschke, R. (2022). Aluminum, arsenic, beryllium, cadmium, Chromium, cobalt, copper, Iron, Lead, mercury, molybdenum, nickel, platinum, thallium, titanium, vanadium, and zinc: molecular aspects in experimental liver injury. *Int. J. Mol. Sci.* 23:2213. doi: 10.3390/ijms232012213

Vincent, J. B. (2019). Effects of chromium supplementation on body composition, human and animal health, and insulin and glucose metabolism. *Curr. Opin. Clin. Nutr. Metab. Care* 22, 483–489. doi: 10.1097/MCO.0000000000000604

Vincent, J. B., and Lukaski, H. C. (2018). Chromium. *Adv. Nutr.* 9, 505–506. doi: 10.1093/advances/nmx021

Wan, X., Lei, M., Chen, T., Tan, Y., and Yang, J. (2017). Safe utilization of heavy-metal-contaminated farmland by mulberry tree cultivation and silk production. *Sci. Total Environ.* 599-600, 1867–1873. doi: 10.1016/j.scitotenv.2017.05.150

Wang, S., Wang, L., Fan, X., Yu, C., Feng, L., and Yi, L. (2020). An insight into diversity and functionalities of gut microbiota in insects. *Curr. Microbiol.* 77, 1976–1986. doi: 10.1007/s00284-020-02084-2

Wheelock, Å. M., and Wheelock, C. E. (2013). Trials and tribulations of 'omics data analysis: assessing quality of SIMCA-based multivariate models using examples from pulmonary medicine. *Mol. BioSyst.* 9, 2589–2596. doi: 10.1039/c3mb70194h

Wróbel, M., Śliwakowski, W., Kowalczyk, P., Kramkowski, K., and Dobrzyński, J. (2023). Bioremediation of heavy metals by the genus Bacillus. *Int. J. Environ. Res. Public Health* 20:4964. doi: 10.3390/ijerph20064964

Wu, D. N., Guan, L., Jiang, Y. X., Ma, S. H., Sun, Y. N., Lei, H. T., et al. (2019). Microbiome and metabonomics study of quercetin for the treatment of atherosclerosis. *Cardiovasc. Diagn. Ther.* 9, 545–560. doi: 10.21037/cdt.2019.12.04

Wurm, P., Stampfer, L., Greimel, T., Leitner, E., Zechner, E. L., Bauchinger, S., et al. (2023). Gut microbiota Dysbiosis in suspected food protein induced Proctocolitis-a prospective comparative cohort trial. *J. Pediatr. Gastroenterol. Nutr.* 77, 31–38. doi: 10.1097/MPG.0000000000003789

Xia, Y., Chen, F., Du, Y., Liu, C., Bu, G., Xin, Y., et al. (2019). A modified SDS-based DNA extraction method from raw soybean. *Biosci. Rep.* 39:2271. doi: 10.1042/BSR20182271

Xu, K., Lan, H., He, C., Wei, Y., Lu, Q., Cai, K., et al. (2022). Toxicological effects of trace amounts of pyriproxyfen on the midgut of non-target insect silkworm. *Pestic. Biochem. Physiol.* 188:105266. doi: 10.1016/j.pestbp.2022.105266

Zang, Y., Wang, M., Shohag, M. J. I., Lu, L., He, T., Liao, C., et al. (2023). Biochar performance for preventing cadmium and arsenic accumulation, and the health risks associated with mustard (*Brassica juncea*) grown in co-contaminated soils. *Ecotoxicol. Environ. Saf.* 263:115216. doi: 10.1016/j.ecoenv.2023.115216

Zhao, L., Wu, B., Liang, S., Min, D., and Jiang, H. (2022). Insight of silkworm Pupa oil regulating oxidative stress and lipid metabolism in *Caenorhabditis elegans*. *Foods* 11:4084. doi: 10.3390/foods11244084

frontiers | Frontiers in Microbiology

TYPE Original Research
PUBLISHED 26 October 2023
DOI 10.3389/fmicb.2023.1294177

OPEN ACCESS

EDITED BY
Hector Alex Saka,
Centro de Investigaciones en Bioquímica Clínica e Inmunología (CIBICI), CONICET, Argentina

REVIEWED BY
Pengsong Li,
Beijing Forestry University, China
Parviz Heidari,
Shahrood University of Technology, Iran

*CORRESPONDENCE
Lanming Chen
✉ lmchen@shou.edu.cn

RECEIVED 14 September 2023
ACCEPTED 10 October 2023
PUBLISHED 26 October 2023

CITATION
Zhang B, Xu J, Sun M, Yu P, Ma Y, Xie L and Chen L (2023) Comparative secretomic and proteomic analysis reveal multiple defensive strategies developed by *Vibrio cholerae* against the heavy metal (Cd^{2+}, Ni^{2+}, Pb^{2+}, and Zn^{2+}) stresses.
Front. Microbiol. 14:1294177.
doi: 10.3389/fmicb.2023.1294177

Comparative secretomic and proteomic analysis reveal multiple defensive strategies developed by *Vibrio cholerae* against the heavy metal (Cd^{2+}, Ni^{2+}, Pb^{2+}, and Zn^{2+}) stresses

Beiyu Zhang[1,2], Jingjing Xu[1,2], Meng Sun[1,2], Pan Yu[1,2], Yuming Ma[1,2], Lu Xie[3] and Lanming Chen[1,2]*

[1]Key Laboratory of Quality and Safety Risk Assessment for Aquatic Products on Storage and Preservation (Shanghai), Ministry of Agriculture and Rural Affairs of the People's Republic of China, Shanghai, China, [2]College of Food Science and Technology, Shanghai Ocean University, Shanghai, China, [3]Shanghai-MOST Key Laboratory of Health and Disease Genomics (Chinese National Human Genome Center at Shanghai), Institute of Genome and Bioinformatics, Shanghai Institute for Biomedical and Pharmaceutical Technologies, Shanghai, China

Vibrio cholerae is a common waterborne pathogen that can cause pandemic cholera in humans. The bacterium with heavy metal-tolerant phenotypes is frequently isolated from aquatic products, however, its tolerance mechanisms remain unclear. In this study, we investigated for the first time the response of such *V. cholerae* isolates ($n = 3$) toward the heavy metal (Cd^{2+}, Ni^{2+}, Pb^{2+}, and Zn^{2+}) stresses by comparative secretomic and proteomic analyses. The results showed that sublethal concentrations of the Pb^{2+} (200 μg/mL), Cd^{2+} (12.5 μg/mL), and Zn^{2+} (50 μg/mL) stresses for 2 h significantly decreased the bacterial cell membrane fluidity, but increased cell surface hydrophobicity and inner membrane permeability, whereas the Ni^{2+} (50 μg/mL) stress increased cell membrane fluidity ($p < 0.05$). The comparative secretomic and proteomic analysis revealed differentially expressed extracellular and intracellular proteins involved in common metabolic pathways in the *V. cholerae* isolates to reduce cytotoxicity of the heavy metal stresses, such as biosorption, transportation and effluxing, extracellular sequestration, and intracellular antioxidative defense. Meanwhile, different defensive strategies were also found in the *V. cholerae* isolates to cope with different heavy metal damage. Remarkably, a number of putative virulence and resistance-associated proteins were produced and/or secreted by the *V. cholerae* isolates under the heavy metal stresses, suggesting an increased health risk in the aquatic products.

KEYWORDS

***Vibrio cholerae*, heavy metal, secretome, proteome, tolerance mechanism, food safety**

Introduction

Vibrio cholerae can cause pandemic cholera in humans (Baker-Austin et al., 2018). The bacterium colonizes on intestinal mucosal cells and causes watery diarrhea and vomiting, even death (Sit et al., 2022). *V. cholerae* was detected positive in a variety of aquatic products (Xu et al., 2019; Fu et al., 2020; Chen et al., 2021). Aquatic ecosystems are challenged by anthropogenic activities, such as wastes from industrial processes (e.g., tanning, electroplating, manufacturing of chemicals and textiles, mining, and smelting), agricultural fertilizers and pesticides, leading to heavy metal pollution (Zamora-Ledezma et al., 2021; Tong et al., 2022). Due to toxicity, persistence and bioaccumulation, heavy metals in aquatic environments pose a huge risk to human health, such as lead (Pb), cadmium (Cd), nickel (Ni), and zinc (Zn) (Yu S. et al., 2022). For example, Pb (II) induced persistent hypertension and myocardial dysfunction, which adversely affected the function of cardiovascular organs (Carmignani et al., 1999). Cd induced various epigenetic changes in mammalian cells, leading to the development of breast, lung, pancreas, and kidney cancers (Genchi et al., 2020). Ni exposure caused allergy, cardiovascular disease, kidney disease, pulmonary fibrosis, and lung and nasal cancers (Yang et al., 2023). Zn is one of the most crucial trace elements required for cells in animals and humans. However, consuming too much dietary Zn (>40 mg/kg) resulted in arteriosclerosis and pancreatic damage (Arslan et al., 2010). Hazardous heavy metals were detected in waters, sediments and aquatic products, particularly in developing nations (Wang et al., 2020; Zamora-Ledezma et al., 2021; Wang Y. et al., 2022). The Cd and Pb had high cytotoxicity even in low concentrations (Carmignani et al., 1999; Sadeq and Beckerman, 2019).

Low levels of heavy metals (far lower than minimal inhibitory concentrations, MICs) also enabled bacteria to obtain resistance (Li et al., 2019). Heavy metal resistant *V. cholerae* isolates have been found in aquatic products in our recent reports (Xu et al., 2019; Fu et al., 2020; Chen et al., 2021). For example, Chen et al. surveyed the prevalence of *V. cholerae* in 36 species of edible aquatic animals sampled in Fuzhou and Shanghai in 2019 in China. They found high incidence of tolerance to heavy metals Hg^{2+} (67.0%), Pb^{2+} (57.6%), and Zn^{2+} (57.6%) among *V. cholerae* isolates ($n = 203$) (Chen et al., 2021). Fu et al. investigated genetic diversity of *V. cholerae* isolates ($n = 370$) originated from 15 species of edible aquatic animals collected in 2018 in Shanghai, China. High percentages of tolerance to Hg^{2+} (69.5%), Ni^{2+} (32.4%), and Cd^{2+} (30.8%) were observed among the isolates (Fu et al., 2020). It has been reported that heavy metals in sublethal levels increased mutation rates and enriched *de novo* mutants to resist multiple antibiotics (Li et al., 2019; Zhong et al., 2021). The emergence and spread of multidrug resistant (MDR) pathogenic bacteria including *V. cholerae* has become one of the most challenging issues in clinical treatment, due to the limited therapeutic options (Das et al., 2020; Salamm et al., 2023). Therefore, to decipher molecular mechanisms underlying heavy metal tolerance of *V. cholerae* is imperative for effectively controlling infectious disease caused by the MDR pathogen.

Stress response or resistance to heavy metals are complex biological processes with numerous proteins involved or at least affected (Okay et al., 2020). Two-dimensional gel electrophoresis (2D-GE) coupled with liquid chromatography–tandem mass spectrometry (LC–MS/MS) are useful techniques for the global identification of protein changes in different organisms in response to biotic and abiotic stresses. For example, Sun et al. identified a total of 1,424 differentially expressed proteins (DEPs) in plant *Brassica campestris* L. hairy roots in response to Cd^{2+} (200 μM) stress (Sun et al., 2023). Sánchez-Rojas et al. (2022) reported 252 and 118 differentially regulated proteins in yeast *Yarrowia lipolytica* under the treatment with Cd^{2+} (0.11 mM) and Cr^{6+} (0.19 mM), respectively.

In our previous studies, the 2D-GE combined with LC–MS/MS techniques were also applied in global identification of DEPs in *Vibrio* species (Zhu et al., 2020; Shan et al., 2022; Yan et al., 2022). For example, Zhu et al. (2020) compared secretomes and proteomes of *Vibrio parahaemolyticus* strains isolated from 12 species of aquatic animals and identified 28 differential extracellular proteins. On the basis of our previous studies, in the study we deciphered molecular mechanisms underlying the heavy metal (Cd^{2+}, Ni^{2+}, Pb^{2+}, and Zn^{2+}) tolerance of *V. cholerae* isolated from aquatic animals. The major objectives of this study were: (1) to examine the growth of the *V. cholerae* isolates ($n = 3$) with heavy metal-tolerant phenotypes under different concentrations of heavy metals (3.125–3,200 μg/mL); (2) to obtain secretomes and proteomes of the *V. cholerae* isolates under the sublethal concentrations of Cd^{2+} (12.5 μg/mL), Ni^{2+}(50 μg/mL), Pb^{2+} (200 μg/mL), or Zn^{2+}(50 μg/mL) stresses using the 2D-GE and LC–MS/MS techniques; and (3) to figure out defensive strategies adopted by the *V. cholerae* isolates toward the Cd^{2+}, Ni^{2+}, Pb^{2+}, and Zn^{2+} stresses. To the best of our knowledge, this study was the first to investigate the response of *V. cholerae* toward the heavy metal stresses by comparative secretomic and proteomic analyses. The results of this study facilitate the better understanding of the bacterial resistance and persistence worldwide.

Materials and methods

Bacterial strains and culture conditions

The non O1/O139 *V. cholerae* J9-62, Q6-10, and N9-4 strains studied in this study were isolated from edible aquatic products including fish *Carassius auratus* and *Ctenopharyngodon idellus*, and shellfish *Saxidomus purpuratus*, respectively, and their genotypes and resistance phenotypes were determined (Chen et al., 2021; Supplementary Table S1). The *V. cholerae* isolates were routinely incubated in trypsin soybean broth (TSB) (3% NaCl, pH 8.5) (Beijing Luqiao Technology Co., Ltd., Beijing, China) at 37°C with shaking at 180 rpm (Xu et al., 2019; Fu et al., 2020; Chen et al., 2021).

Determination of MICs of heavy metals

The MICs of heavy metals against the *V. cholerae* isolates were determined using the broth dilution testing (microdilution) approved by Clinical and Laboratory Standards Institute (CLSI, M2-A9, 2006), USA. Heavy metals included $CdCl_2$, $NiCl_2$, $PbCl_2$, and $ZnCl_2$ (Sinopharm Chemical Reagent Co., Ltd., Shanghai, China). *Escherichia coli* K-12 (Institute of Industrial Microbiology, Shanghai, China) was used as a quality control strain (Xu et al., 2019; Fu et al., 2020; Chen et al., 2021).

Growth curve assay

The *V. cholerae* isolates were incubated in the TSB medium supplemented with different concentrations (3200–3.125 μg/mL) of the heavy metals ($CdCl_2$, $NiCl_2$, $PbCl_2$, or $ZnCl_2$) at 37°C for 40 h, respectively. Growth curves were measured using Bioscreen Automatic Growth Curve Analyzer (BioTek Instruments, Inc., Winooski, VT, USA) (Yang et al., 2020). Bacterial survival was examined using the standard plate counting method (Yu P. et al., 2022). The sublethal concentrations of the heavy metals were defined as fatality rates less than 50% under the treatment conditions for 2 h (Yu P. et al., 2022).

Scanning Electron Microscopy (SEM) analysis

The *V. cholerae* isolates were incubated in the TSB medium to the mid logarithmic growth phase (mid-LGP) at 37°C. A final concentration of Cd^{2+} (12.5 μg/mL), Ni^{2+}(50 μg/mL), Pb^{2+} (200 μg/mL), or Zn^{2+}(50 μg/mL) was added to the bacterial culture (5 mL), and then continuously incubated at 37°C for 2 h, 4 h, and 6 h. The cell mixture (1.5 mL) was then harvested, washed, fixed, and observed using thermal field emission SEM (Hitachi, SU5000, Tokyo, Japan, 5.0 kV, ×30,000) as described in our recent report (Yu P. et al., 2022). The untreated bacterial culture was used as a negative control.

Bacterial cell membrane fluidity and permeability, and surface hydrophobicity assays

The *V. cholerae* isolates were treated with the heavy metals for 2 h as described in the Scanning Electron Microscopy (SEM) Analysis section. The bacterial cell membrane fluidity was examined using the 1, 6-Diphenyl-1, 3, 5-hexatrine (DPH, National Pharmaceutical Group Corporation Co., Ltd., Shanghai, China) as a probe (Voss and Montville, 2014). The bacterial inner membrane permeability was examined using the O-nitrophenyl-β-D galactopyranoside (ONPG, Beijing Solarbio Science & Technology Co., Ltd., Beijing, China) as a probe (Huang et al., 2021). The OD_{415} values were determined using BioTek Synergy 2 (BioTek, Burlington, VT, USA) every 30 min for 2 h. The bacterial cell surface hydrophobicity was measured using the n-hexadecane (National Pharmaceutical Group Corporation Co., Ltd., Shanghai, China) as a probe (Yan et al., 2016). The untreated bacterial culture was used as a negative control.

2D-GE analysis

The *V. cholerae* isolates were treated with the heavy metals for 2 h as described in the Scanning Electron Microscopy (SEM) Analysis section, but incubated without shaking. Extracellular proteins of the *V. cholerae* isolates were extracted as described in our recent reports (Zhu et al., 2020; Shan et al., 2022; Yan et al., 2022). Isoelectric focusing (IEF) was performed using immobilized pH gradient (IPG) gels (pH 4–7, 7 cm; Bio-Rad, Hercules, USA). The second-dimension sodium dodecyl sulfate–polyacrylamide gel electrophoresis (SDS-PAGE), gel staining, protein spot detection, spot matching, and quantitative intensity analysis were performed as described previously (Zhu et al., 2020; Shan et al., 2022; Yan et al., 2022). In addition, intracellular proteins were extracted using Bacterial Protein Extraction Kit (Shanghai Sangon Biological Engineering Technology and Service Co., Ltd., Shanghai, China), and analyzed as described previously (Zhu et al., 2020; Shan et al., 2022; Yan et al., 2022). The untreated bacterial culture was used as a negative control.

LC–MS/MS analysis

The LC–MS/MS analysis was carried out by HooGen Biotech, Shanghai, China using Q Executive Mass Spectrometer (Thermo Fisher Scientific, Waltham, MA, USA) coupled with Easy nLC 1200 Chromatography System (Zhu et al., 2020; Shan et al., 2022; Yan et al., 2022). The automated peptide identification and protein calls were performed using Uniprot *V. cholerae* 80449 20221026 databases in Mascot version 2.2 server (Matrix Science, London, United Kingdom) with the same criteria described in our previous report (Zhu et al., 2020). A false discovery rate (FDR) was set below 0.01 for both peptides and proteins. The lable-free relative protein quantitation was performed based on peak areas of corresponding peptides. To reveal intensities that were significant between the treatment groups under the heavy metal stresses and the control group, the p values of <0.01, and fold changes of >1.5 were set for significant difference. Three independent biological replicates were prepared and combined for each sample.

Quantitative reverse transcription-PCR (qRT-PCR) assay

The *V. cholerae* isolates were treated with the heavy metals as described in the 2D-GE Analysis section. Total RNA was extracted, qRT-PCR was performed, the relative expression of representative genes were calculated according to the method described in our recent reports (Zhu et al., 2020; Shan et al., 2022; Yan et al., 2022). Primers were synthesized by Biotech Bioengineering (Shanghai, China). The untreated bacterial culture was used as a negative control.

Data analysis

In this study, all tests were performed in triplicate. The data were analyzed using the SPSS software version 17.0 (SPSS Inc., Armonk, NY, USA). The one-way analysis of variance (ANOVA) followed by appropriate post-hoc test (Tukey) was used to determine significant difference ($p < 0.05$).

Results

MICs of the heavy metals against the *Vibrio cholerae* isolates

The *V. cholerae* J9-62, Q6-10, and N9-4 isolates of aquatic animal origins showed different heavy metal tolerant profiles (Chen et al., 2021). The tolerance of *V. cholerae* J9-62 to Pb^{2+}, *V. cholerae* Q6-10 to

10.3389/fmicb.2023.1294177

Cd^{2+} and Zn^{2+}; and *V. cholerae* N9-4 to Ni^{2+} was chosen for the further analyses in this study (Supplementary Table S1).

The MICs of the heavy metals were determined, and the results showed that when compared to the quality control strain *E. coli* K-12, *V. cholerae* J9-62 was tolerant to Pb^{2+} with MIC value of 3,200 μg/mL; *V. cholerae* Q6-10 to Cd^{2+}, and Zn^{2+} with MIC values of 400 μg/mL, and 800 μg/mL, respectively; and *V. cholerae* N9-4 to Ni^{2+} with MIC value of 400 μg/mL (Supplementary Table S2). These results underlined the high heavy metal tolerance of the *V. cholerae* isolates of the aquatic animal origins.

Growth of the *Vibrio cholerae* isolates under different concentrations of the heavy metals

Based on the above results, we determined growth curves of *V. cholerae* J9-62, Q6-10, and N9-4 isolates in the TSB medium supplemented with different concentrations of the heavy metals at 37°C, and the results are shown in Figure 1.

After supplemented with the Pb^{2+} (3200–200 μg/mL), we observed that the growth of *V. cholerae* J9-62 was greatly inhibited at 3200 μg/mL of Pb^{2+}. Upon the decreased Pb^{2+} concentrations (1600–400 μg/mL), the increased growth of *V. cholerae* J9-62 was observed. The maximum biomass was detected at 200 μg/mL of Pb^{2+} with the OD_{600} value of 0.544, as compared to the control group (Figure 1A).

Similarly, growth curves of *V. cholerae* Q6-10 were determined under the Cd^{2+} (400–12.5 μg/mL) or Zn^{2+} (800–50 μg/mL) conditions. As shown in Figure 1B1, *V. cholerae* Q6-10 was highly inhibited at 400 and 200 μg/mL of Cd^{2+}, while little growth was observed at 100 and 50 μg/mL of Cd^{2+}, respectively. *V. cholerae* Q6-10 was slightly inhibited at 25 and 12.5 μg/mL of Cd^{2+} with the maximum OD_{600} values of 0.578 and 0.636, respectively. In addition, under the Zn^{2+} (800–50 μg/mL) treatment conditions, the growth of *V. cholerae* Q6-10 was fully inhibited at 800 and 400 μg/mL of Zn^{2+}, respectively. The isolate still grew poorly at 200 μg/mL of Zn^{2+}, whereas slight inhibition was observed at 50 μg/mL of Zn^{2+} with the maximum OD_{600} values of 0.625, as compared to the control group (Figure 1B2).

Growth curves of *V. cholerae* N9-4 were determined under the Ni^{2+} (400–50 μg/mL) conditions. As shown in Figure 1C, the growth

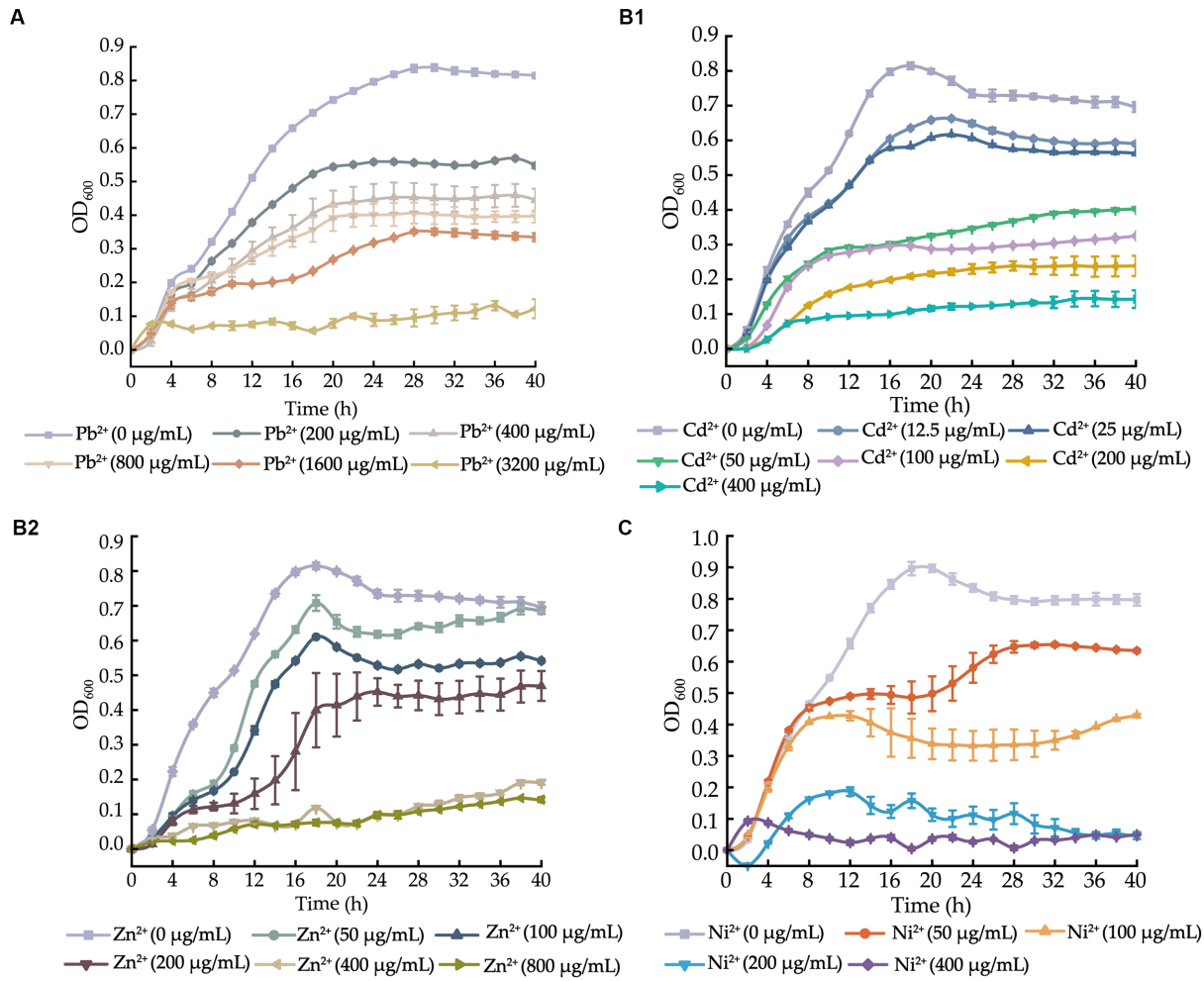

FIGURE 1
Growth curves of the *V. cholerae* isolates incubated in the TSB medium supplemented with different concentrations of heavy metals at 37°C. **(A–C)** *V. cholerae* J9–62 **(A)**, Q6–10 **(B1,B2)**, and N9–4 **(C)** isolates, respectively.

of *V. cholerae* N9-4 was highly inhibited at 400 μg/mL and 200 μg/mL of Ni^{2+}, respectively. The isolate still grew poorly at 100 μg/mL of Ni^{2+}, whereas a slight decrease in growth was observed at 50 μg/mL of Ni^{2+}, with the maximum OD_{600} value of 0.624, as compared to the control group (Figure 1C).

Taken together, based on these results, the 200 μg/mL of Pb^{2+} for *V. cholerae* J9-62; the 12.5 μg/mL of Cd^{2+} or 50 μg/mL of Zn^{2+} for *V. cholerae* Q6-10; and the 50 μg/mL of Ni^{2+} for *V. cholerae* N9-4 were chosen as the treatment conditions in the further analyses, respectively.

Changes in cell morphological structure of the *Vibrio cholerae* isolates under the heavy metal stresses

As shown in Figure 2, bacterial cells in the control groups were flat, intact and rod-shaped (Figures 2A1,B1,C1), however, after being treated with the Pb^{2+} (200 μg/mL) for 2 h, the cell surface of *V. cholerae* J9-62 was slightly deformed, with obvious depressions and wrinkles (Figure 2A2). Similarly, after treated with the Cd^{2+} (12.5 μg/mL), the cell surface of *V. cholerae* Q6-10 slightly folded (Figure 2B2); and the same case was observed under the Zn^{2+} (50 μg/mL) treatment (Figure 2B3). For *V. cholerae* N9-4, the treatment with the Ni^{2+} (50 μg/mL) also led to the bacterial cell surface slightly shrank (Figure 2C2). Additionally, we observed that the extended treatment time (≥4 h) resulted in the bacterial cell broke (Figures not shown).

Survival of the *Vibrio cholerae* isolates under the heavy metal stresses

Based on the above results, we also examined fatality rates of the *V. cholerae* isolates under the heavy metal stresses, and the results are shown in Supplementary Table S2. Approximately 42.75% of *V. cholerae* J9-62 cells could not survive after being treated with the Pb^{2+} (200 μg/mL) for 2 h. Similarly, the fatality rates of *V. cholerae* Q6-10 under the Cd^{2+} (12.5 μg/mL), or Zn^{2+} (50 μg/mL) stresses were 27.98%, or 29.70%, respectively, while that of *V. cholerae* N9-4 under the Ni^{2+}(50 μg/mL) stress was 34.42%. These results highlighted that the *V. cholerae* isolates were capable of surviving under the heavy metal stresses, with the fatality rates ranging from 27.98 to 42.75%.

The effects of the heavy metal stresses on cell membrane permeability and fluidity, and cell surface hydrophobicity of the *Vibrio cholerae* isolates

Bacterial cell membrane fluidity and permeability, and cell surface hydrophobicity are key parameters of cell membrane that undergoes quick adaptation to environmental changes (Rogers et al., 2021). Therefore, based on the above results, we further investigated the effects of the heavy metal stresses on the *V. cholerae* cell membrane integrity (Figure 3).

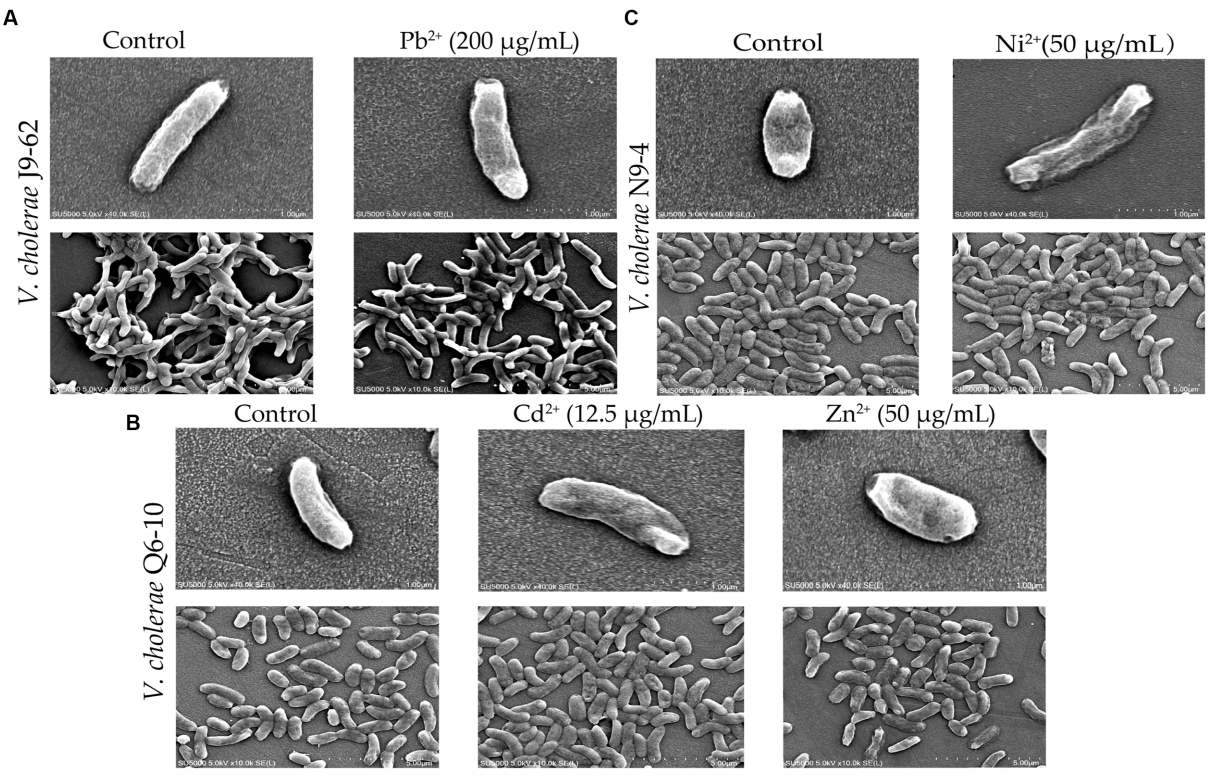

FIGURE 2
The SEM assay of cell surface structure of the *V. cholerae* isolates under the heavy metal stresses. *V. cholerae* J9–62, Q6–10, and N9–4 isolates were treated with 200 μg/mL of Pb^{2+} **(A)** 12.5 μg/mL of Cd^{2+} **(B)** or 50 μg/mL of Zn^{2+} **(B)** and 50 μg/mL of Ni^{2+} **(C)** for 2 h, respectively. The untreated bacterial cells were used as controls.

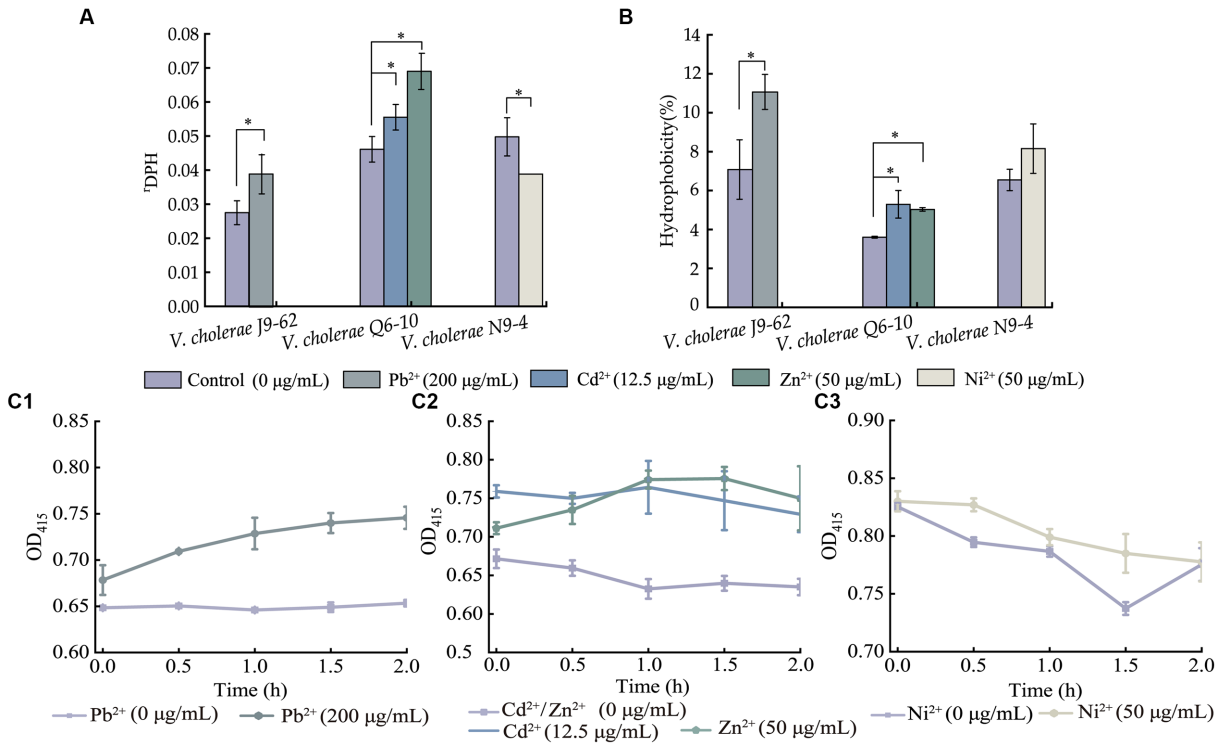

FIGURE 3
The cell membrane fluidity **(A)**, surface hydrophobicity **(B)**, and inner cell membrane permeability **(C)** of the *V. cholerae* isolates under the heavy metal stresses. *V. cholerae* J9–62, Q6–10, and N9–4 isolates **(C1–C3)** grown in the TSB medium were treated with the heavy metals at 37°C for 2 h, respectively. *$p < 0.05$.

As shown in Figure 3A, when compared to the control group, the cell membrane fluidity of *V. cholerae* J9-62 was significantly reduced by 1.422–fold after being treated with the Pb^{2+} (200 μg/mL) for 2 h ($p < 0.05$). Similarly, the cell membrane fluidity of *V. cholerae* Q6-10 was also reduced by 1.204–fold and 1.495–fold under the treatment with Cd^{2+} (12.5 μg/mL) and Zn^{2+} (50 μg/mL) stresses, respectively ($p < 0.05$). Conversely, the treatment with the Ni^{2+} (50 μg/mL) increased the cell membrane fluidity of *V. cholerae* N9-4 by 1.285–fold ($p < 0.05$).

As shown in Figure 3B, as compared with the control group, cell surface hydrophobicity of *V. cholerae* J9-62 was significantly enhanced by 1.563–fold after treated with the Pb^{2+} for 2 h ($p < 0.05$). Similarly, an increase by 1.468–fold, and 1.397–fold was observed in cell surface hydrophobicity of *V. cholerae* Q6-10 after treated with the Cd^{2+}, and Zn^{2+}, respectively ($p < 0.05$). In addition, there was no significant change in cell surface hydrophobicity of *V. cholerae* N9-4 after treated with the Ni^{2+} (50 μg/mL) ($p > 0.05$).

As shown in Figure 3C, as compared to the control group, after being treated with the Pb^{2+}, the inner cell membrane permeability of *V. cholerae* J9-62 was significantly increased ($p < 0.05$) (Figure 3A). The similar cases were observed after *V. cholerae* Q6-10 being treated with the Cd^{2+} or Zn^{2+}, respectively (Figure 3B). Additionally, there was no significant change in the inner membrane permeability of *V. cholerae* N9-4 under the treatment with Ni^{2+} (Figure 3C).

Taken together, the results demonstrated that the Pb^{2+} (200 μg/mL), Cd^{2+} (12.5 μg/mL), and Zn^{2+} (50 μg/mL) stresses significantly decreased cell membrane fluidity of *V. cholerae* J9-62, and Q6-10 isolates ($p < 0.05$), but increased the bacterial cell surface hydrophobicity, and inner membrane permeability, respectively ($p < 0.05$). Exceptionally, the Ni^{2+} (50 μg/mL) stress only significantly increased the cell membrane fluidity of *V. cholerae* N9-4 ($p < 0.05$).

Distinct secretomes of the *Vibrio cholerae* isolates under the heavy metal stresses

Secretomes of the *V. cholerae* isolates under the heavy metal stresses were obtained by the 2D-GE analysis (Figures 4A–C). Secretome patterns produced by three independent 2D-GE experiments of each isolate were consistent (Figures not shown). Comparative secretomic analysis revealed that *V. cholerae* J9-62, Q6-10, and N9-4 isolates secreted 30 common proteins (marked with different red letters, Figure 4 and Supplementary Table S3), and 32 differential proteins (marked with different red numbers, Figure 4 and Supplementary Table S4) under the Pb^{2+} (200 μg/mL), Cd^{2+} (12.5 μg/mL) and Zn^{2+} (50 μg/mL), and Ni^{2+} (50 μg/mL) stresses, respectively, as compared to the control groups. Amino acid sequences of each of these extracellular proteins were further determined by the LC–MS/MS analysis.

Remarkably, some differential extracellular proteins of *V. cholerae* J9-62, N9-4, and Q6-10 isolates were identified ($n = 5$ to 10) under the heavy metal stresses. For example, after treated with the Pb^{2+} (200 μg/mL) for 2 h, *V. cholerae* J9-62 secreted seven more extracellular proteins than the control group; *V. cholerae* Q6-10 secreted ten more, but five less extracellular proteins under the Zn^{2+}

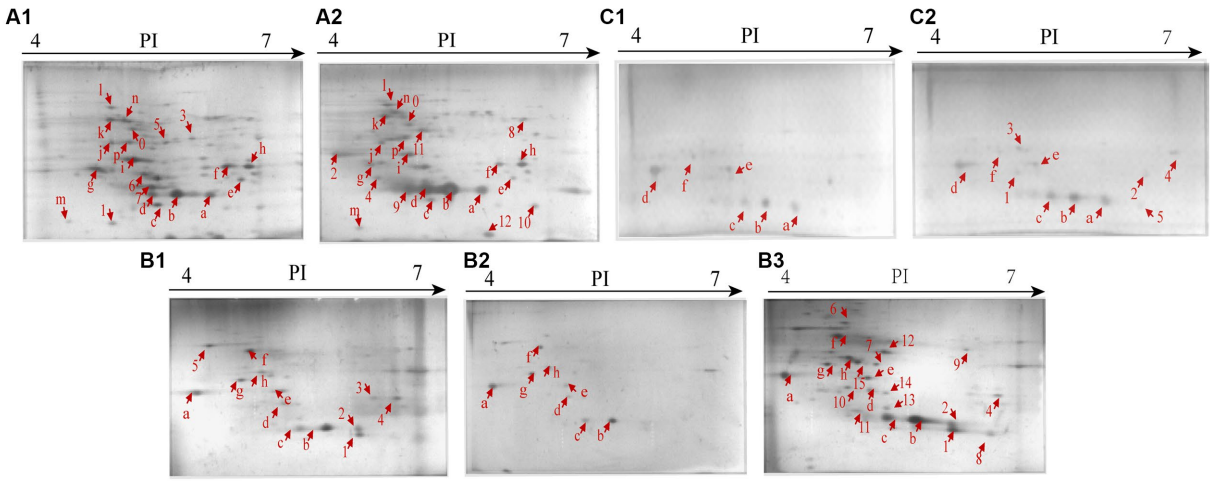

FIGURE 4
Secretomic profiles of the *V. cholerae* isolates under the heavy metal stresses by the 2D-GE analysis. **(A1,A2)** *V. cholerae* J9–62 incubated in the TSB medium without and with the Pb^{2+}(200 μg/mL) treatment, respectively. **(B1–B3)** *V. cholerae* Q6–10 without and with the Cd^{2+}(12.5 μg/mL) or Zn^{2+} (50 μg/mL) treatment, respectively. **(C1,C2)** *V. cholerae* N9–4 without and with the Ni^{2+} (50 μg/mL) treatment, respectively.

(50 μg/mL), and Cd^{2+}(12.5 μg/mL) stresses, respectively; and *V. cholerae* N9-4 secreted five more extracellular proteins under the Ni^{2+} (50 μg/mL) stress.

Identification of differential extracellular proteins of the *Vibrio cholerae* isolates under the heavy metal stresses

A total of 32 differential extracellular proteins were identified using the LC–MS/MS analysis (Supplementary Table S4). Of these, 20 extracellular proteins were grouped into three main Gene Onotology (GO) categories, whereas 12 had unknown function (Figure not shown).

The Pb^{2+} (200 μg/mL), Zn^{2+} (50 μg/mL), and Ni^{2+} (50 μg/mL) stresses increased extracellular protein secretion of *V. cholerae* J9-62, Q6-10, and N9-4 isolates, respectively (Figure 4). For example, approximately seven extracellular proteins were secreted by *V. cholerae* J9-62 under the Pb^{2+} (200 μg/mL) stress, including a gntP family permease (Spot A-8), a hydroxyacylglutathione hydrolase (Spot A-9), a Thiol: disulfide interchange protein (Spot A-10), an enolase (Spot A-11), a leucine aminopeptidase (Spot A-12), a porin_4 domain-containing protein (Spot A-2), and a DUF91 domain-containing protein (Spot A-4) (Figure 4A2).

Approximately ten extracellular proteins were secreted by *V. cholerae* Q6-10 under the Zn^{2+} (50 μg/mL) stress, e.g., a putrescine-binding periplasmic protein (Spot B-7), a S8 family peptidase (Spot B-9), and an outer membrane protein A (OmpA) (Spot B-10) (Figure 4B3), while approximately five differential extracellular proteins were identified from secretomic profiles of *V. cholerae* N9-4 under the Ni^{2+}(50 μg/mL) stress, e.g., a maltodextrin-binding protein (Spot C-1), a flagellin (Spot C-3), and a periplasmic thiosulfate-binding protein (Spot C-4) (Figure 4C2).

Conversely, under the Cd^{2+}(12.5 μg/mL) stress, *V. cholerae* Q6-10 secreted less extracellular proteins ($n = 5$) than those in the control group (Figure 4B2).

Identification of differential intracellular proteins (DIPs) in the *Vibrio cholerae* isolates under the heavy metal stresses

Identification of DIPs in *Vibrio cholerae* J9-62 under the Pb^{2+} stress

A total of 417 DIPs in *V. cholerae* J9-62 under the Pb^{2+} (200 μg/mL) stress for 2 h were identified by the LC–MS/MS analysis, as compared to the control group. Of these, 316 DIPs were grouped into GO categories, whereas 101 DIPs had unknown function. The most abundant GO term of the DIPs was the cellular process (79.75%, 252/316), followed by metabolic processes (75.95%, 240/316), and single-organism process (73.10%, 231/316) (Figure 5A).

The DIPs were significantly enriched in eleven metabolic pathways, including the butanoate metabolism, beta-lactam resistance, fatty acid metabolism, fatty acid biosynthesis, valine, leucine and isoleucine biosynthesis, bacterial secretion system, starch and sucrose metabolism, phosphotransferase system (PTS), carbon metabolism, amino sugar and nucleotide sugar metabolism, and oxidative phosphorylation ($p < 0.05$).

For example, in the beta-lactam resistance, the DIPs involved in heavy metal tolerance were found in *V. cholerae* J9-62 under the Pb^{2+} stress, e.g., an efflux transporter outer membrane subunit, a putative multidrug resistance protein, an ATP-binding protein, and a Co/Zn/Cd efflux system membrane fusion protein. Metal ion transportation occurs in active mode by ATP-binding cassette (ABC) transporters in bacterial cells (Mitra et al., 2021). It has been reported that metal exclusion occurred *via* resistance-nodulation cell division proteins across the proton gradient in *E. coli*, *Candida albicans*, and *Pseudomonas putida* to reduce cytotoxicity of heavy metals (Mitra et al., 2021).

In the butanoate metabolism, the expression of a glutathione peroxidase and a succinate-semialdehyde dehydrogenase was also induced in *V. cholerae* J9-62 under the Pb^{2+} stress. The glutathione peroxidase is an important antioxidant enzyme. The elevation of glutathione after the Pb treatment of *Rhodotorula mucilaginosa*

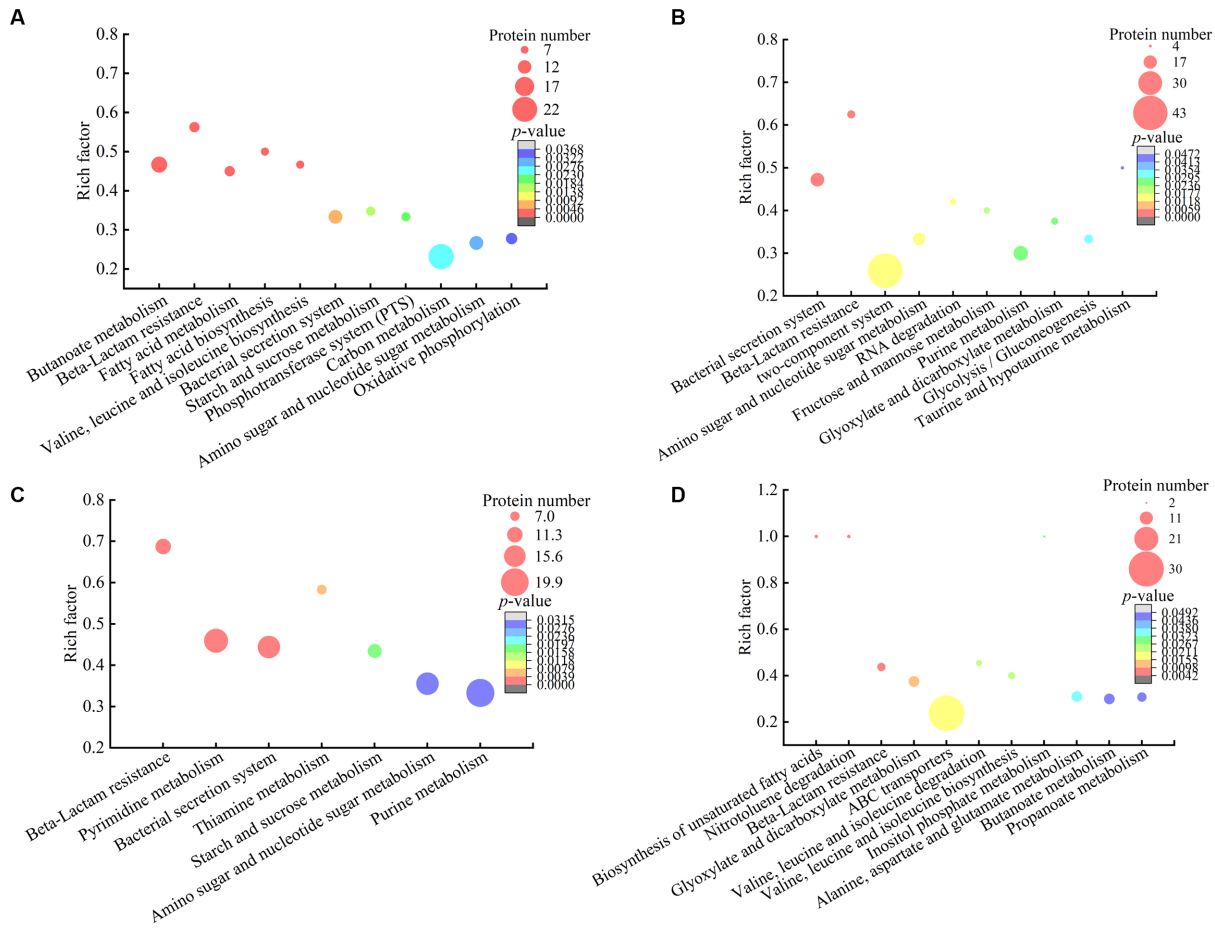

FIGURE 5
The metabolic pathways with significant enrichment of DIP produced by the *V. cholerae* isolates. **(A–D)** *V. cholerae* J9–62, Q6–10, and N9–4 under the Pb^{2+}; Cd^{2+}or Zn^{2+}; and Ni^{2+} stresses, respectively.

contributed to the enhanced detoxification of Pb (Chen et al., 2022). The succinate semialdehyde dehydrogenase directly participates in the formation of α-ketoglutarate that is an essential metabolite involved in anti-oxidative defense, energy production, signaling modules, and genetic modification in cells (Legendre et al., 2020).

In energy metabolic pathways such as the carbon metabolism, starch and sucrose metabolism, oxidative phosphorylation, as well as amino sugar and nucleotide sugar metabolism, the expression of some DIPs was enriched under the Pb^{2+} stress, e.g., a glyceraldehyde 3-phosphate dehydrogenase (GAPDH), a glucose-6-phosphate isomerase (GPI), an acetyl-CoA acetyltransferase, and a putative NADH oxidase. The coordination of these pathways may have provided critical material flux and energy for cell processes toward the Pb stress in *V. cholerae* J9-62.

Taken together, under the Pb^{2+} stress, *V. cholerae* J9-62 developed multiple defensive strategies for reducing cytotoxicity of the Pb: (1) induced the expression of transportation, efflux, and secretion systems-related proteins; (2) triggered the expression of antioxidative defense enzymes; (3) elicited the biosynthesis of hydrophobic amino acids; and (4) enriched the energy metabolism-related proteins.

Identification of DIPs in *Vibrio cholerae* Q6-10 under the Cd^{2+} stress

A total of 521 DIPs were identified in *V. cholerae* Q6-10 under the Cd^{2+} (12.5 μg/mL) stress for 2 h by the LC–MS/MS analysis, as compared to the control group. Of these, 427 DIPs were grouped into GO categories, whereas 94 DIPs had unknown function. The most abundant GO term of the DIPs was the cellular process (77.98%, 333/427), followed by metabolic processes (72.83%, 311/427), and single-organism process (64.87%, 277/427) (Figure 5B).

The DIPs were significantly enriched in bacterial secretion system, beta-lactam resistance, two-component system, amino sugar and nucleotide sugar metabolism, RNA degradation, fructose and mannose metabolism, purine metabolism, glyoxylate and dicarboxylate metabolism, glycolysis/gluconeogenesis, and taurine and hypotaurine metabolism ($p < 0.05$). Three of these metabolic pathways (bacterial secretion system, beta-lactam resistance, as well as amino sugar and nucleotide sugar metabolism) were also altered in the Pb^{2+}-induced *V. cholerae* J9-62.

For example, in the bacterial secretion system, the DIPs related to heavy metal Cd^{2+} resistance were identified, including type VI secretion system (T6SS) ATPase TssH, and IcmF. T6SS can secret various metal-binding proteins to promote bacterial survival in

harmful environments through metal ion acquisition (Wang et al., 2021; Dang et al., 2022). For instance, Hu et al. reported that T6SS contributed to zinc stress resistance in a BaeSR system-dependent manner (Hu et al., 2020).

In the beta-lactam resistance, the expression of a multidrug efflux resistance-nodulation-cell division (RND) transporter permease subunit VexB, an oligopeptide ABC transporter, an ATP-binding protein, and a vibriobactin export RND transporter periplasmic adaptor subunit VexG was induced under the Cd^{2+} stress in *V. cholerae* Q6-10. The RND family protein was able to efflux Cd from the cytoplasm to the periplasm in *Bacillus vietamensis* thereby alleviating its toxicity (Yu et al., 2020).

In the fructose and mannose metabolism, the expression of an exopolysaccharide (EPS) biosynthesis protein was identified. Fang et al. (2022) reported that *Cupriavidus nantongensis* $X1^T$ strain produced EPS under the stress of Cd^{2+}, which immobilized Cd^{2+} to protect the cells against the Cd^{2+} toxicity (Fang et al., 2022). Extracellular adsorption was the main pathway for microorganisms to remove Cd^{2+} from media to reduce its cytotoxicity (Heidari and Panico, 2020).

Taken together, under the Cd^{2+} (12.5 μg/mL) stress, *V. cholerae* Q6-10 developed multiple strategies to efficiently alleviate the Cd cytotoxicity: (1) induced the expression of transportation and efflux of multidrug efflux RND transporters; (2) elicited the expression of proteins related to the regulation of glutathione metabolism; (3) triggered the accumulation of taurine; (4) induced the expression of the EPS biosynthesis proteins; and (5) enriched the energy metabolism-related proteins.

Identification of DIPs in *Vibrio cholerae* Q6-10 under the Zn^{2+} stress

A total of 655 DIPs were identified in *V. cholerae* Q6-10 under the Zn^{2+} (50 μg/mL) stress for 2 h by the LC–MS/MS analysis, as compared to the control group. Of these, 498 DIPs were grouped into GO categories, whereas 157 DIPs had unknown function. The most abundant GO term of the DIPs was the cellular process (79.92%, 398/498), followed by metabolic processes (79.52%, 396/498), and catalytic activity (68.88%, 343/498) (Figure 5C).

The DIPs were significantly enriched in beta-lactam resistance, pyrimidine metabolism, bacterial secretion system, thiamine metabolism, starch and sucrose metabolism, amino sugar and nucleotide sugar metabolism, and purine metabolism ($p < 0.05$). Three of these metabolic pathways (bacterial secretion system, beta-lactam resistance, as well as amino sugar and nucleotide sugar metabolism) were also altered in the Pb^{2+}-induced *V. cholerae* J9-62, and the Cd^{2+}-induced *V. cholerae* Q6-10. Moreover, the starch and sucrose metabolism was also altered in the Pb^{2+}-induced *V. cholerae* J9-62.

For example, in the beta-lactam resistance, the expression of the DIPs involved in the Zn^{2+} resistance was identified in *V. cholerae* Q6-10, including a multidrug efflux RND transporter permease subunit VexB, a multidrug efflux RND transporter periplasmic adaptor subunit VexA, and a peptide ABC transporter. Bacterial drug-efflux transporters acted synergistically as diffusion barriers of cellular membranes to protect cells from heavy metals and toxic metabolites (Zgurskaya et al., 2022).

In the amino sugar and nucleotide sugar metabolism, the expression of an iron–sulfur cluster assembly protein CyaY, and an iron–sulfur cluster carrier protein was induced in *V. cholerae* Q6-10 under the Zn^{2+} stress. The metal-binding domain of iron–sulfur proteins functioned to entrap metallic elements inside the cells (Huang et al., 2019). Extracellular adsorption and intracellular accumulation were found to be the main pathways for microorganisms to remove Zn^{2+} from media to get rid of the Zn^{2+} toxicity (Vargas-García Mdel et al., 2012). In addition, amino sugar and nucleotide sugar metabolism, and starch and sucrose metabolism likely provided energy for cellular activities and maintained stability of the bacterial cell under the Zn^{2+} stress (Lee et al., 2016).

Taken together, under the Zn^{2+} (50 μg/mL) stress, *V. cholerae* Q6-10 employed multiple strategies to efficiently alleviate its cytotoxicity: (1) induced the expression of multidrug efflux RND transporters, and ABC transporters; (2) triggered the expression of extracellular adsorption and intracellular accumulation-related proteins; (3) elicited the expression of stress-related proteins; and (4) enriched the energy metabolism-related proteins.

Identification of DIPs in *Vibrio cholerae* N9-4 under the Ni^{2+} stress

A total of 441 DIPs were identified in *V. cholerae* N9-4 under the Ni^{2+} (50 μg/mL) stress for 2 h by the LC–MS/MS analysis, as compared to the control group. Of these, 378 DIPs were grouped into GO categories, whereas 63 DIPs had unknown function. The most abundant GO term of the DIPs was metabolic process (78.31%, 296/378), followed by catalytic activity (70.37%, 266/378), and single-organism process (65.87%, 249/378) (Figure 5D).

The DIPs were significantly enriched in the biosynthesis of unsaturated fatty acids, nitrotoluene degradation, beta-lactam resistance, glyoxylate and dicarboxylate metabolism, ABC transporters, valine, leucine and isoleucine degradation, valine, leucine and isoleucine biosynthesis, inositol phosphate metabolism, alanine, aspartate and glutamate metabolism, butanoate metabolism, and propanoate metabolism ($p < 0.05$). Of these, the bacterial secretion system was also altered in the Pb^{2+}-induced *V. cholerae* J9-62, Cd^{2+}-induced *V. cholerae* Q6-10, and Zn^{2+}-induced *V. cholerae* Q6-10; the butanoate metabolism, and valine, leucine and isoleucine biosynthesis were changed in the Pb^{2+}-induced *V. cholerae* J9-62 as well; the glyoxylate and dicarboxylate metabolism was also altered in the Cd^{2+}-induced *V. cholerae* Q6-10.

For instance, in the ABC transporters, the expression of an ABC transporter substrate-binding protein, an arginine ABC transporter, a sulfate ABC transporter substrate-binding protein, a peptide/nickel transport system substrate-binding protein, and a cysteine/glutathione ABC transporter permease was induced in *V. cholerae* N9-4 under the Ni^{2+} stress. ABC transporters can secret and excret foreign substances across cell membrane to maintain cellular homeostasis (Fan et al., 2023). They can export the cations as a metal-glutathione complex to reduce cytotoxicity of certain metals (Pearson and Cowan, 2021).

In the glyoxylate and dicarboxylate metabolism, the expression of a short-chain dehydrogenase/reductase (SDR) family oxidoreductase, a dihydrolipoamide dehydrogenase (DLD), and a bifunctional glutamine synthetase adenylyltransferase/adenylyl-removing enzyme was induced in *V. cholerae* N9-4 under the Ni^{2+} stress. For example, aldehyde reductases were identified as critical enzymes for catalyzing the detoxification reactions of aldehydes in *Saccharomyces cerevisiae* (Wang et al., 2019).

Taken together, under the Ni^{2+} (50 μg/mL) stress, *V. cholerae* N9-4 developed multiple strategies to efficiently reduce its cytotoxicity: (1) induced the expression of efflux pump RND transporters, ABC transporters, and T6SS-associated proteins; (2) triggered the expression of extracellular adsorption-associated proteins; (3) elicited the expression of stress-related proteins; and (4) triggered the glyoxylate and dicarboxylate metabolism pathways.

The main defensive strategies of the *Vibrio cholerae* isolates under the Pb^{2+}, Cd^{2+}, Zn^{2+}, and Ni^{2+} stresses

The comparative secretomic and proteomic analyses revealed common strategies developed by the *V. cholerae* isolates under different heavy metal (Pb^{2+}, Cd^{2+}, Zn^{2+}, and Ni^{2+}) stresses, such as the activation of efflux pump RND transporters, ABC transporters and metal chelators for effluxing; the expression of glutathione peroxidase for reducing oxidative stress damage; the biosynthesis of EPS for extracellular biosorption and sequestration; and the activation of energy metabolism-related pathways.

Notably, different strategies were also found in the *V. cholerae* isolates to cope with different heavy metal stresses. For example, *V. cholerae* J9-62 reduced the Pb^{2+} cytotoxicity by inducing the biosynthesis of hydrophobic amino acids; *V. cholerae* Q6-10 mitigated the Cd^{2+} damage by inducing taurine accumulation; *V. cholerae* Q6-10 reduced the Zn^{2+} hazard by elicting the iron–sulfur protein expression and thiamin biosynthesis; and *V. cholerae* N9-4 reduced the Ni^{2+} cytotoxicity by triggering the expression of T6SS-associated proteins (Figure 6).

The effects of the heavy metal stresses on putative virulence-associated proteins in the *Vibrio cholerae* isolates

In this study, among the 32 identified differential extracellular proteins, four virulence-associated proteins were secreted by the *V. cholerae* J9-62, N9-4, and Q6-10 isolates. Among the 2,034 identified DIPs produced by the *V. cholerae* isolates, approximately 108 were directly or indirectly involved in the virulence of pathogenic bacteria, such as adhesion, invasion, damage of host cells, and regulation of virulence (Supplementary Table S5).

For example, under the Zn^{2+} (50 μg/mL) stress, *V. cholerae* Q6-10 secreted more extracellular virulence-associated proteins ($n = 3$) than the control group, including an OmpA (Spot B-10), a high-affinity zinc uptake system protein ZnuA (Spot B-13), and a PrkA serine protein kinase (Spot B-14). It has been reported that OmpA was a highly multifunctional protein required for bacterial virulence in *Pseudomonas aeruginosa* (Paulsson et al., 2021). PrkA is required for cell wall stress responses, and virulence in *Listeria monocytogenes* (Kelliher et al., 2021).

Approximately 89 intracellular virulence-associated proteins were produced by *V. cholerae* J9-62, and Q6-10 isolates under the Pb^{2+} (200 μg/mL) ($n = 25$), Cd^{2+} (12.5 μg/mL) ($n = 26$), and Zn^{2+} (50 μg/mL) ($n = 38$) stresses (Supplementary Table S5), e.g., a T6SS-associated forkhead-associated (FHA) domain protein TagH (Spot 558), a transmembrane regulator ToxS (Spot 980), and a cholix toxin (Spot 927). For example, it has been reported that the TagH regulated the hemolytic activity and virulence of *V. cholerae* (Wang G. et al., 2022).

Under the Ni^{2+} (50 μg/mL) stress, *V. cholerae* N9-4 expressed more intracellular virulence-associated proteins ($n = 20$) than the control

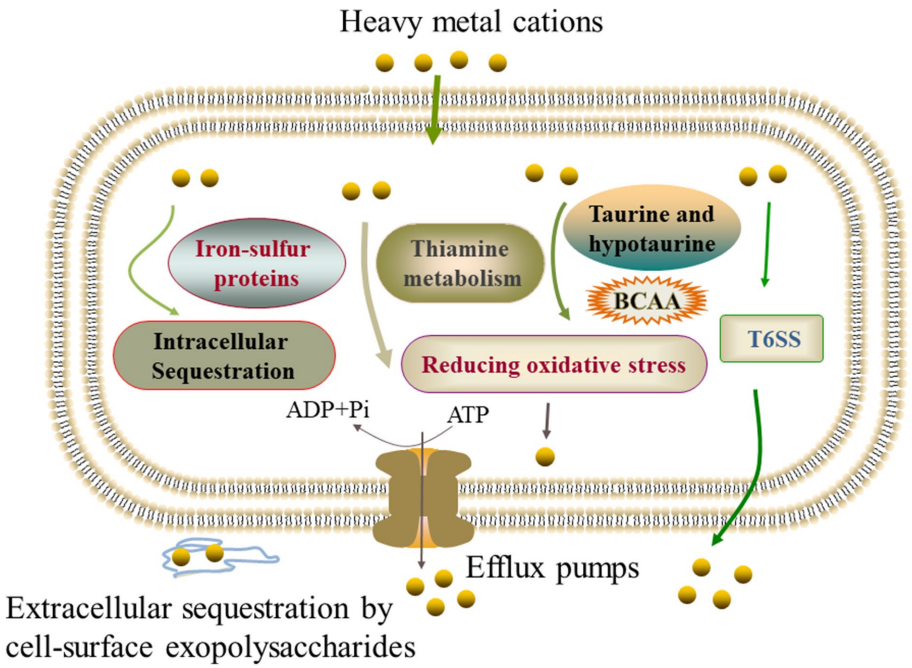

FIGURE 6
The mechanistic diagram of the *V. cholerae* tolerance toward the heavy metals Pb^{2+}, Cd^{2+}, Zn^{2+}, and Ni^{2+} stresses. BCAA, branched-chain amino acid, e.g., isoleucine, valine, and leucine.

group, e.g., a NADH-dependent flavin oxidoreductase (NFOR) (Spot 729), a T6SS protein VasJ (Spot 1147), a transcriptional activator HlyU (Spot 1046), and an OmpV (Spot 812). For instance, Xie et al. (2021) reported that NFOR was involved in the pathogenicity of *Mycoplasma hyopneumoniae*. HlyU is a transcriptional regulator essential for the virulence of *Vibrio vulnificus* (Lee et al., 2019). OmpV played a vital role in the pathogenesis of *Salmonella typhimurium*, including the adhesion and invasion to intestinal epithelial cells (Kaur et al., 2021).

These results highlighted that a number of putative virulence-associated proteins ($n = 112$) were differently produced and or secreted by the *V. cholerae* isolates under the heavy metal stresses, implying an increased health risk of the *V. cholerae* isolates in aquatic products triggered by the heavy metal stresses.

The effects of the heavy metal stresses on putative resistance-associated proteins in the *Vibrio cholerae* isolates

In this study, one differential extracellular protein, and approximately 55 DIPs involved in bacterial resistance were identified in the *V. cholerae* isolates under the heavy metal stresses (Supplementary Table S6).

For instance, there were 35 intracellular resistance-associated proteins produced by *V. cholerae* J9-62, and Q6-10 isolates under the Pb^{2+} (200 μg/mL) ($n = 10$), Cd^{2+} (12.5 μg/mL) ($n = 6$), and Zn^{2+} (50 μg/mL) ($n = 19$) stresses, e.g., a multidrug transporter AcrB (Spot 563), and a tetR family transcriptional regulator (Spot 1133). Under the Ni^{2+} (50 μg/mL) stress, *V. cholerae* N9-4 produced more intracellular resistance-associated proteins ($n = 23$) than the control group, e.g., a lytic transglycosylases (Spot 1115), and a putative glutathione S-transferase (Spot 1058).

In addition, to confirm the identified proteins by the 2D-GE and LC–MS/MS methods, the qRT-PCR was carried out to examine the expression of randomly chosen differential proteins. The obtained results were in agreement with those by the secretomic and proteomic analyses in this study (Supplementary Table S7 and Supplementary Figure S1).

Discussion

V. cholerae is frequently isolated from aquatic products (Xu et al., 2019; Fu et al., 2020; Chen et al., 2021). China is the largest producer, exporter, and consumer of aquatic products worldwide. Thus, it is of great significance to investigate molecular mechanisms of *V. cholerae* of aquatic animal origins toward the heavy metal stresses in order to effectively control the pathogen in aquatic products.

The MIC is currently the best available parameter to reflect the effectiveness of an antibiotic or heavy metal against bacterial strains (Kowalska-Krochmal and Dudek-Wicher, 2021). In this study, the MIC values of Cd^{2+}, and Zn^{2+} was 400 μg/mL, and 800 μg/mL against *V. cholerae* Q6-10, respectively, while those of Pb^{2+}, and Ni^{2+} agaist *V. cholerae* J9-62, and N9-4 were 3,200 μg/mL, and 400 μg/mL, respectively. Chen et al. (2021) reported that the maximum MIC values against the *V. cholerae* isolates ($n = 203$) were 800 μg/mL for Cd^{2+}, 1600 μg/mL for Zn^{2+}, 3200 μg/mL for Pb^{2+}, and 1600 μg/mL for Ni^{2+}. Similarly, the higher MICs of heavy metals against *V. cholerae* isolates of aquatic animal origins were also reported by Fu et al. (2020). These results suggested possible heavy metal exposure or pollution sources in the aquaculture environments.

Changes in cell biophysical properties have been disclosed as stressors affecting compound and ion transport and cell integrity (Yu P. et al., 2022). Bacterial strains applied different mechanisms to response to heavy metals, such as bond formation between bacterial cell surface and metal ions to decrease their toxicity (Heidari and Panico, 2020; Wróbel et al., 2023). The compositions of the cell surface (e.g., hydroxyl, phosphate, carboxyl, and sulfate) are more involved in linking to metal ions, leading to the deposition of metal ions on the cell surface or the accumulation between the space of the cell membranes (Jarosławiecka and Piotrowska-Seget, 2014; Ashrafi et al., 2022). In this study, our results revealed that the cytoplasma membrane permeability of *V. cholerae* J9-62 and Q6-10 isolates was significantly increased under the Pb^{2+} (200 μg/mL), and Cd^{2+} (12.5 μg/mL) or Zn^{2+} (50 μg/mL) stresses, respectively ($p < 0.05$). The increased inner membrane permeability was also found in *V. parahaemolyticus* N10-8 after treated with a sublethal concentration of Cd^{2+} (50 μg/mL) in our recent study (Yu P. et al., 2022). Likewise, cell membrane fluidity affected most compounds and ions (such as nutrients and heavy metals) to cross the bacterial cytoplasma membrane (Bessa et al., 2018). In this study, we found that the cell membrane fluidity of *V. cholerae* J9-62, and Q6-10 isolates was significantly decreased under the Pb^{2+}, and Cd^{2+} or Zn^{2+} stresses, respectively ($p < 0.05$). Hu et al. (2019) reported that the plasma membrane fluidity of *E. coli* and *Phanerochaete chrysosporium* decreased gradually with the increased concentrations of Cd^{2+} (0–80 nM). Most recently, Yu S. et al. (2022) found that the cell membrane fluidity of *V. parahaemolyticus* N10-18 was significantly decreased after treated with the 50 μg/mL of Cd^{2+}. Bacteria can adjust membrane lipid composition to control membrane homeostasis in response to environmental changes (Bessa et al., 2018). In this study, the proteome-level analysis provided certain evidence for the results by the biochemical assays. For example, the comparative proteomic analysis revealed that the expression of fatty acid biosynthesis-associated proteins was significantly induced in *V. cholerae* J9-62 under the Pb^{2+} stress ($p < 0.05$). The altered abundance of lipid-metabolism-related proteins likely led to the reduced cell membrane fluidity (Li D. et al., 2022). In addition, cell membrane hydrophobicity affected the activation free energy of passive lipid transport (Rogers et al., 2021). In this study, we observed that the cell membrane hydrophobicity of *V. cholerae* J9-62, and Q6-10 isolates was significantly increased under the Pb^{2+}, and Cd^{2+} or Zn^{2+} stresses ($p < 0.05$). Similar case was also found in *V. parahaemolyticus* N10-8 after treated with the Cd^{2+} (50 μg/mL) in our recent study (Yu P. et al., 2022). Exceptionally, the Ni^{2+} (50 μg/mL) stress only increased the cell membrane fluidity of *V. cholerae* N9-4 ($p < 0.05$). Taken, our results, coupled with the previous studies, suggested that the changes in cell biophysical properties were likely additional strategies for *V. cholerae* to survive under the heavy metal stresses.

Consistent with the changes in the bacterial cell biophysical properties, comparative secretomic and proteomic analyses revealed differential extracellular and intracellular proteins in *V. cholerae* J9-62, Q6-10, and N9-4 isolates elicited by the Pb^{2+}, Cd^{2+}, Zn^{2+}, or Ni^{2+} stresses, respectively. Interestingly, the Pb^{2+}, Zn^{2+}, and Ni^{2+} stresses increased extracellular protein secretion in *V. cholerae* J9-62, Q6-10, and N9-4 isolates ($n = 5$–10), respectively, whereas under the Cd^{2+} stress, *V. cholerae* Q6-10 secreted less extracellular proteins ($n = 5$)

than those in the control group. For example, the secretion of enolase (spot A-11) was induced in *V. cholerae* J9-62 under the Pb^{2+} stress. Ling et al. reported that enolase was secreted by alkaliphilic bacterium *Bacillus lehensis* G1 in the alkaline pH condition (Ling et al., 2018). Recently, Zhao et al. (2023) reported that enolase, a Cd resistance-related protein from hyperaccumulator plant *Phytolacca americana,* increased the tolerance of *E. coli* to Cd stress. These results, coupled with our finding in this study, provided evidence for enolase serving as a stress protein under different environmental stresses. In addition, seven to ten metabolic pathways in *V. cholerae* J9-62, Q6-10, and N9-4 isolates were significantly altered under the Pb^{2+}, Cd^{2+}, Zn^{2+}, or Ni^{2+} stresses, respectively. For example, many DIPs were enriched in the starch and sucrose, fructose and mannose, glycolysis and gluconeogenesis, amino acid sugar and nucleotide sugar metabolic pathways in *V. cholerae* J9-62, and Q6-10 under the Pb^{2+}, and Cd^{2+} stresses, respectively. Notably, all these pathways were associated with glucose metabolism, the coordination of which may have provided critical material fluxes and energy for cellular activity, especially under the heavy metal stress. Additionally, a close link between the purine/pyrimidine metabolism and antimicrobial stress has been suggested (Sung et al., 2022). In this study, our comparative proteomic data provided the first evidence for such metabolism-related proteins involved in the Zn^{2+} stress in *V. cholerae* Q6-10.

An effective regulation of metal ion homeostasis is essential for bacterial survival in any environment. An eminent mechanism for such homeostasis is ABC transporters (Mandal et al., 2019). In this study, many proteins involved in ABC transporters were produced in the *V. cholerae* isolates under the heavy metal stresses. For example, an ABC transporter substrate-binding protein, an arginine ABC transporter, a sulfate ABC transporter substrate-binding protein, a peptide/nickel transport system substrate-binding protein, and a cysteine/glutathione ABC transporter permease were produced in *V. cholerae* N9-4 under the Ni^{2+} stress. In this study, we found that efflux pumps-associated proteins were produced in the *V. cholerae* isolates under the heavy metal stresses. For example, an efflux transporter outer membrane subunit, and a Co/Zn/Cd efflux system membrane fusion protein were expressed in *V. cholerae* J9-62 under the Pb^{2+} stress; a multidrug efflux RND transporter permease subunit VexB, and a vibriobactin export RND transporter periplasmic adaptor subunit VexG were produced in *V. cholerae* Q6-10 under the Cd^{2+} stress; a multidrug efflux RND transporter permease subunit VexB, and a multidrug efflux RND transporter periplasmic adaptor subunit VexA were expressed in *V. cholerae* Q6-10 under the Zn^{2+} stress. In addition, the expression of iron carriers in *V. cholerae* J9-62, and Q6-10 isolates were induced under the Pb^{2+}, and Zn^{2+} stresses, respectively. Most recently, we also found the greatly enhanced expression of Zn/Cd/Hg/Pb-transportation and efflux, and ABC transporters in *V. parahaemolyticus* N10-18 under the Cd stress (Yu P. et al., 2022).

Thiamine was involved in various abiotic stress response in microorganisms, such as drought, high salt, and oxidative stress (Li Y. et al., 2022). In this study, thiamine biosynthesis-associated proteins were produced in *V. cholerae* Q6-10 under the Zn^{2+} stress. The expression of glutathione peroxidase and glutathione reductase were also induced in *V. cholerae* Q6-10 under the Cd^{2+} stress. Fang et al. reported that *C. nantongensis* $X1^T$ strain could reduce the cytotoxicity of Cd^{2+} and improve resistance to Cd^{2+} by regulating glutathione metabolism and reducing oxidative stress (Fang et al., 2022). Moreover, in this study, *V. cholerae* Q6-10 was found to significantly enrich the taurine and hypotaurine metabolism under the Cd^{2+} stress. Taurine has been proven to have clear alleviating effects on the damage caused by Cd, Mn, and Pb (Duan et al., 2023).

In this study, we found that the expression of extracellular polysaccharides was induced in *V. cholerae* N9-4, and Q6-10 isolates under the Ni^{2+}, and Cd^{2+} stresses, respectively, and that a high-affinity zinc uptake system protein ZnuA (Spot B-13) was secreted by *V. cholerae* Q6-10 under the Zn^{2+} stress, suggesting possible extracellular sequestration of the heavy metals. Overall, our data revealed common defensive strategies developed by the *V. cholerae* isolates under different heavy metal (Pb^{2+}, Cd^{2+}, Zn^{2+}, and Ni^{2+}) stresses. On the other hand, different strategies were also observed in the *V. cholerae* isolates to cope with different heavy metal stresses.

Notably, a number of putative virulence-associated proteins were differently produced ($n = 108$) and secreted ($n = 4$) in the *V. cholerae* isolates under the heavy metal stresses. For example, the expression of T6SS-related proteins in *V. cholerae* Q6-10, and N9-4 was induced under the Cd^{2+}, and Ni^{2+} stresses, respectively, which are closely associated with the virulence of *V. cholerae* (Crisan and Hammer, 2020). Fang et al. reported that Cd^{2+} (20 mg/L) elicited differential expression of 1,157 genes in *C. nantongensis* $X1^T$, including the T6SS-related genes. In addition, in this study, some putative resistance-associated proteins were also differently produced in the *V. cholerae* isolates under the heavy metal stresses. These data suggested an increased health risk of the *V. cholerae* isolates in aquatic products triggered by the heavy metal stresses.

Although the 2D-GE is a powerful technique to study protein alternations in bacteria under environmental stresses, due to the technique limitations of protein spot separation on the 2D-GE gels, not all of the differential extracellular proteins could be identified from the *V. cholerae* isolates under the heavy metal stresses. Similar case for the proteomics data, particularly to the proteins with weaker abundance or at lower expression levels. Additionally, *V. cholerae* is usually challenged by multiple heavy metals in aquatic environments. Therefore, it will be interesting to investigate synergistic effects of different heavy metals on the *V. cholerae* survival in the future research.

Conclusion

The *V. cholerae* J9-62, Q6-10, and N9-4 isolates of aquatic animal origins showed different heavy metal tolerant profiles. The sublethal concentrations of the Pb^{2+} (200 μg/mL), Cd^{2+} (12.5 μg/mL) and Zn^{2+} (50 μg/mL) stresses at 37°C for 2 h decreased cell membrane fluidity of *V. cholerae* J9-62, and Q6-10 ($p < 0.05$), but increased the bacterial cell surface hydrophobicity and inner membrane permeability ($p < 0.05$). Exceptionally, the Ni^{2+} (50 μg/mL) stress only increased the cell membrane fluidity of *V. cholerae* N9-4 ($p < 0.05$).

The comparative secretomic analysis revealed that *V. cholerae* J9-62, Q6-10, and N9-4 isolates secreted 32 differential proteins under the Cd^{2+} (12.5 μg/mL), Pb^{2+} (200 μg/mL), Ni^{2+} (50 μg/mL), or Zn^{2+} (50 μg/mL) stresses. Meanwhile, a number of DIPs were also identified in the *V. cholerae* isolates, which significantly altered seven to eleven metabolic pathways under the Pb^{2+}, Cd^{2+}, Zn^{2+}, or Ni^{2+} stresses. The comparative secretomic and proteomic analyses revealed common defensive strategies developed by the *V. cholerae* isolates to ameliorate cytotoxicity of the heavy metal (Pb^{2+}, Cd^{2+}, Zn^{2+}, and Ni^{2+}) stresses, such as the activation of efflux pump RND transporters, ABC

transporters and metal chelators for transportation and effluxing; the expression of glutathione peroxidase for reducing oxidative stress damage; the biosynthesis of EPS for extracellular biosorption and sequestration; and the activation of energy metabolism-related pathways. In addition, different strategies were also observed in the *V. cholerae* isolates to cope with different heavy metal stresses: *V. cholerae* J9-62 reduced the Pb^{2+} cytotoxicity by inducing the biosynthesis of hydrophobic amino acids; *V. cholerae* Q6-10 mitigated the Cd^{2+} damage by inducing taurine accumulation; *V. cholerae* Q6-10 reduced the Zn^{2+} hazard by eliciting the iron–sulfur protein expression and thiamin biosynthesis; and *V. cholerae* N9-4 reduced the Ni^{2+} cytotoxicity by triggering the expression of T6SS-associated proteins.

Remarkably, a number of putative virulence and resistance-associated proteins were differently produced and/or secreted in the *V. cholerae* isolates under the heavy metal stresses, suggested an increased health risk of the *V. cholerae* isolates in aquatic products under the heavy metal conditions.

Overall, the results of this study fill prior gaps of *V. cholerae* in response to the heavy metal stresses, and facilitate better understanding of pathogenesis and MDR resistance of the common waterborne pathogen worldwide.

Data availability statement

The raw LC-MS/MS data have been deposited in the ProteomeXchange Consortium via the PRoteomics IDEntifications (PRIDE) database (iPRIDE) partner respiratory under the accession number PXD046079.

Author contributions

BZ: Data curation, Formal analysis, Investigation, Writing – original draft. JX: Data curation, Formal analysis, Writing – original draft. MS: Investigation, Writing – original draft. PY: Writing – original draft. YM: Data curation, Formal analysis, Writing – original draft. LX: Supervision, Writing – review & editing. LC: Conceptualization, Funding acquisition, Project administration, Supervision, Writing – review & editing.

Funding

The author(s) declare financial support was received for the research, authorship, and/or publication of this article. This research was financially supported by the Science and Technology Commission of Shanghai Municipality, grant number 17050502200, and the National Natural Science Foundation of China, grant number 31671946.

Acknowledgments

The authors would like to express gratitude to Lili Yan, Huanhuan Fan, Tingting Gu, and Fengfeng Cao in College of Food Science and Technology, Shanghai Ocean University for their help in comparative secretomic and/or proteomic analysis.

Conflict of interest

The authors declare that the research was conducted in the absence of any commercial or financial relationships that could be construed as a potential conflict of interest.

Publisher's note

Supplementary material

The Supplementary material for this article can be found online at: https://www.frontiersin.org/articles/10.3389/fmicb.2023.1294177/full#supplementary-material

References

Arslan, C., Altan, H., Akgün, O. O., Kiziler, A. R., Aydemir, B., Güzel, S., et al. (2010). Trace elements and toxic heavy metals play a role in Buerger disease and atherosclerotic peripheral arterial occlusive disease. *Int. Angiol.* 29, 489–495.

Ashrafi, Z., Heidari, P., and Mojerlou, S. (2022). Does the long-term contamination of lead (PbII) affect the bioremediation mechanisms of *Microbacterium oxydans* strain CM3 and CM7? *Soil Sediment Contamin.* 31, 959–973. doi: 10.1080/15320383.2022.2028719

Baker-Austin, C., Oliver, J. D., Alam, M., Ali, A., Waldor, M. K., Qadri, F., et al. (2018). *Vibrio* spp. infections. *Nat. Rev. Dis. Primers.* 4, 1–19. doi: 10.1038/s41572-018-0005-8

Bessa, L. J., Ferreira, M., and Gameiro, P. (2018). Evaluation of membrane fluidity of multidrug-resistant isolates of Escherichia coli and *Staphylococcus aureus* in presence and absence of antibiotics. *J. Photochem. Photobiol. B* 181, 150–156. doi: 10.1016/j.jphotobiol.2018.03.002

Carmignani, M., Boscolo, P., Poma, A., and Volpe, A. R. (1999). Kininergic system and arterial hypertension following chronic exposure to inorganic lead. *Immunopharmacology* 44, 105–110. doi: 10.1016/s0162-3109(99)00115-0

Chen, D., Li, X., Ni, L., Xu, D., Xu, Y., Ding, Y., et al. (2021). First experimental evidence for the presence of potentially toxic *Vibrio cholerae* in snails, and virulence, cross-resistance and genetic diversity of the bacterium in 36 species of aquatic food animals. *Antibiotics* 10:412. doi: 10.3390/antibiotics10040412

Chen, T., Shi, Y., Peng, C., Tang, L., Chen, Y., Wang, T., et al. (2022). Transcriptome analysis on key metabolic pathways in *Rhodotorula mucilaginosa* under Pb(II) stress. *Appl. Environ. Microbiol.* 88:e0221521. doi: 10.1128/aem.02215-21

Crisan, C. V., and Hammer, B. K. (2020). The *Vibrio cholerae* type VI secretion system: toxins, regulators and consequences. *Environ. Microbiol.* 22, 4112–4122. doi: 10.1111/1462-2920.14976

Dang, J., Wang, T., Wen, J., and Liang, H. (2022). An important role of the type VI secretion system of *Pseudomonas aeruginosa* regulated by Dnr in response to anaerobic en-vironments. *Microbiol. Spectr.* 10:e0153322. doi: 10.1128/spectrum.01533-22

Das, B., Verma, J., Kumar, P., Ghosh, A., and Ramamurthy, T. (2020). Antibiotic resistance in *Vibrio cholerae*: understanding the ecology of resistance genes and mechanisms. *Vaccine* 38, A83–A92. doi: 10.1016/j.vaccine.2019.06.031

Duan, Y., Zhao, Y., Wang, T., Sun, J., Ali, W., Ma, Y., et al. (2023). Taurine alleviates cadmium-induced hepatotoxicity by regulating autophagy flux. *Int. J. Mol. Sci.* 24:1205. doi: 10.3390/ijms24021205

Fan, J., To, K. K. W., Chen, Z.-S., and Fu, L. (2023). ABC transporters affects tumor immune microenvironment to regulate cancer immunotherapy and multidrug resistance. *Drug Resist. Updat.* 66:100905. doi: 10.1016/j.drup.2022.100905

Fang, L., Zhu, H., Geng, Y., Zhang, G., Zhang, H., Shi, T., et al. (2022). Resistance properties and adaptation mechanism of cadmium in an enriched strain, Cupriavidus nantongensis X1(T). *J. Hazard. Mater.* 434:128935. doi: 10.1016/j.jhazmat.2022.128935

Fu, H., Yu, P., Liang, W., Kan, B., Peng, X., and Chen, L. (2020). Virulence, resistance, and genomic fingerprint traits of *Vibrio cholerae* isolated from 12 species of aquatic products in Shang-hai, China. *Microb. Drug Resist.* 26, 1526–1539. doi: 10.1089/mdr.2020.0269

Genchi, G., Sinicropi, M. S., Lauria, G., Carocci, A., and Catalano, A. (2020). The effects of cadmium toxicity. *Int. J. Environ. Res. Public Health* 17:3782. doi: 10.3390/ijerph17113782

Heidari, P., and Panico, A. (2020). Sorption mechanism and optimization study for the bioremediation of Pb(II) and cd(II) contamination by two novel isolat-ed strains Q3 and Q5 of *Bacillus* sp. *Int. J. Environ. Res. Public Health* 17:4059. doi: 10.3390/ijerph17114059

Hu, L., Wang, C., Lu, W., Lu, H., Chen, H., and Tan, C. (2020). BaeSR activates type VI secretion system expression in porcine extra-intestinal pathogenic *Escherichia coli* to enhance bacterial resistance to zinc stress. *Microb. Pathog.* 147:104357. doi: 10.1016/j.micpath.2020.104357

Hu, L., Zhong, H., and He, Z. (2019). The cytotoxicities in prokaryote and eukaryote varied for CdSe and CdSe/ZnS quantum dots and differed from cadmium ions. *Ecotoxicol. Approximately. Saf.* 181, 336–344. doi: 10.1016/j.ecoenv.2019.06.027

Huang, B., Liu, X., Li, Z., Zheng, Y., Wai Kwok Yeung, K., Cui, Z., et al. (2021). Rapid bacteria capturing and killing by AgNPs/N-CD@ZnO hybrids strengthened photo-responsive xerogel for rapid healing of bacteria-infected wounds. *Chem. Eng. J.* 414:128805. doi: 10.1016/j.cej.2021.128805

Huang, N., Mao, J., Zhao, Y., Hu, M., and Wang, X. (2019). Multiple transcriptional mechanisms collectively mediate copper resistance in *Cupriavidus gilardii* CR3. *Environ. Sci. Technol.* 53, 4609–4618. doi: 10.1021/acs.est.8b06787

Jarosławiecka, A., and Piotrowska-Seget, Z. (2014). Lead resistance in micro-organisms. *Microbiology* 160, 12–25. doi: 10.1099/mic.0.070284-0

Kaur, D., Gandhi, S., and Mukhopadhaya, A. (2021). *Salmonella typhimurium* adhesin OmpV activates host immunity to confer protection against systemic and gastrointestinal infection in mice. *Infect. Immun.* 89:e0012121. doi: 10.1128/iai.00121-21

Kelliher, J. L., Grunenwald, C. M., Abrahams, R. R., Daanen, M. E., Lew, C. I., Rose, W. E., et al. (2021). PASTA kinase-dependent control of peptidoglycan synthesis via ReoM is required for cell wall stress responses, cytosolic survival, and virulence in *Listeria monocytogenes*. *PLoS Pathog.* 17:e1009881. doi: 10.1371/journal.ppat.1009881

Kowalska-Krochmal, B., and Dudek-Wicher, R. (2021). The minimum inhibitory concentration of antibiotics: methods, interpretation, clinical relevance. *Pathogens* 10:165. doi: 10.3390/pathogens10020165

Lee, D. K., Ahn, S., Cho, H. Y., Yun, H. Y., Park, J. H., Lim, J., et al. (2016). Metabolic response induced by parasitic plant-fungus interactions hinder amino sugar and nucleotide sugar metabolism in the host. *Sci. Rep.* 6:37434. doi: 10.1038/srep37434

Lee, Z. W., Kim, B. S., Jang, K. K., Bang, Y. J., Kim, S., Ha, N. C., et al. (2019). Small-molecule inhibitor of HlyU attenuates virulence of Vibrio species. *Sci. Rep.* 9:4346. doi: 10.1038/s41598-019-39554-y

Legendre, F., MacLean, A., Appanna, V. P., and Appanna, V. D. (2020). Biochemical pathways to α-ketoglutarate, a multi-faceted metabolite. *World J. Microbiol. Biotechnol.* 36:123. doi: 10.1007/s11274-020-02900-8

Li, X., Gu, A. Z., Zhang, Y., Xie, B., Li, D., and Chen, J. (2019). Sub-lethal concentrations of heavy metals induce antibiotic resistance via mutagenesis. *J. Hazard. Mater.* 369, 9–16. doi: 10.1016/j.jhazmat.2019.02.006

Li, D., He, S., Dong, R., Cui, Y., and Shi, X. (2022). Stress response mechanisms of *Salmonella enteritidis* to sodium hypochlorite at the proteomic level. *Foods* 11:2918. doi: 10.3390/foods11182912

Li, Y., Long, H., Jiang, G., Yu, Z., Huang, M., Zou, S., et al. (2022). Protective effects of thiamine on *Wickerhamomyces anomalus* against ethanol stress. *Front. Microbiol.* 13:1057284. doi: 10.3389/fmicb.2022.1057284

Ling, H. L., Rahmat, Z., Bakar, F. D. A., Murad, A. M. A., and Illias, R. M. (2018). Secretome analysis of alkaliphilic bacterium *Bacillus lehensis* G1 in response to pH changes. *Microbiol. Res.* 215, 46–54. doi: 10.1016/j.micres.2018.06.006

Mandal, S. K., Adhikari, R., Sharma, A., Chandravanshi, M., Gogoi, P., and Kanaujia, S. P. (2019). Designating ligand specificities to metal uptake ABC transporters in *Thermus thermophilus* HB8. *Metallomics* 11, 597–612. doi: 10.1039/c8mt00374b

Mitra, A., Chatterjee, S., Kataki, S., Rastogi, R. P., and Gupta, D. K. (2021). Bacterial tolerance strategies against lead toxicity and their relevance in bioremediation application. *Environ. Sci. Pollut. Res. Int.* 28, 14271–14284. doi: 10.1007/s11356-021-12583-9

Okay, S., Yildirim, V., Buttner, K., Becher, D., and Ozcengiz, G. (2020). Dynamic proteomic analysis of *Phanerochaete chrysosporium* under copper stress. *Ecotoxicol. Environ. Saf.* 198:110694. doi: 10.1016/j.ecoenv.2020.110694

Paulsson, M., Kragh, K. N., Su, Y. C., Sandblad, L., Singh, B., Bjarnsholt, T., et al. (2021). Peptidoglycan-binding anchor is a *Pseudomonas aeruginosa* OmpA family lipoprotein with importance for outer membrane vesicles, biofilms, and the periplasmic shape. *Front. Microbiol.* 12:639582. doi: 10.3389/fmicb.2021.639582

Pearson, S. A., and Cowan, J. A. (2021). Glutathione-coordinated metal complexes as substrates for cellular transporters. *Metallomics* 13:mfab015. doi: 10.1093/mtomcs/mfab015

Rogers, J. R., Espinoza Garcia, G., and Geissler, P. L. (2021). Membrane hydrophobicity determines the activation free energy of passive lipid transport. *Biophys. J.* 120, 3718–3731. doi: 10.1016/j.bpj.2021.07.016

Sadeq, S. A., and Beckerman, A. P. (2019). The chronic effects of copper and cadmium on life history traits across Cladocera species: a meta-analysis. *Arch. Environ. Contam. Toxicol.* 76, 1–16. doi: 10.1007/s00244-018-0555-5

Salamm, M. A., Al-Amin, M. Y., Salam, M. T., Pawar, J. S., Akhter, N., Rabaan, A. A., et al. (2023). Antimicrobial resistance: a growing serious threat for global public health. *Healthcare* 11:1946. doi: 10.3390/healthcare11131946

Sánchez-Rojas, T., Espinoza-Culupú, A., Ramírez, P., Iwai, L. K., Montoni, F., Macedo-Prada, D., et al. (2022). Proteomic study of response to copper, cadmium, and chrome ion stress in Yarrowia lipolytica strains isolated from andean mine tailings in Peru. *Microorganisms* 10:2002. doi: 10.3390/microorganisms10102002

Shan, X., Fu, J., Li, X., Peng, X., and Chen, L. (2022). Comparative proteomics and secretomics revealed virulence, and coresistance-related factors in non O1/O139 *Vibrio cholerae* recovered from 16 species of consumable aquatic animals. *J. Proteome* 251:104408. doi: 10.1016/j.jprot.2021.104408

Sit, B., Fakoya, B., and Waldor, M. K. (2022). Animal models for dissecting *Vibrio cholerae* intestinal pathogenesis and immunity. *Curr. Opin. Microbiol.* 65, 1–7. doi: 10.1016/j.mib.2021.09.007

Sun, Y., Liu, X., Li, W., Wang, X., Zhong, X., Gao, Y., et al. (2023). The regulatory metabolic networks of the *Brassica campestris* L. hairy roots in response to cadmium stress revealed from proteome studies combined with a transcriptome analysis. *Ecotoxicol. Environ. Saf.* 263:115214. doi: 10.1016/j.ecoenv.2023.115214

Sung, K., Park, M., Chon, J., Kweon, O., Khan, S. A., Shen, A., et al. (2022). Concentration-dependent global quantitative proteome response of *Staphylococcus epidermidis* RP62A biofilms to subinhibi-tory tigecycline. *Cells* 11:3488. doi: 10.3390/cells11213488

Tong, S., Bambrick, H., Beggs, P. J., Chen, L., Hu, Y., Ma, W., et al. (2022). Current and future threats to human health in the anthropocene. *Env. Int.* 158:106892. doi: 10.1016/j.envint.2021.106892

Vargas-García Mdel, C., López, M. J., Suárez-Estrella, F., and Moreno, J. (2012). Compost as a source of microbial isolates for the bioremediation of heavy metals: in vitro selection. *Sci. Total Environ.* 431, 62–67. doi: 10.1016/j.scitotenv.2012.05.026

Voss, D., and Montville, T. J. (2014). 1,6-Diphenyl-1,3,5-hexatrine as a reporter of inner spore membrane fluidity in *Bacillus subtilis* and *Alicyclobacillus acidoterrestris*. *J. Microbiol. Methods* 96, 101–103. doi: 10.1016/j.mimet.2013.11.009

Wang, T., Du, X., Ji, L., Han, Y., Dang, J., Wen, J., et al. (2021). *Pseudomonas aeruginosa* T6SS-mediated molybdate transport contributes to bacterial competition during anaerobiosis. *Cell Rep.* 35:108957. doi: 10.1016/j.celrep.2021.108957

Wang, G., Fan, C., Wang, H., Jia, C., Li, X., Yang, J., et al. (2022). Type VI secretion system-associated FHA domain protein TagH regulates the hemolytic activity and virulence of *Vibrio cholerae*. *Gut Microbes* 14:2055440. doi: 10.1080/19490976.2022.2055440

Wang, H., Li, Q., Zhang, Z., Zhou, C., Ayepa, E., Abrha, G. T., et al. (2019). YKL107W from *Saccharomyces cerevisiae* encodes a novel aldehyde reductase for detoxification of acetaldehyde, glycolaldehyde, and furfural. *Appl. Microbiol. Biotechnol.* 103, 5699–5713. doi: 10.1007/s00253-019-09885-x

Wang, Y., Rume, T., Islam, S. M. D., Fan, W., Wu, J., and Li, X. (2022). Water quality criteria and ecological risk assessment of typical transition metals in South Asia. *Int. J. Environ. Res. Public Health* 19:16125. doi: 10.3390/ijerph192316125

Wang, X., Wu, J., Yu, B., Dong, K. F., Ma, D., Xiao, G., et al. (2020). Heavy metals in aquatic products and the health risk assessment to population in China. *Environ. Sci. Pollut. Res. Int.* 27, 22708–22719. doi: 10.1007/s11356-020-08685-5

Wróbel, M., Śliwakowski, W., Kowalczyk, P., Kramkowski, K., and Dobrzyński, J. (2023). Bioremediation of heavy metals by the genus Bacillus. *Int. J. Environ. Res. Public Health* 20:4964. doi: 10.3390/ijerph20064964

Xie, X., Hao, F., Chen, R., Wang, J., Wei, Y., Liu, J., et al. (2021). Nicotinamide adenine dinucleotide-dependent flavin oxidoreductase of *Mycoplasma hyopneumoniae* functions as a potential novel virulence factor and not only as a metabolic enzyme. *Front. Microbiol.* 12:747421. doi: 10.3389/fmicb.2021.747421

Xu, M., Wu, J., and Chen, L. (2019). Virulence, antimicrobial and heavy metal tolerance, and genetic diversity of *Vibrio cholerae* recovered from commonly consumed freshwater fish. *Environ. Sci. Pollut. Res.* 26, 27338–27352. doi: 10.1007/s11356-019-05287-8

Yan, F., Dang, Q., Liu, C., Yan, J., Wang, T., Fan, B., et al. (2016). 3,6-O-[N-(2-Aminoethyl)-acetamideyl]-chitosan exerts antibacterial activity by a membrane damage mechanism. *Carbohydr. Polym.* 149, 102–111. doi: 10.1016/j.carbpol.2016.04.098

Yan, L., Jin, Y., Zhang, B., Xu, Y., Peng, X., Qin, S., et al. (2022). Diverse aquatic animal matrices play a key role in survival and potential virulence of non-O1/O139 *Vibrio cholerae* isolates. *Front. Microbiol.* 13:896767. doi: 10.3389/fmicb.2022.896767

Yang, L., Wang, Y., Yu, P., Ren, S., Zhu, Z., Jin, Y., et al. (2020). Prophage-related gene VpaChn25_0724 contributes to cell membrane integrity and growth of *Vibrio parahaemolyticus* CHN25. *Front. Cell. Infect. Microbiol.* 10:595709. doi: 10.3389/fcimb.2020.595709

Yang, Q., Zuo, Z., Zeng, Y., Ouyang, Y., Cui, H., Deng, H., et al. (2023). Autophagy-mediated ferroptosis involved in nickel-induced nephrotoxicity in the mice. *Ecotoxicol. Environ. Saf.* 259:115049. doi: 10.1016/j.ecoenv.2023.115049

Yu, X., Ding, Z., Ji, Y., Zhao, J., Liu, X., Tian, J., et al. (2020). An operon consisting of a P-type ATPase gene and a transcriptional regulator gene responsible for cadmium resistances in *Bacillus vietamensis* 151-6 and *Bacillus marisflavi* 151-25. *BMC Microbiol.* 20:18. doi: 10.1186/s12866-020-1705-2

Yu, P., Yang, L., Wang, J., Su, C., Qin, S., Zeng, C., et al. (2022). Genomic and transcriptomic analysis reveal multiple strategies for the cadmium tolerance in *Vibrio parahaemolyticus* N10-18 isolated from aquatic animal ostrea gigas thunberg. *Foods* 11:3777. doi: 10.3390/foods11233777

Yu, S., Zhang, W., Miao, X., Wang, Y., and Fu, R. (2022). Spatial distribution, source analysis and health risk study of heavy metals in the Liujiang River basin in different seasons. *Int. J. Environ. Res. Public Health* 19:15435. doi: 10.3390/ijerph192315435

Zamora-Ledezma, C., Negrete-Bolagay, D., Figueroa, F., Zamora-Ledezma, E., Ni, M., Alexis, F., et al. (2021). Heavy metal water pollution: a fresh look about hazards, novel and conventional remediation methods. *Environ. Technol. Innov.* 22:101504. doi: 10.1016/j.eti.2021.101504

Zgurskaya, H. I., Adamiak, J. W., and Leus, I. V. (2022). Making sense of drug-efflux transporters in the physiological environment. *Curr. Opin. Microbiol.* 69:102179. doi: 10.1016/j.mib.2022.102179

Zhao, L., Zhu, Y., Wang, M., Han, Y., Xu, J., Feng, W., et al. (2023). Enolase, a cadmium resistance related protein from hyperaccumulator plant *Phytolacca americana*, increase the tolerance of *Escherichia coli* to cadmium stress. *Int. J. Phytoremediation* 25, 562–571. doi: 10.1080/15226514.2022.2092064

Zhong, Q., Cruz-Paredes, C., Zhang, S., and Rousk, J. (2021). Can heavy metal pollution induce bacterial resistance to heavy metals and antibiotics in soils from an ancient land-mine? *J. Hazard. Mater.* 411:124962. doi: 10.1016/j.jhazmat.2020.124962

Zhu, Z., Yang, L., Yu, P., Wang, Y., Peng, X., and Chen, L. (2020). Comparative proteomics and secretomics revealed virulence and antibiotic resistance-associated factors in *Vibrio parahaemolyticus* recovered from commonly consumed aquatic products. *Front. Microbiol.* 11:1453. doi: 10.3389/fmicb.2020.01453

frontiers | Frontiers in Microbiology

TYPE Original Research
PUBLISHED 16 November 2023
DOI 10.3389/fmicb.2023.1294518

OPEN ACCESS

EDITED BY
Hector Alex Saka,
CONICET, Argentina

REVIEWED BY
Anne J. Anderson,
Utah State University, United States
Samina Mehnaz,
Forman Christian College, Pakistan

*CORRESPONDENCE
Joerg Overhage
✉ joergoverhage@cunet.carleton.ca

RECEIVED 14 September 2023
ACCEPTED 01 November 2023
PUBLISHED 16 November 2023

CITATION
da Cruz Nizer WS, Adams ME, Inkovskiy V, Beaulieu C and Overhage J (2023) The secondary metabolite hydrogen cyanide protects *Pseudomonas aeruginosa* against sodium hypochlorite-induced oxidative stress. *Front. Microbiol.* 14:1294518. doi: 10.3389/fmicb.2023.1294518

The secondary metabolite hydrogen cyanide protects *Pseudomonas aeruginosa* against sodium hypochlorite-induced oxidative stress

Waleska Stephanie da Cruz Nizer, Madison Elisabeth Adams, Vasily Inkovskiy, Carole Beaulieu and Joerg Overhage*

Department of Health Sciences, Carleton University, Ottawa, ON, Canada

The high pathogenicity of *Pseudomonas aeruginosa* is attributed to the production of many virulence factors and its resistance to several antimicrobials. Among them, sodium hypochlorite (NaOCl) is a widely used disinfectant due to its strong antimicrobial effect. However, bacteria develop many mechanisms to survive the damage caused by this agent. Therefore, this study aimed to identify novel mechanisms employed by *P. aeruginosa* to resist oxidative stress induced by the strong oxidizing agent NaOCl. We analyzed the growth of the *P. aeruginosa* mutants Δ*katA*, Δ*katE*, Δ*ahpC*, Δ*ahpF*, Δ*msrA* at 1μg/mL NaOCl, and showed that these known H_2O_2 resistance mechanisms are also important for the survival of *P. aeruginosa* under NaOCl stress. We then conducted a screening of the *P. aeruginosa* PA14 transposon insertion mutant library and identified 48 mutants with increased susceptibility toward NaOCl. Among them were 10 mutants with a disrupted *nrdJa, bvlR, hcnA, orn, sucC, cysZ, nuoJ,* PA4166, *opmQ,* or *thiC* gene, which also exhibited a significant growth defect in the presence of NaOCl. We focussed our follow-up experiments (i.e., growth analyzes and kill-kinetics) on mutants with defect in the synthesis of the secondary metabolite hydrogen cyanide (HCN). We showed that HCN produced by *P. aeruginosa* contributes to its resistance toward NaOCl as it acts as a scavenger molecule, quenching the toxic effects of NaOCl.

KEYWORDS

***Pseudomonas aeruginosa*, oxidative stress, sodium hypochlorite, hydrogen cyanide, reactive chlorine species, oxidative stress response, antimicrobial resistance**

1. Introduction

Pseudomonas aeruginosa is an ubiquitous environmental, Gram-negative bacterium and a highly versatile opportunistic human pathogen that can be isolated from soil, water, plants, and animals (Ambreetha and Balachandar, 2022). In humans, it can cause severe and diverse infections of considerable medical importance, such as ventilator-associated pneumonia, endocarditis, urinary tract, and systemic infections, mainly in immunocompromised individuals (Bassetti et al., 2018). One remarkable characteristic of *P. aeruginosa* is its ability to adapt and survive under various and harsh environmental conditions due to a sophisticated network of stress responses, including cold, heat, and oxidative stress responses (Craig et al., 2021; Da Cruz Nizer et al., 2021).

Oxidizing agents are low-molecular-weight compounds that have an increased ability to oxidize other substances by removing electrons and, therefore, are considered potent antimicrobial agents (Finnegan et al., 2010). Among them, reactive oxygen (e.g., hydrogen peroxide, H_2O_2) and chlorine (e.g., hypochlorous acid, HOCl) species (ROS and RCS, respectively) are highly reactive molecules produced as by-products of the metabolism of oxygen of living organisms (endogenous production) or encountered by bacterial cells from exogenous sources, such as disinfectants (Bardaweel et al., 2018). In bacterial cells, these molecules oxidize several molecules and disrupt numerous cellular processes. For instance, they react with lipids, proteins, and nucleic acids resulting in membrane damage and affecting protein, DNA, RNA, and energy synthesis (Da Cruz Nizer et al., 2021). Due to their potent activity, ROS and RCS are widely used in many applications as disinfectants in domestic, industrial and hospital settings, water and wastewater treatment, cleaning of wounds, and as antiseptic agents (Da Cruz Nizer et al., 2020, 2021; Gold et al., 2020). Furthermore, H_2O_2 and HOCl are also produced by human immune cells as a defense against invading pathogens (Da Cruz Nizer et al., 2020). Overall, HOCl is a more potent oxidizing agent with a much faster antimicrobial effect than H_2O_2 (Peskin and Winterbourn, 2001; Winterbourn et al., 2016). It is the active ingredient of sodium hypochlorite (NaOCl; household bleach) and is considered the most commonly used chlorine-based disinfectant and oxidant in drinking water disinfection (Fukuzaki, 2006; Deborde and von Gunten, 2008).

Pseudomonas aeruginosa is constantly exposed to oxidative stress, either from endogenous production or exogenous sources, by the use of disinfectants. In this context, this bacterium has developed many mechanisms to survive the toxic effects of these agents. Although HOCl is a stronger oxidant than H_2O_2, most research has focused on the H_2O_2 responses adopted by *P. aeruginosa,* and only a few studies have identified and characterized specific stress responses and resistance mechanisms against HOCl (Da Cruz Nizer et al., 2020). However, most of these adaptive responses are not specific to a single agent but are part of a general oxidative stress response in *P. aeruginosa*. For instance, detoxifying enzymes, such as catalases, alkyl hydroperoxides, and protein repair systems, such as MrsR, are well-known to be involved in the resistance of *P. aeruginosa* against H_2O_2 (Panmanee and Hassett, 2009; Romsang et al., 2013). Furthermore, transcriptional regulators, mainly OxyR, are also crucial for the survival of *P. aeruginosa* under oxidizing conditions (Ochsner et al., 2000). Previous studies have used gene expression analyzes or screening for regulatory proteins to characterize the adaptation of *P. aeruginosa* to HOCl (Groitl et al., 2017; Farrant et al., 2020).

This study aims to identify novel genes involved in the resistance of *P. aeruginosa* to the strong oxidant NaOCl by a targeted screening of genes known to be involved in H_2O_2 resistance as well as screening the comprehensive *P. aeruginosa* PA14 mutant library (Liberati et al., 2006) for mutants with increased susceptibility to NaOCl.

2. Materials and methods

2.1. Bacterial strains, plasmids, and growth conditions

The bacterial strains used in this study included *P. aeruginosa* PA14 wild-type (PA14 WT) (Rahme et al., 1995), *P. aeruginosa* PAO1 WT (Stover et al., 2000) and the entire *P. aeruginosa* PA14 transposon mutant library from Harvard University (Liberati et al., 2006), which was used to screen susceptible mutants. After the selection of PA14 mutants, PAO1 homologs from the PAO1 comprehensive transposon mutant library (Jacobs et al., 2003) were also tested for further verification of our findings. The list of strains used in this study is shown in Supplementary Table S1. Unless otherwise stated, all strains were grown in Lysogeny broth (LB) overnight at 37°C under shaking conditions (220 rpm) and the experiments were conducted using cells in the stationary growth phase. Oxidative stress assays were conducted in BM2 minimal medium [7 mM $(NH_4)_2SO_4$, 40 mM K_2HPO_4, 22 mM KH_2PO, 0.4% (w/v) glucose, 0.5 mM $MgSO_4$, 0.01 mM $FeSO_4$, pH 7.0] (Overhage et al., 2008). For easier readability, we used the PAO1 gene numbers for our genes when the gene names were unknown.

The PA2194 PW4739 (Δ*hcnB*) mutant from the PAO1 transposon mutant library (Jacobs et al., 2003) was complemented by the transfer of the *phcnBC* plasmid expressing *hcnBC* (Létoffé et al., 2022), which was kindly provided by Dr. Jean-Marc Ghigo. The complemented mutant Δ*hcnB-phcnBC* was grown overnight in LB medium supplemented with 400 μg/mL kanamycin and 2 mM sodium benzoate for inducible gene expression (Létoffé et al., 2022).

2.2. Measurement of RCS

NaOCl aqueous solution was used to induce RCS stress. Free chlorine concentration of NaOCl aqueous solutions was determined weekly using DPD Free Chlorine Powder Packs (Thermo Scientific Orion), according to the manufacturer's instructions. BM2 minimal medium was used to mitigate side reactions between NaOCl and growth medium components. Additionally, to confirm that the addition of NaOCl to BM2 did not reduce the amount of overall RCS, RCS concentration was measured as previously described (Ashby et al., 2020). In this context, addition of 1, 2, and 4 μg/mL NaOCl to BM2 minimal medium did not result in significant reduction in overall RCS levels. In contrast, NaOCl was completely quenched by LB in our control experiment.

2.3. Pre-liminary screening for susceptible mutants

To identify genes involved in *P. aeruginosa* stress resistance to NaOCl, we initially screened the *P. aeruginosa* PA14 transposon insertion mutant library (Liberati et al., 2006) for mutants with increased susceptibility to NaOCl. For this, frozen stocks of PA14 mutants arranged in 96-well microtiter plates were transferred to fresh LB medium and incubated for 24 h at 37°C. Then, the mutants were stamped with a 96-pin metal replicator into new 96-well microtiter plates containing NaOCl at 1 μg/mL (½ x MIC) in BM2 growth medium and incubated for 24 h at 37°C. Susceptible mutants (i.e., mutants that did not grow at 1 μg/mL NaOCl) were selected for further analysis.

2.4. Minimal inhibitory concentration assay

The MIC for NaOCl and H_2O_2 was determined by the standard broth microdilution method in BM2 minimal medium, as described previously (Wiegand et al., 2008). Briefly, *P. aeruginosa* strains were

grown overnight in LB at 37°C and 220 rpm. Cells were collected by centrifugation (10,000 rpm for 2 min), washed twice with phosphate-buffered saline (PBS), and resuspended in BM2 medium. The optical density at 600 nm (OD_{600nm}) was adjusted to 0.2 (2×10^8 CFU/mL), and 50 µL was mixed in 96-well plates with 50 µL of serial dilutions of NaOCl (0.125–128 µg/mL) or H_2O_2 (98–50,000 µg/mL) prepared in BM2 (final cell concentration of 1×10^8 CFU/mL). The plates were incubated for 24 h at 37°C, and the MIC was considered the lowest concentration of oxidizing agent that inhibits the visual growth of bacteria.

2.5. Growth curves

Pseudomonas aeruginosa overnight cultures grown at 37°C and 220 rpm in LB were washed twice with PBS, resuspended in BM2, and the OD_{600nm} was adjusted to 0.2 (2×10^8 CFU/mL). Then, 50 µL of bacterial suspension and 50 µL of oxidizing agent were mixed in flat-bottom polystyrene 96-well microtiter plates, leading to a final concentration of NaOCl of 1 µg/mL and H_2O_2 of 400 µg/mL and the final cell concentration of 1×10^8 CFU/mL. The OD_{600nm} was read every hour for 20 h at 37°C using the Epoch plate reader (Biotek, United States). Growth curves were statistically analyzed by measuring the area under the curve (AUC) using GraphPad Prism version 9.5.1 (San Diego, United States).

2.6. Semiquantitative analysis of Hydrogen cyanide (HCN) production

Volatile Hydrogen cyanide production was quantified by the semiquantitative method previously described (Castric, 1977; Létoffé et al., 2022). Briefly, 2 mL of overnight cultures of PAO1 WT, Δ*hcnB*, and Δ*hcnB-phcnBC* grown in LB were collected by centrifugation and washed twice with PBS. The cells were resuspended in 2 mL of LB and transferred to a small Petri dish (35 cm diameter) placed in the middle of a 100-mm diameter Petri dish. The small petri dish was covered with chromatography paper soaked in HCN detection reagent: 100 mg of copper (II) ethyl acetoacetate and 100 mg of 4,4′-methylenebis-(*N,N*-dimethylaniline) solubilized in 20 mL chloroform (Létoffé et al., 2022). The large petri dish was then closed and incubated at 37°C for 24 h under static conditions. HCN production was detected by blue color formation on the chromatography paper. Two mM sodium benzoate was added to Δ*hcnB-phcnBC* cells.

2.7. Time-kill kinetics experiments

Pseudomonas aeruginosa was grown overnight in LB at 37°C under shaking conditions, collected by centrifugation, washed twice, and resuspended in PBS. The OD_{600nm} was adjusted to 0.1, and the bacterial suspensions were treated with NaOCl at 2 µg/mL for 5, 15, 30, and 60 min. For the experiments using the supernatant, PAO1 WT, Δ*hcnB* and Δ*hcnB-phcnBC* were grown in BM2 overnight. Then, PAO1 WT, Δ*hcnB*, or Δ*hcnB-phcnBC* culture supernatants were collected by centrifugation followed by sterile filtration using a 0.22 µm filter. On the other hand, Δ*hcnB* cells were collected by centrifugation, washed twice with PBS, and the OD_{600nm} was adjusted to 0.1 by diluting the cells in PAO1 WT, Δ*hcnB*, or Δ*hcnB-phcnBC* supernatants. The bacterial suspensions were treated with 4 µg/mL NaOCl for 60 min.

After the treatments, 10 mM $Na_2S_2O_3$ was added to the samples to quench NaOCl, and the cells were serially diluted and plated out on LB agar plates using the drop plate method previously described (Herigstad et al., 2001).

2.8. Statistical analysis

Statistical analyzes were performed using GraphPad Prism software version 9.5.1 (San Diego, United States). The Shapiro–Wilk test was used to confirm the normality of the data. Parametric data were analyzed by One Way ANOVA, followed by Tukey or Dunnett's post-test for multiple comparisons or Student's t-test for comparison between two groups. Non-parametric data were analyzed by the t-test and Mann–Whitney test for comparison between two groups. All experiments were performed in at least three independent experiments, and results were considered statistically significant when $p < 0.05$.

3. Results

3.1. H_2O_2 Detoxifying mechanisms also contribute to the NaOCl survival of *Pseudomonas aeruginosa*

Previous work on H_2O_2 has identified several detoxifying enzymes and oxidative stress repair systems in *P. aeruginosa*. To evaluate if these previously described genes involved in H_2O_2 adaptation also play a role in the adaptation of *P. aeruginosa* to NaOCl, we examined growth of the *P. aeruginosa* PAO1 and PA14 mutants Δ*katA* and Δ*katE* (catalases), Δ*ahpC* and Δ*ahpF* (alkyl hydroperoxide reductase), Δ*msrA* (methionine sulfoxide reductase), and Δ*ohrR* (organic hydroperoxide resistance protein) exposed to NaOCl at 1 µg/mL for 20 h at 37°C. This sub-lethal concentration was chosen based on the MIC of the WT strains (2 µg/mL). In accordance with Farrant et al. (2020), mutants were considered to possess a susceptibility phenotype when they presented an increased lag phase of >3 h compared to the WT strain. Furthermore, to statistically analyze the growth curves obtained, we measured the AUC. AUC, also known as growth potential (Todor et al., 2014), is a metric to quantify the cumulative effect of overall growth over time (Sprouffske and Wagner, 2016).

Pseudomonas aeruginosa PAO1 and PA14 WT treated with 1 µg/mL NaOCl took approximately 5–6 h to reach an OD_{600nm} of 0.2 (double the initial OD). Overall, all mutants presented reduced growth at 1 µg/mL NaOCl compared to the WT strains. Furthermore, the AUCs were statistically significant for both the PA14 and PAO1 mutant strains compared to the WT strains treated with 1 µg/mL NaOCl. An OhrR mutant, a transcriptional repressor involved in oxidative stress response in *P. aeruginosa*, was used as a control and presented growth compared to the untreated controls and WT strains (Figure 1; Table 1). Of note, the PA14 Δ*katA* mutant (Figure 1A)

required 11 h to reach an OD_{600nm} of 0.2, nearly twice as long as the time needed for the PA14 WT strain, and the PAO1 mutant did not show any growth. Furthermore, the Δ*katA* PA14 mutant exhibited an AUC approximately 2x smaller than that of the PA14 WT strain, whereas the Δ*katA* PAO1 mutant had an AUC more than 4x smaller than the PAO1 WT strain.

In addition to the increased susceptibility in the growth analyzes, these mutants presented a 2-fold increase in susceptibility in MIC testing (MIC of 1 μg/mL; ½ x MIC of the WT), except for OhrR, which presented a MIC of 4 μg/mL (Table 1). These results demonstrate the importance of these repair systems in detoxifying toxic oxygen species, including NaOCl.

3.2. PA14 transposon mutant library screening for identification of novel genes involved in NaOCl resistance

To identify novel genes involved in NaOCl resistance, we screened the comprehensive Harvard PA14 transposon insertion mutant library (Liberati et al., 2006) for mutants with increased susceptibility to NaOCl. In the preliminary screening, we exposed the PA14 mutants to NaOCl at 1 μg/mL in BM2 minimal growth medium. Mutants not showing visual growth at this concentration were selected for further MIC testing to confirm their phenotypes. In total, 48 PA14 mutants with MIC of 0.5 and 1 μg/mL (¼ and ½ x MIC of PA14 WT) were identified and selected for further analysis (Figure 2A; Supplementary Table S2). Most of the mutants identified in this preliminary screening have a mutation in genes with unknown function (17/48), followed by genes involved in the transport of small molecules (8/48), such as ABC transporter, sulfate uptake protein, and major facilitator superfamily (MFS) transporter (Figure 2B). Furthermore, among the 48 mutants identified, 9 presented MIC values of 0.5 μg/mL [PA2077 (hypothetical protein), PA2193 (Δ*hcnA*, cyanide production), PA0846 (sulfate uptake protein), PA4110 (Δ*ampC*, cephalosporinase), PA5446 (hypothetical protein), PA0040 (hemolysin activation/secretion protein), PA1046 (hypothetical protein), PA4973 (Δ*thiC*, thiamin biosynthesis protein ThiC), and PA1315 (transcriptional regulator)].

3.3. Growth kinetic analyzes of mutants identified in the planktonic screening

To further characterize the susceptibility phenotype of the mutants identified in the MIC screening in more detail, we analyzed the growth of these 48 mutants in the presence of 1 μg/mL NaOCl for 20 h at 37°C in microtiter plates. Overall, 10 PA14 mutants identified in the library screening also presented a significant delay in growth in the presence of NaOCl compared to the WT-treated strains (i.e., more than 10 h to double the initial OD). Table 2 shows the 10 mutants identified in the PA14 mutant library screening, and Figure 3 illustrates their growth kinetics at 1 μg/mL NaOCl. Most of the mutants reached the OD_{600nm} of 0.2 (double the initial cell concentration) after 11 h of incubation, while it took approximately 5–6 h for the WT strains to get to this OD. Among them, Δ*bvlR*, Δ*hcnA*, and Δ*thiC* presented overall reduced growth at 1 μg/mL NaOCl, reaching the maximum OD_{600nm} of 0.364, 0.382, and 0.405, respectively, after 20 h compared to the PA14 WT (OD_{600nm} of 0.6 after 20 h).

To evaluate if our findings are strain-specific, we also assessed the growth of the PAO1 mutant homologs from the PAO1 two-allele transposon mutant library from the University of Washington Genome Center (Jacobs et al., 2003) under the same experimental conditions over time (Figure 3). Moreover, to statistically analyze the growth curves obtained for the PA14 and PAO1 mutants, we calculated the AUC and compared the values obtained with the AUC of 1 μg/mL NaOCl-treated WT strains (Table 3). The mutants Δ*nrdJa*, Δ*cysZ*, Δ*opmQ*, and Δ*thiC* presented delayed growth (i.e., lag phase >3 h than the WT strains) and statistically different AUCs compared to the NaOCl-treated

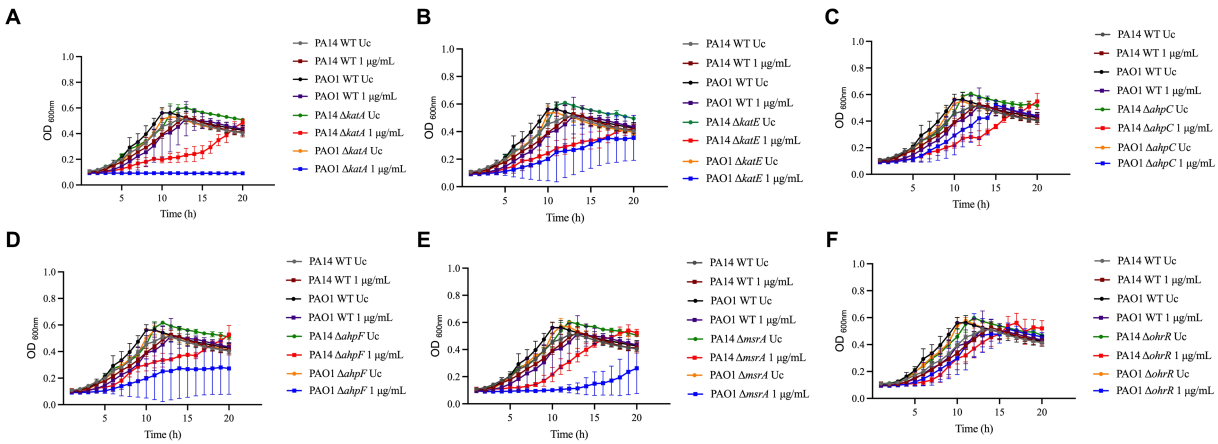

FIGURE 1
Susceptibility of known-H_2O_2 resistance mechanisms to NaOCl. Overnight cultures were grown in LB at 37°C and 220 rpm. Then, cells were washed twice with PBS, resuspended in BM2 minimal medium, and treated with NaOCl at 1 μg/mL (final cell concentration of 1×10^8 CFU/mL) for 20 h at 37°C. OD_{600nm} was recorded every hour using an epoch plate reader. **(A)** Δ*katA*; **(B)** Δ*katE*; **(C)** Δ*ahpC*; **(D)** Δ*ahpF*; **(E)** Δ*msrA*; **(F)** Δ*ohrR*. WT: wild-type; Uc, untreated control.

TABLE 1 MIC and area under the curve (AUC) of growth curves of *Pseudomonas aeruginosa* strains exposed to 1 μg/mL NaOCl.

P. aeruginosa strains		MIC (μg/mL)	Area under the curve (AUC)	
			Untreated Control	1 μg/mL NaOCl
PAO1 WT		2	9.288 ± 0.875	7.946 ± 0.874
PA14 WT		2	8.115 ± 0.983	7.310 ± 0.912
ΔkatA	PA4236	1	6.823 ± 0.012	1.761 ± 0.054*
	PA14_09150	1	7.767 ± 0.097	4.269 ± 0.545*
ΔkatE	PA2147	1	6.797 ± 0.137	3.823 ± 1.790*
	PA14_36810	1	7.687 ± 0.049	4.093 ± 0.989*
ΔahpC	PA0139	1	6.965 ± 0.045	5.417 ± 1.017*
	PA14_01710	1	7.616 ± 0.184	5.002 ± 0.313*
ΔahpF	PA0140	1	6.924 ± 0.023	3.812 ± 0.645*
	PA14_01720	1	7.704 ± 0.203	5.410 ± 0.369*
ΔmsrA	PA5018	1	7.133 ± 0.092	2.394 ± 0.883*
	PA14_66330	1	7.651 ± 0.207	5.346 ± 0.520*
ΔohrR	PA2849	4	7.198 ± 0.154	6.106 ± 0.877
	PA14_27230	4	7.455 ± 0.188	5.871 ± 0.783

WT, wild-type. Data were analyzed by One-Way ANOVA and compared with the PA14 or PAO1 WT strains treated with 1 μg/mL NaOCl. *$p < 0.05$. AUC represents the average ± standard deviation of at least three independent experiments.

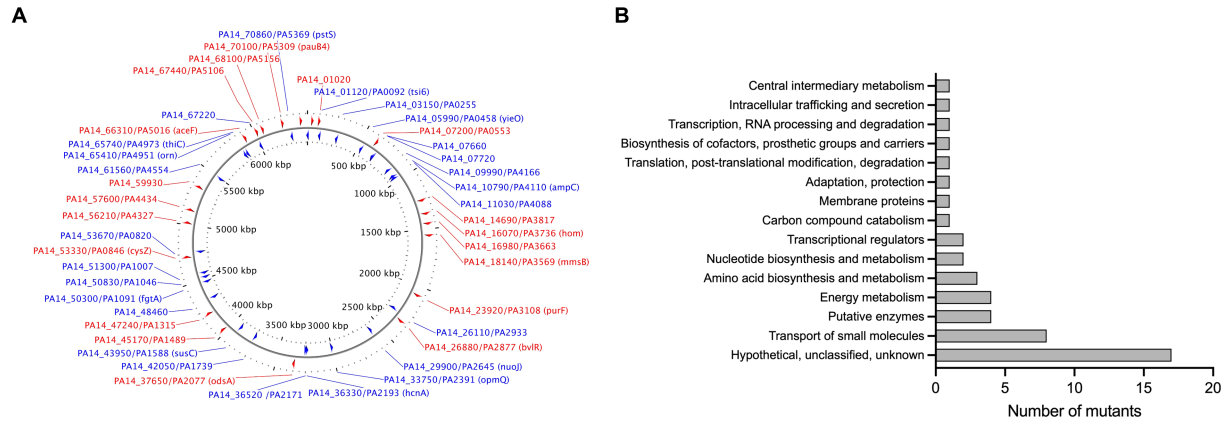

FIGURE 2
(A) Map of the *P. aeruginosa* genome with genes identified in the MIC screening. The image was generated by CGview (Stothard and Wishart, 2005). Red: Forward genes; Blue, Reverse genes. **(B)** Functional classification of genes identified in the MIC screening based on the *P. aeruginosa* genome classification.

WT strains for both PA14 and PAO1 mutants, suggesting that the phenotype found is not strain specific. PAO1 homologs for the mutants Δ*hcnA* and Δ*sucC* were unavailable for testing.

Most of the NaOCl responses previously reported in other studies are not specific to NaOCl but are rather employed by bacteria to survive the stress caused by different oxidizing agents (Da Cruz Nizer et al., 2021). Therefore, we conducted growth kinetics over time of the PA14 mutants identified and their PAO1 homologs to investigate if these genes are NaOCl-specific by exposing the mutants to 400 μg/mL H_2O_2. This concentration was chosen based on the growth curve of PA14 and PAO1 WT strains previously conducted (Supplementary Figure S1). As shown in the growth analyzes of Figure 4 and the AUC values in Table 3, the PA14 and PAO1 homologs tested were not susceptible to H_2O_2 under our experimental conditions, except for Δ*thiC*, which did not grow in the presence of 400 μg/mL H_2O_2. These results indicate that the susceptibility phenotypes found in our experiments are rather specific to NaOCl under our experimental conditions.

3.4. HCN affects NaOCl resistance in *Pseudomonas aeruginosa*

Among the mutants identified in our screening and follow-up MIC and growth analyzes (Table 2) was the Δ*hcnA* mutant, which presented increased susceptibility to NaOCl. For instance, it took

TABLE 2 Susceptibility to *Pseudomonas aeruginosa* mutants to NaOCl.

Locus name	PAO1 homolog	Gene name	Gene description	Functional category	MIC (μg/mL)
PA14_72540	PA5497	*nrdJa*	Putative ribonucleotide reductase	Nucleotide biosynthesis and metabolism	1
PA14_26880	PA2877	*bvlR*	Putative transcriptional regulator, LysR family	Transcriptional regulators	1
PA14_36330	PA2193*	*hcnA*	Hydrogen cyanide synthase	Central intermediary metabolism	0.5
PA14_65410	PA4951	*orn*	Oligoribonuclease	Transcription, RNA processing, and degradation	1
PA14_43950	PA1588*	*sucC*	Succinyl-CoA synthetase beta subunit	Energy metabolism	1
PA14_53330	PA0846	*cysZ*	Probable sulfate uptake protein	Transport of small molecules	0.5
PA14_29900	PA2645	*nuoJ*	NADH dehydrogenase I chain J	Energy metabolism	1
PA14_09990	PA4166		Putative acetyltransferase	Putative enzymes	1
PA14_33750	PA2391	*opmQ*	Putative outer membrane protein precursor	Transport of small molecules	1
PA14_65740	PA4973	*thiC*	Thiamin biosynthesis protein ThiC	Biosynthesis of cofactors, prosthetic groups, and carriers	0.5
PA14 WT					2
PA01 WT					2

*PAO1 homolog unavailable for testing.

approximately 11 h for the Δ*hcnA* mutant to reach an OD_{600nm} of 0.2, while the PA14 WT strain grew to an OD_{600nm} of 0.2 in only 5–6 h. After 20 h of growth, the Δ*hcnA* mutant exhibited an OD_{600nm} of 0.382, while the PA14 WT showed an OD_{600nm} of 0.6. Furthermore, the Δ*hcnA* mutant presented a MIC of 0.5 μg/mL, which was ¼ x MIC of PA14 WT. Given this pronounced increase in susceptibility, we focused the following analyzes on HCN and its contribution to NaOCl resistance.

Since HCN is produced by the *hcnABC* gene cluster in *P. aeruginosa* (Gilchrist et al., 2011), we evaluated if the absence of *hcnB* and *hcnC* also affects the susceptibility of *P. aeruginosa* to NaOCl by analyzing the growth of the corresponding PA14 and PAO1 Δ*hcnB* and Δ*hcnC* mutants at 1 μg/mL NaOCl for 20 h at 37°C. Like the Δ*hcnA* PA14 mutant, the corresponding PA14 and PAO1 Δ*hcnB* and Δ*hcnC* mutants showed an increase in susceptibility to NaOCl, presenting extended lag phase and reduced AUC compared to the WT strains at 1 μg/mL NaOCl. This phenotype seemed specific to NaOCl since these mutants did not present altered susceptibility to H_2O_2 at a final concentration of 400 μg/mL compared to WT strains (Figure 5; Table 4). These results confirm the importance of HCN production for *P. aeruginosa* survival under NaOCl stress conditions.

To test whether the increased susceptibility of the *hcn* mutants was due to the absence of HCN, we complemented the PAO1 mutant PA2194 PW4739 (Δ*hcnB*) by the transfer of the *phcnBC* plasmid, which expresses the genes *hcnBC*. Since both PA14 and PAO1 mutants presented increased susceptibility to NaOCl, we focused our analyzes on the PAO1 Δ*hcnB* mutant since this mutant has been characterized in a recent study (Létoffé et al., 2022). We assessed if the Δ*hcnB* mutant could be complemented by evaluating the release of HCN by our PAO1 strains using a semiquantitative method for HCN detection (Létoffé et al., 2022). When grown in LB for 24 h, both PAO1 WT and the Δ*hcnB-phcnBC* produced a detectable amount of HCN, while the Δ*hcnB* mutant did not produce HCN (Figure 6A).

Then, we conducted growth kinetic analyzes to determine whether the production of HCN by *P. aeruginosa* increases its resistance to NaOCl. As shown in Figure 6B, it took 6 h for the complemented strain Δ*hcnB-phcnBC* to reach the OD_{600nm} of 0.2, similar to the PAO1 WT strain. Furthermore, no statistical difference in growth was found for the AUC of Δ*hcnB-phcnBC* and PAO1 WT when treated with 1 μg/mL NaOCl (Table 5). Together, these results indicate that growth delay in response to NaOCl in the PAO1 Δ*hcnB* mutant could be complemented by the insertion of the *hcnBC*-producing plasmid *phcnBC*, demonstrating that HCN plays a role in the resistance of *P. aeruginosa* to NaOCl.

3.5. Characterization of HCN-mediated resistance to NaOCl in *Pseudomonas aeruginosa*

In order to provide further insight into the underlying mechanism of the HCN phenotype found in this study, we formulated two hypotheses: (i) HCN-related NaOCl resistance is mediated by cellular effects caused by HCN, or (ii) HCN acts as an extracellular metabolite, directly reacting with NaOCl and quenching its antimicrobial effect. In a previous study, Frangipani et al. (2014) investigated the effect of endogenously produced HCN on *P. aeruginosa* by transcriptomic analysis. The authors identified four *P. aeruginosa* genes that were repressed in response to endogenously produced HCN and 12 genes induced in response to HCN. To test if any of these HCN-controlled genes are involved in NaOCl resistance, we conducted growth analyzes by exposing *P. aeruginosa* PAO1 strains with mutations on the identified genes to 1 μg/mL NaOCl and measured their growth for 20 h. Among the mutants tested, only the

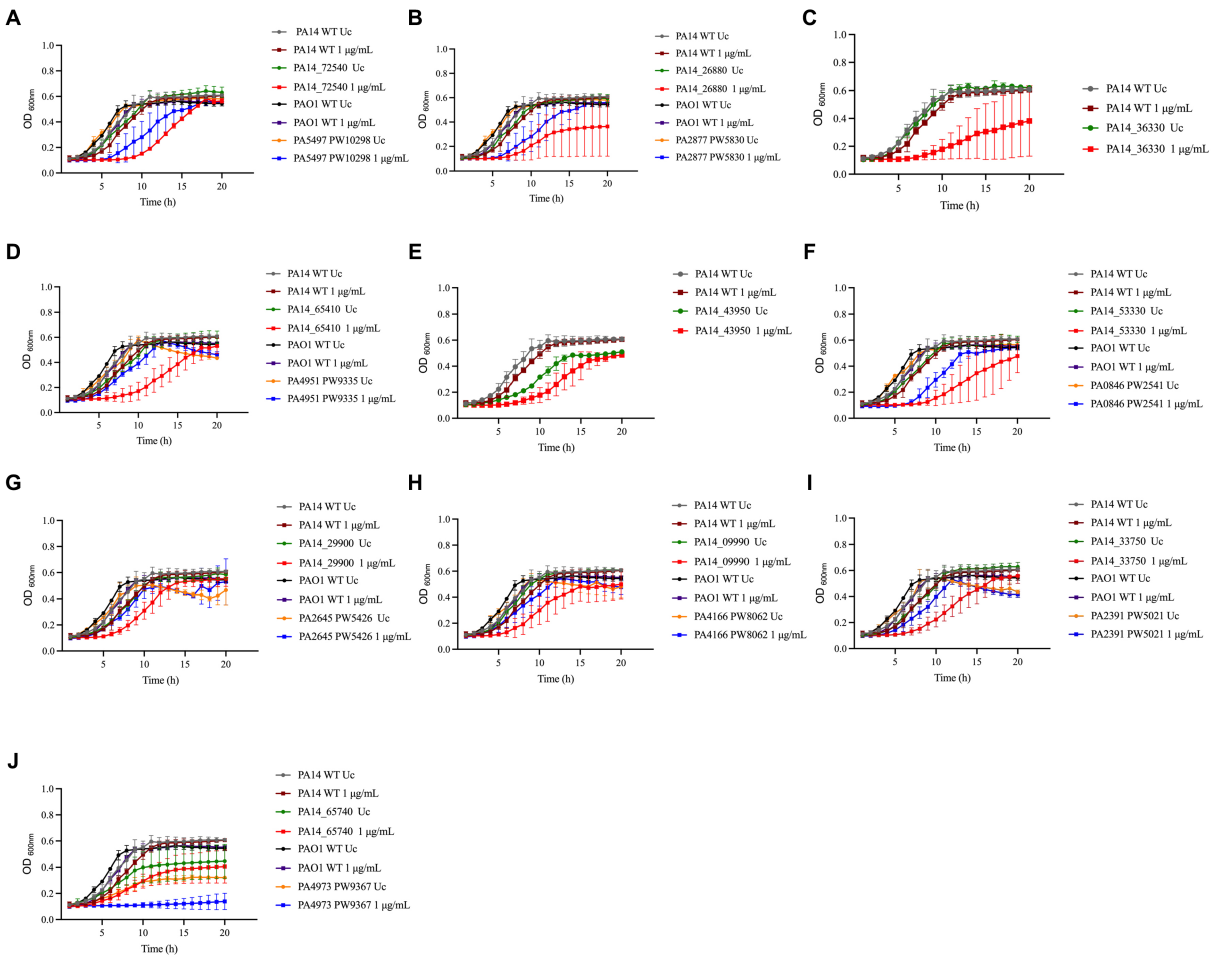

FIGURE 3
Susceptibility of PA14 mutants and PAO1 homologs identified in the screening to NaOCl. Overnight cultures were grown in LB at 37°C and 220 rpm. Then, cells were washed twice, resuspended in BM2 minimal medium, and treated with NaOCl at 1 µg/mL (final cell concentration of 1×10^8 CFU/mL) for 20 h at 37°C. OD_{600nm} was recorded every hour using an epoch plate reader. **(A)** Δ*nrdJa* (PA14_72540/PA5497); **(B)** Δ*bvlR* (PA14_26880/PA2877); **(C)** Δ*hcnA* (PA14_36330); **(D)** Δ*orn* (PA14_65410/PA4951); **(E)** Δ*sucC* (PA14_43950); **(F)** Δ*cysZ* (PA14_53330/PA0846); **(G)** Δ*nuoJ* (PA14_29900/PA2645); **(H)** PA14_09990/PA4166; **(I)** Δ*opmQ* (PA14_33750/PA2391); **(J)** Δ*thiC* (PA14_65740/PA4973). WT: wild-type; Uc: untreated control.

mutant with a mutation in the PA4134 gene, which synthesizes a hypothetical protein with unknown function, presented statistically different AUC compared to the PAO1 WT strain treated with NaOCl (Supplementary Figure S2; Table 6). This mutant strain presented an AUC (5.785 ± 3.059) similar to Δ*hcnB* (6.214 ± 1.074). The PA4134 gene forms a gene cluster together with PA4133, with PA4133 being located upstream of PA4134;[1] however, the PA4133 mutant did not show any significant difference in NaOCl susceptibility.

We then tested if the metabolite HCN itself would directly react with NaOCl and quench its toxic effect. For this, we first analyzed if removing HCN from the medium would change the susceptibility of Δ*hcnB* and PAO1 WT strains by evaluating the kill kinetics in response to NaOCl. Cells grown overnight were washed twice, resuspended in PBS to remove the HCN from the medium, and NaOCl was added to a final concentration of 2 µg/mL. The absence of HCN in the medium did not provoke a difference in the NaOCl susceptibility of PAO1 WT and Δ*hcnB* (Figure 7A), in which no statistical difference was found for the cell concentration over time for both strains. Overall, the growth analyzes and kill-kinetic results suggested that the susceptibility phenotype found for Δ*hcnB* is likely not due to a cellular effect.

Next, we aimed to complement the susceptibility phenotype of Δ*hcnB* with the supernatant from PAO1 WT and the complemented strain Δ*hcnB-phcnBC*. We used the culture supernatant of HCN-producing strains instead of the pure chemical HCN due to the high toxicity of HCN and its related forms [e.g., sodium cyanide (NaCN) and potassium cyanide (KCN)]. For this, we resuspended overnight Δ*hcnB* cells in the supernatants of Δ*hcnB*, PAO1 WT, and Δ*hcnB-phcnBC* grown in BM2 minimal medium. Then, the bacterial suspensions were treated with NaOCl at 4 µg/mL for 60 min. Figure 7B shows that the addition of PAO1 WT and Δ*hcnB-phcnBC* supernatants to cells of Δ*hcnB* complemented the Δ*hcnB* phenotype, and Δ*hcnB* cells showed increased resistance to NaOCl (percentage survival of 88 and 83%, respectively) compared to the Δ*hcnB* cells resuspended in Δ*hcnB* supernatant (17% survival).

1 pseudomonas.com

TABLE 3 Area under the curve (AUC) of NaOCl and H_2O_2 growth curves of NaOCl-susceptible *Pseudomonas aeruginosa* strains identified in the screening.

Gene name	*P. aeruginosa* strains	NaOCl		H_2O_2	
		Untreated	1 μg/mL	Untreated	400 μg/mL
	PAO1 WT	9.288 ± 0.875	7.946 ± 0.874	9.385 ± 0.747	5.542 ± 0.775
	PA14 WT	8.115 ± 0.983	7.310 ± 0.912	8.279 ± 0.748	4.253 ± 0.956
nrdJa	PA5497 PW10298	8.776 ± 0.056	6.058 ± 1.027*	8.626 ± 0.195	4.264 ± 0.416
	PA14_72540	8.572 ± 0.525	5.031 ± 0.122*	7.555 ± 0.149	4.644 ± 1.003
bvlR	PA2877 PW10298	8.776 ± 0.056	6.877± 0.665	8.846 ± 0.254	6.494 ± 0.68
	PA14_26880	8.096 ± 0.110	4.295 ± 2.310*	7.506 ± 0.115	4.872 ± 1.934
hcnA	PA14_36330	8.695 ± 0.365	4.034 ± 1.968*	8.178 ± 0.192	3.863 ± 0.674
orn	PA4951 PW9335	7.635 ± 0.308	6.868 ± 0.372	9.055 ± 0.553	4.645 ± 0.518
	PA14_65410	7.991 ± 0.327	4.880 ± 1.049*	7.502 ± 0.031	3.828 ± 0.452
sucC	PA14_43950	6.094 ± 0.136	4.787 ± 0.747*	6.927 ± 0.181	3.254 ± 0.509
cysZ	PA0846 PW2541	8.520 ± 0.068	5.991 ± 0.442*	8.385 ± 0.152	5.324 ± 0.150
	PA14_53330	8.229 ± 0.283	4.302 ± 1.661*	7.563 ± 0.144	4.216 ± 0.679
nuoJ	PA2645 PW5426	7.327 ± 0.543	6.765 ± 0.840	7.619 ± 0.212	5.524 ± 0.564
	PA14_29900	7.851 ± 0.119	6.328 ± 0.503	6.146 ± 0.214	3.429 ± 1.247
	PA4166 PW8062	7.812 ± 0.670	7.102 ± 0.814	8.552 ± 0.116	4.919 ± 0.609
	PA14_09990	8.414 ± 0.260	5.794 ± 1.315	7.793 ± 0.159	4.171 ± 0.928
opmQ	PA2391 PW5021	7.711 ± 0.348	6.339 ± 0.236*	8.639 ± 0.048	4.529 ± 0.775
	PA14_33750	8.222 ± 0.337	5.525 ± 0.978*	7.657 ± 0.030	4.226 ± 0.051
thiC	PA4973 PW9367	4.765 ± 0.356	2.194 ± 0.354*	4.609 ± 0.241	1.864 ± 0.015*
	PA14_65740	6.383 ± 1.677	5.272 ± 1.088*	4.974 ± 0.381	1.891 ± 0.098*

WT, wild-type. Data were analyzed by One-Way ANOVA and compared with the PA14 or PAO1 WT strains treated with 1 μg/mL NaOCl. *$p < 0.05$. AUC represents the average ± standard deviation of at least three independent experiments.

These results suggest that HCN reacts with NaOCl, quenching its lethal effect.

4. Discussion

Bacteria have developed several mechanisms to mitigate the harmful and often irreversible damage caused by oxidizing agents. Most of these resistance mechanisms are not specific but rather provide a general defense against a broad range of oxidizing agents. In this context, the knowledge of HOCl-specific responses is still limited (Gray et al., 2013; da Cruz Nizer et al., 2020). Among the HOCl responses described so far, ATP-independent chaperones are considered the immediate response against HOCl since they are readily activated by the oxidation of amino acid residues. These enzymes are essential for HOCl response since they do not require the expression of sensor mechanisms, which takes a long time compared to the fast action of HOCl on proteins (Goemans and Collet, 2019; Sultana et al., 2020). Other mechanisms include the activation of the transcriptional regulators HypT, NemR, and RclR and the formation of biofilms (Gray et al., 2013; Strempel et al., 2017; Da Cruz Nizer et al., 2020).

In this study, we demonstrated that the loss of KatA, KatE, AhpC, AhpF, and MsrA increases the susceptibility of *P. aeruginosa* PAO1 and PA14 to NaOCl compared to the WT strains, showing that these H_2O_2 responses are employed by this bacterium as a general response against oxidizing agents. We then identified 48 mutants with increased susceptibility to NaOCl and characterized 10 mutants in more detail. Among them, we found that HCN acts as a scavenger molecule and increases the survival of *P. aeruginosa* in the presence of NaOCl.

Most oxidative stress responses have been characterized for H_2O_2 and other ROS, while their roles in RCS and NaOCl resistance remain mostly unknown. Therefore, in the first part of this study, we showed by growth kinetics analyzes that well-known H_2O_2 responses are also involved in the survival of *P. aeruginosa* to NaOCl. Catalases and peroxidases are specialized enzymes that convert H_2O_2 into less toxic species (i.e., $H_2O + O_2$ and alcohol + H_2O, respectively; Cavinato et al., 2020). These enzymes are widely distributed among bacteria (Yuan et al., 2021) and are the primary response against oxidative stress (Romsang et al., 2013). *P. aeruginosa* has three catalases (*katA, katB,* and *katE*) and four alkyl hydroperoxide reductases (*ahpA*, *ahpB*, *ahpCF*, and *ohr*), in which KatA is considered the main catalase and its expression is controlled by various systems, such as OxyR, quorum sensing, and ANR (anaerobic regulator; Heo et al., 2010; Su et al., 2014). KatA and AhpA are continually expressed during bacterial growth, implying their importance as a defense not only during harmful conditions but also against endogenously produced ROS (Ochsner et al., 2000; Lee et al., 2005). Many studies have shown that the production of these detoxifying systems is upregulated by oxidizing agents in *P. aeruginosa*, such as H_2O_2 (Salunkhe et al., 2002; Palma et al., 2004; Chang et al., 2005; Small et al., 2007a,b), NaOCl (Small et al., 2007a,b; Groitl et al., 2017), hypobromous acid (Groitl

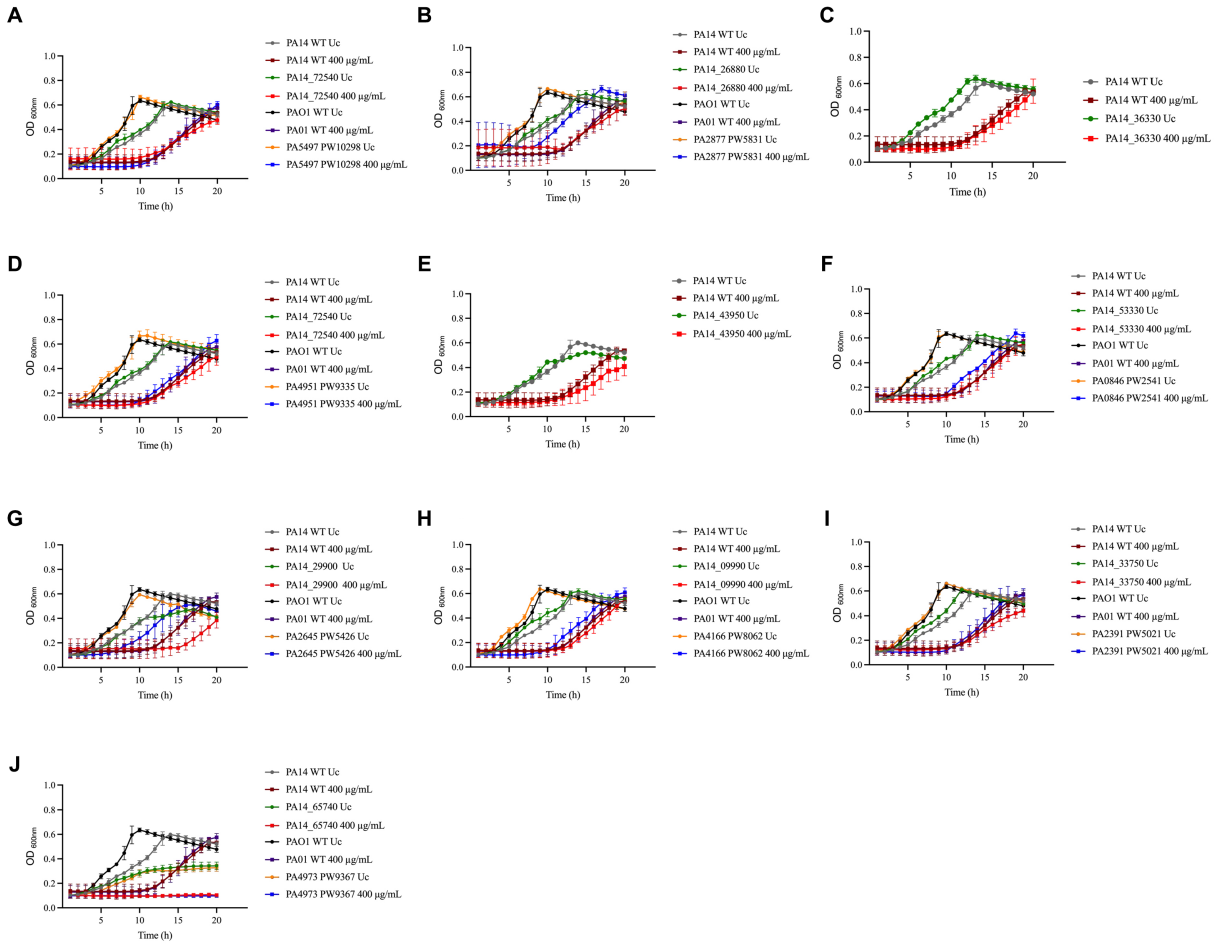

FIGURE 4
Susceptibility of PA14 mutants and PAO1 homologs identified in the screening to H_2O_2. Overnight cultures were grown in LB at 37°C and 220 rpm. Then, cells were washed twice, resuspended in BM2 minimal medium, and treated with H_2O_2 at 400 μg/mL (final cell concentration of 1×10^8 CFU/mL) for 20 h at 37°C. OD_{600nm} was recorded every hour using an epoch plate reader. **(A)** Δ*nrdJa* (PA14_72540/PA5497); **(B)** Δ*bvlR* (PA14_26880/PA2877); **(C)** Δ*hcnA* (PA14_36330); **(D)** Δ*orn* (PA14_65410/PA4951); **(E)** Δ*sucC* (PA14_43950); **(F)** Δ*cysZ* (PA14_53330/PA0846); **(G)** Δ*nuoJ* (PA14_29900/PA2645); **(H)** PA14_09990/PA4166; **(I)** Δ*opmQ* (PA14_33750/PA2391); **(J)** Δ*thiC* (PA14_65740/PA4973). WT: wild-type; Uc: untreated control.

et al., 2017), hypothiocyaous acid (Groitl et al., 2017) and peracetic acid (Chang et al., 2005). Furthermore, *P. aeruginosa katA*, *katB*, *ahpB*, and *oxyR* mutant strains were consistently more susceptible to H_2O_2 than the WT strains (Ochsner et al., 2000; Lee et al., 2005), corroborating our results. This susceptibility phenotype of *kat* and *ahp* mutants was also reported for other bacterial strains, such as *Vibrio cholerae* (Wang et al., 2012) and *Stenotrophomonas maltophilia* (Li et al., 2020). In the context of HOCl resistance, little has been explored on the roles of these enzymes in the resistance of *P. aeruginosa* toward this oxidant. The importance of detoxifying enzymes such as catalases has been described for *Escherichia coli* and *Helicobacter pylori* (Dukan and Touati, 1996; Benoit and Maier, 2016), in which catalases are considered a ubiquitous enzymes with quenching ability toward oxidizing agents in general (Benoit and Maier, 2016), corroborating our findings for *P. aeruginosa*. Considering that proteins are the main target of HOCl, another important stress response mechanism is the protein repair system Msr. *P. aeruginosa* and most bacterial species have two highly conserved Msr systems: MsrA and MsrB (Romsang et al., 2013). As for KatA and AhpA, MsrA is expressed during all growth phases, while MsrB is overproduced under oxidative stress conditions (Romsang et al., 2013). In accordance with our PA14 susceptibility results, PAO1 *msrA* and *msrB* mutants presented increased susceptibility to H_2O_2 and NaOCl in the study by Romsang et al. (2013). Hence, our findings report the involvement of *kat*, *ahp*, and *msr* genes in NaOCl resistance, adding to the previously described function of these response mechanisms.

We then performed a genome-wide mutant library screening of the PA14 transposon mutant library (Liberati et al., 2006) to find mutants with increased susceptibility to NaOCl. We were able to identify 48 genes with reduced MIC values toward NaOCl compared to PA14 WT, and we characterized 10 mutants (disrupted *nrdJa*, *bvlR*, *hcnA*, *orn*, *sucC*, *cysZ*, *nuoJ*, PA4166, *opmQ*, and *thiC* gene, respectively) in more detail (Table 2). Library screenings allow access to a large number of mutants carrying specific genetic alterations; therefore, researchers can simultaneously screen multiple mutants for the phenotype of interest in a short period. This approach is valuable for uncovering novel genes and pathways that contribute to bacterial resistance (Moser et al., 2014). Among them, two mutant strains, Δ*cysZ* and Δ*opmQ*, lacked genes involved in the transport of small molecules. The first one (Δ*cysZ*) has a mutation in a sulfate uptake

10.3389/fmicb.2023.1294518

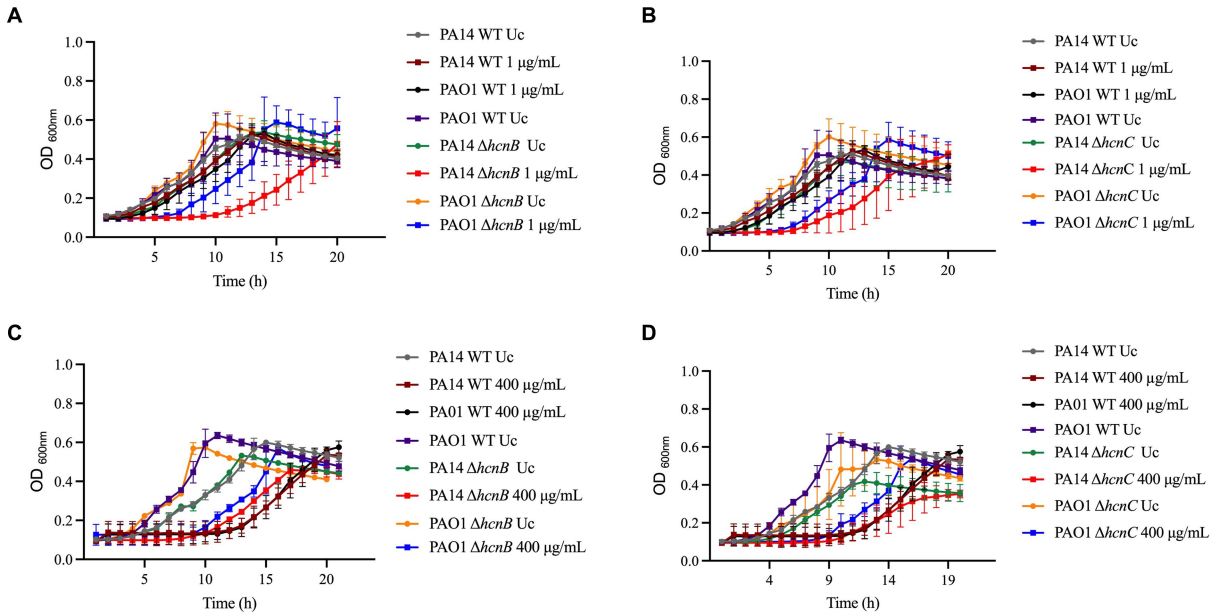

FIGURE 5
Susceptibility of *hcn* PA14 and PAO1 mutants to NaOCl and H_2O_2. Susceptibility to NaOCl of **(A)** Δ*hcnB* and **(B)** Δ*hcnC* PA14 and PAO1 mutants. Susceptibility to H_2O_2 of **(C)** Δ*hcnB* and **(D)** Δ*hcnC* PA14 and PAO1 mutants. Overnight cultures were grown in LB at 37°C and 220 rpm. Then, cells were washed twice, resuspended in BM2 minimal medium, and treated with NaOCl at 1 µg/mL or H_2O_2 at 400 µg/mL (final cell concentration of 1×10^8 CFU/mL) for 20 h at 37°C. OD_{600nm} was recorded every hour using an epoch plate reader. WT: wild-type; Uc: untreated control.

TABLE 4 Area under the curve (AUC) of NaOCl and H_2O_2 growth curves of *hcn Pseudomonas aeruginosa* mutants.

Gene name	*P. aeruginosa* strains	NaOCl		H_2O_2	
		Untreated	1 µg/mL	Untreated	400 µg/mL
	PAO1 WT	9.288 ± 0.875	7.946 ± 0.874	9.385 ± 0.747	5.542 ± 0.775
	PA14 WT	8.115 ± 0.983	7.310 ± 0.912	8.279 ± 0.748	4.253 ± 0.956
hcnB	PA2194 PW4739	7.507 ± 0.813	6.214 ± 1.074*	7.148 ± 0.092	5.199 ± 0.514
	PA14_36320	6.823 ± 0.504	3.626 ± 0.367*	6.739 ± 0.043	4.727 ± 0.161
hcnC	PA2195 PW4740	7.297 ± 112	5.727 ± 0.389*	6.718 ± 1.199	5.005 ± 0.395
	PA14_36310	5.389 ± 0.194	3.456 ± 0.294*	5.846 ± 0.337	3.407 ± 0.839

WT, wild-type. Data were analyzed by One-Way ANOVA and compared with the PA14 or PAO1 WT strains treated with 1 µg/mL NaOCl. *$p < 0.05$. AUC represents the average ± standard deviation of at least three independent experiments.

protein. Proteins, mainly the sulfur-containing ones, are the main target of HOCl in the cells (Da Cruz Nizer et al., 2020); therefore, due to the reduction of the amount of sulfur in the cells due to its reaction with HOCl, the transport of this compound to the cells seems to be necessary (Farrant et al., 2020). The upregulation of transport and metabolism of sulfur genes by HOCl has also been described for *E. coli* and *Salmonella enterica* Serovars Enteritidis (Wang et al., 2009, 2010). Overexpression of genes involved in the transport of small molecules (Small et al., 2007a,b) has been detected by transcriptomic studies and has been implicated in the need of cells to allow the entry or exit of metabolites, such as toxic HOCl-by-products and compounds needed for cell metabolism (Albrich et al., 1986).

In accordance with previous reports about the oxidation of DNA by HOCl (Prütz, 1996), we found the *nrdJa* gene, which encodes for a ribonucleotide reductase and was previously reported to be involved in DNA repair (Torrents et al., 2005). NrdJa is crucial for growth under anaerobic conditions (Wu et al., 2005; Filiatrault et al., 2013) and was upregulated after ciprofloxacin exposure (Cirz et al., 2006). Furthermore, Crespo et al. (2017) also found increased transcription of *nrdJ* under H_2O_2 stress, supporting our findings (Crespo et al., 2017). Ribonucleotide reductases have also been shown to be used by many other bacteria, such as *Bifidobacterium longum* (Zuo et al., 2018), *Bacillus subtilis* (Castro-Cerritos et al., 2017) and *E. coli* (Monje-Casas et al., 2001) as a response mechanism to oxidative stress, mainly H_2O_2.

Considering the high metabolic diversity of *P. aeruginosa*, many genes and pathways remain to be explored regarding their secondary effects and possible roles in resistance. In this context, we identified two genes involved in energy metabolism (i.e., *sucC* and *nuoJ*) and one implicated in thiamine biosynthesis (*thiC*). Thiamine, for example, has been explored as a target in the development of antibiotics (Lünse et al., 2014; Kim et al., 2020), while energy metabolism genes, such as *sucC* and *nuoH*, *nuoM*, and *nuoN* have been shown to be downregulated in response to

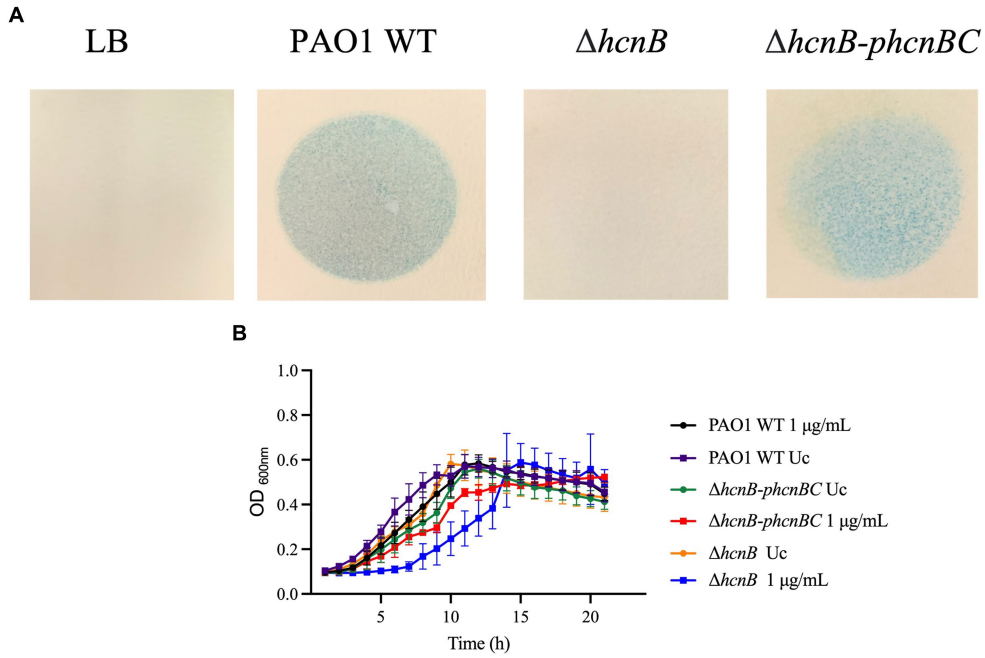

FIGURE 6
(A) Semiquantitative detection of HCN production by *P. aeruginosa* strains. cultures were grown in LB at 37°C and 220 rpm. Then, cells were washed twice and resuspended in LB. Two mL of overnight cultures were transferred to a small petri dish, which was covered by chromatography paper soaked in HCN detection reagent composed of copper (II) ethyl acetoacetate and 4,4′-methylenebis-(*N,N*-dimethylaniline) solubilized in chloroform. The small plates were placed in larger petri dish plates, which were covered. Production of volatile HCN was measured as the formation of blue color in the chromatography paper. The figures are representative of at least two independent experiments. **(B)** Susceptibility Δ*hcnB-phcnBC* complemented strain to NaOCl compared to PAO1 WT and PAO1 Δ*hcnB*. Overnight cultures were grown in LB at 37°C and 220 rpm. Then, cells were washed twice, resuspended in BM2 minimal medium, and treated with NaOCl at 1 µg/mL or (final cell concentration of 1×10^8 CFU/mL) for 20 h at 37°C. OD_{600nm} was recorded every hour using an epoch plate reader. WT, wild-type; Uc, untreated control.

TABLE 5 **Area under the curve (AUC) of NaOCl growth curves of PAO1-Δ*hcnB- phcnBC*.**

	NaOCl	
	Untreated	1 µg/mL
PAO1 WT	9.288 ± 0.875	7.946 ± 0.874
Δ*hcnB- phcnBC*	7.21 ± 0.050	7.078 ± 0.038

AUC represents the average ± standard deviation of at least three independent experiments.

tobramycin in *A. baumannii* (Kashyap et al., 2022). Furthermore, transcriptomic studies have shown the downregulation of energy production genes in cells under HOCl (Small et al., 2007a,b). However, their contribution to oxidative stress remains to be elucidated.

In our screening, we also identified genes involved in the pathogenicity of *P. aeruginosa* by controlling virulence factors and resistance production (*bvlR* and *orn*). BvlR is a transcriptional repressor that belongs to the LysR-type transcriptional regulator (LTTR) family. It is upregulated during exposure to epithelial cells (Frisk et al., 2004) and controls several virulence factors in *P. aeruginosa*, indicating a role in the pathogenicity of this bacterium. BvlR represses the expression of the type 3 secretion system (T3SS), *cupA*-associated fimbrial-based surface attachment, and toxin A. Furthermore, it was shown to promote tight microcolony formation, which is associated with the formation of biofilms in the lung of cystic fibrosis (*CF*) patients (McCarthy et al., 2014). The oligorribonuclease Orn also affects T3SS production (Chen et al., 2016) and contributes to bacterial resistance to fluoroquinolones by a pyocin-mediated mechanism (Chen et al., 2017) and aminoglycosides, β-lactams and oxidative stress by influencing the translation of *katA* mRNA (Xia et al., 2019).

Another finding in our screening was a mutant with a disrupted *hcnA* gene. The absence of HCN in our *P. aeruginosa* mutant strains increased their susceptibility to NaOCl, while the complementation of Δ*hcnB* with an HCN-producing plasmid recovered the phenotype in our growth kinetic analyzes. HCN is a toxic volatile secondary metabolite as it has no apparent function in primary metabolism and is produced at later stages during the exponential phase and offers an advantage for the producing strain, which is tolerant to it (Blumer and Haas, 2000). It is synthesized by many bacterial genera, including *Alcaligenes*, *Aeromonas*, *Bacillus*, *Pseudomonas*, and *Rhizobium* (Blumer and Haas, 2000; Abd El-Rahman et al., 2019). In *P. aeruginosa*, HCN is synthesized by the HCN synthase, encoded by the *hcnABC* operon, and regulated by quorum sensing and the ANR regulator (Pessi and Haas, 2000). *P. aeruginosa* cultures produce up to 300 µM of HCN by the decarboxylation of glycine, and the *hcnABC* operon is induced by low oxygen (Blumer and Haas, 2000) and high cell density, with maximum production at the end of the exponential phase (Blier et al., 2012). The toxic effect of HCN is due to the inhibition of cytochrome c oxidase, impairing cell oxygen consumption and energy production (Zuhra and Szabo, 2022). *P. aeruginosa* has two systems to avoid HCN intoxication. One involves a cyanide-insensitive terminal oxidase, CioAB, which allows aerobic respiration in the presence of

TABLE 6 Area under the curve (AUC) of NaOCl growth curves of *Pseudomonas aeruginosa* PAO1 and PA14 strains.

P. aeruginosa strains		Regulation by HCN[#]	AUC ± SD	
			Untreated	1 μg/mL NaOCl
PAO1 WT			9.288 ± 0.875	7.946 ± 0.874
PA14 WT			8.115 ± 0.983	7.310 ± 0.912
PA0433	PA0433 PW1792	↓	9.110 ± 0.503	7.682 ± 3.079
	PA14_05630		7.952 ± 0.268	7.624 ± 1.822
PA0434	PA0434 PW1793	↓	9.074 ± 0.311	6.904 ± 4.3
	PA14_05640		8.051 ± 0.323	6.828 ± 2.660
PA0435	PA0435 PW1795	↓	9.452 ± 0.502	7.005 ± 4.078
	PA14_05650		8.162 ± 0.38	7.520 ± 1.772
PA2299	PA2299 PW4885	↓	9.393 ± 0.366	8.354 ± 1.937
	PA14_15830		8.208 ± 0.190	7.609 ± 1.386
PA2328	PA2328 PW4927	↑	9.510 ± 0.164	8.565 ± 1.505
	PA14_41480		8.365 ± 0.455	7.592 ± 1.655
PA2329	PA14_02330	↑	8.137 ± 0.621	7.728 ± 1.317
PA2330	PA2330 PW4930	↑	9.368 ± 0.305	8.775 ± 0.830
	PA14_34490		7.709 ± 1.227	7.802 ± 1.517
PA2331	PA2331 PW7998	↑	9.490 ± 0.232	7.544 ± 1.839
	PA14_10540		8.232 ± 0.359	7.617 ± 0.615
PA3022	PA3022 PW6063	↑	9.181 ± 0.331	7.228 ± 2.425
	PA14_24980		8.038 ± 0.505	6.325 ± 1.978
PA4129	PA4129 PW7993	↑	9.113 ± 0.397	6.482 ± 1.977
PA4130	PA4130 PW7996	↑	9.290 ± 0.083	7.835 ± 0.936
	PA14_10550		6.401 ± 0.398	6.176 ± 0.577
PA4131	PA4131 PW7998	↑	9.367 ± 0.115	7.331 ± 0.316
	PA14_10540		8.238 ± 0.105	7.278 ± 0.483
PA4132	PA4132 PW8001	↑	8.879 ± 0.457	7.095 ± 1.207
	PA14_10530		7.652 ± 0.176	6.651 ± 0.933
PA4133	PA4133 PW8002	↑	9.595 ± 0.243	7.832 ± 0.309
	PA14_10500		6.479 ± 0.112	5.895 ± 0.227
PA4134	PA4134 PW8004	↑	9.748 ± 0.522	5.785 ± 3.059*

[#]Gene regulation by endogenously produced HCN by transcriptomic analysis conducted by Frangipani et al. (2014). WT, wild-type. Data were analyzed by One-Way ANOVA and compared with the PA14 or PAO1 WT strains treated with 1 μg/mL NaOCl. ↓ gene downregulated and ↑ upregulated in the study conducted by Frangipani et al. (2014). *$p < 0.05$. AUC represents the average ± standard deviation of at least three independent experiments.

cyanide (Cunningham et al., 1997) and the other system is the enzyme rhodonase, which forms thiocyanate by the reaction with HCN (Cipollone et al., 2007).

HCN has been detected in the breath (Enderby et al., 2009; Smith et al., 2013) and the sputum and lung of *CF* patients (Ryall et al., 2008; Sanderson et al., 2008), suggesting that *P. aeruginosa* could also employ this metabolite as a virulence factor to increase its pathogenicity. Due to its high toxicity, HCN also exerts a toxic effect on non-producing strains (Zdor, 2015; Biswas and Götz, 2022). In this context, HCN produced by *P. aeruginosa* has been shown to control the growth of *S. aureus*, contributing to *P. aeruginosa* competition (Létoffé et al., 2022). Here we show that HCN also contributes to the survival of *P. aeruginosa* to the strong antioxidant NaOCl. Recently, studies have shown the effect of signaling molecules on the resistance profile of bacterial species (Li et al., 2022). Therefore, to investigate the HCN-mediated response to NaOCl in *P. aeruginosa*, we first tested the hypothesis that the production of HCN induces cellular mechanisms that, in turn, activate resistance mechanisms. For instance, indole produced by bacterial species induces bacterial resistance endogenously and exogenously by many mechanisms, including efflux pump regulation, biofilm formation, and induction of the persister state (Li et al., 2022). We then tested a list of *P. aeruginosa* genes that were up or down-regulated under endogenously produced HCN (Frangipani et al., 2014). Except for the gene PA4134, no NaOCl susceptibility was found for the mutant strains tested, suggesting that the NaOCl phenotype found in this study is likely not due to cellular regulation.

10.3389/fmicb.2023.1294518

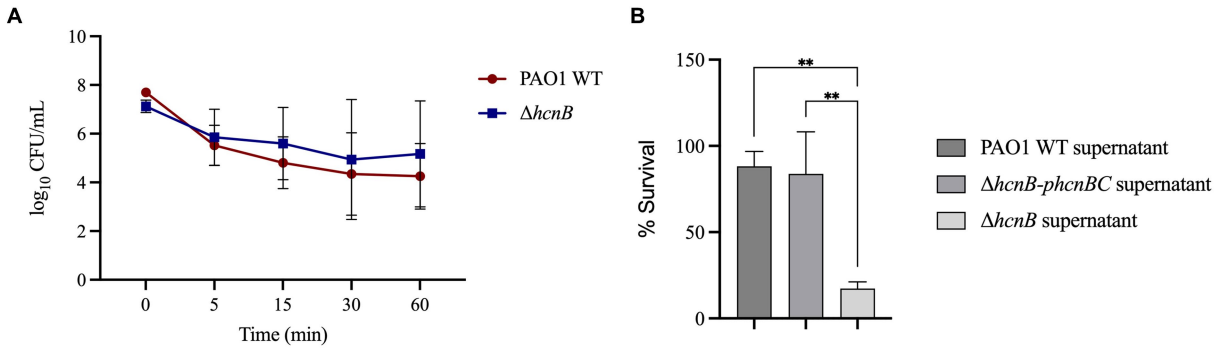

FIGURE 7
Effect of exogenous HCN on the susceptibility of *P. aeruginosa* to NaOCl. **(A)** PAO1 WT and Δ*hcnB* were grown overnight, washed twice, and resuspended in PBS. The OD_{600nm} was adjusted to 0.1, and the cell suspension was treated with 2 μg/mL NaOCl for 5, 15, 30, and 60 min. Then, CFU counts were determined by the drop plate method. **(B)** Δ*hcnB*, PAO1 WT, and Δ*hcnB-phcnBC* were grown overnight in BM2, and the supernatant was collected by centrifugation followed by filtration in a 0.22 μm filter. Δ*hcnB* overnight cells were resuspended in each supernatant to an OD_{600nm} of 0.1, treated with NaOCl at 4 μg/mL, and the CFU counts were determined by the drop plate method. ** $p < 0.01$.

We then assessed if the NaOCl susceptibility found was due to the reaction of HCN with NaOCl and found evidence supporting the scavenger effect of HCN in the presence of NaOCl, quenching the toxic effect of this oxidizing agent. Due to its high reactivity, HOCl is known to react rapidly with sulfur- and nitrogen-containing compounds, producing chlorinated derivatives with impaired functions (Winterbourn, 1985; Pattison et al., 2012). In this context, the reaction between HCN and HOCl, the active ingredient of NaOCl in aqueous solution (Fukuzaki, 2006), forms CO_2, N_2, and HCl. However, due to its toxicity, we could not evaluate if adding HCN to *P. aeruginosa* would rescue the NaOCl-susceptibility phenotype found for the Δ*hcnB* mutant, and we used different supernatants from WT and HCN-deficient strains as an alternative approach.

It is believed that the production of HCN by bacteria serves various purposes, including defense mechanisms, helping the bacteria compete with other microorganisms for resources, and antimicrobial effect, inhibiting the growth of other microorganisms. Here, we have identified a new role for HCN produced by pathogenic bacteria as a NaOCl scavenger molecule, contributing to bacterial resistance under NaOCl stress conditions. We hypothesize that HCN is produced in the context of *P. aeruginosa* infection, such as wound infection in which the environment presents low oxygen levels, favoring anaerobic microorganisms (Versey et al., 2021), and helping in the fight against oxidative stress produced by the immune system or from exogenous sources. Many bacteria produce a wide array of virulence factors and secreted metabolites. Many of these secreted molecules have been shown to quench and neutralize the toxic effect of oxidizing agents. For example, melanin produced by bacteria is a free radical scavenger (Sichel et al., 1991; Agodi et al., 1996) that protects bacterial cells against oxidative stress (Rodríguez-Rojas et al., 2009; Thippakorn et al., 2018). The search for molecules that act as scavengers for antimicrobial agents or immune system factors and understanding these metabolites help develop new strategies to eradicate *P. aeruginosa* and fight infections and the spread of this bacterium.

Of note, due to the high reactivity of NaOCl and its active ingredient, HOCl, the chemistry behind the formation and consumption of RCS in media is complex (Peskin et al., 2005; Pattison and Davies, 2006). For instance, rich media such as LB have been shown to completely quench the oxidizing effect of HOCl, while in some buffers such as PBS, no change in the levels of RCS was detected (Ashby et al., 2020). In this context, in minimal growth media containing amine, chloramines can be formed by the chlorination of amino groups by the chlorine present in HOCl (Pál Fehér et al., 2019). Therefore, the amount of HOCl and other RCS will depend on the type of media used and their ability to quench HOCl as well as to produce other RCS.

5. Conclusion

Although much effort has been made to uncover the mechanisms employed by bacteria to resist oxidative stress, most of the studies have focused on H_2O_2, and the knowledge on adaption to RCS, including NaOCl, is still in its infancy. Our PA14 mutant library screening identified 48 genes and showed that *P. aeruginosa* relies on diverse mechanisms to survive the potent and often irreversible stress caused by NaOCl. Among them, we identified the *hcnA* gene and showed that HCN contributes to the resistance of *P. aeruginosa* by quenching the toxic effect of NaOCl. To our knowledge, this is the first study reporting the roles of HCN in NaOCl resistance.

Data availability statement

The original contributions presented in the study are included in the article/Supplementary material, further inquiries can be directed to the corresponding author.

Author contributions

WSdCN: Conceptualization, Formal analysis, Investigation, Methodology, Project administration, Visualization, Writing – original draft, Writing – review & editing. MEA: Formal analysis,

Investigation, Methodology, Writing – original draft. VI: Formal analysis, Investigation, Methodology, Writing – original draft. CB: Methodology, Writing – original draft, Investigation. JO: Methodology, Writing – original draft, Conceptualization, Funding acquisition, Project administration, Resources, Supervision, Writing – review & editing.

Funding

The author(s) declare financial support was received for the research, authorship, and/or publication of this article. This research was funded by Carleton University and the Natural Sciences and Engineering Research Council of Canada (NSERC, RGPIN-2019-06335).

Acknowledgments

We would like to thank Jean-Marc Ghigo for providing the *phcnBC* plasmid used in this study.

Conflict of interest

The authors declare that the research was conducted in the absence of any commercial or financial relationships that could be construed as a potential conflict of interest.

Publisher's note

Supplementary material

The Supplementary material for this article can be found online at: https://www.frontiersin.org/articles/10.3389/fmicb.2023.1294518/full#supplementary-material

References

Abd El-Rahman, A. F., Shaheen, H. A., Abd El-Aziz, R. M., and Ibrahim, D. S. S. (2019). Influence of hydrogen cyanide-producing rhizobacteria in controlling the crown gall and root-knot nematode, Meloidogyne incognita. *Egypt. J. Biol. Pest Control* 29:41. doi: 10.1186/s41938-019-0143-7

Agodi, A., Stefani, S., Corsaro, C., Campanile, F., Gribaldo, S., and Sichel, G. (1996). Study of a melanic pigment of *Proteus mirabilis*. *Res. Microbiol.* 147, 167–174. doi: 10.1016/0923-2508(96)80216-6

Albrich, J. M., Gilbaugh, J. H., Callahan, K. B., and Hurst, J. K. (1986). Effects of the putative neutrophil-generated toxin, hypochlorous acid, on membrane permeability and transport systems of *Escherichia coli*. *J. Clin. Invest.* 78, 177–184. doi: 10.1172/JCI112548

Ambreetha, S., and Balachandar, D. (2022). Pathogenesis of plant-associated *Pseudomonas aeruginosa* in *Caenorhabditis elegans* model. *BMC Microbiol.* 22:269. doi: 10.1186/s12866-022-02682-z

Ashby, L. V., Springer, R., Hampton, M. B., Kettle, A. J., and Winterbourn, C. C. (2020). Evaluating the bactericidal action of hypochlorous acid in culture media. *Free Radic. Biol. Med.* 159, 119–124. doi: 10.1016/j.freeradbiomed.2020.07.033

Bardaweel, S. K., Gul, M., Alzweiri, M., Ishaqat, A., ALSalamat, H. A., and Bashatwah, R. M. (2018). Reactive oxygen species: the dual role in physiological and pathological conditions of the human body. *Eurasian J Med* 50, 193–201. doi: 10.5152/eurasianjmed.2018.17397

Bassetti, M., Vena, A., Croxatto, A., Righi, E., and Guery, B. (2018). How to manage *Pseudomonas aeruginosa* infections. *Drugs Context* 7:212527, 1–18. doi: 10.7573/dic.212527

Benoit, S. L., and Maier, R. J. (2016). Helicobacter catalase devoid of catalytic activity protects the bacterium against oxidative stress. *J. Biol. Chem.* 291, 23366–23373. doi: 10.1074/jbc.M116.747881

Biswas, L., and Götz, F. (2022). Molecular mechanisms of Staphylococcus and Pseudomonas interactions in cystic fibrosis. *Front. Cell. Infect. Microbiol.* 11:4042. doi: 10.3389/fcimb.2021.824042

Blier, A.-S., Vieillard, J., Gerault, E., Dagorn, A., Varacavoudin, T., Le Derf, F., et al. (2012). Quantification of *Pseudomonas aeruginosa* hydrogen cyanide production by a polarographic approach. *J. Microbiol. Methods* 90, 20–24. doi: 10.1016/j.mimet.2012.04.005

Blumer, C., and Haas, D. (2000). Mechanism, regulation, and ecological role of bacterial cyanide biosynthesis. *Arch. Microbiol.* 173, 170–177. doi: 10.1007/s002039900127

Castric, P. A. (1977). Glycine metabolism by *Pseudomonas aeruginosa*: hydrogen cyanide biosynthesis. *J. Bacteriol.* 130, 826–831. doi: 10.1128/jb.130.2.826-831.1977

Castro-Cerritos, K. V., Yasbin, R. E., Robleto, E. A., and Pedraza-Reyes, M. (2017). Role of ribonucleotide reductase in *Bacillus subtilis* stress-associated mutagenesis. *J. Bacteriol.* 199, e00715–e00716. doi: 10.1128/JB.00715-16

Cavinato, L., Genise, E., Luly, F. R., Di Domenico, E. G., Del Porto, P., and Ascenzioni, F. (2020). Escaping the phagocytic oxidative burst: the role of SODB in the survival of *Pseudomonas aeruginosa* within macrophages. *Front. Microbiol.* 11:326. doi: 10.3389/fmicb.2020.00326

Chang, W., Small, D. A., Toghrol, F., and Bentley, W. E. (2005). Microarray analysis of *Pseudomonas aeruginosa* reveals induction of pyocin genes in response to hydrogen peroxide. *BMC Genomics* 6:115. doi: 10.1186/1471-2164-6-115

Chen, F., Chen, G., Liu, Y., Jin, Y., Cheng, Z., Liu, Y., et al. (2017). *Pseudomonas aeruginosa* Oligoribonuclease contributes to tolerance to ciprofloxacin by regulating Pyocin biosynthesis. *Antimicrob. Agents Chemother.* 61, e02256–e02216. doi: 10.1128/AAC.02256-16

Chen, G., Zhao, Q., Zhu, F., Chen, R., Jin, Y., Liu, C., et al. (2016). Oligoribonuclease is required for the type III secretion system and pathogenesis of *Pseudomonas aeruginosa*. *Microbiol. Res.* 188-189, 90–96. doi: 10.1016/j.micres.2016.05.002

Cipollone, R., Frangipani, E., Tiburzi, F., Imperi, F., Ascenzi, P., and Visca, P. (2007). Involvement of *Pseudomonas aeruginosa* Rhodanese in protection from cyanide toxicity. *Appl. Environ. Microbiol.* 73, 390–398. doi: 10.1128/AEM.02143-06

Cirz, R. T., O'Neill, B. M., Hammond, J. A., Head, S. R., and Romesberg, F. E. (2006). Defining the *Pseudomonas aeruginosa* SOS response and its role in the global response to the antibiotic ciprofloxacin. *J. Bacteriol.* 188, 7101–7110. doi: 10.1128/JB.00807-06

Craig, K., Johnson, B. R., and Grunden, A. (2021). Leveraging Pseudomonas stress response mechanisms for industrial applications. *Front. Microbiol.* 12:134. doi: 10.3389/fmicb.2021.660134

Crespo, A., Pedraz, L., Van Der Hofstadt, M., Gomila, G., and Torrents, E. (2017). Regulation of ribonucleotide synthesis by the *Pseudomonas aeruginosa* two-component system AlgR in response to oxidative stress. *Sci. Rep.* 7, 17892–17815. doi: 10.1038/s41598-017-17917-7

Cunningham, L., Pitt, M., and Williams, H. D. (1997). The cioAB genes from *Pseudomonas aeruginosa* code for a novel cyanide-insensitive terminal oxidase related to the cytochrome bd quinol oxidases. *Mol. Microbiol.* 24, 579–591. doi: 10.1046/j.1365-2958.1997.3561728.x

da Cruz Nizer, W. S., Inkovskiy, V., and Overhage, J. (2020). Surviving reactive chlorine stress: responses of gram-negative Bacteria to Hypochlorous acid. *Microorganisms* 8:1220. doi: 10.3390/microorganisms8081220

Da Cruz Nizer, W. S., Inkovskiy, V., Versey, Z., Strempel, N., Cassol, E., and Overhage, J. (2021). Oxidative stress response in *Pseudomonas aeruginosa*. *Pathogens* 10:1187. doi: 10.3390/pathogens10091187

Deborde, M., and von Gunten, U. (2008). Reactions of chlorine with inorganic and organic compounds during water treatment—kinetics and mechanisms: a critical review. *Water Res.* 42, 13–51. doi: 10.1016/j.watres.2007.07.025

Dukan, S., and Touati, D. (1996). Hypochlorous acid stress in *Escherichia coli*: resistance, DNA damage, and comparison with hydrogen peroxide stress. *J. Bacteriol.* 178, 6145–6150. doi: 10.1128/jb.178.21.6145-6150.1996

Enderby, B., Smith, D., Carroll, W., and Lenney, W. (2009). Hydrogen cyanide as a biomarker for *Pseudomonas aeruginosa* in the breath of children with cystic fibrosis. *Pediatr. Pulmonol.* 44, 142–147. doi: 10.1002/ppul.20963

Farrant, K. V., Spiga, L., Davies, J. C., and Williams, H. D. (2020). Response of *Pseudomonas aeruginosa* to the innate immune system-derived oxidants Hypochlorous acid and Hypothiocyanous acid. *J. Bacteriol.* 203, e00300–e00320. doi: 10.1128/JB.00300-20

Filiatrault, M. J., Tombline, G., Wagner, V. E., Alst, N. V., Rumbaugh, K., Sokol, P., et al. (2013). *Pseudomonas aeruginosa* PA1006, which plays a role in molybdenum homeostasis, is required for nitrate utilization, biofilm formation, and virulence. *PLoS One* 8:e55594. doi: 10.1371/journal.pone.0055594

Finnegan, M., Linley, E., Denyer, S. P., McDonnell, G., Simons, C., and Maillard, J.-Y. (2010). Mode of action of hydrogen peroxide and other oxidizing agents: differences between liquid and gas forms. *J. Antimicrob. Chemother.* 65, 2108–2115. doi: 10.1093/jac/dkq308

Frangipani, E., Pérez-Martínez, I., Williams, H. D., Cherbuin, G., and Haas, D. (2014). A novel cyanide-inducible gene cluster helps protect *Pseudomonas aeruginosa* from cyanide. *Environ. Microbiol. Rep.* 6, 28–34. doi: 10.1111/1758-2229.12105

Frisk, A., Schurr, J. R., Wang, G., Bertucci, D. C., Marrero, L., Hwang, S. H., et al. (2004). Transcriptome analysis of *Pseudomonas aeruginosa* after interaction with human airway epithelial cells. *Infect. Immun.* 72, 5433–5438. doi: 10.1128/iai.72.9.5433-5438.2004

Fukuzaki, S. (2006). Mechanisms of actions of sodium hypochlorite in cleaning and disinfection processes. *Biocontrol Sci.* 11, 147–157. doi: 10.4265/bio.11.147

Gilchrist, F. J., Alcock, A., Belcher, J., Brady, M., Jones, A., Smith, D., et al. (2011). Variation in hydrogen cyanide production between different strains of *Pseudomonas aeruginosa*. *Eur. Respir. J.* 38, 409–414. doi: 10.1183/09031936.00166510

Goemans, C. V., and Collet, J.-F. (2019). Stress-induced chaperones: a first line of defense against the powerful oxidant hypochlorous acid. *F1000Res* 8:1678. doi: 10.12688/f1000research.19517.1

Gold, M. H., Andriessen, A., Bhatia, A. C., Bitter, P. Jr., Chilukuri, S., Cohen, J. L., et al. (2020). Topical stabilized hypochlorous acid: the future gold standard for wound care and scar management in dermatologic and plastic surgery procedures. *J. Cosmet. Dermatol.* 19, 270–277. doi: 10.1111/jocd.13280

Gray, M. J., Wholey, W.-Y., and Jakob, U. (2013). Bacterial responses to reactive chlorine species. *Annu. Rev. Microbiol.* 67, 141–160. doi: 10.1146/annurev-micro-102912-142520

Groitl, B., Dahl, J.-U., Schroeder, J. W., and Jakob, U. (2017). *Pseudomonas aeruginosa* defense systems against microbicidal oxidants. *Mol. Microbiol.* 106, 335–350. doi: 10.1111/mmi.13768

Heo, Y.-J., Chung, I.-Y., Cho, W.-J., Lee, B.-Y., Kim, J.-H., Choi, K.-H., et al. (2010). The major catalase gene (katA) of *Pseudomonas aeruginosa* PA14 is under both positive and negative control of the global Transactivator OxyR in response to hydrogen peroxide. *J. Bacteriol.* 192, 381–390. doi: 10.1128/JB.00980-09

Herigstad, B., Hamilton, M., and Heersink, J. (2001). How to optimize the drop plate method for enumerating bacteria. *J. Microbiol. Methods* 44, 121–129. doi: 10.1016/s0167-7012(00)00241-4

Jacobs, M. A., Alwood, A., Thaipisuttikul, I., Spencer, D., Haugen, E., Ernst, S., et al. (2003). Comprehensive transposon mutant library of *Pseudomonas aeruginosa*. *Proc. Natl. Acad. Sci.* 100, 14339–14344. doi: 10.1073/pnas.2036282100

Kashyap, S., Sharma, P., and Capalash, N. (2022). Tobramycin stress induced differential gene expression in *Acinetobacter baumannii*. *Curr. Microbiol.* 79:88. doi: 10.1007/s00284-022-02788-7

Kim, H. J., Lee, H., Lee, Y., Choi, I., Ko, Y., Lee, S., et al. (2020). The ThiL enzyme is a valid antibacterial target essential for both thiamine biosynthesis and salvage pathways in *Pseudomonas aeruginosa*. *J. Biol. Chem.* 295, 10081–10091. doi: 10.1074/jbc.RA120.013295

Lee, J.-S., Heo, Y.-J., Lee, J. K., and Cho, Y.-H. (2005). KatA, the major catalase, is critical for Osmoprotection and virulence in *Pseudomonas aeruginosa* PA14. *Infect. Immun.* 73, 4399–4403. doi: 10.1128/IAI.73.7.4399-4403.2005

Létoffé, S., Wu, Y., Darch, S. E., Beloin, C., Whiteley, M., Touqui, L., et al. (2022). *Pseudomonas aeruginosa* production of hydrogen cyanide leads to airborne control of *Staphylococcus aureus* growth in biofilm and in vivo lung. *Environments* 13:e0215422. doi: 10.1128/mbio.02154-22

Li, Y., Feng, T., and Wang, Y. (2022). The role of bacterial signaling networks in antibiotics response and resistance regulation. *Mar Life Sci Technol* 4, 163–178. doi: 10.1007/s42995-022-00126-1

Li, L.-H., Shih, Y.-L., Huang, J.-Y., Wu, C.-J., Huang, Y.-W., Huang, H.-H., et al. (2020). Protection from hydrogen peroxide stress relies mainly on AhpCF and KatA2 in *Stenotrophomonas maltophilia*. *J. Biomed. Sci.* 27:37. doi: 10.1186/s12929-020-00631-4

Liberati, N. T., Urbach, J. M., Miyata, S., Lee, D. G., Drenkard, E., Wu, G., et al. (2006). An ordered, nonredundant library of *Pseudomonas aeruginosa* strain PA14 transposon insertion mutants. *Proc. Natl. Acad. Sci.* 103, 2833–2838. doi: 10.1073/pnas.0511100103

Lünse, C. E., Schüller, A., and Mayer, G. (2014). The promise of riboswitches as potential antibacterial drug targets. *Int. J. Med. Microbiol.* 304, 79–92. doi: 10.1016/j.ijmm.2013.09.002

McCarthy, R. R., Mooij, M. J., Reen, F. J., Lesouhaitier, O., and O'Gara, F. (2014). A new regulator of pathogenicity (bvlR) is required for full virulence and tight microcolony formation in *Pseudomonas aeruginosa*. *Microbiology* 160, 1488–1500. doi: 10.1099/mic.0.075291-0

Monje-Casas, F., Jurado, J., Prieto-Alamo, M. J., Holmgren, A., and Pueyo, C. (2001). Expression analysis of the nrdHIEF operon from *Escherichia coli*. Conditions that trigger the transcript level in vivo. *J. Biol. Chem.* 276, 18031–18037. doi: 10.1074/jbc.M011728200

Moser, S., Chileveru, H. R., Tomaras, J., and Nolan, E. M. (2014). A bacterial mutant library as a tool to study the attack of a Defensin peptide. *Chembiochem* 15, 2684–2688. doi: 10.1002/cbic.201402354

Ochsner, U. A., Vasil, M. L., Alsabbagh, E., Parvatiyar, K., and Hassett, D. J. (2000). Role of the *Pseudomonas aeruginosa* oxyR-recG operon in oxidative stress defense and DNA repair: OxyR-dependent regulation of katB-ankB, ahpB, and ahpC-ahpF. *J. Bacteriol.* 182, 4533–4544. doi: 10.1128/JB.182.16.4533-4544.2000

Overhage, J., Bains, M., Brazas, M. D., and Hancock, R. E. W. (2008). Swarming of *Pseudomonas aeruginosa* is a complex adaptation leading to increased production of virulence factors and antibiotic resistance. *J. Bacteriol.* 190, 2671–2679. doi: 10.1128/jb.01659-07

Pál Fehér, P., Purgel, M., Lengyel, A., Stirling, A., and Fábián, I. (2019). The mechanism of monochloramine disproportionation under acidic conditions. *Dalton Trans.* 48, 16713–16721. doi: 10.1039/C9DT03789F

Palma, M., DeLuca, D., Worgall, S., and Quadri, L. E. N. (2004). Transcriptome analysis of the response of *Pseudomonas aeruginosa* to hydrogen peroxide. *J. Bacteriol.* 186, 248–252. doi: 10.1128/JB.186.1.248-252.2004

Panmanee, W., and Hassett, D. J. (2009). Differential roles of OxyR-controlled antioxidant enzymes alkyl hydroperoxide reductase (AhpCF) and catalase (KatB) in the protection of *Pseudomonas aeruginosa* against hydrogen peroxide in biofilm vs. planktonic culture. *FEMS Microbiol. Lett.* 295, 238–244. doi: 10.1111/j.1574-6968.2009.01605.x

Pattison, D. I., and Davies, M. J. (2006). Reactions of myeloperoxidase-derived oxidants with biological substrates: gaining chemical insight into human inflammatory diseases. *Curr. Med. Chem.* 13, 3271–3290. doi: 10.2174/092986706778773095

Pattison, D. I., Davies, M. J., and Hawkins, C. L. (2012). Reactions and reactivity of myeloperoxidase-derived oxidants: differential biological effects of hypochlorous and hypothiocyanous acids. *Free Radic. Res.* 46, 975–995. doi: 10.3109/10715762.2012.667566

Peskin, A. V., Midwinter, R. G., Harwood, D. T., and Winterbourn, C. C. (2005). Chlorine transfer between glycine, taurine, and histamine: reaction rates and impact on cellular reactivity. *Free Radic. Biol. Med.* 38, 397–405. doi: 10.1016/j.freeradbiomed.2004.11.006

Peskin, A. V., and Winterbourn, C. C. (2001). Kinetics of the reactions of hypochlorous acid and amino acid chloramines with thiols, methionine, and ascorbate. *Free Radic. Biol. Med.* 30, 572–579. doi: 10.1016/S0891-5849(00)00506-2

Pessi, G., and Haas, D. (2000). Transcriptional control of the hydrogen cyanide biosynthetic genes hcnABC by the anaerobic regulator ANR and the quorum-sensing regulators LasR and RhlR In *Pseudomonas aeruginosa*. *J. Bacteriol.* 182, 6940–6949. doi: 10.1128/jb.182.24.6940-6949.2000

Prütz, W. A. (1996). Hypochlorous acid interactions with thiols, nucleotides, DNA, and other biological substrates. *Arch. Biochem. Biophys.* 332, 110–120. doi: 10.1006/abbi.1996.0322

Rahme, L. G., Stevens, E. J., Wolfort, S. F., Shao, J., Tompkins, R. G., and Ausubel, F. M. (1995). Common virulence factors for bacterial pathogenicity in plants and animals. *Science* 268, 1899–1902. doi: 10.1126/science.7604262

Rodríguez-Rojas, A., Mena, A., Martín, S., Borrell, N., Oliver, A., and Blázquez, J. (2009). Inactivation of the hmgA gene of *Pseudomonas aeruginosa* leads to pyomelanin hyperproduction, stress resistance and increased persistence in chronic lung infection. *Microbiology* 155, 1050–1057. doi: 10.1099/mic.0.024745-0

Romsang, A., Atichartpongkul, S., Trinachartvanit, W., Vattanaviboon, P., and Mongkolsuk, S. (2013). Gene expression and physiological role of *Pseudomonas aeruginosa* methionine sulfoxide reductases during oxidative stress. *J. Bacteriol.* 195, 3299–3308. doi: 10.1128/JB.00167-13

Ryall, B., Davies, J. C., Wilson, R., Shoemark, A., and Williams, H. D. (2008). *Pseudomonas aeruginosa*, cyanide accumulation and lung function in CF and non-CF bronchiectasis patients. *Eur. Respir. J.* 32, 740–747. doi: 10.1183/09031936.00159607

Salunkhe, P., von Götz, F., Wiehlmann, L., Lauber, J., Buer, J., and Tümmler, B. (2002). GeneChip expression analysis of the response of *Pseudomonas aeruginosa* to Paraquat-induced superoxide stress. *Genome Lett* 1, 165–174. doi: 10.1166/gl.2002.019

Sanderson, K., Wescombe, L., Kirov, S. M., Champion, A., and Reid, D. W. (2008). Bacterial cyanogenesis occurs in the cystic fibrosis lung. *Eur. Respir. J.* 32, 329–333. doi: 10.1183/09031936.00152407

Sichel, G., Corsaro, C., Scalia, M., Di Bilio, A. J., and Bonomo, R. P. (1991). In vitro scavenger activity of some flavonoids and melanins against O2-(.). *Free Radic. Biol. Med.* 11, 1–8. doi: 10.1016/0891-5849(91)90181-2

Small, D. A., Chang, W., Toghrol, F., and Bentley, W. E. (2007a). Comparative global transcription analysis of sodium hypochlorite, peracetic acid, and hydrogen peroxide

on *Pseudomonas aeruginosa*. *Appl. Microbiol. Biotechnol.* 76, 1093–1105. doi: 10.1007/s00253-007-1072-z

Small, D. A., Chang, W., Toghrol, F., and Bentley, W. E. (2007b). Toxicogenomic analysis of sodium hypochlorite antimicrobial mechanisms in *Pseudomonas aeruginosa*. *Appl. Microbiol. Biotechnol.* 74, 176–185. doi: 10.1007/s00253-006-0644-7

Smith, D., Spaněl, P., Gilchrist, F. J., and Lenney, W. (2013). Hydrogen cyanide, a volatile biomarker of *Pseudomonas aeruginosa* infection. *J. Breath Res.* 7:044001. doi: 10.1088/1752-7155/7/4/044001

Sprouffske, K., and Wagner, A. (2016). Growthcurver: an R package for obtaining interpretable metrics from microbial growth curves. *BMC Bioinformatics* 17:172. doi: 10.1186/s12859-016-1016-7

Stothard, P., and Wishart, D. S. (2005). Circular genome visualization and exploration using CGView. *Bioinformatics* 21, 537–539. doi: 10.1093/bioinformatics/bti054

Stover, C. K., Pham, X. Q., Erwin, A. L., Mizoguchi, S. D., Warrener, P., Hickey, M. J., et al. (2000). Complete genome sequence of Pseudomonas aeruginosa PAO1, an opportunistic pathogen. *Nature* 406, 959–964. doi: 10.1038/35023079

Strempel, N., Nusser, M., Neidig, A., Brenner-Weiss, G., and Overhage, J. (2017). The oxidative stress agent hypochlorite stimulates c-di-GMP synthesis and biofilm formation in *Pseudomonas aeruginosa*. *Front. Microbiol.* 8:2311. doi: 10.3389/fmicb.2017.02311

Su, S., Panmanee, W., Wilson, J. J., Mahtani, H. K., Li, Q., VanderWielen, B. D., et al. (2014). Catalase (KatA) plays a role in protection against anaerobic nitric oxide in *Pseudomonas aeruginosa*. *PLoS One* 9:e91813. doi: 10.1371/journal.pone.0091813

Sultana, S., Foti, A., and Dahl, J.-U. (2020). Bacterial defense systems against the neutrophilic oxidant Hypochlorous acid. *Infect. Immun.* 88, e00964–e00919. doi: 10.1128/IAI.00964-19

Thippakorn, C., Isarankura-Na-Ayudhya, C., Pannengpetch, S., Isarankura-Na-Ayudhya, P., Schaduangrat, N., Nantasenamat, C., et al. (2018). Oxidative responses and defense mechanism of hyperpigmented *P. aeruginosa* as characterized by proteomics and metabolomics. *EXCLI J.* 17, 544–562. doi: 10.17179/excli2018-1238

Todor, H., Dulmage, K., Gillum, N., Bain, J. R., Muehlbauer, M. J., and Schmid, A. K. (2014). A transcription factor links growth rate and metabolism in the hypersaline adapted archaeon *Halobacterium salinarum*. *Mol. Microbiol.* 93, 1172–1182. doi: 10.1111/mmi.12726

Torrents, E., Poplawski, A., and Sjöberg, B.-M. (2005). Two proteins mediate class II ribonucleotide reductase activity in *Pseudomonas aeruginosa*: expression and transcriptional analysis of the aerobic enzymes. *J. Biol. Chem.* 280, 16571–16578. doi: 10.1074/jbc.M501322200

Versey, Z., Da Cruz Nizer, W. S., Russell, E., Zigic, S., DeZeeuw, K. G., Marek, J. E., et al. (2021). Biofilm-innate immune Interface: contribution to chronic wound formation. *Front. Immunol.* 12:648554. doi: 10.3389/fimmu.2021.648554

Wang, H., Chen, S., Zhang, J., Rothenbacher, F. P., Jiang, T., Kan, B., et al. (2012). Catalases promote resistance of oxidative stress in *Vibrio cholerae*. *PLoS One* 7:e53383. doi: 10.1371/journal.pone.0053383

Wang, S., Deng, K., Zaremba, S., Deng, X., Lin, C., Wang, Q., et al. (2009). Transcriptomic response of *Escherichia coli* O157:H7 to oxidative stress. *Appl. Environ. Microbiol.* 75, 6110–6123. doi: 10.1128/AEM.00914-09

Wang, S., Phillippy, A. M., Deng, K., Rui, X., Li, Z., Tortorello, M. L., et al. (2010). Transcriptomic responses of *Salmonella enterica* Serovars Enteritidis and typhimurium to chlorine-based oxidative stress. *Appl. Environ. Microbiol.* 76, 5013–5024. doi: 10.1128/AEM.00823-10

Wiegand, I., Hilpert, K., and Hancock, R. E. W. (2008). Agar and broth dilution methods to determine the minimal inhibitory concentration (MIC) of antimicrobial substances. *Nat. Protoc.* 3, 163–175. doi: 10.1038/nprot.2007.521

Winterbourn, C. C. (1985). Comparative reactivities of various biological compounds with myeloperoxidase-hydrogen peroxide-chloride, and similarity of oxidant to hypochlorite. *Biochim. Biophys. Acta Gen. Subj.* 840, 204–210. doi: 10.1016/0304-4165(85)90120-5

Winterbourn, C. C., Kettle, A. J., and Hampton, M. B. (2016). Reactive oxygen species and neutrophil function. *Annu. Rev. Biochem.* 85, 765–792. doi: 10.1146/annurev-biochem-060815-014442

Wu, M., Guina, T., Brittnacher, M., Nguyen, H., Eng, J., and Miller, S. I. (2005). The *Pseudomonas aeruginosa* proteome during anaerobic growth. *J. Bacteriol.* 187, 8185–8190. doi: 10.1128/JB.187.23.8185-8190.2005

Xia, B., Li, M., Tian, Z., Chen, G., Liu, C., Xia, Y., et al. (2019). Oligoribonuclease contributes to tolerance to aminoglycoside and β-lactam antibiotics by regulating KatA in *Pseudomonas aeruginosa*. *Antimicrob. Agents Chemother.* 63, e00212–e00219. doi: 10.1128/AAC.00212-19

Yuan, F., Yin, S., Xu, Y., Xiang, L., Wang, H., Li, Z., et al. (2021). The richness and diversity of catalases in Bacteria. *Front. Microbiol.* 12:477. doi: 10.3389/fmicb.2021.645477

Zdor, R. E. (2015). Bacterial cyanogenesis: impact on biotic interactions. *J. Appl. Microbiol.* 118, 267–274. doi: 10.1111/jam.12697

Zuhra, K., and Szabo, C. (2022). The two faces of cyanide: an environmental toxin and a potential novel mammalian gasotransmitter. *FEBS J.* 289, 2481–2515. doi: 10.1111/febs.16135

Zuo, F., Yu, R., Xiao, M., Khaskheli, G. B., Sun, X., Ma, H., et al. (2018). Transcriptomic analysis of *Bifidobacterium longum* subsp. *longum* BBMN68 in response to oxidative shock. *Sci. Rep.* 8:17085. doi: 10.1038/s41598-018-35286-7

frontiers | Frontiers in Microbiology

TYPE Original Research
PUBLISHED 22 November 2023
DOI 10.3389/fmicb.2023.1281058

OPEN ACCESS

EDITED BY
Jose Echenique,
National University of Cordoba, Argentina

REVIEWED BY
Jan-Ulrik Dahl,
Illinois State University, United States
Markus J. Tamás,
University of Gothenburg, Sweden

*CORRESPONDENCE
Felipe A. Arenas
✉ felipe.arenass@usach.cl

†Deceased

‡PRESENT ADDRESS
Fabián A. Cornejo,
Max Planck Unit for the Science of Pathogens,
Berlin, Germany

RECEIVED 21 August 2023
ACCEPTED 01 November 2023
PUBLISHED 22 November 2023

CITATION
Cornejo FA, Muñoz-Villagrán C, Luraschi RA, Sandoval-Díaz MP, Cancino CA, Pugin B, Morales EH, Piotrowski JS, Sandoval JM, Vásquez CC and Arenas FA (2023) Soft-metal(loid)s induce protein aggregation in *Escherichia coli*.
Front. Microbiol. 14:1281058.
doi: 10.3389/fmicb.2023.1281058

Soft-metal(loid)s induce protein aggregation in *Escherichia coli*

Fabián A. Cornejo[1‡], Claudia Muñoz-Villagrán[1], Roberto A. Luraschi[1], María P. Sandoval-Díaz[1], Camila A. Cancino[1], Benoit Pugin[2], Eduardo H. Morales[3], Jeff S. Piotrowski[3], Juan M. Sandoval[4], Claudio C. Vásquez[1†] and Felipe A. Arenas[1*]

[1]Laboratorio de Microbiología Molecular, Departamento de Biología, Facultad de Química y Biología, Universidad de Santiago de Chile, Santiago, Chile, [2]Laboratory of Food Biotechnology, Department of Health Sciences and Technology, ETH, Zürich, Switzerland, [3]E. & J. Gallo Winery, Modesto, CA, United States, [4]Facultad de Ciencias, Universidad Arturo Prat, Iquique, Chile

Metal(loid) salts were used to treat infectious diseases in the past due to their exceptional biocidal properties at low concentrations. However, the mechanism of their toxicity has yet to be fully elucidated. The production of reactive oxygen species (ROS) has been linked to the toxicity of soft metal(loid)s such as Ag(I), Au(III), As(III), Cd(II), Hg(II), and Te(IV). Nevertheless, few reports have described the direct, or ROS-independent, effects of some of these soft-metal(loid)s on bacteria, including the dismantling of iron–sulfur clusters [4Fe-4S] and the accumulation of porphyrin IX. Here, we used genome-wide genetic, proteomic, and biochemical approaches under anaerobic conditions to evaluate the direct mechanisms of toxicity of these metal(loid)s in *Escherichia coli*. We found that certain soft-metal(loid)s promote protein aggregation in a ROS-independent manner. This aggregation occurs during translation in the presence of Ag(I), Au(III), Hg(II), or Te(IV) and post-translationally in cells exposed to Cd(II) or As(III). We determined that aggregated proteins were involved in several essential biological processes that could lead to cell death. For instance, several enzymes involved in amino acid biosynthesis were aggregated after soft-metal(loid) exposure, disrupting intracellular amino acid concentration. We also propose a possible mechanism to explain how soft-metal(loid)s act as proteotoxic agents.

KEYWORDS

***Escherichia coli*, soft-metal(loid)s, anaerobiosis, protein aggregation, proteotoxicity, amino acid metabolism**

1 Introduction

Some metallic elements (e.g., sodium, iron, copper, and cobalt) are essential for life because their unique chemical properties are indispensable for cellular functions. These metals participate in redox reactions, provide structural stability, and enable critical cellular processes such as electron transfer and catalysis (Lemire et al., 2013; Foster et al., 2022). However, in excess, these metals can become toxic (Nies, 1999). On the other hand, non-essential metal(loid) ions such as mercury, arsenic, tellurium, and silver are highly toxic to most organisms, even at micromolar concentrations (Daum et al., 1993; Tchounwou et al., 2012; Kim et al., 2019; Noreen et al., 2019; Zarei et al., 2019; Li et al., 2021). Metal-based molecules were used as treatment against syphilis, such as the As(III)-based drug Arsphenamine (Williams, 2009). Other metal-based drugs or metallodrugs hold great potential as a new generation of antimicrobials, cancer treatment, psychotropics, among others (Mjos and Orvig, 2014).

Ions of these elements, due to their high polarizability, are classified as soft acids or soft-metal(loid)s. They tend to react with intracellular molecules containing soft bases like sulfhydryl, thioesters, phenyl, or imidazole groups, forming covalently bound adducts (Pearson, 1966; Lemire et al., 2013). Conversely, metals such as Mg(II), Na(I), and K(I) are classified as hard metals and primarily interact through ionic bonds with hard bases like sulfate, carboxylate, phosphate, and amine groups (Pearson, 1966; Lemire et al., 2013).

Soft-metal(loid)s toxify cells by producing Reactive Oxygen Species (ROS) and inducing oxidative stress damage (Parvatiyar et al., 2005; Pérez et al., 2007; Tremaroli et al., 2007; Pacheco et al., 2008; Park et al., 2009; Lemire et al., 2013; Muñoz-Villagrán et al., 2020). Some metal(loid)s can produce ROS directly via Fenton chemistry [e.g., Fe(II) and Cu(I)], or indirectly, where Fenton-inactive metal(oid)s such as As(III), Cd(II), and Te(IV) deplete reduced glutathione, compromising the redox state and oxidative stress response of the cell (Valko et al., 2005; Baba and Bhatnagar, 2018; Ouyang et al., 2018). The depletion of major cellular sulfhydryl reserves seems to be a critical indirect mechanism for oxidative stress induced by metal(loid)s (Ouyang et al., 2018). The consequences of cells under oxidative stress include various dysfunctions mediated by direct damage to lipids, proteins, and DNA (Sies et al., 2017; Hawkins and Davies, 2019; Poetsch, 2020). Metals like Cd(II), Cu(I), Hg(II), Te(IV), and Ni(II) can trigger lipid peroxidation in different organisms (Company et al., 2004; Paraszkiewicz et al., 2010; Pradenas et al., 2013). Membrane damage caused by Cu(II), Cd(II) or Ag(I) can produce a loss of membrane potential (Dibrov et al., 2002; Hong et al., 2012). Double-stranded DNA can be damaged by oxidation, thereby inducing cell death and mutagenicity (Sies et al., 2017; Poetsch, 2020), as demonstrated with iron (Nunoshiba et al., 1999) and via genotoxicity assays with Mn, Cr, Cd, and other metals (Lemire et al., 2013). ROS can also induce protein oxidation and dysfunction, forming carbonyl derivatives through the metal-catalyzed oxidation of several amino acid side chains (such as histidine, arginine, lysine, and proline). Hence, carbonyl group levels are often used as a marker of oxidative protein damage (Stadtman and Levine, 2003). In other instances, metal(loid)-induced ROS dismantle Fe-S clusters in some dehydratases (Imlay, 2006; Calderón et al., 2009; Gomez et al., 2014).

The soft or hard acid nature of a specific metal(loid) can explain its toxicity and reactivity toward soft-base ligands within the protein matrix (Medici et al., 2021; Peana et al., 2021). For instance, Ni(II) can replace the structural Zn(II) present in the metal-binding sites of some proteins. These metal-binding sites can be exchanged by other more competitive divalent soft-metals, resulting in mismetallation and protein function loss (Macomber et al., 2011; Quintal et al., 2011). Certain metal(loid)s can damage enzymes that display reactive Cys residues at their active sites (Rajanna et al., 1990; Fadeeva et al., 2011). The soft-metal(loid)s Cu(I), Hg(II), Ag(I), Cd(II), and Te(IV) can dismantle solvent-exposed [4Fe-4S] clusters of *Escherichia coli* aconitases (Calderón et al., 2009; Macomber and Imlay, 2009; Xu and Imlay, 2012), releasing Fenton-active iron into the cytoplasm, which in turn generates ROS.

Despite the similar chemical reactivity of soft-metal(loid)s, few studies have identified cell targets beyond ROS-mediated oxidative stress. In this study, we conducted a genome-wide screening of an *E. coli* deletion collection challenged with soft-metal(loid)s under anaerobic conditions to identify ROS-independent targets. Strains lacking genes involved in protein homeostasis showed reduced fitness under these conditions, suggesting that proteins aggregated when exposed to Ag(I), Au(III), As(III), Cd(II), Hg(II), or Te(IV). Protein aggregation induced by Ag(I), Au(III), Hg(II), and Te(IV) required active translation, whereas As(III) and Cd(II) do not, suggesting that the mechanism by which these metals act during protein aggregation is different. In summary, we demonstrated that, in a ROS-independent manner, soft-metal(loid)s act as proteotoxic agents, leading to the accumulation of aggregated proteins, most likely due to at least two distinct mechanisms.

2 Methods

2.1 Bacterial strains

Escherichia coli K-12 BW25113 (National Institute of Genetics, Microbial Genetics Laboratory, NBRP, Japan) was used as the model strain. Unless otherwise indicated, all cultures were grown at 37°C in an anaerobic chamber (Coy Laboratory Products Inc., 100% N_2 atmosphere) with constant shaking (150 rpm) in MOPS minimal medium supplemented with 0.2% (w/v) glucose. The barcoded deletion collection was derived from *E. coli* K-12 BW38028 (Otsuka et al., 2015).

2.2 Chemical genomic profiling of soft-metal(loid)s in *Escherichia coli*

The pooled *E. coli* deletion collection was independently inoculated in media supplemented with the following soft-metal(loid) salts (resuspended in H_2O) at concentrations that resulted in a 20–30% reduction of OD_{600} compared to unexposed controls after 24 h: $AgNO_3$ (625 nM), $HAuCl_4$ (2 μM), $NaAsO_2$ (125 μM), $CdCl_2$ (31.25 μM), $HgCl_2$ (375 nM) or K_2TeO_3 (14.7 μM). For control experiments, salts were replaced with H_2O. Each pooled competition experiment was conducted in 200 μL cultures in triplicate at 37°C for 24 h. Genomic DNA was extracted using the Wizard Genomic DNA Purification Kit (Promega, Cat. No. A1120). Strain-specific barcodes from each culture were amplified using indexed primers designed for multiplexed Illumina sequencing. The forward primer contained the Illumina-specific P5 sequence, a 10 bp index tag (x's), and the 19 bp *E. coli* deletion collection common priming site: 5′-AATGATACGGCGACCACCGAGATCTACACTCTTTCCCTACACGACGCTCTTCCGATCTxxxxxxxxxxAATCTTCGGTAGTCCAGCG-3′. The reverse primer included the Illumina-specific P7 sequence and 20 bp *E. coli* common priming site: 5′-CAAGCAGAAGACGGCATACGAGCTCTTCCGATCTTGTAGGCTGGAGCTGCTTCG-3′.

As previously described, barcodes were amplified by PCR, pooled, gel-purified, and quantified by quantitative PCR (Piotrowski et al., 2015). For barcode sequencing, samples were run on an Illumina HiSeq2500 in rapid run mode for 50 cycles at a loading concentration of 15 pM. The resulting fastq file was used for the analysis of sensitive and resistant mutants. Normalized counts were compared to a control solvent (water) to identify compound-specific responses among gene deletion mutants (chemical-genetic interaction score).

Sequence data were processed using BEANcounter (Simpkins et al., 2019) and EdgeR (Robinson et al., 2010). The chemical-genetic interaction score was computed as z-scores, representing the standardized deviation of each strain in treatments compared to their

counterpart strain in the control solvent, for the 3,551 mutants quantified (Piotrowski et al., 2017; Simpkins et al., 2019). In this way, deletion-mutants whose abundance (compared to the mean of the population) was decrease as result of the treatment show a negative CG-score, while those having a higher abundance show positive CG-scores. CG-scores were analyzed using the DAVID database (Huang et al., 2009). Gene functional annotations were retrieved from EcoCyc (Keseler et al., 2017).

2.3 Isolation of aggregated proteins

Protein aggregation was assessed using the method described by Tomoyasu et al. (2001). Briefly, saturated cultures (16 h) were inoculated into 250 mL flasks containing 60 mL of MOPS medium, to a starting OD_{600} of approximately 0.05, and grown anaerobically at 37°C with constant shaking until they reached an OD_{600} of approximately 0.3. Cultures were individually exposed to soft-metal(loid) concentrations (as indicated in each figure) and incubated for 2 h at 37°C. Fifty mL of each treated culture were centrifuged at 5,000 × g for 10 min at 4°C. The resulting cell pellets were suspended in 250 µL of 10 mM potassium phosphate buffer pH 6.5 containing 1 mM EDTA (buffer A), supplemented with 20% (w/v) sucrose and 1 mg/mL lysozyme, and incubated on ice for 30 min. Then, 360 µL of buffer A was added, and cells were disrupted by sonication on ice (eight 15-s cycles with 45-s rests at 60% amplitude). Cell debris was removed by centrifugation at 2,000 × *g* for 15 min at 4°C. Both aggregated and membrane proteins were centrifuged at 15,000 × *g* for 20 min at 4°C and frozen at −80°C for later processing. Sedimented proteins were suspended in 400 µL of buffer A by brief sonication (one pulse, 5 s at 60% amplitude) and sedimented again at 15,000 × *g* for 20 min at 4°C. Membrane proteins were removed by suspending the pellet via brief sonication (one pulse, 5 s at 60% amplitude) in 320 µL of buffer A containing 2% (v/v) NP-40 (Abcam, Cat. No. ab142227). The aggregated proteins were sedimented at 15,000 × *g* for 30 min at 4°C. This washing procedure was repeated four times. The NP-40 insoluble pellet was rinsed with 400 µL of buffer A and finally suspended in 200 µL of the same buffer. Aggregated proteins were quantified by the Bradford method (Bradford, 1976), resolved by SDS-PAGE (12%), and visualized by silver staining.

2.4 Translation-arrested cells and pulse-chase of aggregated proteins

For experiments involving translation arrest, 100 µg/mL of chloramphenicol (CHL) was added to the cultures 5 min prior to the soft-metal(loid) treatment. For pulse-chase experiments, cultures (with an OD_{600} of approximately 0.3) were pulse-labeled with 250 µM 4-azido-L-homoalanine (AHA, Jena Bioscience, Cat. No. CLK-AA005) and incubated for 15 min at 37°C. The chase was initiated by adding L-methionine (Sigma-Aldrich, Cat. No. M9625) to a final concentration of 250 µM and incubated for 30 min at 37°C. Cells were then exposed to soft-metal(loid)s at the indicated concentrations for 2 h at the same temperature. Aggregated proteins were isolated as described above, but EDTA was omitted from the buffers to prevent Cu chelation in subsequent reactions. Protein aggregates were washed with phosphate saline buffer (PBS) and suspended through a brief (5-s) sonication in 200 µL of Click reaction buffer. This buffer contained 50 µM acetylene-PEG4-Biotin (Jena Bioscience, Cat. No. CLK-TA105), 1 mM TCEP (Tris(2-carboxyethyl)phosphine hydrochloride Sigma-Aldrich, Cat. No. C4706), 100 µM THPTA (Tris(3-hydroxypropyltriazolylmethyl) amine, Jena Bioscience, Cat. No. CLK-1010), and 1 mM $CuSO_4$ (Sigma-Aldrich, Cat. No. C8027) in PBS, and incubated for 30 min at 37°C. Biotinylated protein aggregates were washed twice with PBS and then analyzed via Western blotting.

2.5 Western blotting of biotinylated aggregated proteins

Five hundred nanograms of aggregated proteins were fractionated using SDS-PAGE (12%). Proteins were then transferred to PVDF membranes (Bio-Rad, Cat. No. 1620177) at 40 mA overnight at 4°C. The membranes were blocked for 1 h in a Tris-buffered saline (TBS) buffer that was supplemented with 1% (v/v) Tween-20 (TBS-T) and 3% (w/v) BSA. After an overnight incubation at 4°C with a 1:10,000 dilution of Streptavidin-HRP (Sigma-Aldrich, Cat. No. S5512) in TBS-T plus 3% (w/v) BSA, the biotinylated proteins were visualized using SuperSignal Western blot FEMTO substrate (Thermo Scientific, Cat. No. 34094).

2.6 Proteomic profiling of aggregated proteins

Samples of aggregated proteins, obtained after a 2 h exposure to metal(loid) concentrations affecting the cell viability in a similar extend (10 µM $AgNO_3$, 5 µM $HAuCl_4$, 200 mM $NaAsO_2$, 500 µM $CdCl_2$, 5 µM $HgCl_2$, or 20 µM K_2TeO_3), were flash-frozen in an ethanol dry-ice bath and processed for label-free quantification at Bioproximity in Virginia, USA. Only proteins identified with at least two unique peptides were included in the analysis. All proteins identified in the control sample were excluded from the analysis, mainly ribosomal proteins and translation factors. Functional protein associations and enrichment analysis were evaluated using the stringApp in Cytoscape (Doncheva et al., 2018). Enrichment analysis of aggregated proteins in each treatment was conducted using the DAVID database (Huang et al., 2009). All properties and subcellular locations of *E. coli* proteins were retrieved from EcoCyc (Keseler et al., 2017).

2.7 Cell viability

Cell viability was determined by diluting 20 µL of each treatment with 180 µL of a sterilized 0.9% (w/v) NaCl solution. After diluting up to 10^{-7}, 4 µL of each dilution was spotted on LB (Luria Bertani broth) agar plates and incubated overnight at 37°C in anaerobic conditions.

2.8 Amino acids extraction and quantification

Amino acids were extracted using the method described by Steinfeld et al. (2014). Briefly, 60 mL of anaerobic *E. coli* cultures at

OD_{600} 0.3 in MOPS media were treated for 2 h with defined concentrations of soft-metal(loid)s. Twenty mL from each treatment were centrifuged at 4,000 × *g* for 10 min at 4°C. Cell pellets were resuspended in 1 mL of ice-cold MOPS media and centrifuged as described above. Then, cells were lysed with 1 mL of 1 N HCl, incubated for 5 min at room temperature, and centrifuged at 19,000 × *g* for 20 min at 20°C. The supernatant was dried in a Vacuum Concentrator SpeedVac SPD120 for 3 h at 50°C and 1.5 h at 35°C. The resulting pellets were flash-frozen at −80°C until use. Pellets were resuspended in 300 µL of water by sonication for 5 s, and two consecutive extractions with 500 and 300 µL of chloroform were performed. The aqueous layers were combined, filtered through a 0.22 µm PVDF filter (4 mm), and dried for 80 min at 65°C and 80 min at 55°C. The pellets were kept flash-frozen at −80°C until used.

Amino acids were quantified using diethyl ethoxymethylenemalonate (DEEMM) derivatization followed by UPLC-DAD quantification as described in Otaru et al. (2021), with few modifications. Each pellet was resuspended in 50 µL of 0.1 N HCl. After dissolution, 87.5 µL of 1 M borate buffer pH 9.0, 37.5 µL methanol, 2 µL of 2 g/L L-2-aminoadipic acid (in 0.1 M HCl; internal standard), and 1.75 µL DEEMM were added. Analytes were derivatized for 45 min at room temperature in an ultrasonic water bath, and the samples were then heated for 2 h at 70°C to stop the reaction. After that, samples were filtered (0.45 µm membrane) and transferred into glass vials for analysis.

Quantification was carried out using an H-Class Acquity UPLC system (Waters Corp., Milford, MA, USA) equipped with a photodiode array detector (DAD). The derivatized molecules were separated using a gradient of (A) 25 mM acetate buffer pH 6.6, (B) methanol, and (C) acetonitrile in a Waters Acquity UPLC BEH C18 1.7 µm column (2.1 × 100 mm) at 40°C, as described in Otaru et al. (2021). One µL sample was applied to the column and eluted at a flow rate of 0.46 mL/min. Individual compounds were quantified at 280 nm using the internal standard method. Data processing was performed using Empower 3 software (Waters).

2.9 Statistical analysis

Biochemical assays were repeated at least three times, and the data were represented as bar plots (mean with standard deviation or standard error), scatter plots (mean with standard error), or heatmaps (mean). In the case of SDS-PAGE and Western blot, representative gels were shown.

The DAVID platform was used to compute enrichment analysis statistics. Two-sample student's *t*-tests, ANOVA, *post hoc* tests, and normal distribution statistics were calculated using R.

3 Results and discussion

3.1 Chemical genomic analysis of soft-metal(loid) toxicity in *Escherichia coli*

The toxicity of metal(loid)s in bacteria has been extensively studied and has been mostly related to the production of ROS. These highly reactive molecules rapidly oxidize several macromolecules, including DNA, membranes, and proteins. Moreover, protein aggregation was observed in yeast exposed to As(III) or Cd(II) under aerobic conditions (Jacobson et al., 2012, 2017). As(III) and Cd(II) displayed mutagenic activities dependent on the presence of RecA, suggesting single or double breaks in the DNA molecule (Lemire et al., 2013). However, the presence of oxygen in these experiments makes it difficult to determine whether the observed effect is a direct result of metal(loid) damage or ROS production. To directly identify the direct intracellular targets of soft-metal(loid)s, we challenged *E. coli* cells under anaerobic conditions where ROS cannot be formed.

We conducted chemical-genomic profiling of *E. coli* to identify deletions responsive to the soft-metal(loid)s Ag(I), Au(III), As(III), Cd(II), Hg(II), and Te(IV) under anaerobic conditions by using a published barcoded deletion collection (Otsuka et al., 2015; Morales et al., 2017). Each mutant in this barcoded collection has a unique 20-nucleotide barcode that allows quantification of its abundance through next-generation sequencing in a pooled competition experiment. We challenged the pooled collection with soft-metal(loid) concentrations that produced a mild (20–30%) reduction of the optical density (OD_{600}) after 24 h compared to the non-treated control to avoid depletion of mutants involved in the general stress response. The chemical-genetic score (from now on, CG-scores, see Supplementary Table S1) of each knockout strain served as an indicator of the relative abundance after the challenge (Simpkins et al., 2019). A negative CG-score means that the abundance of the deletion mutant, compared to the rest of the population, was negatively affected by the treatment, while a positive score means an increased abundance on those conditions.

Deletion of genes involved in fundamental processes such as cell division, lipopolysaccharide core region synthesis, protein import, homologous recombination, conjugation, and cell shape regulation was detrimental to soft-metal(loid) exposure (Supplementary Figure S1). These results suggest that soft-metal(loid)s have a pleiotropic effect and affect multiple molecular targets, which ultimately leads to cell death.

Deleting *prc*, *nlpI*, *ompA*, *galU*, and *ldcA* resulted in reduced tolerance to most treatments (Supplementary Figure S2A,B). For example, the *prc* and *nlpI* gene deletions have a very low CG-score in most soft-metal(loid) treatments, except Te(IV). Prc (or Tsp) is a periplasmic protease indispensable for *E. coli* to survive under low osmolality at 42°C due to a potential role in regulating peptidoglycan biogenesis (Hsu et al., 2020). NlpI is a lipoprotein and adaptor protein for Prc (Tadokoro et al., 2004), targeting the murein endopeptidase MepS for degradation. Other gene deletions related to peptidoglycan synthesis showed a negative CG-score, such as *mrcB* in treatment with Cd(II) (Sugawara et al., 2021), and *ybgF* in treatment with Te(IV) (Gray et al., 2015) and *ftsN* in the treatment with As(III) (Müller et al., 2007) (Supplementary Figure S2B). Therefore, our data suggest that peptidoglycan biosynthesis might be a potential soft-metal(loid) s target.

Strikingly, our analyses revealed that mutants in genes encoding proteins required for homologous recombination-DNA repair and protein aggregation (Figure 1A), were among the most impacted by toxic exposure, strongly suggesting that soft-metal(loid)s could damage DNA and proteins under anoxic conditions. In contrast, no common pathway or biological process could give tolerance to all metal(loid)s under study (Supplementary Figures S2A,C), suggesting that their common chemical properties could explain some toxicity mechanisms, but tolerance mechanisms are rather diverse. Notably,

the deletion of members of importers such as CysPUWA or MetNIQ gave resistance to Au(III) or As(III), respectively, implying that these metals could get inside the cell by those amino acid transporters (Supplementary Figure S2A). An alternative explanation is that importing Cys or Met could increase sensitivity to Au(III) or As(III), respectively. However, these experiments were performed in MOPS minimal media without amino acid addition.

3.2 Soft-metal(loid)s induce protein aggregation

Previous research has suggested that soft metal(loid)s can induce protein aggregation and damage proteins under aerobic conditions. A prominent example of this is the interaction of Hg(II) and Cd(II) with luciferase during an *in vitro* refolding process, leading to its inactivation (Sharma et al., 2008). A recent study discovered that the soft-metal Cu(I) can cause protein aggregation in *E. coli* independently of ROS (Zuily et al., 2022).

Our analysis showed that deletion mutants in genes implicated in the protein quality control (PQC) network had decreased fitness in *E. coli* exposed to soft-metal(loid)s, suggesting these metal(loid)s can induce protein misfolding and aggregation in a ROS-independent manner (Figure 1A).

Under standard conditions, misfolded proteins can be refolded by chaperones or degraded by various proteolytic systems, preventing their accumulation. However, the protein quality control network can be overwhelmed under stress conditions, leading to an accumulation of protein aggregates (Tyedmers et al., 2010). Once these aggregated proteins are formed in *E. coli*, they can be refolded by ClpB (assisted by DnaK, DnaJ, and GrpE) or degraded by AAA+ proteases like ClpAP, HslUV, or Lon (Dougan et al., 2002; Haslberger et al., 2007; Tyedmers et al., 2010). DegS and DegP are two critical proteases involved in detecting misfolded and aggregated proteins in the periplasmic compartment. DegS functions as a regulatory protease that detects misfolded proteins through its PDZ domain and catalyzes the proteolysis of the anti-sigma factor RseA (Wilken et al., 2004) (Figure 1B, right panel). This process releases the alternative sigma factor RpoE, initiating a transcriptional response to manage misfolded proteins in the cytoplasmic and periplasmic compartments (Erickson and Gross, 1989; Danese and Silhavy, 1997). Egler et al. (2005) found that a Δ*rpoE* strain is sensitive to Cu(II), Cd(II), and Zn(II), but the authors did not speculate about a potential metal-mediated proteotoxic effect. DegP is a RpoE-induced serine protease/chaperone that degrades misfolded proteins in the periplasm. In our analysis, mutants lacking cytoplasmic and periplasmic proteases and chaperones, such as DegP, DegQ, the AAA+ protease ClpAP, and its adaptor ClpS (Dougan et al., 2002), displayed negative fitness when exposed to soft-metal(loid)s (Figure 1B). A similar negative fitness was observed for mutants lacking the refoldase ClpB and other cytoplasmic chaperones like DnaK and the small heat shock proteins IbpA and IbpB, all of which form an intricate network for protein disaggregation (Tyedmers et al., 2010). Consistent with this, previous transcriptomic analyses of *E. coli* exposed to Cd(II), Hg(II), and Te(IV) showed the induction of chaperone and protease systems such as ClpB, DnaK, and ClpP, among others (Wang and Crowley, 2005; Molina-Quiroz et al., 2014; LaVoie and Summers, 2018), supporting a proteotoxic effect of these metal(loid)s.

An intriguing observation was that *lon* deletion mutants showed improved fitness following soft-metal(loid) treatment. Lon is one of the main AAA+ proteases involved in the degradation of misfolded proteins, thereby preventing aggregation (Rosen et al., 2002). Some researchers have reported that it plays a minor role in protein aggregate clearance (Vera et al., 2005), but this does not explain the increased resistance to soft-metal(loid)s. This phenotype could result from Lon-dependent regulatory proteolysis of an unknown factor that when stabilized, could help combat soft-metal(loid) toxicity. Further studies are required to elucidate the role of Lon in this process.

To directly test if soft-metal(loid)s caused protein misfolding and aggregation under anaerobic conditions, we challenged exponentially growing wild type *E. coli* BW25113 to increasing concentrations of soft-metal(loid)s for 2 h and immediately quantified aggregated proteins (Figures 2A–C; Supplementary Figure S3). For all soft-metal(loid)s tested, treatment led to protein aggregation in a concentration-dependent manner and started even at low toxic concentrations (Figure 2B; Supplementary Figure S3A).

Interestingly, while all the tested soft-metal(loid)s caused protein aggregation, their effects on cell viability varied considerably (Figures 2B,C). For instance, 9.5 μM Hg(II) induced approximately 150 μg of aggregated proteins per mg of total protein, significantly decreasing viability by 5 orders of magnitude. In contrast, 200 mM As(III) produced similar number of aggregated proteins to Hg(II), but its impact on cell viability was noticeably less (Figures 2B,C). Others, like Te(IV) and Au(III), strongly affected viability at 20 and 10 μM, respectively; however, they induced less protein aggregation compared to Ag(I), Hg(II), and As(III). This indicates that for each metal(loid) there is no direct correlation between its effect on viability and the amount of protein aggregates (Figures 2B,C).

Recently, Zuily et al. (2022) demonstrated that the soft-metal Cu(I), and to a lesser extent Cu(II), can cause protein aggregation independent of ROS. In agreement with these results, we observed protein aggregation induced by Cu(II) at millimolar concentrations (1 mM), comparable to protein aggregation induced by some other soft-metal(loid)s tested (Figure 2D; Supplementary Figure S3B). Altogether, this suggests that the soft-acid property of these metal(loid)s could explain their reactivity toward proteins and cause aggregation. To test this, we exposed *E. coli* to the hard-acid metal Mg(II) and the borderline metal Ni(II) (Figure 2D; Supplementary Figure S3B). Exposure to Mg(II) or Ni(II) in the millimolar range did not result in protein aggregation, which is even reduced in the presence of Mg(II), suggesting that the soft-acid property, and thus the covalent nature of the metal–ligand interaction, might be important for inducing protein aggregation.

We next sought to assess whether protein aggregation could happen during or required active translation, as nascent proteins are not fully folded. The exposed soft residues may interact with these metal(loid)s through covalent bond formation, leading to unexpected geometries that could cause protein misfolding. To test this, we halted active translation by using chloramphenicol (CHL) for 5 min prior to toxic exposure and measured aggregated proteins (Figure 3). CHL pre-treatment did not affect protein aggregation mediated by As(III) and Cd(II), suggesting that it does not depend on active translation (Figures 3B,C). Conversely, Au(III)-induced aggregation was completely inhibited when the translation was blocked (Figures 3B,C), while for Ag(I), Hg(II), and Te(IV) it was inhibited by 85, 65, and 80%, respectively (Figure 3C). We hypothesize that the metal(loid) Ag(I), Hg(II), Au(III),

10.3389/fmicb.2023.1281058

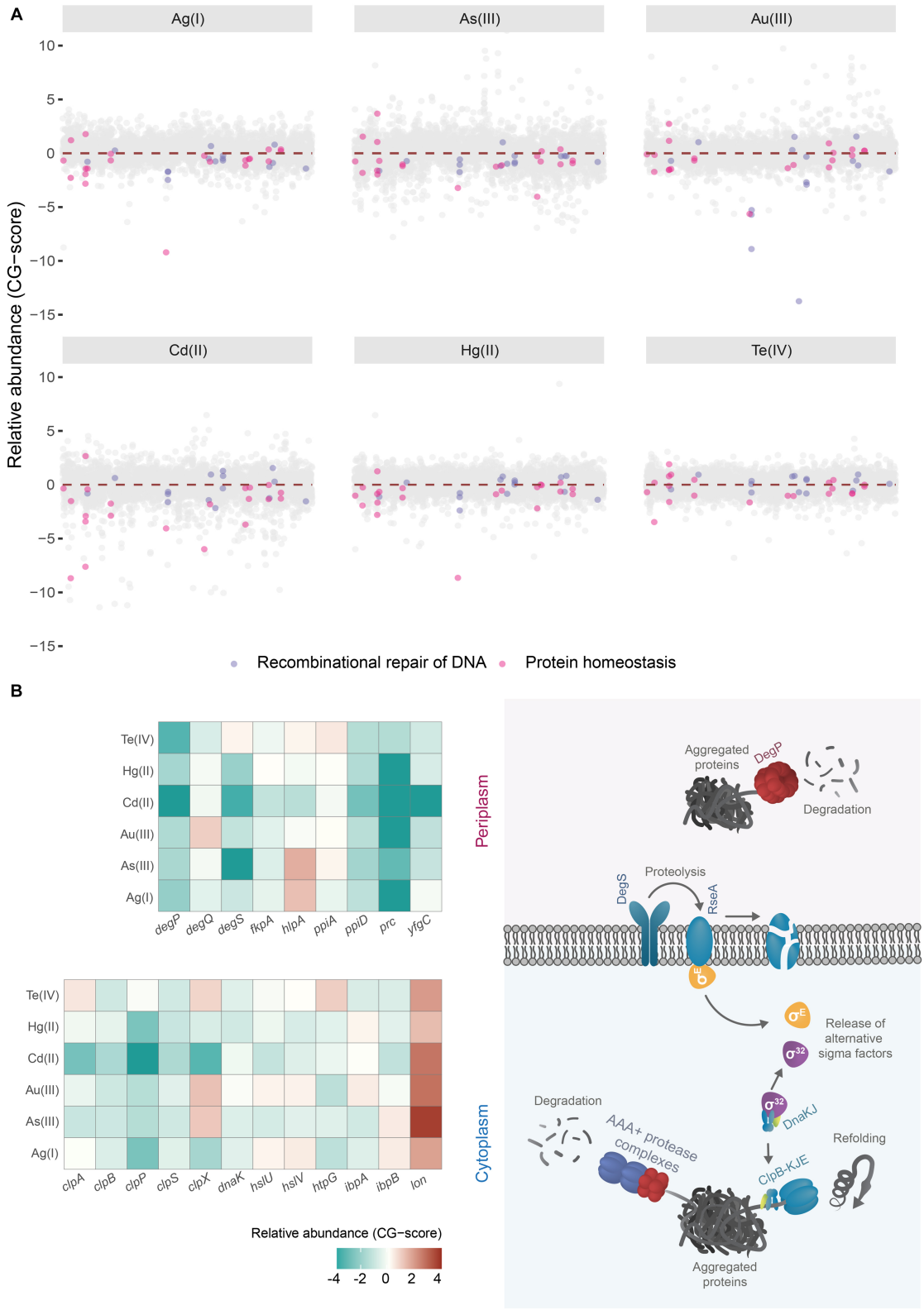

FIGURE 1
Chemical genomic analysis of soft-metal(loid) toxicity in *E. coli*. **(A)** Relative abundance (CG-score) of single gene deletion mutants after soft-metal(loid)s 24 h treatment. Mutants lacking genes involved in the recombinational repair of DNA (lavender dots) and protein homeostasis (pink dots) are highlighted. **(B)** In the left panel, a heat map of the relative abundance of deletion mutants in genes implicated in proteins homeostasis present in the periplasmic and cytoplasmic compartments after soft metal(loid)s treatments. In the right panel, a simplified model of chaperones/proteases involved in aggregated protein clearance in both periplasm and cytoplasm. ClpAPS and other AAA+ protease complexes and ClpB-DnaKJ-GrpE (refoldase) act in the cytoplasm; meanwhile, DegP (protease) functions in the periplasm. Misfolded proteins in this last compartment are detected by DegS, which catalyzes the degradation of the antisigma factor RseA. In the cytoplasm, on the other hand, sigma 32 is controlled through titration of DnaKJ by protein aggregates.

10.3389/fmicb.2023.1281058

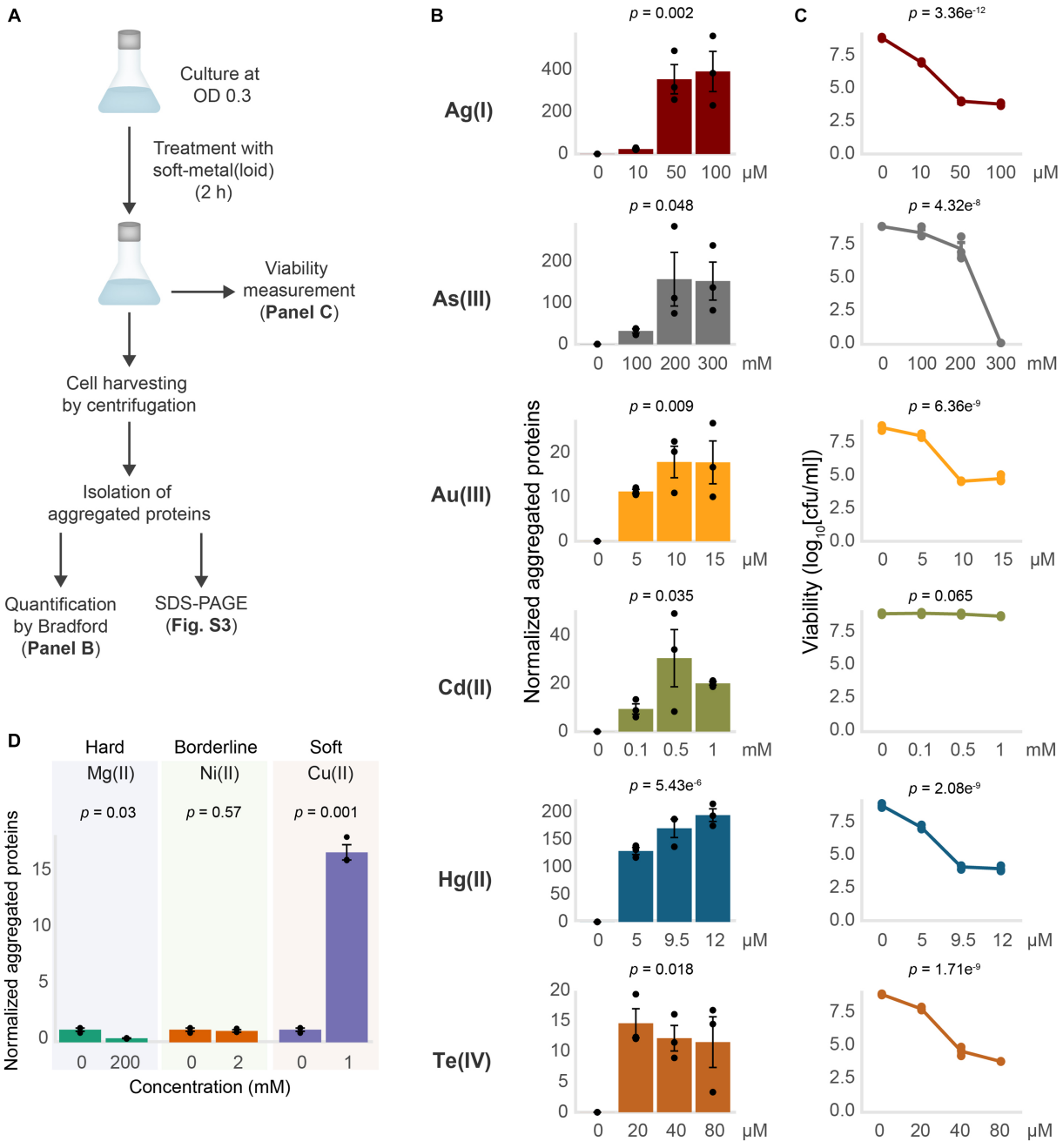

FIGURE 2
Soft-metal(loid)s induce protein aggregation. **(A)** Outline of the methodology for soft-metal(loid) treatment and aggregated protein quantification (Bradford) and visualization (SDS-PAGE). **(B)** Amount of aggregated proteins isolated from *E. coli* after the treatment with increasing concentrations of soft-metal(loid)s in anaerobic conditions. The amount of protein aggregated (μg) was normalized by the total protein amount in crude extracts (mg). The bars represent the mean and standard deviation of three biological replicates. *p* values were calculated by one-way ANOVA **(C)** Viability curve of *E. coli* treated with increasing concentrations of soft-metal(loid)s. The graph displays the mean and standard deviation of three biological replicates. *p* values were calculated using one-way ANOVA **(D)** Amount of aggregated proteins isolated from *E. coli* exposed to 200 mM of the hard-acid metal Mg(II), 2 mM of the borderline metal Ni(II), or 2 mM of the borderline/soft metal Cu(II). The bars represent the mean and standard deviation of three biological replicates. *p* values were calculated using the student's *t*-test.

and Te(IV) primarily cause protein aggregation by interacting with nascent proteins, while Cd(II) or As(III) can also interact with pre-folded proteins and produce aggregation by different mechanism. To directly test this, we conducted pulse-chase experiments in cells treated with the metalloids As(III) and Te(IV) as models. Proteins were pulse-labeled with 4-azido-L-homoalanine (AHA) for 15 min and chased with excess L-Met for 30 min to produce labeled folded proteins and unlabeled nascent proteins during toxicant exposure (Supplementary Figure S4). As hypothesized, the label was only detected in aggregates from cells treated with As(III), confirming that this oxyanion causes aggregation of proteins that are already folded, while Te(IV) appears to target nascent proteins (Supplementary Figure S4).

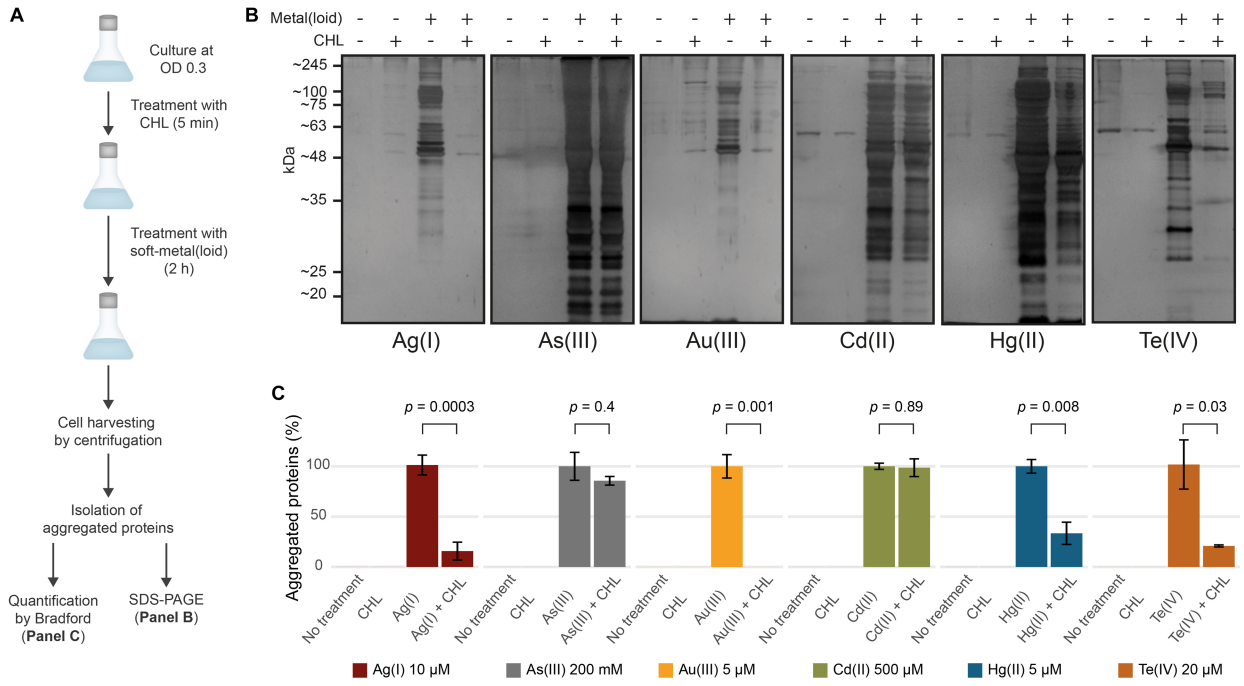

FIGURE 3
Soft-metal(loid)s induce protein aggregation of nascent and mature proteins. **(A)** Outline of the methodology used in the CHL treatment. Briefly, cells were grown to OD 0.3 and treated with 100 µg/mL of chloramphenicol (CHL) to stop protein synthesis before soft-metal(loid) treatment. After 2 h, protein aggregates were isolated and resolved on SDS-PAGE and quantified by Bradford. **(B,C)** Effect of protein synthesis inhibition on soft metal(loid)-induced protein aggregation in *E. coli*. **(B)** Ten microliters of the aggregated protein isolation were resolved in a denaturing SDS-PAGE (12%) and silver stained. **(C)** The amount of aggregated proteins in CHL-treated samples were compared against the respective soft-metal(loid) treatment (100%). Values represent the mean and the standard deviation of at least three biological replicates. *p* values were calculated using the student's *t*-test.

In summary, our results show that exposure to soft-metal(loid)s caused protein aggregation in a ROS-independent manner. In *E. coli*, soft-metal(loid)s could cause protein aggregation through at least two hypothetically distinct mechanisms: (i) a translational-dependent mechanism where Hg(II), Au(III), Ag(I), and Te(IV) react with nascent proteins, causing misfolding, and (ii) a translational-independent (or post-translational) one, where As(III) and Cd(II) preferentially target mature proteins. Alternatively, the latter could be attributed to the inhibition of disaggregation or protein degradation pathways by Cd(II) and As(III), which might ultimately lead to an imbalance in proteostasis and an accumulation of protein aggregates. In this context, Cd(II), Hg(II), and Pb(II) have been found to inhibit DnaK-, DnaJ-, and GrpE-assisted refolding and disaggregation *in vitro* (Sharma et al., 2008).

Protein aggregation at the translational level could be explained by the interaction between Hg(II), Au(III), Ag(I), and Te(IV) with soft-side chains such as those from Cys, His, Met, and Phe residues (Stadtman and Levine, 2003). This may hinder proper folding by introducing different coordination geometries and impacting folding rates, leading to misfolding, aggregation, and the sequestration of other proteins. Proteins likely react with these metal(loid)s through metal binding sites as they are being synthesized, resulting in incorrect metallation and misfolding. For instance, the Cu, Zn superoxide dismutase (Cu, Zn - SOD) from *S. cerevisiae* undergoes the exchange of Cu(I) for Ag(I) when the yeast is exposed to silver nitrate, generating an inactive Ag, Zn - SOD. Interestingly, Ag, Zn - SOD is less immunoreactive to conformational antibodies against Cu, Zn - SOD, suggesting a change in the protein's folding or conformation (Ciriolo et al., 1994).

3.3 Identification of aggregated proteins

The reduction of soluble proteins and their diversion to the insoluble fraction may account for the toxicity of protein aggregates, consequently impacting normal metabolism and appropriate cell development (Mogk et al., 2018). To gain further insights on how this process impacts the resistance of *E. coli* against soft-metal(loid)s, we identified the aggregated proteins derived from the exposure to each toxic by mass spectrometry (label-free quantification) (Figure 4; Supplementary Table S2).

After treatment with Te(IV), Au(III), As(III), Hg(II), Cd(II), or Ag(I), we identified 335, 737, 718, 798, 719, and 831 insoluble proteins, respectively (Figure 4A). This represents between 7.5 and 18.6% of the proteins encoded by *E. coli*. Although the removal of periplasmic chaperones and proteases resulted in decreased fitness after toxic exposure, the aggregated proteins that we identified are mainly cytoplasmic. For example, 78.5, 85.7, 87.2, 82.8, 88.9, and 87.1% of the identified proteins in aggregates induced by Te(IV), Au(III), As(III), Ag(I), Cd(II), and Hg(II), respectively, were cytoplasmic proteins.

To assess if aggregated proteins where enriched in residues with a soft-base nature such as Cys (C), Met (M), His (H) or Phe (F), we quantified the frequency of each residue on aggregated proteins compared to the total coding sequences of *E. coli* (Supplementary Figure S5A). When comparing cytoplasmic proteins, which represent the biggest share of aggregated proteins, a slight increase of frequency of Cys was observed in Ag(I) and Cd(II) treatments. On the other hand, a different effect is observed in aggregated membrane proteins, where the frequency of residues such

10.3389/fmicb.2023.1281058

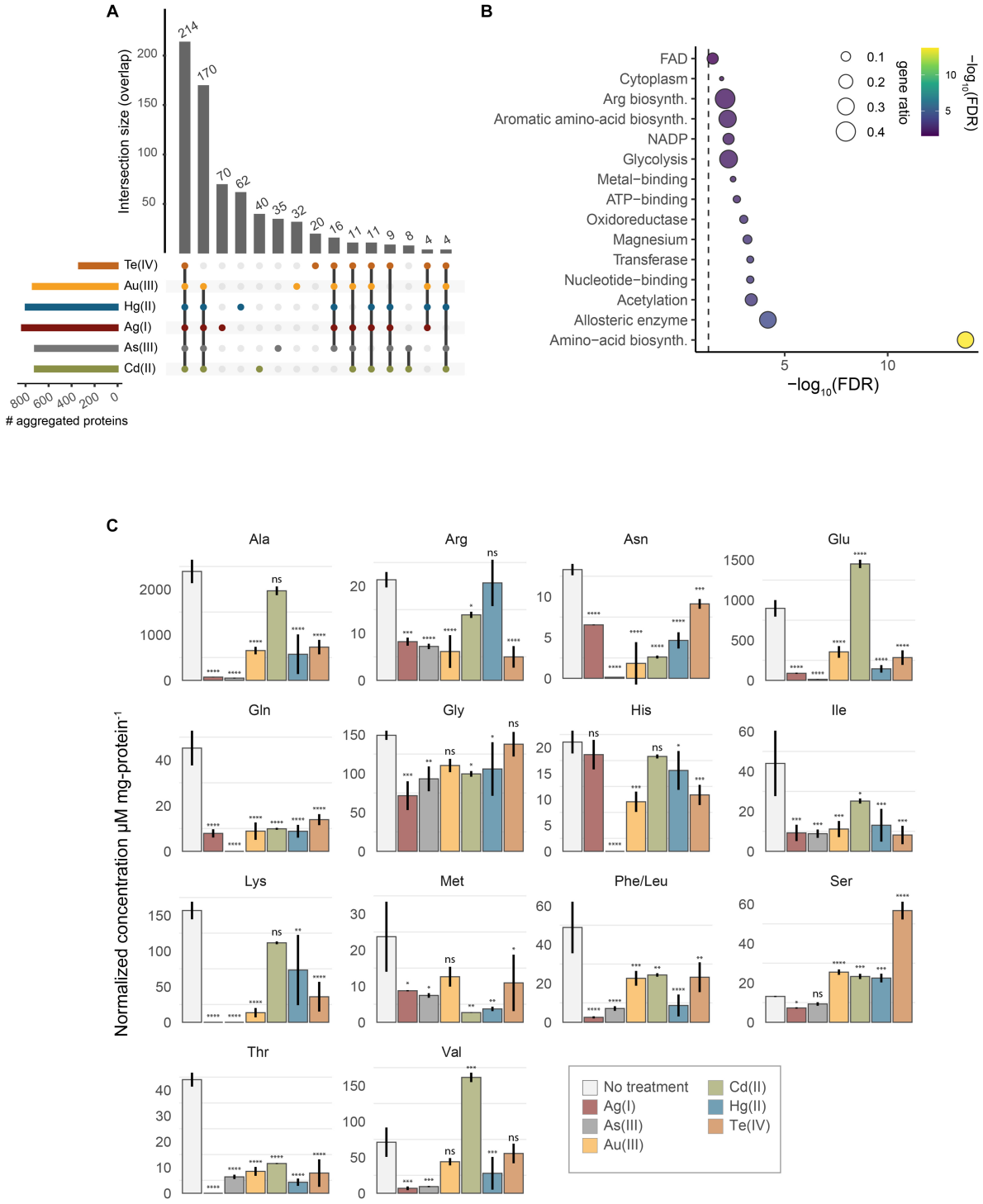

FIGURE 4
Identification of aggregated proteins. **(A)** UpSet plot representing the overlap of identified aggregated proteins after treatment with Te(IV), Au(III), Hg(II), Ag(I), As(III), or Cd(II). **(B)** UniProt keywords enrichment analysis of aggregated proteins by all soft-metal(loid)s. Gene ratio (size) is the fraction of significant genes over the total genes in a given pathway, ranked by FDR-adjusted *p* value **(C)** Normalized intracellular concentration of 15 amino acids measured from exponentially-grown *E. coli* exposed to 10 µM Ag(I), 200 mM As(III), 5 µM Au(III), 500 µM Cd(II), 5 µM Hg(II), or 20 µM Te(IV). Phe/Leu represents the sum of both amino acids. Statistical significance was calculated by one-way ANOVA and Dunnett's posthoc test using no treatment as the control mean. Values represent the mean of three biological replicates and the standard error. ns: not significant; *: adjusted *p* value < 0.05; **: adjusted *p* value < 0.01; ***: adjusted *p* value < 0.001; ****: adjusted *p* value < 0.0001.

as Asp (D), Glu (E), Arg (R) was overrepresented in all treatments with all metal(oid)s, and a lower representation of tryptophan (W) was observed in 5 of the metals analyzed (Supplementary Figure S5A). Furthermore, soft-metal(loid)-induced aggregated proteins have a similar hydrophobicity index compared to the *E. coli* proteome (Supplementary Figure S5B). Aggregated cytoplasmic proteins do not

show a bias to specific pI or molecular weight. In contrast, aggregation of membrane proteins seems to mainly affect acidic proteins (Supplementary Figure S5C), which coincides with what was observed in a greater number of acidic amino acids, such as D (in Ag(I), As(III), Au(III), Cd(II) and Hg(II)) and E (in all metal(loid)s). In addition, a slight shift to a higher molecular weight is observed in the aggregated proteins (Supplementary Figure S5C). This suggest that ionic interaction seems to be more relevant for aggregation of membrane proteins than covalent interactions.

The results described above suggest that there is no clear physicochemical property that can explain the aggregation of cytoplasmic proteins induced by soft metal(loid)s. Then, we ought to see if proteins that are highly translated might be targeted by soft metal(loid)s given that we observed a dependency on active translation for Ag(I), Au(III), Hg(II) and Te(IV)-mediated protein aggregation. For this, we took advantage of the already published protein synthesis rate for *E. coli* in MOPS minimal media (Li et al., 2014). Remarkably, the proteins detected in soft metal(loid)-induced aggregates are among the highly expressed proteins from *E. coli* (Supplementary Figure S5D). This correlates with the observed translation-dependent protein aggregation for Te(IV), Au(III), Ag(I) and Hg(II); however, protein aggregated by As(III) or Cd(II) show a similar trend.

During their synthesis, proteins can be assisted for correct folding by chaperones such as DnaK, GroE and the trigger factor. In *E. coli*, deletion of *dnaK* and *tig* (trigger factor) leads to disrupted proteostasis, producing aggregation of more than 1,000 proteins (Calloni et al., 2012). Therefore, we examined if proteins aggregated by soft metal(loid) treatments are preferentially clients of one of these chaperone systems (Supplementary Figure S5E). Noticeably, around 50% of the proteins aggregated by soft metal(loid) treatments are known clients of DnaK, according to STEPdb. This effect is not observed for trigger factor or GroE clients. These results agree with Sharma and collaborators (2008) that observed inhibition of DnaKJ-GrpE *in vitro* refolding of unfolded luciferase by Cd(II); probably by interaction of Cd(II) with the zinc-binding domain of DnaJ.

Next, to assess the presence of essential proteins within the aggregated material, we compared sets of aggregated proteins in each treatment to essential genes identified for a genome-wide deletion collection in MOPS media (Baba et al., 2006). The number of essential proteins in aggregates varied depending on the metal(loid) treatment: aggregates induced by Ag(I), Te(IV), As(III), Au(III), Hg(II), and Cd(II) contained 110, 21, 98, 102, 109, and 96 essential proteins, respectively. This indicates that protein aggregation induced by soft metal(loid)s disrupts crucial cellular processes by decreasing the soluble levels of essential proteins, leading to cell death. An interesting documented example of this phenomenon is MetA from *E. coli*, an essential thermosensitive protein in minimal media; depletion of this protein from soluble media due to high temperature-dependent aggregation causes a decrease in L-Met biosynthesis, impacting cell growth (Gur et al., 2002).

We collated the results of chemical genomics and protein aggregation to identify if, among the aggregated proteins, we could identify the ones that are important for soft metal(loid) tolerance (Supplementary Figure S6). The rationale was that deleting the gene coding for those proteins would negatively impact strain abundance (CG scores) in the treatments. Overall, there is no clear correlation between proteins identified in the aggregates, observing that deletion of genes of identified aggregated proteins can have favorable, deleterious or no effect on resistance to the metals analyzed. However, in 5 of the 6 metals analyzed (Ag(I), As(III), Au(III), Cd(II) and Hg(II)), the RfaG (WaaG) protein is detected in the aggregates, and its deletion increases sensitivity to them. Also, other proteins part of LPS biosynthesis are found, such as RfaH, RfaF, and RfaQ, confirming that the biosynthesis of liposaccharides is affected by these soft metal(loid)s (Figure 1B). In *E. coli*, deletion of *waaG* resulted in a truncated LPS core section lacking most of the negatively charged phosphate groups where the UO22+ cation binds (Thorgersen et al., 2021). In addition, Chromium exposure induces a membrane response, and lipopolysaccharide biosynthesis is a mechanism upregulated in *Caulobacter crescentus* (Hu et al., 2005).

Among the total number of proteins identified in the aggregates induced by soft metal(loid)s, 214 were shared by all treatments (Figure 4A). A KEGG pathway enrichment analysis revealed that these proteins are primarily involved in metabolic pathways such as amino acid biosynthesis, pyruvate metabolism, central metabolism, and the biosynthesis of secondary metabolites (Figure 4B; Supplementary Table S3). When proteins identified in every soft-metal(loid) treatment are examined individually, they participate in the same cellular processes and metabolic pathways as the aforementioned 214 proteins (Figures 4A,B). A UniProt keywords enrichment analysis of those proteins showed a clear enrichment of proteins involved in amino acid biosynthesis. Notably, metal and magnesium binding proteins were also enriched, suggesting a possible role of mismetallation on protein aggregation. Surprisingly, Cd(II) and As(III) influenced the same processes as the other soft-metal(loid)s, despite inducing aggregation through a potentially different mechanism. Nonetheless, in our analysis, it is challenging to determine which proteins were directly misfolded by the metal(loid) treatment and which were subsequently trapped by the aggregates.

Our results support the observations made by Weids and collaborators (2016) that described that As(III), H_2O_2 and azetidine-2-carboxylic acid promote the aggregation of highly expressed proteins, which are involved in metabolic processes such as amino acid biosynthesis, and a large fraction interacts with the Hsp70 chaperone (DnaK in *E. coli*).

3.4 Soft-metal(loid)s perturb intracellular amino acid concentration

Since proteins involved in amino acid biosynthesis were among the most represented in protein aggregates for all treatments (Figure 4B), we speculated that amino acid levels might be affected after toxicant exposure. Furthermore, amino acid biosynthesis is an essential process for *E. coli* growing in minimal media, and its disruption would explain part of their toxicity mechanisms. We measured the intracellular concentration of 15 amino acids in exponentially growing *E. coli* exposed to soft-metal(loid)s under the same conditions as in the protein identification analysis. Peaks for phenylalanine and leucine were not resolved, and their concentration represents the sum of both amino acids. Although none of the metal(loid)s depleted all amino acids, they impacted the levels of a significant number of them, ranging from 8 [Cd(II)] to 14 [Ag(I) and As(III)]. All soft-metal(loid) treatments decreased the intracellular concentration of asparagine, glutamine, isoleucine, phenylalanine + leucine, and threonine (Figure 4C). For

asparagine, isoleucine, and leucine, we detected proteins involved in their biosynthesis in the aggregates of most of the soft-metal treatments (Figure 4C; Supplementary Table S2). AsnA (aspartate-ammonia ligase (ADP-forming) (EC 6.3.1.4)) and IlvA (threonine ammonia-lyase, EC 4.3.1.19) have been previously detected in aggregates during anaerobic copper treatment (Zuily et al., 2022). LeuB (3-isopropylmalate dehydrogenase, EC 1.1.1.85) has been detected in protein aggregates when the gene was overexpressed in *E. coli* (Śmigiel et al., 2022) and in yeast deficient in the shock protein Hsp70 of type-Ssa (Amm et al., 2016).

Decreased intracellular amino acid concentrations may result in numerous deleterious effects on bacterial physiology. These could include deficiencies in protein and other cell structure synthesis (e.g., cell wall), metabolism of various cell pathway intermediates, cellular buffering, and osmotolerance, among several others (Nelson and Cox, 2017; Xiao et al., 2017; Aliashkevich et al., 2018; Idrees et al., 2020). Interestingly, this metabolic condition could be somewhat beneficial; under physiological conditions of anaerobic amino acid limitation, the efflux system pump CusCFBA is induced to protect iron–sulfur cluster proteins on *E. coli* cells exposed to Cu(I) (Fung et al., 2013).

We also observed the accumulation of certain amino acids after metal(loid) exposure. For instance, serine accumulates after Au(III), Cd(II), Hg(II), and Te(IV) treatments, with the latter inducing the highest accumulation (4.3-fold) (Figure 4C). Similarly, Cd(II) treatment also resulted in an accumulation of glutamic acid and valine. The excess of intracellular serine is toxic for *E. coli* as it inhibits the biosynthesis of isoleucine and aromatic amino acids (Hama et al., 1990; Tazuya-Murayama et al., 2006), disrupts cell division (Zhang and Newman, 2008), and generates the misincorporation of serine instead of alanine in peptidoglycan crosslinks (Zhang et al., 2010). Serine excess is removed to the extracellular medium by SdaC or can be deaminated to pyruvate and ammonia by SdaA, SdaB, TdcG, TdcB, or Thr/Ser dehydrogenase IlvA (Shizuta et al., 1969; Su et al., 1989; Su and Newman, 1991; Burman et al., 2004; Borchert and Downs, 2018; Kriner and Subramaniam, 2019). Mutants lacking these proteins did not display significant changes in fitness (CG z-scores) after soft-metal(loid) exposure, and only IlvA was detected in the aggregated material produced by Te(IV) (Supplementary Table S1). IlvA was also aggregated in treatments that did not induce serine accumulation, so it may not solely explain the phenomena observed with Te(IV). Our data do not suggest that serine accumulation is a direct result of protein aggregation. Altogether, our results demonstrate that soft-metal(loid)s result in the aggregation of proteins required for amino acid biosynthesis, which in turn leads to perturbations in the intracellular levels of amino acids.

In summary, we demonstrate that proteins can be aggregated in a ROS-independent manner by soft-metal(loid)s, mainly affecting proteins involved in anabolic pathways. Protein aggregation might be primarily induced at the translational level by Ag(I), Au(III), Hg(II), and Te(IV), or at the post-translational level by Cd(II) and As(III). Initial protein aggregates might sequester other proteins by exposing hydrophobic or disordered regions to the surface, leading to secondary loss of function (Mogk et al., 2018). Regardless of the mechanism, it can be expected that amino acid biosynthesis is hindered as a cellular response under our experimental conditions, also impacting the tRNA charging process, ribosome stalling and limited translation, induction of the stringent response, and altered synthesis of various metabolites that use amino acids as precursors (Traxler et al., 2008; Nedialkova and Leidel, 2015; Wang et al., 2020). The fact that we did not observe a direct correlation between protein aggregation and cell viability suggests that soft-metal(loid) toxicity is a multifactorial phenomenon, an observation further confirmed by the wide variety of gene deletions that can lead to decreased fitness upon soft-metal(loid) challenges. These various targets could explain why these types of metal(loid)s are effective biocides.

Data availability statement

The original contributions presented in the study are included in the article/Supplementary material, further inquiries can be directed to the corresponding author.

Author contributions

FC: Conceptualization, Formal analysis, Investigation, Methodology, Writing – original draft. CM-V: Conceptualization, Data curation, Formal analysis, Methodology, Investigation, Writing – original draft. RL: Data curation, Formal analysis, Investigation, Writing – original draft. MS-D: Conceptualization, Data curation, Investigation, Methodology, Writing – original draft. CC: Conceptualization, Data curation, Formal analysis, Project administration, Writing – original draft. BP: Conceptualization, Investigation, Methodology, Writing – original draft. EM: Conceptualization, Data curation, Methodology, Writing – original draft. JP: Data curation, Formal analysis, Writing – original draft. JS: Conceptualization, Data curation, Formal analysis, Writing – original draft. CV: Conceptualization, Writing – original draft. FA: Conceptualization, Funding acquisition, Investigation, Resources, Writing – original draft.

In memoriam

This paper is dedicated to the memory of CV. We report with great sadness that CV died on 17th July 2020. He had seen and approved a previous version of this manuscript.

Funding

The author(s) declare financial support was received for the research, authorship, and/or publication of this article. This work received financial support from Fondecyt Regular 1230724 (FA), USA1799 Vridei 021943FA_GO Universidad de Santiago de Chile (FC and FA), Beca Doctorado Nacional 21150690 (FC), and Dicyt (FA and CV).

Acknowledgments

We thank Dr. Roberto Molina-Quiroz (CECS, Valdivia, Chile) and Dr. James Imlay (Department of Microbiology, University of Illinois Urbana-Champaign) for critically reading the manuscript.

Conflict of interest

EM and JP were employed by E. & J. Gallo Winery.

The remaining authors declare that the research was conducted in the absence of any commercial or financial relationships that could be construed as a potential conflict of interest.

Publisher's note

All claims expressed in this article are solely those of the authors and do not necessarily represent those of their affiliated organizations, or those of the publisher, the editors and the reviewers. Any product that may be evaluated in this article, or claim that may be made by its manufacturer, is not guaranteed or endorsed by the publisher.

Supplementary material

The Supplementary material for this article can be found online at: https://www.frontiersin.org/articles/10.3389/fmicb.2023.1281058/full#supplementary-material

References

Aliashkevich, A., Alvarez, L., and Cava, F. (2018). New insights into the mechanisms and biological roles of D-amino acids in complex eco-systems. *Front. Microbiol.* 9:683. doi: 10.3389/fmicb.2018.00683

Amm, I., Kawan, M., and Wolf, D. H. (2016). Characterization of protein quality control components via dual reporter-containing misfolded cytosolic model substrates. *Anal. Biochem.* 515, 14–21. doi: 10.1016/j.ab.2016.09.012

Baba, T., Ara, T., Hasegawa, M., Takai, Y., Okumura, Y., Baba, M., et al. (2006). Construction of *Escherichia coli* K-12 in-frame, single-gene knockout mutants: the Keio collection. *Mol. Syst. Biol.* 2:0008. doi: 10.1038/msb4100050

Baba, S. P., and Bhatnagar, A. (2018). Role of thiols in oxidative stress. *Curr. Opin. Toxicol.* 7, 133–139. doi: 10.1016/j.cotox.2018.03.005

Borchert, A. J., and Downs, D. M. (2018). Analyses of variants of the Ser/Thr dehydratase IlvA provide insight into 2-aminoacrylate metabolism in *Salmonella enterica*. *J. Biol. Chem.* 293, 19240–19249. doi: 10.1074/jbc.RA118.005626

Bradford, M. M. (1976). A rapid and sensitive method for the quantitation of microgram quantities of protein utilizing the principle of protein-dye binding. *Anal. Biochem.* 72, 248–254. doi: 10.1016/0003-2697(76)90527-3

Burman, J. D., Harris, R. L., Hauton, K. A., Lawson, D. M., and Sawers, R. G. (2004). The iron–sulfur cluster in the l-serine dehydratase TdcG from *Escherichia coli* is required for enzyme activity. *FEBS Lett.* 576, 442–444. doi: 10.1016/j.febslet.2004.09.058

Calderón, I. L., Elías, A. O., Fuentes, E. L., Pradenas, G. A., Castro, M. E., Arenas, F. A., et al. (2009). Tellurite-mediated disabling of [4Fe-4S] clusters of *Escherichia coli* dehydratases. *Microbiology* 155, 1840–1846. doi: 10.1099/mic.0.026260-0

Calloni, G., Chen, T., Schermann, S. M., Chang, H. C., Genevaux, P., Agostini, F., et al. (2012). DnaK functions as a central hub in the *E. coli* chaperone network. *Cell Rep.* 1, 251–264. doi: 10.1016/j.celrep.2011.12.007

Ciriolo, M. R., Civitareale, P., Carrì, M. T., De Martino, A., Galiazzo, F., and Rotilio, G. (1994). Purification and characterization of ag,Zn-superoxide dismutase from *Saccharomyces cerevisiae* exposed to silver. *J. Biol. Chem.* 269, 25783–25787. doi: 10.1016/S0021-9258(18)47316-4

Company, R., Serafim, A., Bebianno, M. J., Cosson, R., Shillito, B., and Fiala-Medioni, A. (2004). Effect of cadmium, copper and mercury on antioxidant enzyme activities and lipid peroxidation in the gills of the hydrothermal vent mussel Bathymodiolus azoricus. *Mar. Environ. Res.* 58, 377–381. doi: 10.1016/j.marenvres.2004.03.083

Danese, P. N., and Silhavy, T. J. (1997). The sigma (E) and the Cpx signal transduction systems control the synthesis of periplasmic protein-folding enzymes in *Escherichia coli*. *Genes Dev.* 11, 1183–1193. doi: 10.1101/gad.11.9.1183

Daum, J. R., Shepherd, D. M., and Noelle, R. J. (1993). Immunotoxicology of cadmium and mercury on B-lymphocytes--I. Effects on lymphocyte function. *Int. J. Immunopharmacol.* 15, 383–394. doi: 10.1016/0192-0561(93)90049-5

Dibrov, P., Dzioba, J., Gosink, K. K., and Häse, C. C. (2002). Chemiosmotic mechanism of antimicrobial activity of ag+ in *Vibrio cholerae*. *Antimicrob. Agents Chemother.* 46, 2668–2670. doi: 10.1128/AAC.46.8.2668-2670.2002

Doncheva, N. T., Morris, J. H., Gorodkin, J., and Jensen, L. J. (2018). Cytoscape StringApp: network analysis and visualization of proteomics data. *J. Proteome Res.* 18, 623–632. doi: 10.1021/acs.jproteome.8b00702

Dougan, D. A., Reid, B. G., Horwich, A. L., and Bukau, B. (2002). ClpS, a substrate modulator of the ClpAP machine. *Mol. Cell* 9, 673–683. doi: 10.1016/S1097-2765(02)00485-9

Egler, M., Grosse, C., Grass, G., and Nies, D. H. (2005). Role of the extracytoplasmic function protein family sigma factor RpoE in metal resistance of *Escherichia coli*. *J. Bacteriol.* 187, 2297–2307. doi: 10.1128/JB.187.7.2297-2307.2005

Erickson, J. W., and Gross, C. A. (1989). Identification of the sigma E subunit of *Escherichia coli* RNA polymerase: a second alternate sigma factor involved in high-temperature gene expression. *Genes Dev.* 3, 1462–1471. doi: 10.1101/gad.3.9.1462

Fadeeva, M. S., Bertsova, Y. V., Euro, L., and Bogachev, A. V. (2011). Cys377 residue in NqrF subunit confers ag(+) sensitivity of Na^+-translocating NADH:quinone oxidoreductase from *Vibrio harveyi*. *Biochemistry* 76, 186–195. doi: 10.1134/s0006297911020040

Foster, A. W., Young, T. R., Chivers, P. T., and Robinson, N. J. (2022). Protein metalation in biology. *Curr. Opin. Chem. Biol.* 66:102095. doi: 10.1016/j.cbpa.2021.102095

Fung, D. K., Lau, W. Y., Chan, W. T., and Yan, A. (2013). Copper efflux is induced during anaerobic amino acid limitation in *Escherichia coli* to protect iron-sulfur cluster enzymes and biogenesis. *J. Bacteriol.* 195, 4556–4568. doi: 10.1128/JB.00543-13

Gomez, M., Pérez-Gallardo, R. V., Sánchez, L. A., Díaz-Pérez, A. L., Cortés-Rojo, C., Meza Carmen, V., et al. (2014). Malfunctioning of the iron–sulfur cluster assembly machinery in *Saccharomyces cerevisiae* produces oxidative stress via an iron-dependent mechanism, causing dysfunction in respiratory complexes. *PLoS One* 9:e111585. doi: 10.1371/journal.pone.0111585

Gray, A. N., Egan, A. J. F., Van't Veer, I., Verheul, J., Colavin, A., Koumoutsi, A., et al. (2015). Coordination of peptidoglycan synthesis and outer membrane constriction during *Escherichia coli* cell division. *eLife* 4:e07118. doi: 10.7554/eLife.07118

Gur, E., Biran, D., Gazit, E., and Ron, E. Z. (2002). In vivo aggregation of a single enzyme limits growth of *Escherichia coli* at elevated temperatures. *Mol. Microbiol.* 46, 1391–1397. doi: 10.1046/j.1365-2958.2002.03257.x

Hama, H., Sumita, Y., Kakutani, Y., Tsuda, M., and Tsuchiya, T. (1990). Target of serine inhibition in *Escherichia coli*. *Biochem. Biophys. Res. Commun.* 168, 1211–1216. doi: 10.1016/0006-291X(90)91157-N

Haslberger, T., Weibezahn, J., Zahn, R., Lee, S., Tsai, F. T., Bukau, B., et al. (2007). M domains couple the ClpB threading motor with the DnaK chaperone activity. *Mol. Cell* 25, 247–260. doi: 10.1016/j.molcel.2006.11.008

Hawkins, C. L., and Davies, M. J. (2019). Detection, identification, and quantification of oxidative protein modifications. *J. Biol. Chem.* 294, 19683–19708. doi: 10.1074/jbc.REV119.006217

Hong, R., Kang, T. Y., Michels, C. A., and Gadura, N. (2012). Membrane lipid peroxidation in copper alloy-mediated contact killing of *Escherichia coli*. *Appl. Environ. Microbiol.* 78, 1776–1784. doi: 10.1128/AEM.07068-11

Hsu, P., Chen, C., Wang, S., Hashimoto, M., Huang, W., and Teng, C. (2020). Identification of Mlt G as a Prc protease substrate whose dysregulation contributes to the conditional growth defect of prc-deficiente *Escherichia coli*. *Front. Microbiol.* 11:2000. doi: 10.3389/fmicb.2020.02000

Hu, P., Brodie, E. L., Suzuki, Y., McAdams, H. H., and Andersen, G. L. (2005). Whole-genome transcriptional analysis of heavy metal stresses in *Caulobacter crescentus*. *J. Bacteriol.* 187, 8437–8449. doi: 10.1128/JB.187.24.8437-8449.2005

Huang, d. W., Sherman, B. T., and Lempicki, R. A. (2009). Systematic and integrative analysis of large gene lists using DAVID bioinformatics resources. *Nat. Protoc.* 4, 44–57. doi: 10.1038/nprot.2008.211

Idrees, M., Mohammad, A. R., Karodia, N., and Rahman, A. (2020). Multimodal role of amino acids in microbial control and drug development. *Antibiotics* 9:330. doi: 10.3390/antibiotics9060330

Imlay, J. A. (2006). Iron-sulphur clusters and the problem with oxygen. *Mol. Microbiol.* 59, 1073–1082. doi: 10.1111/j.1365-2958.2006.05028.x

Jacobson, T., Navarrete, C., Sharma, S. K., Sideri, T. C., Ibstedt, S., Priya, S., et al. (2012). Arsenite interferes with protein folding and triggers formation of protein aggregates in yeast. *J. Cell Sci.* 125, 5073–5083. doi: 10.1242/jcs.107029

Jacobson, T., Priya, S., Sharma, S. K., Andersson, S., Jakobsson, S., Tanghe, R., et al. (2017). Cadmium causes misfolding and aggregation of cytosolic proteins in yeast. *Mol. Cell. Biol.* 37:e00490-16. doi: 10.1128/MCB.00490-16

Keseler, I. M., Mackie, A., Santos-Zavaleta, A., Billington, R., Bonavides-Martínez, C., Caspi, R., et al. (2017). The EcoCyc database: reflecting new knowledge about *Escherichia coli* K-12. *Nucleic Acids Res.* 45, D543–D550. doi: 10.1093/nar/gkw1003

Kim, J. J., Kim, Y. S., and Kumar, V. (2019). Heavy metal toxicity: an update of chelating therapeutic strategies. *J. Trace Elem. Med. Biol.* 54, 226–231. doi: 10.1016/j.jtemb.2019.05.003

Kriner, M. A., and Subramaniam, A. R. (2019). The serine transporter SdaC prevents cell lysis upon glucose depletion in *Escherichia coli*. *Microbiology* 9:e960. doi: 10.1002/mbo3.960

LaVoie, S. P., and Summers, A. O. (2018). Transcriptional responses of *Escherichia coli* during recovery from inorganic or organic mercury exposure. *BMC Genomics* 19:52. doi: 10.1186/s12864-017-4413-z

Lemire, J. A., Harrison, J. J., and Turner, R. J. (2013). Antimicrobial activity of metals: mechanisms, molecular targets and applications. *Nat. Rev. Microbiol.* 11, 371–384. doi: 10.1038/nrmicro3028

Li, Y. P., Ben Fekih, I., Chi Fru, E., Moraleda-Munoz, A., Li, X., Rosen, B. P., et al. (2021). Antimicrobial activity of metals and metalloids. *Annu. Rev. Microbiol.* 75, 175–197. doi: 10.1146/annurev-micro-032921-123231

Li, G. W., Burkhardt, D., Gross, C., and Weissman, J. S. (2014). Quantifying absolute protein synthesis rates reveals principles underlying allocation of cellular resources. *Cells* 157, 624–635. doi: 10.1016/j.cell.2014.02.033

Macomber, L., Elsey, S. P., and Hausinger, R. P. (2011). Fructose-1,6-bisphosphate aldose (class II) is the primary site of nickel toxicity in *Escherichia coli*. *Mol. Microbiol.* 82, 1291–1300. doi: 10.1111/j.1365-2958.2011.07891.x

Macomber, L., and Imlay, J. A. (2009). The iron-sulfur clusters of dehydratases are primary intracellular targets of copper toxicity. *Proc. Natl. Acad. Sci. U. S. A.* 106, 8344–8349. doi: 10.1073/pnas.0812808106

Medici, S., Peana, M., Pelucelli, A., and Zoroddu, M. A. (2021). An updated overview on metal nanoparticles toxicity. *Semin. Cancer Biol.* 76, 17–26. doi: 10.1016/j.semcancer.2021.06.020

Mjos, K. D., and Orvig, C. (2014). Metallodrugs in medicinal inorganic chemistry. *Chem. Rev.* 114, 4540–4563. doi: 10.1021/cr400460s

Mogk, A., Bukau, B., and Kampinga, H. H. (2018). Cellular handling of protein aggregates by disaggregation machines. *Mol. Cell* 69, 214–226. doi: 10.1016/j.molcel.2018.01.004

Molina-Quiroz, R. C., Loyola, D. E., Díaz-Vásquez, W. A., Arenas, F. A., Urzúa, U., Pérez-Donoso, J. M., et al. (2014). Global transcriptomic analysis uncovers a switch to anaerobic metabolism in tellurite-exposed *Escherichia coli*. *Res. Microbiol.* 165, 566–570. doi: 10.1016/j.resmic.2014.07.003

Morales, E. H., Pinto, C. A., Luraschi, R., Muñoz-Villagrán, C. M., Cornejo, F. A., Simpkins, S. W., et al. (2017). Accumulation of heme biosynthesis intermediates contributes to the antibacterial action of the metalloid tellurite. *Nat. Commun.* 8:15320. doi: 10.1038/ncomms15320

Müller, P., Ewers, C., Bertsche, U., Anstett, M., Kallis, T., Breukink, E., et al. (2007). The essential cell division protein FtsN interacts with the murein (peptidoglycan) synthase PBP1B in *Escherichia coli*. *J. Biol. Chem.* 282, 36394–36402. doi: 10.1074/jbc.M706390200

Muñoz-Villagrán, C., Contreras, F., Cornejo, F., Figueroa, M., Valenzuela-Bezanilla, D., Luraschi, R., et al. (2020). Understanding gold toxicity in aerobically-grown *Escherichia coli*. *Biol. Res.* 53:26. doi: 10.1186/s40659-020-00292-5

Nedialkova, D. D., and Leidel, S. A. (2015). Optimization of codon translation rates via tRNA modifications maintains proteome integrity. *Cells* 161, 1606–1618. doi: 10.1016/j.cell.2015.05.022

Nelson, D. L., and Cox, M. M. (2017). *Lehninger: Principles of biochemistry* (*7th ed.*). Hamilton, NJ. American Metro Center.

Nies, D. H. (1999). Microbial heavy-metal resistance. *Appl. Microbiol. Biotechnol.* 51, 730–750. doi: 10.1007/s002530051457

Noreen, A., Rehman, A., Aftab, S., and Shakoori, A. R. (2019). Antiproliferative effect of oxidative stress induced by tellurite in breast carcinoma cells. *J. Cancer Res. Prac.* 6, 68–75. doi: 10.4103/JCRP.JCRP_5_19

Nunoshiba, T., Obata, F., Boss, A. C., Oikawa, S., Mori, T., Kawanishi, S., et al. (1999). Role of iron and superoxide for generation of hydroxyl radical, oxidative DNA lesions, and mutagenesis in *Escherichia coli*. *J. Biol. Chem.* 274, 34832–34837. doi: 10.1074/jbc.274.49.34832

Otaru, N., Ye, K., Mujezinovic, D., Berchtold, L., Constancias, F., Cornejo, F. A., et al. (2021). GABA production by human intestinal Bacteroides spp.: prevalence, regulation, and role in acid stress tolerance. *Front. Microbiol.* 12:656895. doi: 10.3389/fmicb.2021.656895

Otsuka, Y., Muto, A., Takeuchi, R., Okada, C., Ishikawa, M., Nakamura, K., et al. (2015). GenoBase: comprehensive resource database of *Escherichia coli* K-12. *Nucleic Acids Res.* 43, D606–D617. doi: 10.1093/nar/gku1164

Ouyang, Y., Peng, Y., Li, J., Holmgren, A., and Lu, J. (2018). Modulation of thiol-dependent redox system by metal ions via thioredoxin and glutaredoxin systems. *Metallomics* 10, 218–228. doi: 10.1039/C7MT00327G

Pacheco, C. C., Passos, J. F., Castro, A. R., Moradas-Ferreira, P., and De Marco, P. (2008). Role of respiration and glutathione in cadmium-induced oxidative stress in *Escherichia coli* K-12. *Arch. Microbiol.* 189, 271–278. doi: 10.1007/s00203-007-0316-8

Paraszkiewicz, K., Bernat, P., Naliwajski, M., and Długoński, J. (2010). Lipid peroxidation in the fungus curvularia lunata exposed to nickel. *Arch. Microbiol.* 192, 135–141. doi: 10.1007/s00203-009-0542-3

Park, H. J., Kim, J. Y., Kim, J., Lee, J. H., Hahn, J. S., Gu, M. B., et al. (2009). Silver-ion-mediated reactive oxygen species generation affecting bactericidal activity. *Water Res.* 43, 1027–1032. doi: 10.1016/j.watres.2008.12.002

Parvatiyar, K., Alsabbagh, E. M., Ochsner, U. A., Stegemeyer, M. A., Smulian, A. G., Hwang, S. H., et al. (2005). Global analysis of cellular factors and responses involved in *Pseudomonas aeruginosa* resistance to arsenite. *J. Bacteriol.* 187, 4853–4864. doi: 10.1128/JB.187.14.4853-4864.2005

Peana, M., Pelucelli, A., Medici, S., Cappai, R., Nurchi, V. M., and Zoroddu, M. A. (2021). Metal toxicity and speciation: a review. *Curr. Med. Chem.* 28, 7190–7208. doi: 10.2174/0929867328666210324161205

Pearson, R. G. (1966). Acids and bases. *Science* 151, 172–177. doi: 10.1126/science.151.3707.172

Pérez, J. M., Calderón, I. L., Arenas, F. A., Fuentes, D. E., Pradenas, G. A., Fuentes, E. L., et al. (2007). Bacterial toxicity of potassium tellurite: unveiling an ancient enigma. *PLoS One* 2:e211. doi: 10.1371/journal.pone.0000211

Piotrowski, J. S., Li, S. C., Deshpande, R., Simpkins, S. W., Nelson, J., Yashiroda, Y., et al. (2017). Functional annotation of chemical libraries across diverse biological processes. *Nat. Chem. Biol.* 13, 982–993. doi: 10.1038/nchembio.2436

Piotrowski, J. S., Simpkins, S. W., Li, S. C., Deshpande, R., McIlwain, S. J., Ong, I. M., et al. (2015). Chemical genomic profiling via barcode sequencing to predict compound mode of action. *Methods Mol. Biol.* 1263, 299–318. doi: 10.1007/978-1-4939-2269-7_23

Poetsch, A. R. (2020). The genomics of oxidative DNA damage, repair, and resulting mutagenesis. *Comput. Struct. Biotechnol. J.* 18, 207–219. doi: 10.1016/j.csbj.2019.12.013

Pradenas, G. A., Díaz-Vásquez, W. A., Pérez-Donoso, J. M., and Vásquez, C. C. (2013). Monounsaturated fatty acids are substrates for aldehyde generation in tellurite-exposed *Escherichia coli*. *Biomed. Res. Int.* 2013:563756. doi: 10.1155/2013/563756

Quintal, S. M., dePaula, Q. A., and Farrell, N. P. (2011). Zinc finger proteins as templates for metal ion exchange and ligand reactivity. Chemical and biological consequences. *Metallomics* 3, 121–139. doi: 10.1039/c0mt00070a

Rajanna, B., Hobson, M., Harris, L., Ware, L., and Chetty, C. S. (1990). Effects of cadmium and mercury on Na^+-K^+ ATPase and uptake of ^{3}H-dopamine in rat brain synaptosomes. *Arch. Int. Phys. Bioch.* 98, 291–296. doi: 10.3109/13813459009113989

Robinson, M. D., McCarthy, D. J., and Smyth, G. K. (2010). edgeR: a bioconductor package for differential expression analysis of digital gene expression data. *Bioinformatics* 26, 139–140. doi: 10.1093/bioinformatics/btp616

Rosen, R., Biran, D., Gur, E., Becher, D., Hecker, M., and Ron, E. Z. (2002). Protein aggregation in *Escherichia coli*: role of proteases. *FEMS Microbiol. Lett.* 207, 9–12. doi: 10.1111/j.1574-6968.2002.tb11020.x

Sharma, S. K., Goloubinoff, P., and Christen, P. (2008). Heavy metal ions are potent inhibitors of protein folding. *Biochem. Biophys. Res. Commun.* 372, 341–345. doi: 10.1016/j.bbrc.2008.05.052

Shizuta, Y., Nakazawa, A., Tokushige, M., and Hayaishi, O. (1969). Studies on the interaction between regulatory enzymes and effectors. III. Crystallization and characterization of adenosine 5′-monophosphate-dependent threonine deaminase from *Escherichia coli*. *J. Biol. Chem.* 244, 1883–1889. doi: 10.1016/S0021-9258(18)91763-1

Sies, H., Berndt, C., and Jones, D. P. (2017). Oxidative stress. *Annu. Rev. Biochem.* 86, 715–748. doi: 10.1146/annurev-biochem-061516-045037

Simpkins, S. W., Deshpande, R., Nelson, J., Li, S. C., Piotrowski, J. S., Ward, H. N., et al. (2019). Using BEAN-counter to quantify genetic interactions from multiplexed barcode sequencing experiments. *Nat. Protoc.* 14, 415–440. doi: 10.1038/s41596-018-0099-1

Śmigiel, W. M., Mantovanelli, L., Linnik, D. S., Punter, M., Silberberg, J., Xiang, L., et al. (2022). Protein diffusion in *Escherichia coli* cytoplasm scales with the mass of the complexes and is location dependent. *Sci. Adv.* 8:eabo5387. doi: 10.1126/sciadv.abo5387

Stadtman, E. R., and Levine, R. L. (2003). Free radical-mediated oxidation of free amino acids and amino acid residues in proteins. *Amino Acids* 25, 207–218. doi: 10.1007/s00726-003-0011-2

Steinfeld, J. B., Aerni, H. R., Rogulina, S., Liu, Y., and Rinehart, J. (2014). Expanded cellular amino acid pools containing phosphoserine, phosphothreonine, and phosphotyrosine. *ACS Chem. Biol.* 9, 1104–1112. doi: 10.1021/cb5000532

Su, H. S., Lang, B. F., and Newman, E. B. (1989). L-serine degradation in *Escherichia coli* K-12: cloning and sequencing of the sdaA gene. *J. Bacteriol.* 171, 5095–5102. doi: 10.1128/jb.171.9.5095-5102.1989

Su, H., and Newman, E. B. (1991). A novel L-serine deaminase activity in *Escherichia coli* K-12. *J. Bacteriol.* 173, 2473–2480. doi: 10.1128/jb.173.8.2473-2480.1991

Sugawara, K., Toyoda, H., Kimura, M., Hayasaka, S., Saito, H., Kobayashi, H., et al. (2021). Loss of cell wall integrity genes cpxA and mrcB causes flocculation in *Escherichia coli*. *Biochem. J.* 478, 41–59. doi: 10.1042/BCJ20200723

Tadokoro, A., Hayashi, H., Kishimoto, T., Makino, Y., Fujisaki, S., and Nishimura, Y. (2004). Interacción of the *Escherichia coli* lipoportein NlpI with periplasmic Prc (tsp) protease. *J. Biochem.* 135, 185–191. doi: 10.1093/jb/mvh022

Tazuya-Murayama, K., Aramaki, H., Mishima, M., Saito, K., Ishida, S., and Yamada, K. (2006). Effect of L-serine on the biosynthesis of aromatic amino acids in *Escherichia coli*. *J. Nutr. Sci. Vitaminol.* 52, 256–260. doi: 10.3177/jnsv.52.256

Tchounwou, P. B., Yedjou, C. G., Patlolla, A. K., and Sutton, D. J. (2012). Heavy metal toxicity and the environment. *EXS* 101, 133–164. doi: 10.1007/978-3-7643-8340-4_6

Thorgersen, M. P., Xue, J., Majumder, E., Trotter, V. V., Ge, X., Poole, F., et al. (2021). Deciphering microbial metal toxicity responses via random bar code transposon site sequencing and activity-based metabolomics. *Appl. Environ. Microbiol.* 87:e0103721. doi: 10.1128/AEM.01037-21

Tomoyasu, T., Mogk, A., Langen, H., Goloubinoff, P., and Bukau, B. (2001). Genetic dissection of the roles of chaperones and proteases in protein folding and degradation in the *Escherichia coli* cytosol. *Mol. Microbiol.* 40, 397–413. doi: 10.1046/j.1365-2958.2001.02383.x

Traxler, M. F., Summers, S. M., Nguyen, H. T., Zacharia, V. M., Hightower, G. A., Smith, J. T., et al. (2008). The global, ppGpp-mediated stringent response to amino acid starvation in *Escherichia coli*. *Mol. Microbiol.* 68, 1128–1148. doi: 10.1111/j.1365-2958.2008.06229.x

Tremaroli, V., Fedi, S., and Zannoni, D. (2007). Evidence for a tellurite-dependent generation of reactive oxygen species and absence of a tellurite-mediated adaptive response to oxidative stress in cells of *Pseudomonas pseudoalcaligenes* KF707. *Arch. Microbiol.* 187, 127–135. doi: 10.1007/s00203-006-0179-4

Tyedmers, J., Mogk, A., and Bukau, B. (2010). Cellular strategies for controlling protein aggregation. *Nat. Rev. Mol. Cell Biol.* 11, 777–788. doi: 10.1038/nrm2993

Valko, M., Morris, H., and Cronin, M. T. (2005). Metals, toxicity and oxidative stress. *Curr. Med. Chem.* 12, 1161–1208. doi: 10.2174/0929867053764635

Vera, A., Arís, A., Carrió, M., González-Montalbán, N., and Villaverde, A. (2005). Lon and ClpP proteases participate in the physiological disintegration of bacterial inclusion bodies. *J. Biotechnol.* 119, 163–171. doi: 10.1016/j.jbiotec.2005.04.006

Wang, A., and Crowley, D. E. (2005). Global gene expression responses to cadmium toxicity in *Escherichia coli*. *J. Bacteriol.* 187, 3259–3266. doi: 10.1128/JB.187.9.3259-3266.2005

Wang, B., Grant, R. A., and Laub, M. T. (2020). ppGpp coordinates nucleotide and amino-acid synthesis in *E. coli* during starvation. *Mol. Cell* 80, 29–42.e10. doi: 10.1016/j.molcel.2020.08.005

Weids, A. J., Ibstedt, S., Tamás, M. J., and Grant, C. M. (2016). Distinct stress conditions result in aggregation of proteins with similar properties. *Sci. Rep.* 6: 24554.

Wilken, C., Kitzing, K., Kurzbauer, R., Ehrmann, M., and Clausen, T. (2004). Crystal structure of the DegS stress sensor: how a PDZ domain recognizes misfolded protein and activates a protease. *Cells* 117, 483–494. doi: 10.1016/S0092-8674(04)00454-4

Williams, K. J. (2009). The introduction of ´chemotherapy'using arsphenamine the first magic bullet. *J. R. Soc. Med.* 102, 343–348. doi: 10.1258/jrsm.2009.09k036

Xiao, M., Zhu, X., Fan, F., Xu, H., Tang, J., Qin, Y., et al. (2017). Osmotolerance in *Escherichia coli* is improved by activation of copper efflux genes or supplementation with sulfur-containing amino acids. *Appl. Environ. Microbiol.* 83, e03050–e03016. doi: 10.1128/AEM.03050-16

Xu, F. F., and Imlay, J. A. (2012). Silver(I), mercury(II), cadmium(II), and zinc(II) target exposed enzymic iron-sulfur clusters when they toxify *Escherichia coli*. *Appl. Environ. Microbiol.* 78, 3614–3621. doi: 10.1128/AEM.07368-11

Zarei, M. H., Pourahmad, J., and Nassireslami, E. (2019). Toxicity of arsenic on isolated human lymphocytes: the key role of cytokines and intracellular calcium enhancement in arsenic-induced cell death. *Main Group Met. Chem.* 42, 125–134. doi: 10.1515/mgmc-2019-0014

Zhang, X., El-Hajj, Z. W., and Newman, E. (2010). Deficiency in L-serine deaminase interferes with one-carbon metabolism and cell wall synthesis in *Escherichia coli* K-12. *J. Bacteriol.* 192, 5515–5525. doi: 10.1128/JB.00748-10

Zhang, X., and Newman, E. (2008). Deficiency in l-serine deaminase results in abnormal growth and cell division of *Escherichia coli* K-12. *Mol. Microbiol.* 69, 870–881. doi: 10.1111/j.1365-2958.2008.06315.x

Zuily, L., Lahrach, N., Fassler, R., Genest, O., Faller, P., Sénèque, O., et al. (2022). Copper induces protein aggregation, a toxic process compensated by molecular chaperones. *MBio* 13, e03251–e03221. doi: 10.1128/mbio.03251-21

frontiers | Frontiers in Microbiology

TYPE Original Research
PUBLISHED 13 December 2023
DOI 10.3389/fmicb.2023.1305973

OPEN ACCESS

EDITED BY
Z. Petek Cakar,
Istanbul Technical University, Türkiye

REVIEWED BY
Robert Hondal,
University of Vermont, United States
Nina Dickerhof,
University of Otago, Christchurch,
New Zealand

*CORRESPONDENCE
James A. Imlay
✉ jimlay@illinois.edu

RECEIVED 02 October 2023
ACCEPTED 27 November 2023
PUBLISHED 13 December 2023

CITATION
Eben SS and Imlay JA (2023) Evidence that protein thiols are not primary targets of intracellular reactive oxygen species in growing *Escherichia coli*.
Front. Microbiol. 14:1305973.
doi: 10.3389/fmicb.2023.1305973

Evidence that protein thiols are not primary targets of intracellular reactive oxygen species in growing *Escherichia coli*

Stefanie S. Eben and James A. Imlay*

Department of Microbiology, University of Illinois, Urbana, IL, United States

The oxidizability of cysteine residues is exploited in redox chemistry and as a source of stabilizing disulfide bonds, but it also raises the possibility that these side chains will be oxidized when they should not be. It has often been suggested that intracellular oxidative stress from hydrogen peroxide or superoxide may result in the oxidation of the cysteine residues of cytoplasmic proteins. That view seemed to be supported by the discovery that one cellular response to hydrogen peroxide is the induction of glutaredoxin 1 and thioredoxin 2. In this study we used model compounds as well as alkaline phosphatase to test this idea. Our results indicate that molecular oxygen, superoxide, and hydrogen peroxide are very poor oxidants of N-acetylcysteine and of the protein thiols of alkaline phosphatase *in vitro*. Copper could accelerate thiol oxidation, but iron did not. When alkaline phosphatase was engineered to remain in the cytoplasm of live cells, unnaturally high concentrations of hydrogen peroxide were required to oxidize it to its active, disulfide-dependent form, and toxic levels of superoxide had no effect. At the same time, far lower concentrations of these oxidants were sufficient to poison key metalloenzymes. The elimination of glutaredoxin 1 and thioredoxin 2 did not change these results, raising the question of why *E. coli* induces them during peroxide stress. In fact, when catalase/peroxidase mutants were chronically stressed with hydrogen peroxide, the absence of glutaredoxin 1 and thioredoxin 2 did not impair growth at all, even in a minimal medium over many generations. We conclude that physiological levels of reduced oxygen species are not potent oxidants of typical protein thiols. Glutaredoxin and thioredoxin must either have an alternative purpose or else play a role under culture conditions that differ from the ones we tested.

KEYWORDS

oxidative stress, glutaredoxin, thioredoxin, *E. coli*, disulfide bond formation

Introduction

Cysteine is a uniquely reactive amino acid. While it is employed in some enzymes as a nucleophile or as a metal ligand, its most distinctive feature is its redox activity. Cysteine residues are systematically oxidized to disulfide bonds in proteins that are exported to the bacterial periplasm; these bonds stabilize proteins in an environment that can be hazardous. Structural disulfide bonds are absent from proteins in the cytoplasm; however, a small group of cytoplasmic enzymes use cysteine residues as electron donors to their substrates, with the concomitant generation of transient disulfide bonds. Ribonucleotide reductase and 3-phosphoadenylyl-sulfate (PAPS) reductase are familiar examples. The catalytic cycles of these enzymes are

completed when the disulfide bonds are reduced by cellular glutaredoxins and thioredoxins. These redoxins are small proteins that themselves employ solvent-exposed cysteine residues to transfer electrons to client proteins; in turn, they acquire electrons from NADPH via glutathione/glutathione reductase or thioredoxin reductase. These routes of disulfide bond formation and resolution have been worked out most completely in *Escherichia coli* and are depicted in Figure 1.

It seems unlikely that *E. coli* synthesizes two thioredoxins (encoded by *trxA* and *trxC*) and three glutaredoxins (*grxA*, *grxB*, and *grxC*) to reduce a mere handful of disulfide-dependent enzymes, and genetic analysis has confirmed that not all of these redoxins are needed for that purpose (Ritz and Beckwith, 2001). This observation raises the question of whether they have additional, discrete roles. A common suggestion is that redoxins also defend proteins against adventitious cysteine oxidations by oxygen species (Tao, 1997; Luikenhuis et al., 1998; Jakob et al., 1999; Carmel-Harel and Storz, 2000; Ritz et al., 2000; Li et al., 2004; Leichert et al., 2008; Wolf et al., 2008; Depuydt et al., 2009; Hillion and Antelmann, 2015; Xie et al., 2019). Potential oxidants might include not only molecular oxygen itself but also superoxide and hydrogen peroxide, both of which are formed as inadvertent by-products of metabolism.

A supporting piece of evidence is that *E. coli* induces glutaredoxin 1 and thioredoxin 2 when the bacterium is exposed to environmental hydrogen peroxide (H_2O_2) (Tao, 1997; Ritz et al., 2000). Hydrogen peroxide is produced in bacterial habitats by chemical events at oxic/anoxic interfaces, by photochemistry, by lactic acid bacteria, and as a major component of the cell-based immune response (Glass et al., 1986; Mehdy, 1994; Bedard et al., 2007). Because it is small and uncharged, it readily passes through membranes into cells (Lynch and Fridovich, 1978; Seaver and Imlay, 2004). Virtually all organisms possess scavenging enzymes—a mixture of catalases and peroxidases—to keep intracellular H_2O_2 scant, but concentrations can still become hazardous if the rate of influx is high enough. Studies of *E. coli* mutants that lack scavenging enzymes have identified two classes of metalloenzymes that H_2O_2 damages. It can inactivate dehydratases by oxidizing their catalytic [4Fe-4S] clusters, which then fall apart. Damage of this type affects aconitase and isopropylmalate isomerase, for example, and thereby impairs the TCA cycle and the synthesis of branched-chain amino acids (Jang and Imlay, 2007). Peroxide also reacts with mononuclear enzymes that use a single Fe(II) cofactor; the pentose-phosphate pathway and the synthesis of aromatic amino acids both rely on such enzymes, and these pathways fail during stress (Anjem and Imlay, 2012). Cells respond to these injuries by re-building the clusters and re-metallating the mononuclear sites, and the steady-state activities of affected enzymes represents the balance between the damage and repair processes. Notably, both cluster reconstruction and remetallation involve steps that require thiols (Jang and Imlay, 2007; Anjem and Imlay, 2012).

A more obvious demand for redoxins would arise if oxidants were to directly oxidize accessible cysteine residues on protein surfaces. This rationale was suggested in the studies that found that redoxins are induced in stressed cells (Tao, 1997; Luikenhuis et al., 1998; Ritz et al., 2000; Depuydt et al., 2009). *In vitro* studies have confirmed that molecular oxygen, superoxide, and H_2O_2 all have the capacity to oxidize thiols, and among these H_2O_2 stands out (Winterbourn and Metodiewa, 1999; Winterbourn, 2016). The primary scavenging system in *E. coli*, in fact, is an NADH peroxidase (AhpCF) that uses thiol-based chemistry to reduce H_2O_2 to water (Seaver and Imlay, 2001; Parsonage et al., 2015). And the cytoplasmic transcription factor that senses elevated H_2O_2—OxyR—does so when H_2O_2 oxidizes its sensory cysteine (Zheng et al., 1998; Choi et al., 2001). These proteins are highly evolved to react with H_2O_2, but they provide a chemical argument that unwanted thiol oxidations are also plausible.

Proteomic studies have repeatedly shown that the cysteine residues of cytoplasmic proteins are oxidized inside cells that are exposed to exogenous H_2O_2, and those data have been cited to support the notion that protein thiols are modified during oxidative stress (Leichert and Jakob, 2004; Hochgrafe et al., 2005; Leichert et al., 2008; Wolf et al., 2008; Deng et al., 2013). However, these experiments

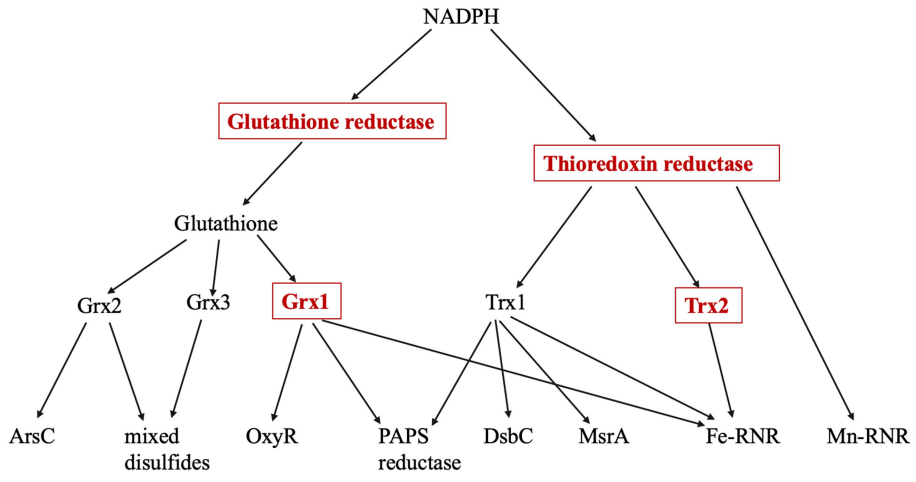

FIGURE 1
Thioredoxin and Glutaredoxin pathways. The four enzymes marked in red boxes are induced by the OxyR regulon. Glutathione reductase (*gor*), thioredoxin reductase (*trxB*), Grx1 (*grxA*), Grx2 (*grxB*), Grx3 (*grxC*), Trx1 (*trxA*), Trx2 (*trxC*), arsenate reductase (*arsC*), methionine sulfoxide reductase (*msrA*), PAPS reductase (*cysH*), Fe-RNR (*nrdAB*), Mn-RNR (*nrdHIEF*), periplasmic protein disulfide isomerase (*dsbC*). PAPS reductase is involved in the sulfate assimilation pathway; RNR denotes isozymes of ribonucleotide reductase.

imposed H_2O_2 concentrations in the millimolar range—far in excess of the sub-micromolar concentrations that pertain to model bacteria (Imlay, 2013). It would be more relevant to test protein oxidation in concentrations that are likely to obtain inside natural environments.

In this study we measured the abilities of different oxygen species to oxidize either model thiols or protein cysteine residues *in vitro*. We also used alkaline phosphatase, a disulfide-dependent enzyme that had been engineered not to be secreted, to detect thiol oxidation events inside the cytoplasm. Forcing conditions were applied using strains with exceptionally high levels of internal superoxide and H_2O_2. The combination of these approaches permits a higher sensitivity to disulfide-bond formation than traditional proteomics. The data indicate that chemical cysteine oxidations were rare events. This result does not explain why cells induce glutaredoxin and thioredoxin systems, and it suggests either that these redoxins have undiscovered roles or that their action is important under growth conditions other than those we employed.

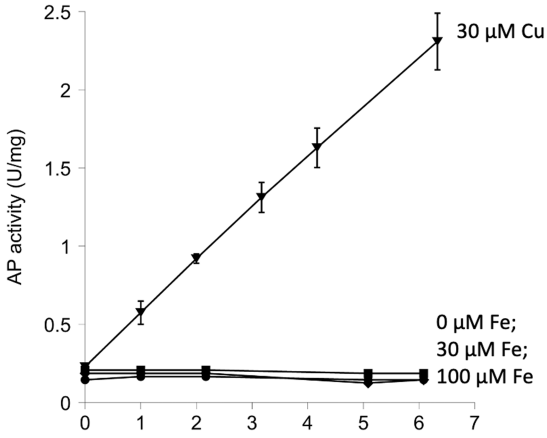

FIGURE 2
Iron does not catalyze the activation of reduced alkaline phosphatase (AP) *in vitro*. The activation of AP can be achieved by oxidation of its cysteine residues. Reduced AP was incubated at 37°C with iron (30 and 100 µM) in oxic buffers. Copper (30 µM) was provided as a positive control. In this figure and all others that follow, experiments were performed in triplicate, and error bars represent the standard error of the mean. Small error bars may be obscured by symbols.

Results

Molecular oxygen is a very slow oxidant of protein thiols

The abundance of disulfide-reducing systems inside cells has generally been rationalized by the notion that either molecular oxygen or species derived from it readily oxidize the cysteine residues of proteins. The immediate product of cysteine oxidation would be a sulfenic acid; if another cysteine residue is nearby, they can condense, forming a disulfide bond. This process can be observed in cell extracts and in preparations of purified protein. Biochemists often suppress thiol oxidation by the inclusion of chelators such as EDTA, indicating that this process is metal-catalyzed and they reverse it by inclusion of reductants such as dithiothreitol (DTT) (Cleland, 1964).

Those observations of thiol oxidation are typically made on a time scale of hours to days. For thiol oxidations to be consequential inside cells—for example, to inactivate an enzyme population to the extent that a pathway bottleneck arises—the rate of thiol oxidation must be fast, with a majority of enzyme molecules being oxidized within a cell generation. We selected alkaline phosphatase (AP) as a model protein to quantify the oxidation rate. This enzyme is normally exported to the periplasm, and its activity requires that two disulfide bonds be generated, customarily by the Dsb system (Derman et al., 1993). In its reduced form the relevant cysteine residues are likely to display the oxidizability of typical protein thiols. We denatured, reduced, and renatured purified AP, generating an inactive, reduced enzyme that could regain activity through thiol oxidation. The assay detects a signal of enzyme activation that rises from a low background, rather than the loss of an enzyme activity; therefore, signal/background provides good sensitivity. Prior experiments have shown that even a modest degree of oxidation is perceptible by a rise in its activity (Eben and Imlay, 2023).

When reduced AP was simply incubated in air-saturated buffer for as long as 6 h, no significant activation could be seen (Figure 2). Previous work showed that AP can be activated under these conditions if the system includes copper, a redox-active transition metal with high affinity for sulfur atoms (Eben and Imlay, 2023). Copper acts as a bridge that transfers electrons from cysteine side chains to oxygen. That observation was reproduced in these experiments (Figure 2). Copper, however, is excluded from the cytoplasms of bacteria (Andrei et al., 2020) and cannot drive thiol oxidation *in vivo*, so we tested whether iron might catalyze the same reaction. Loose iron is relatively abundant (20–60 micromolar) inside bacterial cytoplasms (Keyer and Imlay, 1996; Liu et al., 2011), where it is needed to metallate numerous enzymes, and it has the capacity to oxidize thiols. However, when iron was added to AP incubations, we did not observe any boost in AP activity (Figure 2).

A more relevant test would be to monitor the activity of AP *in vivo*. We use a modified form of AP designed by Beckwith and colleagues (Derman and Beckwith, 1991). This enzyme derivative lacks a leader sequence, so the vast majority of the protein accumulates in the cytoplasm (cAP). A very small minority of the cAP harvested from cells is active, and we have shown that this background activity primarily derives from a small fraction that, despite the absence of the N-terminal leader sequence, is nevertheless exported and oxidized by the periplasmic disulfide-bond forming system (Dsb) (Eben and Imlay, 2023). To evaluate whether the majority of protein—in the cytoplasm—can be adventitiously oxidized by oxygen, we compared the amount of AP activity in cells gassed with 22% oxygen with the activity in cells that had been gassed with 100% oxygen. The data (Figure 3A) suggested a modest rise (~ 15%) in mean activity among replicate samples, but the sample-to-sample variation was large enough that statistical significance was not achieved ($p = 0.57$). The experiment was repeated in a *trxC grxA* double mutant, which lacks the inducible redoxins that are hypothesized to deal with chemical oxidation; in this strain, the apparent rise in cAP activity was larger, and the p value was smaller (0.20) but still in excess of the conventional line for statistical significance (Figure 3A). We tentatively conclude that hyperoxia may have a slight effect upon protein-thiol oxidation; however, because air-saturated medium has only 22% this level of oxygen, the impact in normoxic cells would be minimal. In the Discussion we consider whether the oxidation of cysteine residues

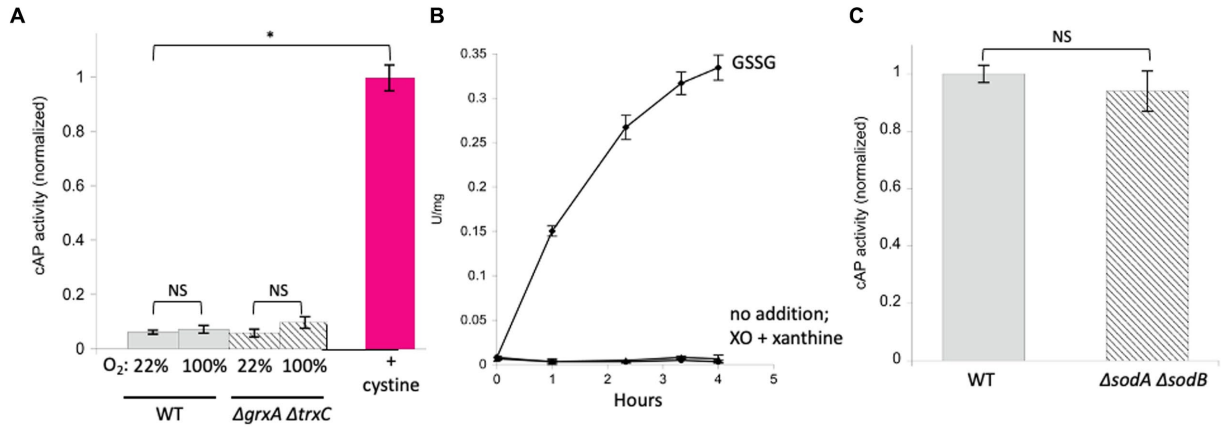

FIGURE 3
High oxygen concentrations were ineffective at activating alkaline phosphatase localized in the cytoplasm (cAP). Superoxide does not activate reduced AP *in vitro* or cAP *in vivo*. **(A)** Wild-type and *ΔgrxA ΔtrxC* strains were gassed with 22% or 100% oxygen for 40 min. The positive control was cystine (0.5 mM), the disulfide-bonded amino acid that is imported by *E. coli* and that can exchange disulfide bonds with cellular proteins. Data have been normalized to the cystine control. **(B)** Reduced AP was incubated at 37°C with xanthine oxidase and xanthine to produce superoxide. Oxidized glutathione (GSSG, 3 mM) was used as a positive control. **(C)** cAP activity was assessed in a WT strain and in a strain lacking superoxide dismutase (*ΔsodA ΔsodB*). Data have been normalized to WT; signals were as low as in Figure 1.

might still be obscured by other routes of countervailing sulfenate/disulfide reduction.

Superoxide does not oxidize protein thiols at a relevant pace

In a previous study we did not detect oxidation of N-acetylcysteine, a cysteine analog, when it was incubated in oxic buffer (Eben and Imlay, 2023). The apparent rate constant must therefore lie $<0.3\,M^{-1}\,s^{-1}$. By comparison, the rate constant for thiol oxidation by superoxide ($O_2^{\cdot-}$) has been estimated to be in the range of $100\,M^{-1}\,s^{-1}$ (Benrahmoune et al., 2000; Winterbourn, 2016). In wild-type cells, where the steady-state $O_2^{\cdot-}$-concentration is restricted by superoxide dismutase to approximately 10^{-10} M (Imlay, 2013), this rate constant is still far too low to be important, as it would project a half-time for thiol oxidation of 2 years (see calculation in Material & Methods). To test this inference, we exposed reduced AP *in vitro* to $O_2^{\cdot-}$-that was steadily produced by xanthine oxidase (2 μM/min over a period of 4 h). Under these conditions the calculated steady-state level of $O_2^{\cdot-}$-was 0.8 μM, but no activation was observed (Figure 3B). As this concentration is 10,000 times that of wild-type cells, we infer that even conditions that substantially elevate $O_2^{\cdot-}$-production would not trigger oxidation of typical protein thiols.

Superoxide ($pK_A = 4.8$) is deprotonated at physiological pH, so its capacity as an oxidant is impaired due to the impossibility of transferring another electron onto a species that is already anionic. A more plausible oxidant is its conjugate acid $HO_2^{\cdot}$, but with a pK_A of 4.8 it comprises only 0.25% of the superoxide at the cytoplasmic pH 7.4. The most plausible route for thiol oxidation by $O_2^{\cdot-}$-is therefore when it oxidizes a thiol-bound Fe (Kawasaki et al., 2005) ion, forming a protein thiol-Fe(III)-OOH complex. For example, the standard model for bleomycin action is that an Fe(III)-OOH complex is created on the surface of DNA, from which the complex then abstracts an electron (Chow et al., 2008). We did not have a reliable way to generate such species *in vitro*, particularly because added iron can inhibit xanthine oxidase. Therefore, we tested whether $O_2^{\cdot-}$-stress oxidizes cAP *in vivo*, inside cells where iron might be available.

The cAP construct was expressed in an SOD-mutant. This mutant cannot scavenge cytoplasmic $O_2^{\cdot-}$, and when it is aerated, the activities of superoxide-sensitive metalloenzymes immediately decline (Gardner and Fridovich, 1991; Gu and Imlay, 2013). However, we did not detect any activation of cAP (Figure 3C). The level of superoxide in this strain is extremely high, and so we conclude that $O_2^{\cdot-}$-does not drive the general oxidation of protein thiols *in vivo*.

Hydrogen peroxide can oxidize AP thiols, but only at non-physiological concentrations

Hydrogen peroxide seemed to be the best candidate to oxidize thiols, because that chemistry is used for H_2O_2 detection by OxyR and for scavenging by Ahp. Those two proteins are highly evolved for this function—but their rate constants for reaction with H_2O_2 ($10^5\,M^{-1}\,s^{-1}$ for OxyR and $10^7\,M^{-1}\,s^{-1}$ for AhpC) (Zheng et al., 1998; Parsonage et al., 2015) are so high that even a lower rate for adventitious reactions might be fast enough to have physiological consequences. In line with that reasoning, workers have shown that redoxin pathways are induced when *E. coli* senses H_2O_2 stress. When intracellular H_2O_2 concentrations exceed 0.2 micromolar, the OxyR system turns on both glutathione reductase (encoded by *gor*) and glutaredoxin 1 (*grxA*), as if to enhance glutaredoxin activity, and thioredoxin 2 (*trxC*) (Christman et al., 1985; Tao, 1997; Ritz et al., 2000). These data imply that H_2O_2-exposed cells must amplify systems to repair oxidized cysteine residues.

The OxyR and AhpC reactions with H_2O_2 involve a direct attack by a deprotonated cysteine residue upon the H_2O_2 (Parsonage et al., 2015; Jo et al., 2017). We first tested the rate at which H_2O_2 oxidizes N-acetylcysteine *in vitro*. N-acetylcysteine is a cysteine analog whose amino terminus is derivatized—as is that of cysteine in

polypeptides—in order to avoid effects that its positive charge might otherwise exert upon thiol behavior. A chelator was included to avoid metal-dependent reactions. A reaction was detected that was first-order in both H_2O_2 and the thiol (Supplementary Figure S1). The overall rate constant was low: 0.07 M^{-1} s^{-1}. This experiment was conducted at pH 8, when only 3% of the thiol (pKa = 9.5) (Zhitkovich, 2019) is deprotonated; the rate constant for fully deprotonated thiolate would therefore be 2.3 M^{-1} s^{-1}. This is in the range of rate constants that have been previously determined for N-acetylcysteine (Aruoma et al., 1989; Xie et al., 2019) and for free cysteine (2 M^{-1} s^{-1} at neutral pH, and 20 M^{-1} s^{-1} for the thiolate) (Winterbourn and Metodiewa, 1999) and for dithiothreitol (15 M^{-1} s^{-1} for the thiolate) (Li and Imlay, 2018). At 1 micromolar H_2O_2, which fully induces the OxyR system, the N-acetylcysteine rate constant implies a half-time for thiolate oxidation of 84 h—which is too long to be impactful.

The experiment was repeated with AP *in vitro* (Figure 4A). Because the AP cysteine residues have evolved to be oxidized by Dsb, it seemed possible that the reaction might also be quick with H_2O_2. Indeed, some activation was detected, but concentrations of 100 micromolar were required.

Finally, we tested AP oxidation *in vivo*. A strain lacking scavengers of H_2O_2 was used, and with these cells the external and internal H_2O_2 concentrations are equivalent. Dipyridyl, a cell-permeable iron chelator, was initially added to prohibit iron-mediated thiol oxidation. Activation of cAP was not detected at 10 micromolar H_2O_2 but became apparent at 100 micromolar and quite substantial at millimolar concentrations (Figure 4B). Those data fit what had been observed *in vitro*. They also suggest that physiological levels of H_2O_2—which are 50 nM in unstressed cells and 200 nM during OxyR activation (Imlay, 2013)—are unlikely to directly oxidize typical cysteine residues at a consequential rate.

Those results fail to explain why OxyR induces disulfide-reducing systems. One possibility might be that iron catalyzes the oxidation. We have observed this chemistry when H_2O_2 attacks mononuclear enzymes whose Fe (Kawasaki et al., 2005) cofactor is coordinated by a cysteine ligand: the oxidation of iron by H_2O_2 is unfailingly coupled to the oxidation of the cysteine residue. Because H_2O_2 reacts rapidly with iron, the rate constants can be as high as 10^4 M^{-1} s^{-1} (Sobota and Imlay, 2011; Anjem and Imlay, 2012). Accordingly, we wondered whether loose iron might generally help H_2O_2 to oxidize protein cysteine residues. We incubated AP *in vitro* in the presence of iron and ascorbate (Figure 5A). In this system the oxidation of Fe(II) by oxygen generates O_2-and, by dismutation, H_2O_2, while ascorbate reduces the oxidized Fe(III) back to Fe(II) to make the process continuous and to ensure the availability of Fe(II) to bind to enzymes. The resultant mixture of H_2O_2 and Fe(II) drives the Fenton reaction and has been shown to fully inactivate iron-binding enzymes (Sobota and Imlay, 2011). However, we did not observe any activation of AP.

The *in vitro* experiment may not accurately reproduce the disposition of loose iron as it occurs *in vivo*, so this model was then tested inside cells. Non-scavenging catalase/peroxidase mutants were aerated, which leads to approximately 1 micromolar H_2O_2 inside the cytoplasm (Mancini and Imlay, 2015). This experiment was then repeated with the additional deletion of the gene encoding Dps, an iron-sequestering miniferritin that is induced by the OxyR system. When catalase/peroxidase *dps* strains are cultured in aerobic medium, cellular levels of free iron are high, and substantial Fenton-mediated damage to DNA and to cell proteins occurs (Park et al., 2005; Anjem et al., 2009). We detected a small but statistically significant (~ 30%) increase in cAP activation (Figure 5B).

We then tested whether even higher H_2O_2 levels might drive cAP oxidation. The catalase/peroxidase mutant was cultured for 90 min in the presence of 10 micromolar H_2O_2, a dose that was continuously sustained as described in Materials and methods. The cAP activity did not rise (Figure 5C). A small decline was observed, which could reflect the slower growth rate of the stressed cells and hence cAP turnover.

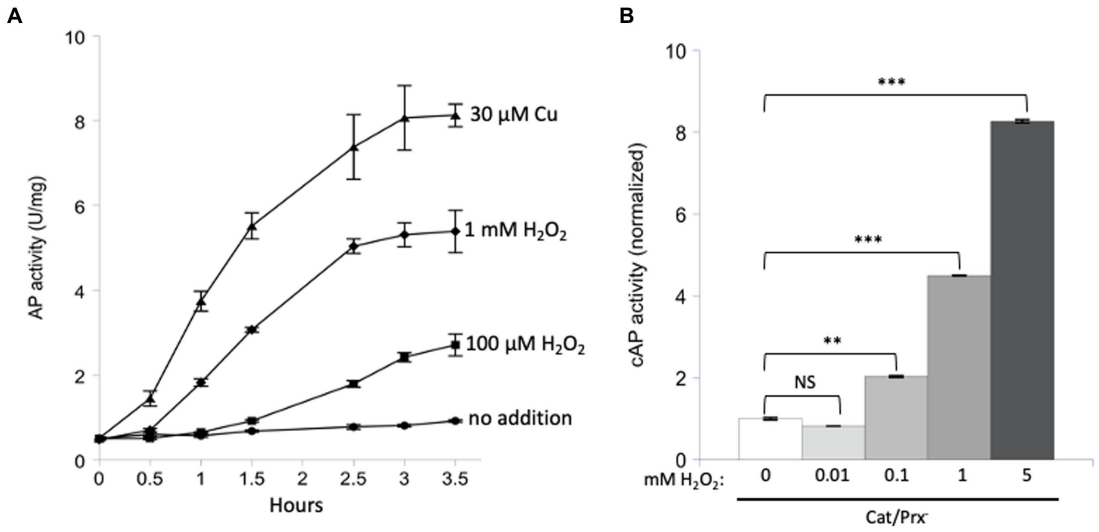

FIGURE 4
Unnaturally high concentrations of hydrogen peroxide are needed to directly activate reduced AP *in vitro* and cAP *in vivo*. **(A)** Reduced AP was incubated at 37°C with 0, 100 µM, and 1 mM H_2O_2 and with 30 µM copper. **(B)** cAP activity was assayed in a catalase/peroxidase-mutant exposed to a range of H_2O_2 concentrations (10, 100, 1, 5 mM). Dipyridyl was added to prevent metal-catalyzed oxidation, and chloramphenicol was added to stop new protein synthesis. Data have been normalized to untreated sample. For comparison: The concentration of H_2O_2 in WT cells has been calculated to be ~50 nM, and 1 µM cytoplasmic H_2O_2 fully induces the OxyR defensive response. *** indicates that $p < 0.001$; ** indicates $p < 0.01$; * indicates $p < 0.05$; NS indicates $p > 0.05$.

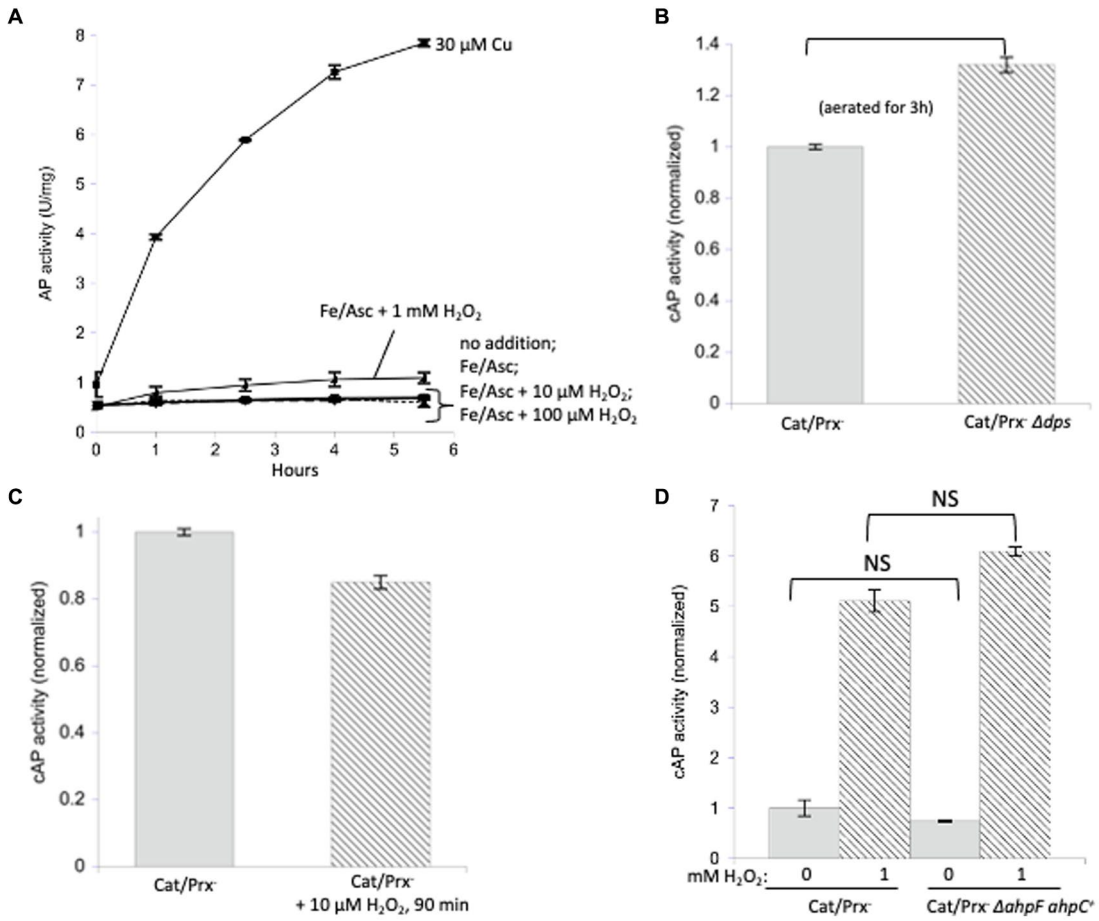

FIGURE 5
Protein disulfide bonds are not made efficiently by either iron/H_2O_2 Fenton chemistry or disulfide transfer from oxidized AhpC. **(A)** Reduced AP was incubated *in vitro* at 37°C with iron (50 μM) and ascorbate (10 mM) as well as increasing amounts of H_2O_2 (10 μM, 100 μM, 1 mM). Ascorbate ensured the constant presence of Fe (Kawasaki et al., 2005) to participate in Fenton chemistry. Control: 30 μM copper activated reduced AP. **(B)** Catalase/peroxidase-and catalase/peroxidase-Δdps strains were aerated for 3 h, and cAP activity was measured. The *dps* mutant lacks mini-ferritin and has elevated levels of intracellular free iron. Data have been normalized to the catalase/peroxidase-sample. **(C)** cAP activity did not increase in a catalase/peroxidase-mutant continuously stressed with 10 μM H_2O_2 over 90 min. Data have been normalized to the catalase/peroxidase-sample. **(D)** cAP activity was assessed in a catalase/peroxidase-and catalase/peroxidase-AhpC$^+$ strain with and without 1 mM H_2O_2 for 40 min. Data have been normalized to the untreated sample.

The fact that there was no detectable oxidation by 10 micromolar H_2O_2—a concentration 50-fold above what is sufficient to activate OxyR—implies that intracellular H_2O_2 does not cause the general oxidation of protein thiols.

A final possibility was that during H_2O_2 stress disulfide bonds might be disseminated from oxidized AhpC to other cellular proteins. Protein–protein disulfide transfer has been reported in two specialized circumstances: in *E. coli*, when Trx1 was forced into its oxidized, disulfide form; and in yeast, when a thiol-based peroxidase transfers a disulfide bond to Yap1 transcription factor (Stewart et al., 1998; Delaunay and AI Toledano, 2000). To create similarly forcing conditions, we knocked out *ahpF*, which encodes the disulfide reductase that reduces AhpC disulfide back to its dithiol form, so that this abundant protein would accumulate intracellularly in its oxidized form. However, upon aeration the non-scavenging AhpC$^+$ AhpF- strain did not activate cAP any more than did the double mutant that lacked AhpC (Figure 5D). This remained true even when 1 mM H_2O_2 was added. In sum, despite multiple approaches, we were unable to find conditions under which physiological doses of H_2O_2 generally oxidize protein thiols.

The inductions of grxA and trxC are strong, but these genes do not play any obvious role under the H_2O_2 stress conditions that we employed

Under the conditions of our experiments, the level of H_2O_2 inside the catalase/peroxide mutants rises to 1–2 micromolar, and the resultant activation of OxyR induces *grxA* 20-fold and *trxC* 30-fold (Figure 6A). We considered the possibility that Grx1 and/or Trx2 reversed disulfide bonds in catalase/peroxidase mutants so rapidly that cAP activation was prevented. Therefore, we probed for cAP activation in scavenging mutants that additionally lacked both redoxins. Again, we did not see any increase in cAP activity (Figure 6B). This was true even when the constant H_2O_2 concentration

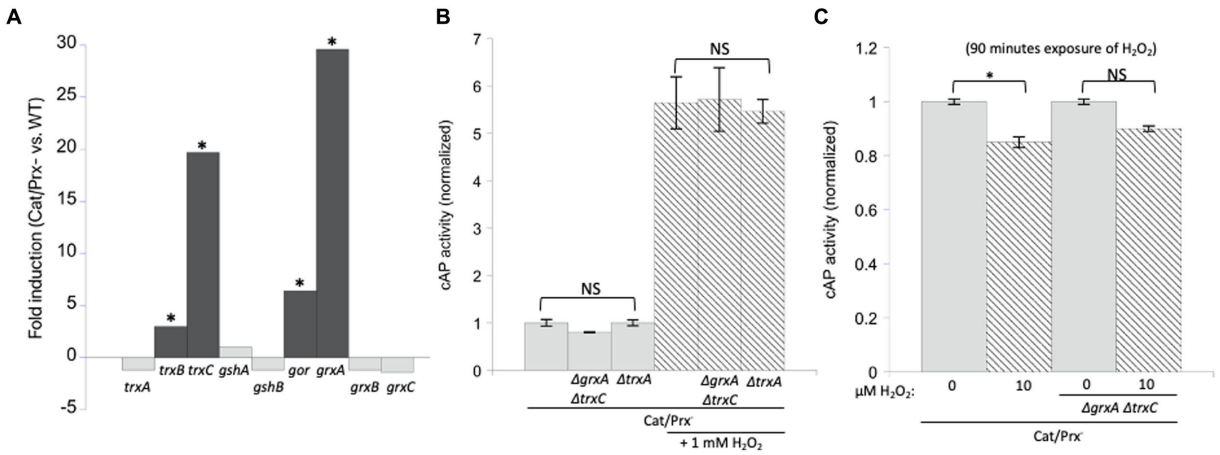

FIGURE 6
Glutaredoxin 1 (encoded by *grxA*) and thioredoxin 2 (*trxC*) are induced by H_2O_2 but are not needed to suppress H_2O_2-driven disulfide bonds. **(A)** RNA sequencing data showed that *grxA* and *trxC* are induced 30-and 20-fold, respectively, in an aerated catalase/peroxidase-strain compared to unstressed WT cells (Mancini and Imlay, 2015). The four redoxins in the dark gray bars are statistically significant. The FDR (false discovery rate adjusted *p*-values) is $<100^{-100}$ for *gor, grxA, trxB, and trxC*. **(B)** No increase in cAP activity was observed in catalase/peroxidase-mutants lacking Grx1 and Trx2. Where indicated, cells were exposed to 1 mM additional H_2O_2 for 40 min. Data are normalized to the catalase/peroxidase-mutant. **(C)** Catalase/peroxidase-and catalase/peroxidase-ΔgrxA *ΔtrxC* strains were exposed to 10 μM H_2O_2 over 90 min. Data have been normalized to the respective untreated samples. *** indicates that $p < 0.001$; ** indicates $p < 0.01$; * indicates $p < 0.05$; NS indicates $p > 0.05$.

was raised to 10 micromolar (Figure 6C). We also examined a mutant lacking Trx1, which appears to be the key disulfide reductase when disulfide bonds are introduced by agents such as diamide. It, too, had no impact upon cAP activity.

These results suggested that during H_2O_2 stress Grx1 and Trx2 provide an action other than the reduction of typical cysteine residues. OxyR-inducing doses of H_2O_2 are known to damage enzymes through two mechanisms: the destruction of [4Fe-4S] clusters in dehydratases, and the oxidation of Fe (Kawasaki et al., 2005) cofactors in mononuclear enzymes (Jang and Imlay, 2007; Anjem and Imlay, 2012; Figures 7A,B). As mentioned, the oxidation of the Fe (Kawasaki et al., 2005) cofactor in mononuclear enzymes causes the co-oxidation of any cysteine ligand. This occurs in the cases of both threonine dehydrogenase (Tdh) and peptide deformylase (Pdf), each of which has a single cysteine ligand that is quantitatively oxidized when H_2O_2 reacts with the iron atom. When these enzymes are isolated after H_2O_2 stress, *in vitro* or *in vivo*, they can be reactivated only if the cysteine residue is reduced so that iron can re-bind. Both DTT and TCEP suffice *in vitro* (Anjem and Imlay, 2012); we wondered whether Grx1 or Trx2 might serve this purpose *in vivo*. Accordingly, we tracked the activities of Tdh and Pdf when catalase/peroxidase mutants were cultured in aerobic medium. Under these conditions the steady-state level of enzyme activity represents the balance between damage and repair. Tdh activity declined by ~85% and Pdf activity by ~70% in the catalase/peroxidase mutant (Figure 7C). Strikingly, the additional absence of Grx1/Trx2 had no impact, indicating that they are not needed for the reactivation process.

Cluster oxidation in dehydratases yields an inactive [3Fe-4S] cluster that lacks its substrate-binding iron atom (Figure 7B). The repair of this damage requires the provision of an electron and then an atom of ferrous iron. This process occurs with a half-time of about 5 min *in vivo*, and it can be replicated *in vitro* by incubating the damaged enzyme with Fe (Kawasaki et al., 2005) and DTT (Djaman et al., 2004). Intriguingly, the reactivation does not succeed if a monothiol is substituted for DTT, suggesting that perhaps DTT not only provides an electron but additionally helps to rearrange the cluster-binding cysteine ligands during conversion from the [3Fe-4S] to the [4Fe-4S] form. If true, it seemed plausible that the redoxins might fulfill the DTT role *in vivo*. Isopropylmalate isomerase (Jang and Imlay, 2007) was examined. Again, activity was low in catalase/peroxidase mutants (Figure 7C). The absence of Grx1 and Trx2 had no further effect. It seems clear that these two redoxins are not needed for the repair of either of the two known families of H_2O_2-sensitive enzymes.

In a final effort to detect any value to Grx1 and Trx2 induction, we conducted a competition experiment in which a catalase/peroxidase Grx1-Trx2$^-$ mutant competed with its catalase/peroxidase Grx1$^+$ Trx2$^+$ sibling. Simple growth curves did not reveal apparent differences in either rate or final biomass of the two strains. A more sensitive approach is to mix the two strains and track their ratio over many generations of growth, using selective drug-resistance markers to distinguish them. We conducted the experiment both in LB medium and in a simple glucose medium; periodic dilutions kept the cell densities below 0.2 OD_{600} so that a slower strain would not have the opportunity to catch up in stationary phase. The data are shown in Figure 8.

In LB medium the two strains competed exactly evenly for 50 generations (Figure 8A). The mutant share of the population declined by <1%, indicating that over 50 generations its growth rate was >99.9% that of its GrxA$^+$ TrxC$^+$ parent. In the minimal glucose medium, in which cells were required to synthesize all their amino acids and cofactors, the *grxA trxC* mutant slightly but consistently outcompeted its GrxA$^+$ TrxC$^+$ parent (Figure 8B). This phenotype was absent from the catalase/peroxidase-proficient parent, showing that it depends upon H_2O_2 stress (Figure 8C). In the Discussion we suggest ideas to explain this contrarian result. In any case, it appears that Grx1 and Trx2 do not play important roles when cells are stressed with H_2O_2 under the standard growth conditions that we used.

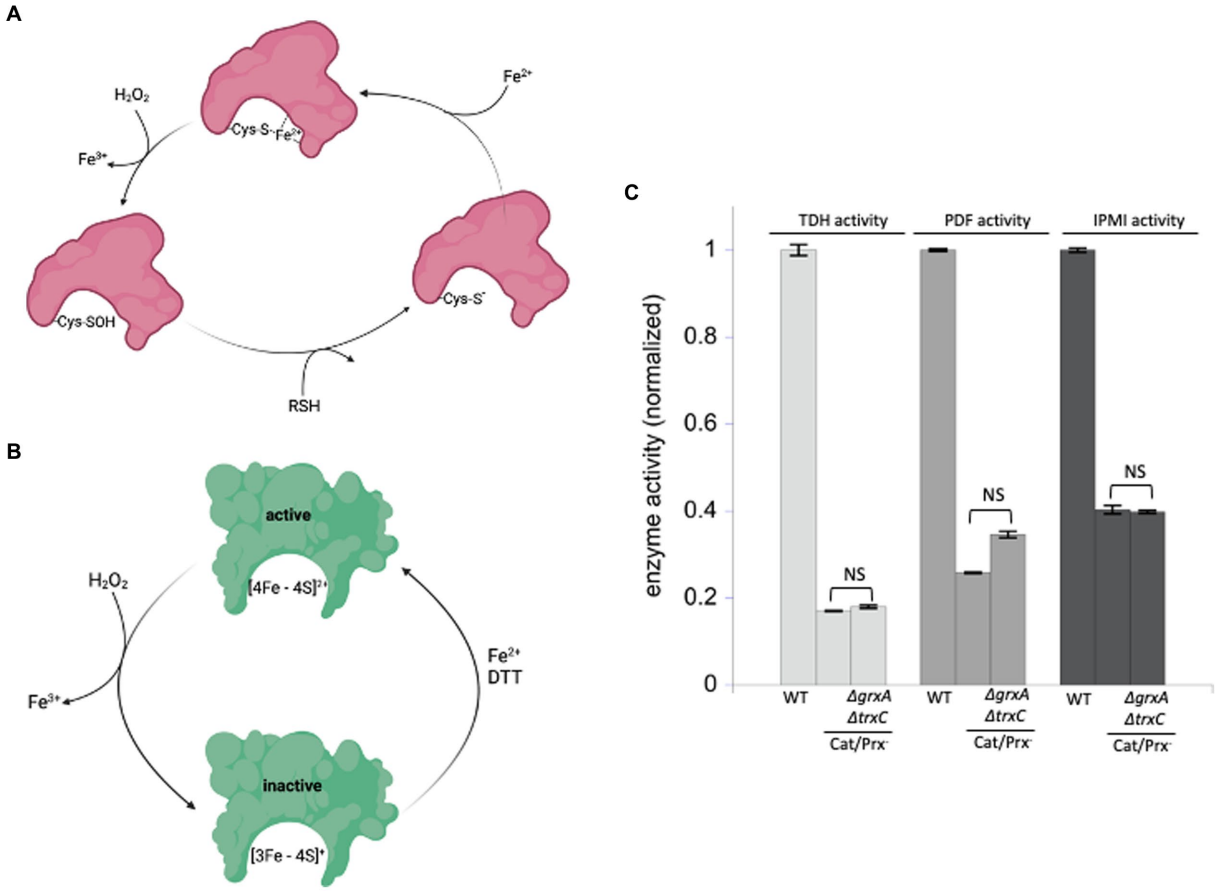

FIGURE 7
Glutaredoxin 1 and thioredoxin 2 do not aid in the repair of mononuclear iron enzymes or [4Fe-4S] cluster dehydratases. **(A)** Mononuclear iron enzymes are inactivated by H_2O_2. The coordinating cysteine ligand is concomitantly oxidized to a sulfenic acid; repair *in vitro* requires a thiol compound to reduce the sulfenate adduct prior to remetallation. **(B)** Dehydratase [4Fe-4S] clusters are oxidized by H_2O_2, and a dithiol compound is needed for cluster reactivation *in vitro*. **(C)** The mononuclear enzymes threonine dehydrogenase (TDH) and peptide deformylase (PDF), and the [4Fe-4S] dehydratase isopropylmalate isomerase (IPMI), were substantially inactivated by the ambient 1 μM H_2O_2 in catalase/peroxidase-mutants. Activities were not further diminished by the addition of *ΔgrxA ΔtrxC* mutations. Data have been normalized to the respective WT control. NS indicates $p > 0.05$.

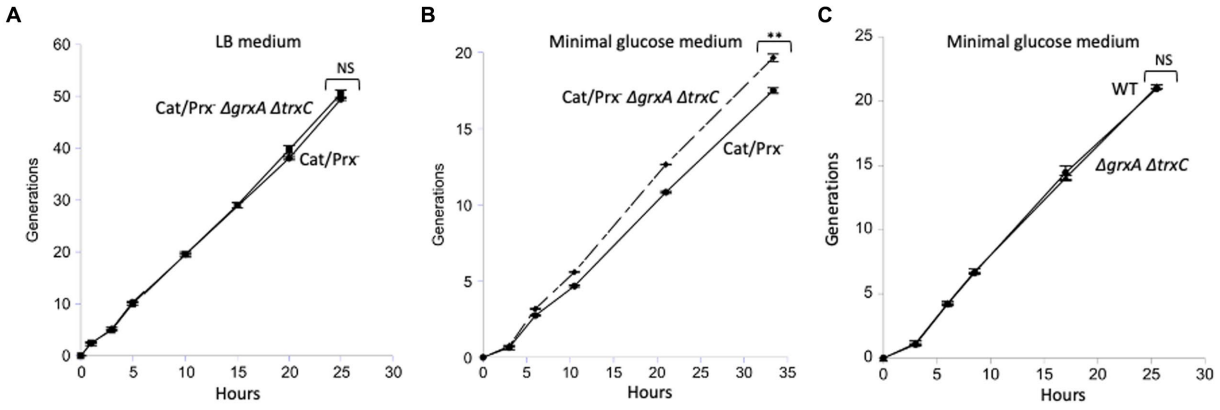

FIGURE 8
The *ΔgrxA ΔtrxC* mutations do not confer a growth disadvantage upon catalase/peroxidase-mutants. **(A)** Catalase/peroxidase-strains were cultured for 50 generations in LB medium. **(B)** The same strains were grown over 20 generations in minimal glucose medium; reproducibly, the *ΔgrxA ΔtrxC* mutants slightly outperformed the redoxin-proficient parent. **(C)** As a control, scavenging-proficient strains were cultured over 20 generations. ** indicates $p < 0.01$; * indicates $p < 0.05$; NS indicates $p > 0.05$.

Discussion

It has frequently been proposed that oxidative stress will generate protein disulfide bonds that can disable enzymes and aggregate proteins (McDuffee et al., 1997). In this study we applied forcing conditions in order to sharply elevate the intracellular concentrations of molecular oxygen, superoxide, hydrogen peroxide, and hydroxyl radicals in a model bacterium, but our analysis found little evidence for the oxidation of cysteine residues. *In vitro* experiments appear to explain this outcome, as they indicated that these oxidants react too slowly with typical protein thiols to constitute a threat during natural levels of stress.

In mammalian cells an indirect route of protein oxidation exists. Those cells contain glutathione peroxidase (Gpx), which scavenges hydrogen peroxide. In oxidant-stressed cells Gpx turnover produces oxidized glutathione, which through exchange reactions can introduce disulfide bonds into cellular proteins. However, in bacteria the primary scavenging enzyme is AhpCF, an NADH peroxidase, and so the Gpx-dependent pathway of disulfide bond formation is absent. Instead, any formation of disulfide bonds would depend upon the direct oxidation of thiols. Our *in vivo* data, however, showed little sign that oxygen species have this effect. We will consider each species in turn.

Reactive oxygen species do not oxidize thiols quickly

Molecular oxygen, a diradical species, is constrained to accept electrons one at a time from potential donors—and its univalent reduction potential (−0.16 V) is so low that this reaction must be slow (Imlay, 2013). The rate can be amplified by transition metals, and we and others have documented metal-driven oxidation of enzyme thiols *in vitro* and in the bacterial periplasm (Hiniker et al., 2005; Lippa and Goulian, 2012; Eben and Imlay, 2023). Copper in particular accelerates the reaction. However, efflux pumps successfully keep copper out of the bacterial cytoplasm, and iron, which is relatively abundant there, does not complex with thiols nearly as well.

From a thermodynamic view superoxide is a far stronger oxidant (Eo' = + 0.94 V) than molecular oxygen, but because it is already an anion at physiological pH, it is unable to accept another electron. Accordingly, the rate constant for its oxidation of N-acetylcysteine was measured to be only 67 M^{-1} s^{-1}; the mechanism of this reaction may not be simple electron transfer (Benrahmoune et al., 2000). Because superoxide dismutase keeps endogenous cytoplasmic O_2-scant (10^{-10} M), this rate constant is at least three orders of magnitude too low to threaten the status of cellular thiols. In contrast, O_2-is an efficient oxidant of metalloenzymes (10^4 M^{-1} s^{-1}), presumably because anionic O_2-forms a stable electrostatic complex with cationic iron cofactors (Kuo et al., 1987; Flint et al., 1993). It seems likely that a momentary protonation event then triggers electron transfer, thereby generating a Fe(III)-OOH species, which ultimately decomposes to Fe(III) and H_2O_2. Interestingly, when this reaction was studied in enzymes whose Fe(II) atoms are liganded by a cysteine residue, the cysteine ligand itself was left untouched by the nascent Fe(III)-OOH (Gu and Imlay, 2013). Therefore, the results of this work provide no mechanism by which superoxide could directly or indirectly oxidize cysteine moieties at a relevant rate *in vivo*.

The direct oxidation of thiol compounds by H_2O_2 is a divalent event, initiated when a thiolate anion attacks an oxygen atom. A sulfenic acid (RSOH) is formed, and a hydroxide anion is the leaving group. Thiol-based peroxidases and OxyR have evolved several features that optimize this reaction. It is believed that they place a cationic residue near the key cysteine to ensure it is deprotonated, provide a cavity that orients H_2O_2 for nucleophilic attack, polarize the oxygen–oxygen bond that must be split, and provide a proton donor to stabilize the hydroxide product. These adaptations allow cysteine oxidation to occur in seconds at sub-micromolar concentrations of H_2O_2. We wondered whether, absent these enhancements, standard thiols might still react with H_2O_2 at a meaningful rate, at least on a minute time scale at micromolar H_2O_2. This pace would entail a second-order rate constant for the thiolate of at least 1,000 M^{-1} s^{-1}. Instead, in our experiments we observed a far lower rate using N-acetylcysteine, and other studies of other thiol compounds reported rates that were similar. The cysteine residues in AP exhibited the same behavior. Enzymes whose chemistry is initiated by nucleophilic cysteine residues display rate constants that are higher—50 M^{-1} s^{-1} and 20 M^{-1} s^{-1} for *E. coli* glyceraldehyde-3-phosphate dehydrogenase and isocitrate lysase, respectively (Anjem and Imlay, 2012), and 10–20 M^{-1} s^{-1} for assorted eukaryotic tyrosine phosphatases (Denu and Tanner, 1998). But even these enzymes would exhibit an oxidation half-time in micromolar H_2O_2 of at least 2 h. The time would be even longer *in vivo*, where substrate competes for the active site.

In an effort to identify proteins with especially oxidizable cysteine residues, proteomic studies have typically imposed millimolar concentrations of H_2O_2 upon cells (Leichert and Jakob, 2004; Hochgrafe et al., 2005; Leichert et al., 2008; Wolf et al., 2008; Deng et al., 2013). Both the AP data, and consideration of fundamental rate constants, indicate that such an experimental design will cause most solvent-exposed cysteine residues to be oxidized. Indeed, such MS-based studies often identify hundreds of oxidized proteins. Consideration of the H_2O_2 levels in unstressed aerobic cells (50 nM) and in OxyR-activated stressed cells (1 μM) argues that millimolar H_2O_2 concentrations are hugely excessive and will detect oxidation events that are vanishingly rare in nature. Conversely, while a minor amount of protein disulfide bonds have been detected in unstressed cells, too, there is no evidence that these were generated by reduced oxygen species.

One mechanism of cysteine oxidation has been verified at physiological H_2O_2 concentrations. Rate constants are very high for Fenton reactions (10^4 M^{-1} s^{-1}) (Park et al., 2005), and the ferryl or hydroxyl radicals that they form are efficient oxidants of thiols (Davies, 2005). This chemistry was observed when low micromolar H_2O_2 inactivated the mononuclear enzymes peptide deformylase, threonine dehydrogenase, and cytosine deaminase (Anjem and Imlay, 2012). Each of those enzymes use cysteine, histidine, and aspartate residues to bind the Fe (Kawasaki et al., 2005) cofactor, and when H_2O_2 oxidizes the iron atom, the oxidation of the cysteine residue occurs concomitantly. However, the adventitious binding of loose iron to typical cysteine residues on protein surfaces would be far weaker and probably rare inside a cytoplasm that distributes its limited iron pool to many surfaces.

In our view these observations sufficiently explain why even supraphysiological levels of oxygen species were ineffective at

TABLE 1 Genes induced by OxyR during H_2O_2 stress in *E. coli*.

Gene	Activity	Fold induction in Hpx- vs. WT	Role during H_2O_2 stress	H_2O_2 phenotype?
trxC	Thioredoxin 2	20.	Unknown	**No**
trxB	Thioredoxin reductase	3.0	Reduce Trx2	**No**
grxA	Glutaredoxin 1	30.	Reduce OxyR	**No**
gor	Glutathione reductase	6.4	Reduce Grx1	**No**
ahpCF	NADH peroxidase	20.[a]	Scavenge H_2O_2	Yes
katG	Catalase	57.	Scavenge H_2O_2	Yes
ccp	Cytochrome *c* peroxidase	10.[b]	Use H_2O_2 as a terminal electron acceptor	Yes
dps	Mini ferritin	9.0	Sequester iron	Yes
fur	Repressor for iron import	3.1	Repress iron import	Yes
yaaA	Unknown	15.	Minimize free iron	Yes
clpSA	Protease adapter protein	4.1	Activate Fe-S enzymes	Yes
sufABCDE	Fe-S assembly	16.	Fe-S cluster assembly	Yes
hemF	Coproporphyrinogen III oxidase	5.7	Heme synthesis	Yes
hemH	Ferrochelatase	14.	Heme synthesis	Yes
mntH	Manganese importer	8.6	Activate mononuclear Fe enzymes	Yes
xthA	Exonuclease III	5.0[c]	DNA repair	Yes
oxyS	Non-coding RNA	261.	Unknown	Untested
flu	Antigen 43	53.	Cell adhesion	Untested

Hpx-means that this strain is deficient in scavenging hydrogen peroxide (ΔkatG ΔkatE ΔahpCF). For an extended discussion of the roles of these proteins, see publication: (Sen and Imlay, 2021). References for table: [a]Zheng et al. (2001), [b]Khademian and Imlay (2017), [c]Gupta and Imlay (2021), rest of table: Mancini and Imlay (2015). Bolded genes are induced by OxyR and do no exhibit a phenotype under H_2O_2 stress.

oxidizing AP thiols in our cell experiments. We must look for alternative reasons that the cell induces Grx1 and Trx2 when it senses H_2O_2 stress.

Why does OxyR induce glutaredoxin 1 and thioredoxin 2?

Of course, OxyR does not induce glutaredoxin 1 and thioredoxin 2 for no reason—so we were surprised by our inability to observe any phenotype for *grxA* and *trxC* deletions during H_2O_2 stress. This failure stands in complete contrast to other members of the OxyR regulon. The products of *katG*, *ahpCF*, *xthA*, *dps*, *clpSA*, *fur*, *yaaA*, *mntH*, *sufABCDE*, *hemF*, *hemH*, and *ccp* either sustain the activities of oxidant-sensitive enzymes or protect the DNA during periods of H_2O_2 stress; accordingly, growth and/or survival defects were apparent when any of these mutations were introduced into catalase/peroxidase mutants. Not so with *grxA* and *trxC* (Table 1).

This result has forced us to consider several possibilities, and these are discussed below. One is that Grx1 and Trx2 are involved in repairing metalloenzymes but that alternative routes of reduction are available in well-fed cells. Both cysteine and glutathione suffice to reduce these adducts *in vitro*, and if the levels of these thiols are high in our growing cultures, then the roles of specialized redoxins may be obscured. The other redoxins (Trx1, Grx2, and Grx3) might similarly compensate. More broadly, it is possible that rapid growth *per se* compensates for damage to an enzyme population, by rapidly replacing them through ongoing synthesis. If true, perhaps a defect may emerge when cells are carbon-limited or in stationary phase. Indeed, one study reported that thioredoxin 1 (*trxA*) is induced at low growth rates via the stringent response, as if nutritional inadequacy somehow requires a boost in redoxin activity (Lim et al., 2000).

Alternatively, these redoxins may not be generalists, like Trx1, but may have specific client proteins whose function happens to be expendable in our growth medium. Precedents exist: AhpF is dedicated to the reduction of AhpC, and NrdH acts exclusively upon the NrdEF ribonucleotide reductase. The AhpF and NrdH disulfide reductases are encoded by genes in a common operon with their target proteins; in contrast, the *grxA* and *trxC* genes are each monocistronic, providing no hint of a co-evolved partner.[1] Nevertheless, Grx1 has been identified as the primary reductant of OxyR, and so its induction during H_2O_2 stress may provide a quick way to turn off the response once H_2O_2 levels decline (Aslund et al., 1999). Further, Potamitou et al. observed that Trx2 levels are high in some mutants defective in Grx1 function and that Grx1 levels are high in other mutants lacking Trx2 (Potamitou et al., 2002). A parsimonious explanation would be that Grx1 and Trx2 collaborate in turning off OxyR, which regulates them both. Yet it seems improbable that the cell induces two redoxin systems merely to accomplish this task.

In a recent study Winterbourn and colleagues observed that H_2O_2 rapidly oxidizes the active-site cysteine of mammalian glyceraldehyde-3-phosphate dehydrogenase (GAPDH), specifically when solution levels of carbon dioxide are high. The rate they observed approaches the rates at which H_2O_2 damages metalloenzymes, so this reaction

1 https://ecocyc.org

should be biologically relevant. The effect, however, may be specific to this particular mammalian enzyme. They inferred that HCO_4^-, the oxidizing species, is formed by reaction between H_2O_2 and CO_2 within the enzyme, enabling it to quickly oxidize the key thiol and redirect carbon flux from glycolysis to the NADPH-generating pentose-phosphate pathway (Winterbourn et al., 2023). That metabolic strategy may make sense in mammalian cells, which use NADPH as the ultimate electron donor for H_2O_2 scavenging, but it would be pointless for *E. coli*, which relies upon NADH. In fact, in a previous study we measured a rate constant for *E. coli* GAPDH inactivation by H_2O_2 of only 50 M^{-1} s^{-1} in anoxic buffer that had equilibrated with a CO_2-rich (5%) atmosphere (Anjem and Imlay, 2012).

A very different notion is that the OxyR regulon moonlights as a defense against electrophiles other than H_2O_2. In this view *grxA* and *trxC* were incorporated into the regulon in order to reduce disulfide bonds created not by H_2O_2 but by other disulfide-generating stressors. Such compounds might include neutrophil-generated species such as hypochlorous acid (HOCl), hypothiocyanous acid (HOSCN), and nitric oxide (NO). The high efficiency with which these chemicals attack protein thiols would predispose them to activate the OxyR transcription factor. One piece of supporting evidence comes from bacteria that use PerR rather than OxyR to turn on H_2O_2 defenses. The PerR transcription factor is triggered not by oxidation of a sensory thiol but by the oxidation of a prosthetic iron atom, in a Fenton-type reaction—an event that seems likely to be H_2O_2-specific (Lee and Helmann, 2006). PerR regulons include familiar H_2O_2 defenses like AhpCF and catalase and the miniferritin Dps, but they do not usually include thioredoxins and glutaredoxins (Sen and Imlay, 2021). Instead, PerR-containing organisms often control redoxin synthesis using separate transcription factors that seem to be activated specifically by disulfide stress. The SigR-RsrA system of *Streptomyces coelicolor* and the Spx systems of *Bacillus subtilis* and *Staphylococcus aureus* have been most closely studied (Kang et al., 1999; Nakano et al., 2003). Workers discovered those regulons by exposing cells to diamide, a synthetic chemical (Kosower et al., 1969) designed to generate intracellular disulfide bonds; H_2O_2 is not an effective trigger for these regulons, and the natural inducers remain unknown. The separation of disulfide and H_2O_2 responses in these bacteria seems to support our conclusion that these phenomena can be unlinked.

In sum, our results suggest that we know a little bit less about disulfide stress than we thought we did. Superoxide and hydrogen peroxide are not potent producers of disulfide bonds. Thioredoxins and glutaredoxins are certainly required for routine electron delivery to a short list of enzymes, but their long-suspected role in suppressing adventitious disulfide bonds has not been confirmed. Either these proteins have a role that we have not yet imagined, or else they become important under a growth condition other than the ones we examined. Further study is warranted.

Materials and methods

Chemicals

Medium and buffer components were purchased from Fisher Chemical. Amino acids, casamino acids (acid-hydrolyzed), copper sulfate, ferrous ammonium sulfate, cytochrome *c*, horseradish peroxidase (HRP), Amplex Red, hydrogen peroxide solution (30% w/w), bovine catalase, ascorbic acid, ovalbumin, β-mercaptoethanol, N-acetylcysteine, bovine superoxide dismutase, reduced (GSH) and oxidized (GSSG) glutathione, *E. coli* alkaline phosphatase (catalog P5931), ascorbate, p-nitrophenylphosphate, zinc(II) diacetate, guanidinium HCl, citraconate, diethylenetriaminepentaacetic acid (DTPA), EDTA, NADH, NAD^+, recombinant *E. coli* formate dehydrogenase (FDH), rabbit L-lactate dehydrogenase, xanthine, bovine xanthine oxidase, and antibiotics were from Sigma Aldrich. Coomassie reagent was from Thermo Scientific. Formyl-Met-Ala-Ser was from Bachem.

Strains and plasmids

The full list of strains and plasmids can be found in Supplementary Table S1. Null mutations were made using the lambda red recombinase method to replace the open reading frame (Gebendorfer et al., 2012) with a chloramphenicol resistance cassette amplified from the pKD3 template (Datsenko and Wanner, 2000). P1 transduction was used to introduce mutations into new strains (Miller, 1972). All mutations were verified by PCR and gel analysis.

Growth conditions

Strains were grown at 37°C in either M9 medium or minimal A medium (Miller, 1972) containing 0.2% glucose, 0.2% casamino acids, 0.5 mM histidine, 0.5 mM tryptophan, 0.5 mM thiamine, 0.01% $MgSO_4$, and 0.01% $CaCl_2$, unless otherwise noted. The growth medium was supplemented with 200 μg/mL ampicillin to maintain pAID135. Cultures grown aerobically were shaken vigorously. Where indicated, cultures were bubbled with 22% or 100% oxygen from an O_2 or air gas tank with the aid of a frit.

Experiments under anoxic conditions were conducted inside an anaerobic Coy chamber. The reagents were moved into the chamber while still hot (from autoclaving) to minimize dissolved oxygen, and they were further stored overnight in the chamber to enable further degassing.

Experiments were conducted with log-phase cultures. Cells were grown overnight, subcultured to low densities (~0.0125 OD_{600}), and grown for at least three generations before dilution into stress conditions for subsequent measurements. Cell density was tracked by absorbance at 600 nm.

H_2O_2 measurement assay

The Amplex Red (AR)/horseradish peroxidase (HRP) assay was used to track the disappearance of H_2O_2 when reacting with thiols (N-acetylcysteine; NAC). The HRP reaction was set up as described in Li and Imlay (2018). The excitation and emission wavelengths used to measure fluorescence using a Shimadzu RF-150 fLuorometer were 520 and 620 nm, respectively. The buffer was 50 mM KPi, pH 8.0. All reagents were dissolved and diluted in 50 mM KPi, pH 8.0.

Preparation of reduced alkaline phosphatase *in vitro*

To prepare *E. coli* alkaline phosphatase (AP) that was reduced and inactive, the purified enzyme (200 U, 4 mg) in 50 mM Tris, pH 8.0, was denatured with 3.6 M guanidinium HCl and reduced with 25 mM β-mercaptoethanol under aerobic conditions, as described (Eben and Imlay, 2023). The AP solution was then transferred to the anaerobic chamber and held in an incubator at 37°C overnight. Activity was checked the next day. If activity was not fully eliminated, incubation was continued at 37°C. The guanidinium HCl and β-mercaptoethanol were then removed using an Amicon Ultra-0.5 (Millipore) Centrifugal Filter Device. The denatured AP (400 µL) was loaded onto a 30 kD spin column, and the samples were centrifuged at 14,000 × g at RT for 15 min, leaving 40 µL of sample. The filtrate was discarded, and 400 µL of anoxic folding buffer was added (1 mM $ZnAc_2$, 1 mM $MgCl_2$, 100 mM Tris, pH 8). The column was re-centrifuged as above. For protein collection, the column was then inverted and centrifuged into a fresh tube, 1,000 × g for 2 min. The volume was adjusted to 400 µL with folding buffer. The reduced, inactive enzyme typically retained ~0.1% of the original activity. It was stored on ice in the anaerobic chamber to avoid activation in air; it was stable in this form for at least 1 month.

Activation of purified AP

Stock solutions of 100 mM copper sulfate and 50 mM GSSG were prepared in water. H_2O_2 stocks were made fresh daily and also diluted in water.

Unless otherwise indicated, reduced AP (diluted 1:50) was exposed to oxidizing agents in 100 mM Tris, pH 8, at 37°C. This reaction mixture also included 10 mM $MgCl_2$ and 10 mM Zn (Kawasaki et al., 2005) diacetate, as zinc is a cofactor of AP. Unless otherwise indicated, reactions were conducted in air-equilibrated buffer. Where indicated, reactions included 20 U/mL superoxide dismutase and/or 30 U/mL catalase. At time points 50 µl aliquots were removed to 1 mL 1 mM p-nitrophenylphosphate in 1 M Tris, pH 8. AP activity was measured based on its ability to hydrolyze p-nitrophenylphosphate to p-nitrophenol, a chromogenic product that absorbs at 405 nm (Bessey et al., 1946). All reactants were incubated with reduced AP at 37°C, and AP was assayed at different time points at room temperature.

To test the ability of Fe (Kawasaki et al., 2005)/oxygen to activate the enzyme, 10 mM of ferrous ammonium sulfate were prepared in water and then diluted into the reaction with reduced AP.

Activation by superoxide was tested using xanthine oxidase as the superoxide source. Xanthine oxidase was diluted 1:200 from the stock suspension (from bovine milk) shortly before use. A stock of 1 mM of xanthine was prepared in 50 mM Tris, pH 8.0, and stored at room temperature; it was diluted to 50 µM in the AP reaction. The rate of O_2-production was measured using cytochrome *c*, and the xanthine oxidase amount was adjusted so O_2-was generated at 2 µM/min. After 15 min, another bolus of 50 µM xanthine was added to extend the reaction. AP activity was measured at different time points.

Activation of AP with iron and ascorbate was tested in air-saturated buffer. Stock solutions of 10 mM ferrous ammonium sulfate and 100 mM ascorbate were prepared in 1 M Tris, pH 8.0. Fifty µM of ferrous ammonium sulfate and 10 mM of ascorbate were added to reduced AP, and activity was determined at intervals.

Hydrogen peroxide was also tested. H_2O_2 stock solution (30%) was diluted in water immediately before the experiment. Enzyme exposure to H_2O_2 occurred before adding zinc and magnesium. One mM $ZnAc_2$ and 1 mM $MgCl_2$ were added to the cuvette and incubated for 2 min before assaying. The assay buffer was 1 M Tris, pH 8.0. Time points were taken periodically.

Activation of alkaline phosphatase in the cytoplasm

A leaderless *phoA* construct (*phoA* Δ2–22) encodes a form of alkaline phosphatase that has been used to detect disulfide bond formation in the *E. coli* cytoplasm (Derman et al., 1993). Without its signal sequence, AP accumulates in the cytoplasm, and only a tiny fraction is exported to the periplasm (Eben and Imlay, 2023). AP is only active when it acquires disulfide bonds; once those bonds are formed AP folds around them, stabilizing them against potential reductants during continued culture, cell harvesting, and extract preparation (Akiyama and Ito, 1993). AP is expressed from a pBR322-based plasmid (pAID135; Derman et al., 1993) which is ampicillin-resistant, and the *phoA* gene is under the control of a *tac* promotor. We observed that it was not necessary to induce the *tac* promoter to establish sufficient AP synthesis for our purpose, and so we did not do so, preferring steady AP production.

H_2O_2 and other potential oxidative stressors were added to the growth medium as described in experimental captions. To quantify AP activity inside cells, 15–20 mL of culture (at *ca.* 0.1 OD_{600}) was centrifuged, resuspended in ice-cold lysis buffer (20 mM aerobic Tris pH 8.0, 10 mM EDTA), re-centrifuged, resuspended in 1 mL lysis buffer, and lysed by passage through a French press. The extract was clarified by centrifugation (17,000 × g for 20′) and then diluted 1:10 into post-lysis buffer (10 mM $MgCl_2$, 10 mM Zn(II) diacetate, 1 M Tris pH 8.0). The extract was incubated for ~10 min at RT for remetallation. Then 100 µL was assayed for AP activity as above. These steps were performed using air-saturated buffers. A Bradford assay (Thermo Scientific) was used to determine the total protein concentration, with ovalbumin as the protein standard.

Activation of cAP in an Hpx⁻strain

Cells were grown overnight in an anaerobic chamber in minimal A medium with 0.2% glucose, 0.5 mM casamino acids, 0.5 mM tryptophan, and 200 µg/mL ampicillin. The next day cells were subcultured in the same anoxic medium and grown from OD_{600} 0.0125–0.1, subcultured again to OD_{600} 0.0125, and shaken vigorously under oxic conditions for 3 h. Cells were then harvested and cAP activity was determined.

In some experiments H_2O_2 was added to 10 µM. In this case the overnight cultures were diluted to OD_{600} of 0.05, grown anaerobically to an OD_{600} of 0.2, and then subcultured to OD_{600}

0.025 in air-saturated medium. The H_2O_2 was then added, and flasks were shaken vigorously under oxic conditions. Because H_2O_2 is a pseudosubstrate for the respiratory cytochrome oxidases, slow H_2O_2 consumption occurs in the Hpx-strain despite the absence of dedicated catalase and peroxidase enzymes. To compensate, the H_2O_2 concentration was measured at intervals and periodically augmented to restore the level to 10 μM. Concentrations were not allowed to fall below 8 H_2O_2. After 90 min the cells were harvested and cAP activity was determined.

Activation of cAP in a SOD⁻strain

Cells were grown overnight in an anaerobic chamber in minimal A medium with 0.2% glucose, 0.5 mM casamino acids, 0.5 mM tryptophan, and 200 μg/mL ampicillin. The overnight culture was diluted in the anaerobic chamber and cultured from OD_{600} 0.0125 to 0.1; it was then subcultured to OD_{600} 0.05 in air-saturated medium and shaken vigorously under oxic conditions for 40 min. The cellular cAP activity was then determined.

Assay of threonine dehydrogenase

Threonine dehydrogenase is a mononuclear Fe (Kawasaki et al., 2005) enzyme that is inactivated when cellular levels of H_2O_2 rise. Cells were grown overnight in an anaerobic chamber in minimal A medium with 1% casamino acids (acid-hydrolyzed), 0.5 mM tryptophan, and then precultured from OD_{600} 0.0125 to 0.1. Cells were then inoculated into the same air-saturated medium and grown from OD_{600} 0.006 to 0.1 in the same aerobic medium. Fifty mL of culture was harvested. Cells were centrifuged aerobically at 6,000 rpm for 10 min at 4°C. Pellets were then moved into an anaerobic chamber, washed with ice-cold anoxic 50 mM Tris pH 8.4, and centrifuged. Pellets were then resuspended in 1 mL ice-cold lysis buffer (50 mM Tris pH 8.4, 30 mM threonine, 0.1 mM DTPA) and lysed by sonication, still inside the anaerobic chamber. Threonine was included in the lysis buffer to stabilize the iron atom in the active site. The lysate was then assayed at 340 nm for 10 min in 500 μL cuvettes, which were capped to allow anoxia to continue when cuvettes were moved outside the chamber to the spectrophotometer. The assay buffer was the same as the lysis buffer. The NAD^+ was prepared in anoxic buffer, and 1 mM NAD^+ was used in the assay.

Assay of peptide deformylase

Peptide deformylase is an essential Fe (Kawasaki et al., 2005) enzyme that removes the formyl moiety from the N-terminal formylmethionine of nascent proteins. Cells were grown overnight in an anaerobic chamber in minimal A medium with 0.2% glucose, 0.2% casamino acids, and 0.5 mM tryptophan. The overnight cultures were diluted in the same anoxic medium to OD_{600} 0.0125 and cultured to OD_{600} 0.1. Cells were then diluted into the same air-saturated medium to OD_{600} 0.0125 and grown to 0.2. Fifty milliliter of culture was harvested. Cells were moved into an anaerobic chamber, centrifuged for 5 min at 6,000 rpm at 4°C, and pellets were resuspended in ice-cold anoxic 50 mM Hepes, pH 7.5, with 25 mM NaCl. Cells were resuspended in 1 mL of the same buffer and sonicated. Cell lysates were centrifuged for 2 min at 14,000 rpm at 4°C to remove debris. Lysates were then assayed at 340 nm for 10 min in 500 μL cuvettes with caps at room temperature. Reagents for the assay were prepared fresh anoxically. A typical assay consisted of 5 mM NAD^+, 1 unit of formate dehydrogenase, and 1 mM formyl-Met-Ala-Ser tripeptide as substrate. The reaction progress was tracked by coupling formate release to NADH oxidation by formate dehydrogenase. Activity was tracked by absorbance at 340 nm.

Assay of serine deaminase

Serine deaminase is a dehydratase dependent upon its [4Fe-4S] cluster; it converts serine into pyruvate and NH_4^+. Cells were grown in minimal A medium containing 0.2% glucose and 0.5 mM 18 amino acids. Overnight cultures in the anaerobic chamber were diluted to anoxic medium and grown from OD_{600} 0.0125 to 0.1. They were then diluted to OD_{600} 0.0125 in the same air-saturated medium and grown to 0.1. Fifty milliliter of culture was transferred to the anaerobic chamber. Cells were centrifuged for 8.5 min at 7,000 rpm at 4°C, and the pellet was resuspended in ice-cold anoxic 0.15 M Tris, pH 8.0, and re-centrifuged. Finally, cells were resuspended in 1 mL of the same anoxic buffer and sonicated. The lysate was centrifuged for 20 min at 4°C at 14 K rpm to remove debris. Cell extracts were assayed for 10 min in 500 μL cuvettes with caps at room temperature. A typical assay consisted of 0.15 M Tris buffer, pH 8.0, 100 mM serine, 100 μM NADH, and 10 μL LDH of a 1:100 stock. The reaction progress was tracked by coupling pyruvate formation to NADH oxidation by lactate dehydrogenase; NADH oxidation was monitored at 340 nm. NADH and LDH were prepared fresh. Serine was stored in the anaerobic chamber.

Assay of isopropylmalate isomerase

Isopropylmalate isomerase is a dehydratase whose activity requires an intact oxidant-sensitive [4Fe-4S] cluster. Activity was measured by its action upon a pseudo substrate, citraconate. Cells were grown in minimal A medium with 0.2% glucose, 0.5 aromatic amino acids, and 0.5 mM histidine. Aromatic amino acids were provided to circumvent the inactivating effect of H_2O_2 upon the aromatic biosynthetic pathway (Sobota et al., 2014); histidine was provided because some MG1655 strains exhibit an anaerobic histidine bradytrophy. Anaerobic overnight cultures were diluted to 0.005 OD_{600} and grown anaerobically to 0.1 OD_{600}. At that time the flasks were aerated and shaken vigorously for 2 h. Cells were then centrifuged aerobically at 4°C; the pellet was then moved to the anaerobic chamber, and all subsequent steps were performed in the anaerobic chamber with anoxic solutions. The cell pellet was resuspended in ice-cold 100 mM Tris, pH 7.6, centrifuged again, and finally resuspended in 1 mL of the same buffer. Cells were lysed by sonication, and the cell debris was removed by centrifugation at 14,000 rpm for 5 min. IPMI was promptly assayed at 235 nm in an anoxic reaction at room temperature. The enzyme gradually loses

activity during storage (Jang and Imlay, 2007), so assays were performed shortly after cell lysis. Citraconate (20 mM) was used as a substrate; it was always freshly prepared, and it was dissolved in anoxic 100 mM Tris, pH 7, which was also used as the reaction buffer.

Competition experiments

Cells were grown either in LB or M9 medium containing 0.2% glucose and 0.5 mM histidine. Overnight cultures and precultures were grown in the anaerobic chamber. Precultures were grown for at least three generations from OD_{600} 0.0125 to 0.1–0.2. Cultures grown in LB were then inoculated to OD_{600} 0.0001 in air-saturated medium, and cultures grown in M9 medium were inoculated to a starting OD_{600} of 0.001. The competing strains were mixed 1:1. Overall growth was monitored by tracking OD_{600}; cultures were diluted before reaching OD_{600} of 0.3, so that the competition continued for many generations under exponential growth conditions. At different time points, aliquots were moved into the anaerobic chamber, diluted, and spread onto LB plates containing 0.2% glucose and either 12 μg/mL tetracycline or 10 μg/mL chloramphenicol, in order to quantify the viable cell number of each strain. Plates were incubated overnight at 37°C in the anaerobic chamber, and colonies were counted the next day.

Illumina RNA sequencing

Precultures were grown in the anaerobic chamber in glucose medium to $OD_{600} \sim 0.1$. Cells were centrifuged 5 min at 7,000 × *g*, and pellets were resuspended in fresh oxic medium to obtain an initial $OD_{600} \sim 0.005$. Cultures were incubated aerobically with vigorous shaking until they reached an $OD_{600} \sim 0.1$–0.15. Total RNA was isolated from cells by hot phenol extraction (Mancini and Imlay, 2015).

Calculations

For second-order reactions, the half-life of a reactant (with the second reactant concentration remaining constant) is described by a simple exponential equation: $Ln(0.5) = -k[R_2]t_{1.2}$, where k is the rate constant, $[R_2]$ represents the concentration of the second reactant, and $t_{1.2}$ is the half-life. E.g., if the rate constant for N-acetylcysteine oxidation by H_2O_2 is 2.3 M^{-1} s^{-1}, and the H_2O_2 concentration is 1 μM, then the half-time for NAC oxidation is 3×10^5 s, or 84 h.

The steady-state concentration of O_2-can be calculated by setting the measured rate of O_2-formation equal to the rate of spontaneous dismutation (Imlay and Fridovich, 1991). The latter = $k[O_2^-][HO_2]$, where $k = 8 \times 10^7$ M^{-1} s^{-1}. The pKa of superoxide is 4.8, so at pH 8 the concentration of protonated superoxide $[HO_2] = 6.3 \times 10^{-4}$ $[O_2^-]$. Therefore, if the measured rate of O_2-production is 2 μM/min, the steady-state O_2-concentration is 0.8 μM.

Error bars in this paper represent the SEM of triplicate measurements. Error bars in this paper represent the SEM of triplicate measurements. Tests for statistical significance were conducted by unpaired *t*-tests using GraphPad software.[2] *** indicates that $p < 0.001$; ** indicates $p < 0.05$; * indicates $p < 0.05$; NS indicates $p > 0.05$.

Data availability statement

The original contributions presented in the study are included in the article/Supplementary material, further inquiries can be directed to the corresponding author.

Author contributions

SE: Conceptualization, Investigation, Methodology, Writing – original draft, Writing – review & editing. JI: Funding acquisition, Resources, Writing – review & editing.

Funding

The author(s) declare financial support was received for the research, authorship, and/or publication of this article. This work was supported the National Institutes of Health (grant no. GM49640).

Acknowledgments

We thank Jon Beckwith (Harvard Medical School) for providing pAID135, which enabled us to track the activity of alkaline phosphatase that is restricted to the cytoplasm.

Conflict of interest

The authors declare that the research was conducted in the absence of any commercial or financial relationships that could be construed as a potential conflict of interest.

Publisher's note

Supplementary material

The Supplementary material for this article can be found online at: https://www.frontiersin.org/articles/10.3389/fmicb.2023.1305973/full#supplementary-material

2 https://www.graphpad.com

References

Akiyama, Y., and Ito, K. (1993). Folding and assembly of bacterial alkaline phosphatase *in vitro* and *in vivo*. *J. Biol. Chem.* 268, 8146–8150. doi: 10.1016/S0021-9258(18)53073-8

Andrei, A., Öztürk, Y., Khalfaoui-Hassani, B., Rauch, J., Marckmann, D., Trasnea, P.-I., et al. (2020). Cu homeostasis in bacteria: the ins and outs. *Membranes* 10:242. doi: 10.3390/membranes10090242

Anjem, A., and Imlay, J. A. (2012). Mononuclear iron enzymes are primary targets of hydrogen peroxide stress. *J. Biol. Chem.* 287, 15544–15556. doi: 10.1074/jbc.M111.330365

Anjem, A., Varghese, S., and Imlay, J. A. (2009). Manganese import is a key element of the OxyR response to hydrogen peroxide in *Escherichia coli*. *Mol. Microbiol.* 72, 844–858. doi: 10.1111/j.1365-2958.2009.06699.x

Aruoma, O. I., Halliwell, B., Hoey, B. M., and Butler, J. (1989). The antioxidant action of N-acetyl cysteine: its reaction with hydrogen peroxide, hydroxyl radical, superoxide, and hypochlorous acid. *Free Radic. Biol. Med.* 6, 593–597. doi: 10.1016/0891-5849(89)90066-X

Aslund, F., Zheng, M., Beckwith, J., and Storz, G. (1999). Regulation of the OxyR transcription factor by hydrogen peroxide and the cellular thiol-disulfide status. *Proc. Natl. Acad. Sci. U. S. A.* 96, 6161–6165. doi: 10.1073/pnas.96.11.6161

Bedard, K., Lardy, B., and Krause, K.-H. (2007). NOX family NADPH oxidases: not just in mammals. *Biochimie* 89, 1107–1112. doi: 10.1016/j.biochi.2007.01.012

Benrahmoune, M., Thérond, P., and Abedinzadeh, Z. (2000). The reaction of superoxide radical with N-acetylcysteine. *Free Radic. Biol. Med.* 29, 775–782. doi: 10.1016/S0891-5849(00)00380-4

Bessey, O. A., Lowry, O. H., and Brock, M. J. (1946). A method for the rapid determination of alkaline phosphates with five cubic millimeters of serum. *J. Biol. Chem.* 164, 321–329.

Carmel-Harel, O., and Storz, G. (2000). Roles of the glutathione-and thioredoxin-dependent reduction systems in the *Escherichia coli* and *Saccharomyces cerevisiae* responses to oxidative stress. *Annu. Rev. Microbiol.* 54, 439–461. doi: 10.1146/annurev.micro.54.1.439

Choi, H., Kim, S., Mukhopadhyay, P., Cho, S., Woo, J., Storz, G., et al. (2001). Structural basis of the redox switch in the OxyR transcription factor. *Cells* 105, 103–113. doi: 10.1016/S0092-8674(01)00300-2

Chow, M. S., Liu, L. V., and Solomon, E. I. (2008). Further insights into the mechanism of the reaction of activated bleomycin with DNA. *Proc. Natl. Acad. Sci. U. S. A.* 105, 13241–13245. doi: 10.1073/pnas.0806378105

Christman, M. F., Morgan, R. W., Jacobson, F. S., and Ames, B. N. (1985). Positive control of a regulon for defenses against oxidative stress and some heat-shock proteins in *Salmonella typhimurium*. *Cells* 41, 753–762. doi: 10.1016/S0092-8674(85)80056-8

Cleland, W. W. (1964). Dithiothreitol, a new protective reagent for SH groups*. *Biochemistry* 3, 480–482. doi: 10.1021/bi00892a002

Datsenko, K. A., and Wanner, B. L. (2000). One-step inactivation of chromosomal genes in *Escherichia coli* K-12 using PCR products. *Proc. Natl. Acad. Sci. U. S. A.* 97, 6640–6645. doi: 10.1073/pnas.120163297

Davies, M. J. (2005). The oxidative environment and protein damage. *Biochim. Biophys. Acta* 1703, 93–109. doi: 10.1016/j.bbapap.2004.08.007

Delaunay, A., and AI Toledano, M. B. (2000). H_2O_2 sensing through oxidation of the Yap1 transcription factor. *EMBO J.* 19, 5157–5166. doi: 10.1093/emboj/19.19.5157

Deng, X., Weerapana, E., Ulanovskaya, O., Sun, F., Liang, H., Ji, Q., et al. (2013). Proteome-wide quantification and characterization of oxidation-sensitive cysteines in pathogenic bacteria. *Cell Host Microbe* 13, 358–370. doi: 10.1016/j.chom.2013.02.004

Denu, J. M., and Tanner, K. G. (1998). Specific and reversible inactivation of protein tyrosine phosphatases by hydrogen peroxide: evidence for a sulfenic acid intermediate and implications for redox regulation. *Biochemistry* 37, 5633–5642. doi: 10.1021/bi973035t

Depuydt, M., Leonard, S. E., Vertommen, D., Denoncin, K., Morsomme, P., Wahni, K., et al. (2009). A periplasmic reducing system protects single cysteine residues from oxidation. *Science* 326, 1109–1111. doi: 10.1126/science.1179557

Derman, A. I., and Beckwith, J. (1991). *Escherichia coli* alkaline phosphatase fails to acquire disulfide bonds when retained in the cytoplasm. *J. Bacteriol.* 173, 7719–7722. doi: 10.1128/jb.173.23.7719-7722.1991

Derman, A. I., Prinz, W. A., Belin, D., and Beckwith, J. (1993). Mutations that allow disulfide bond formation in the cytoplasm of *Escherichia coli*. *Science* 262, 1744–1747. doi: 10.1126/science.8259521

Derman, A. I., Puziss, J. W., Bassford, P. J., and Beckwith, J. (1993). A signal sequence is not required for protein export in priA mutants of *Escherichia coli*. *EMBO J.* 12, 879–888. doi: 10.1002/j.1460-2075.1993.tb05728.x

Djaman, O., Outten, F. W., and Imlay, J. A. (2004). Repair of oxidized iron-sulfur clusters in *Escherichia coli*. *J. Biol. Chem.* 279, 44590–44599. doi: 10.1074/jbc.M406487200

Eben, S. S., and Imlay, J. A. (2023). Excess copper catalyzes protein disulfide bond formation in the bacterial periplasm but not in the cytoplasm. *Mol. Microbiol.* 119, 423–438. doi: 10.1111/mmi.15032

Flint, D. H., Tuminello, J. F., and Emptage, M. H. (1993). The inactivation of Fe-S cluster containing hydro-lyases by superoxide. *J. Biol. Chem.* 268, 22369–22376. doi: 10.1016/S0021-9258(18)41538-4

Gardner, P. R., and Fridovich, I. (1991). Superoxide sensitivity of the *Escherichia coli* aconitase. *J. Biol. Chem.* 266, 19328–19333. doi: 10.1016/S0021-9258(18)55001-8

Gebendorfer, K. M., Drazic, A., Le, Y., Gundlach, J., Bepperling, A., Kastenmüller, A., et al. (2012). Identification of a hypochlorite-specific transcription factor from *Escherichia coli*. *J. Biol. Chem.* 287, 6892–6903. doi: 10.1074/jbc.M111.287219

Glass, G. A., DeLisle, D., DeTogni, P., Gabig, T., Magee, B., Markert, M., et al. (1986). The respiratory burst oxidase of human neutrophils. Further studies of the purified enzyme. *J. Biol. Chem.* 261, 13247–13251. doi: 10.1016/S0021-9258(18)69297-X

Gu, M., and Imlay, J. A. (2013). Superoxide poisons mononuclear iron enzymes by causing mismetallation. *Mol. Microbiol.* 89, 123–134. doi: 10.1111/mmi.12263

Gupta, A., and Imlay, J. A. (2021). *Escherichia coli* induces DNA repair enzymes to protect itself from low-grade hydrogen peroxide stress. *Mol. Microbiol.* 117, 754–769. doi: 10.1111/mmi.14870

Hillion, M., and Antelmann, H. (2015). Thiol-based redox switches in prokaryotes. *Biol. Chem.* 396, 415–444. doi: 10.1515/hsz-2015-0102

Hiniker, A., Collet, J.-F., and Bardwell, J. C. A. (2005). Copper stress causes an *in vivo* requirement for the *Escherichia coli* disulfide isomerase DsbC*. *J. Biol. Chem.* 280, 33785–33791. doi: 10.1074/jbc.M505742200

Hochgrafe, F., Mostertz, J., Albrecht, D., and Hecker, M. (2005). Fluorescence thiol modification assay: oxidatively modified proteins in *Bacillus subtilis*. *Mol. Microbiol.* 58, 409–425. doi: 10.1111/j.1365-2958.2005.04845.x

Imlay, J. A. (2013). The molecular mechanisms and physiological consequences of oxidative stress: lessons from a model bacterium. *Nat. Rev. Microbiol.* 11, 443–454. doi: 10.1038/nrmicro3032

Imlay, J. A., and Fridovich, I. (1991). Assay of metabolic superoxide production in *Escherichia coli*. *J. Biol. Chem.* 266, 6957–6965. doi: 10.1016/S0021-9258(20)89596-9

Jakob, U., Muse, W., Eser, M., and Bardwell, J. C. (1999). Chaperone activity with a redox switch. *Cells* 96, 341–352. doi: 10.1016/S0092-8674(00)80547-4

Jang, S., and Imlay, J. A. (2007). Micromolar intracellular hydrogen peroxide disrupts metabolism by damaging iron-sulfur enzymes. *J. Biol. Chem.* 282, 929–937. doi: 10.1074/jbc.M607646200

Jo, I., Kim, D., Bang, Y.-J., Ahn, J., Choi, S. H., and Ha, N.-C. (2017). The hydrogen peroxide hypersensitivity of OxyR2 in *Vibrio vulnificus* depends on conformational constraints. *J. Biol. Chem.* 292, 7223–7232. doi: 10.1074/jbc.M116.743765

Kang, J.-G., Paget, M. S., Seok, Y.-J., Hahn, M.-Y., Bae, J.-B., Hahn, J.-S., et al. (1999). RsrA, an anti-sigma factor regulated by redox change. *EMBO J.* 18, 4292–4298. doi: 10.1093/emboj/18.15.4292

Kawasaki, S., Watamura, Y., Ono, M., Watanabe, T., Takeda, K., and Niimura, Y. (2005). Adaptive responses to oxygen stress in obligatory anaerobes clostridium acetobutylicum and *Clostridium aminovalericum*. *Appl. Environ. Microbiol.* 71, 8442–8450. doi: 10.1128/AEM.71.12.8442-8450.2005

Keyer, K., and Imlay, J. A. (1996). Superoxide accelerates DNA damage by elevating free-iron levels. *Proc. Natl. Acad. Sci. U. S. A.* 93, 13635–13640. doi: 10.1073/pnas.93.24.13635

Khademian, M., and Imlay, J. A. (2017). *Escherichia coli* cytochrome *c* peroxidase is a respiratory oxidase that enables the use of hydrogen peroxide as a terminal electron acceptor. *Proc. Natl. Acad. Sci. U. S. A.* 114, E6922–E6931. doi: 10.1073/pnas.1701587114

Kosower, N. S., Kosower, E. M., and Wertheim, B. (1969). Diamide, a new reagent for the intracellular oxidation of glutathione to the disulfide. *Biochem. Biophys. Res. Commun.* 37, 593–596. doi: 10.1016/0006-291X(69)90850-X

Kuo, C. F., Mashino, T., and Fridovich, I. (1987). α,β-dihydroxyisovalerate dehydratase: a superoxide-sensitive enzyme. *J. Biol. Chem.* 262, 4724–4727. doi: 10.1016/S0021-9258(18)61255-4

Lee, J.-W., and Helmann, J. D. (2006). The PerR transcription factor senses H_2O_2 by metal-catalysed histidine oxidation. *Nature* 440, 363–367. doi: 10.1038/nature04537

Leichert, L. I., Gehrke, F., Gudiseva, H. V., Blackwell, T., Ilbert, M., Walker, A. K., et al. (2008). Quantifying changes in the thiol redox proteome upon oxidative stress *in vivo*. *Proc. Natl. Acad. Sci. U. S. A.* 105, 8197–8202. doi: 10.1073/pnas.0707723105

Leichert, L. I., and Jakob, U. (2004). Protein thiol modifications visualized *in vivo*. *PLoS Biol.* 2:e333. doi: 10.1371/journal.pbio.0020333

Li, K., Hein, S., Zou, W., and Klug, G. (2004). The glutathione-glutaredoxin system in *Rhodobacter capsulatus*: part of a complex regulatory network controlling defense against oxidative stress. *J. Bacteriol.* 186, 6800–6808. doi: 10.1128/JB.186.20.6800-6808.2004

Li, X., and Imlay, J. A. (2018). Improved measurements of scant hydrogen peroxide enable experiments that define its threshold of toxicity for *Escherichia coli*. *Free Rad. Biol. Med.* 120, 217–227. doi: 10.1016/j.freeradbiomed.2018.03.025

Lim, C.-J., Daws, T., Gerami-Nejad, M., and Fuchs, J. A. (2000). Growth-phase regulation of the *Escherichia coli* thioredoxin gene. *Biochim. Biophys. Acta* 1491, 1–6. doi: 10.1016/S0167-4781(00)00026-9

Lippa, A. M., and Goulian, M. (2012). Perturbation of the oxidizing enviornment of the periplasm stimulates the PhoQ/PhoP system in *Escherichia coli*. *J. Bacteriol.* 194, 1457–1463. doi: 10.1128/JB.06055-11

Liu, Y., Bauer, S. C., and Imlay, J. A. (2011). The YaaA protein of the *Escherichia coli* OxyR regulon lessens hydrogen peroxide toxicity by diminishing the amount of intracellular unincorporated iron. *J. Bacteriol.* 193, 2186–2196. doi: 10.1128/JB.00001-11

Luikenhuis, S., Perrone, G., Dawes, I. W., and Grant, C. M. (1998). The yeast *Saccharomyces cerevisiae* contains two glutaredoxin genes that are required for protection against reactive oxygen species. *Mol. Biol. Cell.* 9, 1081–1091. doi: 10.1091/mbc.9.5.1081

Lynch, R., and Fridovich, I. (1978). Permeation of the erythrocyte stroma by superoxide radical. *J. Biol. Chem.* 253, 4697–4699. doi: 10.1016/S0021-9258(17)30446-5

Mancini, S., and Imlay, J. A. (2015). The induction of two biosynthetic enzymes helps *Escherichia coli* sustain heme synthesis and activate catalase during hydrogen peroxide stress. *Mol. Microbiol.* 96, 744–763. doi: 10.1111/mmi.12967

McDuffee, A. T., Senisterra, G., Huntley, S., Lepock, J. R., Sekhar, K. R., Meredith, M. J., et al. (1997). Proteins containing non-native disulfide bonds generated by oxidative stress can act as signals for the induction of the heat shock response. *J. Cell. Physiol.* 171, 143–151. doi: 10.1002/(SICI)1097-4652(199705)171:2<143::AID-JCP4>3.0.CO;2-O

Mehdy, M. C. (1994). Active oxygen species in plant defense against pathogens. *Plant Physiol.* 105, 467–472. doi: 10.1104/pp.105.2.467

Miller, J. H. *Experiments in molecular genetics*. Cold Spring Harbor, NY: Cold Spring Harbor Laboratory (1972).

Nakano, S., Küster-Schöck, E., Grossman, A. D., and Zuber, P. (2003). Spx-dependent global transcriptional control is induced by thiol-specific oxidative stress in *Bacillus subtilis*. *Proc. Natl. Acad. Sci. U. S. A.* 100, 13603–13608. doi: 10.1073/pnas.2235180100

Park, S., You, X., and Imlay, J. A. (2005). Substantial DNA damage from submicromolar intracellular hydrogen peroxide detected in Hpx-mutants of *Escherichia coli*. *Proc. Natl. Acad. Sci. U. S. A.* 102, 9317–9322. doi: 10.1073/pnas.0502051102

Parsonage, D., Nelson, K. J., Ferrer-Sueta, G., Alley, S., Karplus, P. A., Furdui, C. M., et al. (2015). Dissecting peroxiredoxin catalysis: separating binding, peroxidation, and resolution for a bacterial AhpC. *Biochemistry* 54, 1567–1575. doi: 10.1021/bi501515w

Potamitou, A., Holmgren, A., and Vlamis-Gardikas, A. (2002). Protein levels of *Escherichia coli* thioredoxins and glutaredoxins and their relation to null mutants, growth phase, and function. *J. Biol. Chem.* 277, 18561–18567. doi: 10.1074/jbc.M201225200

Ritz, D., and Beckwith, J. (2001). Roles of thiol-redox pathways in bacteria. *Annu. Rev. Biochem.* 55, 21–48. doi: 10.1146/annurev.micro.55.1.21

Ritz, D., Patel, H., Doan, B., Zheng, M., Aslund, F., Storz, G., et al. (2000). Thioredoxin 2 is involved in the oxidative stress response in *Escherichia coli*. *J. Biol. Chem.* 275, 2505–2512. doi: 10.1074/jbc.275.4.2505

Seaver, L. C., and Imlay, J. A. (2001). Alkyl hydroperoxide reductase is the primary scavenger of endogenous hydrogen peroxide in *Escherichia coli*. *J. Bacteriol.* 183, 7173–7181. doi: 10.1128/JB.183.24.7173-7181.2001

Seaver, L. C., and Imlay, J. A. (2004). Are respiratory enzymes the primary sources of intracellular hydrogen peroxide? *J. Biol. Chem.* 279, 48742–48750. doi: 10.1074/jbc.M408754200

Sen, A., and Imlay, J. A. (2021). How microbes defend themselves from incoming hydrogen peroxide. *Front. Immunol.* 12:667343. doi: 10.3389/fimmu.2021.667343

Sobota, J. M., Gu, M., and Imlay, J. A. (2014). Intracellular hydrogen peroxide and superoxide poison 3-deoxy-D-arabinoheptulosonate 7-phosphate synthase, the first committed enzyme in the aromatic biosynthetic pathway of *Escherichia coli*. *J. Bacteriol.* 196, 1980–1991. doi: 10.1128/JB.01573-14

Sobota, J. M., and Imlay, J. A. (2011). Iron enzyme ribulose-5-phosphate 3-epimerase in *Escherichia coli* is rapidly damaged by hydrogen peroxide but can be protected by manganese. *Proc. Natl. Acad. Sci. U. S. A.* 108, 5402–5407. doi: 10.1073/pnas.1100410108

Stewart, E. J., Aslund, F., and Beckwith, J. (1998). Disulfide bond formation in the *Escherichia coli* cytoplasm: an *in vivo* role reversal for the thioredoxins. *EMBO J.* 17, 5543–5550. doi: 10.1093/emboj/17.19.5543

Tao, K. (1997). oxyR-dependent induction of *Escherichia coli* grx gene expression by peroxide stress. *J. Bacteriol.* 179, 5967–5970. doi: 10.1128/jb.179.18.5967-5970.1997

Winterbourn, C. C. (2016). Revisiting the reactions of superoxide with glutathione and other thiols. *Arch. Biochem. Biophys.* 595, 68–71. doi: 10.1016/j.abb.2015.11.028

Winterbourn, C. C., and Metodiewa, D. (1999). Reactivity of biologically important thiol compounds with superoxide and hydrogen peroxide. *Free Radic. Biol. Med.* 27, 322–328. doi: 10.1016/S0891-5849(99)00051-9

Winterbourn, C. C., Peskin, A. V., Kleffmann, T., Radi, R., and Pace, P. E. (2023). Carbon dioxide/bicarbonate is required for sensitive inactivation of mammalian glyceraldehyde-3-phosphate dehydrogenase by hydrogen peroxide. *Proc. Natl. Acad. Sci. U. S. A.* 120:e2221047120. doi: 10.1073/pnas.2221047120

Wolf, C., Hochgräfe, F., Kusch, H., Albrecht, D., Hecker, M., and Engelmann, S. (2008). Proteomic analysis of antioxidant strategies of *Staphylococcus aureus*: diverse responses to different oxidants. *Proteomics* 8, 3139–3153. doi: 10.1002/pmic.200701062

Xie, K., Bunse, C., Marcus, K., and Leichert, L. I. (2019). Quantifying changes in the bacterial thiol redox proteome during host-pathogen interaction. *Redox Biol.* 21:101087. doi: 10.1016/j.redox.2018.101087

Zheng, M., Åslund, F., and Storz, G. (1998). Activation of the OxyR transcription factor by reversible disulfide bond formation. *Science* 279, 1718–1722. doi: 10.1126/science.279.5357.1718

Zheng, M., Wang, X., Templeton, L. J., Smulski, D. R., LaRossa, R. A., and Storz, G. (2001). DNA microarray-mediated transcriptional profiling of the *Escherichia coli* response to hydrogen peroxide. *J. Bacteriol.* 183, 4562–4570. doi: 10.1128/JB.183.15.4562-4570.2001

Zhitkovich, A. (2019). N-acetylcysteine: antioxidant, aldehyde scavenger, and more. *Chem. Res. Toxicol.* 15, 1318–1319. doi: 10.1021/acs.chemrestox.9b00152

frontiers | Frontiers in Microbiology

TYPE Original Research
PUBLISHED 04 January 2024
DOI 10.3389/fmicb.2023.1324062

OPEN ACCESS

EDITED BY
Jose Echenique,
National University of Cordoba, Argentina

REVIEWED BY
Changyong Cheng,
Zhejiang A & F University, China
Filipe Carvalho,
INRAE Centre Jouy-en-Josas, France

*CORRESPONDENCE
Agata Krawczyk-Balska
✉ a.krawczyk-bal@uw.edu.pl

RECEIVED 18 October 2023
ACCEPTED 05 December 2023
PUBLISHED 04 January 2024

CITATION
Ładziak M, Prochwicz E, Gut K, Gomza P, Jaworska K, Ścibek K, Młyńska-Witek M, Kadej-Zajączkowska K, Lillebaek EMS, Kallipolitis BH and Krawczyk-Balska A (2024) Inactivation of *lmo0946* (*sif*) induces the SOS response and MGEs mobilization and silences the general stress response and virulence program in *Listeria monocytogenes*. *Front. Microbiol.* 14:1324062. doi: 10.3389/fmicb.2023.1324062

Inactivation of *lmo0946* (*sif*) induces the SOS response and MGEs mobilization and silences the general stress response and virulence program in *Listeria monocytogenes*

Magdalena Ładziak[1], Emilia Prochwicz[1], Karina Gut[1], Patrycja Gomza[1], Karolina Jaworska[1], Katarzyna Ścibek[1], Marta Młyńska-Witek[1], Katarzyna Kadej-Zajączkowska[1], Eva M. S. Lillebaek[2], Birgitte H. Kallipolitis[2] and Agata Krawczyk-Balska[1]*

[1]Department of Molecular Microbiology, Biological and Chemical Research Centre, Faculty of Biology, University of Warsaw, Warsaw, Poland, [2]Department of Biochemistry and Molecular Biology, University of Southern Denmark, Odense, Denmark

Bacteria have evolved numerous regulatory pathways to survive in changing environments. The SOS response is an inducible DNA damage repair system that plays an indispensable role in bacterial adaptation and pathogenesis. Here we report a discovery of the previously uncharacterized protein Lmo0946 as an SOS response interfering factor (Sif) in the human pathogen *Listeria monocytogenes*. Functional genetic studies demonstrated that *sif* is indispensable for normal growth of *L. monocytogenes* in stress-free as well as multi-stress conditions, and *sif* contributes to susceptibility to β-lactam antibiotics, biofilm formation and virulence. Absence of Sif promoted the SOS response and elevated expression of mobilome genes accompanied by mobilization of the A118 prophage and ICELm-1 mobile genetic elements (MGEs). These changes were found to be associated with decreased expression of general stress response genes from the σB regulon as well as virulence genes, including the PrfA regulon. Together, this study uncovers an unexpected role of a previously uncharacterized factor, Sif, as an inhibitor of the SOS response in *L. monocytogenes*.

KEYWORDS

SOS response, MGEs mobilization, stress response, virulence, *Listeria monocytogenes*

Introduction

Listeria monocytogenes is a Gram-positive foodborne human pathogen that is exquisitely well adapted to survive exposure to severe environmental challenges including high salt concentrations, a wide range of temperatures and extreme pH, and high concentration of β-lactam antibiotics used in the treatment of listeriosis. The versatility of *L. monocytogenes* allows for its adaptation to the natural environment, survival under food processing, successful infection of host organisms and survival under antibiotic therapy (Hof, 2003; NicAogáin and

O'Byrne, 2016). Although infections are not very common, the high mortality rate of listeriosis combined with the widespread dissemination of this organism in the environment makes it a serious public health risk (European Food Safety Authority and European Centre for Disease Prevention and Control, 2022). Regarding this, the primary goals of most research are focused on the detailed understanding of mechanisms which enable survival of *L. monocytogenes* in different environments. Such an understanding could lead to finding the Achilles heel of this pathogen and rational design of new control measures that prevent the survival of *L. monocytogenes* in clinical and non-clinical settings.

A key step in adapting to new stresses is coordination of gene expression with the physiological needs. This is achieved by reprogramming of the transcriptional landscape in response to different physical and chemical signals sensed by *L. monocytogenes*. So far, the best documented role in the response of *L. monocytogenes* to stressful conditions has been established for genes coding for multiple regulatory proteins including, among others, the alternative sigma factor B (σB), the virulence master regulator PrfA, the nutrient-responsive regulator CodY, the RNA chaperone Hfq and two-component signal transduction systems (Christiansen et al., 2004; Williams et al., 2005; Bennett et al., 2007; Reniere et al., 2016; Dorey et al., 2019).

One of the important factors involved in the response of *L. monocytogenes* to multiple stresses is a ferritin-like protein (Fri) belonging to the Dps (DNA-binding proteins from starved cells) family of proteins. The role of Dps-like proteins is to counteract the adverse effects of iron under aerobic conditions (Haikarainen and Papageorgiou, 2010). While Fri of *L. monocytogenes* has no regulatory properties, it contributes to virulence and plays a role in protection against various stresses including acid stress, oxidative stress, iron-starvation, cold- and heat-shock (Dussurget et al., 2005; Olsen et al., 2005; Milecka et al., 2015). Furthermore, inactivation of the *fri* gene was shown to disturb the level of the global regulators catabolite control protein A (CcpA) and anti-σB factor (RsbW), thus indicating the importance of Fri for *L. monocytogenes'* gene regulatory networks (Dussurget et al., 2005; Milecka et al., 2015). In a previous study, we showed that Fri also is a mediator of β-lactam tolerance and innate resistance to cephalosporins. Interestingly, we observed that *fri* is co-transcribed with the two downstream genes, *lmo0944* and *lmo0945* (Krawczyk-Balska et al., 2012). We hypothesized that genes co-transcribed with *fri* could play an important role in stress adaptation and/or virulence. Therefore, the aim of the present study was to characterize these genes functionally. Firstly, we have undertaken an extended co-transcription analysis revealing that *fri* is transcribed together with four downstream genes, namely *lmo0944*, *lmo0945, lmo0946* and *lhrC5*. Subsequent functional analyses revealed that *lmo0946* of unknown function (conserved in Firmicutes) is indispensable for normal growth of *L. monocytogenes* in a stress-free environment and required under multi-stress conditions. To answer the question why inactivation of *lmo0946* results in severe phenotypic changes of *L. monocytogenes*, we performed comparative RNA-seq analysis of wild type and the mutant strain with inactivated *lmo0946* gene. We found that inactivation of *lmo0946* leads to activation of the SOS response which is a conserved bacterial pathway induced upon various types of DNA damage and regulated by the repressor LexA and the activator RecA. Based on this finding, we propose to rename the *lmo0946* gene to *sif* (*S*OS *i*nterfering *f*actor). Furthermore, inactivation of *sif* leads to downregulation of stress response genes from the σB regulon, virulence genes from the PrfA regulon, and highly upregulated expression of *hfq* encoding an RNA chaperone involved in post-transcriptional regulation of genes in *L. monocytogenes*. Interestingly, inactivation of *sif* resulted in mobilization of two mobile genetic elements (MGEs), namely prophage A118 and ICELm-1. Taken together, our studies led to identification of Sif as an important factor in the physiology of *L. monocytogenes*. Considering the severe phenotypic disorders caused by the inactivation of *sif* in virtually all conditions tested, we propose that Sif represents a good candidate for an Achilles heel of *L. monocytogenes.*

Materials and methods

Bacterial strains and growth conditions

The wild-type strain *L. monocytogenes* EGD-e, its derivative mutant strains in ferritin operon genes (described in detail below) and strain with complemented mutation of *lmo0946* were used in this study. *L. monocytogenes* was routinely grown in brain heart infusion broth (BHI, Oxoid) at 37°C with aeration. When appropriate, cultures were supplemented with chloramphenicol (7.5 μg/mL), erythromycin (5 μg/mL) or X-gal (50 mg/mL).

For growth experiments, overnight cultures grown at 37°C with aeration in BHI medium were diluted 1:1000 in fresh BHI broth in titration plates. Depending on the experiment, BHI medium was supplemented with 5% ethanol, 0.09 μg/mL penicillin G, acidified with HCl to pH 5 or alkalized with NaOH to pH 9. The cultures were grown at 37°C with aeration and bacterial growth was monitored by measuring the optical density at 600 nm (OD_{600}). For thermal stress, the cultures were grown at 37°C to an OD_{600} of 0.03 and at this point the incubation temperature was shifted to 43°C. *Escherichia coli* strain Top10 and BL21 (DE3) (Invitrogen) were used in cloning experiments and purification of Lmo0946-His_6, respectively. *E. coli* strains were grown on Luria-Bertani medium. When required, the LB medium was supplemented with ampicillin (100 μg/mL), chloramphenicol (25 μg/mL) or kanamycin (30 μg/mL).

Construction of ferritin operon mutant strains and complementation of *lmo0946* mutation

For the construction of in-frame mutants with deletions of *lmo0944*, *lmo0945*, *lhrC1-4*, *lhrC6* (*rli22*), and *lhrC7* (*rli33.1*) *L. monocytogenes* EGD-e chromosomal DNA was used as the template for the PCR amplification of DNA fragments representing either the 5′ end and upstream sequences or the 3′ end and downstream sequences of the respective genes. The Splicing of the amplified 5′ and 3′ fragments were performed by overlap extension PCR and the obtained products were subsequently cloned into the temperature-sensitive shuttle vector pMAD (Arnaud et al., 2004). For the construction of nonsense mutants of *fri* and *lmo0946* and mutant with disabled −10 promoter region of *lhrC5 L. monocytogenes* EGD-e chromosomal DNA was used as the template for the PCR amplification of DNA fragments covering intended mutagenesis site of the

respective genes. The obtained PCR products were cloned into the temperature-sensitive shuttle vector pMAD and obtained derivatives of pMAD vector were used as the templates for site-directed mutagenesis (SDM). In case of *fri*, the introduced nucleotide substitutions changed the TTA codon at position 58–60 bp of the open reading frame to the STOP codon TAG. In case of *lmo0946*, the introduced nucleotide substitutions changed the GAA codon at position 70–72 bp of the open reading frame of *lmo0946* to the STOP codon TAG. In case of *lhrC5*, the introduced nucleotide substitutions changed the-10 promoter consensus sequence TATTAT to CAGTGC. Primers used for constructing the in-frame deletions as well as site-directed mutagenesis are listed in Supplementary Table S1. The obtained pMAD derivatives were used for genes replacement which was performed via double-crossover homologous recombination as described previously (Arnaud et al., 2004). Erythromycin-sensitive clones were screened for the presence of the mutations by PCR. Accuracy of the desired DNA modifications in the obtained mutant strains was confirmed by the sequencing of obtained PCR products.

For the construction of the strain with complemented *lmo0946* mutation *L. monocytogenes*Δ*lmo0945* chromosomal DNA was used as the template for the PCR amplification of DNA fragment covering ORFs of *lmo0945* and *lmo0946*. The obtained PCR product was cloned into the pPL2 vector and subsequently introduced into *lmo0946** mutant strain as described previously (Lauer et al., 2002).

Biofilm formation analysis

Biofilm formation was carried out essentially as described previously (Djordjevic et al., 2002). Briefly, 12-well polystyrene plates containing 1 mL of BHI broth were inoculated with the overnight culture of each strain to $OD_{600} = 0.01$. The plates were then incubated at 37°C under static condition. At different time points (14, 24, and 72 h), the wells were emptied and washed with sterile distilled water. After fixation with methanol, the wells were air dried and stained with crystal violet solution for 5 min. After washing, wells were air dried and the bound dye was solubilized with an solution of acetic acid. Following 10-fold dilution in distilled water, the absorbance of the solubilized dye was measured at 570 nm.

Susceptibility tests

The susceptibility to antibiotics and cadmium as well as the tolerance to penicillin G were examined essentially as described previously (Krawczyk-Balska et al., 2012). Briefly, the susceptibility to antibiotics and cadmium were examined using a microdilution test. 96-well microdilution plates containing 100 µL of two-fold dilutions of antibiotics or cadmium chloride (Merck) in BHI broth were inoculated with 10^5 CFU/mL of overnight culture of each strain. The plates were then incubated at 37°C. The MIC endpoints were read after 18–22 h of incubation for antibiotics susceptibility testing and after 48 h of incubation for cadmium susceptibility testing. The MIC was determined as the lowest tested compound concentration that resulted in the absence of apparent growth of the bacteria.

The tolerance to penicillin G was examined by inoculation of BHI broth supplemented with 32 µg/mL penicillin G with 5×10^7 CFU/mL of mid-exponential phase cultures. The cultures were subsequently incubated with aeration at 37°C and at indicated points of time viable cell counts were performed by standard plate counting.

In vitro infection experiment

Infection experiments with *L. monocytogenes* strains were performed using P388.D1 murine macrophage (ECACC Collection) essentially as described previously (Chatterjee et al., 2006). Briefly, macrophages were grown in 12-well plates until reached at least 80% confluence. Bacteria were added at MOI (multiplicity of infection) of 10. After 45 min remaining extracellular bacteria were removed and macrophages were washed twice with 1 × phosphate buffered saline (PBS), and subsequently incubated with fresh medium supplemented with gentamycin (20 µg/mL). After 1 and 4 h post infection macrophages were washed three times with 1 × PBS, lysed in 0.1% Triton X-100 and viable cell counts were performed by standard plate counting.

Murine infection model

In vivo infection experiments were performed essentially as described previously (Cabanes et al., 2008). Briefly, 2×10^3 bacteria in 200 µL of 1 × PBS were administered intravenously to 6–8 old BALB/c female mice. After 72 h post infection bacterial growth in mice spleens and livers was determined by plating 10-fold serial dilutions of organ homogenates on BHI.

Total RNA isolation and purification

For northern blot analysis in stationary phase, *L. monocytogenes* EGD-e was inoculated from single colony into BHI broth and cultured for 18 h. For northern blot analysis in exponential phase, *L. monocytogenes* EGD-e was grown to $OD_{600} \sim 0.35$, split, and half stressed with 0.09 µg/mL penicyllin G for 60 min. 10 mL samples from stationary phase cultures and 20 mL from exponential phase cultures were immediately cooled down in liquid nitrogen and centrifuged at 12,000 × g for 3 min at 4°C. The cell pellets were frozen in liquid nitrogen and stored at −80°C until further processing. The cells were disrupted by the FastPrep instrument and total RNA was extracted using 1 mL of TRItidy G™ Reagent (Applichem) as described previously (Nielsen et al., 2010). The concentration and purity of RNA were determined with a NanoDrop ND-1000 spectrophotometer and integrity of RNA was confirmed by agarose gel electrophoresis.

For transcriptomic and RT-qPCR analysis, *L. monocytogenes* cultures were grown to $OD_{600} \sim 0.35$. 5 mL samples of each culture were stabilized with RNA protect Cell Reagent (Qiagen) and subsequently collected by centrifugation at 5,000 × g for 10 min at 4°C. The cell pellets were frozen immediately in liquid nitrogen and stored at −80°C until further processing. The pellets were suspended in 1 mL of TRItidy G™ Reagent (Applichem) and cells were disrupted by the FastPrep instrument. Total RNA was isolated with Direct-zol RNA MiniPrep (Zymo Research) according to the manufacturer's

instructions. Contaminating DNA was removed from the samples using the TURBO DNA-free™ Kit (Invitrogen) following the manufacturer's instructions, except that DNAse treatment was performed in presence of SUPERase•In™ RNase Inhibitor (Invitrogen). The concentration and purity of the RNA preparations were then estimated by measuring the A260 and A280 with a NanoDrop ND-1000 spectrophotometer. The absence of DNA from RNA preparations was verified by the failure to amplify a *rpoB* gene fragment in a 30-cycle PCR using 100 ng of each RNA isolation as the template. A 2100 Bioanalyzer (Agilent Technologies) was used to measure the RNA quality. The prepared RNA was stored at −80°C before further analysis.

rRNA depletion, library preparation, RNA sequencing, and data analysis

Ribosomal RNA depletion, library preparation and sequencing were performed by Eurofins Genomics AT GmbH (Vienna, Austria). To enrich mRNA and remove ribosomal RNA (rRNA) from total RNA, total RNA was treated with Bacterial rRNA Depletion Kit (NEB). Preparation of cDNA fragment libraries was performed using the NEBNext® Ultra™ II Directional RNA Library Prep Kit for Illumina® (Illumina). Sequencing was carried out on the Illumina NovaSeq platform (10 M paired-end reads, 2 × 150 bp per read). The obtained raw data were further analyzed by DDG Bioinformatics, University of Warsaw. Briefly, sequenced reads were quality-checked using FastQC, and Illumina adapter sequences and low-quality base pairs were removed using fastp (Chen et al., 2018). Reads were mapped against the complete sequenced genome of the *L. monocytogenes* reference strain EGD-e (ENSEMBL ASM19603v1) and 154 genes of ncRNA from Listeriomics database, using Bowtie 2 with standard parameters and sensitive-local (Langmead and Salzberg, 2012). Differential expression (DE) analyses were performed using DESeq2 (Love et al., 2014). DE was reported as $\log_2$fold changes and *p* values were adjusted by the DESeq2 default Benjamini–Hochberg (BH) adjustment method. The reading counts obtained from the Salmon program (Patro et al., 2017) were submitted to the DEseq2 tool using the tximport (Soneson et al., 2015) library. The results of the differential gene expression analysis were additionally scaled using the apeglm library (Zitovsky and Love, 2019), the aim of which was to reduce the influence of high variability of low-expressed genes on the results of the analysis. The fold changes were calculated by comparing expression levels of *lmo0946* mutant strain vs. wild-type strain. Genes with changed expression and an adjusted *p* value <0.01 were considered as DE in the interpretation applied in this study. The transcriptomic data has been deposited on the Array Express database and is available via the Experiment ArrayExpress accession E-MTAB-10809.

Reverse transcriptase-quantitative polymerase chain reaction (RT-qPCR)

100 ng of total RNA was used for synthesis of first strand cDNA. Reverse transcription was performed with RevertAid First Strand cDNA Synthesis Kit and random hexamers used as primers (Thermo Fisher Scientific) according to the manufacturer's protocol. Quantitative PCR reactions were performed using the LightCycler® 480 SYBR Green I Master (Roche) and specific primer sets for the gene of interest (Supplementary Table S1). The samples were run on LightCycler®96 thermocycler (Roche) with an initial step at 95°C for 10 min, 45 cycles of 10 s at 95°C, 10 s at 60°C, and 15 s at 72°C. Data was analyzed using LightCycler® 96 SW 1.1 Software. The relative amount of target cDNA was normalized using the *rpoB* gene. The experiment was carried out in three biological replicates, each in technical duplicates.

Co-transcription and northern blotting analysis

For co-transcription analysis, 100 ng of total RNA was used for synthesis of first strand cDNA. Reverse transcription was performed with RevertAid First Strand cDNA Synthesis Kit (Thermo Fisher Scientific) and primer specific for the *lhrC5* gene. The obtained cDNA was then used as the template for PCR performed with primers specific for internal fragments of the *fri* and *lmo0944* genes. Primers used for the co-transcription analysis are listed in Supplementary Table S1.

For northern blotting, 20 µg of total RNA in loading buffer containing 50% formamide and 20% formaldehyde was separated on a formaldehyde agarose gel and subsequently transferred to a Zeta probe nylon membrane (Bio-Rad) by capillarity blotting. For detection of RNA, the membranes were preincubated for 1 h in PerfectHyb hybridization buffer (Sigma-Aldrich) and then hybridized overnight with a specific ^{32}P-labeled DNA double-stranded probes. Probes were generated using [α-32P] dATP and Megaprime DNA labeling system (Amersham Biosciences), according to the manufacturer's protocol. Primers used for preparing DNA double-stranded probes are listed in Supplementary Table S1. RNA bands were visualized by phosphor imaging using a Typhoon scanner and analyzed with ImageQuant™ TL software (GE Healthcare).

MGE mobilization analysis

15 mL of exponential phase cultures (OD_{600} ~ 0.35) were centrifuged at 5,000 × g for 10 min. The cell pellets were suspended in buffer containing 0.2 mg/mL lysozyme and 20% saccharose and incubated at 37°C for 5 min. Total DNA was subsequently isolated with GeneJetGenomic DNA Purification Kit (ThermoScientific) according to the manufacturer's instructions. The concentration of DNA was determined with a NanoDrop ND-1000 spectrophotometer. PCR reactions were performed using 0.1 ng of DNA and specific primer sets (Supplementary Table S1).

Purification of Sif protein and electrophoretic mobility shift assay (EMSA)

The His-tag system (Novagen) was used for Sif purification. The fragment representing the entire *lmo0946* coding sequence was PCR-amplified on the template of *L. monocytogenes* EGD-e chromosomal DNA using primers listed in Supplementary Table S1. PCR product was cloned into vector pET28a (Novagen) and the

obtained construct was used to transform *E. coli* BL21 (DE3). The N-terminal His-tagged Sif protein (Lmo0946-His_6) was expressed and purified using Ni-NTA resin (Qiagen) according to the manufacturer's recommendations. Briefly, the cells were suspended in 20 mM Tris–HCl (pH 8.0) buffer containing 500 mM NaCl, 1 mM PMSF and 5 mM imidazol and disrupted by sonication. After centrifuging the cell lysate to remove unbroken cells, the supernatant was passed through a Ni-NTA agarose column. The column was washed with 20 mM Tris–HCl (pH 8.0) buffer containing 500 mM NaCl, 10% glicerol, 5 mM imidazol, and subsequently the Lmo0946-His_6 protein was eluted using a gradient of imidazole buffer. Finally, the protein was dialyzed against 20 mM Tris–HCl (pH 8.0), 150 mM NaCl and 1% glicerol. The concentration of the purified Sif was determined using the Pierce™ BCA Protein Assay Kit (ThermoScientific).

For EMSA analysis, DNA fragments comprising the regulatory regions upstream of genes of interest were PCR-amplified using primers listed in Supplementary Table S1. The amplicons were purified using a GeneJET Gel Extraction & DNA Cleanup Micro Kit (ThermoScientific) and the concentration of DNA was determined with a NanoDrop ND-1000 spectrophotometer. EMSA reactions contained appropriate DNA fragments of the studied promoters (0.1 pmol) and Lmo0946-His_6 in concentration ranging from 0 to 40 μM. The purified protein was used in EMSAs with and without *in vitro* phosphorylation. A 202-bp fragment of *L. monocytogenes* 16S rDNA generated by PCR was included as a non-specific competitor in binding reactions. Sif binding to the DNA targets was performed at 37°C for 30 min and subsequently samples were separated on 4.2% native polyacrylamide gels. After electrophoresis the gels were stained with ethidium bromide and DNA bands were visualized using a AI600 imager (GE Healthcare).

Statistics

For all assays, data were pooled from three biological repetition of experiments. Differences between *L. monocytogenes* strains were analyzed by ANOVA with a Tukey's multiple comparisons posttest (for comparison of multiple groups with each other), or by unpaired *t* test (for assays with only 2 groups). Adjusted *p* values were calculated (for comparison of multiple groups with each other), or two-tailed *p* values were calculated (for assays with only 2 groups), and $p < 0.05$ was considered significant. Prism 8 (Graph Pad Software) was used for statistical calculations.

Results

Analysis of the co-transcription of *fri* with downstream genes

The study concerning identification of penicillin G-inducible genes of *L. monocytogenes* revealed that *fri* is transcribed together with its downstream genes *lmo0944* and *lmo0945* (Krawczyk-Balska et al., 2012). Further *in silico* analysis of the genomic region comprising the *fri* gene indicated that *lmo0946* and *lhrC5* are located downstream from, and in orientation consistent with, *lmo0945*. This led us to hypothesize that these two genes may also be a part of the *fri* operon (Figure 1A). To evaluate this hypothesis, RT-PCR analysis was performed that verified the co-transcription of *fri*, *lmo0944*, *lmo0945*, *lmo0946*, and *lhrC5* genes (Figure 1B). Importantly, in addition to the observed co-transcription event, transcription of *lmo0944*, *lmo0945* and *lhrC5* genes is expected to proceed from their own promoters. To get more detailed information about individual transcripts produced within the ferritin operon and their level of co-transcription, northern blot analysis was performed on total RNA extracted from *L. monocytogenes* EGD-e grown in BHI in exponential phase, with and without penicillin G exposure. The results of the northern blotting, shown in Figure 1C, demonstrate signals corresponding to each gene transcript from the *fri* operon. According to these signals, *fri*, *lmo0944*, and *lhrC5* are predominantly transcribed as monocistronic transcripts with size ~500 nt, ~ 400 nt and ~ 100 nt, respectively, with the *lhrC5* transcript clearly visible only in presence of penicillin G. For *lmo0945* and *lmo0946*, the signals in the northern blot analysis indicate that these two genes are co-transcribed as no signal with a size corresponding to a monocistronic transcript of any of them is visible. Each of the analyzed genes gave additional bands in the northern blot which may originate from co-transcription with downstream genes and/or processing of the larger co-transcripts. Noteworthy is that signals corresponding to a larger co-transcript with size ~2,300 nt are visible for each of the analyzed genes, providing proof for co-transcription of *fri* with all the genes analyzed. The signal intensity of this co-transcript is much lower than signals corresponding to the monocistronic transcripts of *fri*, *lmo0944*, and *lhrC5*, and the bicistronic transcript of *lmo0945* and *lmo0946*, indicating that co-transcription of *fri* with downstream genes does not proceed very effectively in the analyzed conditions of growth. We were wondering if co-transcription level depends on the conditions of growth. To answer this, further northern blot analysis with probes specific for *fri* and *lmo0946* was performed on total RNA extracted from *L. monocytogenes* EGD-e in stationary phase of growth. According to the signals in the northern blot analysis, shown in Figure 1D, *fri* is still predominantly transcribed as the monocistronic transcript with size ~500 nt, however the co-transcript with size ~2,300 nt is clearly visible in stationary phase. In case of *lmo0946*, the intensity of the signal corresponding to this co-transcript is much higher than the signal corresponding to the bicistronic transcript of *lmo0945-lmo0946*. These observations suggest that co-transcription of *fri* with downstream genes occurs more readily in stationary phase cells. Generally, northern blotting confirmed co-transcription of *fri* with *lmo0944*, *lmo0945*, *lmo0946* and *lhrC5* genes. Thus, these genes constitute an operon, named afterwards, the ferritin operon.

Inactivation of *lmo0946* impairs the growth under different conditions

To investigate the relevance of the ferritin operon in the physiology of *L. monocytogenes*, each gene of the operon was subjected to inactivation. In case of *lmo0944* and *lmo0945*, in frame deletion mutants were constructed. Due to the presence of genes coding for antisense RNAs Anti0943, Anti0945 and Anti0946 within the operon (Figure 1A), single point mutations were designed for inactivation of *fri*, *lmo0946* and *lhrC5* to minimize the risk of undesirable changes in the expression of these asRNAs. In case of *fri* and *lmo0946* the nucleotide substitutions were introduced to create nonsense mutations (named *fri** and *lmo0946**), and in case of *lhrC5*, nucleotide substitutions in the-10 promoter region were introduced to prevent initiation of transcription (named *lhrC5**). Moreover, due to high sequence similarity between LhrC5 and six other sRNAs from the

10.3389/fmicb.2023.1324062

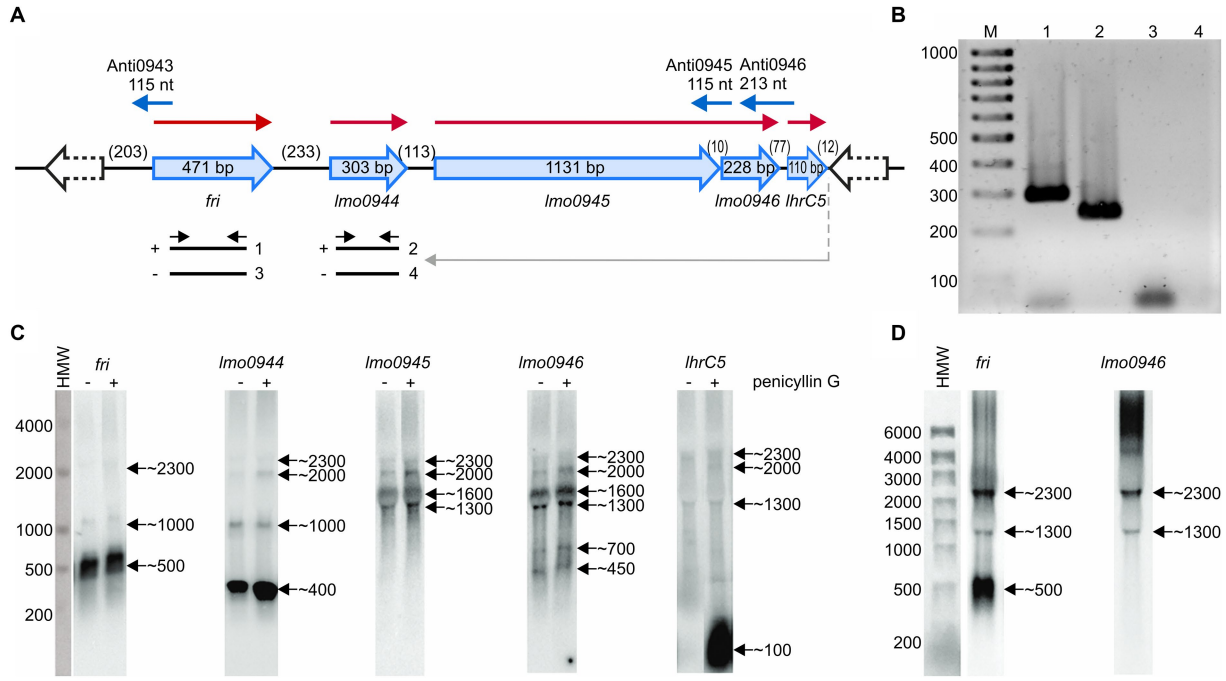

FIGURE 1
Analysis of co-transcription of *fri* with downstream genes. **(A)** Schematic representation of the genomic region comprising the *fri*, *lmo0944*, *lmo0945*, *lmo0946*, and *lhrC5* genes. Red arrows indicate mRNAs corresponding to the individual genes of the operon and blue arrows represent small antisense transcripts encoded from this genome region. Scheme for co-transcription analysis by RT-PCR is shown below. The template RNA was isolated from exponential-phase cultures of *Listeria monocytogenes* EGD-e grown in BHI broth at 37°C with 0.09 μg/mL penicillin G. Gray arrow indicates the position of the primer used in RT reaction and black arrows indicate the positions of primers used for PCR. (–) or (+) indicate the expected products amplified on template of RT reactions performed without or with reverse transcriptase, respectively. **(B)** The products obtained in RT-PCR reactions. The numbering of the agarose gel lanes corresponds to the expected products presented in panel **(A)**. The expected size of the amplified fragments of fri and lmo0944 was 288 bp and 212 bp, respectively. A 100-bp ladder (lane M) is shown as a size marker. **(C)** Northern blot analysis of *fri*, *lmo0944*, *lmo0945*, *lmo0946*, and *lhrC5* in exponential-phase of *L. monocytogenes* EGD-e growth. Samples were taken from EGD-e wild type mid-exponential cultures exposed to 1 h of penicillin G stress (+) as well as from non-stressed cultures (–). Northern blots were probed for *fri* mRNA, *lmo0944* mRNA, *lmo0945* mRNA, *lmo0946* mRNA, and LhrC5. Numbers on the right side of each panel indicate the estimated lengths of the transcripts in nucleotides. **(D)** Northern blot analysis of *fri* and *lmo0946* in stationary-phase of *L. monocytogenes* EGD-e growth. Samples were taken from EGD-e wild type overnight culture. Northern blots were probed for *fri* mRNA and *lmo0946* mRNA. Numbers on the right side of each panel indicate the estimated lengths of the transcripts in nucleotides.

LhrC family, the functional analysis of LhrC5 may be difficult or impossible when the other LhrCs remain functional. To resolve this problem, the genes encoding for these six LhrCs were deleted in the background of the wild-type and *lhrC5* mutant strains. First, the growth rates of the mutants and the parent strain in BHI broth at 37°C were compared. Interestingly, in these stress-free conditions the inactivation of all the studied genes but *lmo0946* had no effect on rate of growth (Figure 2).

The observed growth impairment of the *lmo0946** mutant strain prompted us to focus on assessing the effects of inactivation of this gene. Prior to detailed analysis, complementation of *lmo0946* was performed in the background of the mutant strain. The wild-type, *lmo0946** mutant and complemented strain (*lmo0946**-*lmo0946*) were compared with respect to their abilities to grow in stress-free conditions. The growth of the *lmo0946** mutant was clearly impaired relative to the wild type and *lmo0946**-*lmo0946* strains (Figure 3A; Supplementary Table S2). Subsequent analysis of the ability of the *lmo0946** mutant to grown under various stress conditions, including the presence of subinhibitory concentrations of ethanol and penicillin G, acid and alkaline environments, or high temperature, revealed that Lmo0946 is necessary for normal growth of *L. monocytogenes* under various environmental conditions (Figures 3B–F; Supplementary Table S2).

Inactivation of *lmo0946* reduces the ability of *Listeria monocytogenes* to form biofilm

In order to study the effect of *lmo0946* inactivation on biofilm formed by *L. monocytogenes*, the sessile biomass of the studied strains was stained by crystal violet. The biofilm formation assay revealed significant differences between the *lmo0946** mutant, and wild-type or complemented strains (Figure 4). The amount of sessile biomass for the *lmo0946** mutant was significantly diminished up to 72 h of sessile growth compared to the wild-type and complemented strains (Figure 4). These results indicate that inactivation of *lmo0946* reduces the ability of *L. monocytogenes* to create biofilm.

Lmo0946 contributes to the resistance of *Listeria monocytogenes* to cephalosporins and tolerance to penicillin G

To investigate whether inactivation of *lmo0946* affects the susceptibility of *L. monocytogenes* to antibiotics, the parent and mutant strains were subjected to antibiotic disk assays. This assay revealed that

10.3389/fmicb.2023.1324062

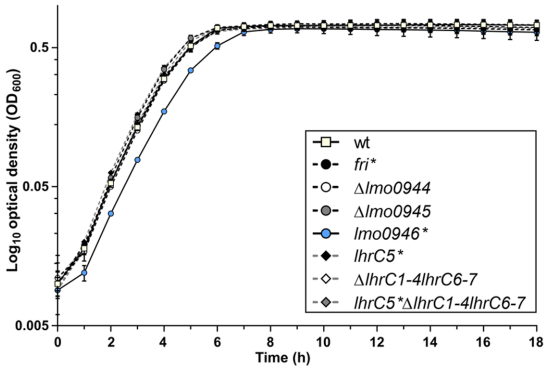

FIGURE 2
Growth of wild-type *L. monocytogenes* EGD-e and the ferritin operon mutants in stress-free conditions. BHI broth was inoculated with an overnight culture of each strain (1:1000) and incubated with shaking at 37°C. Cell growth was measured spectrophotometrically by determining the OD_{600}. The mean values from three independent experiments are plotted and the error bars represent the standard deviation.

the wild-type and *lmo0946** strains displayed similar levels of resistance to various antibiotics (ampicillin, penicillin G, vancomycin, aztreonam, meropenem, tetracycline, rifampicin, gentamicin, trimethoprim, and ciprofloxacin), however significantly greater zones of growth inhibition were observed for the mutant with cefuroxime and cefoxitin (Supplementary Table S3). The MICs of these specific cephalosporin antibiotics were then determined for *L. monocytogenes* EGD-e and the *lmo0946** mutant. In confirmation of the antibiotic disk assay result, the MIC of cefuroxime for wild-type and *lmo0946** was 8 μg/mL and 4 μg/mL, respectively, whereas the MIC of cefoxitin for wild-type and *lmo0946** was 32 μg/mL and 16 μg/mL, respectively. Thus, inactivation of the *lmo0946* gene caused a 2-fold increase in the sensitivity of *L. monocytogenes* to these cephalosporins. Next, tolerance was examined by testing the ability of the strains to survive in concentrations of penicillin G over 100-fold higher than the MIC value which is 0.12 μg/mL (Supplementary Table S3). The tolerance assay revealed that the survival of *lmo0946** was significantly impaired since reduced numbers of viable cells were recovered for the mutant relative to the wild-type strain after exposure to high concentration of penicillin G (Figure 5). In summary, our results indicate that Lmo0946 contributes to the resistance to cephalosporins and tolerance to penicillin G of *L. monocytogenes*.

Inactivation of *lmo0946* impairs the virulence of *Listeria monocytogenes*

To determine whether Lmo0946 is important for the virulence of *L. monocytogenes*, *in vitro* infection studies were performed using the *lmo0946** mutant and wild-type *L. monocytogenes* EGD-e. The infection assay showed that the *lmo0946** mutant was significantly impaired in the ability to proliferate intracellularly in the murine macrophage cell line P388D1 relative to the wild-type strain (Figure 6A). Subsequently, the mouse infection model was used to assess the virulence properties of the *lmo0946** mutant relative to that of wild-type. For the mutant, survival and/or growth in the liver and spleen was significantly reduced at day 3 post-infection when compared with wild-type (Figure 6B). These results indicate that Lmo0946 contributes to the virulence of *L. monocytogenes*.

Inactivation of *lmo0946* causes global changes of genes expression including upregulation of the mobilome and downregulation of metabolism

In silico analysis of Lmo0946 indicates that it is a small (75 aa) conserved bacterial protein of unknown function, and the function of its homologs, found mainly in *Bacilli* and *Clostridia* classes of the Firmicutes phylum (Supplementary Figure S1), has not been established yet. To further elucidate why inactivation of *lmo0946* results in severe phenotypic changes of *L. monocytogenes*, a transcriptomic analysis of *L. monocytogenes lmo0946** mutant and the parental strain EGD-e was performed using RNA-seq during exponential phase of growth at 37°C in BHI. The RNA-seq analysis revealed that inactivation of *lmo0946* caused 589 genes to be differentially expressed when compared to the wild-type strain using an adjusted p value < 0.01, corresponding to approximately 20% of protein encoding genes and 10% of the sRNAs (Figure 7A; Supplementary Table S4). The relative abundance of each COG category in the set of differentially transcribed genes was further determined. A set of 320 genes showed higher transcript levels while 269 showed lower transcript levels in the *lmo0946** mutant relative to the wild-type strain (Figure 7B; Supplementary Table S5). COGs analysis revealed that genes involved in carbohydrate transport and metabolism, energy production and conversion, lipid transport and metabolism, amino acid transport and metabolism, transcription, and translation were highly represented in the downregulated set of genes, indicating that inactivation of *lmo0946* results in a general slowdown of metabolism. The analysis also showed that genes related to nucleotide transport and metabolism, replication, recombination and repair as well as the mobilome were highly represented among the upregulated genes, suggesting that inactivation of *lmo0946* leads to disorders of processes related to DNA metabolism and replication.

To better understand the causes of global changes in gene expression resulting from *lmo0946* inactivation we further analyzed the genes that were at least fourfold up-or downregulated in the background of *lmo0946** (corresponding to 83 and 45 genes, respectively) (Supplementary Table S6). The most up-regulated genes with more than 20-fold change were *lmo1097* (encoding an integrase), *hfq* (encoding an RNA chaperone), genes involved in cadmium resistance, and few genes coding for hypothetical proteins (Supplementary Table S6; Figure 7A). Going through the most numerous parts of the up-regulated genes, it was noticeable that most of them are phage-related genes. These genes accounted for over 50% of the upregulated genes and most of them, though not all, were genes of the A118 prophage which is one of the four mobile genetic elements (MGEs) found in the *L. monocytogenes* EGD-e strain. The three other MGEs are the monocin (or *lma*) locus, the integrative and conjugative element ICELm1 (Tn*916*-like) and IS3-1 (Kuenne et al., 2013).

Given the high frequency of prophage genes in the set of up-regulated genes, the expression of all MGE genes in the *lmo0946** strain was further analyzed. This analysis showed that genes of three of the four MGEs, i.e., prophage A118, monocin locus and ICELm-1, are highly expressed in the *lmo0946** mutant (Supplementary Table S7).

10.3389/fmicb.2023.1324062

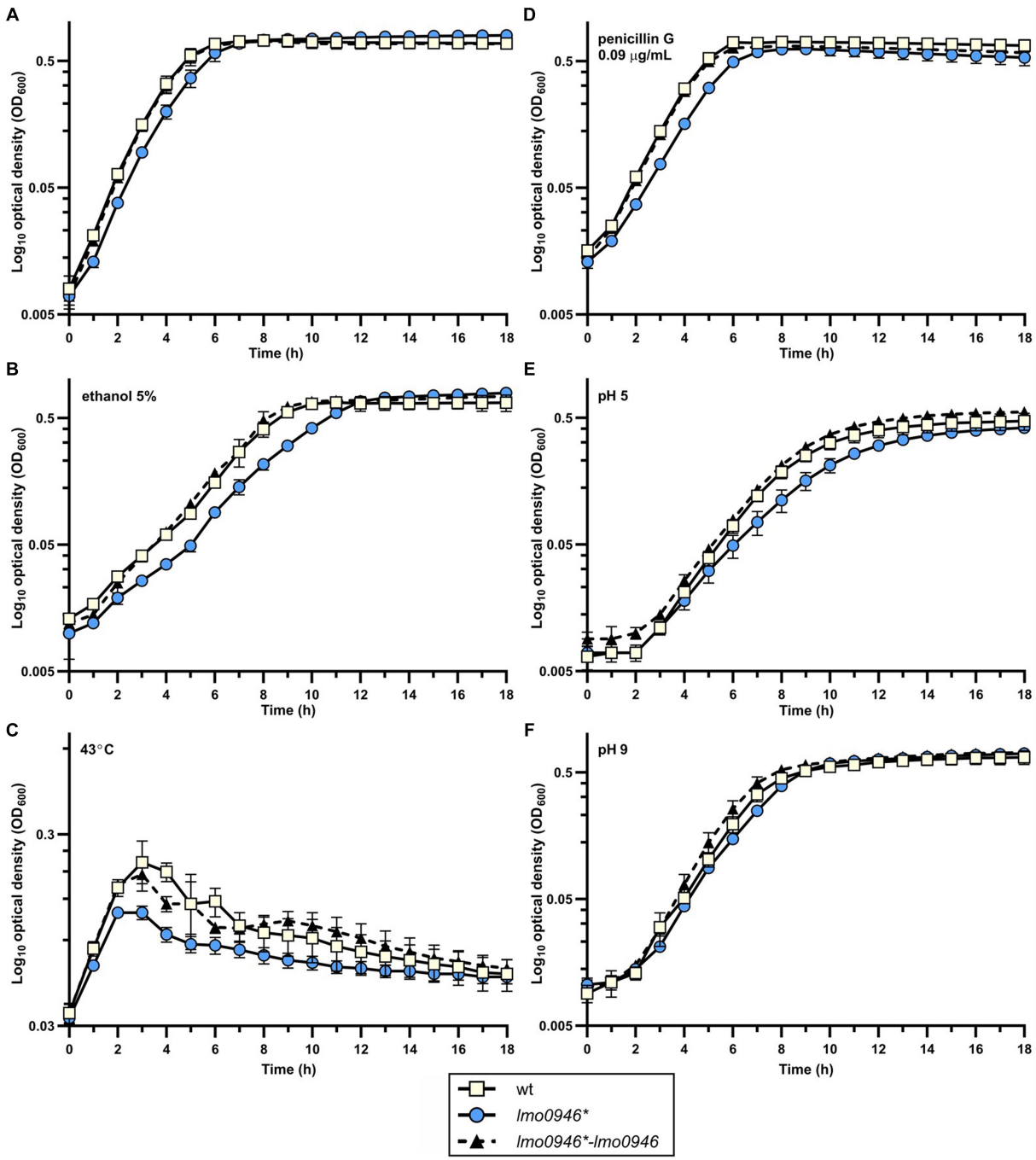

FIGURE 3
Inactivation of *lmo0946* impairs growth of *L. monocytogenes* under different conditions. Growth of wild-type *L. monocytogenes* EGD, *lmo0946** mutant and the complemented strain *lmo0946**-*lmo0946* in **(A)** BHI broth, **(B)** BHI broth supplemented with 5% ethanol, **(C)** BHI broth at 43°C, **(D)** BHI broth supplemented with 0.09 µg/mL penicillin G, **(E)** BHI broth pH 5 **(F)** and BHI broth pH 9. BHI broth was inoculated with an overnight culture of each strain (1:1000) and incubated with shaking at 37°C except high temperature stress **(C)**. Cell growth was measured spectrophotometrically by determining the OD_{600}. The mean values from three independent experiments are plotted and the error bars represent the standard deviation. Calculated generation times are shown in Supplementary Table S2.

The monocin locus, a cryptic prophage region, is conserved in all *L. monocytogenes* lineages and includes the *lmaDCBA* operon with an important role in virulence of *L. monocytogenes* (Hain et al., 2012). The expression of all genes from the monocin locus is up-regulated in the *lmo0946** mutant, and for most of them more than 10-fold up-regulation is observed. ICELm1 is an MGE specific for *L. monocytogenes* EGD-e. It consists of 19 genes, including an integrase-encoding gene (*lmo1097*), cadmium resistance genes *lmo1100* (*cadA*), *lmo1101* (*lspB*) and *lmo1102* (*cadC*), a gene coding for a fibrinogen-binding protein with an LPXTG domain (*lmo1115*) and Tn*916*-like genes of unknown function (Kuenne et al., 2013; Pombinho et al., 2017; Parsons et al., 2018). In case of this MGE, eight genes were found to be upregulated in *lmo0946** including

10.3389/fmicb.2023.1324062

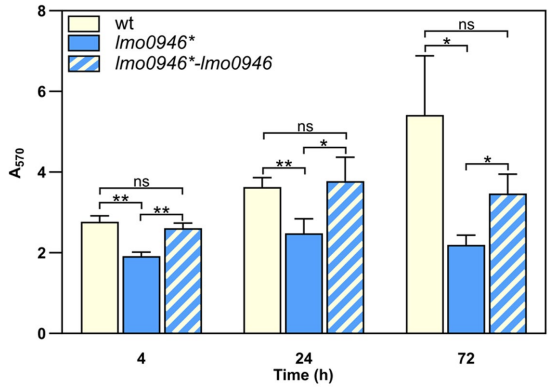

FIGURE 4
Inactivation of *lmo0946* reduces biofilm formation by *L. monocytogenes*. Sessile development of wild-type *L. monocytogenes* EGD-e, *lmo0946** mutant and the complemented strain *lmo0946**-*lmo0946* are assayed with the crystal violet method. The data represent the means and standard deviations of three biological repeats. ANOVA with a Tukey's multiple comparisons posttest was used to determine statistical significances. The asterisks indicate significant differences (*$p < 0.05$, **$p < 0.01$); ns, non-significant.

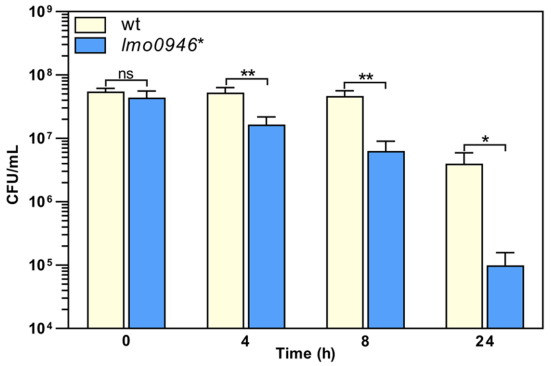

FIGURE 5
Inactivation of *lmo0946* impairs tolerance of *L. monocytogenes* to penicillin G. BHI broth supplemented with 32 µg/mL penicillin G was inoculated with a mid-exponential culture of wild-type *L. monocytogenes* EGD-e (wt) and *lmo0946** mutant strains and incubated with shaking at 37°C. Viable cell counts were measured on agar plates following serial dilutions of culture samples. The mean values from three independent experiments are plotted and the error bars indicate standard deviations. Unpaired two-tailed *t* test was used to determine statistical significances. The asterisks indicate significant differences (*$p < 0.05$, **$p < 0.01$); ns, non-significant.

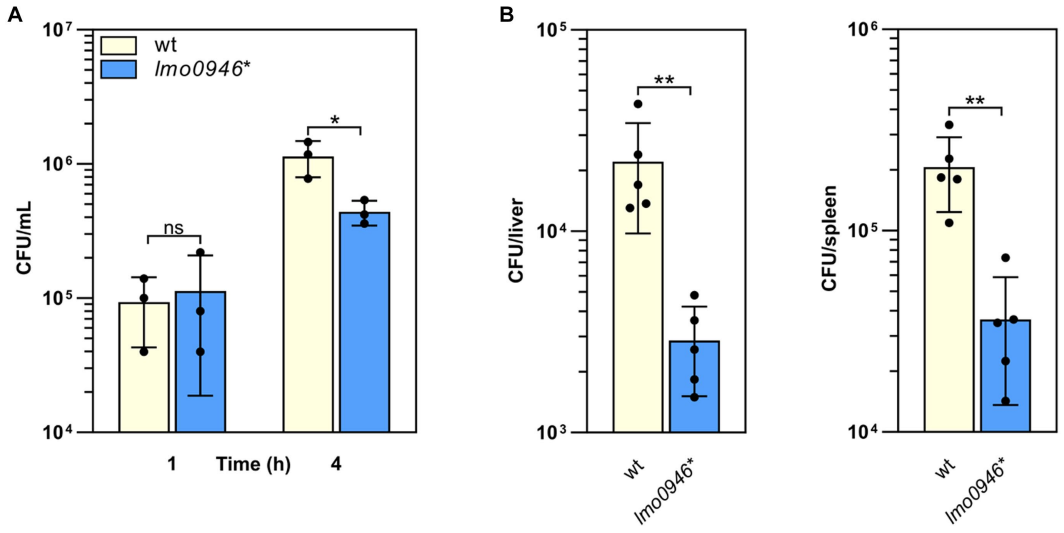

FIGURE 6
Inactivation of *lmo0946* impairs virulence of *L. monocytogenes*. **(A)** The effect of *lmo0946* inactivation on the intracellular replication of *L. monocytogenes* in the murine macrophage cell line P388D1. Cell monolayers were infected with the wild-type *L. monocytogenes* EGD-e (wt) and *lmo0946** mutant strains with an MOI of 10 in 24-well plates. Bacterial CFU counts were measured on agar plates following lysis of the infected cells at the indicated time of post-infection. The mean values from three independent experiments are plotted and the error bars indicate standard deviations. **(B)** Mice infection with wild-type *L. monocytogenes* EGD-e and *lmo0946** mutant strains. Bacterial load in BALB/c mice organs were determined following intravenous inoculation with 2000 CFU of *L. monocytogenes* EGD-e as well as *lmo0946** mutant. On day 3 after infection, the numbers of viable bacteria in livers and spleens of five animals per group were determined. Error bars indicate standard deviations. Unpaired two-tailed *t* test was used to determine statistical significances. The asterisks indicate significant differences (*$p < 0.05$, **$p < 0.01$); ns, non-significant.

the aforementioned genes with known function (Supplementary Table S7). Interestingly, genes belonging to ICELm1 showed over 30-fold up-regulation of expression in the *lmo0946** mutant strain, and this was the highest increase in expression recorded in these studies. An analysis of the A118 prophage showed that the expression of 50 of 62 prophage genes is up-regulated in the *lmo0946** strain with more than 4-fold up-regulation observed for 45 of these genes (Supplementary Table S7). Interestingly, the upregulated genes belong to virtually all functional modules of prophage A118 including genes encoding phage lysis proteins holin and lysin. In summary, these data indicate that inactivation of *lmo0946* led to upregulation of a large portion of the mobilome of *L. monocytogenes*.

The most highly down-regulated gene in the *lmo0946** mutant was *lmo1634*. It encodes the Listeria adhesion protein (LAP), a

10.3389/fmicb.2023.1324062

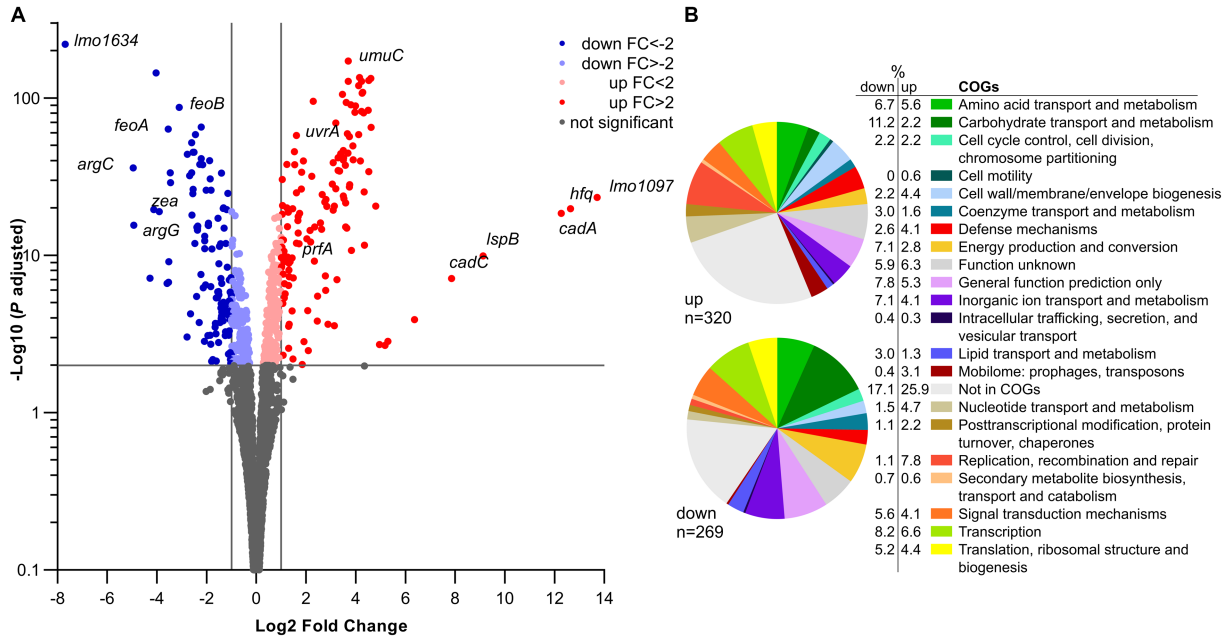

FIGURE 7
RNA-seq analysis of genes differentially transcribed by *L. monocytogenes lmo0946** mutant grown to exponential phase in BHI medium. **(A)** Volcano plots displaying differentially expressed genes in *L. monocytogenes lmo0946** mutant compared to the wild-type EGD-e. The negative log10 of an adjusted *p* value is plotted on the Y-axis, and the log2FC is plotted on the X-axis. The horizontal line represents an adjusted *p* value > 0.01 cutoff. The vertical lines represent a − 1.0 > log2FC > 1.0 cutoffs. **(B)** Relative abundance of categories of genes differentially expressed by *L. monocytogenes lmo0946** mutant comparatively to the wild-type EGD-e corresponding to categories in the COGs database. Upper pie chart, genes upregulated in the mutant compared with wild-type; Lower pie chart, genes downregulated in the mutant compared with wild-type.

putative bifunctional acetaldehyde-CoA/alcohol dehydrogenase involved in pyruvate metabolism. Three pyruvate-formate lyase encoding genes were found to be downregulated as well (*pflB*, *pflA* and *pflC*). Additionally, genes involved in arginine biosynthesis (*argC*, *argG*, *argH*), ferrous iron transport (*feoA* and *feoB*), and amino acid transport and metabolism (*arpJ* and *gadD*) were found to be highly down-regulated in the *lmo0946** mutant relative to the wild-type strain (Supplementary Table S6; Figure 7A). Collectively, these findings suggest that inactivation of *lmo0946* led to a decrease in energy production and conversion as well as decreased transport and metabolism of amino-acids and other cell compounds. Interestingly, high level of downregulation was also noticed for *lmo2686* encoding the RNA binding protein Zea which was shown to specifically interact with phage RNAs of *L. monocytogenes* (Pagliuso et al., 2019). This observation further supports a putative link between *lmo0946* and the mobilome of *L. monocytogenes*.

Inactivation of *lmo0946* triggers a variety of stress responses in *Listeria monocytogenes*, including the SOS response

Out of 128 genes with at least a 4-fold change in expression level, 68 were found to be allocated into known regulons, and some of them are under control of more than one regulator (Supplementary Table S6). For these genes the largest overlap was observed with the CodY regulon. The transcriptional regulator CodY responds to different nutritional and environmental stresses and generally controls adaptive responses in conditions that limit bacterial growth (Bennett et al., 2007). We noticed that 30 of the highly upregulated genes, coding for prophage A118 proteins, were under positive control of CodY. In addition, seven of the most downregulated genes were under negative control of CodY. Among them were *arg* genes coding for proteins engaged in the biosynthesis of arginine, and genes involved in the transport and metabolism of amino acids, carbohydrates, and inorganic ion.

In addition to the CodY regulon, five genes belonging to LexA/RecA regulon were upregulated at least fourfold in *lmo0946** mutant strain (Supplementary Table S6). The LexA/RecA regulon covers genes involved in the SOS response that is induced upon various types of DNA damage (van der Veen et al., 2010). This observation led us to further analyze the effect of inactivation of *lmo0946* on level of expression of the SOS regulon. The analysis revealed that nearly all of the 29 genes of LexA/RecA regulon are upregulated in the mutant strain, except from the σB-dependent genes *bilEA* and *bilEB* involved in osmoprotection (Sue et al., 2003), and *lmo2266* with unknown function (Supplementary Table S8). Notably, the expression levels of genes from the SOS response noticed for the *lmo0946** mutant strain is comparable to the levels expressed in wild-type *L. monocytogenes* EGD-e after treatment with the SOS-inducing agent mitomycin C (van der Veen et al., 2010). Among the most highly induced genes were those encoding the cell division inhibitor YneA (*lmo1303*), the translesion DNA polymerases DinB (*lmo1975*) and UmuDC (*lmo2675* and *lmo2676*) (Supplementary Table S8). These findings clearly demonstrate that inactivation of *lmo0946* triggers the expression of SOS response genes known to promote the DNA repair in DNA-damaged cells.

Finally, four genes belonging to the VirR regulon were upregulated at least fourfold in the *lmo0946** mutant strain. VirR is an important regulator of genes involved in bacterial surface components modifications (Mandin et al., 2005). Most of the VirR-dependent upregulated genes code for proteins involved in amino acid transport and metabolism (Supplementary Table S6).

Inactivation of *lmo0946* leads to downregulation of virulence genes and modulation of expression of σB and CodY regulons

An analysis of 45 highly downregulated genes revealed that eight of them belong to the PrfA regulon (Supplementary Table S6). PrfA is the master virulence regulator of *L. monocytogenes* (Reniere et al., 2016). Further analysis of the effect of inactivation of *lmo0946* on the PrfA regulon revealed that expression of 29 from 73 genes was changed with an adjusted p value < 0.01 in the *lmo0946** mutant strain and further 12 genes with an adjusted p value < 0.05 (Supplementary Table S9). Interestingly, all differentially expressed genes from the PrfA regulon, except *prfA and lmo0641*, are downregulated in the *lmo0946** mutant, even though nearly all of them correspond to genes under positive control by PrfA (Supplementary Table S9). Furthermore, decreased level of expression was observed for genes preceded by a PrfA box and belonging to the core set of the PrfA regulon, like *hly*, *inlA* and *inlB* (Milohanic et al., 2003). Additionally, the most highly downregulated gene, *lmo1634*, encodes the LAP protein that promotes bacterial translocation across the intestinal epithelial barrier (Drolia et al., 2018). Furthermore, among the highly downregulated genes were *arpJ* and *pplA* coding for factors playing important roles at different stages of intracellular infection of *L. monocytogenes* but not belonging to PrfA regulon (Supplementary Table S6; Reniere et al., 2016). In addition to the PrfA regulon, five genes belonging to the σB regulon were downregulated at least fourfold in the *lmo0946** mutant strain (Supplementary Table S6). The alternative sigma factor σB positively regulates genes involved in the response of *L. monocytogenes* to multiple stress conditions and has also been implicated in virulence (Dorey et al., 2019). σB-dependent downregulated genes encode proteins with unknown function, except for *lmo2067* (*bsh*) coding for the bile salt hydrolase with an important role in intestinal phase of infection (Begley et al., 2005). As observed for the PrfA regulon, σB positively regulates the genes found to be downregulated in the *lmo0946** mutant (Supplementary Table S6). The only gene positively regulated by σB, and highly upregulated in the *lmo0946** strain, is *hfq* coding for an RNA chaperone involved in post-transcriptional control of gene expression in *L. monocytogenes*. Notably, transcription of *hfq* was shown to proceed from a σB-dependent promoter (Christiansen et al., 2004). These data suggest that modulation of expression of the σB regulon occurs in the *lmo0946** strain. This assumption is supported by a 2-fold decrease in expression of the *rsbV* gene coding for the anti-anti-σB factor (Supplementary Table S4). As *rsbV* plays an important role in a signaling pathway controlling σB activity (Dorey et al., 2019), this observation prompted us to gain insight into the expression of the *rsb* genes coding for components of the stressosome as well as the σB signaling cascade. The *rsb* genes are encoded within the *sigB* operon and are responsible for sensing and subsequent transmission of stress signals to activate the σB factor (Dorey et al., 2019). The analysis revealed that expression of *rsbV* and *rsbW*, the latter encoding an anti-σB factor, is significantly decreased in the *lmo0946** mutant strain (Supplementary Table S10). This observation suggests that the σB signaling cascade is affected by the *lmo0946* mutation. Among the highly downregulated genes were also three genes downregulated by Fur, which is a Fe^{2+} dependent repressor of genes involved in iron/heme uptake and utilization. These genes encode a ferrous iron transport system (*feoA* and *feoB*) and an element of a transport system involved in cytochrome biosynthesis (*cydC*) (Lechowicz and Krawczyk-Balska, 2015).

It should be noted that as many as 16 out of 25 highly downregulated genes belonging to known regulons are regulated in *lmo0946** in a manner opposite to regulation by the appropriate regulators (Supplementary Table S4). Besides the genes from the PrfA and σB regulons described above, seven genes positively regulated by CodY also belong to this group. These observations indicate that inactivation of *lmo0946** result in global modulation of expression of genes belonging to different regulons involved in stress response and virulence of *L. monocytogenes*.

Validation of transcriptomic changes observed in the *lmo0946** mutant strain by RT-qPCR analysis

To ensure that the performed RNA-seq analysis reflects the transcriptional changes in the *lmo0946** mutant strain, the RNA-seq data was subsequently validated by RT-qPCR analyses of 12 genes (including up-, non-and down-regulated genes). The obtained results indicated very good correlation between RNA-seq and RT-qPCR results ($R^2 = 0.945$; Supplementary Figure S2). Subsequently, to verify whether the transcriptomic changes observed in the *lmo0946** mutant strain are the result of inactivation of *lmo0946*, the level of expression of selected genes in wild-type *L. monocytogenes* EGD-e, the *lmo0946** mutant and the complemented strain was examined by RT-qPCR. The analysis of genes from the SOS regulon and mobile genetic elements revealed increased level of expression in the *lmo0946** mutant (Figure 8A). Upon complementation, the expression of these genes was restored to that observed in the wild-type strain, except for the *lmo1097* gene belonging to ICELm1 MGE (Figure 8A). Next, the expression of virulence genes was examined. Increased expression of *prfA* and decreased expression of *hly* was observed in the *lmo0946** mutant, and upon complementation the expression of these genes was restored to that observed in the wild-type strain (Figure 8B). Finally, the expression of genes with potent regulatory roles was studied. Increased expression of *hfq* and decreased expression of *zea* was observed in the *lmo0946** mutant, but upon complementation the expression of these genes was not restored to that observed in the wild-type strain. In case of *rsbV* and *sigB*, expression of these genes is decreased in the *lmo0946** mutant strain, however only in case of *rsbV* the difference in expression between wild-type and mutant strain was significantly important ($p = 0.04$), while for *sigB* the difference was just above the cut-off of statistical significance ($p = 0.08$). Furthermore, the expression of *rsbV* was not restored upon complementation to the level observed in wild-type EGD-e strain (Figure 8C). In conclusion, the results of the RT-qPCR analysis confirmed the changes in gene expression in the mutant strain observed in the RNA-seq analysis.

10.3389/fmicb.2023.1324062

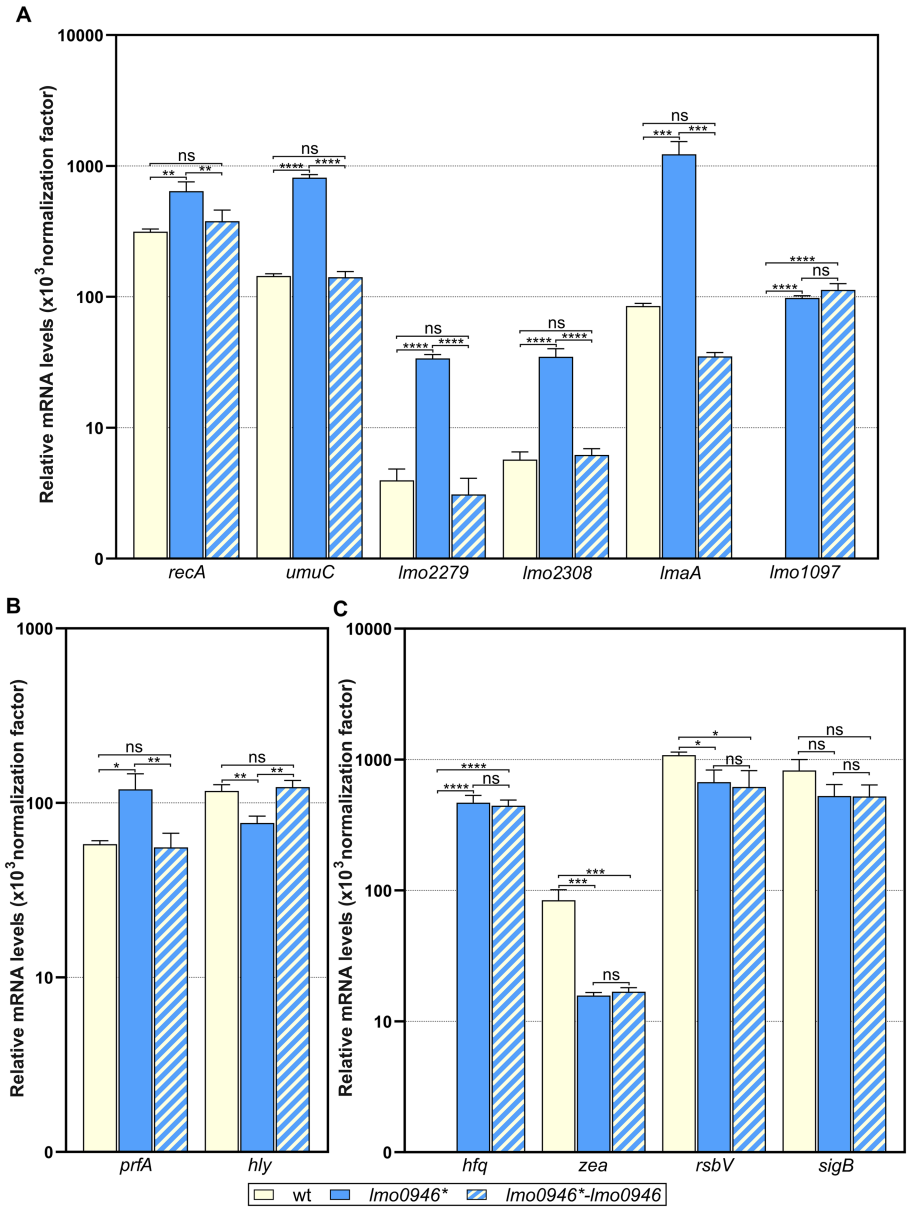

FIGURE 8
Impact of *lmo0946* inactivation and complementation on expression of selected SOS regulon, MGE, virulence and regulatory genes. The expression was determined in exponential growth phase in BHI for wild-type EGD-e, *lmo0946** mutant strain and complemented strain *lmo0946*-lmo0946* by RT-qPCR. Relative transcripts levels of **(A)** *recA*, *umuC*, *lmo2279*, *lmo2308*, *lmaA* and *lmo1097*, **(B)** *prfA* and *hly*, and **(C)** *hfq*, *zea*, *rsbV* and *sigB* were normalized to the amount of *rpoB* gene. The results shown are the average of three biological replicates, error bars indicate standard deviations. ANOVA with a Tukey's multiple comparisons posttest was used to determine statistical significances. The asterisks indicate significant differences (*$p < 0.05$, **$p < 0.01$, ***$p < 0.001$, ****$p < 0.0001$); ns, non-significant.

Furthermore, gene expression was restored in the complemented strain for genes involved in the SOS response and virulence as well as two MGEs, i.e., prophage A118 and monocin locus. However, the expression of genes involved in RNA binding and the σB response as well as ICELm1 MGE was not restored upon complementation.

Lmo0946 protein does not bind to DNA of promoters of selected genes

Frequently, pronounced changes in bacterial transcriptomics and physiology are observed upon inactivation of regulatory genes. Considering that inactivation of Lmo0946 resulted in major changes in gene expression, we wondered whether Lmo0946 could be a DNA-binding transcriptional regulator. To investigate this idea, we performed electrophoretic mobility shift assays (EMSAs) using native polyacrylamide gels to detect binding of the purified Lmo0946-His_6 protein to promoter regions of selected genes with clearly changed expression in the mutant strain and important roles in physiology or stress response of *L. monocytogenes*. EMSA analysis showed that Lmo0946-His_6 lacks the ability to bind DNA fragments corresponding to the promoter regions of *recA*, *prfA*, *lap*, *lmo1097*, *hfq*, *cadA*, and *argC* (Supplementary Figure S3). These results indicate that Lmo0946 itself has no DNA binding properties and changes in

10.3389/fmicb.2023.1324062

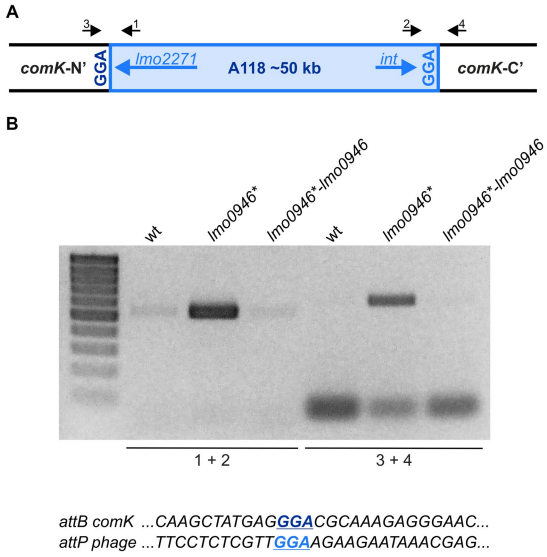

FIGURE 9
The Prophage A118 Is Excised in *lmo0946** mutant strain. **(A)** Schematic representation of the genomic region containing the split *comK* gene with integrated the A118 prophage. Black arrows depict primers used to characterize the *comK*-phage genomic region (primers 1–4). **(B)** PCR analysis of *comK*-phage genomic region in wild-type, *lmo0946** mutant and the complemented strain *lmo0946*-lmo0946* grown to exponential (mid-log) phase in BHI medium. **(C)** DNA sequences of the *comK attB* site and the phage *attP* site.

expression of the analyzed genes in the mutant strain seem not to result from direct regulation of transcription by Lmo0946.

Inactivation of *lmo0946* results in excision of prophage A118 without inducing lysogeny

The prophage A118 is integrated within the *comK* gene of *L. monocytogenes* EGD-e and while it was not extensively studied, it exhibits high similarity to Φ10403S prophage of *L. monocytogenes* 10403S which was shown to excise without switching from lysogeny to the lytic pathway in the process named active lysogeny (Rabinovich et al., 2012; Pasechnek et al., 2020). Based on the highly increased expression of prophage A118 genes in the *lmo0946** mutant strain, we hypothesized that excision of the phage could occur. To address this hypothesis, phage DNA excision and extra-chromosomal replication in the wild-type, *lmo0946** mutant and complemented strain were evaluated by PCR amplification of the intact *comK* gene and a fragment of circularized phage genome, which are formed only upon the phageA118 excision (Figure 9A). This analysis revealed the presence of a PCR product corresponding to a fragment containing the phage genome integration site in the *lmo0946** mutant strain and lack of this product in the wild-type and complemented strain. Furthermore, an intact *comK* gene was not amplified in the wild-type and complemented strain, while the amplification proceeded efficiently on DNA isolated from the *lmo0946** mutant strain (Figure 9B). The sequence analysis of PCR products representing intact *comK* and circular phage-DNA confirmed a precise excision of the phage A118 genome in the *lmo0946** mutant strain which leaves an in-frame coding sequence of the *comK* gene containing *attB* site and a reconstituted phage attachment *attP* site (Figure 9C). These observations indicate that in the *lmo0946** mutant strain precise excision of prophage A118 is induced and it is reversed upon complementation.

We further wondered whether the observed phage excision in *lmo0946** mutant strain is followed by induction of the lytic cycle. To answer this question, infective virion production was monitored in the wild-type, *lmo0946** mutant and complemented strains by using a plaque forming assay. The infective phages production was not detected in any of the strains tested (data not shown). Therefore, prophage A118 does not go into the lytic cycle, even though excision of the prophage occurs in the *lmo0946** mutant strain. Likewise, PCR analysis was performed to detect possible excision of cryptic prophage monocin locus as a high level of expression of this MGE in *lmo0946** mutant was also observed. However, no PCR products were obtained in this analysis indicating that excision of monocin locus in *lmo0946** mutant does not occur (data not shown).

Inactivation of *lmo0946* results in replication of ICELm1 in circular form and increased resistance to cadmium

The integrative and conjugative element ICELm1 is specific for the EGD-e strain and accordingly, it is absent in other widely used *L. monocytogenes* strains. So far, nothing is known about the biological function or mobilization of ICELm1 (Kuenne et al., 2013; Bécavin et al., 2014). As the genes from ICELm1 were found among the most highly upregulated genes in the *lmo0946** mutant strain, we decided to investigate the possible excision of this MGE. To address this hypothesis, ICELm1 DNA excision and extra-chromosomal replication in the wild-type, *lmo0946** mutant and complemented strain were evaluated by PCR amplification of a fragment covering the distal *guaA* and proximal *lmo1116* genes as well as a fragment of circularized ICELm1, which both are formed only upon the ICELm1 excision (Figure 10A). This analysis revealed the presence of a PCR product corresponding to the fragment containing the ICELm1 integration site (primers 1 + 2) in the *lmo0946** mutant and complemented strains, however this product was not detected in the wild-type strain (Figure 10B). Surprisingly, the fragment covering distal *guaA* and proximal *lmo1116* genes (primers 3 + 4) was not amplified in any of the tested strains suggesting the presence of ICELm1 in the genome of the studied strains (Figure 10B). This assumption was evaluated by an additional PCR amplification of an intergenic region of *guaA* and *lmo1097* (primers 1 + 3) which revealed the presence of a PCR product corresponding to intact intergenic region of *guaA* and *lmo1097* in all studied strains (Figure 10B). The sequence analysis of PCR products representing circular ICELm1 confirmed a precise replication of the circular form of ICELm1 in the *lmo0946** mutant strain with preserved duplicated attachment *attR* site and resulted in the arising of a truncated form of sRNA *rli38*, named *rli38-1* (Figure 10C). These observations indicate that while the presence of ICELm1 is preserved in the chromosome of all the strains, a precise extrachromosomal replication of the circular form of

10.3389/fmicb.2023.1324062

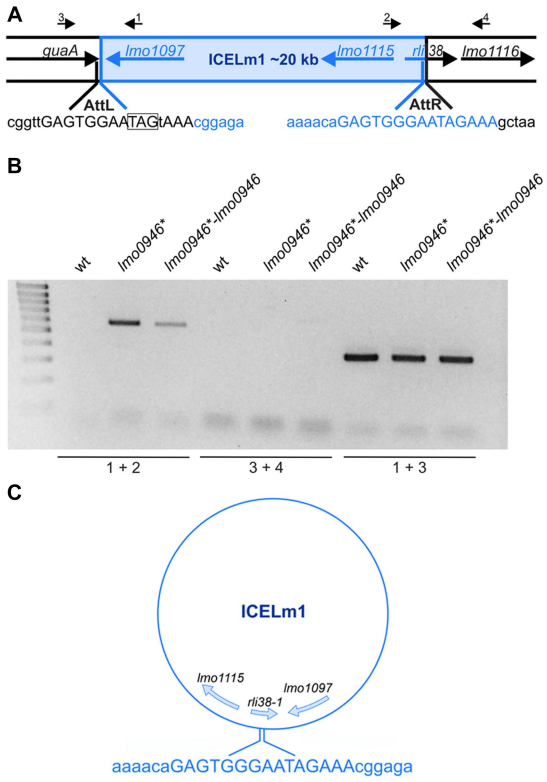

FIGURE 10
The ICELm1 is replicated and present in circular form in *lmo0946** mutant strain. **(A)** Schematic representation of the genomic region containing ICELm1. Black arrows depict primers used to characterize the ICELm1 genomic region (primers 1–4). The *attL* and *attR* sequences are given in uppercase and stop codon of guaA is boxed. **(B)** PCR analysis of ICELm1 genomic region in wild-type, *lmo0946** mutant and the complemented strain grown to exponential (mid-log) phase in BHI medium. **(C)** Schema of circular form of ICELm1 with given sequence of *attR* site.

ICELm1 is induced in the *lmo0946** mutant strain, and it is not reversed upon complementation.

As the genes involved in cadmium resistance are encoded within the ICELm1 (Kuenne et al., 2013) we further wondered whether the observed replication of the circular form of ICELm1 in the *lmo0946** mutant and complemented strain led to an increase in cadmium resistance of these strains. To answer this question, the susceptibility of the wild-type, *lmo0946** mutant and complemented strains to cadmium was tested using an agar and broth dilution assay. This assay revealed that the MIC of cadmium for EGD-e was 200 μg/mL while for the *lmo0946** and complemented strains MIC of cadmium was over 800 μg/mL (Supplementary Table S3). The precise determination of the MIC values for these strains was impossible due to their ability to grow in the presence of cadmium to the limit of its solubility, which was 1,000 μg/mL. Thus, inactivation of the *lmo0946* gene caused over 4-fold decrease in the sensitivity of *L. monocytogenes* to cadmium and the sensitivity was not restored upon complementation to the level observed in the wild-type EGD-e strain. These observations indicate that replication of the circular form of ICELm1 in the *lmo0946** mutant and complemented strain is accompanied by high increase of cadmium resistance.

Discussion

The ferritin-like protein plays an important role in protection against multiple stresses and virulence of *L. monocytogenes* (Dussurget et al., 2005; Olsen et al., 2005; Milecka et al., 2015). We previously showed that the *fri* gene is co-transcribed together with its downstream genes *lmo0944* and *lmo0945* (Krawczyk-Balska et al., 2012). As genes co-transcribed with *fri* could play an important role in stress adaptation and/or virulence, this observation prompted us to extend the co-transcription analysis and functional analyses of genes transcribed together with *fri*. The RT-qPCR revealed that *fri* is co-transcribed with four downstream genes, namely *lmo0944*, *lmo0945, lmo0946* and *lhrC5*, the last of which encodes for an sRNA from the LhrC family known for its role in the stress response of *L. monocytogenes* (Sievers et al., 2014, 2015). As the result from the co-transcription analysis contradicts previous studies showing that Fri is expressed from a monocistronic mRNA both in stress-free conditions and under heat-or cold-shock (Hébraud and Guzzo, 2000), we further analyzed the transcripts of the *fri* operon by northern blot. The analysis showed that the larger co-transcript, corresponding to the mRNA of *fri* and downstream genes, is clearly visible in the stationary phase of growth, however it is barely detectable during growth under stress-free conditions and under penicillin G pressure. These results indicate that the transcriptional terminator of *fri* is regulated in a condition-specific manner that results in generation of full-length mRNA at higher levels in the stationary phase than in other conditions. Therefore, the co-transcription of *fri* with downstream genes could be easily missed in earlier studies. Subsequently, all the genes from the ferritin operon were subjected to functional analysis. The inactivation of *fri, lmo0944, lmo0945 and lhrC5* had no effect on the growth of *L. monocytogenes* in stress-free conditions which in the case of *fri* and *lhrC5* confirms the results of previous studies (Dussurget et al., 2005; Olsen et al., 2005; Sievers et al., 2014), however inactivation of *lmo0946* led to markedly slower growth and reduced number of bacteria. This surprising observation prompted us to focus further research on *lmo0946*. Our analyses revealed that inactivation of *lmo0946* caused slowdown of growth of *L. monocytogenes* in the presence of subinhibitory concentrations of ethanol and penicillin G, in acid and alkaline environments, and high temperature. The *lmo0946** mutant strain also exhibited reduced tolerance to penicillin G, a phenotype that so far is known to be determined by the σB factor and Fri protein (Begley et al., 2006; Krawczyk-Balska et al., 2012). Furthermore, the *lmo0946** mutant strain showed increased sensitivity to some cephalosporins – antibiotics to which *L. monocytogenes* shows high innate resistance (Krawczyk-Balska and Markiewicz, 2016). The experiments examining the effect of *lmo0946* inactivation on sessile growth revealed an important role of *lmo0946* in biofilm formation by *L. monocytogenes* as well. Finally, the mutant with inactivated *lmo0946* exhibited attenuated virulence in *in vitro* and *in vivo* models of infection. The aforementioned phenotypes are likely associated with the inherent growth issue of bacteria lacking Lmo0946. Overall, the results of the phenotypic analysis indicate that inactivation of *lmo0946* results in severe disorders in the physiology of *L. monocytogenes* in virtually all conditions tested. To further explore the role of Lmo0946 in *L. monocytogenes*, a transcriptomic analysis of the *lmo0946** mutant and the parental strain was performed in stress-free conditions, as we assumed that the functional impairment of the mutant strain is

related to the transcriptomic changes already observed in stress-free conditions. Our experiments revealed that the response of *L. monocytogenes* to *lmo0946* inactivation is multifaceted. Firstly, *L. monocytogenes* responds to *lmo0946* inactivation by induction of the SOS response which generally is initiated by accumulation of single-stranded DNA in the cell. This situation results in the activation of RecA, which in turn stimulates autocatalytic cleavage of repressor LexA and, finally, the induction of the SOS response (Maslowska et al., 2019). Notably, RecA-mediated activation of the SOS response factor YneA, responsible for cell division arrest in *L. monocytogenes* (van der Veen et al., 2010), explains the observed growth retardation of the *lmo0946** mutant in different conditions of growth. The SOS response can be induced by a plethora of factors, including physical and chemical DNA damaging-agents present in the environment, and DNA-damaging byproducts and intermediates of cellular metabolism, such as reactive oxygen species (ROS). Since the SOS response in the mutant is induced during growth without harmful factors, it must be related to the changes in cellular processes that occur because of the mutation. The induction of the SOS response observed in the *lmo0946** mutant is not likely caused by induced production of ROS since the transcriptome analysis did not reveal an induction of *kat* (encoding catalase) and *sod* (encoding superoxide dismutase) known to work together in detoxification of ROS (Dallmier and Martin, 1988). Furthermore, these genes were recently reported to be highly co-induced with the SOS response in *L. monocytogenes* exposed to heme stress causing oxidative damage (Dos Santos et al., 2018). This conclusion is further supported by the observation that genes belonging to the PerR regulon dealing with peroxide stress in *L. monocytogenes* (Rea et al., 2005) are lacking among the genes showing greatly upregulated expression in the mutant strain (Supplementary Table S6). Worth of note is that different stimuli can indirectly generate the SOS-inducing signal by activation of endogenous DNA damage mechanisms (Aertsen and Michiels, 2006). Given this, we speculated that Lmo0946 may be a transcriptional regulator of genes with important roles in the physiology or stress response of *L. monocytogenes* and its regulatory activity in turn could lead to activation of the SOS response. However, the results of EMSA analyses led us to reject this hypothesis. Therefore, the specific mechanism underlying the link between Lmo0946 inactivation and activation of the SOS response remains unclear at the current stage of research. Although the present study does not explain how the SOS system is activated in the *lmo0946** mutant, the complementation studies show that this effect is clearly dependent on the *lmo0946* gene. Based on this finding, we propose to rename *lmo0946* gene to *sif* (*S*OS *i*nterfering *f*actor).

Generally, one of the well-known effects of the induction of the SOS response is activation of mobile genetic elements including endogenous prophages (Little and Mount, 1982). Accordingly, we observed phage A118 mobilization in the *sif* mutant strain. The temperate A118 prophage is specific to *L. monocytogenes* serovar 1/2 strains and belongs to the Siphoviridae family of double-stranded DNA bacterial viruses (Zink and Loessner, 1992). This bacteriophage was shown to reproduce by both lytic and lysogenic cycles, in the latter the phage's genome is integrated at a specific attachment site located within the *comK* gene (Loessner et al., 2000). Surprisingly, we observed that phage A118 mobilization is not accompanied by switching from lysogeny to the lytic pathway in a *sif* mutant strain of *L. monocytogenes* EGD-e. This result is consistent with previous reports on hardly induction of the lytic cycle of prophage A118 in the EGD-e strain exposed to UV irradiation or mitomycin C; well known factors inducing the SOS response (Pasechnek et al., 2020). Notably, a similar prophage to A118, named Φ10403S, is integrated like A118 in the *comK* gene of another widely used *L. monocytogenes* laboratory strain, 10403S. Upon UV irradiation or mitomycin C treatment the Φ10403S phage enters the lytic cycle, while the excision without production of progeny virions is specifically induced during intracellular growth to promote bacterial escape from macrophage phagosomes. This process, named active lysogeny, led to modulation of the virulence of *L. monocytogenes* 10403S in the course of infection (Rabinovich et al., 2012; Pasechnek et al., 2020). In the light of these data, we assume that the interplay between *comK*-phages and their *L. monocytogenes* hosts is strain dependent and the active lysogeny triggered by the SOS response in the *sif* mutant may be a specific response of the *L. monocytogenes* EGD-e strain. The active lysogeny in *L. monocytogenes* 10403S is ensured by negative control of the expression of the Φ10403S phage's late genes, including the *lysin* and *holin* genes that mediate bacterial lysis (Pasechnek et al., 2020). In contrary, we observed a high level of transcription of A118 phage late genes, including *holin* and *lysin*. This result indicates that the control of active lysogeny of phage A118 in strain EGD-e is different form that of the Φ10403S phage in strain 10403S. The high level of transcription of *holin* and *lysin* of A118 phage suggests a post-transcriptional control of active lysogeny in the *sif* mutant of the EGD-e strain. This hypothesis may be supported by the observed changed transcription in the *sif* mutant strain of two genes, namely *hfq* and *zea*, with known and putative roles, respectively in post-transcriptional regulation of gene expression in *L. monocytogenes*. The Hfq of *L. monocytogenes* is an RNA chaperone involved in post-transcriptional regulation of gene expression (Nielsen et al., 2010, 2011). The Hfq protein, which is encoded from one of the most highly upregulated genes in the *sif* mutant strain, could inhibit the translation of A118 phage genes and therefore promote active lysogeny. Noteworthy, the Hfq protein was originally identified as HF-I – a host factor for phage Qbeta RNA replication in *E. coli* (Franze de Fernandez et al., 1968), which further supports a putative link between Hfq and A118 phage of *L. monocytogenes*. An intriguing possibility is also the potential involvement of the Zea protein in the post-transcriptional control of A118 phage gene expression. The Zea protein has been described very recently as the protein specifically binding transcripts of A118 phage genes of *L. monocytogenes* EGD-e (Pagliuso et al., 2019). Unfortunately, it is not known whether Zea binding to the phage RNAs influences their translation, however the observed decrease in *zea* expression in the *sif* mutant strain may suggest that it is involved in the control of active lysogeny of A118 phage in the EGD-e strain. Clearly, our speculations on the potential involvement of Hfq and/or Zea proteins in post-transcriptional regulation of A118 phage genes expression require further research.

Our study also revealed that *L. monocytogenes* responds to *lmo0946* inactivation by upregulation of the monocin genetic locus. As the monocin element in *L. monocytogenes* is reported to be activated under UV irradiation (Argov et al., 2017), we assume that high level of expression of this MGE in the *sif* imutant strain, similarly to phage A118, results from activation of the SOS response. It is worth noting that the monocin locus resembles a phage tail module of A118-like phages but it does not contain the DNA region responsible for DNA replication and recombination (Lee et al., 2016). These

observations might explain why this MGE element, unlike phage A118, is not mobilized. Inactivation of the *sif* gene also results in replication of ICELm1 and the presence of this element in circular form in *L. monocytogenes* EGD-e. Generally, integrative and conjugative elements (ICEs), also known as conjugative transposons, are normally integrated into the bacterial chromosome. They can excise, transfer by conjugation and integrate into the chromosome of the recipient (Whittle et al., 2002). Notably, this is the first report on mobilization of the ICE in *L. monocytogenes*. In case of the integrative and conjugative element ICE*Bs1* of *Bacillus subtilis*, capable of transferring to *Bacillus* and *Listeria* species, its excision and transfer is activated by induction of the SOS response (Auchtung et al., 2005). Therefore, we assume that the replication and presence of ICELm1 in circular form in the *sif* mutant strain may be associated with activation of the SOS response which results from *sif* inactivation. The replication and presence of ICELm1 in circular form in the *sif* mutant strain is correlated with increased resistance to cadmium, which confirms the mobilization of this MGE. Curiously, upon complementation ICELm1 is still detected in a circular form and the presence of this MGE in the complemented strain correlates well with high level of expression of *lmo1097* coding for an integrase of ICELm1 and high level of cadmium resistance. Thus, ICELm1 mobilization and associated phenotype is not reversed upon complementation. Moreover, the complementation also fails to restore the expression of several other genes, namely *hfq*, *zea* and *rsbV*, to the level observed in the wild-type strain. At the current stage of research, the reason for the lack of reversion of the expression level of these genes and the mobilization of ICELm1 upon complementation remains unclear. However, we suppose that the lack of complementation may be due to a lower level of Sif protein in the complemented strain as compared to the wild-type strain. In the complemented strain, the *sif* gene is expressed *in trans* from the native promoter of *lmo0945*. As a result, Sif is not translated from the larger co-transcripts corresponding to *sif* mRNA arising in *L. monocytogenes* EGD-e, which in turn leads to an overall lower level of Sif protein in the complemented strain than in the wild-type strain.

Activation of the SOS response and the mobilization of MGEs, is accompanied by a decrease in energy production and conversion as well as transport and metabolism of different cell compounds in the *sif* mutant strain. These changes indicate general metabolic slowdown in response to *sif* inactivation. Our analysis also revealed that *L. monocytogenes* responds to *sif* inactivation by changed expression of multiple genes known to be under control of important regulators involved in stress response and virulence of *L. monocytogenes*, including CodY, σB and PrfA. The largest overlap of genes with highly changed expression in the *sif* mutant is observed for the CodY regulon. The transcriptional regulator CodY plays an important role in carbon and nitrogen assimilation and metabolism. The role of CodY relies on monitoring the overall energetic state of the cell by sensing the levels of GTP, and the nutritional state of the cell by sensing the levels of branched chain amino acid (BCAAs) (Bennett et al., 2007). In the current study, no change in the level of expression of the BCAA biosynthesis operon (*ilv-leu*) was observed (Supplementary Table S4). This suggests that putative modulation of CodY activity in the *sif* mutant strain does not result from BCAAs insufficiency and could be rather GTP-dependent. This assumption is in line with the observed general downregulation of genes involved in energy production and conversion in the *sif* mutant strain. However, it should be noted that only some of the genes overlapping with the CodY regulon are involved in transport and metabolism, while most of them correspond to A118 prophage genes. Therefore, the involvement of CodY in the downregulation of energy production and conversion in the *sif* mutant strain is uncertain. Similarly, the engagement of CodY in the regulation of A118 prophage genes in the *sif* mutant is ambiguous, as the details of CodY-dependent regulation of A118 prophage genes are missing (Bennett et al., 2007), and upregulation of these genes is triggered by activation of the SOS response (Pasechnek et al., 2020).

Among the highly down-regulated genes in the *sif* mutant strain, we found genes positively regulated by the alternative sigma factor σB. The σB factor controls the general stress response in *L. monocytogenes* (Dorey et al., 2019) and plays an indispensable role in the gastrointestinal phase of infection (Toledo-Arana et al., 2009). One of the stresses experienced by *L. monocytogenes* in the gastrointestinal tract is bile stress, and σB-dependent expression of *bsh* encoding the bile salt hydrolase enables bile tolerance (Begley et al., 2005). The downregulation of *bsh* in the *sif* mutant strain suggests that inactivation of *sif* leads to an impairment of stress tolerance during the gastrointestinal phase of infection. Further analysis revealed decreased level of expression of *rsbV* which is an important factor in the signaling pathway controlling σB activity. In stress-free conditions, σB is sequestered by the anti-sigma factor RsbW that prevents interaction of σB with core RNA polymerase, and therefore the σB regulon is not transcribed (Ferreira et al., 2001). When stress signals are sensed, the anti-anti-sigma factor RsbV undergoes dephosphorylation and interacts directly with RsbW. The RsbV-RsbW interaction results in release of σB from RsbW-σB complexes. Subsequently, σB binds to the core RNA polymerase and directs transcription of the σB regulon (Hecker et al., 2007). Therefore, RsbV is required to activate σB in response to stress signals in *L. monocytogenes* (Chaturongakul and Boor, 2004, 2006). It seems likely that the reduced level of *rsbV* expression in the *sif* mutant strain may result in decreased liberation of σB from the RsbW-σB complexes, and thus in inhibition of transcription of the σB regulon despite of stress signals sensed. While the impairment of the σB signaling pathway does not explain the downregulation of numerous genes which are under positive control of σB, it clearly indicates that the σB protective response is prevented in *sif* mutant strain. Interestingly, while *rsbV* is the first gene of the four-gene operon which includes besides *rsbV* also *rsbW*, *sigB* and *rsbX*, we observed that expression of *rsbV* but not *sigB* is downregulated. This result suggests that the expression of this operon is regulated post-transcriptionally in the *sif* mutant strain.

Finally, we found that expression of a large portion of genes regulated by the master virulence regulator PrfA is downregulated in the *sif* mutant strain despite increased expression of *prfA* itself. It should be noted that σB-dependent promoters precede multiple PrfA-dependent genes which are downregulated in the *sif* mutant strain (Supplementary Table S9; Milohanic et al., 2003). This suggests that downregulation of PrfA-dependent genes is related to the downregulation of σB-dependent genes described above for the *sif* mutant strain. However, among the downregulated genes are also those belonging to the core set of genes preceded by a PrfA box (e.g., *hly* encoding listeriolysin O); these genes are most likely expressed in a σA-dependent manner (Milohanic et al., 2003). Furthermore, among highly downregulated genes is *lmo1634*, encoding the LAP protein with a role in crossing the intestinal epithelial barrier (Drolia et al., 2018) as well as *arpJ* and *pplA* coding for factors important at

the intracellular stage of infection (Reniere et al., 2016). Interestingly, the virulence factors mentioned above do not belong to the PrfA-or σB regulons. These findings indicate that inactivation of *sif* impairs virulence of *L. monocytogenes* at different stages of infection. This conclusion is supported by the diminished virulence of the *sif* mutant observed in our *in vitro* and *in vivo* infection studies. While the details of the complex regulatory circuits in the *sif* mutant strain remain to be elucidated, it is clear that inactivation of *sif* leads to general silencing of the virulence program in *L. monocytogenes*.

To summarize, we found that *fri* is transcribed together with four downstream genes, namely *lmo0944*, *lmo0945, lmo0946* and *lhrC5*. Functional analysis of genes from the ferritin operon revealed that inactivation of *lmo0946*, coding for a protein with unknown function, results in severe impairment of *L. monocytogenes* growth in virtually all conditions tested. Inactivation of *lmo0946* results in global changes of gene expression with clearly induced expression of SOS response genes, which prompted us to rename the *lmo0946* gene to *sif* (SOS *i*nterfering *f*actor). Activation of the SOS response in the *sif* mutant strain is accompanied by mobilization of A118 prophage and ICELm-1 mobile genetic elements (MGEs). In parallel to activation of the SOS response and mobilization of MGEs, the absence of Sif results in downregulation of stress response genes from the σ^B regulon and multiple virulence genes, modulation of expression of genes from the CodY regulon, and highly upregulated expression of *hfq* coding for an RNA chaperone. While the function of Sif could not be disclosed in the current study, the results clearly demonstrate the importance of this newly discovered protein in stress adaptation and virulence of *L. monocytogenes*. Future studies should aim at disclosing the function of Sif as well as defining the molecular mechanisms responsible for the transcriptional changes resulting from *sif* inactivation, especially those related to silencing of the general stress response and virulence program in *L. monocytogenes*.

Data availability statement

The datasets presented in this study can be found in online repositories. The names of the repository/repositories and accession number(s) can be found in the article/Supplementary material.

Ethics statement

Ethical approval was not required for the studies on humans in accordance with the local legislation and institutional requirements because only commercially available established cell lines were used. The animal study was approved by 2nd Local IACUC in Kraków (Institute of Pharmacology Polish Academy of Sciences, Permit Number: 48/2017). The study was conducted in accordance with the local legislation and institutional requirements.

Author contributions

MŁ: Formal analysis, Investigation, Methodology, Validation, Visualization, Writing – original draft. EP: Investigation, Methodology, Writing – original draft. KG: Investigation, Methodology, Writing – original draft. PG: Investigation, Validation, Writing – original draft. KJ: Investigation, Methodology, Validation, Visualization, Writing – original draft. KŚ: Investigation, Writing – original draft. MM-W: Investigation, Writing – original draft. KK-Z: Investigation, Writing – original draft. EL: Methodology, Writing – original draft. BK: Conceptualization, Methodology, Resources, Writing – original draft, Writing – review & editing. AK-B: Conceptualization, Data curation, Formal analysis, Funding acquisition, Investigation, Methodology, Project administration, Resources, Supervision, Visualization, Writing – original draft, Writing – review & editing.

Funding

The author(s) declare financial support was received for the research, authorship, and/or publication of this article. The study was supported by the National Science Centre (Poland) through a grant to AK-B (grant no. 2016/21/B/NZ6/00963) and partially supported by EMBO Short-term Fellowship (no. ASTF 137) to AK-B. Publication was co-financed by "Excellence Initiative—Research University (2020–2026)" Program at the University of Warsaw.

Acknowledgments

The authors are grateful to Krzysztof Pyrć from Malopolska Centre of Biotechnology, Jagiellonian University for the organizational care over animal experiments and Inga Drebot from Malopolska Centre of Biotechnology for expert technical assistance in *in vivo* infection experiments. The authors also thank Marta Zapotoczna for help with biofilm analysis, Mikołaj Dziurzyński from DDG Bioinformatics for great expert assistance in transcriptomics data analysis, and Dariusz Bartosik from Department of Bacterial Genetics, University of Warsaw for a constructive discussion on MGEs.

Conflict of interest

The authors declare that the research was conducted in the absence of any commercial or financial relationships that could be construed as a potential conflict of interest.

Publisher's note

Supplementary material

The Supplementary material for this article can be found online at: https://www.frontiersin.org/articles/10.3389/fmicb.2023.1324062/full#supplementary-material

References

Aertsen, A., and Michiels, C. W. (2006). Upstream of the SOS response: figure out the trigger. *Trends Microbiol.* 14, 421–423. doi: 10.1016/j.tim.2006.08.006

Argov, T., Rabinovich, L., Sigal, N., and Herskovits, A. A. (2017). An effective counterselection system for *Listeria monocytogenes* and its use to characterize the monocin genomic region of strain 10403S. *Appl. Environ. Microbiol.* 83, e02927–e02916. doi: 10.1128/AEM.02927-16

Arnaud, M., Chastanet, A., and Débarbouillé, M. (2004). New vector for efficient allelic replacement in naturally nontransformable, low-GC-content, gram-positive bacteria. *Appl. Environ. Microbiol.* 70, 6887–6891. doi: 10.1128/AEM.70.11.6887-6891.2004

Auchtung, J. M., Lee, C. A., Monson, R. E., Lehman, A. P., and Grossman, A. D. (2005). Regulation of a *Bacillus subtilis* mobile genetic element by intercellular signaling and the global DNA damage response. *Proc. Natl. Acad. Sci.* 102, 12554–12559. doi: 10.1073/pnas.0505835102

Bécavin, C., Bouchier, C., Lechat, P., Archambaud, C., Creno, S., Gouin, E., et al. (2014). Comparison of widely used *Listeria monocytogenes* strains EGD, 10403S, and EGD-e highlights genomic differences underlying variations in pathogenicity. *MBio* 5, 10–1128. doi: 10.1128/mBio.00969-14

Begley, M., Hill, C., and Ross, R. P. (2006). Tolerance of *Listeria monocytogenes* to cell envelope-acting antimicrobial agents is dependent on sig B. *Appl. Environ. Microbiol.* 72, 2231–2234. doi: 10.1128/AEM.72.3.2231-2234.2006

Begley, M., Sleator, R. D., Gahan, C. G. M., and Hill, C. (2005). Contribution of three bile-associated loci, bsh, pva, and btl B, to gastrointestinal persistence and bile tolerance of *Listeria monocytogenes*. *Infect. Immun.* 73, 894–904. doi: 10.1128/IAI.73.2.894-904.2005

Bennett, H. J., Pearce, D. M., Glenn, S., Taylor, C. M., Kuhn, M., Sonenshein, A. L., et al. (2007). Characterization of rel a and codY mutants of *Listeria monocytogenes*: identification of the CodY regulon and its role in virulence. *Mol. Microbiol.* 63, 1453–1467. doi: 10.1111/j.1365-2958.2007.05597.x

Cabanes, D., Lecuit, M., and Cossart, P. (2008). Animal models of listeria infection: firmicutes (low G+ C gram positive). *Curr. Protoc. Microbiol.* 10, 9B–1B. doi: 10.1002/9780471729259.mc09b01s10

Chatterjee, S. S., Hossain, H., Otten, S., Kuenne, C., Kuchmina, K., Machata, S., et al. (2006). Intracellular gene expression profile of *Listeria monocytogenes*. *Infect. Immun.* 74, 1323–1338. doi: 10.1128/IAI.74.2.1323-1338.2006

Chaturongakul, S., and Boor, K. J. (2004). RsbT and RsbV contribute to σB-dependent survival under environmental, energy, and intracellular stress conditions in *Listeria monocytogenes*. *Appl. Environ. Microbiol.* 70, 5349–5356. doi: 10.1128/AEM.70.9.5349-5356.2004

Chaturongakul, S., and Boor, K. J. (2006). σB activation under environmental and energy stress conditions in *Listeria monocytogenes*. *Appl. Environ. Microbiol.* 72, 5197–5203. doi: 10.1128/AEM.03058-05

Chen, S., Zhou, Y., Chen, Y., and Gu, J. (2018). Fastp: an ultra-fast all-in-one FASTQ preprocessor. *Bioinformatics* 34, i884–i890. doi: 10.1093/bioinformatics/bty560

Christiansen, J. K., Larsen, M. H., Ingmer, H., Søgaard-Andersen, L., and Kallipolitis, B. H. (2004). The RNA-binding protein Hfq of *Listeria monocytogenes*: role in stress tolerance and virulence. *J. Bacteriol.* 186, 3355–3362. doi: 10.1128/JB.186.11.3355-3362.2004

Dallmier, A. W., and Martin, S. E. (1988). Catalase and superoxide dismutase activities after heat injury of *Listeria monocytogenes*. *Appl. Environ. Microbiol.* 54, 581–582. doi: 10.1128/aem.54.2.581-582.1988

Djordjevic, D., Wiedmann, M., and McLandsborough, L. A. (2002). Microtiter plate assay for assessment of *Listeria monocytogenes* biofilm formation. *Appl. Environ. Microbiol.* 68, 2950–2958. doi: 10.1128/AEM.68.6.2950-2958.2002

Dorey, A., Marinho, C., Piveteau, P., and O'byrne, C. (2019). Role and regulation of the stress activated sigma factor sigma B (σB) in the saprophytic and host-associated life stages of *Listeria monocytogenes*. *Adv. Appl. Microbiol.* 106, 1–48. doi: 10.1016/bs.aambs.2018.11.001

Dos Santos, P. T., Larsen, P. T., Menendez-Gil, P., Lillebaek, E. M. S., and Kallipolitis, B. H. (2018). *Listeria monocytogenes* relies on the Heme-regulated transporter hrtAB to resist Heme toxicity and uses heme as a signal to induce transcription of lmo1634, encoding listeria adhesion protein. *Front. Microbiol.* 9:3090. doi: 10.3389/fmicb.2018.03090

Drolia, R., Tenguria, S., Durkes, A. C., Turner, J. R., and Bhunia, A. K. (2018). Listeria adhesion protein induces intestinal epithelial barrier dysfunction for bacterial translocation. *Cell Host Microbe* 23, 470–484.e7. doi: 10.1016/j.chom.2018.03.004

Dussurget, O., Dumas, E., Archambaud, C., Chafsey, I., Chambon, C., Hébraud, M., et al. (2005). *Listeria monocytogenes* ferritin protects against multiple stresses and is required for virulence. *FEMS Microbiol. Lett.* 250, 253–261. doi: 10.1016/j.femsle.2005.07.015

European Food Safety Authority and European Centre for Disease Prevention and Control (2022). The European Union one health 2021 zoonoses report. *EFSA J.* 20:e07666. doi: 10.2903/j.efsa.2022.7666

Ferreira, A., O'Byrne, C. P., and Boor, K. J. (2001). Role of σB in heat, ethanol, acid, and oxidative stress resistance and during carbon starvation in *Listeria monocytogenes*. *Appl. Environ. Microbiol.* 67, 4454–4457. doi: 10.1128/AEM.67.10.4454-4457.2001

Franze de Fernandez, M. T., Eoyang, L., and August, J. T. (1968). Factor fraction required for the synthesis of bacteriophage QÎ²-RNA. *Nature* 219, 588–590. doi: 10.1038/219588a0

Haikarainen, T., and Papageorgiou, A. C. (2010). Dps-like proteins: structural and functional insights into a versatile protein family. *Cell. Mol. Life Sci.* 67, 341–351. doi: 10.1007/s00018-009-0168-2

Hain, T., Ghai, R., Billion, A., Kuenne, C. T., Steinweg, C., Izar, B., et al. (2012). Comparative genomics and transcriptomics of lineages I, II, and III strains of *Listeria monocytogenes*. *BMC Genomics* 13, 1–17. doi: 10.1186/1471-2164-13-144

Hébraud, M., and Guzzo, J. (2000). The main cold shock protein of *Listeria monocytogenes* belongs to the family of ferritin-like proteins. *FEMS Microbiol. Lett.* 190, 29–34. doi: 10.1016/S0378-1097(00)00310-4

Hecker, M., Pané-Farré, J., and Uwe, V. (2007). SigB-dependent general stress response in *Bacillus subtilis* and related gram-positive bacteria. *Annu. Rev. Microbiol.* 61, 215–236. doi: 10.1146/annurev.micro.61.080706.093445

Hof, H. (2003). Therapeutic options. *FEMS Immunol. Med. Microbiol.* 35, 203–205. doi: 10.1016/S0928-8244(02)00466-2

Krawczyk-Balska, A., Marchlewicz, J., Dudek, D., Wasiak, K., and Samluk, A. (2012). Identification of a ferritin-like protein of *Listeria monocytogenes* as a mediator of β-lactam tolerance and innate resistance to cephalosporins. *BMC Microbiol.* 12, 278–212. doi: 10.1186/1471-2180-12-278

Krawczyk-Balska, A., and Markiewicz, Z. (2016). The intrinsic cephalosporin resistome of *Listeria monocytogenes* in the context of stress response, gene regulation, pathogenesis and therapeutics. *J. Appl. Microbiol.* 120, 251–265. doi: 10.1111/jam.12989

Kuenne, C., Billion, A., Mraheil, M. A., Strittmatter, A., Daniel, R., Goesmann, A., et al. (2013). Reassessment of the *Listeria monocytogenes* pan-genome reveals dynamic integration hotspots and mobile genetic elements as major components of the accessory genome. *BMC Genomics* 14, 1–19. doi: 10.1186/1471-2164-14-47

Langmead, B., and Salzberg, S. L. (2012). Fast gapped-read alignment with bowtie 2. *Nat. Methods* 9, 357–359. doi: 10.1038/nmeth.1923

Lauer, P., Chow, M. Y. N., Loessner, M. J., Portnoy, D. A., and Calendar, R. (2002). Construction, characterization, and use of two *Listeria monocytogenes* site-specific phage integration vectors. *J. Bacteriol.* 184, 4177–4186. doi: 10.1128/JB.184.15.4177-4186.2002

Lechowicz, J., and Krawczyk-Balska, A. (2015). An update on the transport and metabolism of iron in *Listeria monocytogenes*: the role of proteins involved in pathogenicity. *Biometals* 28, 587–603. doi: 10.1007/s10534-015-9849-5

Lee, G., Chakraborty, U., Gebhart, D., Govoni, G. R., Zhou, Z. H., and Scholl, D. (2016). F-type bacteriocins of *Listeria monocytogenes*: a new class of phage tail-like structures reveals broad parallel coevolution between tailed bacteriophages and high-molecular-weight bacteriocins. *J. Bacteriol.* 198, 2784–2793. doi: 10.1128/JB.00489-16

Little, J. W., and Mount, D. W. (1982). The SOS regulatory system of *Escherichia coli*. *Cells* 29, 11–22. doi: 10.1016/0092-8674(82)90085-X

Loessner, M. J., Inman, R. B., Lauer, P., and Calendar, R. (2000). Complete nucleotide sequence, molecular analysis and genome structure of bacteriophage A118 of *Listeria monocytogenes*: implications for phage evolution. *Mol. Microbiol.* 35, 324–340. doi: 10.1046/j.1365-2958.2000.01720.x

Love, M. I., Huber, W., and Anders, S. (2014). Moderated estimation of fold change and dispersion for RNA-seq data with DESeq2. *Genome Biol.* 15, 1–21. doi: 10.1186/s13059-014-0550-8

Mandin, P., Fsihi, H., Dussurget, O., Vergassola, M., Milohanic, E., Toledo-Arana, A., et al. (2005). Vir R, a response regulator critical for *Listeria monocytogenes* virulence. *Mol. Microbiol.* 57, 1367–1380. doi: 10.1111/j.1365-2958.2005.04776.x

Maslowska, K. H., Makiela-Dzbenska, K., and Fijalkowska, I. J. (2019). The SOS system: a complex and tightly regulated response to DNA damage. *Environ. Mol. Mutagen.* 60, 368–384. doi: 10.1002/em.22267

Milecka, D., Samluk, A., Wasiak, K., and Krawczyk-Balska, A. (2015). An essential role of a ferritin-like protein in acid stress tolerance of *Listeria monocytogenes*. *Arch. Microbiol.* 197, 347–351. doi: 10.1007/s00203-014-1053-4

Milohanic, E., Glaser, P., Coppée, J., Frangeul, L., Vega, Y., Vázquez-Boland, J. A., et al. (2003). Transcriptome analysis of *Listeria monocytogenes* identifies three groups of genes differently regulated by PrfA. *Mol. Microbiol.* 47, 1613–1625. doi: 10.1046/j.1365-2958.2003.03413.x

NicAogáin, K., and O'Byrne, C. P. (2016). The role of stress and stress adaptations in determining the fate of the bacterial pathogen *Listeria monocytogenes* in the food chain. *Front. Microbiol.* 7:1865. doi: 10.3389/fmicb.2016.01865

Nielsen, J. S., Larsen, M. H., Lillebæk, E. M. S., Bergholz, T. M., Christiansen, M. H. G., Boor, K. J., et al. (2011). A small RNA controls expression of the chitinase ChiA in *Listeria monocytogenes*. *PLoS One* 6:e19019. doi: 10.1371/journal.pone.0019019

Nielsen, J. S., Lei, L. K., Ebersbach, T., Olsen, A. S., Klitgaard, J. K., Valentin-Hansen, P., et al. (2010). Defining a role for Hfq in gram-positive bacteria: evidence for Hfq-dependent antisense regulation in *Listeria monocytogenes*. *Nucleic Acids Res.* 38, 907–919. doi: 10.1093/nar/gkp1081

Olsen, K. N., Larsen, M. H., Gahan, C. G. M., Kallipolitis, B., Wolf, X. A., Rea, R., et al. (2005). The Dps-like protein Fri of *Listeria monocytogenes* promotes stress tolerance and intracellular multiplication in macrophage-like cells. *Microbiology* 151, 925–933. doi: 10.1099/mic.0.27552-0

Pagliuso, A., Tham, T. N., Allemand, E., Robertin, S., Dupuy, B., Bertrand, Q., et al. (2019). An RNA-binding protein secreted by a bacterial pathogen modulates RIG-I signaling. *Cell Host Microbe* 26, 823–835.e11. doi: 10.1016/j.chom.2019.10.004

Parsons, C., Lee, S., and Kathariou, S. (2018). Heavy metal resistance determinants of the foodborne pathogen *Listeria monocytogenes*. *Genes* 10:11. doi: 10.3390/genes10010011

Pasechnek, A., Rabinovich, L., Stadnyuk, O., Azulay, G., Mioduser, J., Argov, T., et al. (2020). Active lysogeny in *Listeria monocytogenes* is a bacteria-phage adaptive response in the mammalian environment. *Cell Rep.* 32:107956. doi: 10.1016/j.celrep.2020.107956

Patro, R., Duggal, G., Love, M. I., Irizarry, R. A., and Kingsford, C. (2017). Salmon provides fast and bias-aware quantification of transcript expression. *Nat. Methods* 14, 417–419. doi: 10.1038/nmeth.4197

Pombinho, R., Camejo, A., Vieira, A., Reis, O., Carvalho, F., Almeida, M. T., et al. (2017). *Listeria monocytogenes* CadC regulates cadmium efflux and fine-tunes lipoprotein localization to escape the host immune response and promote infection. *J. Infect. Dis.* 215, 1468–1479. doi: 10.1093/infdis/jix118

Rabinovich, L., Sigal, N., Borovok, I., Nir-Paz, R., and Herskovits, A. A. (2012). Prophage excision activates listeria competence genes that promote phagosomal escape and virulence. *Cells* 150, 792–802. doi: 10.1016/j.cell.2012.06.036

Rea, R., Hill, C., and Gahan, C. G. M. (2005). *Listeria monocytogenes* PerR mutants display a small-colony phenotype, increased sensitivity to hydrogen peroxide, and significantly reduced murine virulence. *Appl. Environ. Microbiol.* 71, 8314–8322. doi: 10.1128/AEM.71.12.8314-8322.2005

Reniere, M. L., Whiteley, A. T., and Portnoy, D. A. (2016). An in vivo selection identifies *Listeria monocytogenes* genes required to sense the intracellular environment and activate virulence factor expression. *PLoS Pathog.* 12:e1005741. doi: 10.1371/journal.ppat.1005741

Sievers, S., Lund, A., Menendez-Gil, P., Nielsen, A., Storm Mollerup, M., Lambert Nielsen, S., et al. (2015). The multicopy sRNA LhrC controls expression of the oligopeptide-binding protein OppA in *Listeria monocytogenes*. *RNA Biol.* 12, 985–997. doi: 10.1080/15476286.2015.1071011

Sievers, S., Sternkopf Lillebæk, E. M., Jacobsen, K., Lund, A., Mollerup, M. S., Nielsen, P. K., et al. (2014). A multicopy sRNA of *Listeria monocytogenes* regulates expression of the virulence adhesin LapB. *Nucleic Acids Res.* 42, 9383–9398. doi: 10.1093/nar/gku630

Soneson, C., Love, M. I., and Robinson, M. D. (2015). Differential analyses for RNA-seq: Transcript-level estimates improve gene-level inferences. *F1000Res* 4:1521. doi: 10.12688/f1000research.7563.1

Sue, D., Boor, K. J., and Wiedmann, M. (2003). σ B-dependent expression patterns of compatible solute transporter genes *opuCA* and *lmo1421* and the conjugated bile salt hydrolase gene bsh in *Listeria monocytogenes*. *Microbiology* 149, 3247–3256. doi: 10.1099/mic.0.26526-0

Toledo-Arana, A., Dussurget, O., Nikitas, G., Sesto, N., Guet-Revillet, H., Balestrino, D., et al. (2009). The listeria transcriptional landscape from saprophytism to virulence. *Nature* 459, 950–956. doi: 10.1038/nature08080

van der Veen, S., van Schalkwijk, S., Molenaar, D., De Vos, W. M., Abee, T., and Wells-Bennik, M. H. J. (2010). The SOS response of *Listeria monocytogenes* is involved in stress resistance and mutagenesis. *Microbiology* 156, 374–384. doi: 10.1099/mic.0.035196-0

Whittle, G., Shoemaker, N. B., and Salyers, A. A. (2002). The role of Bacteroides conjugative transposons in the dissemination of antibiotic resistance genes. *Cellular Molecular Life Sci.* 59, 2044–2054. doi: 10.1007/s000180200004

Williams, T., Bauer, S., Beier, D., and Kuhn, M. (2005). Construction and characterization of *Listeria monocytogenes* mutants with in-frame deletions in the response regulator genes identified in the genome sequence. *Infect. Immun.* 73, 3152–3159. doi: 10.1128/IAI.73.5.3152-3159.2005

Zink, R., and Loessner, M. J. (1992). Classification of virulent and temperate bacteriophages of listeria spp. on the basis of morphology and protein analysis. *Appl. Environ. Microbiol.* 58, 296–302. doi: 10.1128/aem.58.1.296-302.1992

Zitovsky, J. P., and Love, M. I. (2019). Fast effect size shrinkage software for beta-binomial models of allelic imbalance. *F1000Res* 8:2024. doi: 10.12688/f1000research.20916.1

frontiers | Frontiers in Microbiology

TYPE Original Research
PUBLISHED 01 February 2024
DOI 10.3389/fmicb.2024.1342584

OPEN ACCESS

EDITED BY
Hector Alex Saka,
CONICET, Argentina

REVIEWED BY
Mei Li,
State Key Laboratory for Biology of Plant Diseases and Insect Pests,
Institute of Plant Protection, China
Vassili N. Kouvelis,
National and Kapodistrian University of Athens, Greece
Samantha Chandranath Karunarathna,
Qujing Normal University, China

*CORRESPONDENCE
Jian Ling
lingjian@caas.cn
Yanlin Li
liyanlin@hunau.edu.cn

†These authors share first authorship

RECEIVED 22 November 2023
ACCEPTED 10 January 2024
PUBLISHED 01 February 2024

CITATION
Yang Q, Mao Z, Hao Y, Zheng S, Zhao J, Li Y, Yang Y, Xie B, Ling J and Li Y (2024) Genome-wide transcriptome profiling reveals molecular response pathways of *Trichoderma harzianum* in response to salt stress. *Front. Microbiol.* 15:1342584. doi: 10.3389/fmicb.2024.1342584

Genome-wide transcriptome profiling reveals molecular response pathways of *Trichoderma harzianum* in response to salt stress

Qihong Yang[1,2†], Zhenchuan Mao[2†], Yali Hao[2], Shijie Zheng[2], Jianlong Zhao[2], Yan Li[2], Yuhong Yang[2], Bingyan Xie[1,2], Jian Ling[2]* and Yanlin Li[1,3]*

[1]College of Horticulture, Engineering Research Center for Horticultural Crop Germplasm Creation and New Variety Breeding (Ministry of Education), Hunan Mid-Subtropical Quality Plant Breeding and Utilization Engineering Technology Research Center, Hunan Agricultural University, Changsha, China, [2]State Key Laboratory of Vegetable Biobreeding, Institute of Vegetables and Flowers, Chinese Academy of Agricultural Sciences, Beijing, China, [3]School of Biological Sciences, Nanyang Technological University, Singapore, Singapore

Trichoderma harzianum exhibits a strong biological control effect on many important plant pathogens, such as *Fusarium oxysporum*, *Botrytis cinerea*, and *Meloidogyne*. However, its biocontrol effectiveness is weakened or reduced under salt stress. The aim of this study was to investigate the molecular response of *T. harzianum* to salt stress at the whole-genome level. Here, we present a 44.47 Mb near-complete genome assembly of the *T. harzianum* qt40003 strain for the first time, which was assembled *de novo* with 7.59 Gb Nanopore sequencing long reads (~170-fold) and 5.2 Gb Illumina short reads (~116-fold). The assembled qt40003 genome contains 12 contigs, with a contig N50 of 4.81 Mb, in which four of the 12 contigs were entirely reconstructed in a single chromosome from telomere to telomere. The qt40003 genome contains 4.27 Mb of repeat sequences and 12,238 protein-coding genes with a BUSCO completeness of 97.5%, indicating the high accuracy and completeness of our gene annotations. Genome-wide transcriptomic analysis was used to investigate gene expression changes related to salt stress in qt40003 at 0, 2% (T2), and 4% (T4) sodium chloride concentrations. A total of 2,937 and 3,527 differentially expressed genes (DEGs) were obtained under T2 and T4 conditions, respectively. GO enrichment analysis showed that the T2-treatment DEGs were highly enriched in detoxification ($p < 0.001$), while the T4 DEGs were mainly enriched in cell components, mostly in cellular detoxification, cell surface, and cell wall. KEGG metabolic pathway analysis showed that 91 and 173 DEGs were significantly enriched in the T2 and T4 treatments, respectively ($p < 0.01$), mainly in the glutathione metabolism pathway. We further experimentally analyzed the differentially expressed glutathione transferase genes in the glutathione metabolic pathway, most of which were downregulated (13/15). In addition, we screened 13 genes related to active oxygen clearance, including six upregulated and seven downregulated genes, alongside five fungal hydrophobic proteins, of which two genes were highly expressed. Our study provides high-quality genome information for the use of *T. harzianum* for biological control and offers significant insights into the molecular responses of *T. harzianum* under salt-stress conditions.

KEYWORDS

genome, metabolic, NaCl, salt tolerance mechanism, transcriptomic

1 Introduction

Soil salinization, the excessive accumulation of salt and alkaline substances in the soil, is one of the major soil degradation threats occurring in the world, leading to an increase in soil pH and salt content, which limits the growth and development of plants. This is a common phenomenon across the globe, especially in arid regions and areas where irrigated agriculture is frequent. Human activities, such as over-reclamation of land, improper irrigation, and large-scale use of chemical fertilizers, have aggravated the problem of soil salinization for a long time, seriously affecting agricultural production, the ecological environment, and human welfare. At present, 0.8–3.6% of soils have become saline globally, about 1,125 million hectares of land are under threat of salinity, and 1.5 million hectares of land are becoming useless for agricultural production (Hossain and Shah, 2019). China's saline–alkali land area is currently about 3.5×10^7 hm^2 and still increasing (Wang et al., 2011), accounting for 4.88% of the country's arable soil area and mainly distributed in the northeast, north, northwest inland areas, and the coastal areas north of the Yangtze River (Zhang, 2020). Poor seed germination, withering of leaves, and, in severe cases, plant death are the signs of reduced water availability and osmotic pressure in saline soil (Kundu et al., 2022). Therefore, the adoption of effective measures to alleviate the harm of saline–alkali land to plants is an important challenge facing world agriculture.

Trichoderma spp. are widely found in nature, primarily in soil. They are one of the most widely used microbes for the biocontrol of plant diseases, and alter the response of plants to abiotic stresses (Zaidi et al., 2014). *T. harzianum* (*TH*), a *Trichoderma* species with great biocontrol potential, has good research value and broad research prospects. *TH* mainly acts on the resistance response of plants through competition, hyperparasitism, antibiosis, growth promotion, induction of plant resistance, and other aspects. Hashem et al. studied the effect of *TH* inoculation on *Ochradenus baccatus* in saline subsurface at soil concentrations of 0, 75, and 150 mM (Hashem et al., 2014), and showed that *TH* can increase the seed germination rate, dry weight of roots and aboveground parts, water content, membrane stability, chlorophyll content, total lipid content, and neutral lipid content of *Ochradenus baccatus* under salt stress, improving the antioxidant capacity and nutrient absorption capacity of plants. Umber et al. studied the effects of *TH* coating on wheat germination and seedling development under salt stress [60 and 120 mM sodium chloride (NaCl)] (Umber et al., 2021). The results showed that *TH* seed coating reduced the amount of hydrogen peroxide, catalase, and malondialdehyde and increased the protein content, ascorbate peroxidase, and total phenolics under salt stress, suggesting that its use is effective in the cultivation of crops in saline areas because it inhibits oxidative damage by triggering various phenolic compounds and scavenging proteins. Ahmad et al. studied the effects of different concentrations of NaCl (0, 100, and 200 mM) on factors including growth, physiobiochemical attributes, antioxidant enzymes, and oil content (Ahmad et al., 2015). Their results show that *TH* mitigated the detrimental effects of NaCl stress in mustard seedlings. Both enzymatic (SOD, POD, CAT, GR, APX, MDHAR, DHAR, GST, GPX), and non-enzymatic (ASA, GSH, GSSG) antioxidants are induced by NaCl, and *TH* further enhanced the synthesis of these phytoconstituents and protected the Brassica plants from further damage. However, the biocontrol effects of *TH* are restricted by various factors, such as chemical pesticides, soil salinization, environmental humidity, and temperature. Xiang et al. found that, as the sodium stress concentration of *TH* increased, the growth rate of the colony slowed down, the colony thinned, and the biomass decreased (Xiang et al., 2019). Nagarajan et al. found that an appropriate salt concentration can promote the metabolism of mycorrhizal fungi cells (Nagarajan and Natarajan, 1999). However, a high salt content affects the metabolism of cellular substances and even inhibits the growth of mycelia. The capacity of *Trichoderma* for biological disease control and environmental restoration depends on whether the strain has a high level of stress resistance (Vinale et al., 2008). In summary, while numerous studies have demonstrated that *TH* alleviates plant damage under salt stress, few have focused on elucidating the fungus's own salt-tolerant mechanisms.

In this study, whole-genome sequencing and RNA sequencing (RNA-seq) technology were used to analyze the differential transcripts of *TH* strain qt40003 under normal conditions and NaCl stress, and to screen for the functional genes that regulate *TH* salt tolerance. The results of this study provide a theoretical basis for exploring the salt tolerance mechanism of *TH*, and have important relevance to making full use of the salt tolerance potential of *TH* and optimizing its application in sustainable agriculture in salinized areas.

2 Materials and methods

2.1 Materials

T. harzianum (*TH*) strain qt40003 was stored in the microbial preservation room of the Institute of Vegetables and Flowers, Chinese Academy of Agricultural Sciences (CAAS). The DNA extraction kit was procured from Sango Biotech Company, while the reverse transcription kit, RNA extraction kit, and qPCR kit were all obtained from TIAN GEN Biotech Company.

2.2 Methods

2.2.1 Morphological and molecular identification of the strain qt40003

In order to determine whether the strain was *TH*, we removed the strain from the −80° refrigerator, picked it out with a vaccination needle and cultured it on PDA medium (28°C, out of light) for 5 days. Microhypha was picked up with tweezers and observed under a microscope. After spore production, spores were filtered with sterile water and four layers of lens paper to obtain a spore suspension, and then observed with a microscope.

The strains in question, namely qt40001, qt40003, and qt40443, were subjected to PCR amplification using the universal fungal primer *RPB2* (Saadaoui et al., 2023) (*RPB2*-5F2: 5′-GGGGWGAYCAG AAGAAGGC-3′, *RPB2*-7Cr: 5′-CCCATRGCTTGYTTRCCCAT-3′). The PCR amplification system was configured as follows: 1 μL of DNA template, 12.5 μL of 2× PCR Master Mix, 1 μL each of primers *RPB2*-5F2 and *RPB2*-7Cr, and 9.5 μL of ddH_2O. The PCR amplification conditions were as follows: initial denaturation at 95°C for 3 min; followed by 35 cycles of denaturation at 95°C for 15 s, annealing at 56°C for 15 s, and extension at 72°C for 15 s; a final extension step at 72°C for 5 min. Subsequently, 5 μL of PCR amplification products

were subjected to electrophoresis in 1 × TAE buffer solution, with DNA Marker serving as the control, and the PCR product bands were visualized using a gel imaging system.

Sequencing services were outsourced to Shenzhen BGI Co., LTD., and the obtained sequencing data were subjected to similarity analysis using Blast against the GenBank database. The clustering analysis was conducted using iqtree (v 2.0), the phylogenetic tree was constructed employing the Neighbor-Joining (NJ) method.

2.2.2 Effects of NaCl stress on mycelial growth of qt40003

The strain was retrieved from the −80°C freezer and cultured at a constant temperature of 28°C without light for 3 days in Potato Dextrose Agar (PDA) medium (containing 200 g of potato, 20 g of glucose, 20 g of agar, and 1,000 mL of water). PDA media containing different concentrations of NaCl (0% as the control, 2, 4, 6, 8, and 10%) were prepared. Using a hole puncher (Φ = 6 mm), fungal cakes were removed from the edge of the activated colony and were then inoculated onto the center of the PDA plates with varying gradients. The plates were incubated at a constant temperature of 28°C without light. Colony morphology was recorded every 12 h. When the CK (0%) colonies occupied the entire culture dish, the colony diameters under different concentration gradients were measured, and the inhibitory rate of NaCl on colony growth was calculated as follows.

$$\text{Colony growth inhibition rate} = \frac{\text{CK colony diameter} - \text{colony diameter after treatment}}{\text{CK colony diameter}} \times 100\%$$

2.2.3 Genome comparison

Using the nucmer module in MUMMER (v 3.23) with the parameter -maxmatch, a genome-wide comparison was made between IIPRTh-33 and qt40003 (Kurtz et al., 2004). The output of nucmer was filtered by delta-filtering (with the parameters -i 85-L1000-1 - r-q) to identify the one-to-one syntenic blocks between two genomes, visualize the results using the mummerplot module (with parameters -R IIPRTh-33.fa -Q qt40003.fa --filter --layout --large --png out.delt.filter > out1.png).

2.2.4 Genome sequencing and assembly

The qt40003 genomic DNA extracted by the kit is sent to the Illumina (CA, United States) platform for sequencing. "k-mer analysis" is performed on the original data using Jellyfish (v2.2.3). When K value is 21, the peak of k-mer distribution curve is 24. The qt40003 genome size is estimated to be 40.79 Mb.

For third-generation sequencing, we used the native barcoding expansion kit (EXP-NBD104 and EXP-NBD114) and the ligation sequencing kit (SQK-LSK109) to prepare the library. Nanopore sequencing was performed on MinION (ONT R9.4.1). Reads generated on the Nanopore MinION platform were evaluated for sequence quality according to manufacturer's protocol. Qt40003 generated a total of 7.59 Gb reads length for subsequent analysis.

We used canu (v 1.5) (Koren et al., 2017) and Nextdenovo (v 2.5.0) for genome *de novo* assembly. To improve assembly quality. We combined the two assembly results using QUICKMERGE (v 0.3) software. The genome was then polished using Racon (v 1.5.0) and Minimap2 (v 2.24), followed by 3 rounds of Pilon (parameters --changes --treads 6 --fix all) using second-generation Illumina's short reads (Walker et al., 2014). A circular map of the genome was obtained using CIRCOS (v 0.69) (Krzywinski et al., 2009).

We conducted a genome evaluation using BUSCO (version 5.3.2, https://busco.ezlab.org/) with the following parameters: -i harzi_40,003.fa -lineage_dataset Fungi_odb10 -out output -m genome.

2.2.5 Repeat content identification

We used homology and *de novo* methods to identify the repeated sequences in qt40003 genome. For the process of *de novo* methods, we used LTR-FINDER, REPEATSCOUT (Price et al., 2005), MITE-HUNTER (Han and Wessler, 2010) and PILER-DF (Edgar and Myers, 2005) to build the *de novo* repeat sequence library. For the process of the homology, we used Repbase database (v 20.05) (Bao et al., 2015). The final repeat sequence library is created from the *de novo* constructed database together with the Repbase database. Finally, we used REPEATMASKER (v 4.0.9) (Tarailo-Graovac and Chen, 2009) (http://repeatmasker.org/) to identify and classify the repeats in qt40003 genome. To detect species-specific repetitive elements, we employed repeatmodeler (v 2.0 with the following parameters: BuildDatabase -name contig.db -engine ncbi qt40003.fa.masked RepeatModeler -pa 10 -database contig.db > & RepeatModeler.log).

2.2.6 Gene structure annotation

We employed three distinct approaches for the prediction of protein-coding genes: *de novo* prediction, gene prediction grounded in protein homology, and facilitated annotation leveraging RNA-seq data. The *ab initio* predictions were executed through the utilization of GENESCAN (Burge and Karlin, 1997), AUGUSTUS (v 2.7) (Stanke and Waack, 2003), GLIMMERHMM (v 3.0.4) (Majoros et al., 2004), GENEID (v 1.4) (Blanco et al., 2007), and SNAP (Korf, 2004). Gene prediction, based on homologous genes, was conducted employing GEMOMA (v 1.3) (Keilwagen et al., 2016) and entailed model training grounded in the coding sequence of *TH* CBS 226.95 (assembly Triha v1.0), as made available by NCBI. The RNA-seq reads of qt40003 were subjected to assembly via HISAT (v 2.0.4) (Kim et al., 2015) and STRINGTIE (v 1.2.3) (Pertea et al., 2015), subsequently facilitated by PASA (v 2.0.2) (Campbell et al., 2006) for elucidating unique i-genes, which contributed to the gene prediction process. Finally, we amalgamated the outcomes employing EVIDENCEMODELER (Haas et al., 2008).

2.2.7 Gene functional annotation analysis

We uploaded the protein sequence of qt40003 to eggnog (v 2.1.12; http://eggnog-mapper.embl.de/) for comparison with some protein sequence databases to annotate gene function. Including Nr (NCBI verbose protein sequence) (Pruitt et al., 2007), Nt (NCBI non-redundant nucleotide sequence) (Bateman et al., 2004), KOG (Galperin et al., 2021) and Swiss-Prot (https://www.ebi.ac.uk/uniprot/).

2.2.8 RNA-seq with different treatments

We employed a 6 mm diameter hole puncher to extract fungal cakes from the periphery of naturally growing 3d qt40003 mycelia. Each treatment was performed with three replicates to ensure the reliability of the results. Subsequently, these fungal cakes were individually inoculated onto Potato Dextrose Broth (PDB) medium containing 0, 2, and 4% concentrations of NaCl. The cultures were

maintained at 28°C in the dark with shaking at 200 rpm/min. After a cultivation period of 3d, the mycelial samples were collected. Subsequently, these samples were submitted to Shanghai Personal Biotechnology Co., Ltd. for subsequent processing, including total RNA extraction, purification, quality assessment, and cDNA library construction. Using the sequencing by synthesis technology, which involves simultaneous synthesis and sequencing, the cDNA libraries were subjected to sequencing using the Illumina Hiseq XTen high-throughput sequencing platform.

2.2.9 GO and KEGG annotation of differentially expressed genes

We employed topGO (Chen et al., 2019) to perform Gene Ontology (GO) enrichment analysis. Within this analysis, differentially expressed genes annotated with GO terms were utilized to compute the gene list and gene count for each specific term. Subsequently, we computed the *p*-value using the hypergeometric distribution method (with significance criteria set at p-value < 0.05) to assess whether the differential genes were significantly enriched within the GO terms, compared to the entire genomic background. This process facilitated the determination of the primary biological functions associated with the differentially expressed genes.

For the Kyoto Encyclopedia of Genes and Genomes (KEGG) enrichment analysis, we utilized clusterprofiler (v 4.0) (Wu et al., 2021). In this analysis, the differentially expressed genes annotated with KEGG pathways were employed to calculate the gene list and gene count for each individual pathway. We subsequently employed the hypergeometric distribution method to compute the *p*-value (with a significance threshold of p-value < 0.05) in order to identify KEGG pathways that exhibited significant enrichment of differentially expressed genes when contrasted with the overall genomic background.

2.2.10 Analysis of differentially expressed genes under salt stress

The identification of significantly enriched metabolic pathways was achieved through an enrichment analysis of KEGG metabolic pathways. Subsequently, the expression levels of differentially expressed genes involved in these pathways were visualized as correlated heat maps using the R language. Multiple sequence comparisons of differentially expressed genes were performed using Muscle (v 3.8.31). The phylogenetic tree was constructed using IQTREE (v 2.2.5 with the following parameters: −nt 20, −m test, −b 1000).

2.2.11 Validation of the RNA-seq results by qPCR

To assess the accuracy of RNA-seq data, we meticulously selected 10 genes exhibiting significant differential expression and designed primers using Primer (v 5.0) and SnapGene (v 2.3.2). Subsequently, we reverse-transcribed RNA from both the control (CK) and T4-treated (T4) samples into complementary DNA (cDNA) utilizing the PrimeScriptTM 1st strand cDNA Synthesis Kit. Utilizing the cDNA as a template and Tubulin (Montero-Barrientos et al., 2011) as the internal reference gene, we performed fluorescence quantification using the TB GreenTM Premix EX TaqTM fluorescence quantitative kit and QuantStudioTM real-time PCR software. Relative expression levels were determined utilizing the −ΔΔCt method, with each sample analyzed in triplicate for both biological and technical replicates.

3 Results

3.1 Morphological and molecular identification of the strain qt40003

The *T. harzianum (TH)* strain qt40003 was derived from the Institute of Vegetable and Flower Research, Chinese Academy of Agricultural Sciences. The morphology of the strain was identified, and the characteristics of colony morphology, mycelia, and conidia were examined. The colony was white in the early stage of growth and turned yellow–green after spore formation. The strain consisted of colorless or light airborne mycelia and basal intracellular mycelia. The airborne mycelia were white, flocculent, dense, and concentric whorled (Figures 1A–C). The conidium was transparent ovoid (Figure 1D).

We further used the universal fungal primers *TEF* and *RPB2* for PCR-based molecular detection. We amplified DNA fragments of

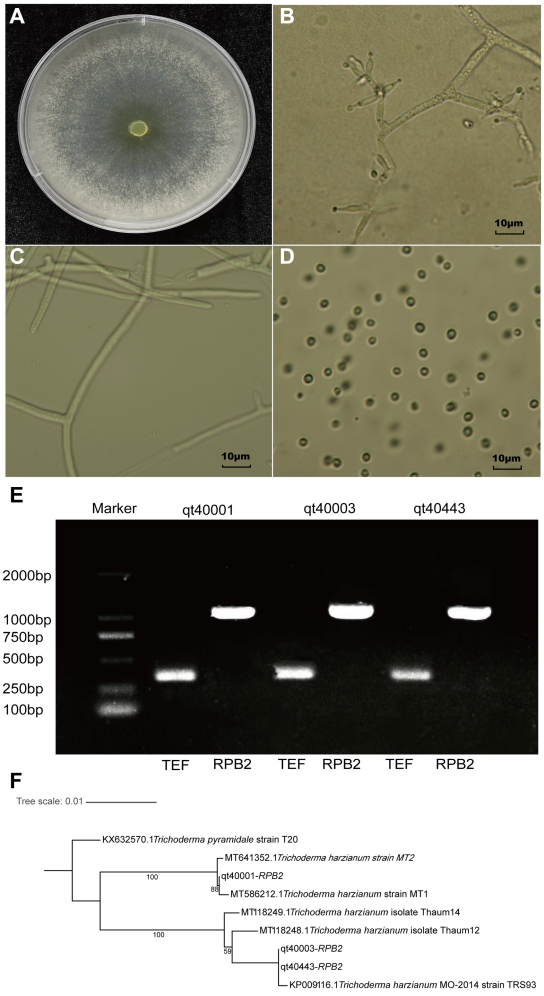

FIGURE 1
The morphological and molecular identification of qt40003. **(A)** The colony morphology of qt40003. **(B)** Microscopic observation of conidiophore. **(C,D)** Microscopic observation of mycelia and conidia. **(E)** PCR molecular identification was performed with specific primers. (Marker: Trans 2Kb DNA Marker, qt40001 and qt40443: other *Trichoderma harzianum* strains, *TEF*: Translation Elongation Factor and *RPB2*: RNA Polymerase II Second Largest Subunit). **(F)** Phylogenetic tree based on *RPB2* sequences of qt40003 and 8 other different *Trichoderma* species.

about 420 bp and 1,000 bp, respectively (Figure 1E). We input the amplified *RPB2* fragments into the BLAST search of the NCBI database. The *RPB2* sequence of this strain showed the highest consistency (99.89%) with the published *TH* MO-2014 strain. To analyze the evolutionary relationship of qt40003 in the *Trichoderma* genus, the *RPB2* sequences of qt40003 and eight other *Trichoderma* species were used to construct phylogenetic trees, and *T. pyramidate* was used as an outgroup (Figure 1F). Strain qt40003 was clustered with the MO-2014 strain, indicating the closest genetic distance between them. Furthermore, we constructed a phylogenetic tree using the *TEF* sequence of this strain and the top five *Trichoderma* species with the highest alignment rates in NCBI, with *T. pyramidate* as the outgroup. The closest genetic distance was between qt40003 and the *TH* TUB F-684 strain (Supplementary Figure S1). Based on morphological and molecular identification, this strain was confirmed as a *TH* strain.

TABLE 1 Statistics of the *Trichoderma harzianum* qt40003 strain genome assembly.

Feature	Statistics
Length of genome assembly (Mb)	44.47
Number of contigs	12
Max contig length (bp)	9,627,940
Contig N50 (bp)	4,809,098
Total length of genes (Mb)	21.89
Repetitive sequence	11,517
Gene number	12,238
GC	47%
Complete BUSCOs (C)	739 (97.5%)

3.2 Genome sequencing and assembly

We employed the Jellyfish tool to evaluate the genome size of qt40003 using Illumina sequence data (5.2 Gb, ~116-fold), based on the k-mer distribution (k-mer = 21). As a result, the estimated qt40003 genome size was approximately 40.79 Mb (Supplementary Figure S2).

The entire genome of strain qt40003 was comprehensively sequenced. For the Nanopore platform, we generated approximately 7.59 Gb of long reads for qt40003, equivalent to approximately 170-fold coverage. The genome assembly process requires separate assembly using NextDenovo and Canu (Koren et al., 2017), and the two assembly results were merged using QUICKMERGE. Subsequently, we enhanced the initial assembly using Racon (Xingxing et al., 2021), incorporating the Nanopore reads for refinement. Following correction with the Illumina short reads (5.2Gb), the genome size of the qt40003 genome final assembly was 44.5 Mb, consisting of 12 contigs The longest contig was 9.63 Mb, and the contig N50 value was 4.81 Mb (Table 1). To assess the assembly completeness, we remapped the Illumina sequences to the assembled qt40003 genome and 97.62% of reads could be mapped to the genome, indicating that the qt40003 assembly covered almost all the genomic region. Four of the 12 contigs (contigs 1, 2, 6, and 7) contained telomeric repeats—(5′-TTAGGG-3′)^n or (5′-CCCTAA-3′)^n—at both contig ends, indicating that these contigs reached the telomere to telomere (T2T)-chromosome level.

On comparison with the published genome of the *TH* strain IIPRTh-33 (accession *SAMN22210987*; 456 contigs with N50 of 0.2 Mb), the two genomes displayed a highly collinear relationship, while some structural variations including inversions and translocations could also be detected (Figure 2B). Furthermore,

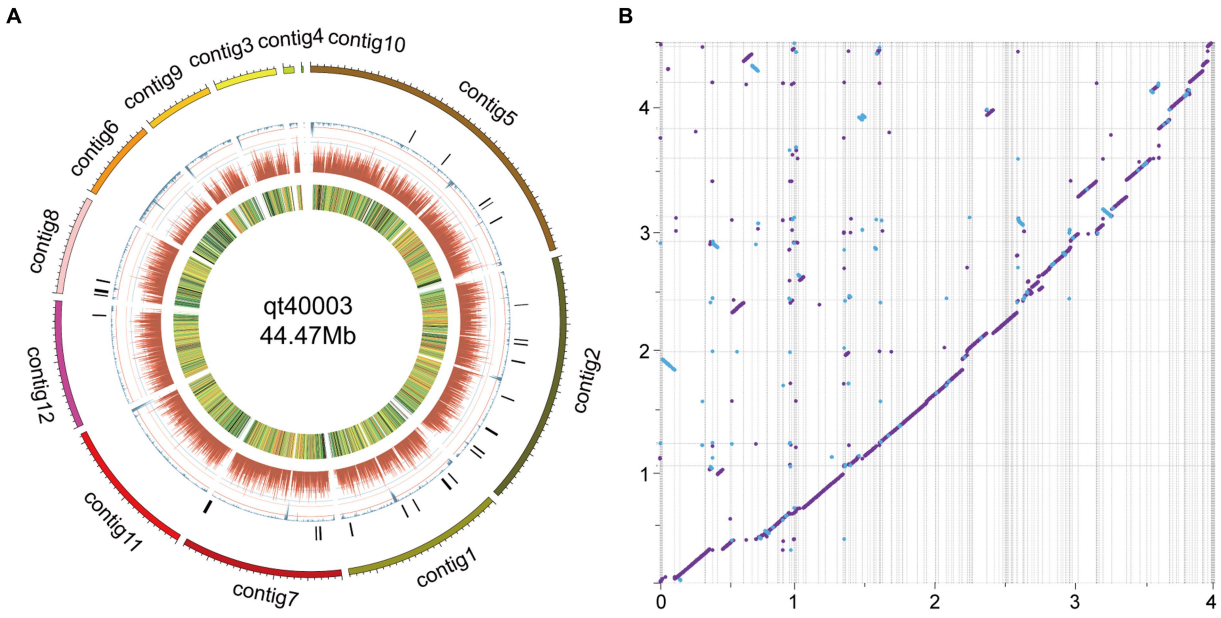

FIGURE 2
Genome features of qt40003 and comparative genomic analysis with published *T. harzianum* genome. **(A)** The outermost circle is the contigs. **(B)** The syntenic relationships between qt40003 and IIPRTh-33. Y-axis represents qt40003 contigs, and x-axis represents IIPRTh-33 genome. The axis tick values represent genome size (x10 Mb). The purple dot or line represents forward matches, and the blue dot or line represents reverse matches between two genomes.

we performed a comparative analysis with the genome of the *TH* strain CDMCC_20739 (accession *SAMN17621345*) at the chromosomal assembly level. The results (Supplementary Figure S3) demonstrated high collinearity between the chromosomes; however, significant structural variations, such as large-scale inversions and translocations, were evident.

We mapped the genome circle of qt40003 (Figure 2A). The outer-to-inner bar charts represent secondary metabolite gene clusters (in black), the repeat sequence density (in blue), gene density (in dark red), and gene expression levels from transcriptome data [in fragments per kilobase of transcript per million mapped reads (FPKM)].

3.3 Genome annotation and assembly assessment

Of the assembled qt40003 sequences, 9.61% (4.27 Mb) were annotated as repeating sequences (Supplementary Table S1). Of these, 4.89% were long terminal repeats (LTRs), and the three longest repeats were LTR/Gypsy (2.16 Mb), LINE/Tad1 (0.54 Mb), and DNA/MITE (96,367 bp). A total of 12,238 protein-coding genes were predicted for qt40003, of which 11,705 (95%) were supported by RNA-seq, and 9,986 (85%) were functionally annotated.

We used the KOG database to classify genes by orthologous lineation (Supplementary Figure S4). A total of 10,270 (87%) genes in the genome of strain qt40003 were annotated to corresponding functions. The most numerous functional classes were carbohydrate transport and metabolism (706), secondary metabolites biosynthesis, transport, and catabolism (679), and posttranslational modification, protein turnover, and chaperones (637), indicating that the strain had abundant carbohydrate metabolism. To assess the accuracy of the assembly, we performed a BUSCO (Benchmarking Universal Single-Copy Orthologs) evaluation of the qt40003 genome, and 739 (97.5%) gene models were complete, indicating that these combinations contained the majority of the qt40003 gene space (Supplementary Table S2).

3.4 Effects of different sodium NaCl on the growth of qt40003

We inoculated qt40003 on PDA medium with different NaCl concentrations and incubated it at 28°C for 48 h without light. Colony size was negatively correlated with NaCl concentration. The control group (CK) grew rapidly, the whole Petri dish was covered with mycelium in 48 h, and the mycelium was dense and wadded. However, as the NaCl concentration increased, the germination time of the qt40003 mycelium was delayed, the growth rate of the colony was significantly slowed, and the colony became thinner (Figure 3A). Under 10% NaCl stress (T10), mycelia did not germinate. The budding time of the CK, 2% (T2), and 4% (T4) NaCl groups was 12 h for mycelia to appear, while at 6% (T6) and 8% (T8) NaCl, mycelia appeared at 24 h and 36 h, respectively (Table 2). At 48 h, the inhibition rates of different NaCl concentrations on qt40003 colonies of CK, T2, T4, T6, T8, and T10 were 0, 11.75, 60.38, 81.75, 94.38, and 100%, respectively, and the overall growth curve for each treatment showed a slightly curved linear shape (Figure 3B). The inhibition rate curve exhibited a pronounced upward trend starting from T2, reaching 100% inhibition at T10 (Figure 3C).

3.5 Transcriptome analysis of qt40003 under NaCl stress

The Illumina HiSeq X Ten platform was used for RNA-seq analysis of nine transcription samples from the CK, T2, and T4 groups. A total of 10.83 Gb of data were obtained, with an average of 3.61 Gb per sample, and the average map ratios were 99.29% for CK, 99.33% for T2, and 99.35% for T4 (Supplementary Table S3). Before performing differential expression analysis, the correlation of the gene expression levels between the samples was checked. We used the Pearson correlation coefficient, *r*, as the evaluation index for inter-sample correlation. The calculated *r* value was used to build a correlation heat map (Supplementary Figure S5). The results showed a high correlation between the samples, which can be used for further analysis.

DESeq was used for differential analysis of gene expression. A total of 2,937 differentially expressed genes (DEGs) were obtained from CK vs. T2, including 1,205 upregulated genes and 1732 downregulated genes. A total of 3,527 DEGs were obtained from CK vs. T4, including 1,484 upregulated genes and 2043 downregulated genes. The number of up- and downregulated genes in qt40003 both increased by 590 genes under a high NaCl concentration (T4) compared with a low NaCl concentration (T2). The comparison of DEGs between the two treatments revealed that the $\log_2$(fold change) of certain upregulated genes also increased with the rise in NaCl concentration.

Significant enrichment analysis was performed on the RNA-seq data structures of the comparison groups treated with NaCl in the GO database (Gene Ontology, http://geneontology.org/), including three first-level classifications and 40 s-level classifications of biological processes (BP), molecular functions (MF), and cell components (CC). Of these, T2 accounted for the highest proportion of BP and T4 accounted for the highest proportion of CC. The DEGs involved in biological processes were mainly concentrated in tRNA aminoacylation for protein translation, amino acid activation, and tRNA aminoacylation, while the DEGs associated with cell components were mainly cytosolic ribosome and the cytosolic large ribosomal subunit (Figure 4).

The Kyoto Encyclopedia of Genes and Genomes (KEGG) pathway database encompasses molecular interaction networks within each biological pathway, along with the distinctive adaptations of organisms. These resources serve to elucidate the primary biological functions carried out by DEGs. KEGG pathway analysis was conducted on qt40003 after treatment under T2 and T4 conditions (Figure 5). This revealed the enrichment of 699 and 932 DEGs for T2 and T4, respectively, across 20 KEGG pathways. Furthermore, within 12 specific pathways, there were 91 and 173 genes exhibiting significant enrichment. Notably, in T2, these pathways included aminoacyl-tRNA biosynthesis, glutathione metabolism, aflatoxin biosynthesis, purine metabolism, tyrosine metabolism, and non-homologous end joining, while in T4, they included the ribosome, glutathione metabolism, tyrosine metabolism, aflatoxin biosynthesis, butanoate metabolism, nicotinate and nicotinamide metabolism, beta-alanine metabolism, and beta-alanine.

10.3389/fmicb.2024.1342584

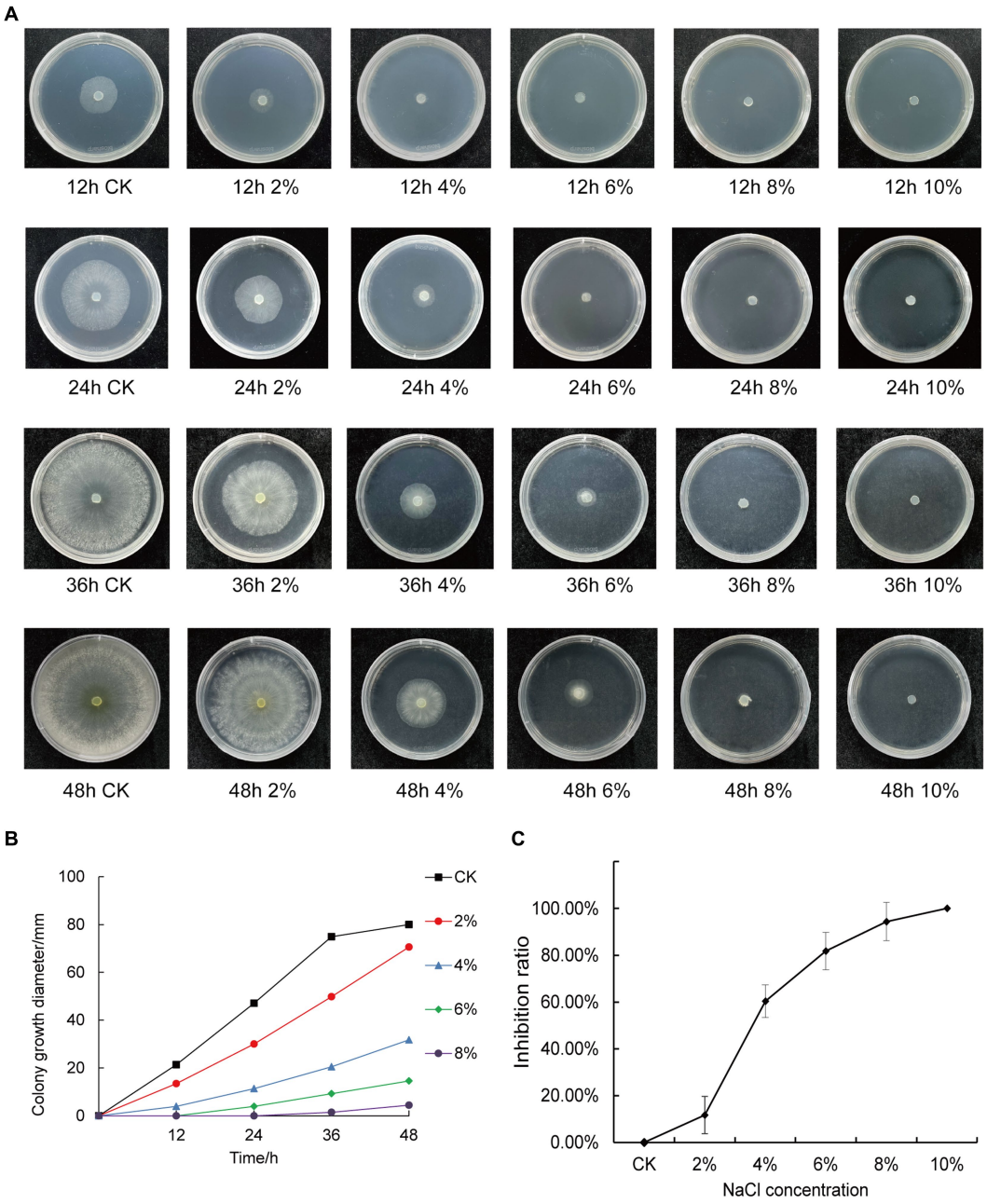

FIGURE 3
Effects of different concentrations of NaCl on the growth of qt40003. **(A)** 48 h growth of strain qt40003 on NaCl PDA. **(B)** Colony size at different NaCl concentrations. **(C)** Inhibition rate of different NaCl concentrations on the growth of strains. Error lines are standard errors.

TABLE 2 **Effects of different NaCl stress on physiological indexes of 40,003 mycelia.**

Concentration	Average daily height growth/mm	Hyphal diameter/mm	Mycelium budding time/h	Inhibition ratio
CK	25.00 ± 2.29	80 ± 0.00	12 h	0.00%
2%	17.66 ± 2.02	70.4 ± 2.61	12 h	11.75%
4%	7.83 ± 2.25	31.2 ± 2.03	12 h	60.38%
6%	3.50 ± 0.50	14.71 ± 2.00	24 h	81.75%
8%	1.1 ± 0.10	4.46 ± 2.10	36 h	94.38%
10%	/	/	/	100.00%

3.6 Analysis of genes related to salt stress

The KEGG metabolic pathway annotation results under T2 and T4 treatments revealed that the most significantly enriched metabolic pathway was glutathione metabolism. Consequently, we conducted a screening of differentially expressed genes within the glutathione metabolism pathway (Figure 6A). The results showed that four genes, namely *g5836*, *g6193*, *g11720*, and *g5530*, exhibited an upregulation in expression with increasing NaCl concentration. Five genes—*g1219*, *g8081*, *g3978*, *g11034*, and *g5841*—displayed no significant changes in expression levels under T2 conditions, while their expression was significantly downregulated under T4 conditions. In contrast, the expression levels of the remaining 13 genes decreased under both T2 and T4 treatments, with nine of them belonging to the glutathione transferase family (Table 3).

Thus, the glutathione transferase family constitutes a significant proportion of these differentially expressed genes. Therefore, we focused on screening for differentially expressed genes within the glutathione transferase family. The results show that, apart from the upregulation of *g9441* and *g1302*, the expression levels of all genes under both T2 and T4 conditions were significantly downregulated. Eight genes (*g9204*, *g4980*, *g12195*, *g1219*, *g484*, *g7830*, *g7443*, and *g9623*) exhibited more pronounced downregulation with increasing salt concentration. Subsequently, phylogenetic tree analysis (Figure 6B) revealed significant homology between two of the upregulated genes (*g9441* and *g1302*).

We identified a shared set of 2,111 differentially expressed genes between the two treatments. Additionally, 826 and 1,416 genes exhibited unique differential expression in T2 and T4, respectively (Figure 7). Subsequently, we conducted KEGG metabolic pathway annotation for these additional genes. The differentially expressed genes in the two treatments were significantly enriched in the porphyrin and chlorophyll metabolic pathway and the valine, leucine, and isoleucine degradation metabolic pathway, respectively. Specifically, five differential genes associated with porphyrin and

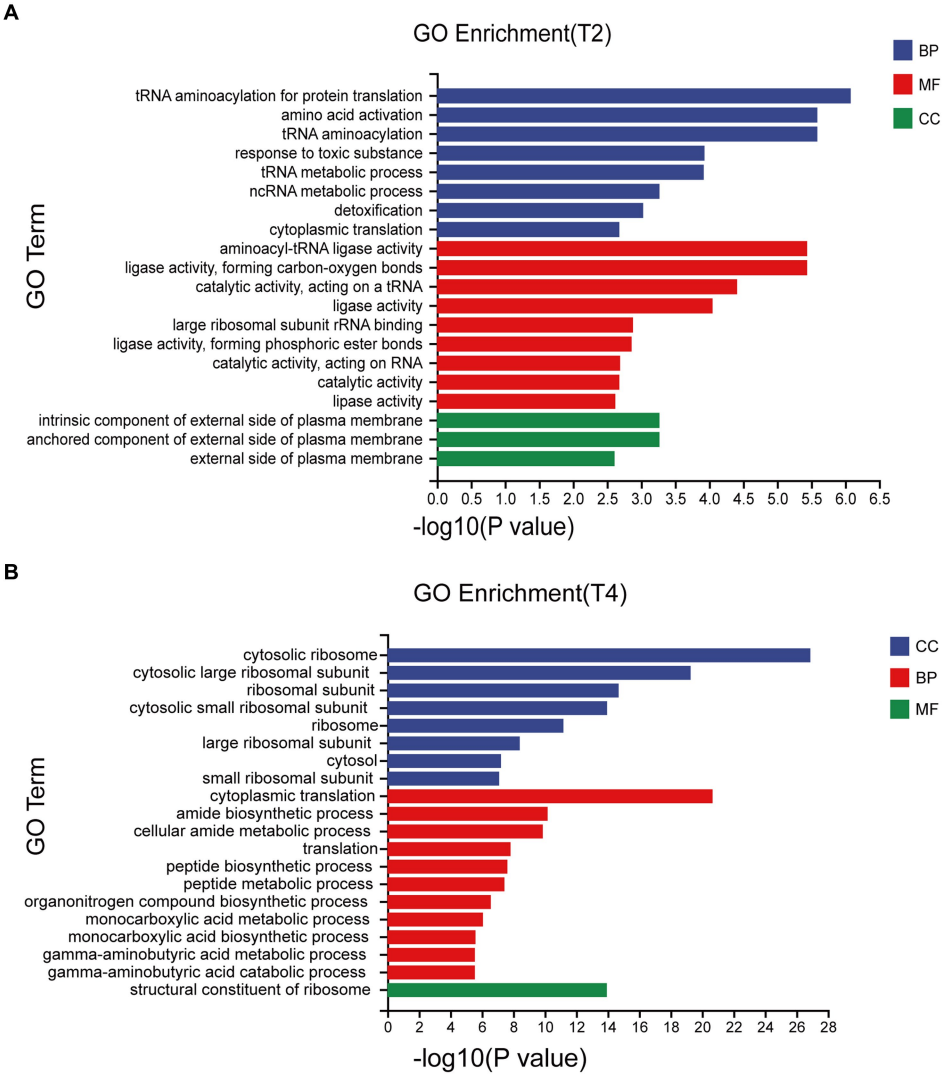

FIGURE 4
Go enrichment classification of differentially expressed genes under different treatments. **(A)** Go enrichment classification of differentially expressed genes treated with T2. **(B)** Go enrichment classification of differentially expressed genes treated with T4.

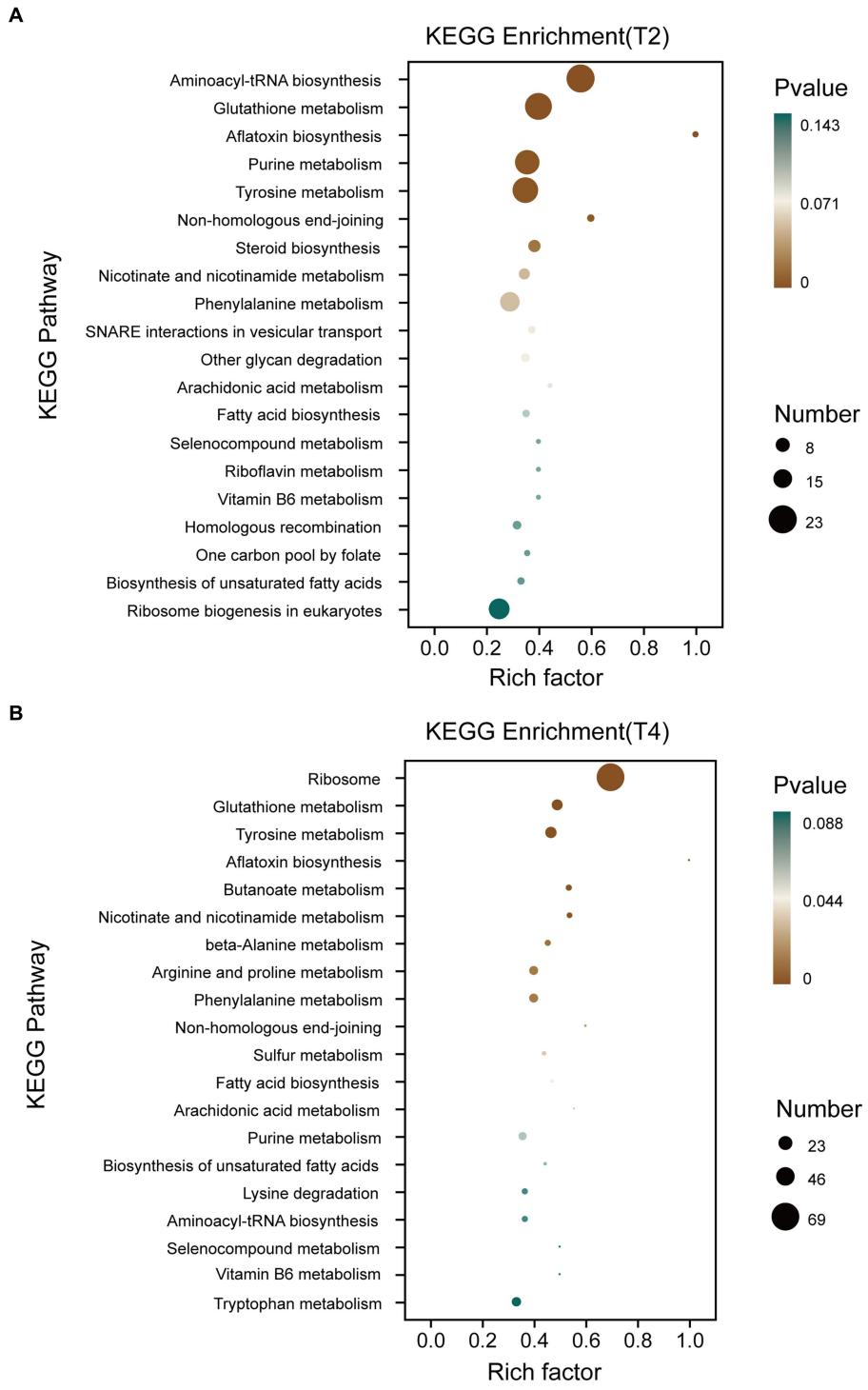

FIGURE 5
KEGG enrichment classification of differentially expressed genes under different treatments. **(A)** KEGG enrichment classification of differentially expressed genes treated with T2. **(B)** KEGG enrichment classification of differentially expressed genes treated with T4.

chlorophyll metabolism in T2 were predominantly upregulated (4/5), with the sole downregulated gene being *g11108* (coproporphyrinogen III oxidase). In contrast, the genes involved in valine, leucine, and isoleucine degradation in T4 were mainly downregulated (10/11), with the only upregulated gene being *g5537* (AMP-binding enzyme) (Table 4).

The effect of NaCl on cell growth is mainly caused by oxidative damage to the biofilm and the denaturation of nucleic acids and proteins caused by reactive oxygen species (ROS) free radicals that are generated, resulting in cell death. Therefore, to reduce ROS damage, an antioxidant system consisting of antioxidant enzymes and non-oxidative enzymes is essential (Xiang et al., 2019). We conducted

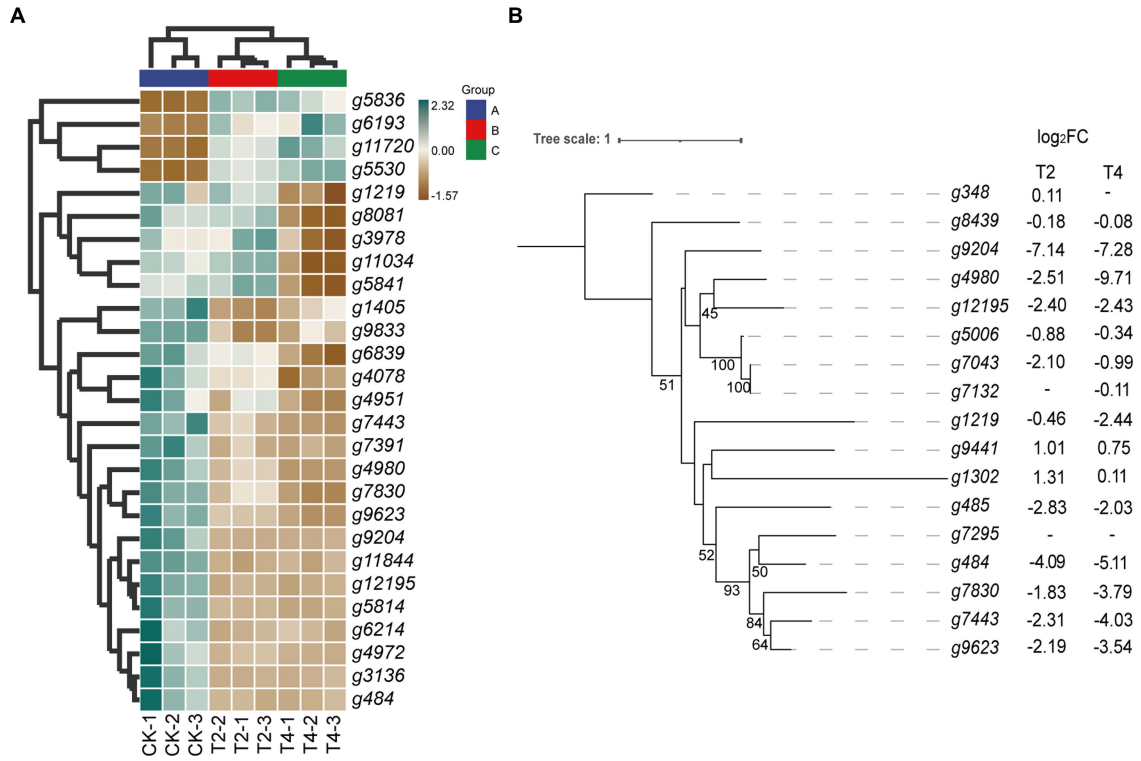

FIGURE 6
Relationship diagram of differentially expressed genes in the glutathione metabolic pathway. **(A)** Heat map of differential expression genes of glutathione metabolic pathways. **(B)** Phylogenetic tree of glutathione transferase gene family showing its evolution. Bootstrap values (n = 1,000).

further screening of 13 active oxygen scavenging genes, including peroxidase, glutathione peroxidase, and catalase. Under T4 treatment, we identified six upregulated and seven downregulated ROS scavenging genes, including peroxidase and catalase. Additionally, we found five DEGs related to the cell wall or extracellular structure, all of which were hydrophobic fungal proteins. Of these, *g2257* and *g10606* exhibited a high level of expression (Table 5).

3.7 Validation of the RNA-seq results by qPCR

To validate the accuracy of the RNA-seq findings, nine genes showing substantial expression changes under T4 conditions were selected from the transcriptomic data, including four upregulated and five downregulated genes. These expression changes were then verified by quantitative PCR (qPCR). Using custom-designed primers (Table 6), qPCR was used for the precise quantification of the expression changes across these nine genes in the CK and T4 groups. This showed a slight variance between the qPCR and RNA-seq results for the differentially expressed genes (Figure 8), but the overall trends were in agreement, confirming the reliability of the RNA-seq results.

4 Discussion

Adverse conditions can cause varying degrees of damage to microorganisms. Currently, research on microbial environmental stress primarily focuses on heavy metals, PAHs (polycyclic aromatic hydrocarbons), organic acids, and other factors (Xiang et al., 2019). *TH* is one of the potent biocontrol fungi today, and studying its salt tolerance is particularly necessary. However, the response mechanisms of fungi to salt stress are highly complex.

Research on *Trichoderma* spp. has accelerated considerably with the availability of fully sequenced genomes. Plant biotechnology will also benefit from *Trichoderma* genome mining (Mukherjee et al., 2013). Rosolen et al. used genome-wide phylogenetic analysis to elucidate the relationships between newly sequenced species and other *Trichoderma* species (Mukherjee et al., 2013). Wang et al. conducted a genomic analysis of *TH*, revealing the biosynthetic diversity of its specialized secondary metabolites (Al-Salihi and Alberti, 2023). Fanelli et al. presented the genome of the *TH* strain ITEM908, a biocontrol agent. Through genomic analysis of ITEM908, they identified the occurrence and correlation of genes associated with biocontrol and slope (Fanelli et al., 2018). Vieira et al. were the first to establish a method for *TH* genome editing. The mutants generated, produced by the overexpression of Cas9 and nutritional markers, serve as tools for functional analysis of biocontrol genes, selection of biocontrol strains, and the generation of novel strains for biotechnological applications (Vieira et al., 2021). Here, for the first time, we have assembled the complete genome sequence (44.47 Mb) of *TH* qt40003, providing a foundational resource for future in-depth exploration of this biocontrol fungus. This comprehensive genomic resource opens new avenues for understanding the biology, evolutionary dynamics, and functional genomics of *TH*. The elucidation of the entire genome provides valuable insights into the

TABLE 3 Functional description of differentially expressed genes of glutathione metabolic pathway.

Gene id	Description
g5836	Belongs to the spermidine spermine synthase family
g6193	Gamma-glutamyltranspeptidase
g11720	Belongs to the Orn Lys Arg decarboxylase class-II family
g5530	Ribonucleotide reductase, small chain
g1219	Glutathione S-transferase, C-terminal domain
g8081	Belongs to the class-I pyridine nucleotide-disulfide oxidoreductase family
g3978	Catalyzes the oxidative decarboxylation of 6- phosphogluconate to ribulose 5-phosphate and CO(2)
g11034	Gamma-glutamyltranspeptidase
g5841	Glutamate-cysteine ligase
g1405	Brf1-like TBP-binding domain
g9833	Gamma-glutamyltranspeptidase
g6839	Glutathione S-transferase, N-terminal domain
g4078	Glutathione S-transferase, N-terminal domain
g4951	Glutathione S-transferase, N-terminal domain
g7443	Belongs to the GST superfamily
g7391	Glutathione S-transferase, C-terminal domain
g4980	Glutathione S-transferase, C-terminal domain
g7830	Belongs to the GST superfamily
g9623	Belongs to the GST superfamily
g9204	Glutathione S-transferase, C-terminal domain
g11844	Belongs to the glutathione peroxidase family
g12195	Glutathione S-transferase, C-terminal domain
g5814	Aldo/keto reductase family
g6214	Glutathione S-transferase, C-terminal domain
g4972	Glutathione S-transferase
g3436	Saccharopine dehydrogenase NADP binding domain
g484	Glutathione S-transferase, C-terminal domain

genetic basis of its biocontrol capabilities and offers opportunities for the development of innovative strategies for sustainable agriculture, disease management, and biotechnological applications. The availability of this high-quality genome sets the stage for further investigations into the molecular mechanisms underlying the biocontrol activities of *TH* and provides a solid foundation for harnessing its potential in diverse fields.

Transcriptome sequencing based on cDNA using second-generation high-throughput sequencing technology has higher detection throughput and a broader detection range than gene chip technology (Liu et al., 2015). In recent years, this technology has been widely applied for research on fungal functional gene discovery and metabolic regulation. To ensure sufficient fungal biomass in this study, we used second-generation high-throughput sequencing technology to conduct RNA-seq on the qt40003 strain under NaCl stress conditions at 0, 2, and 4% NaCl concentrations, with three biological replicates for each condition. It is of note that previous studies have shown significant differences in the salt tolerance response of microorganisms to low and high salt levels (Grada and Weinbrecht, 2013). Therefore, we screened for differentially expressed genes under two treatment concentrations, and obtained a total of 2,937 and 3,527 genes for 2 and 4% NaCl, respectively. T4 conditions resulted in 590 more differentially expressed genes than T2 conditions. Furthermore, we observed that the fold change in the expression of many genes also varied with the increase in NaCl concentration. Therefore, the selection of an appropriate NaCl concentration is crucial for studying the salt tolerance mechanisms of *TH*. The functional enrichment analysis of these differentially expressed genes revealed associations with cellular processes, cellular components, metabolic processes, and other functions. This result is consistent with the experimental research results of Wang et al. on fungal stress (Wang, 2017). In the GO enrichment analysis, differentially expressed genes are categorized into biological processes, molecular functions, and cellular components. Under T2 and T4 treatments, significant enrichments in biological processes are observed in "tRNA aminoacylation for protein translation" and "cytosolic ribosome." Molecular functions show prominent enrichments in "aminoacyl-tRNA ligase activity" and "cytoplasmic translation," while cellular components exhibit significant enrichments in "intrinsic component of external side of plasma membrane" and "structural constituent of ribosome." In the KEGG pathway analysis, differentially expressed genes are mainly classified into two major categories: "Genetic Information Processing" and "Metabolism." Under T2 and T4 treatments, genes related to Genetic Information Processing significantly enrich in "Aminoacyl-tRNA biosynthesis" and "Ribosome," while those associated with Metabolism predominantly enrich in "Glutathione metabolism." Under the two treatment conditions, differentially expressed genes exhibit distinct patterns in GO and KEGG enrichment analyses. This suggests that the fungus may adopt different biological responses and metabolic pathway regulation strategies to adapt to changes in salt concentration under different salt levels. However, in the KEGG metabolic pathways, both treatments significantly enriched in the glutathione metabolism pathway. Therefore, we focused on analyzing differentially expressed genes related to glutathione metabolism.

Glutathione S-transferase (GST) enzymes are present in many evolved organisms and are essential for the defense against reactive oxygen species (Muslu et al., 2023). GSTs play a role in the development of defenses against biotic and abiotic challenges, especially in defending plants from various stresses such as drought, salinity, and heavy metal exposure, and have diverse functions, including the production of oxylipins as precursors to jasmonic acid. GSTs help eliminate cytotoxic or genotoxic components in cells that can damage DNA, RNA, or proteins (Noctor et al., 2002). In our KEGG pathway enrichment analysis, we screened for differentially expressed genes in the glutathione metabolism pathway and found that the expression of GST decreased with increasing NaCl concentration, consistent with results reported by Muslu et al. (2023) and others. The inhibition rate of qt40003 mycelium growth at 2% NaCl concentrations was only 11.75%, while the inhibition rate at 4% NaCl reached 60.38%, indicating that the salt tolerance of qt40003 was significantly reduced at this concentration, which we speculated might be related to the downregulation of GST. Unlike our study, Xiang et al., in their investigation of salt stress in *TH*, revealed through enrichment analysis of KEGG metabolic pathways that, under 0.6 mol/L salt stress, the most significantly downregulated pathway in *TH* is the biosynthesis of amino acids (Xiang et al., 2019). They used a

10.3389/fmicb.2024.1342584

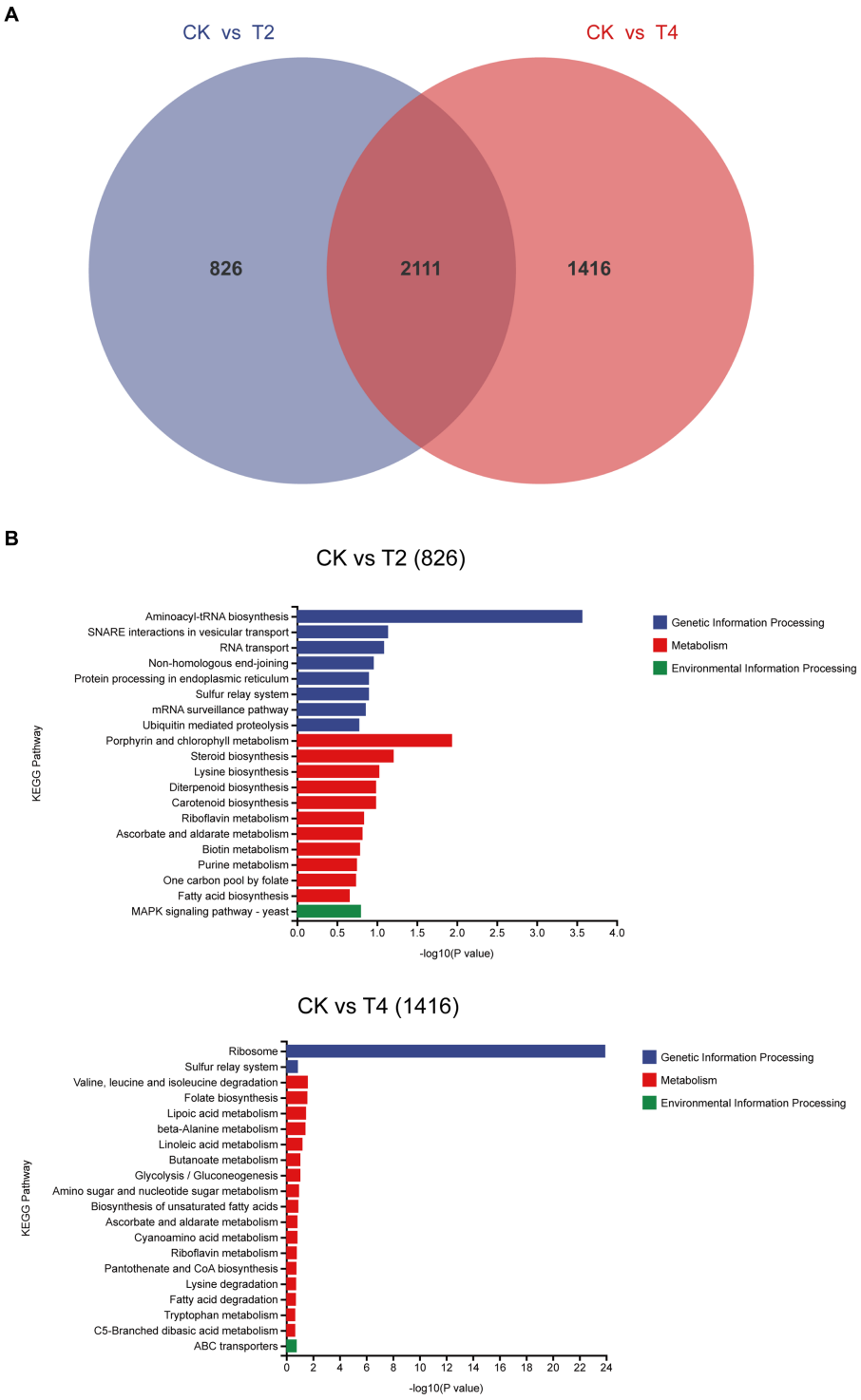

FIGURE 7
Analysis of non-overlapping differentially expressed genes across distinct treatments. **(A)** Venn diagram of differentially expressed genes under T2 and T4 treatments. **(B)** KEGG metabolic pathway annotation of non-overlapping differentially expressed genes under different treatments.

concentration of 0.6 mol/L in their study, while in our research, the concentration was 4%. This difference in concentration may lead to notable variations in the observed biological responses between the two studies. In our study, we observed that, at a concentration of 4% NaCl, downregulated genes in the *TH* transcriptome were primarily enriched in the glutathione metabolism pathway, indicating a cellular preference for addressing oxidative stress and detoxification reactions. In contrast, at 0.6 mol/L concentration in Xiang et al.'s study, the differentially expressed genes, particularly downregulated ones, were predominantly enriched in amino acid metabolism pathways. This observation suggests a potential emphasis on regulating amino acid metabolism to maintain fundamental biological functions under

TABLE 4 Genes involved in the significantly enriched metabolic pathways of non-overlapping genes in T2 and T4 treatments.

	Gene Id	Log_2FC	Functional description
T2	g11979	1.10	Belongs to the class-I aminoacyl-tRNA synthetase family
	g11108	−1.25	Coproporphyrinogen III oxidase
	g3692	1.07	Belongs to the class-I aminoacyl-tRNA synthetase family
	g5198	1.92	short-chain dehydrogenase
	g1609	1.02	Porphobilinogen deaminase, dipyromethane cofactor binding domain
T4	g811	−1.98	Belongs to the aldehyde dehydrogenase family
	g4650	−2.07	Belongs to the 3-hydroxyisobutyrate dehydrogenase family
	g5537	3.95	AMP-binding enzyme
	g11905	−1.27	Belongs to the enoyl-CoA hydratase isomerase family
	g8039	−1.28	Aldehyde dehydrogenase family
	g3935	−1.12	It is involved in ketone body synthesis and cholesterol synthesis
	g1401	−1.10	Belongs to the class-IV pyridoxal-phosphate-dependent aminotransferase family
	g569	−1.08	Belongs to the class-III pyridoxal-phosphate-dependent aminotransferase family
	g3500	−3.17	Aldehyde dehydrogenase family
	g9014	−1.04	Thiolase, N-terminal domain
	g12065	−1.755	AMP-binding enzyme C-terminal domain

TABLE 5 The predicted genes related to osmotic protection and cell wall of qt40003 under NaCl stress.

	Gene id	$T4(log_2FC)$	Function description
Cell wall	*g2257*	4.311234	Fungal hydrophobin
	g10606	8.41909	Fungal hydrophobin
	g12011	0.858408	Fungal hydrophobin
	g8412	−1.38319	Fungal hydrophobin
	g10244	0.710579	Fungal hydrophobin
Scavenging	*g1424*	−1.1314	Peroxidase catalase subfamily
	g11844	−1.32796	Belongs to the glutathione peroxidase family
	g8864	−5.06323	Belongs to the peroxidase familyactivity
	g10787	−0.82274	Peroxidase
	g1127	−0.31405	Belongs to the peroxidase family
	g3402	1.042145	Belongs to the peroxidase family
	g10014	0.543035	Belongs to the peroxidase family
	g5387	−1.09096	Peroxidase
	g9374	0.474377	Peroxidase
Ros	*g594*	1.692462	Catalase
	g7039	0.790193	Catalase
	g4507	−0.7587	Catalase
	g12119	0.591896	Catalase

TABLE 6 Primer sequences used for qPCR analysis.

Gene	Forward (5′-3′)	Reverse (5′-3′)
g2354	CGAGGCAGTAGGCTTCCATTTTC	CGAGGCAGTAGGCTTCCATTTTC
g7283	GCCAAGACTCAACATCCATACG	GCCTTCACCTTCAACGACCAC
g3306	TCCTATTTCGTATTCTTCCACCCG	GGTAATGCCTGATCCCTTTTG
g10826	TTTCCCATTGAGAAGGTCCAGG	TTCGCTACCGCTAAGACGCC
g6208	TCGCCTCCCTCTTCTCCAAC	GAAAGTGTCCACAAGCCCCTC
g4966	GCCACATCTCAGAATACAACAACG	GACCGCAGAAATCAGCCAAG
g12093	CTATGGCGTCTTCGGTCTCAC	GGATCTTTGGAAACTGCCCTCTT
g11988	TCGGCAACGGCACATCAGCAG	GCTTCGCTCAACAAAGGCATAC
g8774	CTGTCGCTTCTTGTCCTCCG	TGGTGAGCATCTGGCTGTAGTC
Tubulin	GCTACCTGACCTGCTGCTCT	TCGCCGACACGCTTGAACAG

higher salt concentrations. Glutathione metabolism is primarily involved in cellular detoxification and antioxidant responses, while amino acid metabolism plays a crucial role in various biological processes. Amino acids serve as the building blocks for protein synthesis, provide energy through metabolic pathways, supply carbon sources, and contribute significantly to immune responses (Ling et al., 2023). Therefore, under 0.6 mol/L salt stress, *TH* may prioritize the regulation of amino acid metabolism to sustain basic biological functions. On the other hand, at 4% concentration, there appears to be a heightened emphasis on defense against oxidative stress, as evidenced by the significant enrichment in glutathione metabolism. This difference likely reflects the varying responses and physiological adaptations of *TH* to stress under different salt concentrations.

High NaCl concentrations cause osmotic stress on cells, and can also lead to the accumulation of excessive reactive oxygen species in cells, triggering the free radical chain reaction of membrane lipid peroxidation, producing excessive harmful free radicals and aggravating the toxicity on cells. In this study, 13 genes related to active oxygen clearance were detected under 4% NaCl stress, including peroxidase, glutathione peroxidase, and catalase, and 10 of these genes were upregulated, indicating that the qt40003 antioxidant oxidase system can actively respond to oxidative damage caused by salt stress.

Fungal hydrophobic proteins are low-molecular-weight amphoteric proteins secreted by higher filamentous fungi with special physical and chemical properties, which play an important role in the growth and development of fungi and environmental communication (Wösten and Wessels, 1997). Hydrophobic proteins typically play a role in stabilizing membrane structures, and their high expression may contribute to maintaining the integrity of cellular membranes, thereby slowing down or alleviating the damage caused by salt stress to the cell membrane. Hydrophobic proteins may be involved in counteracting oxidative stress induced by salt stress. Under adverse conditions, organisms may produce an excess of reactive oxygen species, and the high expression of hydrophobic proteins may aid in clearing these harmful substances, protecting cells from oxidative

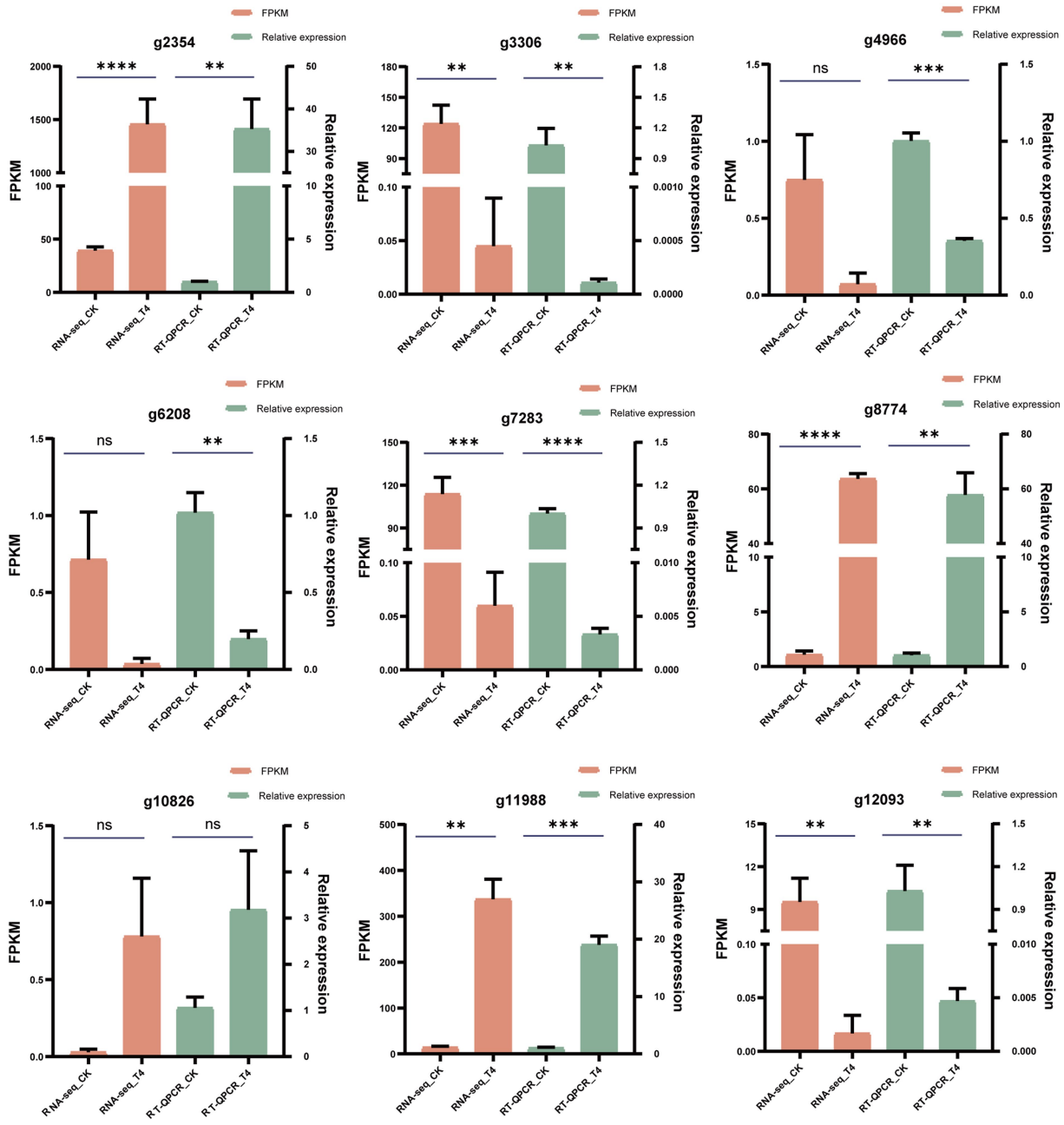

FIGURE 8
qPCR validation of differentially expressed genes. The reliability of RNA-seq results for 10 differentially expressed genes was substantiated through qPCR validation. FPKM values from the RNA-seq analysis were presented in the orange column, while qPCR measurements were displayed in the green column. The data were expressed as the mean ± standard error ($n = 3$). In the context of an unpaired *t*-test, "*" signified a significance level of $p < 0.05$, "**" indicated $p < 0.01$, "***" denoted $p < 0.001$, "****" represented an exceptionally profound significance, and "ns" indicated a lack of statistical significance.

damage. *Trichoderma* species contain a high diversity of hydrophobic proteins (Kubicek et al., 2008). Huang et al. found that expression of the *T. asperellum* ACCC30526 class II hydrophobic protein gene *HFB2-6* was induced under carbon and nitrogen stress, and may be involved in plant rhizosphere colonization (Huang et al., 2015). We screened five fungal hydrophobic proteins under 4% NaCl stress, and two hydrophobic proteins were highly induced.

The current research provides valuable insights into the physiological and molecular response mechanisms of *TH* under salt-stress conditions. However, there are still many future research directions that will further expand our understanding of this field. Deeper research is needed into the differentially expressed genes identified herein to determine their exact functions in the salt-stress response. This may involve gene knockout or overexpression experiments to validate their roles in salt tolerance. In addition to gene-level research, future studies should focus on understanding the changes to proteins and metabolites under salt-stress conditions. This will help to reveal a more comprehensive response mechanism.

In summary, research on the salt-stress response of *TH* provides profound insights and has the potential to positively impact fields such as agriculture, ecology, and biotechnology. Future research will contribute to unlocking more potential applications and ecosystem effects, better addressing the challenges posed by salt stress.

5 Conclusion

The complete genome sequence of *TH* strain qt40003, which is 44.47 Mb in length, is reported here for the first time. Under NaCl stress, a concentration of 10% was the lethal threshold for qt40003. On transcriptomic analysis, 2,937 and 3,527 differentially expressed genes were obtained in control vs. 2% NaCl and control vs. 4% NaCl, respectively. The expression of GST was significantly inhibited on 4% NaCl treatment, and we speculate that the expression of GST is regulated by the salt stress response pathway. The decline in GST expression may be an attempt to allocate resources to other, more urgent survival strategies while responding to salt stress. In this case, the decline in GST may be the result of a cellular stress response that could make organisms more vulnerable to damage in high-salt environments, and so may be related to the decreased tolerance of this strain in salt-stress conditions.

Data availability statement

The datasets presented in this study can be found in online repositories. The names of the repository/repositories and accession number(s) can be found in the article/Supplementary material.

Author contributions

QY: Data curation, Investigation, Methodology, Software, Validation, Visualization, Writing – original draft, Writing – review & editing. ZM: Project administration, Resources, Supervision, Writing – review & editing. YH: Resources, Writing – review & editing. SZ: Investigation, Software, Writing – review & editing. JZ: Supervision, Writing – review & editing. YanL: Supervision, Writing – review & editing. YY: Supervision, Writing – review & editing. BX: Project administration, Supervision, Writing – review & editing. JL: Funding acquisition, Methodology, Project administration, Resources, Supervision, Writing – review & editing. YanlL: Resources, Supervision, Validation, Writing – review & editing.

Funding

The author(s) declare financial support was received for the research, authorship, and/or publication of this article. Funding for this research was provided by the National Key R&D Program of China, 2022YFD1401200; Central Public-interest Scientific Institution Basal Research Fund (No. IVF-BRF2022013), Key Laboratory of Biology and Genetic Improvement of Horticultural Crops, Ministry of Agriculture, P.R. China (CARS-25), the Science and Technology Innovation Program of the Chinese Academy of Agricultural Sciences (CAAS-ASTIP-2017-IVF), the National Natural Science Foundation of China (grant number: 32372508); The Forestry Science and Technology Innovation Foundation of Hunan Province for Distinguished Young Scholarship (XLKJ202205), the Foundation of Changsha Municipal Science and Technology Bureau (KQ2202227), the key project of Hunan Provincial Education Department (22A0155), the Forestry Bureau for Industrialization Management of Hunan Province (2130221), and the Graduate Innovation Project of Hunan Province (2023XC108), the College Student Innovation and Entrepreneurship Project of China (S202310537005). The Project fund of Hunan Province Philosophy and social science achievements Evaluation Committee (XSP20YBZ123).

Conflict of interest

The authors declare that the research was conducted in the absence of any commercial or financial relationships that could be construed as a potential conflict of interest.

Publisher's note

All claims expressed in this article are solely those of the authors and do not necessarily represent those of their affiliated organizations, or those of the publisher, the editors and the reviewers. Any product that may be evaluated in this article, or claim that may be made by its manufacturer, is not guaranteed or endorsed by the publisher.

Supplementary material

The Supplementary material for this article can be found online at: https://www.frontiersin.org/articles/10.3389/fmicb.2024.1342584/full#supplementary-material

References

Ahmad, P., Hashem, A., Abd-Allah, E. F., Alqarawi, A. A., John, R., Egamberdieva, D., et al. (2015). Role of *Trichoderma harzianum* in mitigating NaCl stress in Indian mustard (*Brassica juncea* L) through antioxidative defense system. *Front. Plant Sci.* 6:868. doi: 10.3389/fpls.2015.00868

Al-Salihi, S. A. A., and Alberti, F. (2023). genomic based analysis of the biocontrol species *Trichoderma harzianum*: a model resource of structurally diverse pharmaceuticals and biopesticides. *J Fungi* 9:895. doi: 10.3390/jof9090895

Bao, W., Kojima, K. K., and Kohany, O. (2015). Repbase update, a database of repetitive elements in eukaryotic genomes. *Mob. DNA* 6:11. doi: 10.1186/s13100-015-0041-9

Bateman, A., Coin, L., Durbin, R., Finn, R. D., Hollich, V., Griffiths-Jones, S., et al. (2004). The PFAM protein families database. *Nucleic Acids Res.* 32, 138D–1141D. doi: 10.1093/nar/gkh121

Blanco, E., Parra, G., and Guigó, R. (2007). Using geneid to identify genes. *Curr. Protoc. Bioinformatics* 18:Unit 4.3. doi: 10.1002/0471250953.bi0403s18

Burge, C., and Karlin, S. (1997). Prediction of complete gene structures in human genomic DNA. *J. Mol. Biol.* 268, 78–94. doi: 10.1006/jmbi.1997.0951

Campbell, M. A., Haas, B. J., Hamilton, J. P., Mount, S. M., and Robin, C. R. (2006). Comprehensive analysis of alternative splicing in rice and comparative analyses with Arabidopsis. *BMC Genomics* 7:327. doi: 10.1186/1471-2164-7-327

Chen, J., Xing, C., Yan, L., Wang, Y., Wang, H., Zhang, Z., et al. (2019). Transcriptome profiling reveals the role of ZBTB38 knock-down in human neuroblastoma. *PeerJ* 7:e6352. doi: 10.7717/peerj.6352

Edgar, R. C., and Myers, E. W. (2005). PILER: Identification and classification of genomic repeats. *Bioinformatics* 21, i152–i158. doi: 10.1093/bioinformatics/bti1003

Fanelli, F., Liuzzi, V. C., Logrieco, A. F., and Altomare, C. (2018). Genomic characterization of Trichoderma atrobrunneum (*T. harzianum* species complex) ITEM 908: insight into the genetic endowment of a multi-target biocontrol strain. *BMC Genomics* 19:662. doi: 10.1186/s12864-018-5049-3

Galperin, M. Y., Wolf, Y. I., Makarova, K. S., Alvarez, R. V., Landsman, D., and Koonin, E. V. (2021). COG database update: Focus on microbial diversity, model organisms, and widespread pathogens. *Nucleic Acids Res.* 49, D274–D281. doi: 10.1093/nar/gkaa1018

Grada, A., and Weinbrecht, K. (2013). Next-generation sequencing: Methodology and application. *J. Investig. Dermatol.* 133, 1–4. doi: 10.1038/jid.2013.248

Haas, B. J., Salzberg, S. L., Zhu, W., Pertea, M., Allen, J. E., Orvis, J., et al. (2008). Automated eukaryotic gene structure annotation using Evidence Modeler and the Program to Assemble Spliced Alignments. *Genome Biol.* 9:R7. doi: 10.1186/gb-2008-9-1-r7

Han, Y., and Wessler, S. R. (2010). MITE-Hunter: A program for discovering miniature inverted-repeat transposable elements from genomic sequences. *Nucleic Acids Res.* 38:e199. doi: 10.1093/nar/gkq862

Hashem, A., Abd Allah, E. F., Alqarawi, A. A., Al Huqail, A. A., and Egamberdieva, D. (2014). Alleviation of abiotic salt stress in *Ochradenus baccatus* (Del.) by *Trichoderma hamatum* (Bonord.) Bainier. *J. Plant Interact.* 9, 857–868. doi: 10.1080/17429145.2014.983568

Hossain, M. S., and Shah, J. S. A. (2019). Present scenario of global salt affected soils, its management and Importance of salinity research. *Int. Res. J. Biol. Scie. Perspect.* 1: 1–3 https://www.researchgate.net/profile/Md-Hossain-72/publication/334773002_Present_Scenario_of_Global_Salt_Affected_Soils_its_Management_and_Importance_of_Salinity_Research/links/5d7150a292851cacdb23c8d9/Present-Scenario-of-Global-Salt-Affected-Soils-its-Management-and-Importance-of-Salinity-Research.pdf

Huang, Y., Mijiti, G., Wang, Z., Yu, W., Fan, H., Zhang, R., et al. (2015). Functional analysis of the class II hydrophobin gene HFB2-6 from the biocontrol agent *Trichoderma asperellum* ACCC30536. *Microbiol. Res.* 171, 8–20. doi: 10.1016/j.micres.2014.12.004

Keilwagen, J., Wenk, M., Erickson, J. L., Schattat, M. H., Grau, J., and Hartung, F. (2016). Using intron position conservation for homology-based gene prediction. *Nucleic Acids Res.* 44:e89. doi: 10.1093/nar/gkw092

Kim, D., Langmead, B., and Salzberg, S. L. (2015). HISAT: A fast spliced aligner with low memory requirements. *Nat. Methods* 12, 357–360. doi: 10.1038/nmeth.3317

Koren, S., Walenz, B. P., Berlin, K., Miller, J. R., Bergman, N. H., and Phillippy, A. M. (2017). Canu: Scalable and accurate long-read assembly via adaptive κ-mer weighting and repeat separation. *Genome Res.* 27, 722–736. doi: 10.1101/gr.215087.116

Korf, I. (2004). Gene finding in novel genomes. *BMC Bioinformatics* 5:59. doi: 10.1186/1471-2105-5-59

Krzywinski, M., Schein, J., Birol, I., Connors, J., Gascoyne, R., Horsman, D., et al. (2009). Circos: An information aesthetic for comparative genomics. *Genome Res.* 19, 1639–1645. doi: 10.1101/gr.092759.109

Kubicek, C. P., Baker, S., Gamauf, C., Kenerley, C. M., and Druzhinina, I. S. (2008). Purifying selection and birth-and-death evolution in the class II hydrophobin gene families of the ascomycete Trichoderma/Hypocrea. *BMC Evol. Biol.* 8:4. doi: 10.1186/1471-2148-8-4

Kundu, S., Perinjelil, S. J., and Thakur, N. D. (2022). "Soil salinization and bioremediation using halophiles and halotolerant microorganisms" in *Mitigation of Plant Abiotic Stress by Microorganisms: Applicability and Future Directions*

Kurtz, S., Phillippy, A., Delcher, A. L., Smoot, M., Shumway, M., Antonescu, C., et al. (2004). Versatile and open software for comparing large genomes. *Genome Biol.* 5:R12. doi: 10.1186/gb-2004-5-2-r12

Ling, Z. N., Jiang, Y. F., Ru, J. N., Lu, J. H., Ding, B., and Wu, J. (2023). Amino acid metabolism in health and disease. *Signal Transduct. Target. Ther.* 8:345. doi: 10.1038/s41392-023-01569-3

Liu, L., Si, L., Meng, X., and Luo, L. (2015). Comparative transcriptomic analysis reveals novel genes and regulatory mechanisms of *Tetragenococcus halophilus* in response to salt stress. *J. Ind. Microbiol. Biotechnol.* 42, 601–616. doi: 10.1007/s10295-014-1579-0

Majoros, W. H., Pertea, M., and Salzberg, S. L. (2004). TigrScan and Glimmer HMM: Two open source ab initio eukaryotic gene-finders. *Bioinformatics* 20, 2878–2879. doi: 10.1093/bioinformatics/bth315

Montero-Barrientos, M., Hermosa, R., Cardoza, R. E., Gutiérrez, S., and Monte, E. (2011). Functional analysis of the *Trichoderma harzianum* nox1 gene, encoding an NADPH oxidase, relates production of reactive oxygen species to specific biocontrol activity against *Pythium ultimum*. *Appl. Environ. Microbiol.* 77, 3009–3016. doi: 10.1128/AEM.02486-10

Mukherjee, P. K., Horwitz, B. A., Herrera-Estrella, A., Schmoll, M., and Kenerley, C. M. (2013). Trichoderma research in the genome era. *Annu. Rev. Phytopathol.* 51, 105–129. doi: 10.1146/annurev-phyto-082712-102353

Muslu, S., Kasapoğlu, A. G., Güneş, E., Aygören, A. S., Yiğider, E., İlhan, E., et al. (2023). Genome-wide analysis of glutathione S-transferase gene family in *P. vulgaris* under drought and salinity stress. *Plant Mol. Biol. Report.*, 41, 1–20. doi: 10.1007/s11105-023-01400-x

Nagarajan, G., and Natarajan, K. (1999). The use of Box-Behnken design of experiments to study *in vitro* salt tolerance by Pisolithus tinctorius. *World J. Microbiol. Biotechnol.* 15, 197–203. doi: 10.1023/A:1008834725272

Noctor, G., Gomez, L., Vanacker, H., and Foyer, C. H. (2002). Interactions between biosynthesis, compartmentation and transport in the control of glutathione homeostasis and signalling. *J. Exp. Bot.* 53, 1283–1304. doi: 10.1093/jexbot/53.372.1283

Pertea, M., Pertea, G. M., Antonescu, C. M., Chang, T. C., Mendell, J. T., and Salzberg, S. L. (2015). StringTie enables improved reconstruction of a transcriptome from RNA-seq reads. *Nat. Biotechnol.* 33, 290–295. doi: 10.1038/nbt.3122

Price, A. L., Jones, N. C., and Pevzner, P. A. (2005). De novo identification of repeat families in large genomes. *Bioinformatics* 21, i351–i358. doi: 10.1093/bioinformatics/bti1018

Pruitt, K. D., Tatusova, T., and Maglott, D. R. (2007). NCBI reference sequences (RefSeq): A curated non-redundant sequence database of genomes, transcripts and proteins. *Nucleic Acids Res.* 35, D61–D65. doi: 10.1093/nar/gkl842

Saadaoui, M., Faize, M., Bonhomme, L., Benyoussef, N. O., Kharrat, M., Chaar, H., et al. (2023). Assessment of Tunisian *Trichoderma* isolates on wheat seed germination, seedling growth and fusarium seedling blight suppression. *Microorganisms* 11:1512. doi: 10.3390/microorganisms11061512

Stanke, M., and Waack, S. (2003). Gene prediction with a hidden Markov model and a new intron submodel. *Bioinformatics* 19, ii215–ii225. doi: 10.1093/bioinformatics/btg1080

Tarailo-Graovac, M., and Chen, N. (2009). Using Repeat Masker to identify repetitive elements in genomic sequences. *Curr. Protoc. Bioinformatics* 25, 4.10.1–4.10.14. doi: 10.1002/0471250953.bi0410s25

Umber, M., Sultana, R., Nasir, F., Mubashir, R., and Sehar, R. (2021). Influence of *Trichoderma harzianum*-seed coating on the biochemical characteristics of wheat (*Triticum aestivum* L.) under salt stress. *Pak. J. Anal. Environ. Chem.* 22, 288–296. doi: 10.21743/pjaec/2021.12.08

Vieira, A. A., Vianna, G. R., Carrijo, J., Aragão, F. J. L., and Vieira, P. M. (2021). Generation of *Trichoderma harzianum* with pyr4 auxotrophic marker by using the CRISPR/Cas9 system. *Sci. Rep.* 11:1085. doi: 10.1038/s41598-020-80186-4

Vinale, F., Sivasithamparam, K., Ghisalberti, E. L., Marra, R., Barbetti, M. J., Li, H., et al. (2008). A novel role for Trichoderma secondary metabolites in the interactions with plants. *Physiol. Mol. Plant Pathol.* 72, 80–86. doi: 10.1016/j.pmpp.2008.05.005

Walker, B. J., Abeel, T., Shea, T., Priest, M., Abouelliel, A., Sakthikumar, S., et al. (2014). Pilon: An integrated tool for comprehensive microbial variant detection and genome assembly improvement. *PLoS One* 9:e112963. doi: 10.1371/journal.pone.0112963

Wang, Lirong (2017). Transcription analysis of two *Trichoderma* species response to copper stress. [dissertation/master's thesis]. Beijing: Chinese Academy of Agricultural Sciences

Wang, J., Huang, X., Zhong, T., and Chen, Z. (2011). Review on sustainable utilization of salt-affected land. *Dili Xuebao/Acta Geogr. Sin.* 66, 673–684. doi: 10.11821/xb201105010

Wösten, H. A. B., and Wessels, J. G. H. (1997). Hydrophobins, from molecular structure to multiple functions in fungal development. *Mycoscience* 38, 363–374. doi: 10.1007/bf02464099

Wu, T., Hu, E., Xu, S., Chen, M., Guo, P., Dai, Z., et al. (2021). clusterProfiler 4.0: A universal enrichment tool for interpreting omics data. *Innovation (New York)* 2:100141. doi: 10.1016/j.xinn.2021.100141

Xiang, J., Chen, J., Xia, X., Liu, K., Li, S., and Gu, J. (2019). Transcriptome-metabolome analysis of *Trichoderma harzianum* ACCC32524 under NaCl stress. 59:2165–2181. doi: 10.13343/j.cnki.wsxb.20180565

Xingxing, P., Khan, R. A. A., Yan, L., Yuhong, Y., Bingyan, X., Zhenchuan, M., et al. (2021). Draft genome resource of fusarium oxysporum f. sp. capsici, the infectious agent of pepper fusarium wilt. *Mol. Plant-Microbe Interact.* 34, 715–717. doi: 10.1094/MPMI-12-20-0355-A

Zaidi, N. W., Dar, M. H., Singh, S., and Singh, U. S. (2014). *Trichoderma* species as abiotic stress relievers in plants. in Biotechnology and Biology of Trichoderma, eds. Vijai K. Gupta, Monika Schmoll, Alfredo Herrera-Estrella, R.S. Upadhyay, Irina Druzhinina, Maria G. Tuohy (Elsevier, Press). 515–525. doi: 10.1016/B978-0-444-59576-8.00038-2

Zhang, J. (2020). "Forestry Ecological Engineering in Coastal Saline–Alkali Soils" in *Study of Ecological Engineering of Human Settlements* doi: 10.1007/978-981-15-1373-2_4

frontiers | Frontiers in Microbiology

TYPE Original Research
PUBLISHED 14 March 2024
DOI 10.3389/fmicb.2024.1360650

OPEN ACCESS

EDITED BY
Z. Petek Cakar,
Istanbul Technical University, Türkiye

REVIEWED BY
Ayşe Meral Yucel,
Middle East Technical University, Türkiye
Haijun Liu,
Saint Louis University, United States
Suleyman I. Allakhverdiev,
Russian Academy of Sciences (RAS), Russia

*CORRESPONDENCE
Rajagopal Subramanyam
✉ srgsl@uohyd.ac.in

RECEIVED 23 December 2023
ACCEPTED 05 February 2024
PUBLISHED 14 March 2024

CITATION
Zamal MY, Madireddi S, Mekala NR, Chintalapati VR and Subramanyam R (2024) Differential stability of bacterial photosynthetic apparatus of *Rhodobacter alkalitolerans* strain JA916^{T} under alkaline and light environment.
Front. Microbiol. 15:1360650.
doi: 10.3389/fmicb.2024.1360650

Differential stability of bacterial photosynthetic apparatus of *Rhodobacter alkalitolerans* strain JA916^{T} under alkaline and light environment

Mohammad Yusuf Zamal, Saikiran Madireddi, Nageswara Rao Mekala, Venkata Ramana Chintalapati and Rajagopal Subramanyam*

Department of Plant Science, School of Life Sciences, University of Hyderabad, Gachibowli, Telangana, India

In purple bacteria, photosynthesis is performed by densely packed pigment-protein complexes, including the light-harvesting complexes known as RC-LH1 and LH2, with carotenoids to assist in the functioning of photosynthesis. Most photosynthetic bacteria are exposed to various abiotic stresses such as light, temperature, alkalinity–acidity, and salinity. *Rhodobacter (R.) alkalitolerans* was discovered from the alkaline pond; here, we report the comparative study of the photosynthetic apparatus of *R. alkalitolerans* in various light intensities in relation to its high pH tolerance ability. With increased light intensity, the stability of photosystem complexes decreased in normal pH (npH pH 6.80 ± 0.05) conditions, whereas in high pH (hpH pH 8.60 ± 0.05), acclimation was observed to high light. The content of bacteriochlorophyll *a*, absorbance spectra, and circular dichroism data shows that the integrity of photosystem complexes is less affected in hpH compared with npH conditions. Large pore blue native polyacrylamide gel electrophoresis of photosystem protein complexes and sucrose density gradient of n-dodecyl β-D-maltoside solubilized intracytoplasmic membranes show that LH2 is more affected in npH than in hpH, whereas RC-LH1 monomer or dimer has shown interplay between monomer and dimer in hpH, although the dimer and monomer both increased in npH. Increased content and expression level of ATPase protein complex and subunit—"c" of ATPase, fast relaxation kinetics of p515, and relatively higher membrane lipid content in hpH along with less photooxidative stress and subsequently lesser superoxide dismutase activity exemplify photoprotection in hpH. Furthermore, the increased expression levels of antiporter NhaD in hpH signify its role in the maintenance of homeostatic balance in hpH.

KEYWORDS

light-harvesting complexes (LH1 andLH2), high light, intracytoplasmic membranes (ICMs), reaction center-light-harvesting complex (RC-LH1), *Rhodobacter alkalitolerans* strain JA916T

Introduction

Photosynthesis is the primary source of energy nearly for all sorts of life forms on Earth. It starts with the absorption of sunlight and subsequently converts the light energy to different forms of hydrocarbon energy. In purple bacteria, photosynthesis is performed by a properly

oriented network of densely packed pigment-protein complexes known as light-harvesting comlex2 (LH2) and light harvesting complex1 (LH1), capturing photons and transferring the energy to the reaction center (RC) (van Grondelle et al., 1994; Niedzwiedzki et al., 2018). Electron passes from RC to the cytochrome (Cyt) bc1 via quinone/quinol exchange at the Qb site of the RC (Okamura et al., 2000; Francia et al., 2004). Light harvesting complexes comprise roughly circularly (elliptically) arranged α-helixes with bound carotenoids and bacterial chlorophyll (BChl) pigments (Bahatyrova et al., 2004). The α-helixes comprise α and β proteins forming the oligomeric light-harvesting complexes LH2 and LH1, and LH1 also encompasses the reaction center (RC), making the complex RC-LH1 (Roszak et al., 2003; Semchonok et al., 2012). RC-LH1 is found in two forms: monomeric form, where the RC is surrounded by C-shaped LH1, and dimeric form, where the S-shaped LH1 complex aggregation surrounds the two reaction centers (Jungas et al., 1999; Crouch and Jones, 2012). The LH2 and RC-LH1 complexes follow a certain pathway of electron transfer in order to generate reducing equivalents, wherein the photon absorbed by the LH2 is transferred to the LH1 and from LH1 to the reaction center, where charge separation takes place between the donor and acceptor molecules. The electron transfer pathway is constituted by a dimer of bacterial chlorophyll, bacterial pheophytin (BPhe), and Cyt bc1 complex, making a cyclic electron flow (Meyer and Donohue, 1995; Jungas et al., 1999). The purple non-sulfur gram-negative bacteria house LH1-RC and LH2 by invaginating the bacterial cytoplasmic membranes, leading to the formation of vesicular membranous structures known as intracytoplasmic membranes (ICMs), also called chromatophores (Niederman, 2013). Some of the ICMs are attached to the plasma membrane as they are developing, whereas matured ICMs are now in the cytoplasm as the development of the cell proceeds (Naylor et al., 1999; Adams and Hunter, 2012; Niederman, 2013).

Rhodobacter is a genus of metabolically versatile bacteria that can grow in aerobic and anaerobic conditions. *Rhodobacter* has been used to study photosynthesis, hydrogen production, and bioplastic polyhydroxy butyrate (PHB) production (Mougiakos et al., 2019). In the present study, the model organism, *Rhodobacter (R.) alkalitolerans* strain JA916^{T}, can grow in alkaline culture conditions and discovered in an alkaline pond (Gandham et al., 2018). The strategies adopted by bacteria, while grown in alkaline conditions, include (a) increased metabolic acid production through amino acid deaminases and sugar fermentation; (ii) increased ATP synthase that couples H^{+} entry to ATP generation; (iii) changes in cell surface properties, and (iv) increased expression and activity of monovalent cation/proton antiporters (Padan et al., 2005). Since *R. alkalitolerans* is a photosynthetic bacterium that utilizes photosynthesis to produce ATP, it could pave the way to understanding the relation between alkaline (high pH) tolerance and production of ATP by photosynthetic machinery and its own functioning in relation to alkaline conditions. Many bacteria have been discovered to have adoptive strategies to grow in extreme environmental conditions, such as alkaliphilic acidophiles halophiles which use several antiporters, such as monocationic and dicationic proton antiporters, e.g., sodium/proton antiporters and calcium/proton antiporters (Padan et al., 2005; Preiss et al., 2015).

Previously, many species from the genus *Rhodobacter* have been studied for its basic mechanism of photosynthesis and its photosynthetic membrane protein complexes, i.e., RC-LH1 monomer, dimer, and LH2 housed in chromatophore/intracytoplasmic membranes (Ng et al., 2011; Crouch and Jones, 2012). They have also been studied at biophysical level to investigate the electron transfer efficiency using femtosecond transient absorption spectroscopy and metabolite study (Yen et al., 2010; Niedzwiedzki et al., 2018). Many species of purple non-sulfur photosynthetic bacteria such as *Rhodobacter sphaeroides 2.4.1*, *Rhodospirillum rubrum* (Hustede et al., 1993; Ryu et al., 2014), and *Rhodobacter capsulatus KU002* (Merugu et al., 2012) have been studied for the production of hydrogen gas and a bioplastic known as polyhydorxybutyrate (PHB). *R. alkalitolerans was* discovered from an alkaline pond, and being a photosynthetic organism and ability to grow in hpH, it promises the existence of interplay between homeostasis and photosynthesis, which can be investigated.

In nature, light intensity is never constant; as a result, photosynthetic organisms face extreme and low light intensity. Moreover, it is important to study how a bacterium that uses light to produce ATP while growing in alkaline conditions maintains the integrity of its photosynthetic machinery. Since it is a new photosynthetic bacterium, it has not been characterized by how it can cope with various stresses, especially high light and alkalinity. Thus, in the current study, we are trying to understand the effect of high light in relation to the high pH tolerance ability of *R. alkalitolerans* on the organization of photosynthetic complexes.

Materials and methods

Growth curve, calculation of generation time and pH measurement

For calculating the generation time, 8 mL screw-capped tubes were inoculated with 5% of inoculum (v/v) from mother cultures in the log phase. Triplicates of each bacterial culture were taken, and growth in terms of optical density was measured by taking reading at 660 nm. Generation time was calculated after plotting the growth curve (Willey et al., 2008; Tucker et al., 2010). pH of the culture was measured in all the conditions just before harvesting the cell using pH tutor of Eutech instruments.

Culturing and harvesting of cells

Cultures were grown in Biebl and Pfennig's medium in two pH conditions of pH 6.80 ± 0.05 and pH 8.60 ± 0.05 with sodium pyruvate (3 g/L) as carbon source and ammonium chloride as nitrogen source (0.4 g/L) in light/anaerobically at room temperature (25°C) in filled glass bottles with glass cork stoppers to avoid infiltration of air without any void space left as described previously (Lakshmi et al., 2011; Crouch and Jones, 2012; Gandham et al., 2018). The cultures were grown in three light intensities of 28–30 μmol photons

Abbreviations: RT, Room temperature; β-DM, *n*-dodecyl β-d-maltoside; ACA, Amino caproic acid; CD, Circular dichroism; HEPES, (4-(2-hydroxyethyl)-1-piperazineethanesulfonic acid); ICMs, Intracytoplasmic membranes; SQDG, Sufoquinovocyl diacylglycerol; PC, Phosphatidylcholine; PG, Phosphatidylglycerol; PE, Phosphatidylethanolamine; CL, Cardiolipin; RC-LH1, Reaction center- light-harvesting complex; LH2, Light-harvesting antenna 2.

m^{-2} s^{-1}(optimum light), 250–255 μmol photons m^{-2} s^{-1}, and 500 ± 5 μmol photons m^{-2} s^{-1} by inoculating 1.125 mL of inoculum culture in 300 mL of Biebl and Pfennig's medium prepared in 25 mM Tris buffer medium, and the pH was set to 6.80 ± 0.05 with hydrochloric acid, and in hpH, the pH was reached to 8.60 ± 0.05 after adding all media components. Cells were harvested in the late log phase (~at OD of 1.4–1.5) (Scheuring et al., 2014) to get maximum number of intracytoplasmic membranes by centrifuging the cells at 15,000 × g for 20 min, washed with 20 mM HEPES pH 7.5, and then stored at −80°C until required.

Harvesting of intracytoplasmic membranes

The pellet was washed with 20 mM of HEPES buffer with pH of 7.5. To harvest the ICMs cell in 15 ml HEPES buffer were sonicated on ice for 6 min at 30% amplitude by giving 45 s of relaxation and 15 min on (Tucker et al., 2010). Before sonication, protease inhibitor cocktail (sigma) was also added to avoid protein degradation. The cell lysate was ultracentrifuged in a 15/40% discontinuous sucrose density gradient at 50,000×g in a Beckman Type SW32 Ti rotor at 4°C for 12 h. A pigmented band of ICM formed at the 15/40% interface and was collected using a fixed needle (Mothersole et al., 2016) and stored at −20°C and − 80°C for long storage. The membranes were solubilized with 1% n-dodecyl-beta-D-maltoside (β-DM) for 30 min, and the non-solubilized material was removed by centrifugation at 10,000 × g for 30 min (D'Haene et al., 2014). The supernatant was loaded in either BN-PAGE or in sucrose density gradient.

Bacteriochlorophyll *a* estimation and carotenoid/BChl *a*

The content of BChl *a* and carotenoid was measured by resuspending the cell pellet in seven parts of acetone and two parts of methanol (v/v), and the absorbance readings were measured at 775 nm and 456 nm, respectively. The contents of BChl *a* and carotenoid were calculated as described (Cohen-Bazire et al., 1957). The carotenoid to Bach *a* ratio was also calculated (Supplementary Excel Sheet S1).

Absorbance spectroscopy

Absorbance spectra of isolated intracytoplasmic membranes were measured in a quartz cuvette of 1 cm path length between 400 and 900 nm at room temperature (RT) at a protein concentration of 50 μg/mL using perkinelmer 1,500 UV–Visible spectrophotometer (Georgakopoulou et al., 2006). Protein concentrations were measured by the Bradford method (Quick Start Bradford 1x Dye Reagent, cat:5000205) using bovine serum albumin (BSA) as standard. The same method was used for all other protein estimations.

Sucrose density gradient sedimentation

Sucrose density gradients were formed in transparent ultracentrifuge tubes by carefully layering five steps of 20, 21.3, 22.5, 23.8, and 25% (w/w) sucrose in 20 mM HEPES (pH 7.5) and 0.03% β-DM. Solubilized membrane proteins (300 μL at 1 μg/μL concentration) were loaded onto each gradient, and these were centrifuged in a Beckman coulter swing-out bucket rotor SW41Ti at 180,000 × g for 18 h at 4°C (D'Haene et al., 2014). For each growth condition, multiple gradients were run.

Circular dichroism spectroscopy

Circular dichroism (CD) spectra of ICMs (in 20 mM HEPES buffer with 10 mM $MgCl_2$) at protein concentration of 50 μg/mL were measured at room temperature using a Jasco J-1500 CD spectrometer and a 10-mm path length quartz cuvette with a protein concentration of 50 μg/mL. The NIR photomultiplier parameters were set: data pitch: 1 nm, bandwidth: 4 nm, response: 1 s. Two scans for each sample were collected at a speed of 100 nm/min (Southall et al., 2018), and each sample was in triplicate from three different biological replicates.

Large pore blue native PAGE

The Blue native gel separation of photosynthetic complexes was carried out in gradient gel of 3.5–12% by solubilization of intracytoplasmic membranes (ICMs) in 1% β-DM along with the protease inhibitors 1 mM Amino Caproic Acid (ACA), 1 mM benzamidine hydrochloride, the gel with 50 mM ACA is run at 4°C with a constant current of 4 mA (Kügler et al., 1997; Madireddi et al., 2014).

Identification of subunit protein of super-complexes separated by blue native-PAGE

Blue-native gel strips were carefully cut and stored at −20°C. BN strips were solubilized in laemmli buffer by gently shaking for 1 h with 6 M urea containing β-mercaptoethanol as a reducing agent. Solubilized BN strips were run with 15% SDS-urea gel. Individual protein subunits of the protein complex from BN-PAGE were spotted, excised, and given for identification by orbitrap high-resolution liquid chromatography-mass spectrometry (OHRLCMS, Agilent Technology USA), and subsequent quantitative studies were conducted in different treatments.

Transmission electron microscopy

To investigate the morphology and number of ICMs in varying light intensities in relation to high pH tolerance, TEM imaging was performed. Harvested cells were washed with 50 mM potassium phosphate (KPi buffer) buffer pH 6.80, and primary fixation was performed with 2% glutaraldehyde Grade-I (Sigma) for 1 h at 4°C in the dark, and then, cells were washed three times with KPi buffer for 15 min each, post-fixed in $KMNO_4$ (4% w/v) for 1 h, and washed with autoclaved distilled water five times each for 5 min. After this, cells were fixed with 2% (w/v) uranyl acetate for 1 h at room temperature (RT), and after washing with distilled water five times each for 5 min, cells were subjected to the dehydration step with ethanol (50, 70, 80, 90, and 95%) and four washes with 100% ethanol. The last two washes were performed with propylene oxide (≥ 99% from Sigma CAS:

75–56-9) two times each for 1 h. These cells were infiltrated with Spurr's low-viscosity embedding medium, and blocks were prepared. Ultra-thin sections were cut and mounted on copper grids. Sections were stained with an alcoholic solution of 2% (w/v) uranyl acetate and Reynolds lead citrate stain (Fedotova and Zeilstra-Ryalls, 2014). The thin sections of cells were visualized using a Technai instrument.

Electrochromic shift measurement

Fast relaxation kinetics measurements were performed in Dual PAM-100 (Walz) equipped with P515/P535 emitter detector module by saturating single turnover flash to intact cells of *R. alkalitolerans*. Cells at 1.4–1.5 OD were incubated in the dark for 1 h in the same culture medium before the measurement (Feniouk et al., 2002).

RNA extraction, cDNA synthesis, and quantitative real-time PCR

Total RNA was extracted from STRN50-1KTspectrum ™ Plant Total RNA Kit, according to the manufacturer's protocol. RNA concentration was calculated at 260/280 nm with a NanoDrop1000 spectrophotometer from Thermo Scientific. Single-stranded cDNA is synthesized from total RNA by cDNA synthesis kit (TAKARA) by priming at 65°C and reverse transcription for 1 h at 42°C in a 20 µL reaction mixture.

To investigate the expression level of some important genes, primers were designed for ATPase subunit "c" and antiporter NhaD based on the available genome sequence of closely related species *Rhodobacter sphaeroides ATH 2.4.1*^{T} *(X53853)* (Supplementary Table S1). Using *R. alkalitolerans,* cDNA genes were amplified, and the $2^{-\Delta\Delta CT}$ method was used to measure the accurate gene expression of target and housekeeping gene recA. RT-PCR was carried out in Eppendorf Mx3000P multiplex quantitative PCR system with SYBR Green PCR Master Mix (Kappa).

Extraction and separation of polar lipids

To extract the polar lipids, 5 mg of lyophilized cells was taken. An extraction mixture of methanol-chloroform-water (1.1:0.9, v/v) was added to cells (De Leo et al., 2009), and phase separation was performed by centrifuging the mixture at 10,000 rpm for 6 min. The lower layer of chloroform was carefully collected, transferred to another fresh tube, and dried in a speed vacuum. Lipid dried was redissolved in 50 µL of chloroform and kept at −20°C until use. Total lipid extracts were analyzed by TLC on silica gel (20 × 20 cm, layer thickness 0.2 mm). The plate was developed with the solvent chloroform-methanol-acetic acid-water (85, 15, 10:3.5, v/v) and detected by iodine vapor. Lipid membrane bands were quantified by ImageJ software.

Estimation of total ROS and analysis of SOD activity

To estimate the total amount of reactive oxygen species (ROS), cells from all the conditions were collected in logarithmic phase at equal OD of 1.4–1.5. Fluorescent dye 2′,7′-dichlorofluorescein diacetate (H_2DCFDA) (Sigma–Aldrich) was used to quantify the total ROS. Cells were washed in culture medium and then incubated in the dark by adding 5 µM of dye for 1 h at room temperature. After incubation, the cells were washed in culture medium to remove excess dye. Fluorescence intensity was measured using a microplate reader (Tecan M250) at the excitation wavelength of 485 nm and emission at 530 nm (Devadasu et al., 2021).

In addition, to analyze the superoxide dismutase activity by native polyacrylamide gel electrophoresis, cells were lysed by sonication, and the supernatant was collected. Protein concentration was measured in all the samples by the Bradford method, and 20 µg of protein was loaded to check the type of superoxide dismutase expressed during the photoheterotrophic growth of bacteria. To visualize the SOD bands, gel was stained in 0.05 mM riboflavin, 0.1 mM nitro blue tetrazolium, and 1 mM EDTA, and 0.3% N,N,N′,N′-tetramethylethylenediamine made in 50 mM potassium phosphate buffer (pH 7.8) as described previously (Kho et al., 2006; Alves et al., 2020).

Statistical analysis

All physiological and biochemical results are the average of at least three independent experiments performed separately. The results were analyzed by analysis of variance (ANOVA Tukey's Test). Each data point averages three replicates, and error bars are represented as ±SE. Asterisks indicated the level of significance of hight light treated versus control (optimum light) with *P*-value style: GP: 0.1234 (ns), 0.0332(*), 0.0021(**), 0.0002 (***), and <0.0001 (****) respectively.

Results

Growth and generation time

The growth curve of *R. alkalitolerans* in different light intensities in high pH and normal pH conditions was plotted (Figure 1A). There has been an effect of high pH on the attainment of the stationary phase. hpH grown cells entered the stationary phase around the optical density of 1.6, which took 40 h in high light (250 and 500 µmol photons $m^{-2}s^{-1}$), whereas at 30 µmol photons $m^{-2}s^{-1}$, it took nearly 60 h to enter the stationary phase. The npH grown cells took 1.9 optical density, which took 40 h to enter the stationary phase. The light affects the generation time as it decreases as light intensity increases (Figure 1B). Generation time remains almost the same at 30 µmol photons $m^{-2}s^{-1}$ being 13.07 hrs in npH and 13.21 hrs in hpH. At 250 µmol photons $m^{-2}s^{-1}$, 9.24 hrs in npH and 10.36 h in hpH, and at 500 µmol photons $m^{-2}s^{-1}$, 6.80 hrs in npH and 6.83 hrs in hpH.

Bacteriochlorophyll *a* estimation and carotenoid to BChl *a* ratio

Bacteriochlorophyll *a* is one of the major pigments and, along with carotenoids, plays an essential role in bacterial photosynthesis, contributing to the assembly and structural stability of photosystem complexes. It is the major component of LH1-RC and LH2 and constitutes a special pair of RC (Cao et al., 2022). *R. alkalitolerans* photosystem also contains the pigment spheroidene, which plays a very important role in photoprotection and energy transfer being the

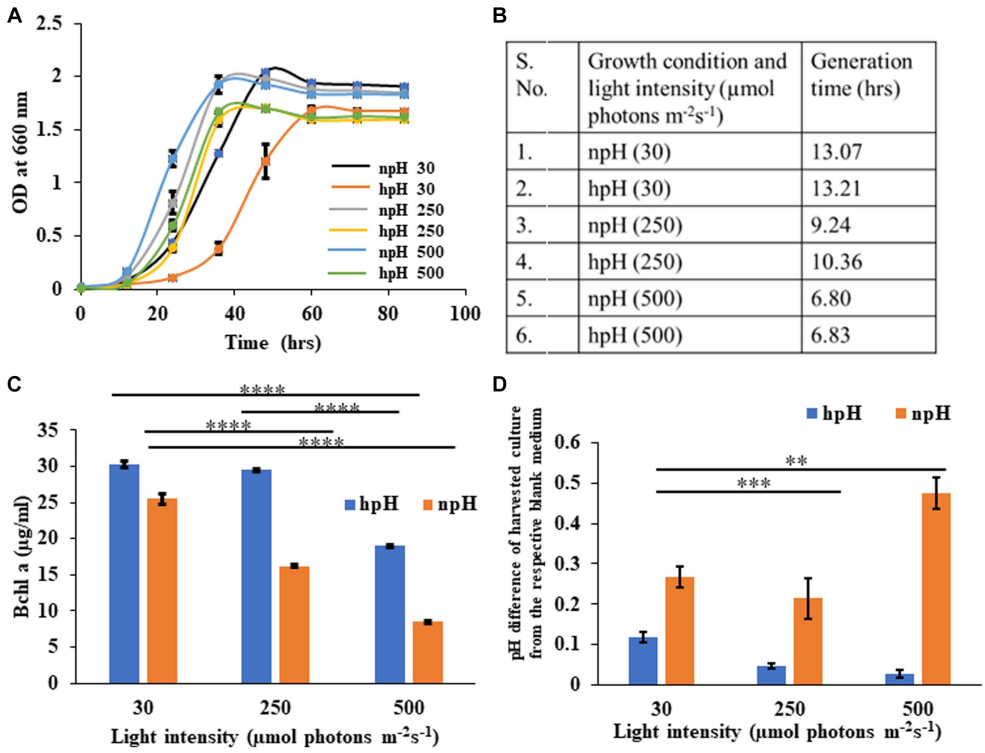

S. No.	Growth condition and light intensity (µmol photons $m^{-2}s^{-1}$)	Generation time (hrs)
1.	npH (30)	13.07
2.	hpH (30)	13.21
3.	npH (250)	9.24
4.	hpH (250)	10.36
5.	npH (500)	6.80
6.	hpH (500)	6.83

FIGURE 1
(A) Growth curve of *R. alkalitolerans* in alkaline (pH 8.60 ± 0.05, hpH) and at normal pH (pH 6.80±0.05, npH) in light intensities of 30 µmol photons m^{-2} s^{-1}, 250 µmol photons m^{-2} s^{-1}, and 500 µmol photons m^{-2} s^{-1}. Cultures were grown anaerobically in 8 mL screw-capped tubes at room temperature (25°C). **(B)** Generation time: Calculation of generation time/doubling time at 30 µmol photons m^{-2} s^{-1}, 250 µmol photons m^{-2} s^{-1}, and 500 µmol photons m^{-2} s^{-1}in npH and hpH culture media. **(C)** Comparative representation of the content of BChl *a* in hpH and npH conditions in all the three light conditions (30 µmol photons m^{-2} s^{-1}, 250 µmol photons m^{-2} s^{-1}, and 500 µmol photons m^{-2} s^{-1}). **(D)** Measurement of pH difference of the culture from that of blank medium in hpH and npH culture grown at light intensity of 30, 250, and 500 µmol photons m^{-2} s^{-1}. Asterisks indicated the level of significance of hight light (treated) versus control (normal light) with *p*-value style: GP: 0.1234 (ns), 0.0332(*), 0.0021(**), 0.0002 (***), and <0.0001 (****) respectively.

accessory light-harvesting pigment (Nagy et al., 2004). Carotenoids have been shown to scavenge the ROS to safeguard the photosystem complexes during the photooxidative stress as a result of increased light stress (Nagy et al., 2004). The content of BChl *a* (Cohen-Bazire et al., 1957) is more in cultures grown in hpH conditions compared with hpH condition (Figure 1C), indicating that *R. alkalitolerans* accumulate more bacteriochlorophyll in hpH conditions. As carotenoids play an important role in scavenging ROS whereas BChl *a* majorly absorbs the energy, we calculated the carotenoid to BChl *a* ratio as a function of the state of the cell under photooxidative stress. Here, we found that the ratio has increased with an increase in light intensity, but it is more in npH than hpH (Supplementary Figure S1).

Measurement of pH of culture media while harvesting

Here, we have plotted the pH difference between the npH-harvested culture and the blank and the hpH-harvested culture and its blank. Uninoculated culture medium was used as blank separately for each pH condition. The pH of culture in normal pH medium has increased as the light intensity increases, except for the culture grown at 250 µmol photons $m^{-2}s^{-1}$ (Figure 1D). In contrast, in high pH grown medium, the pH difference in harvested culture from that of the blank has subsequently decreased.

Absorbance spectroscopy analysis

A comparative study of the absorbance spectrum of ICMs shows that in hpH (pH 8.60 ± 0.05), the absorbance intensity is higher in all light conditions compared with npH (pH 6.80 ± 0.05) (Figures 2A–C). The absorbance spectrum is also an indication of photosystem integrity and stability of the photosystem in relation to given stress conditions (Niedzwiedzki et al., 2018). When increasing light intensity, the ICMs in both normal and high pH complexes are reduced, but in npH, the complexes are more sensitive than hpH. Absorbance data at equal protein concentration show that the spectrum intensity is comparatively higher in high pH conditions compared with normal pH conditions, indicating the role of high pH tolerance ability in photoprotection. The shoulder peak in the absorbance spectrum at 875 nm represents the RC-LH1 complex. In hpH its peak intensity is less compared to that of the npH ICMs which signifies that in npH condition the RC-LH1 has increased with an increase in light intensity (Figures 2D–F).

Large pore blue native page and identification of protein subunit from selected protein complex

The blue native page separates the photosystem complexes without denaturing the photosynthetic pigment-protein complexes. Here,

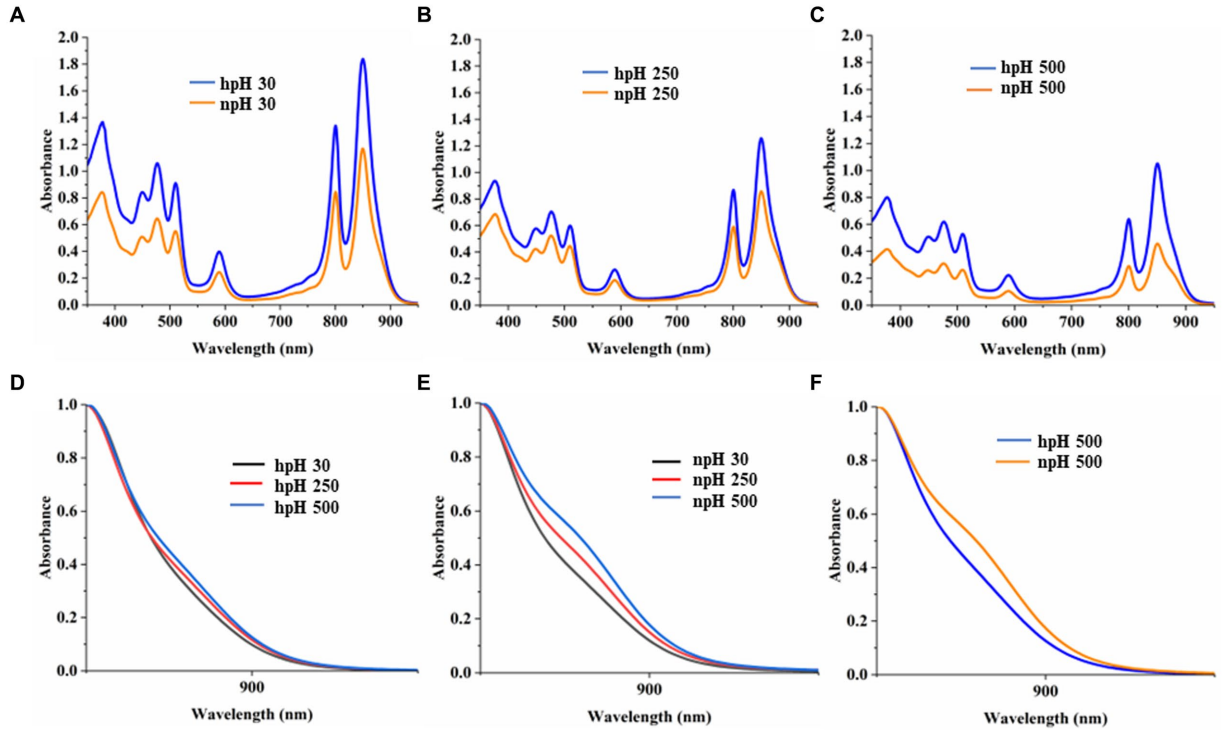

FIGURE 2
Comparative representation of absorbance spectrum of ICMs isolated from hpH-grown and npH-grown cells. ICMs were harvested from the interface of 15/40% discontinuous sucrose density gradient run overnight. **(A)** Absorbance spectra of npH and hpH from 30 µmol photons m^{-2} s^{-1}. **(B)** Absorbance spectra of npH and hpH from 250 µmol photons m^{-2} s^{-1}. **(C)** Absorbance spectra of npH and hpH from 500 µmol photons m^{-2} s^{-1}. **(D)** Enlarged view of shoulder peak at 875 nm of hpH ICM absorbance. **(E)** Enlarged view of shoulder peak at 875 nm of npH ICM absorbance. **(F)** Enlarged comparative view of absorbance the npH and hpH ICM at 500 µmol photons m^{-2} s^{-1} light intensity.

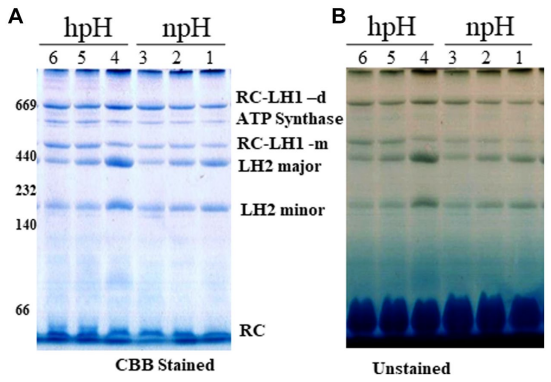

FIGURE 3
Large pore blue native page (LP-BN) of photosynthetic complexes. After centrifugation, supernatant was loaded in wells of native gradient gel of 3.5–12% by solubilization of intracytoplasmic membranes (ICMs) in 1% β-DM. Lane 1,2,3 represents the photosystem complexes from npH grown at light intensity of 30, 250 and 500 µmol photons m^{-2} s^{-1}. Lane 4,5,6 represent photosystem complexes from hpH grown at a light intensity of 30,250 and 500 µmol photons m^{-2} s^{-1}. At respective growth conditions, CBB stained with native marker lane **(A)** without stain **(B)**. Fifteen microgram of protein was loaded in each lane.

we found that as the light intensity increases, it affects the photosystem protein complex stability. A decrease is observed in the case of RC-LH1 dimer, although at 500 µmol photons $m^{-2}s^{-1}$, it is increased a little, and an increase is observed in RC-LH1 monomer in hpH condition which could be because of the conversion of dimer to monomer. In contrast, in npH-grown cells, it is the inverse of the hpH, wherein both dimeric and monomeric reaction centers have increased with the increase in light intensity (Figure 3; Supplementary Figures S2A,C). This could be an interesting phenomenon to pave the way to understanding the real reason for dimer monomer interconversion. The LH2 major and minor both have decreased with light intensity, but the extent is less in hpH conditions than in npH conditions (Figure 3; Supplementary Figures S2D,E). Even in normal growth conditions, the alkaline pH shows a stronger band of photosystem protein complexes than the normal pH. The protein complex separation pattern is in accordance with the previous study (Mothersole et al., 2016).

After staining the gel with colloidal Coomassie brilliant blue G -250, a non-pigmented band appeared below RC-LH1 dimeric band is enhanced with an increase in light intensity in both npH and hpH conditions (Supplementary Figure S2B). To identify this protein complex band, second dimension of the LP-BN strip was performed. The upper subunit protein bands were identified by mass spectrometry. Out of these, four protein bands were identified to be ATP synthase α (55.12 kDa), β (50.45 kDa), γ (31.2 kDa), and δ (19.34 kDa) (Supplementary Figure S3). The protein complex is found to be as ATP synthase complex with relatively increased expression with an increase in light intensity, and its expression is more in hpH conditions compared with npH conditions.

Furthermore, SDS-PAGE of ICMs from each condition shows that the protein abundance of photosystem complex proteins is higher in hpH than that in npH (Supplementary Figure S2F).

Sucrose density gradient sedimentation and absorbance spectra of fractions from npH

Equal protein amounts of ICMs were solubilized in 1% β-DM loaded on the sucrose density gradient to separate the photosystem protein complexes of LH2 and RC-LH1 monomer and RC-LH1 dimer. Sucrose density gradient fractions were carefully collected, and their absorbance spectra were measured. SDG of npH condition shows that the F1 fraction, originating from light-harvesting antenna 2 (LH2), has decreased with increasing light intensity (Figures 4A,B; Supplementary Figure S4A). The same has also been found in LP-BN (Figure 3; Supplementary Figures S2D,E), although LH2 minor could not be separated in SDG because of minor difference in molecular weight (Mothersole et al., 2016), whereas both the F2 and F3 fractions have increased with an increase in light intensity. F2 represents RC-LH1 monomer and F3 represents RC-LH1 dimer (Figures 4B,C; Supplementary Figures S4B,C). The same is visible in the absorbance spectroscopy of each fraction of SDG. With an increase in light intensity, the RC-LH1 monomer and dimer have increased as the shoulder peak at 875 nm has enhanced while increasing in light intensity (Figures 2D–F, 4C,D). The same result is also observed in the LP-BN PAGE of ICM in npH, where both monomeric and dimeric reaction centers have elevated with an increase in light intensity (Figures 3, 4; Supplementary Figures S2A,C).

Sucrose density gradient sedimentation and absorbance spectra of fractions from hpH

Sucrose density gradient fractions were carefully collected, and their absorbance spectra were measured. SDG shows that the F1 fraction, which is for light harvesting (LH2), has decreased with increasing light intensity (Figures 5A,B; Supplementary Figure S4A). However, the F2 fraction, which is for the monomeric reaction center, has increased with light intensity. This could be because of the decrease in the F3 fraction which represented the dimeric reaction center complex, and its content was decreased (Figure 5A; Supplementary Figures S4B,C). It is also in agreement with Blue native

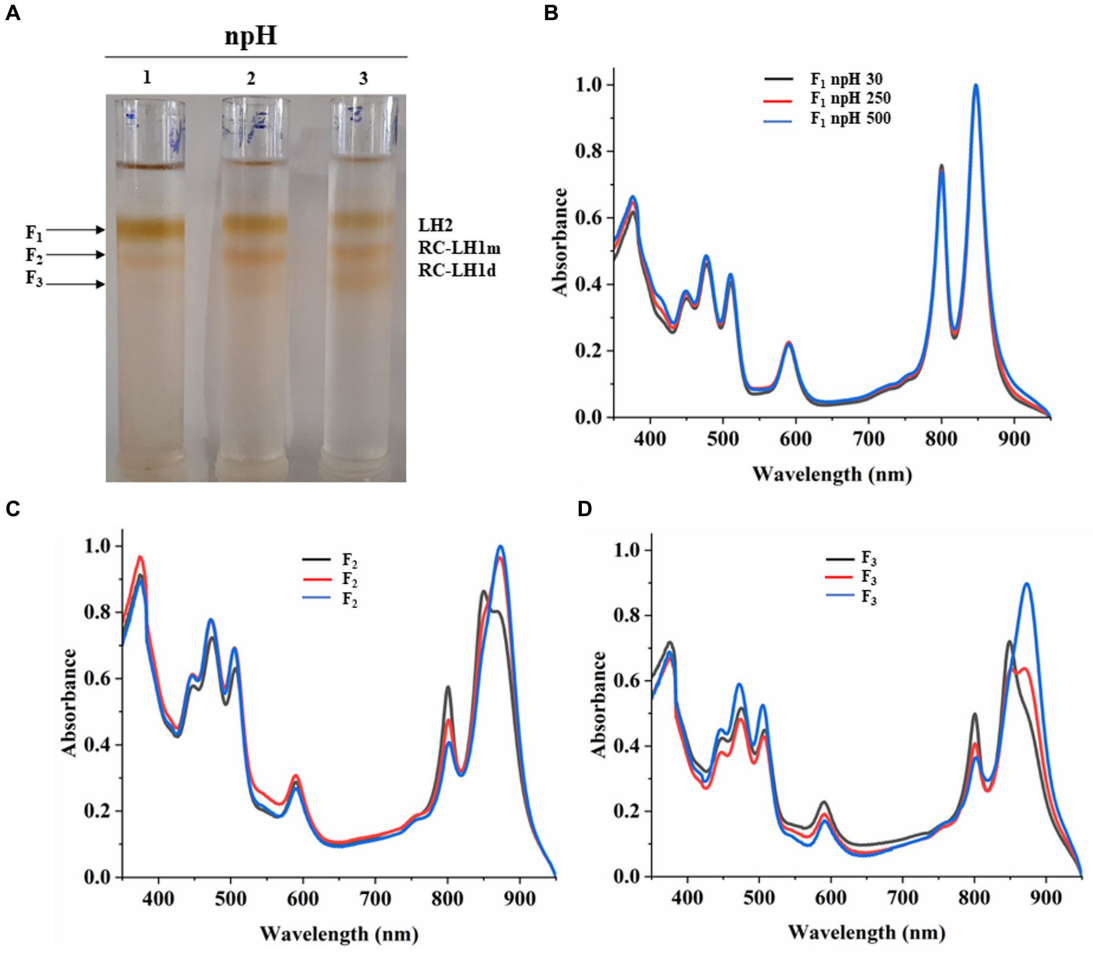

FIGURE 4
Sucrose density gradient of ICMs solubilized in 1% β-DM from npH. Five steps gradient of sucrose 20, 21.3, 22.5, and 23.8%, 25% (w/w) were made in 20 mM HEPES (pH 7.5) and 0.03% β-DM. Fractions were carefully harvested and their absorbance spectra was measured. 1,2,3 represent samples from light intensity of 30,250 and 500 μmol photons m^{-2} s^{-1}, respectively **(A)**. Absorbance spectra of all three-fractions obtained F1 (LH2) **(B)**, F2 (RC-LH1m) **(C)**, F3(RC-LH1d) **(D)** in all three light conditions of 30, 250 and 500 μmol photons m^{-2} s^{-1}.

PAGE (Figure 3; Supplementary Figures S2A,C). The absorbance spectroscopy of each fraction further confirms that the dimeric reaction center has converted to the monomeric reaction center (Figures 5C,D). However, a slight increase is observed in the dimeric reaction center (RC-LH1 d) at 500 µmol photons $m^{-2}s^{-1}$ of light intensity (Figure 5; Supplementary Figure S2A).

Circular dichroism analysis

It is important to investigate the basic arrangement of the BChls in the complex in all the respective growth conditions. CD spectrum of ICMs from all these six conditions can provide detailed information about the organization and optically active pigments. In the CD spectrum, it is obvious that organizational pattern of pigment protein interaction remains the same. In contrast, the intensity of CD peaks is much stronger in hpH conditions than in npH-grown cells. The near-infrared (NIR) Q_Y region shows the doublet band with a strong positive band at 850 nm and a strong negative peak at 860 nm, pertaining to LH2 and LH1-RC (Tokita et al., 2011; Southall et al., 2018) (Figure 6). CD spectra have also shown the absorption peaks for the Q_x region at 590 nm and in the carotenoid region from 400 to 550 nm. Like the absorption spectra results, the CD spectra data also depict the changes in pigment-pigment/protein complexes during an increase in light intensity. These changes are much lesser in hpH than in npH, indicating that the complexes are stabilized in high pH. In addition, under high pH and high light, these complexes are relatively stable.

Electrochromic shift analysis of whole cells

P515 measurement measures chromatophore lumen acidification in relation to ATPase activity by measuring flash-induced relaxation kinetics of carotenoids. Figure 7 shows the electrochromic shift measurement by P515 signal measurement of intact *R. alkalitolerans* cells grown in different conditions. The relaxation of the P515 normalized signal is also an indicator of ATPase activity. In this study, in high pH conditions, the relaxation is quite faster than that of the npH cells and has enhanced with an increase in light intensity (Figures 7A,B). Although in npH cells, the relaxation time has decreased, it is comparatively lesser than that of the hpH cells. The qPCR of the "c" subunit of ATPase expression level has also enhanced with an increase in light intensity which is more in hpH-grown cells (Figure 8B). It further confirms from LP-BN-2D and protein identification that the level of ATP synthase is

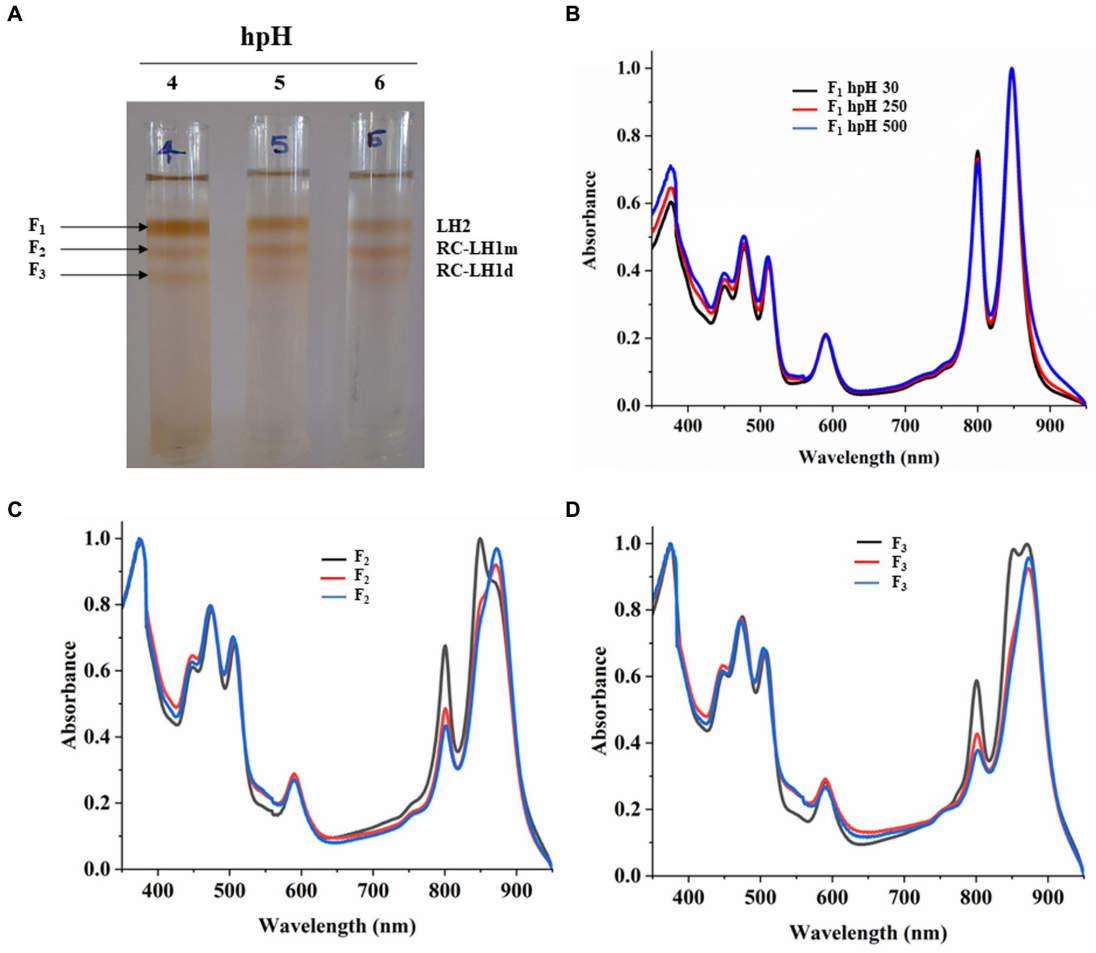

FIGURE 5
Sucrose density gradient of ICMs solubilized in 1% β-DM from hpH. Five steps gradient of sucrose 20, 21.3, 22.5, and 23.8%, 25% (w/w) were made in 20 mM HEPES (pH 7.5) and 0.03% β-DM. Fractions were carefully harvested and their absorbance spectra was measured. 4,5,6 represent samples from light intensity of 30,250 and 500 µmol photons m^{-2} s^{-1} **(A)**. Absorbance spectra of all the three-fractions obtained F1 (LH2) **(B)**, F2 (RC-LH1m) **(C)**, F3 (RC-LH1d) **(D)** and in all three light conditions of 30,250 and 500 µmol photons m^{-2} s^{-1}.

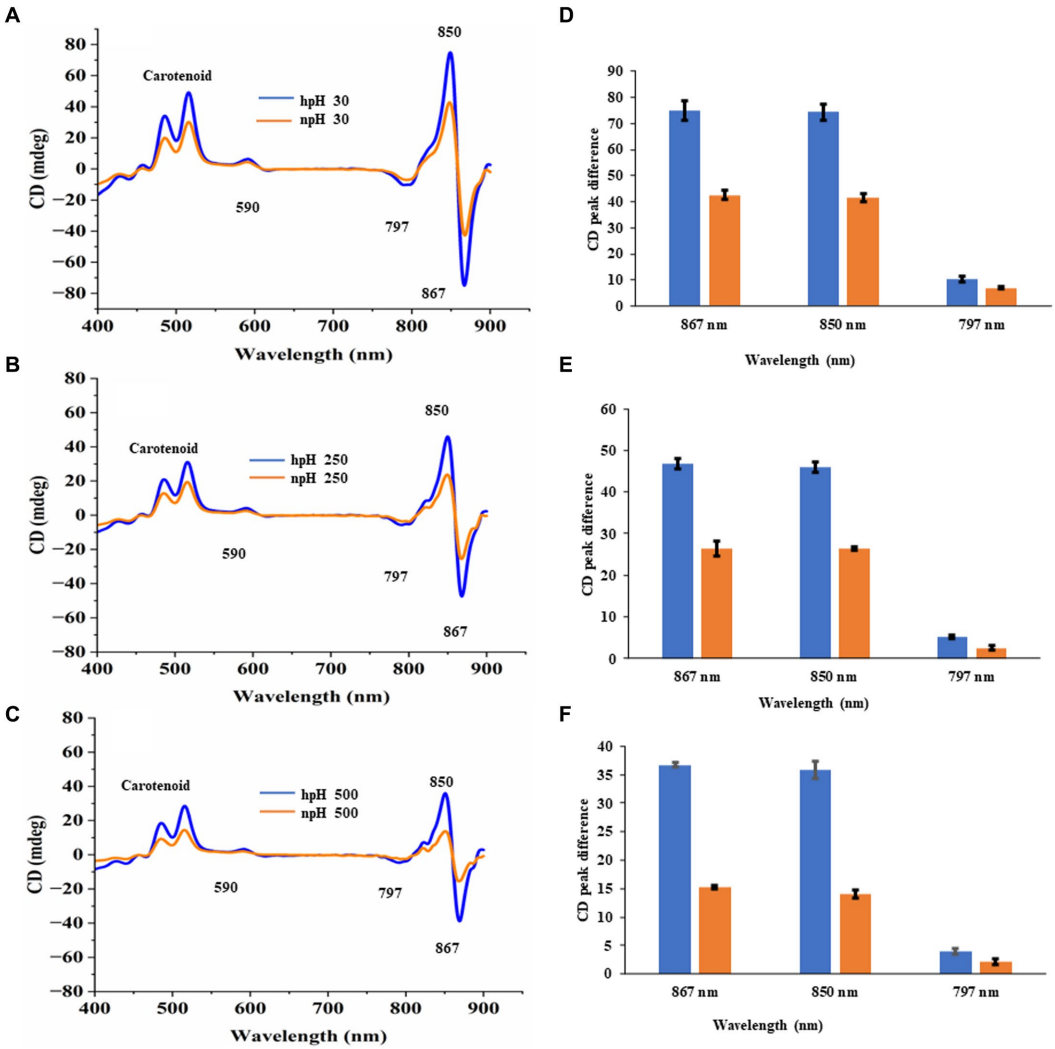

FIGURE 6
Comparative representation of circular dichroism of ICMs isolated from hpH and npH grown cells. CD spectra of ICMs (in 20 mM HEPES buffer with 10 mM $MgCl_2$) at protein concentration of 50 µg/mL, were measured at room temperature using a Jasco J-1500 CD spectrometer. **(A)** Circular dichroism spectra of npH and hpH from 30 µmol photons m^{-2} s^{-1}. **(B)** Circular dichroism spectra of npH and hpH from 250 µmol photons m^{-2} s^{-1}. **(C)** Circular dichroism spectra of npH and hpH from 500 µmol photons m^{-2} s^{-1}. Major peak intensity differences of circular dichroism spectra of ICMs from npH and hpH in all three light conditions **(D–F)**.

higher in hpH-grown cells (Supplementary Figure S2B). This helps in less acidification in the chromatophore lumen and less detrimental effect on photosystem complexes.

Quantitative real-time PCR and polar lipids

To assess the transcript level of the ATPase and the antiporter NhaD, qPCR was performed for subunit "c" of ATPase and NhaD. Both proteins play a crucial role in the dissipation of the proton gradient. NhaD has been shown to play a significant role in the homeostasis of bacterial cells when shifted in culture media of different alkaline conditions (Padan et al., 2005). ATP synthase also plays a very similar role to that of the NhaD, but it utilizes ADP (adenosine diphosphate and inorganic phosphate) to make ATP, which is used as an energy source in various metabolic processes and during photosynthesis by making the use of the proton gradient made in the cell. In this result, it is evident that the transcript level of both genes has increased significantly in hpH-grown cells compared with that of the npH-grown cells (Figures 8B,C). Moreover, expression levels of both genes have increased in response to an increase in light intensity.

Thin layer chromatography of polar lipids isolated from complete cells shows that this bacterium has sufoquinovocyl diacylglycerol (SQDG), phosphatidylcholine (PC), phosphatidylglycerol (PG), phosphatidylethanolamine (PE), and cardiolipin (CL) as major polar lipids, making lipid bilayer (Figure 8A). After analyzing the separation of lipids, the hpH-grown cells have a slightly higher amount of membrane lipids (Supplementary Figure S5). Out of this, phosphatidylcholine (PC) is present in higher amounts in hpH than in npH in all light intensities.

Transmission electron microscopy

Electron micrograph of ICMs from *R. alkalitolerans* cells in all three light conditions in relation to culture condition npH shows that high light of 250 and 500 µmol photons $m^{-2}s^{-1}$ has drastically affected

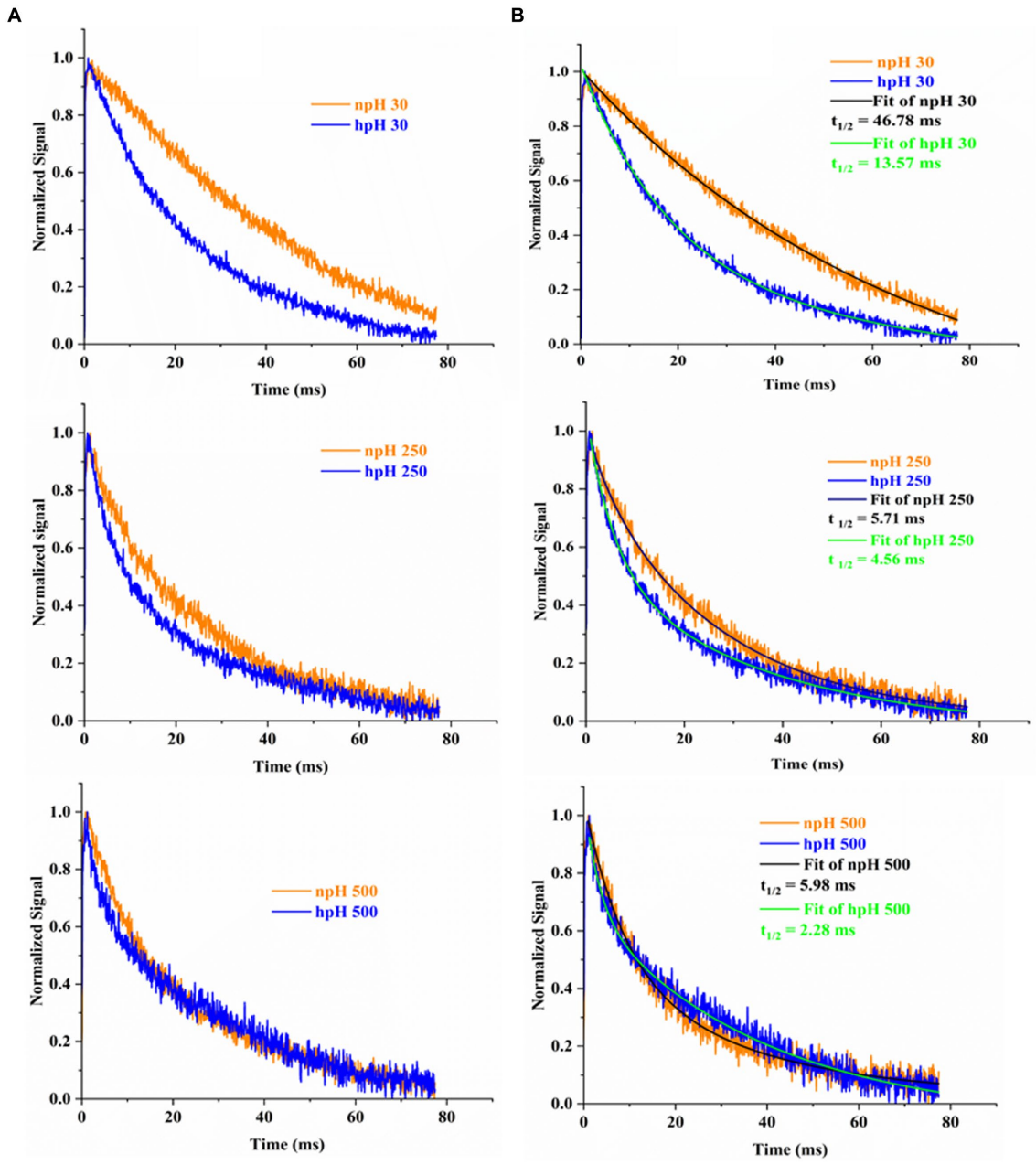

FIGURE 7
Flash-induced absorption changes in cells of *R. alakalitolerans* measured at 515 nm wavelength. Cells were adopted for 1 h in dark incubation before the measurement **(A)**. Calculation of $t_{1/2}$ for each light intensity. Half-life of each decay kinetics was calculated by double fitting in origin software (Origin 2023). Half-life ($t_{1/2}$) for npH and hpH at 30 μm photons m^{-2} s^{-1}, $t_{1/2}$ npH_{30}=46.78 ms, $t_{1/2}$ hpH $_{30}$=13.57 ms. For 250 μmol photons m^{-2} s^{-1}. npH and hpH $t_{1/2}$ npH_{250}=5.71 ms, $t_{1/2}$ hpH_{250}=4.56 ms and for 500 μmol photons m^{-2} s^{-1}.in npH and hpH half-life were $t_{1/2}$ npH_{500}=5.98 ms, $t_{1/2}$ hpH_{500}=2.28 ms, respectively **(B)**.

the ICMs compared with that of the hpH-grown cells. ImageJ analysis of TEM images from 250 to 500 μmol photons $m^{-2}s^{-1}$ of light intensity shows that npH-grown cells are much more affected than that of hpH-grown cells, and the number of ICMs has also decreased (Figures 9A,B). Another phenomenon is also apparent in hpH-grown cells that the cell size is increased (Figure 9C). In previous studies, in *E. coli,* cells grown in alkaline conditions were increased in size and length compared with cells grown at neutral pH (Mueller et al., 2020). In our study, the cell size has increased in high pH grown cells compared with that of the npH-grown cells. This property of elongation in cell size is more visible in normal light, whereas with an increase in light intensity, the cell size has decreased more in npH but in hpH, it remained almost the same at 250 and 500 μmol photons $m^{-2}s^{-1}$ of light intensity (Figures 9A,C).

Estimation of total ROS and quantification of SOD

To measure the stress level in the cell in all conditions, the total ROS was measured by H_2DCFDA fluorescent dye (Devadasu et al., 2021). ROS level has enhanced with an increase in light

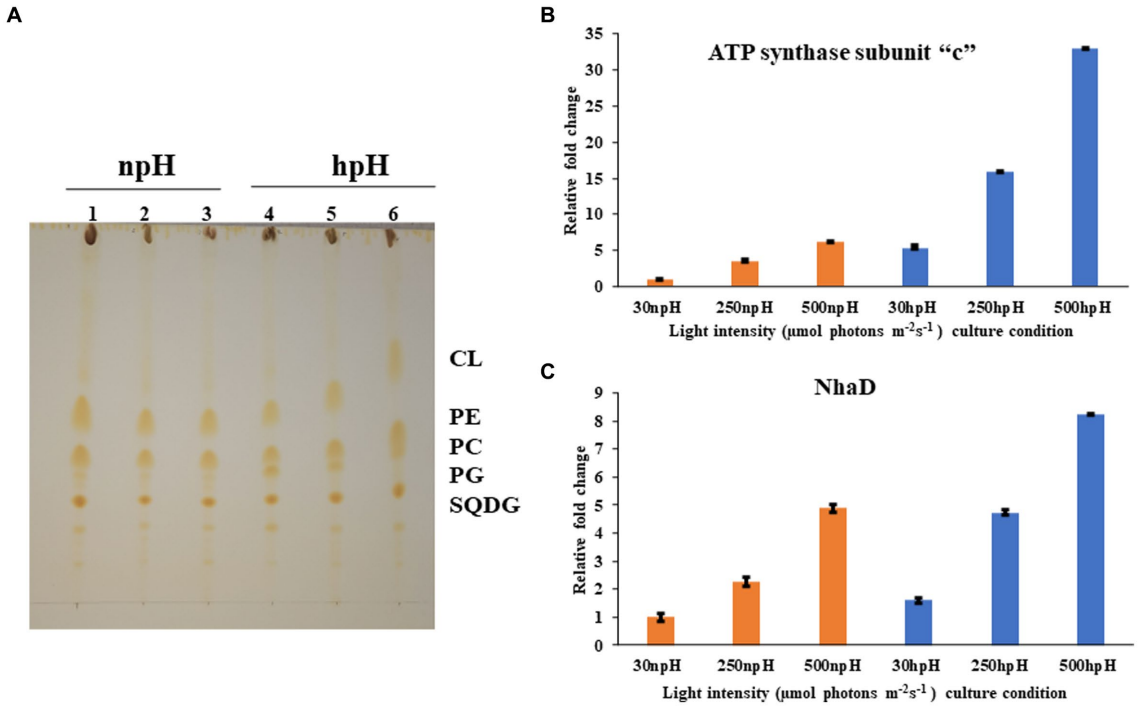

FIGURE 8
(A) Thin layer chromatographic separation of isolated polar lipids; Cardiolipin (CL) Phosphatidylethanolamine (PE) phosphatidylcholine (PC) phosphatidylglycerol (PG) and sufoquinovocyl diacylglycerol (SQDG). Membrane lipids were extracted in a mixture of methanol-chloroform-water (1:1:0.9, v/v) was added to 5 mg of lyophilized cells, separated by TLC on silica gel (20 × 20 cm, layer thickness 0.2 mm). and detected by iodine vapor. In npH (1,2,3 represent light intensity of 30,250,500 µmol photons m^{-2} s^{-1} in npH) and hpH (4,5,6 represent the light intensity of 30,250,500, in hpH µmol photons m^{-2} s^{-1}). **(B)** q-PCR of subunit -c of ATPase in npH and hpH at light intensity of 30,250 and 500 µmol photons m^{-2} s^{-1}. **(C)** q-PCR of sodium proton antiporter NhaD in npH and hpH at light intensity of 30,250 and 500 µmol photons m^{-2} s^{-1}.

intensity in both npH and hpH conditions. It was found that the level of ROS is relatively high in npH-grown cells in all three light conditions compared with that in hpH condition (Figure 10A). To further investigate the level of superoxide dismutase expressed in the cell, the after-sonication cell supernatant was used to quantify the level of SOD. Only one band of SOD appeared after staining the gel with a staining solution containing nitroblutetrazolium chloride (NBT) (Figures 10B,C). According to Kho et al. (2006), the CuZnSOD is expressed, and its expression level has enhanced with an increase in light intensity in both npH and hpH conditions, but it is relatively less in hpH conditions.

Discussion

Effect of high light on growth pattern, external milieu, bacteriochlorophyll, carotenoid, and absorbance spectra

R. alkalitolerans when grown in npH and hpH, in relation to an increase in light intensity, shows not much difference in terms of growth pattern at 250 and 500 µmol photons $m^{-2}s^{-1}$, except at 30 µmol photons $m^{-2}s^{-1}$, where it takes a bit longer to enter the log phase (Figure 1A). The generation time of the bacterium is almost similarly decreased in all light intensities in both npH and hpH conditions (Figure 1B). hpH-grown cells entered the stationary phase at a less optical density, which could be because of the nutrient exhaust relatively early in hpH as cells have to expend more energy in hpH to maintain the homeostatic balance (Padan et al., 2005), leading to the consumption of more nutrients. Bacteriochlorophyll *a* is the major photosynthetic pigment present in *R. alkalitolerans* along with carotenoids, such as spheroidene, which along with photosystem protein RC- L, M, H, and light-harvesting antenna LH1 and LH2 make the photosystem (Qian et al., 2005). The content of Bchl *a* has decreased with an increase in light intensity, but the relative content is high in hpH-grown cells. This could be because of the cell metabolism, where more ATP is required to maintain the homeostatic balance in hpH, leading to very little damage to the photosystem because of high light; on the contrary, the cells in npH comparatively do not require much ATP. We also measured the pH of culture medium as to what happens to the extracellular pH while harvesting the cells. We found that there is an increase in the pH of culture medium by 0.5 units in npH conditions, whereas in hpH, the pH of culture has decreased with an increase in light intensity (Figure 1D). This indicates that growing the culture at high pH leads to the expression of antiporters (Padan et al., 2005; Adams and Hunter, 2012) (Figure 8C). This helps in maintaining the cytoplasmic pH of the cell, and subsequently, photoprotection of photosystem protein complex integrity in hpH condition relatively more than in npH condition (Figure 4). It is already been reported that when bacteria are grown in an alkaline environment, extracellular pH decreases (Padan et al., 2005), whereas when grown in npH, the extracellular pH of the culture medium increases (Farrell and Finkel, 2003; Padan et al., 2005; Sánchez-Clemente et al., 2018). The less increase in pH of hpH-grown culture compared to blank indicated that the cells are efficiently able to maintain the homeostatic balance by acid production

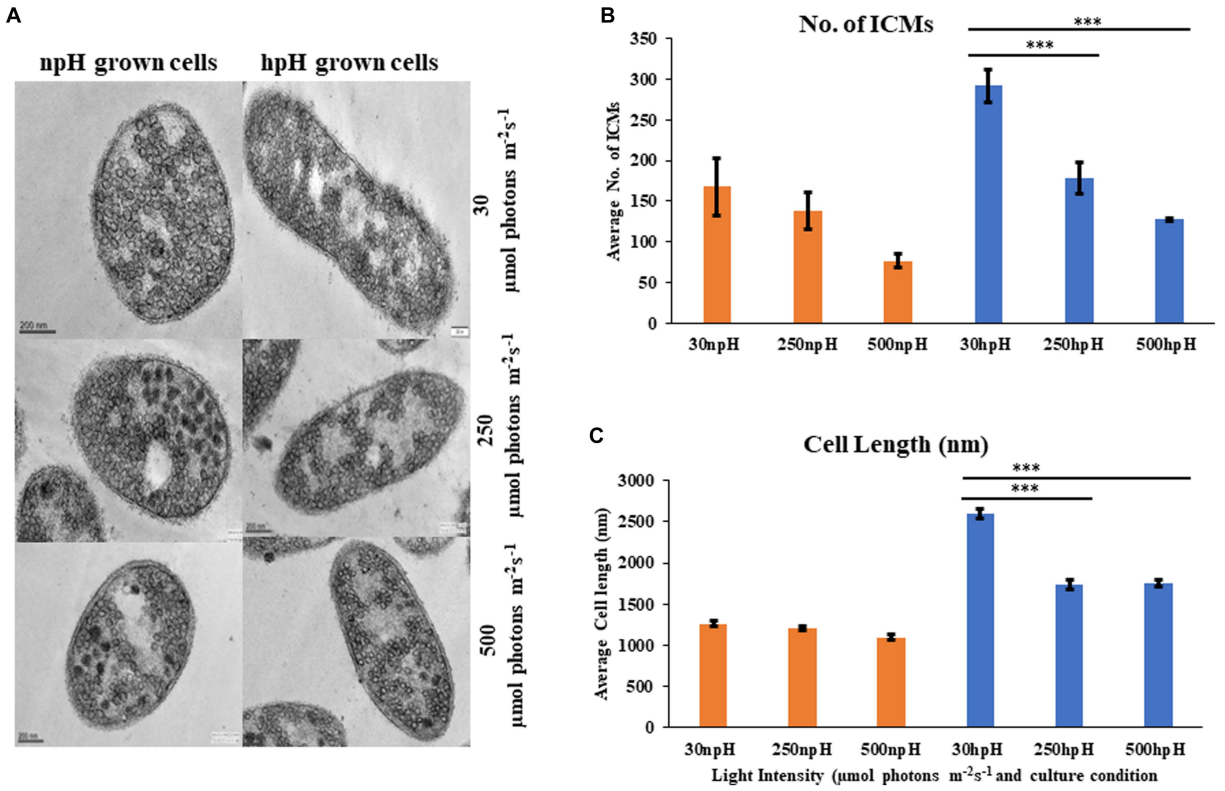

FIGURE 9
(A) Transmission electron micrograph of thin sections of *R. alkalitolerans* cells in various light intensities in npH and hpH culture condition. **(B)** Number of chromatophore/ICMs from npH and hpH condition at light intensity of 30, 250 and 500 µmol photons m^{-2} s^{-1}. **(C)** Measurement of cell length (nm as imaged in the TEM instrument) in each growth condition from TEM images by ImageJ software ($n = 3$ cells were used). Asterisks indicated the level of significance of hight light (treated) versus control (normal light) with *p*-value style: GP: 0.1234 (ns), 0.0332(*), 0.0021(**), 0.0002 (***), and <0.0001 (****) respectively.

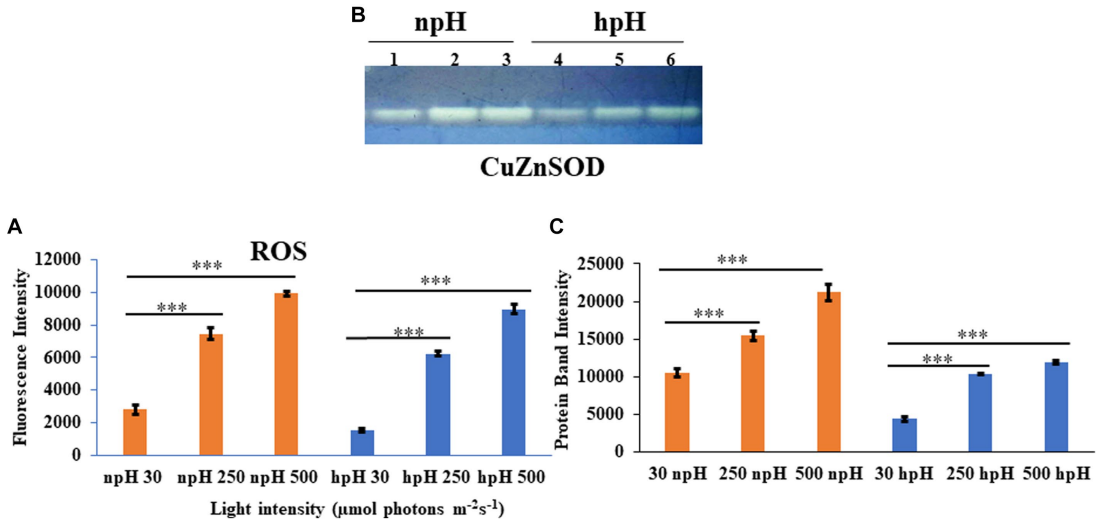

FIGURE 10
(A) Estimation of total reaction oxygen species (ROS) in cells grown in npH and hpH conditions. Cells from all the conditions were collected in logarithmic phase, and fluorescence intensity was measured at the excitation wavelength of 485 nm and emission at 530 nm. **(B)** Native polyacrylamide gel to detect level of Superoxide dismutase activity in npH and hpH conditions. After sonication lysate was centrifuged and supernatant was taken to estimate the protein concentration. Twenty microgram of protein was load in native gel to separate the protein. SOD bands were visualized after staining the gel in staining solution as described in materials and methods. Lane 1,2,3 represent samples from npH grown at 30,250 and 500 µmol photons m^{-2} s^{-1}. Likewise lane 4,5,6 sequentially represent sample from hpH grown at 30,250 and 500 µmol photons m^{-2} s^{-1}. **(C)** ImageJ quantification SOD bands from figure **(B)**. Asterisks indicated the level of significance of hight light (treated) versus control (normal light) with *p*-value style: GP: 0.1234 (ns), 0.0332(*), 0.0021(**), 0.0002 (***), and <0.0001 (****) respectively.

and by proton antiporters not letting it increase but decreasing (Padan et al., 2005), where protons produced might be coming from photosynthetic machinery because increased expression enhanced ATPase activity (Figures 7A,B) has been observed along with relatively stable photosynthetic supercomplexes in hpH (Figures 3–5). From the data, it must be found out that the expression of antiporters might help in the dissipation of excess proton gradient built during high light in hpH culture, which leads to photoprotection in high light compared with that of the high light npH-grown cells (Padan et al., 2005), which is evidenced in the further experiments.

Absorbance spectroscopy of photosystem complexes represents the intactness and openness of the photosystems. The absorbance spectra of the isolated intracytoplasmic membranes in alkaline (hpH) conditions exhibit a more stable photosystem with high absorbance intensity compared with npH (Figures 2A–C). It clearly shows less impact of light stress on the photosystem of bacteria in hpH than that in npH (Figure 2). It is evident from Figures 2A–C that the shoulder peak at 875 nm which represents the RC-LH1 complex, either monomer or dimer, increased with an increase in light intensity. Comparing with the high light of 500 µmol photons $m^{-2}s^{-1}$, it is evident that the peak at 875 nm is higher in npH conditions, which could represent either RC-LH1 dimer or RC-LH1 monomer (Figures 2D–F). It also provides evidence that per RC-LH1, the number of LH2 is less in npH than in hpH, harnessing more energy required for hpH tolerance.

LP-BN PAGE, sucrose density gradient of β- DM solubilized ICMs, and circular dichroism show relatively stable photosystem protein complexes in hpH

LP-BN- PAGE separates the photosynthetic protein complexes in native conditions (Kügler et al., 1997; Southall et al., 2018). Five major photosystem protein complexes were identified in each condition when compared with native page of *R. sphaeroides* (Mothersole et al., 2016), which is phylogenetically very near to *R. alkalitolerans* (Gandham et al., 2018). LP-BN shows major changes in RC-LH1 dimeric and monomeric complexes and light-harvesting antenna LH2. RC-LH1 complexes have decreased in hpH, and monomeric RC-LH1 complexes increased, which could be because of the conversion of dimeric RC-LH1 to monomer (Figure 3; Supplementary Figures S2A,C). This pattern is reversed in npH-grown cells, where both the dimeric and monomeric reaction centers have increased with an increase in light intensity. The increase in the content of both monomeric and dimeric RC-LH1 complexes in npH condition could be an adoptive and local microenvironmental strategy (Chenchiliyan et al., 2016) to cope with the effect of high light. In addition, it might be the photoprotective mechanism as the membrane lipids (bilayer and non-bilayer forming) are relatively less in npH with effect of high light and lesser ATPase activity. On the contrary, in hpH, it is opposite of npH. This pattern of conversion could be attributed to three factors as follows: (1) The microenvironment of the photosynthetic protein super complex includes the membrane bilayer forming PC, PG, and SQDG and non-bilayer forming lipids CL and PE. These membrane lipids provide differing environments around the protein complexes as and when they are changing, depending upon the growth condition. This has been previously shown to increase the photosystem protein complex stability by interacting with primary and secondary quinones along with other reaction center proteins (Ng et al., 2011). As in hpH, the membrane lipids CL, PC, PG, and SQDG are in relatively high content (Figure 8A; Supplementary Figure S5), which can provide a stable environment to protein complexes that are opposite in npH conditions. (2) Along with the membrane lipid environment, the level of ICM lumen acidification is also important in relation to the ATPase activity, which acts as the dissipater of proton gradient made as a result of photosynthesis. As light intensity increases, photons are absorbed, and the chromatophore lumen becomes more acidified because of proton accumulation. The acidic luminal condition of chromatophore leads to protein instability (Järvi et al., 2013; Krishnan-Schmieden et al., 2021). The level of ATPase complex has increased with an increase in light intensity in all conditions, but it is relatively high in hpH condition, which comparatively dissipates more proton gradient in hpH, leading to photoprotection. Previous studies show that in plant, thylakoid also has been shown to affect the photosynthetic protein complexes by high light-induced lumen acidification, activating many other photoprotective gene expressions, such as PsbS (Liu and Last, 2017; Krishnan-Schmieden et al., 2021). (3) Moreover, relatively fast relaxation of the P515 signal in hpH conditions compared with npH conditions, less lumen acidification effect on the protein complexes. Although at 500 µmol photons $m^{-2}s^{-1}$ in hpH, the content of RC-LH1 dimer increased a little bit, where it might start making dimers again as stress level increased. The light-harvesting antenna LH2 major and minor have also been drastically affected (Figure 3; Supplementary Figures S2D,E, S4A) in npH compared with hpH, which further confirms less photoprotection in npH. The sucrose density gradient from npH and hpH again proves the same pattern of protein super-complexes (RC-LH1 d, RC-LH1 m, and LH2) as of LP-BN. F1 represents the LH2, F2 represents the RC-LH1 monomer, and F3 represents the RC-LH dimer (Figures 4, 5). From this data, we can conclude that the photosystem protein complexes, antenna (LH2 major and LH2 minor) and core (RC-LH1 monomer and dimer), are relatively more stable in hpH condition. It can also be said that in hpH, the cell requires more energy to maintain the homeostatic balance. Moreover, to harvest more energy, the antenna size (higher content of LH2 is observed) is more in hpH than that in npH conditions.

To investigate the interactions between the pigment and protein which also represents protein complex integrity, we performed CD of ICMs at room temperature (RT) from the visible region to the far-red region (400–900 nm) (Clayton and Clayton, 1981; Davis et al., 1995), wherein the doublet bands at 875–850 nm show a particular orientational interaction of BChl *a* with that of the scaffold proteins of LH1and LH2. However, the CD pattern in NIR shows almost the same interaction pattern in complexes in three different light conditions (Figures 6A–C). The CD signal is affected as the culture grows in higher light intensities. However, less reduction was observed in pigment-protein interaction from hpH-grown ICMs (Figures 6D–F). It has been shown in the studies that the position of the carotenoid bands and the bacteriochlorophyll carotenoid ratio affect the NIR-CD spectra (Georgakopoulou et al., 2006).

ECS measurement, membrane lipids, qPCR of ATP "c," and NhaD have increased activity and levels of expression in hpH

The electrochromic shift measurement (Feniouk et al., 2002; Yakovlev et al., 2022) measures the ATPase activity as an electronic absorbance transient of intrinsic carotenoid spheroidene (Tokita et al., 2011). Spheroidene is the only carotenoid present in *R. alkalitolerans* cells (Gandham et al., 2018). The electrochromic shift in carotenoid spheroidene and spheroidenone results from increased membrane

potential and membrane energization due to more chromatophore lumen acidification and absorption of light (Feniouk et al., 2002). Change in the permanent dipole moment of carotenoids upon excitation, and because of change in the electronic interaction, caused alterations in the protein organization (Gottfried et al., 1991; Feniouk et al., 2002). The experiment was performed in whole cells in all growth conditions, which shows that relaxation of the P515 signal is very fast in hpH compared with npH, which signifies the role of ATPase in hpH and its more immediate activity (Figure 7). The half-time of relaxation kinetics has decreased with an increase in light intensity. Although the half-life at 250 µmol photons $m^{-2}s^{-1}$ is less than 500 µmol photons $m^{-2}s^{-1}$ (5.71 ms < 5.98 ms) in npH, in LP-BN quantification, protein band has sequentially increased, although it (half-life) has sequentially decreased in hpH. The reason could be at the activity level that it might have retarded a little, whereas protein content might remain the same. Further qPCR of subunit "c" level has also increased with an increase in light intensity (Figure 8B), which supports the ECS measurement results.

Membrane lipids play a very important role when it comes in membrane proteins. They are the ones that provide the microenvironment for the well-functioning of these membrane proteins (Ng et al., 2011). So, it is important to study the membrane lipids while investigating the role of photosystem protein complexes as membrane energization is an important part of photosynthesis when it houses the carotenoids and bacteriochlorophylls (Ng et al., 2011). Since SQDG, PC, PG, PE, and CL are proven to be involved in the stabilization of the reaction center, especially PC has been shown to fasten the electron transfer rates in charge recombination states of Q_A and Q_B (Ng et al., 2011) and mediate more efficient formation of ICMs (Kim et al., 2007). These membrane lipids from whole cells and membrane lipids from ICMs have relatively no significant difference and are present in the same ratio (De Leo et al., 2009). SQDG, PC, and CL have previously been shown to interact with bacterial pheophytin and quinone (Ng et al., 2011) and reaction center proteins to enhance the stability of photosystem protein supercomplexes (Cao et al., 2022). Even CL and PG have been shown to increase the electron transfer rate between quinones (Ng et al., 2011). A case study in *R. sphaeroides* focused on the role of PC in the stability of the B800-850 complex, playing an important role in the efficient formation of ICMs (Kim et al., 2007), and ICM formation also confirms the importance of this lipid in the current study. At the same time, CL also plays an essential role in photosystem complex stability (De Leo et al., 2009). Overall, the increased membrane lipid in hpH conditions provides a relatively stable microenvironment and, subsequently, provides photoprotection.

Apart from membrane lipids, proton antiporters present in the plasma membrane also utilize intracellular protons to maintain homeostatic balance to the cells in hpH (Padan et al., 2005). Comparatively increased level of sodium proton antiporter NhaD in the hpH condition shows that to maintain the homeostatic balance in hpH, the antiporter level has increased. As previously reported, the sodium/potassium/calcium proton antiporter expression increases when bacteria are shifted to an alkaline environment (Padan et al., 2005).

Transmission electron microscopy of cells and ROS estimation show relatively less oxidative stress in hpH

From TEM data, it is visible that high light impacts not only the cell size but also the number of ICMs in both npH and hpH conditions (Figure 9). However, as the cell length is more in hpH, it is because of the less frequent cell division culminated by the hpH environment. As reported earlier in *Escherichia coli* (*E. coli*), cell length increases as it is subjected to growth in increasing pH media cultures (Mueller et al., 2020). The cell division proteins, FtsZ and FtsN, are not able to mobilize to the middle of the cell, and cell divisome is not formed as efficiently as in npH-grown cells (Mueller et al., 2020); inverse to hpH, cells in acidic medium have been reported to divide fast (Mueller et al., 2020). As evident from TEM in npH, ICM count is more affected than hpH, but how the photosynthetic supercomplexes are affected is not clear from TEM data. It is only evident from LP-BN, SDG data and by membrane lipid data, where they are more stable in hpH condition than in npH. As ICMs are present freely in the cytosol, it would get affected by the intracellular environment, and its protein complex stability would depend on both the ICM lumen environment and cytosolic environment. In continuation to the cellular environment, it is also necessary to measure the redox level of the cell. We quantified the total reactive oxygen species (ROS) to measure the stress inside the cell generated because of high light (Ziegelhoffer and Donohue, 2009). Here, it should be noted that cells are grown anaerobically; therefore, ROS generated is because of photooxidative stress. The level of reactive oxygen species has increased with an increase in light intensity in both npH and hpH conditions, but the relative content is less in hpH conditions, which indicates that cells in hpH are in relatively less photooxidative stress (Figure 10A). Further confirmation comes from superoxide dismutase activity in non-denaturing gel, where CuZnSOD level is also increased in relation to ROS level, which is more in npH than in hpH and enhanced with an increase in light intensity (Figures 10A–C). CuZnSOD has been shown to express in photoheterotrophic conditions, confirming that in *R. alkalitolerans,* there is a single type of SOD to express in photoheterotrophic conditions (Kho et al., 2006). In *R. sphaeroides* and *R. capsulatus,* more than one SOD enzyme has been found to be active, but in the case of *R. alkalitolerans,* only one CuZnSOD has been found when grown anaerobically. Overall, the ROS and SOD levels are relatively less in hpH condition, which shows that the cell is under less photooxidative stress in hpH (Figures 10A–C).

Overall, in this study, we tried to investigate the behavior of the photosynthetic apparatus of *R. alkalitolerans* by growing it in alkaline growth conditions as it was discovered in an alkaline pond in Gujrat, India. We found that *R. alkalitolerans* cells have comparatively more ICMs and stable photosystem complexes in hpH. The level of membrane lipids (bilayer and non-bilayer forming) has increased in hpH, which also confers the stability to photosystem complexes. Formation of a more dimeric RC-LH1 complex in npH with an increase in light intensity emphasizes the importance of its role in acclimatizing as ICM lumen gets more acidified, but ATPase activity is not as efficient as in hpH where dimeric RC-LH1 is converting to monomer along with the increased ATPase activity. The reason for dimer to monomer conversion or dimer formation is still elusive, but it is clear that lumen acidification might be playing an important role in dimer formation or its interconversion to monomer in the provided micro lipid environment in either npH or hpH. Overall, *R. alkalitolerans* cells could adapt to hpH conditions photoheterotrophically with a

relatively stable photosystem and homeostatic balance of the intracellular environment. Relatively less photooxidative stress, enhanced activity of ATP synthase from ICMs and high expression of Na^+/H^+ (NhaD) antiporter in hpH in high light indicate the interdependency of homeostasis and photosynthetic machinery functioning in cellular homeostatic balance.

Furthermore, *R. alkalitolerans* opens up the window for an in-depth study into complex interrelation between cellular homeostasis and photosynthesis, applying this knowledge to generate alkali-tolerant algal and plant species to cope with harsh alkaline environments. Being a photosynthetic purple non-sulfur species, it can also emerge as a potential species for biohydrogen and bioplastic production. Furthermore, studies are required to explore the possibility of the potential applications.

Data availability statement

The original contributions presented in the study are included in the article/Supplementary material, further inquiries can be directed to the corresponding authors.

Author contributions

MZ: Conceptualization, Formal analysis, Investigation, Methodology, Validation, Writing – original draft, Writing – review & editing. SM: Formal analysis, Investigation, Methodology, Writing – review & editing. NM: Data curation, Formal analysis, Investigation, Methodology, Writing – review & editing. VC: Conceptualization, Data curation, Formal analysis, Resources, Supervision, Validation, Writing – review & editing. RS: Conceptualization, Data curation, Formal analysis, Funding acquisition, Project administration, Resources, Supervision, Validation, Writing – original draft, Writing – review & editing.

Funding

The author(s) declare financial support was received for the research, authorship, and/or publication of this article. RS was supported by the Institute of Eminence (UoH/IoE/RC1/RC1-20-019), DBT-Builder (BT/INF/22/SP41176/2020), DST-FIST and UGC-SAP, Govt. of India, for financial support.

Conflict of interest

The authors declare that the research was conducted in the absence of any commercial or financial relationships that could be construed as a potential conflict of interest.

Publisher's note

Supplementary material

The Supplementary material for this article can be found online at: https://www.frontiersin.org/articles/10.3389/fmicb.2024.1360650/full#supplementary-material

SUPPLEMENTARY FIGURE S1
Ratio of the content of carotenoid and bacteriochlorophyll a in npH and hpH culture condition at light intensity of 30, 250 and 500 µmol photons $m^{-2}s^{-1}$. Bacteriochlorophyll a and carotenoids were measured at 775 nm and 456 nm from whole after extracing the pigments in 7:2 ratio of acetone and methanol.

SUPPLEMENTARY FIGURE S2
ImageJ analysis of LP-BN protein complex bands to compare the relative protein complex band intensity in npH and hpH condition at 30 µmol photons $m^{-2}s^{-1}$, 250 µmol photons $m^{-2}s^{-1}$, & 500 µmol photons $m^{-2}s^{-1}$. **(A)** RC-LH1 d, **(B)** ATP synthase complex, **(C)** RC-LH1 m **(D)** LH2 major, **(E)** LH2 minor. **(F)** SDS-PAGE of intracytoplasmic membrane protein from all above-mentioned growth conditions to compare the photosynthetic membrane protein complex abundance (lanes 1&4, 2&5, 3&6 sequentially represent 30, 250, and 500 µmol photons $m^{-2}s^{-1}$ of light intensity). Each data point averages three replicates, and error bars are represented as ±SE. Asterisks indicated the le vel of significance of hight light (treated) vs control (normal light) with P value style: GP: 0.1234 (ns), 0.0332(*), 0.0021(**), 0.0002 (***), <0.0001 (****) respectively.

SUPPLEMENTARY FIGURE S3
The second dimension of the LP-BN strip for identification of ATP synthase complex subunits. Subunit proteins were excised and sent for identification **(A)** by Orbitrap Liquid Chromatography Mass Spectrometry (OHRLCMS). The sequence of peptides matched (red-coloured amino acid sequences) with respective full amino acid sequences **(B)**.

SUPPLEMENTARY FIGURE S4
Image-J analysis of sucrose density gradient fractions. **(A)** LH2 (fraction1: F1), **(B)** RC-LH1 m (fraction 2: F2) and (C) RC-LH1 d (fraction 3: F3). Fractions were obtained after 18 hrs of ultracentrifugation. Each data point averages three replicates, and error bars are represented as ±SE. Asterisks indicated the level of significance of high light (treated) vs control (normal light) with P value style: GP: 0.1234 (ns), 0.0332(*), 0.0021(**), 0.0002 (***), <0.0001 (****) respectively.

SUPPLEMENTARY FIGURE S5
ImageJ quantification of membrane lipid band from TLC plate. **(A)** Cardiolipin, **(B)** Phosphatidylethanolamine, **(C)** Phosphatidylcholine, **(D)** Phosphatidylglycerol, **(E)** Sulfoquinovosyldiacylglycerols. Each data point averages three replicates, and error bars are represented as ±SE.

SUPPLEMENTARY TABLE S1
Nucleotide sequence of forward and reverse primer used for RT-PCR study of recA, NhaD and ATP synthase subunit "c" genes.

References

Adams, P. G., and Hunter, C. N. (2012). Adaptation of intracytoplasmic membranes to altered light intensity in *Rhodobacter sphaeroides*. *Biochim. Biophys. Acta* 1817, 1616–1627. doi: 10.1016/j.bbabio.2012.05.013

Alves, L. R., Prado, E. R., de Oliveira, R., Santos, E. F., Lemos de Souza, I., Dos Reis, A. R., et al. (2020). Mechanisms of cadmium-stress avoidance by selenium in tomato plants. *Ecotoxicology* 29, 594–606. doi: 10.1007/s10646-020-02208-1

Bahatyrova, S., Frese, R. N., Siebert, C. A., Olsen, J. D., van Der Werf, K. O., Van Grondelle, R., et al. (2004). The native architecture of a photosynthetic membrane. *Nature* 430, 1058–1062. doi: 10.1038/nature02823

Cao, P., Bracun, L., Yamagata, A., Christianson, B. M., Negami, T., Zou, B., et al. (2022). Structural basis for the assembly and quinone transport mechanisms of the dimeric photosynthetic RC–LH1 supercomplex. *Nat. Commun.* 13:1977. doi: 10.1038/s41467-022-29563-3

Chenchiliyan, M., Timpmann, K., Jalviste, E., Adams, P. G., Hunter, C. N., and Freiberg, A. (2016). Dimerization of core complexes as an efficient strategy for energy trapping in *Rhodobacter sphaeroides*. *Biochim. Biophys. Acta* 1857, 634–642. doi: 10.1016/j.bbabio.2016.03.020

Clayton, R. K., and Clayton, B. J. (1981). B850 pigment-protein complex of *Rhodopseudomonas sphaeroides*: extinction coefficients, circular dichroism, and the reversible binding of bacteriochlorophyll. *Proc. Natl. Acad. Sci. U. S. A.* 78, 5583–5587. doi: 10.1073/pnas.78.9.5583

Cohen-Bazire, G., Sistrom, W. R., and Stanier, R. Y. (1957). Kinetic studies of pigment synthesis by non-sulfur purple bacteria. *J. Cell. Comp. Physiol.* 49, 25–68. doi: 10.1002/jcp.1030490104

Crouch, L. I., and Jones, M. R. (2012). Cross-species investigation of the functions of the Rhodobacter PufX polypeptide and the composition of the RC–LH1 core complex. *Biochim. Biophys. Acta* 1817, 336–352. doi: 10.1016/j.bbabio.2011.10.009

Davis, C. M., Bustamante, P. L., and Loach, P. A. (1995). Reconstitution of the bacterial core light-harvesting complexes of Rhodobacter sphaeroides and *Rhodospirillum rubrum* with isolated α-and β-polypeptides, bacteriochlorophyll a, and carotenoid. *J. Biol. Chem.* 270, 5793–5804. doi: 10.1074/jbc.270.11.5793

De Leo, V., Catucci, L., Ventrella, A., Milano, F., Agostiano, A., and Corcelli, A. (2009). Cardiolipin increases in chromatophores isolated from *Rhodobacter sphaeroides* after osmotic stress: structural and functional roles. *J. Lipid Res.* 50, 256–264. doi: 10.1194/jlr.M800312-JLR200

Devadasu, E., Pandey, J., Dhokne, K., and Subramanyam, R. (2021). Restoration of photosynthetic activity and supercomplexes from severe iron starvation in *Chlamydomonas reinhardtii*. *Biochim. Biophys. Acta* 1862:148331. doi: 10.1016/j.bbabio.2020.148331

D'Haene, S. E., Crouch, L. I., Jones, M. R., and Frese, R. N. (2014). Organization in photosynthetic membranes of purple bacteria in vivo: the role of carotenoids. *Biochim. Biophys. Acta* 1837, 1665–1673. doi: 10.1016/j.bbabio.2014.07.003

Farrell, M. J., and Finkel, S. E. (2003). The growth advantage in stationary-phase PhenotypeConferred by rpoS mutations is dependent on the pH and nutrient environment. *J. Bacteriol.* 185, 7044–7052. doi: 10.1128/JB.185.24.7044-7052.2003

Fedotova, Y., and Zeilstra-Ryalls, J. (2014). Analysis of the role of PrrA, PpsR, and FnrL in intracytoplasmic membrane differentiation of *Rhodobacter sphaeroides 2.4. 1* using transmission electron microscopy. *Photosynth. Res.* 119, 283–290. doi: 10.1007/s11120-013-9944-9

Feniouk, B. A., Cherepanov, D. A., Voskoboynikova, N. E., Mulkidjanian, A. Y., and Junge, W. (2002). Chromatophore vesicles of *Rhodobacter capsulatus* contain on average one FOF1-ATP synthase each. *Biophys. J.* 82, 1115–1122. doi: 10.1016/S0006-3495(02)75470-2

Francia, F., Dezi, M., Rebecchi, A., Mallardi, A., Palazzo, G., Melandri, B. A., et al. (2004). Light-harvesting complex 1 stabilizes P+ QB-charge separation in reaction centers of *Rhodobacter sphaeroides*. *Biochemistry* 43, 14199–14210. doi: 10.1021/bi048629s

Gandham, S., Lodha, T., Chintalapati, S., and Chintalapati, V. R. (2018). Rhodobacter alkalitolerans sp. nov., isolated from an alkaline brown pond. *Arch. Microbiol.* 200, 1487–1492. doi: 10.1007/s00203-018-1561-8

Georgakopoulou, S., van der Zwan, G., Olsen, J. D., Hunter, C. N., Niederman, R. A., and van Grondelle, R. (2006). Investigation of the effects of different carotenoids on the absorption and CD signals of light harvesting 1 complexes. *J. Phys. Chem. B* 110, 3354–3361. doi: 10.1021/jp0517955

Gottfried, D. S., Steffen, M. A., and Boxer, S. G. (1991). Stark effect spectroscopy of carotenoids in photosynthetic antenna and reaction center complexes. *Biochim. Biophys. Acta* 1059, 1, 76–90. doi: 10.1016/S0005-2728(05)80189-6

Hustede, E., Steinbüchel, A., and Schlegel, H. G. (1993). Relationship between the photoproduction of hydrogen and the accumulation of PHB in non-Sulphur purple bacteria. *Appl. Microbiol. Biotechnol.* 39, 87–93. doi: 10.1007/BF00166854

Järvi, S., Gollan, P. J., and Aro, E. M. (2013). Understanding the roles of the thylakoid lumen in photosynthesis regulation. *Front. Plant Sci.* 4:434. doi: 10.3389/fpls.2013.00434

Jungas, C., Ranck, J. L., Rigaud, J. L., Joliot, P., and Verméglio, A. (1999). Supramolecular organization of the photosynthetic apparatus of *Rhodobacter sphaeroides*. *EMBO J.* 18, 534–542. doi: 10.1093/emboj/18.3.534

Kho, D. H., Yoo, S. B., Kim, J. S., Kim, E. J., and Lee, J. K. (2006). Characterization of cu-and Zn-containing superoxide dismutase of *Rhodobacter sphaeroides*. *FEMS Microbiol. Lett.* 234, 261–267. doi: 10.1111/j.1574-6968.2004.tb09542.x

Kim, E. J., Kim, M. S., and Lee, J. K. (2007). Phosphatidylcholine is required for the efficient formation of photosynthetic membrane and B800-850 light-harvesting complex in *Rhodobacter sphaeroides*. *J. Microbiol. Biotechnol.* 17, 373–377.

Krishnan-Schmieden, M., Konold, P. E., Kennis, J. T., and Pandit, A. (2021). The molecular pH-response mechanism of the plant light-stress sensor PsbS. *Nat. Commun.* 12:2291. doi: 10.1038/s41467-021-22530-4

Kügler, M., Jänsch, L., Kruft, V., Schmitz, U. K., and Braun, H. P. (1997). Analysis of the chloroplast protein complexes by blue-native polyacrylamide gel electrophoresis (BN-PAGE). *Photosynth. Res.* 53, 35–44. doi: 10.1023/A:1005882406718

Lakshmi, K. V., Sasikala, C., Takaichi, S., and Ramana, C. V. (2011). *Phaeospirillum oryzae* sp. nov., a spheroplast-forming, phototrophic alphaproteobacterium from a paddy soil. *Int. J. Syst. Evol. Microbiol.* 61, 1656–1661. doi: 10.1099/ijs.0.025544-0

Liu, J., and Last, R. L. (2017). A chloroplast thylakoid lumen protein is required for proper photosynthetic acclimation of plants under fluctuating light environments. *Proc. Natl. Acad. Sci. U. S. A.* 114, E8110–E8117. doi: 10.1073/pnas.1712206114

Madireddi, S. K., Nama, S., Devadasu, E. R., and Subramanyam, R. (2014). Photosynthetic membrane organization and role of state transition in cyt, cpII, stt7 and npq mutants of *Chlamydomonas reinhardtii*. *J. Photochem. Photobiol. B Biol.* 137, 77–83. doi: 10.1016/j.jphotobiol.2014.03.025

Merugu, R., Rudra, M. P., Girisham, S., and Reddy, S. M. (2012). PHB (Polyhydroxy butyrate) production under nitrogen limitation by *Rhodobacter capsulatus KU002* isolated from tannery effluent. *Int. J. Chem. Tech. Res.* 4, 1099–1102.

Meyer, T. E., and Donohue, T. J. (1995). Cytochromes, iron-sulfur, and copper proteins mediating electron transfer from the cyt bc 1 complex to photosynthetic reaction center complexes. *Anoxyg. Photosynth. Bact.*, 2, 725–745. doi: 10.1007/0-306-47954-0_34

Mothersole, D. J., Jackson, P. J., Vasilev, C., Tucker, J. D., Brindley, A. A., Dickman, M. J., et al. (2016). PucC and LhaA direct efficient assembly of the light-harvesting complexes in *Rhodobacter sphaeroides*. *Mol. Microbiol.* 99, 307–327. doi: 10.1111/mmi.13235

Mougiakos, I., Orsi, E., Ghiffary, M. R., Post, W., de Maria, A., Adiego-Perez, B., et al. (2019). Efficient Cas9-based genome editing of *Rhodobacter sphaeroides* for metabolic engineering. *Microb. Cell Factories* 18, 1–3. doi: 10.1186/s12934-019-1255-1

Mueller, E. A., Westfall, C. S., and Levin, P. A. (2020). pH-dependent activation of cytokinesis modulates *Escherichia coli* cell size. *PLoS Genet.* 16:e1008685. doi: 10.1371/journal.pgen.1008685

Nagy, L., Milano, F., Dorogi, M., Agostiano, A., Laczkó, G., Szebényi, K., et al. (2004). Protein/lipid interaction in the bacterial photosynthetic reaction center: phosphatidylcholine and phosphatidylglycerol modify the free energy levels of the quinones. *Biochemistry* 43, 12913–12923. doi: 10.1021/bi0489356

Naylor, G. W., Addlesee, H. A., Gibson, L. C., and Hunter, C. N. (1999). The photosynthesis gene cluster of *Rhodobacter sphaeroides*. *Photosynth. Res.* 62, 121–139. doi: 10.1023/A:1006350405674

Ng, I. W., Adams, P. G., Mothersole, D. J., Vasilev, C., Martin, E. C., Lang, H. P., et al. (2011). Carotenoids are essential for normal levels of dimerisation of the RC–LH1–PufX core complex of *Rhodobacter sphaeroides*: characterisation of R-26 as a crtB (phytoene synthase) mutant. *Biochim. Biophy. Acta* 1807, 1056–1063. doi: 10.1016/j.bbabio.2011.05.020

Niederman, R. A. (2013). Membrane development in purple photosynthetic bacteria in response to alterations in light intensity and oxygen tension. *Photosynth. Res.* 116, 333–348. doi: 10.1007/s11120-013-9851-0

Niedzwiedzki, D. M., Gardiner, A. T., Blankenship, R. E., and Cogdell, R. J. (2018). Energy transfer in purple bacterial photosynthetic units from cells grown in various light intensities. *Photosynth. Res.* 137, 389–402. doi: 10.1007/s11120-018-0512-1

Okamura, M. Y., Paddock, M. L., Graige, M. S., and Feher, G. (2000). Proton and electron transfer in bacterial reaction centers. *Biochim. Biophys. Acta* 1458, 148–163. doi: 10.1016/S0005-2728(00)00065-7

Padan, E., Bibi, E., Ito, M., and Krulwich, T. A. (2005). Alkaline pH homeostasis in bacteria: new insights. *Biochim. Biophys. Acta* 1717, 67–88. doi: 10.1016/j.bbamem.2005.09.010

Preiss, L., Hicks, D. B., Suzuki, S., Meier, T., and Krulwich, T. A. (2015). Alkaliphilic bacteria with impact on industrial applications, concepts of early life forms, and bioenergetics of ATP synthesis. *Front. Bioeng. Biotechnol.* 3:75. doi: 10.3389/fbioe.2015.00075

Qian, P., Hunter, C. N., and Bullough, P. A. (2005). The 8.5 Å projection structure of the core RC–LH1–PufX dimer of *Rhodobacter sphaeroides*. *J. Mol. Biol.* 349, 948–960. doi: 10.1016/j.jmb.2005.04.032

Roszak, A. W., Howard, T. D., Southall, J., Gardiner, A. T., Law, C. J., Isaacs, N. W., et al. (2003). Crystal structure of the RC-LH1 core complex from *Rhodopseudomonas palustris*. *Science* 302, 1969–1972. doi: 10.1126/science.1088892

Ryu, M. H., Hull, N. C., and Gomelsky, M. (2014). Metabolic engineering of *Rhodobacter sphaeroides* for improved hydrogen production. *Int. J. Hydrog. Energy* 39, 6384–6390. doi: 10.1016/j.ijhydene.2014.02.021

Sánchez-Clemente, R., Igeño, M. I., Población, A. G., Guijo, M. I., Merchán, F., and Blasco, R. (2018). Study of pH changes in media during bacterial growth of several environmental strains. *Proceedings* 2:1297. doi: 10.3390/proceedings2201297

Scheuring, S., Nevo, R., Liu, L. N., Mangenot, S., Charuvi, D., Boudier, T., et al. (2014). The architecture of *Rhodobacter sphaeroides* chromatophores. *Biochim. Biophys. Acta* 1837, 1263–1270. doi: 10.1016/j.bbabio.2014.03.011

Semchonok, D. A., Chauvin, J. P., Frese, R. N., Jungas, C., and Boekema, E. J. (2012). Structure of the dimeric RC–LH1–PufX complex from *Rhodobaca bogoriensis* investigated by electron microscopy. *Philos. Trans. R. Soc. B Biol. Sci.* 367, 3412–3419. doi: 10.1098/rstb.2012.0063

Southall, J., Henry, S. L., Gardiner, A. T., Roszak, A. W., Mullen, W., Carey, A. M., et al. (2018). Characterisation of a puc BA deletion mutant from *Rhodopseudomonas palustris*

lacking all but the puc BA d genes. *Photosynth. Res.* 135, 9–21. doi: 10.1007/s11120-017-0386-7

Tokita, S., Shimada, K., Watabe, K., Matsuura, K., and Mimuro, M. (2011). A novel and mild isolation procedure of chlorosomes from the green sulfur bacterium *Chlorobaculum tepidum*. *Photosynth. Res.* 108, 183–190. doi: 10.1007/s11120-011-9679-4

Tucker, J. D., Siebert, C. A., Escalante, M., Adams, P. G., Olsen, J. D., Otto, C., et al. (2010). Membrane invagination in *Rhodobacter sphaeroides* is initiated at curved regions of the cytoplasmic membrane, then forms both budded and fully detached spherical vesicles. *Mol. Microbiol.* 76, 833–847. doi: 10.1111/j.1365-2958.2010.07153.x

van Grondelle, R., Dekker, J. P., Gillbro, T., and Sundstrom, V. (1994). Energy transfer and trapping in photosynthesis. *Biochim. Biophys. Acta* 1187, 1–65. doi: 10.1016/0005-2728(94)90166-X

Willey, J. M., Sherwood, L. M., and Woolverton, C. J. (2008). *Prescott, Harley, and Klein's microbiology*. *7th* Edn. New York, NY: Mc Graw Hill Press.

Yakovlev, A. G., Taisova, A. S., and Fetisova, Z. G. (2022). Dynamic stark effect in β and γ carotenes induced by photoexcitation of bacteriochlorophyll c in chlorosomes from *Chloroflexus aurantiacus*. *Photosynth. Res.* 154, 291–302. doi: 10.1007/s11120-022-00942-7

Yen, H. W., Feng, C. Y., and Kang, J. L. (2010). Cultivation of *Rhodobacter sphaeroides* in the stirred bioreactor with different feeding strategies for CoQ 10 production. *Appl. Biochem. Biotechnol.* 160, 1441–1449. doi: 10.1007/s12010-009-8576-1

Ziegelhoffer, E. C., and Donohue, T. J. (2009). Bacterial responses to photo-oxidative stress. *Nat. Rev. Microbiol.* 7, 856–863. doi: 10.1038/nrmicro2237

frontiers | Frontiers in Microbiology

TYPE Original Research
PUBLISHED 04 April 2024
DOI 10.3389/fmicb.2024.1359513

OPEN ACCESS

EDITED BY
Jose Echenique,
National University of Cordoba, Argentina

REVIEWED BY
Catherine Duport,
University of Avignon, France
Joerg Overhage,
Carleton University, Canada

*CORRESPONDENCE
Ulrike Kappler
✉ u.kappler@uq.edu.au

RECEIVED 21 December 2023
ACCEPTED 11 March 2024
PUBLISHED 04 April 2024

CITATION
Nasreen M, Ellis D, Hosmer J, Essilfie A-T, Fantino E, Sly P, McEwan AG and Kappler U (2024) The DmsABC S-oxide reductase is an essential component of a novel, hypochlorite-inducible system of extracellular stress defense in *Haemophilus influenzae*.
Front. Microbiol. 15:1359513.
doi: 10.3389/fmicb.2024.1359513

The DmsABC S-oxide reductase is an essential component of a novel, hypochlorite-inducible system of extracellular stress defense in *Haemophilus influenzae*

Marufa Nasreen[1], Daniel Ellis[1], Jennifer Hosmer[1], Ama-Tawiah Essilfie[2], Emmanuelle Fantino[3], Peter Sly[3], Alastair G. McEwan[1] and Ulrike Kappler[1]*

[1]School of Chemistry and Molecular Biosciences, Australian Infectious Diseases Research Centre, The University of Queensland, St. Lucia, QLD, Australia, [2]QIMR Berghofer Medical Research Institute, Herston, QLD, Australia, [3]Child Health Research Centre, South Brisbane, QLD, Australia

Defenses against oxidative damage to cell components are essential for survival of bacterial pathogens during infection, and here we have uncovered that the DmsABC S-/N-oxide reductase is essential for virulence and in-host survival of the human-adapted pathogen, *Haemophilus influenzae*. In several different infection models, *H. influenzae* Δ*dmsA* strains showed reduced immunogenicity as well as lower levels of survival in contact with host cells. Expression of DmsABC was induced in the presence of hypochlorite and paraquat, closely linking this enzyme to defense against host-produced antimicrobials. In addition to methionine sulfoxide, DmsABC converted nicotinamide- and pyrimidine-N-oxide, precursors of NAD and pyrimidine for which *H. influenzae* is an auxotroph, at physiologically relevant concentrations, suggesting that these compounds could be natural substrates for DmsABC. Our data show that DmsABC forms part of a novel, periplasmic system for defense against host-induced S- and N-oxide stress that also comprises the functionally related MtsZ S-oxide reductase and the MsrAB peptide methionine sulfoxide reductase. All three enzymes are induced following exposure of the bacteria to hypochlorite. MsrAB is required for physical resistance to HOCl and protein repair. In contrast, DmsABC was required for intracellular colonization of host cells and, together with MtsZ, contributed to resistance to N-Chlorotaurine. Our work expands and redefines the physiological role of DmsABC and highlights the importance of different types of S-oxide reductases for bacterial virulence.

KEYWORDS

respiratory infection, *Haemophilus influenzae*, sulfoxide reduction, oxidative stress, host-pathogen interactions

Introduction

Sulfur-containing molecules such as glutathione, coenzyme A and the amino acids cysteine and methionine are essential for the maintenance of cellular redox balance, metabolic pathways, and enzyme function and regulation. However, the same high reactivity that is essential for their cellular function makes sulfur-containing molecules targets for inactivation by oxidation (Staerck et al., 2017; Gout, 2019; Kappler et al., 2019).

S-oxide reductases are enzymes that can reverse sulfoxide-formation on biomolecules, including proteins, sulfur-containing amino acids and vitamins such as methionine, cysteine and biotin that are highly susceptible to oxidative damage (Baltes et al., 2003; Denkel et al., 2013; Dhouib et al., 2016, 2021; Ezraty et al., 2017; Kappler et al., 2019; Zhong et al., 2020; Nasreen et al., 2021). S-oxide reductases are emerging as essential components for virulence and fitness of bacterial pathogens such as *Escherichia coli*, *Salmonella* sp., *Actinobacillus pleuropneumoniae*, and *Haemophilus influenzae* (Baltes et al., 2003; Denkel et al., 2013; Dhouib et al., 2016, 2021; Ezraty et al., 2017; Kappler et al., 2019; Zhong et al., 2020; Nasreen et al., 2021), where a loss of S-oxide reduction causes a reduction of survival in infection models.

Haemophilus influenzae, the focus of this study, is a human-adapted pathobiont that colonizes the nasopharynx as a commensal but also causes acute diseases such as otitis media, sinusitis or pneumonia on access to the upper or lower respiratory tract (Van Eldere et al., 2014; Wen et al., 2020). Non-encapsulated, so-called 'non-typeable' strains of *H. influenzae* are currently the most common type of clinical isolate. These strains contribute to the pathogenesis and significantly worsen exacerbations of chronic lung diseases such as asthma, chronic obstructive pulmonary disease (COPD), cystic fibrosis and affect recovering COVID-19 patients (King, 2012; Van Eldere et al., 2014; Langereis and de Jonge, 2020; Lansbury et al., 2020; López-López et al., 2021; Short et al., 2021). Diseases caused by *H. influenzae* are characterized by high rates of recurrence and persistence (Ahearn et al., 2017), and sites of *H. influenzae* infections show high levels of inflammation and oxidative stress that lead to sulfoxide damage to proteins and redox molecules (Tufvesson et al., 2015; Saliu et al., 2021).

Sulfoxide formation can be caused by host-produced extracellular stressors such as hypochlorite or N-Chlorotaurine (Gottardi and Nagl, 2010; da Cruz Nizer et al., 2020). These extracellular chemical stressors first impact the bacterial cell envelope and periplasm, where we have recently described three enzymes that have the capacity to protect *H. influenzae* from sulfoxide stress. These include a strictly conserved periplasmic peptide methionine sulfoxide reductase, MsrAB, that repairs sulfoxide damage to proteins using thiol-based catalysis (Nasreen et al., 2020, 2022) and the two molybdenum-containing, periplasmic S- and N-oxide reductases, DmsABC and MtsZ (Dhouib et al., 2016, 2021; Struwe et al., 2021). Of these two enzymes, MtsZ is present in about 80% of strains and is strongly associated with methionine sulfoxide (MetSO) reductase activity, while DmsABC appeared to have a negligible contribution to this activity and had no identifiable *in vitro* phenotype, but is found in all *H. influenzae* strains (Othman et al., 2014; Dhouib et al., 2016). Despite this, in a mouse model of lung infection, attenuation of a *H. influenzae* Hi2019$^{\Delta dmsA}$ strain was much more significant than for the Hi2019$^{\Delta mtsZ}$ strain (Othman et al., 2014; Dhouib et al., 2016, 2021). These results suggest that *H. influenzae* DmsABC is required during conditions that exist only during contact with host cells. However, at present, it is not known what conditions, other than an anaerobic environment, lead to an induction of the operon that encodes DmsABC (Dhouib et al., 2021), and it is also unclear what substrate(s) DmsABC converts during infection. Equally unclear is whether there is a functional connection between the three S-oxide reductases in *H. influenzae*, and specifically DmsABC and MtsZ.

To address these gaps in knowledge, we have investigated the role of DmsABC for virulence of *H. influenzae* strains carrying either both DmsABC and MtsZ or only DmsABC in different infection models, including changes in the host response to infection. We were able to link expression of *dmsABCDE* to the presence of hypochlorite, a reactive chlorine species produced by the human immune system during infection, and identified several small molecule S- and N-oxides as potential natural substrates for DmsABC.

Together with the MsrAB peptide methionine sulfoxide reductase, DmsABC and the functionally related enzymes, MtsZ, form a novel, hypochlorite-inducible extracellular stress defense system in *H. influenzae*. This system protects *H. influenzae* from reactive chlorine and oxygen species and is essential for survival of the bacteria during infection.

Materials and methods

Bacterial strains and growth conditions

E. coli strains (Supplementary Table S1) were grown on liquid or solid Luria–Bertani (LB) medium at 37°C for 16–18 h with shaking at 200 rpm for liquid media. *Haemophilus influenzae* (Hi) 2019 (Campagnari et al., 1987) (NCBI acc. no.: NZ_CP008740.1), NTHi 86-028NP (Bakaletz et al., 1989) (NCBI acc. no.: NC_007146.2) and derivative strains (Supplementary Table S1) were grown on Brain Heart Infusion broth (BHI, BBL) or agar supplemented with hemin (10 μg/mL) and NAD (10 μg/mL) at 37°C for 16 h and 200 rpm shaking for broth cultures. Chemically Defined Medium (CDM) was also used and contained 10 mM glucose, 1 mM sodium pyruvate, 0.08 mg/mL uracil, 0.17 mg/mL inosine, 10 μg/mL β-NAD, 25 mM HEPES, pH 7.4, 10 μg/mL hemin and 2 mg/mL $NaHCO_3$ in RPMI1640 (Coleman et al., 2003). The sBHI and CDM media were also used to cultivate *H. influenzae* clinical isolate strains from our collection. *Actinobacillus pleuropneumoniae* (strain 4074) (Supplementary Table S1) was cultivated on CDM medium under microaerobic conditions at 37°C and 45°C, respectively. Ampicillin (100 μg/mL *E. coli*), kanamycin (100 μg/mL *E. coli*; 10 μg/mL Hi) and tetracycline (10 μg/mL *E. coli*, 1 μg/mL Hi) were added to culture media when needed.

NTHi growth experiments (Hosmer et al., 2022) were conducted in microtiter plates, each well containing 200 μL of CDM medium. Three biological replicates per strain were incubated at 37°C and 200 rpm using a Clariostar multimode plate reader (BMG LabTech). The atmospheric control unit was set up to allow approximately 20% O_2 for aerobic conditions, 2.8% O_2 for microaerobic conditions, and 5% CO_2 with no oxygen for anaerobic conditions (no shaking). Growth rates were calculated according to the method described in Kurokawa and Ying (2017).

Transformation of *Haemophilus influenzae* strains

NTHi transformation was performed as in Poje and Redfield (2003). Briefly, *H. influenzae* cultures (20 mL) were grown to an OD_{600nm} of 0.25 using sBHI, harvested, and washed twice in freshly prepared MIV solution (Poje and Redfield, 2003) before resuspension in 5 mL MIV and incubation at 37°C with shaking for 100 min to develop competence. One microgram of linearized plasmid was added to 1 mL of competent cells and incubated at 37°C for 30 min before 1 mL of sBHI was added. Samples were incubated at 37°C for 1 h before plating on sBHI plates with 20 μg/mL kanamycin. MIV solution was prepared by combining 25 mL solution 21 (per liter: 4 g L-aspartate, 0.2 g L-glutamate, 1 g fumarate, 4.7 g NaCl, 0.87 g K_2HPO_4, 0.76 g KH_2PO_4, 0.2 mL Tween 80, pH 7.0) with 0.25 mL solution 22 (4 mg L-cytosine, 10 mg L-tyrosine dissolved in 1 mL 1 M HCl at 37°C followed by addition of 9 mL H_2O and 6 mg L-citrulline, 20 mg L-phenylalanine, 30 mg L-serine, 20 mg L-alanine), 0.25 mL 0.1 M $CaCl_2$, 0.25 mL 0.05 M $MgCl_2$, and 0.25 mL 5% Difco vitamin-free Casamino acids.

Biofilm formation

Biofilm formation in 96-well microtiter plates used the protocol described in Schembri and Klemm (2001), and bacterial survival in biofilms was determined as in Dhouib et al. (2016) using proteinase K digestion and serial dilution. Briefly, non-typeable *H. influenzae* strains were grown to OD_{600nm} of 0.2–0.3 under microaerobic conditions in sBHI broth at 37°C with shaking. Then, the cultures were diluted to an OD_{600nm} of 0.05 and dispensed into 96-well microtiter plates (100 μL per well, 96-well plate: Techno Plas, cat no: SMPSL) and incubated at 37°C. Following incubation, planktonic cells were removed by washing the wells twice with sterile water, and the wells were subsequently stained using 0.1% crystal violet for 10 min. After plate drying, 30% acetic acid was applied to dissolve the biofilm, and the optical density at 550 nm (OD_{550nm}) was measured using a plate reader. To determine viable cell counts, the wells of the biofilm plate were rinsed twice with sterile water, followed by incubation with 100 μL of 0.1 mg/mL protease K for 10 min at room temperature to dissolve the biofilm. Subsequently, samples were collected, serially diluted in 1xPhosphate Buffered Saline (PBS), and plated on sBHI agar to quantify the colony forming units (CFU) per well. Each strain was analyzed with three biological replicates, and several technical replicates were used for each biological replicate.

Oxidative and nitrosative stress susceptibility testing

Bactericidal assays were conducted following the protocol described in Nasreen et al. (2020) and used 150 and 175 μM HOCl, 0.5–1.5 mM NCT. In all experiments, HOCl was applied as NaOCl. *H. influenzae* 2019 strains, obtained from freshly grown sBHI plates, were resuspended to an OD_{600nm} of 1.0 (~6×10^8 CFU/mL) in 1xPBS. Subsequently, 900 μL of bacterial culture were combined with 100 μL of a freshly prepared 10x stock of the test compound or sterile water as a control. The reactions were incubated at room temperature for 60 min with orbital shaking, followed by immediate serial dilution and plating on sBHI plates for CFU/mL determination.

For S-oxide reductase activity assays in *H. influenzae* strains 2019 and 86-028NP, cultures growing microaerobically in CDM were treated with 0.4 mM HOCl or 10 mM paraquat for 60 min at mid-exponential phase before harvesting.

Nitrosative stress susceptibility was assessed following the method of (27). NTHi strains, with three biological replicates grown on sBHI agar plates, were inoculated in 50 mL sBHI broth in 50 mL tubes and incubated at 37°C in a CO_2 incubator for 16–18 h. These cultures were then used to inoculate sBHI broth buffered to pH 5.5 at an initial $OD_{600\,nm}$ of 0.07. 150 μL of this bacterial suspension were added to each well of a round-bottom 96-well microtiter plate (Costar 3799), followed by addition of 150 μL of 20 mM or 30 mM $NaNO_2$ to each reaction to achieve final concentrations of 10 mM and 15 mM. Sterile water was added to control wells. Plates were incubated at 37°C, 5% CO_2, for 16 h in an anaerobic jar using Anaerocult A catalysts (Merck) to remove oxygen. After 2 h of incubation, the cultures were serially diluted and plated on sBHI plates for CFU/mL determination. Growth rate determinations used the program GrowthRates v.6.2.1 (Hall et al., 2013).

General molecular biology and biochemical methods

Standard methods were used throughout (Ausubel et al., 2005). All chemicals were purchased in analytical grade or equivalent. Genomic DNA was isolated using DNAzol reagent (Thermo Fisher Scientific). GoTaq Green MasterMix (Promega) was used for general PCR (primer sequences, Supplementary Table S2), the GeneJET Plasmid Miniprep Kit and GeneJET PCR Purification kit (both Thermo Fisher Scientific) for plasmid and PCR product purification. Restriction enzymes were from Thermo Fisher Scientific, T4 ligase (NEB) was used for ligations. Cell-free extracts of NTHi were generated using BugBuster Mastermix (Novagen) according to the manufacturer's instructions (750 μL were used for pellets from 50 mL culture). Protein concentrations were determined using the BCA-1 kit (Sigma Aldrich).

Construction of *Haemophilus influenzae* 86-028$^{\Delta dmsA}$

The previously constructed plasmid, pGEM-Hi*dmsA::kan* (Dhouib et al., 2021) was linearized using *NcoI* and transformed into competent NTHi 86-028NP using the method described above.

Construction of double mutants of Hi2019

The *tet* resistance cassette, amplified from pRK415 using primers from Supplementary Table S2, was ligated into two previously constructed plasmids: pGEM-Hi*mtsZ* (Dhouib et al., 2016) and pBlu-Hi*msrAB* (Nasreen et al., 2020). This resulted in the construction of pGEM-Hi*mtsZ::tet* and pBlu-Hi*msrAB::tet* plasmids. The linearized pGEM-Hi*mtsZ::tet* plasmid was transformed into Hi2019$^{\Delta dmsA}$ *and* Hi2019$^{\Delta msrAB}$ to generate

Hi2019$^{\Delta dmsA\Delta mtsZ}$ *and* Hi2019$^{\Delta msrAB\Delta mtsZ}$. Additionally, linearized pBlu-H*imsrAB::tet* was used to create double mutant Hi2019$^{\Delta dmsA\Delta msrAB}$.

RNA isolation and cDNA synthesis

Samples for RNA isolation from bacteria were obtained during the mid-exponential growth phase (OD_{600nm} Hi, Ap ~ 0.45) from cultures growing on CDM under microaerobic conditions. Additionally, RNA samples were collected at 30, 60, and 120 min after treating cultures with 200 µM HOCl, 150 µM H_2O_2, or 5 mM paraquat, following the method outlined in reference (Pauwels et al., 2004).

For each sample, 2 mL of culture was preserved using 2 mL of RNAprotect Bacteria Reagent (Qiagen) before RNA isolation using the Illustra RNAspin Mini RNA isolation kit (Cytiva). RNA from snap-frozen mouse lung tissue was isolated by homogenization in 1 mL Trizol (Thermo Fisher Scientific), followed by centrifugation to remove large cellular debris and RNA isolation according to the manufacturer's instructions. Genomic DNA was removed using the Turbo DNAfree kit (Thermo Fisher Scientific), and RNA concentrations were determined using the Quant-it RNA HS kit (Thermo Fisher Scientific). The absence of genomic DNA was confirmed by PCR using 16S primers and β-actin (*ACTB*, mouse) primers (Supplementary Table S2), with purified RNA serving as the template. Subsequently, cDNA was synthesized from 500 ng of genomic DNA-free RNA using random hexamer primers and either the Superscript IV VILO Master Mix (Thermo Fisher Scientific) or the Lunascript RT SuperMix kit (New England Biolabs), following the manufacturer's instructions.

Quantitative RT-PCR

Quantitative reverse transcription-PCR (qRT-PCR) was conducted following the procedures outlined in reference (Othman et al., 2014). Each qRT-PCR reaction (10 µL) comprised diluted cDNA (1:100) as the template, QuantiNova SYBR Green qPCR Master Mix from Qiagen, and specific oligonucleotide primers (Conc 2 µM) listed in Supplementary Table S2. Reference genes used included gyrase (*gyrA*) genes for *H. influenzae, Actinobacillus pleuropneumoniae,* and β-actin (*ACTB*) for mouse cDNA. Data analysis and normalization were performed as in Kappler et al. (2005). The cycle threshold (CT) value for all samples was determined using QuantstudioTM Real-time PCR software version 1.3 (Thermo Fisher Scientific). The PCR efficiencies were determined using LinRegPCR software version 2016.0 (Ruijter et al., 2009).

S-/N-oxide reductase activity assays

S- and N-oxide reductase activity assays were performed anaerobically in 20 mM sodium phosphate buffer (pH 6.8) containing 0.2 mM Methyl viologen, 0.3 mM sodium dithionite and one of the following terminal electron acceptors: 10 mM Dimethyl Sulfoxide (DMSO), 10 mM L-Methionine Sulfoxide (L-MetSO), 10 mM S-Biotin Sulfoxide (S-BSO), 10 mM racemic methyl p-tolyl sulfoxide (MPTS), 10 mM R-MPTS & S-MPTS, 2 mM Pyrimidine N-Oxide (Pyr N-Ox), and 5 mM Nicotinamide N-Oxide (Nic N-Ox). The re-oxidation of reduced methyl viologen [$\varepsilon_{600} = 13.7\ mM^{-1}\ cm^{-1}$ (Watanabe and Honda, 1982)] was monitored at 37°C in a Cary60 Spectrophotometer (Agilent Technologies) as described in Dickie and Weiner (1979). For determination of kinetic parameters, the concentrations of the substrates were varied. Specific enzyme activities are given as µmoles of substrate reduced per min (U) and mg of protein present. Kinetic data were fitted using Prism 9 (GraphPad). For enzyme assays using purified *H. influenzae* MtsZ, the protein was prepared as described in Dhouib et al. (2016) and Struwe et al. (2021).

NTHi host cell adherence and invasion assays using cultured tissue cells and normal human nasal epithelia

The Human Bronchial Epithelial 16HBE14 cell line was cultured using Minimal Essential Medium (MEM) supplemented with 10% heat-inactivated Fetal Bovine Serum (FBS). Adherence and invasion assays for NTHi were conducted following the procedures outlined in Dhouib et al. (2015). Normal Human Nasal Epithelia (NHNE) were prepared following the protocol outlined in Yeo et al. (2019) using primary nasal cells obtained from healthy donors at the Child Health Research Centre, UQ, Brisbane. Seven days before infection, NHNE were transferred to steroid- and antibiotic-free PneumaCult-ALI medium (Stemcell). NTHi for infection were resuspended in 1xPBS and applied at a Multiplicity of Infection (MOI) of 10:1. Uninfected NHNE were exposed to an equal amount of sterile 1xPBS. Following a 24-h infection period at 37°C with 5% CO_2, the inoculum was removed by washing with 1xPBS, and the basal medium was replaced.

Post-infection, NHNE apical surfaces were washed every second day using 100 µL 1xPBS, and the basal medium was replaced. Lysates were generated by a 10 min incubation of NHNE with 1% saponin at 37°C. Intracellular bacterial Colony Forming Units (CFU) were determined after treating the NHNE surface with gentamycin (100 µg/mL) for 1 h at 37°C. Gentamycin was then aspirated, and the apical compartments were washed five times with 200 µL of 1xPBS before lysing the NHNE with a 10 min incubation at 37°C with 1% saponin. Bacterial loads in lysates were determined by plating serial dilutions on sBHI agar.

NHNE transepithelial electrical resistance (TEER) was measured every 2 days using a Millicell ERS-2 Volt-ohm meter. For competition assays, NHNE were infected with an equal mixture of Hi2019^{WT} and one mutant strain (total MOI 10:1), and bacterial loads were analyzed as described above. However, serial dilutions were plated on sBHI to determine total bacterial numbers and on sBHI with 20 µg/mL kanamycin to assess the load of NTHi carrying a mutation. Hi2019^{WT} cell numbers were determined by subtracting CFU/mL of kanamycin-resistant (mutant) NTHi from total NTHi CFU/mL for the same time point. Each infection and co-infection involved two biological replicates for each strain or strain combination, with three technical replicates used for CFU/mL determination in each biological replicate.

Mouse bone marrow macrophage infection assay

The procedure for isolating Bone Marrow Macrophages (BMM) from C57 Black mice was adapted from Tushinski et al. (1982). In

summary, mice were sacrificed, and femurs and tibias were collected, with muscles and surrounding tissues removed. The tips of the femurs and tibias were excised using surgical scissors, and the bone cavity was flushed with complete macrophage medium [RPMI1640 containing 10% heat-inactivated FBS 2 mM L-glutamine (GlutaMAX, Thermo Fisher Scientific) and 150 ng/mL recombinant colony-stimulating factor-1 (rCSF-1, produced at Protein Expression Facility, The University of Queensland)].

Bone marrow cells were washed twice with complete medium (centrifuged at 300 × g for 5 min each time) before being evenly distributed into eight sterile, 100 mm square petri dishes, each containing 15 mL of complete medium. Penicillin/streptomycin (Stock: Penicillin: 10,000 Units/mL, Streptomycin: 10,000 mg/mL) was added to the media to a final concentration of 1%, and the plates were incubated for 6 days at 37°C with 5% CO_2. On day 3, fresh rCSF-1 (final conc.: 150 ng/mL) was added. On day 6, the growth medium was discarded, and BMMs were washed off the plate using 10 mL of 1xPBS. BMMs were then centrifuged at 300 × g for 5 min and resuspended in antibiotic-free BMM medium. Subsequently, 1×10^5 cells/well were seeded into 24-well tissue culture plates for the infection assay.

The infection assays used a MOI of 1,000:1. After 1 h, the inoculum was removed, and complete macrophage medium with 7 μg/mL polymyxin B was added to the wells for 60 min to eliminate extracellular bacteria. For 2 h infections, cell layers were washed twice with RPMI before 100 μL of 0.1% saponin was used to lyse the macrophages. Intracellular bacteria were quantified through dilution plating. For 4 and 6 h infections, the medium containing 7 μg/mL polymyxin B was replaced with medium containing 0.5 μg/mL polymyxin B for 2 h and 4 h before processing the cells to determine intracellular bacteria.

Haemophilus influenzae murine lung infection

For NTHi pulmonary infection, the mouse model of lung infection we described previously was used (Morey et al., 2013; Dhouib et al., 2016). Hi2019 and Hi2019$^{\Delta dmsA}$ were cultured on sBHI plates for 16 h at 37°C with 5% CO_2. A bacterial suspension in 1xPBS, containing 10^7 CFUs in 30 μL, was intranasally inoculated into female BALB/c mice aged 5 to 6 weeks. Groups of 5 mice were euthanized and necropsied at 0 h, 6 h, 24 h, 48 h, and 72 h, as described in Hosmer et al. (2022). Lungs were aseptically removed from sacrificed mice, and lung tissue was either snap-frozen in liquid nitrogen for RNA isolation or homogenized in 1 mL 1xPBS. The homogenized samples were serially diluted and plated on sBHI agar to determine CFU/mL. Additionally, bronchoalveolar lavage fluid (BALF) was collected, and CFU/mL were determined. CFUs per lung were calculated as described in Essilfie et al. (2012). Giemsa staining of BALF was performed according to the manufacturer's instructions (Sigma-Aldrich). Statistical comparisons of mean CFU/lung and BALF were carried out using two-tailed *t*-tests integrated into the Prism 9 software package.

ELISA assays

Mouse BALF was used for ELISA assays (Thermo Fisher Scientific) according to the manufacturer's instructions to detect the presence of mouse TNFα and IL-6. Data were collected for all mice in each treatment group. The statistical significance of the detected differences among the groups was assessed using Prism 9 (GraphPad).

Statistical analyses

Statistical analyses were carried out using Prism versions 9 and 10 (GraphPad). Statistical comparisons of mean CFU/lung and BALF following mouse lung infection experiments were carried out using two-tailed *t*-tests. All other analyses used either 1-Way of 2-Way ANOVA with an appropriate multi-comparison correction. All analyses used a $p < 0.05$ to determine statistical significance. Details of the analyses are provided in the Figure legends.

Ethics statement

Experimental animal procedures were conducted in strict accordance with the recommendations outlined in the QLD Animal Care and Protection Act (2001) and the Australian Code of Practice for the Care and Use of Animals for Scientific Purposes, 8th edition. The protocols were approved by the Animal Care and Ethics Committees of QIMR Berghofer and the University of Queensland (QIMR/050/19).

Human nasal cell samples were obtained from healthy donors at the Child Health Research Centre, UQ, Brisbane, under the approval of the University of Queensland Ethics Committee (Approval #2017000520). Clinical isolates of *Haemophilus influenzae* were collected from routine pathology samples according to approvals 2021/HE001644, 2014/HE000067.

Results

Infection with an *Haemophilus influenzae* Δ*dmsA* strain elicits a reduced host immune response to infection in a mouse model of lung infection

We have previously reported that *H. influenzae* DmsABC is required for virulence in a mouse model of infection (Dhouib et al., 2021), and to better understand this process, we investigated whether the presence or absence of DmsABC affected the host response to *H. influenzae* infection. Using a mouse model of lung infection (Dhouib et al., 2021), the Hi2019$^{\Delta dmsA}$ strain was cleared significantly faster than the wildtype, with first differences becoming apparent at 24 h post-infection (p.i.) (Figure 1A). Compared to the wildtype, the total lung-associated populations of Hi2019$^{\Delta dmsA}$ were reduced 10x, 28x, and 18x times at 24 h, 48 h, and 72 h post-infection (p.i.) (total CFU/lung: $p < 0.0001$). Attenuation was similar for bacteria detected in bronchoalveolar lavage fluid (BALF) (Supplementary Figure S1A). We then tested the host immune response to infection using qPCR for RNA isolated from lung tissue and ELISA for BALF samples. The faster clearance of Hi2019$^{\Delta dmsA}$ was associated with reduced expression of the pro-inflammatory markers IL6, TNFα and IL1β in mouse lung tissue, with expression levels returning to near baseline by 48 h p.i. In contrast, for infections with the wildtype strain, expression of these genes was still elevated at 72 h p.i. (Figures 1B–D). Similar expression

10.3389/fmicb.2024.1359513

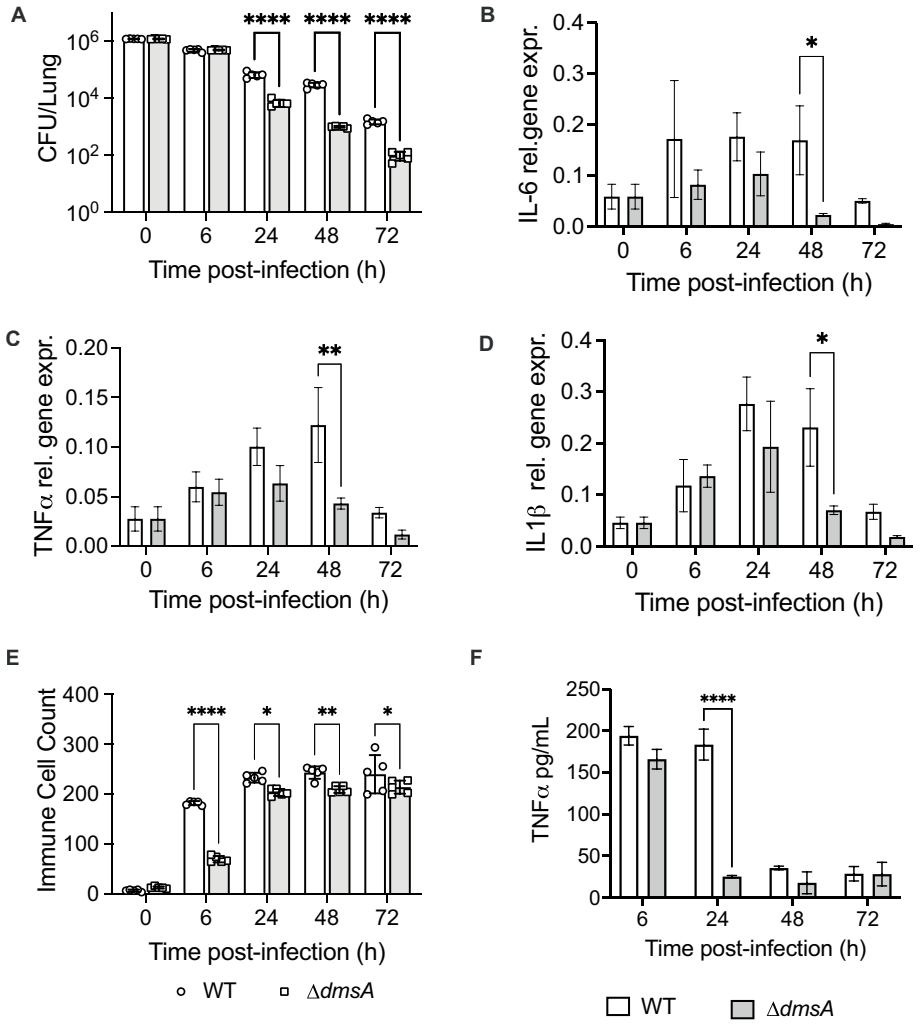

FIGURE 1
Comparison of mouse lung infections with Hi2019^{WT} and Hi2019$^{\Delta dmsA}$. **(A)** Bacterial colony forming unit (CFU) recovered per lung. **(B–D)** Relative expression of IL-6, TNFα and Il1β in mouse lung tissue during infection with NTHi strains. qPCR data was normalized against expression of ACTB, cDNA was generated using random hexamers. **(E)** Immune cell counts (Giemsa stain) in mouse Bronchoalveolar Lavage Fluid (BALF). **(F)** TNFα levels in mouse BALF determined by ELISA. Infection assays used five mice per group, qPCR analyses used RNA isolated from three mice for each data point. Statistical analyses: **(A)** multiple un-paired *t*-tests, ****$p<0.0001$; **(B–F)** 2-Way ANOVA, Sidaks' multiple comparison correction, *$p<0.05$, **$p<0.01$, ****$p<0.0001$.

patterns were also observed for Hif1α, TGFβ and the BIRC3 gene that encodes an anti-apoptotic effector and has shown increased expression in human tissue cells infected with wildtype *H. influenzae* (Nasreen et al., 2020) (Supplementary Figures S1B–D). In mouse BALF, a reduced immune response was also apparent for TNFα, but not IL6 levels (Figure 1F; Supplementary Figure S1E). These data suggested a reduced production of chemo-attractants during infection with Hi2019$^{\Delta dmsA}$ that was accompanied by a reduced influx of immune cells into the lungs of infected mice (Figure 1E; Supplementary Figures S1F–H). The difference was most prominent at 6 h p.i., but persisted up to 72 h p.i. and was primarily due to lower neutrophil numbers. Together with the reduced recovery of Hi2019$^{\Delta dmsA}$ from mouse lungs, this could indicate reduced survival of the Hi2019$^{\Delta dmsA}$ strain in contact with resident lung immune cells.

To investigate this possibility, we tested whether Hi2019$^{\Delta dmsA}$ showed increased susceptibility to killing by bone marrow-derived mouse macrophages. While we had previously demonstrated slightly increased susceptibility of Hi2019$^{\Delta dmsA}$ to neutrophil-mediated killing (Dhouib et al., 2021), in macrophage killing assays, this strain showed a statistically significant increase in intracellular survival compared to the wild type at 6 h p.i. (Supplementary Figure S2). As neutrophil numbers were low in Hi2019$^{\Delta dmsA}$ infection BALF samples, we conclude that the increased clearance of Hi2019$^{\Delta dmsA}$ in the mouse lung was not due to a greater sensitivity to killing by phagocytic cells such as tissue-resident macrophages.

DmsABC is required for survival of *Haemophilus influenzae* in contact with primary human epithelia and transepithelial migration

The human respiratory tract is the only known natural niche of *H. influenzae* (Van Eldere et al., 2014), and as a result, *H. influenzae* infections in healthy mice are not stable and of short duration (Figure 1A). To determine whether the *dmsA* mutation also reduces

H. influenzae survival in contact with human respiratory epithelia, we infected normal human nasal epithelia (NHNE) with either the Hi2019^{WT} or the Hi2019$^{\Delta dmsA}$ strain. NHNE are pseudostratified epithelia that are derived from primary human nasal cells (Pezzulo et al., 2011; Hosmer et al., 2022). NHNE are differentiated at the air-liquid interface and closely resemble primary human respiratory epithelia (Pezzulo et al., 2011; Hosmer et al., 2022).

In NHNE single-strain infections, compared to the wildtype, attenuation of Hi2019$^{\Delta dmsA}$ increased from 3.6- and 2.2 -fold for total and intracellular bacteria on day 3 p.i. to 3×10^3- and 1×10^4- fold, respectively, by day 7 p.i. (Figures 2A,B). Transepithelial migration of Hi2019$^{\Delta dmsA}$ was also reduced, with only ~0.3% of total bacteria recovered for the mutant strain on day 7 p.i., compared to ~1.1% for the wildtype strain (Supplementary Figure S2C).

We then tested the survival of Hi2019$^{\Delta dmsA}$ in competitive infections of NHNE. Using an equal mixture of Hi2019^{WT} and Hi2019$^{\Delta dmsA}$, attenuation of the mutant strain was ~100 fold by day 3 p.i., and this increased to ~1,000 fold by day 7 p.i. for both total and intracellular bacterial populations (Figures 2E–G). Neither infection type appeared to cause significant damage to NHNE, as indicated by the consistency of TEER values between infected and uninfected control NHNE (Figure 2D; Supplementary Figure S3). These data confirmed that DmsABC is also required for the survival and virulence of *H. influenzae* in human nasal epithelia, its primary niche.

Expression of Hi dmsABC is triggered by hypochlorite and other host-produced stressors

Together with our previous investigations that documented the absence of an *in vitro* phenotype of Hi2019$^{\Delta dmsA}$ (Dhouib et al., 2021), the data above confirm that DmsABC is required under conditions that only exist when *H. influenzae* is in contact with host cells. This then suggested that host-produced stressors might play a role in controlling expression of *dmsABC*. To investigate this, we monitored expression of *dmsA* following exposure of actively growing, microaerobic cultures of Hi2019 to hypochlorite, hydrogen peroxide and or paraquat, a superoxide-producing agent. Hypochlorite caused a 3.3-fold increase in *dmsA* expression within 30 min of exposure, followed by a slow decrease in gene expression, while hydrogen peroxide had no or very little effect on *dmsA* expression (Figure 3A). Interestingly, the highest levels of *dmsA* expression were observed following paraquat exposure; however, induction of gene expression only occurred 60 min post-exposure (Figure 3A).

This is the first time that a specific, fast-acting inducer for *dmsA* expression other than general anaerobiosis has been identified in any bacterium, and we therefore tested whether hypochlorite induction of *dmsA* expression also occurs in other *H. influenzae* strains and other bacteria in which *dmsABC* genes are present such as *Actinobacillus pleuropneumoniae*. *A. pleuropneumoniae* is another bacterial pathogen of the Pasteurellaceae family for which a link between virulence and the presence of DmsABC has been previously reported (Baltes et al., 2003) (Figures 3B,C) Hypochlorite induced *dmsA* expression in all bacteria tested, but expression patterns and maximal induction levels varied, especially for the three *H. influenzae* strains. In most cases, increases in *dmsA* expression were measurable after 30 min, and peak expression occurred between 60 and 90 min post HOCl exposure. The smallest relative change, ~2-fold induction at 60 min, was observed for *A. pleuropneumoniae* (Figure 3C). The data clearly establish hypochlorite-induction as a feature of *dmsABC* regulation, suggesting a general role of DmsABC in bacterial stress responses during host-bacteria interactions in *H. influenzae* and other *Pasteurellaceae* (Baltes et al., 2003; Dhouib et al., 2021).

DmsABC activity levels in *Haemophilus influenzae* show high strain-to-strain variation but did not correlate with the presence or absence of *mtsZ* in addition to *dmsABC*

As *H. influenzae dmsA* gene expression levels were very strikingly different between the three strains tested above, we hypothesized that this might correlate with the presence or absence of genes encoding the MtsZ MetSO reductase that is another S-oxide reductase in *H. influenzae* but is not strictly conserved. Accordingly, we compared S-oxide reductase activity levels in five genotypically *dmsABC*$^+$/ *mtsYZ*$^+$ strains and two *dmsABC*$^+$/ *mtsZ*$^-$ strains from our *H. influenzae* isolate strain collection. Hi2019 and Hi 86-028NP were used as reference strains for the two groups, respectively, and had 0.11 and 1.8 U/mg S-oxide reductase activity, respectively. Following anaerobic growth, total S-oxide reductase activities between 0.09 and 1.8 U/mg for the DmsABC-only group, and 0.11–3.44 U/mg for the DmsABC/MtsZ positive group of strains were determined (Figure 3D). Together, this indicates that under standard anaerobic conditions, S-oxide reductase activity varied significantly in a strain- but not genotype-dependent manner. It also shows that high S-oxide reductase activity is not a specific trait of recent clinical isolate strains.

To confirm that the observed induction of gene expression in the presence of HOCl and paraquat leads to an increase in S-oxide reductase activity, we then exposed the two reference strains to HOCl or paraquat prior to S-oxide reductase activity determination. This experiment confirmed induction of activity by 1.5- and 3.2-fold for Hi2019 and 86-028NP following HOCl exposure and 3.2- and 14.4-fold, respectively, for paraquat exposure (Figure 3E).

Loss of DmsABC in an MtsZ-negative *Haemophilus influenzae* strain exacerbates the sensitivity to oxidative stress and loss of virulence

While the *dmsABC*$^+$/ *mtsZ*$^-$-genotype is only present in about 20% of *H. influenzae* isolate strains, these strains offer a unique opportunity to better understand the physiological role of DmsABC in *H. influenzae* pathogenesis and we therefore created and characterized a Hi86-028NP Δ*dmsA* strain.

The mutation was confirmed using PCR, and enzyme assays showed that in crude extracts from the mutant strain, S-oxide reductase activity was reduced by ~80% (Figure 4A). As the Hi2019$^{\Delta dmsA}$ strain lacked a distinct *in vitro* growth phenotype but showed increased biofilm formation, we then tested biofilm formation in Hi86028NP$^{\Delta dmsA}$ to confirm a similarity of phenotypes. Under microaerobic conditions, the Hi86028NP$^{\Delta dmsA}$ strain showed a 5-fold increase in biofilm formation (1-Way ANOVA, Dunnett, $p < 0.0001$)

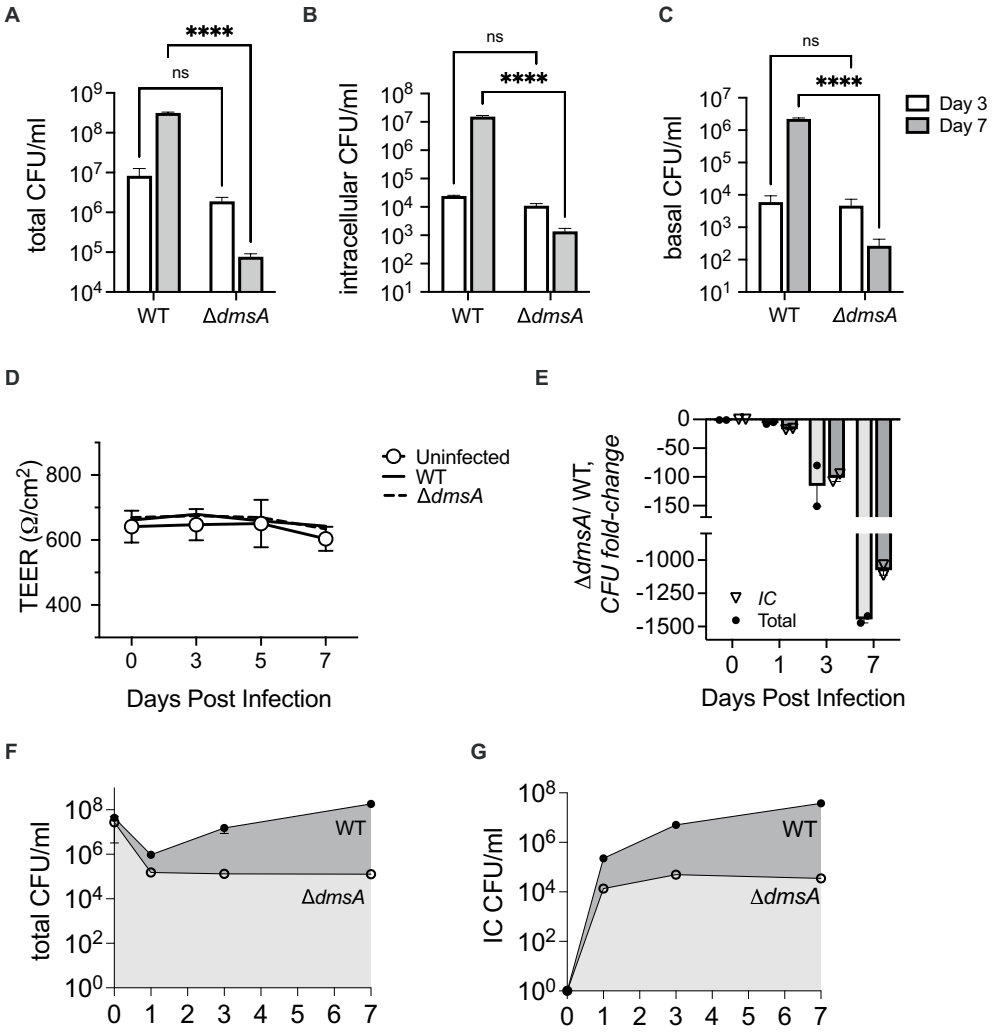

FIGURE 2
Infection of Normal Human Nasal Epithelia (NHNE) with Hi2019^{WT} and Hi2019$^{\Delta dmsA}$. **(A,B)** Total and intracellular bacterial colony forming unit (CFU) recovered from infected NHNE with a single NTHi strain. **(C)** Bacterial CFU/mL recovered from NHNE basal medium during single strain infections. **(D)** NHNE integrity during single strain infections determined using Transepithelial Resistance (TEER) values. **(E)** Changes in strain abundance (fold-change) during competitive infections of NHNE using a 1:1 mixture of Hi2019^{WT} and Hi2019$^{\Delta dmsA}$. IC, intracellular. **(F,G)** Total and intracellular CFU/mL recovered during competitive infections of NHNE using a 1:1 mixture of Hi2019^{WT} and Hi2019$^{\Delta dmsA}$. IC, intracellular. NHNE infections used $n=2$ biological replicates, 3 technical replicates were used per biological replicate. Statistical analyses: 2-Way ANOVA, Sidaks multiple comparison correction, ****$p<0.0001$. For panels **(F,G)**, the day 7 and day 3 and 7 values are significant with $p<0.0001$. All other timepoint comparisons are not significant.

and similar viable cell counts to the wildtype (Figures 4B,C). In addition to oxidizing compounds, reactive nitrogen species are also commonly found at sites of infection (Ulfig and Leichert, 2021), and we therefore tested the susceptibility of the Hi2019 and 86-028NP *dmsA* mutant strains to NO stress, however, both strains behaved the same as the respective wildtype strains (Supplementary Figure S4).

In infection assays using 16HBE14 bronchial epithelial cells, the 86-028NP *dmsA* mutant strain showed a reduction in total cell-associated bacteria of 1.6- and 7.7-fold relative to the wildtype strain at 4 h and 24 h p.i. (2-Way ANOVA, Sidak, $p=0.0255$ & 0.023), while intracellular bacterial loads were reduced 8-fold at 4 h and 100-fold at 24 h p.i. (2-Way ANOVA, Sidak, $p=0.0001$ & 0.001) (Figures 4D,E). Planktonic cell numbers showed no statistically significant differences (Figure 4F). These results resemble the phenotype we reported for Hi2019$^{\Delta dmsA}$ (Dhouib et al., 2021), except that for the 86-028NP Δ*dmsA* strain, the infection phenotype was somewhat more pronounced. In infections of mouse primary macrophages, the 86-028NP Δ*dmsA* strain showed no statistically significant difference in survival compared to the WT strain, which differs from the behavior of the corresponding Hi2019 derivative strain that showed increased survival at 6 h post-infection (Supplementary Figure S2). The slight differences in infection phenotypes may be due to the absence of the MtsZ methionine sulfoxide reductase that provides some functional redundancy in *H. influenzae* 2019.

Together, these experiments demonstrate that the phenotype of the *H. influenzae* 86-028NP Δ*dmsA* strain is similar to what we previously described for the equivalent mutation in Hi2019 (Dhouib et al., 2021), but in the tissue cell infection model, the *H. influenzae* 86-028NP Δ*dmsA* strain showed an increased colonization defect for tissue cell adherent bacteria.

10.3389/fmicb.2024.1359513

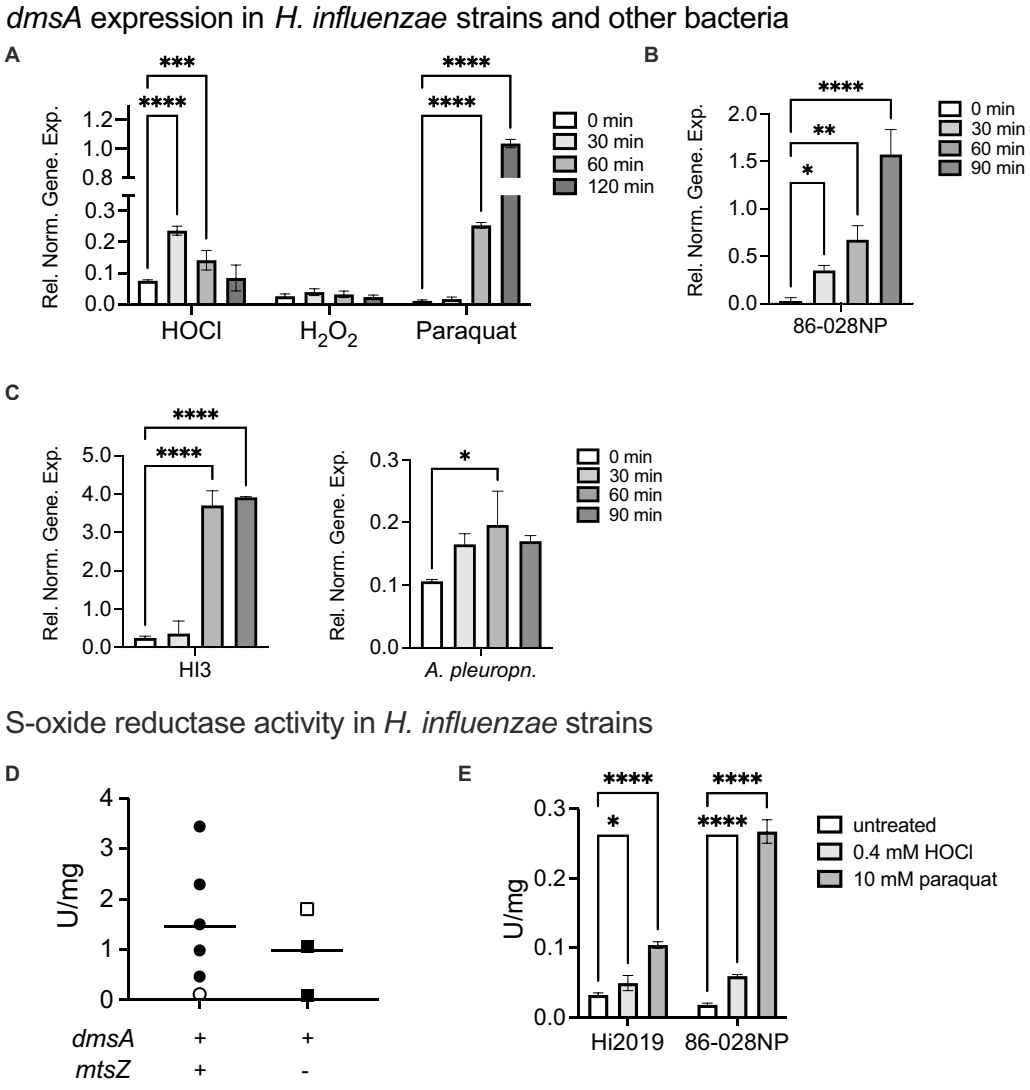

FIGURE 3
Induction of *dmsABC* gene expression and S-oxide reductase activity following exposure of bacteria to oxidative stressors. **(A)** Changes in *dmsABC* gene expression in Hi2019 following exposure of actively growing, microaerobic cultures to different oxidative stress challenges (200 μM HOCl, 150 μM H_2O_2, 5 mM paraquat). **(B,C)** Changes in *dmsABC* gene expression in *H. influenzae* strains 86-028NP and HI3 and *Actinobacillus pleuropneumoniae* 4,074 following exposure of actively growing, microaerobic cultures to 200 μM HOCl over a 90 min time course. **(D)** S-oxide reductase activity in *H. influenzae* strains with either a *dmsA*$^+$/*mtsZ*$^-$, or a *dmsA*$^+$/– genotype following anaerobic growth. Open symbols denote the two control strains, Hi2019 and 86-028NP, respectively. **(E)** S-oxide reductase activity in actively growing, microaerobic cultures of *H. influenzae* strains 2019 and 86-028 following exposure to either 0.4 mM HOCl or 10 mM paraquat for 60 min. qPCR data and enzyme assays shown are averages of three determinations. Statistical testing used 2-Way-ANOVA with Dunnett's multi-comparison correction for panels **(A,E)**, and 1-Way ANOVA (Holm-Sidak correction) for all other panels. *$p < 0.05$, **$p < 0.01$, ***$p < 0.001$, ****$p < 0.0001$. Only statistically significant comparisons are shown. In panel **(C)**, *A. pleuropneumoniae*, the 30 min and 90 min comparisons had *p*-values of 0.0509, i.e., were close to being significant.

HiDmsABC is not only able to convert S-oxides but is also highly specific for several biologically relevant N-oxide molecules

Our data so far indicate that DmsABC is important for full virulence of *H. influenzae*, with strong phenotypes observed only during infection. This strongly suggests that the substrate that DmsABC converts is only available during contact with host cells. As the enzyme is produced in the presence of hypochlorite and paraquat-mediated stress, the natural substrate could be an oxidatively damaged biomolecule. To better understand the catalytic properties of HiDmsABC, we used cell extracts of the MtsZ negative Hi86-028NP wildtype strain that has high S-oxide reductase activity (Figures 3D,E). Initial experiments used the artificial substrate Methyl-p-tolyl-sulfoxide (MPTS) to determine the HiDmsABC stereospecificity. Activity with racemic RS-MPTS was 2.23 U/mg, while R- and S-MPTS resulted in 1.86 U/mg and 0.54 U/mg of activity (Figure 5A). This confirmed that, like its *E. coli* counterpart (SimalaGrant and Weiner, 1996), HiDmsABC is specific for R-sulfoxides and thus has the opposite stereospecificity to HiMtsZ, which is an S-sulfoxide-specific enzyme (Dhouib et al., 2016). We then tested HiDmsABC activity with different S- and N-oxides that could occur in the human respiratory tract and

10.3389/fmicb.2024.1359513

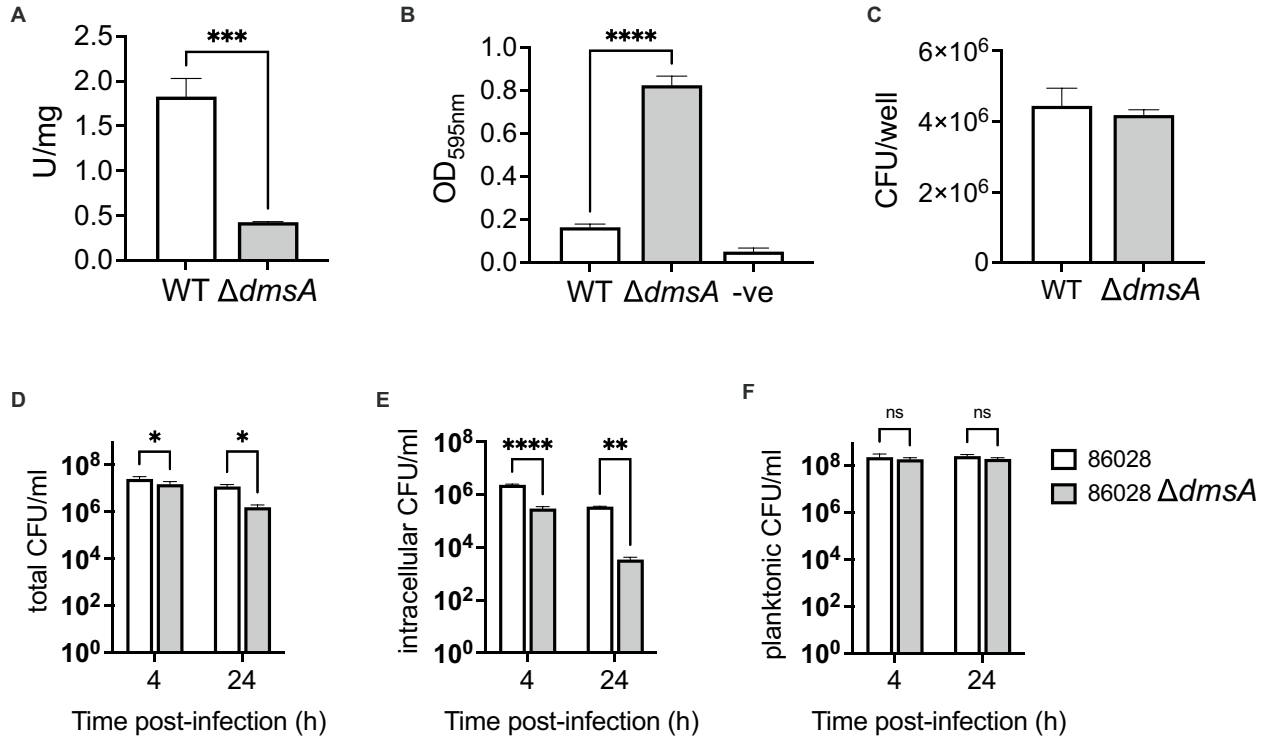

FIGURE 4
Properties of *H. influenzae* 86-028NP^{WT} and 86-028NP$^{\Delta dmsA}$ strains. **(A)** S-oxide reductase activity in *H. influenzae* 86-028NP^{WT} and 86-028NP$^{\Delta dmsA}$. **(B)** Biofilm formation in *H. influenzae* 86-028NP^{WT} and 86-028NP$^{\Delta dmsA}$ in 96-well plates under microaerobic conditions. Control wells (–ve) only contained sterile growth medium. Biofilms were stained using crystal violet. **(C)** Bacterial CFU/mL recovered from *H. influenzae* 86-028NP^{WT} and 86-028NP$^{\Delta dmsA}$ biofilms using protein K digestion. **(D–F)** Total, intracellular and planktonic CFU/mL recovered during infection of 16HBE14 human bronchial epithelial cells with either *H. influenzae* 86-028NP^{WT} or 86-028NP$^{\Delta dmsA}$ for 4h or 24h. Panel **(A)** shows representative averages and standard deviation from three independent assays, data in panels **(B–F)** are averages and standard deviations of data from three biological replicates. Statistical analyses **(A–C)**: unpaired *t*-tests, two-tailed; **(D–F)**: 2-Way ANOVA, Sidaks multiple comparison correction, *p<0.05, **p<0.01, ****p<0.0001.

DMSO as a control substrate. HiDmsABC easily converted L-methionine S/R sulfoxide, nicotinamide-N-oxide, pyrimidine-N-oxide and can also catalyze reduction of adenine-N-1-oxide, while S-Biotin Sulfoxide was not converted and was not investigated further (Figure 5B). As expected, due to the higher reactivity of N-oxides compared to S-oxides, DmsABC activities were highest with nicotinamide-N-oxide and pyrimidine-N-oxide (~4 U/mg), but interestingly, the K_M-values for both substrates were in the low micromolar ranges with 32 ± 13 μM, and 76 ± 17 μM, and were, in fact, in a similar range as the K_M-value for L-methionine S/R sulfoxide (35 ± 9 μM) (Figures 5C–E). These catalytic parameters make all three compounds excellent candidates as natural DmsABC substrates. In contrast, adenine-N-1 oxide had a K_M-value of 793 ± 138 μM, making it an unlikely natural substrate for DmsABC. Effective conversion of nicotinamide- and pyrimidine N-oxide by DmsABC has not previously been described but is an important discovery as *H. influenzae* is an auxotroph for both pyrimidine and NAD, for which nicotinamide is a precursor. With the exception of adenine-N-1-oxide, all K_M-values are not only within a concentration range that is highly likely to be physiologically relevant, but the K_M-value for L-methionine sulfoxide is also comparable to the value of 90 μM that has been previously reported for DmsABC from *E. coli* (SimalaGrant and Weiner, 1996).

DmsABC is an essential part of a novel, conserved defense against sulfoxide stress in *Haemophilus influenzae*

In addition to DmsABC, *H. influenzae* strains contain two other periplasmic sulfoxide reductases, the MtsZ methionine sulfoxide reductase and the MsrAB peptide methionine sulfoxide reductase (Dhouib et al., 2016; Nasreen et al., 2020, 2022). The three enzymes reduce either protein-bound methionine sulfoxide (MsrAB) or free S-/N-oxides (MtsZ, DmsABC), and their expression is upregulated when the bacteria are exposed to hypochlorite (Dhouib et al., 2016; Nasreen et al., 2020). We hypothesized that together, these three enzymes form a new system for protection of *H. influenzae* from oxidative stress, and to fully define the roles of these three methionine sulfoxide reductases in this process, we constructed *H. influenzae* 2019 double mutant strains that each lack two of the three S-oxide reductases.

S-oxide reductase activity assays were used to confirm the contribution of DmsA and MtsZ to the reduction of small-molecule S-oxides in the double mutant strains. As expected, double mutants that lacked MtsZ showed only very low levels of S-oxide reductase activity with both L-methionine sulfoxide and DMSO (Supplementary Figures S5A,B), with lowest activities observed for the

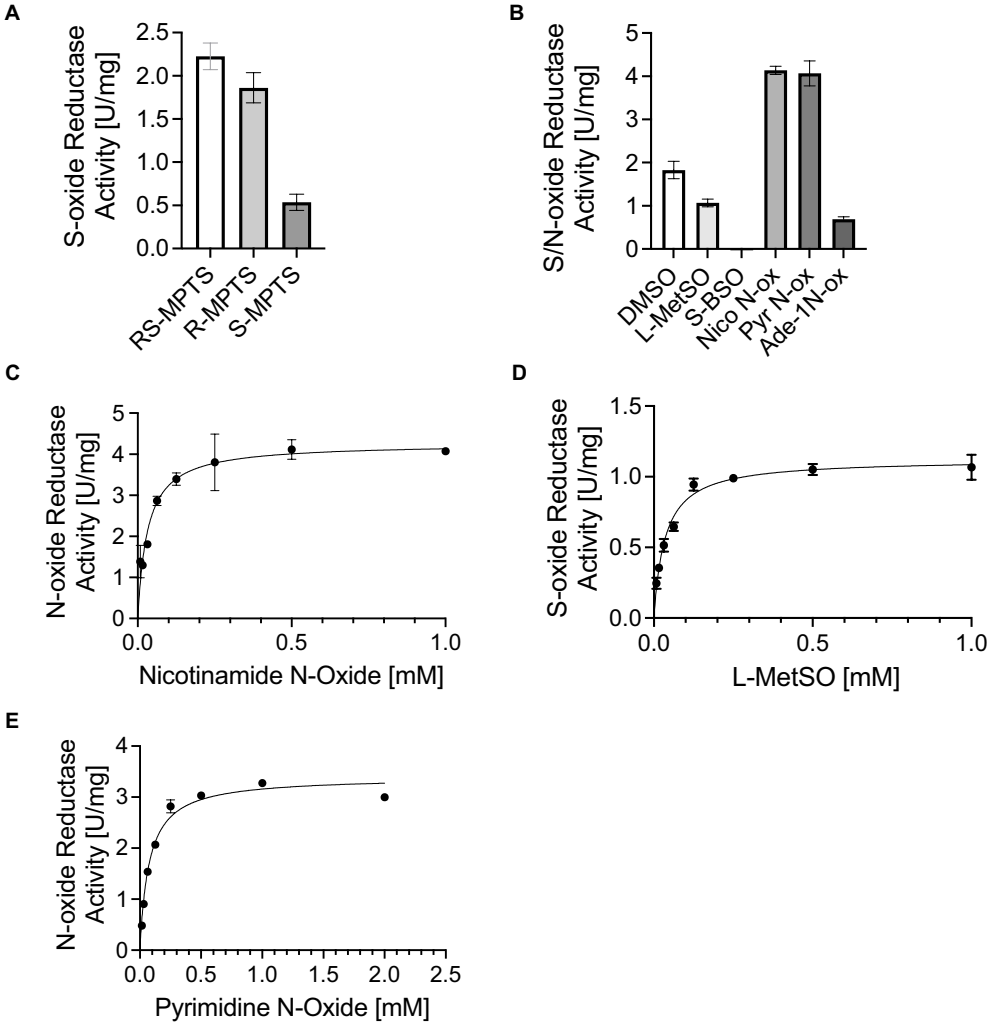

FIGURE 5
H. influenzae DmsABC S- and N-oxide reductase activity. **(A)** Stereospecificity of DmsABC S-oxide reductase activity. **(B)** S-and N-oxide reductase activity in cell extracts of anaerobically grown *H. influenzae* 86-028NP with various substrates. DMSO, dimethyl sulfoxide; L-MetSO, L-methionine (R/S) sulfoxide; S-BSO, S-biotin sulfoxide; Nico-N-ox, Nicotinamide-n-oxide; Pyr-N-ox, pyrimidine-N-oxide; Ade-1 N-ox, Adenine 1-N-oxide. **(C–E)** Substrate dependence of DmsABC activity in cell extracts of anaerobically grown *H. influenzae* 86-028NP with Nicotinamide-n-oxide, L-methionine sulfoxide and pyrimidine N-oxide. All data shown are averages and standard deviation of three independent assays.

Δ*dmsA*Δ*mtsZ* strain. Unexpectedly, the Δ*dmsA*Δ*msrAB* strain in which MtsZ is the only sulfoxide reductase showed about 35% reduced activity, which is about 4x more than expected based on the activity levels (7% of WT) detected in the Δ*msrAB*Δ*mtsZ* strain and could indicate some synergistic effects.

We then determined growth of the double mutant strains in the presence and absence of oxygen. Growth of all strains was very similar under microaerobic conditions. However, compared to the WT strain, strains carrying a *msrAB* gene knockout (Δ*dmsA*Δ*msrAB;* Δ*msrAB*Δ*mtsZ*) showed reduced growth under aerobic conditions, and interestingly, under anaerobic conditions, strains carrying a *dmsA* gene knockout (Δ*dmsA*Δ*msrAB;* Δ*dmsA*Δ*mtsZ*) showed reduced growth (Figures 6A–C; Supplementary Table S3). For the MsrAB sulfoxide reductase, a similar phenotype was already apparent in the single mutant strain. However, the *dmsA* single mutant strain did not show a reduced growth rate compared to the WT strain (Nasreen et al., 2020; Dhouib et al., 2021).

As all three enzymes have a role in oxidative stress responses, we also determined the sensitivity of the double mutant strains to oxidative stress caused by hydrogen peroxide or the two reactive chlorine species, HOCl or N-Chlorotaurine (NCT). Compared to the WT strain, the double mutants showed a small but statistically significant increase in H_2O_2 sensitivity at high concentrations that are unlikely to be physiologically relevant. However, when the double mutant strains were exposed to HOCl, strains that lacked the *msrAB* gene were undetectable following exposure to both 150 and 175 μM HOCl, clearly linking the presence of *msrAB* to *H. influenzae* HOCl resistance (Figure 6D). We then tested resistance of the strains to another reactive chlorine species, N-Chlorotaurine (NCT), expecting to see a similar, but weaker phenotype as NCT is less reactive than HOCl. Following exposure to NCT, strains lacking the *msrAB* gene were again most strongly affected, however, reductions in CFU were more pronounced for the Δ*msrAB*Δ*mtsZ* strain, where a 10^6-fold decrease in CFU/ml relative

to the wildtype strains was observed at concentrations of both 1 mM and 1.5 mM NCT, compared to 10^4- and 10^5-fold reductions for Δ*dmsA*Δ*msrAB*. Unexpectedly, attenuation was also observed for the Δ*dmsA*Δ*mtsZ* strain that was unaffected by HOCl exposure but showed a ~ 600- and 10^4-fold reduction in CFU/ml at 1 mM and 1.5 mM NCT (Figure 6E). These changes in attenuation demonstrate that while MsrAB is the most important enzyme for defense against RCS-induced stress, the two Mo-containing S-oxide reductases, and particularly MtsZ, also contribute to NTHi survival during NCT stress.

The presence and absence of *Haemophilus influenzae* S-oxide reductases alters biofilm formation profiles

Biofilm formation is a typical bacterial response to cellular stress, and in *H. influenzae,* biofilm formation has been linked to colonization of host cells and tissues. Under microaerobic conditions, two of the three mutant strains showed altered biofilm formation. The Δ*dmsA*Δ*msrAB* mutant strain, in which MtsZ is the only sulfoxide reductase, showed a ~ 50% reduction in biofilm formation relative to the wild type. In contrast, in the Δ*msrAB*Δ*mtsZ* strain, where DmsABC is the only sulfoxide reductase, biofilm formation was increased ~2-fold (Figure 6F). The third mutant strain, Δ*dmsA*Δ*mtsZ*, showed wildtype levels of biofilm formation.

The link between the presence and absence of these Mo-containing S-oxide reductases and biofilm formation is currently unknown but warrants further investigation. It is intriguing that when present as the sole S-/N-oxide reductases, MtsZ and DmsABC appear to have opposing effects on biofilm formation.

DmsABC is required for successful invasion of tissue cells

To assess the impact of the double mutants on *H. influenzae* virulence, we infected 16HBE14 cultured bronchial epithelial cells with either the WT or one of the mutant strains. At 4 h post-infection, the mutant strains showed modest reductions in total cell numbers of 12% (Δ*dmsA*Δ*mtsZ*), 21% (Δ*dmsA*Δ*msrAB*) and 24% (Δ*msrAB*Δ*mtsZ*) (Figures 6G,H; Supplementary Figure S6). However, clear differences existed for intracellular populations, which were reduced by 60 and 70% for Δ*dmsA*Δ*msrAB* and Δ*dmsA*Δ*mtsZ*, while for the Δ*msrAB*Δ*mtsZ* mutant, only a modest reduction of intracellular bacteria by 20% compared to the WT was observed. By 24 h, CFUs for all strains had increased, and all mutant strains showed ~40% reduction in total cell numbers compared to the WT. Intracellular cell numbers, however, showed the same trends as at 4 h, with the greatest reductions seen for the *dmsA*Δ*mtsZ* mutant (30% reduction), while the Δ*msrAB*Δ*mtsZ* strain was, again, the least affected (20% reduction) (Figures 6G,H; Supplementary Figure S6). Together, the data indicate that MsrAB (Δ*dmsA*Δ*mtsZ* strain) is not required for invasion of tissue cells but may affect extracellular survival of *H. influenzae*. In contrast, the two Mo-containing S-/N-oxide reductases are required for intracellular survival. Of the two enzymes, DmsABC had the greatest impact on tissue cell invasion, while MtsZ contributed to invasion but was less critical than DmsABC, as documented by the reduction of bacterial populations in the Δ*dmsA*Δ*msrAB* strain.

Discussion

Haemophilus influenzae strains are known for their ability to withstand oxidative stress, which is part of their success as host-adapted human pathogens. The bacterial cell envelope is the area where host-produced stressors such as hydrogen peroxide, hypochlorite and others first impact the bacterial cell. While several oxidative stress defense systems have been previously described in *H. influenzae*, the relevant enzymes, such as peroxiredoxin, catalase and superoxide dismutase, are located in the *H. influenzae* cytoplasm (Harrison et al., 2007, 2012, 2015; Pang et al., 2012). Additionally, these known *H. influenzae* oxidative stress responses were mostly identified using exposure of the bacteria to hydrogen peroxide (Harrison et al., 2007; Wong et al., 2007).

Here, we have characterized a novel, extracellular stress defense system in *H. influenzae* that is composed of two types of sulfoxide reductases, the peptide methionine sulfoxide reductase MsrAB and the two molybdenum-dependent S-oxide reductases DmsABC and MtsZ (Figure 7). Expression of all three enzymes increased in the presence of reactive chlorine species (RCS), but also superoxide-producing compounds such as paraquat. While hypochlorite-induced gene expression had been previously demonstrated for MsrAB and MtsZ, this is the first time that specific inducers of gene expression have been identified for DmsABC. To date, the only regulators that have been shown to modulate expression of DmsABC in bacteria are the Fumarate and Nitrate Reductase regulator (FNR) that controls gene expression in response to anaerobiosis, and the ModE molybdate responsive regulator (McNicholas et al., 1998; Bearson et al., 2002; Harrington et al., 2009). Both of these control gene expression in response to very general conditions that may be frequently encountered by bacteria and specific inducers of *dmsABC* expression had so far not been identified. However, in *E. coli*, nitrate can act as a specific repressor of *dmsABC* expression (Bearson et al., 2002). The induction of *H. influenzae msrAB*, *mtsZ*, and *dmsABC* by reactive oxygen and chlorine species known to be produced by the human immune system documents a novel link between especially the two molybdo-enzymes, MtsZ and DmsABC, and protection from oxidative stress during infection. Traditionally, this type of enzyme has been associated with bacterial energy generation under anaerobic conditions as catalysis uses quinols that mediate electron transfer between respiratory chain complexes as the electron donors (Kappler and Schaefer, 2014; Kappler et al., 2019). At present, only a single hypochlorite-responsive regulator, the RpoE2 extracytoplasmic function—sigma factor, has been identified in *H. influenzae* (Nasreen et al., 2021), and this regulator might mediate the hypochlorite-based induction of *dmsABC* expression.

Although MsrAB, MtsZ, and DmsABC are all induced following exposure of the bacteria to RCS and ROS, the functions of these enzymes in protecting *H. influenzae* from RCS/ROS stress are distinct (Figure 7). Our experiments using S-oxide reductase double mutant strains demonstrate that MsrAB mediates resistance to RCS-killing, likely by repairing oxidative damage to a range of periplasmic and outer membrane proteins that we characterized previously (Nasreen

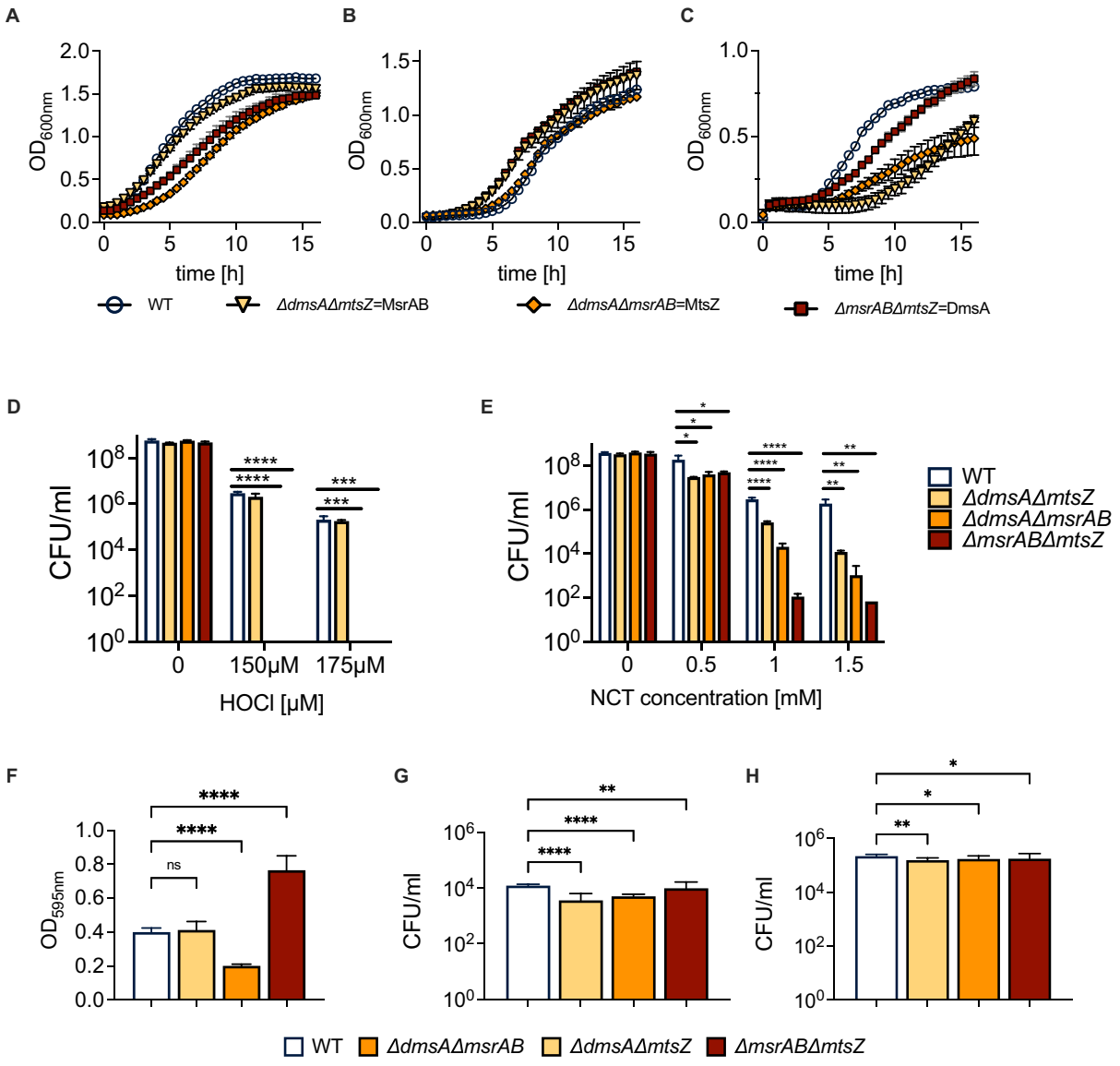

FIGURE 6
Properties of *H. influenzae* S-oxide reductase double mutant strains. **(A–C)** Growth of *H. influenzae* 2019 S-oxide reductase double mutants under aerobic, microaerobic and anaerobic conditions on Chemically Defined Medium (CDM). **(D,E)** Susceptibility of Hi2019 S-oxide reductase double mutants to exposure to HOCl (D) or N-Chlorotaurine **(E)** for 60 min. **(F)** Biofilm formation in Hi2019 S-oxide reductase double mutants in 96-well plates under microaerobic conditions. **(G,H)** Intracellular bacterial CFU/ml following 4 h **(G)** and 24 h **(H)** infection of 16HBE14 bronchial epithelial tissue cells with Hi2019 S-oxide reductase double mutants. All data shown are averages and standard deviations of at least three biological replicates. Statistical analyses **(D,E,G,H)**: 2-Way ANOVA, Dunnett's multiple comparison correction, $*p < 0.05$, $**p < 0.01$, $****p < 0.0001$. **(F)**: 1-Way ANOVA, Dunnett's multiple comparison correction, $****p < 0.0001$.

et al., 2020, 2022). Additionally, MsrAB is also involved in host immunomodulatory activities during *H. influenzae* infections (Nasreen et al., 2020) (Figure 7). Conversely, the two Mo-dependent S/N-oxide reductases, MtsZ and DmsABC, appear to be involved in repairing damage to small molecule S- and N-oxides, and there is some functional redundancy (Dhouib et al., 2016, 2021; Struwe et al., 2021). The double mutant studies showed that both enzymes have a similar functional profile during host interactions, where they are required for efficient colonization of the intracellular environment. Interestingly, our single mutant studies also revealed that in mouse infections, the Hi2019$^{\Delta dmsA}$ strain was less immunogenic and elicited a reduced cytokine response that led to lower numbers of immune cells detected in BALF samples. The reason for this reduced immunogenicity is currently unclear as DmsABC is located in the periplasmic space and thus should not be surface-exposed. We have, however, previously observed a similar effect in Hi2019 strains lacking a membrane-associated enzyme required for energy generation from lactate (Hosmer et al., 2022), and propose that a possible explanation for the reduced immunogenicity in both of these strains might be a sub-optimal use of the metabolic network and lack of redox balancing in these strains. DmsABC and MtsZ also played a minor role in resistance to stressors such as NCT. *H. influenzae* strains lacking either of these enzymes only exhibited pronounced phenotypes during host colonization. DmsABC mutant strains had a much more pronounced

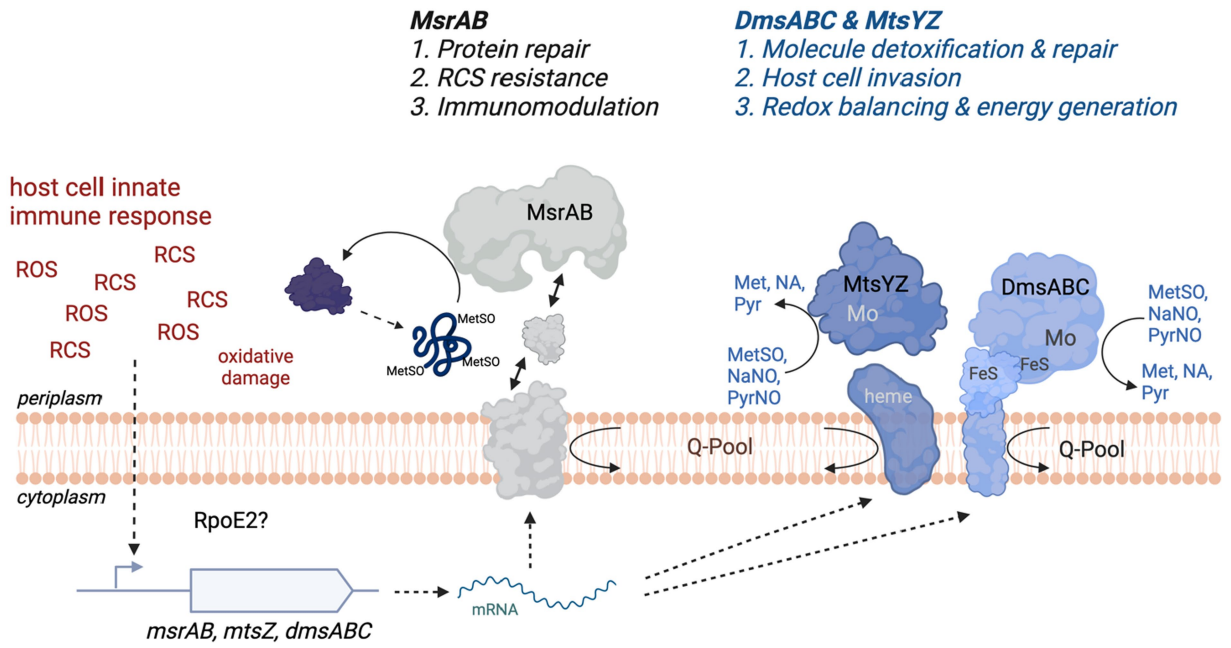

FIGURE 7
Schematic Representation of the function of the S-/N-oxide damage repair system in *H. influenzae*. FeS, iron sulfur cluster; Met, methionine; MetSO, methionine sulfoxide; Mo, molybdenum active site of MtsZ and DmsABC; NA, nicotinamide; NaNO, Nicotinamide-N-oxide; Pyr, pyrimidine; PyrNO, pyrimidine-N-oxide; RCS, Reactive Chlorine Species such as HOCl or N-Chlorotaurine; ROS, Reactive Oxygen Species such as hydrogen peroxide and superoxide; Q-Pool, cellular quinone pool. Figure created with BioRender.com.

phenotype, indicating that this enzyme is more important for *H. influenzae* survival in contact with host cells. In keeping with the greater importance of DmsABC, MtsZ is absent in about 20% of *H. influenzae* strains, while DmsABC, like MsrAB, is strictly conserved in all strains. Our data show that in *H. influenzae* strains that lack MtsZ, phenotypes generated by a *dmsA* gene knockout are more pronounced (Figure 4), supporting the functional redundancy of the two enzymes.

An interesting, yet so far not fully resolved question is what substrates are converted by the Mo-containing S-oxide reductases during contact with the host where they are required for *H. influenzae* survival. Using a selection of biologically relevant S- and N-oxides that could occur at sites of infection where high levels of oxidizing compounds are present (Ulfig and Leichert, 2021), we have shown here that DmsABC converts not only methionine sulfoxide but also nicotinamide- and pyrimidine-N-oxides with great efficiency and K_M-values that are in the physiological range. This is significant, as nicotinamide is a precursor for NAD, for which *H. influenzae* is an auxotroph, and can be converted to NAD via the actions of DeoD, NadN, SurE and NadR. Similarly, *H. influenzae* strains are pyrimidine auxotrophs and rely on pyrimidine salvage to meet cellular pyrimidine requirements (Tatusov et al., 1996). We had previously established that MtsZ, like DmsABC, is an efficient methionine sulfoxide reductase [9; 25], and kinetic analyses with nicotinamide- and pyrimidine-N-oxide as substrates revealed that MtsZ also converts both of these substrates with high specificity (Nicotinamide-N-oxide: K_M: $46 \pm 8\,\mu M$, k_{cat}: $93 \pm 5\,s^{-1}$; Pyrimidine-N-oxide: K_M: $35 \pm 8\,\mu M$, k_{cat}: $33.2 \pm 2.7\,s^{-1}$) (Supplementary Figure S7). Despite the similarities in catalytic profiles, an interesting difference between MtsZ and DmsABC is their opposing stereospecificity (Dhouib et al., 2016; Struwe et al., 2021), which, however, does not appear to affect their ability to fulfill similar physiological roles. We propose that this could be due to the non-chiral nature of the reaction products produced by these enzymes from chiral precursors such as S-oxides, where the final product is the same regardless of the configuration of the substrate molecule.

Lastly, our discovery of the physiological role of *H. influenzae* DmsABC as a major enzyme in host interactions rather than an enzyme mediating anaerobic respiration with DMSO, suggests that the latter role may be an artifact and have little relevance under physiological conditions for *H. influenzae*, i.e., during contact with host respiratory epithelia. Based on our results, we propose that homologs of DmsABC that exist in many pathogenic and commensal bacteria, including in *E. coli,* may, in fact, in most cases, underpin successful host colonization rather than anaerobic respiration with DMSO. As DMSO is a molecule that may occur in some aquatic environments, but generally does not occur in significant amounts in vertebrate bodies, the physiological role of DmsABC in *E. coli* where DMSO respiration is the accepted role should be reinvestigated (Sambasivarao and Weiner, 1991; Kappler and Schaefer, 2014). Our proposal is supported by studies in *Actinobacillus pleuropneumoniae* and *Salmonella enterica* that also identified DmsABC and homologous enzymes as essential for virulence (Baltes et al., 2003; Cruz et al., 2023). If the universality of this role and the interplay between peptide methionine sulfoxide reductases such as MsrAB and Mo-containing S-oxide reductases could be demonstrated, this would make these two classes of enzymes attractive, bacteria-specific drug targets.

Data availability statement

The original contributions presented in the study are included in the article/Supplementary material, further inquiries can be directed to the corresponding author.

Ethics statement

The studies involving humans were approved by University of Queensland Ethics Committee (Approvals #2017000520, 2021/HE001644, 2014/HE000067). The studies were conducted in accordance with the local legislation and institutional requirements. The participants provided their written informed consent to participate in this study. The animal study was approved by the Animal Care and Ethics Committees of QIMR Berghofer and the University of Queensland (QIMR/050/19). The study was conducted in accordance with the local legislation and institutional requirements.

Author contributions

MN: Writing – review & editing, Writing – original draft, Visualization, Methodology, Investigation, Formal Analysis. DE: Writing – review & editing, Visualization, Methodology, Investigation. JH: Writing – review & editing, Visualization, Methodology, Investigation, Formal Analysis. A-TE: Writing – review & editing, Supervision, Project administration, Methodology, Investigation. EF: Writing – review & editing, Supervision, Methodology, Investigation, Formal Analysis. PS: Writing – review & editing, Supervision, Methodology. AM: Writing – review & editing, Supervision, Project administration, Funding acquisition. UK: Writing – review & editing, Writing – original draft, Visualization, Supervision, Project administration, Funding acquisition, Conceptualization.

Funding

The author(s) declare that financial support was received for the research, authorship, and/or publication of this article. This work was supported by a project grant (GNT1158451) from the National Health and Medical Research Council (NHMRC) Australia to UK and AM. Seed funding for studies using normal human nasal epithelia was provided by the Australian Infectious Diseases Research Centre (AID).

Acknowledgments

We thank Prof. Avril Robertson for making N-Chlorotaurine (The University of Queensland) available to us for this study and Prof. Paul V. Bernhardt (The University of Queensland) for supplying S-BSO and Ade-1N-oxide.

Conflict of interest

The authors declare that the research was conducted in the absence of any commercial or financial relationships that could be construed as a potential conflict of interest.

The author(s) declared that they were an editorial board member of Frontiers, at the time of submission. This had no impact on the peer review process and the final decision.

Publisher's note

Supplementary material

The Supplementary material for this article can be found online at: https://www.frontiersin.org/articles/10.3389/fmicb.2024.1359513/full#supplementary-material

References

Ahearn, C. P., Gallo, M. C., and Murphy, T. F. (2017). Insights on persistent airway infection by non-typeable *Haemophilus influenzae* in chronic obstructive pulmonary disease. *Pathog. Dis.* 75:ftx042. doi: 10.1093/femspd/ftx042

Ausubel, F. M., Brent, R., Kingston, R. E., Moore, D. D., Seidman, J. G., Smith, J. A., et al. (2005). "Current protocols in molecular biology" in *Current protocols in molecular biology*. ed. K. Janssen (Hoboken, NJ: John Wiley & Sons Inc.)

Bakaletz, L. O., Tallan, B. M., Andrzejewski, W. J., DeMaria, T. F., and Lim, D. J. (1989). Immunological responsiveness of chinchillas to outer membrane and isolated fimbrial proteins of nontypeable *Haemophilus influenzae*. *Infect. Immun.* 57, 3226–3229. doi: 10.1128/iai.57.10.3226-3229.1989

Baltes, N., Hennig-Pauka, I., Jacobsen, I., Gruber, A. D., and Gerlach, G. F. (2003). Identification of dimethyl sulfoxide reductase in *Actinobacillus pleuropneumoniae* and its role in infection. *Infect. Immun.* 71, 6784–6792. doi: 10.1128/IAI.71.12.6784-6792.2003

Bearson, S. M., Albrecht, J. A., and Gunsalus, R. P. (2002). Oxygen and nitrate-dependent regulation of *dmsABC* operon expression in *Escherichia coli*: sites for Fnr and NarL protein interactions. *BMC Microbiol.* 2:13. doi: 10.1186/1471-2180-2-13

Campagnari, A. A., Gupta, M. R., Dudas, K. C., Murphy, T. F., and Apicella, M. A. (1987). Antigenic diversity of lipooligosaccharides of nontypable *Haemophilus influenzae*. *Infect. Immun.* 55, 882–887. doi: 10.1128/iai.55.4.882-887.1987

Coleman, H. N., Daines, D. A., Jarisch, J., and Smith, A. L. (2003). Chemically defined media for growth of *Haemophilus influenzae* strains. *J. Clin. Microbiol.* 41, 4408–4410. doi: 10.1128/JCM.41.9.4408-4410.2003

Cruz, E., Haeberle, A. L., Westerman, T. L., Durham, M. E., Suyemoto, M. M., Knodler, L. A., et al. (2023). Nonredundant dimethyl sulfoxide reductases influence *Salmonella enterica* serotype typhimurium anaerobic growth and virulence. *Infect. Immun.* 91, e00578–e00522. doi: 10.1128/iai.00578-22

da Cruz Nizer, W. S., Inkovskiy, V., and Overhage, J. (2020). Surviving reactive chlorine stress: responses of gram-negative Bacteria to Hypochlorous acid. *Microorganisms* 8:1220. doi: 10.3390/microorganisms8081220

Denkel, L. A., Rhen, M., and Bange, F.-C. (2013). Biotin sulfoxide reductase contributes to oxidative stress tolerance and virulence in *Salmonella enterica* serovar typhimurium. *Microbiology* 159, 1447–1458. doi: 10.1099/mic.0.067256-0

Dhouib, R., Nasreen, M., Othman, D., Ellis, D., Lee, S., Essilfie, A. T., et al. (2021). The DmsABC sulfoxide reductase supports virulence in non-typeable *Haemophilus influenzae*. *Front. Microbiol.* 12:686833. doi: 10.3389/fmicb.2021.686833

Dhouib, R., Othman, D., Essilfie, A. T., Hansbro, P. M., Hanson, J. O., McEwan, A. G., et al. (2015). Maturation of molybdoenzymes and its influence on the pathogenesis of

non-typeable *Haemophilus influenzae*. *Front. Microbiol.* 6:e01219. doi: 10.3389/fmicb.2015.01219

Dhouib, R., Othman, D. S. M. P., Lin, V., Lai, X. J., Wijesinghe, H. G. S., Essilfie, A.-T., et al. (2016). A novel, molybdenum-containing methionine sulfoxide reductase supports survival of *Haemophilus influenzae* in an *in vivo* model of infection. *Front. Microbiol.* 7:e1743. doi: 10.3389/fmicb.2016.01743

Dickie, P., and Weiner, J. H. (1979). Purification and characterization of membrane-bound fumarate reductase from anaerobically grown *Escherichia coli*. *Can. J. Biochem.* 57, 813–821. doi: 10.1139/o79-101

Essilfie, A. T., Simpson, J. L., Dunkley, M. L., Morgan, L. C., Oliver, B. G., Gibson, P. G., et al. (2012). Combined *Haemophilus influenzae* respiratory infection and allergic airways disease drives chronic infection and features of neutrophilic asthma. *Thorax* 67, 588–599. doi: 10.1136/thoraxjnl-2011-200160

Ezraty, B., Gennaris, A., Barras, F., and Collet, J.-F. (2017). Oxidative stress, protein damage and repair in bacteria. *Nat. Rev. Microbiol.* 15, 385–396. doi: 10.1038/nrmicro.2017.26

Gottardi, W., and Nagl, M. (2010). N-chlorotaurine, a natural antiseptic with outstanding tolerability. *J. Antimicrob. Chemother.* 65, 399–409. doi: 10.1093/jac/dkp466

Gout, I. (2019). Coenzyme a: a protective thiol in bacterial antioxidant defence. *Biochem. Soc. Trans.* 47, 469–476. doi: 10.1042/BST20180415

Hall, B. G., Acar, H., Nandipati, A., and Barlow, M. (2013). Growth rates made easy. *Mol. Biol. Evol.* 31, 232–238. doi: 10.1093/molbev/mst187

Harrington, J. C., Wong, S. M. S., Rosadini, C. V., Garifulin, O., Boyartchuk, V., and Akerley, B. J. (2009). Resistance of *Haemophilus influenzae* to reactive nitrogen donors and gamma interferon-stimulated macrophages requires the Formate-dependent nitrite reductase regulator-activated *ytfE* gene. *Infect. Immun.* 77, 1945–1958. doi: 10.1128/IAI.01365-08

Harrison, A., Bakaletz, L. O., and Munson, R. S. (2012). *Haemophilus influenzae* and oxidative stress. *Front. Cell. Infect. Microbiol.* 2:40. doi: 10.3389/fcimb.2012.00040

Harrison, A., Baker, B. D., and Munson, R. S. (2015). Overlapping and complementary oxidative stress defense mechanisms in Nontypeable *Haemophilus influenzae*. *J. Bacteriol.* 197, 277–285. doi: 10.1128/JB.01973-14

Harrison, A., Ray, W. C., Baker, B. D., Armbruster, D. W., Bakaletz, L. O., and Munson, R. S. (2007). The OxyR regulon in Nontypeable *Haemophilus influenzae*. *J. Bacteriol.* 189, 1004–1012. doi: 10.1128/JB.01040-06

Hosmer, J., Nasreen, M., Dhouib, R., Essilfie, A.-T., Schirra, H. J., Henningham, A., et al. (2022). Access to highly specialized growth substrates and production of epithelial immunomodulatory metabolites determine survival of *Haemophilus influenzae* in human airway epithelial cells. *PLoS Pathog.* 18:e1010209. doi: 10.1371/journal.ppat.1010209

Kappler, U., Nasreen, M., and McEwan, A. (2019). New insights into the molecular physiology of sulfoxide reduction in bacteria. *Adv. Microb. Physiol.* 75, 1–51. doi: 10.1016/bs.ampbs.2019.05.001

Kappler, U., and Schaefer, H. (2014). "Conversions of dimethylsulfide" in *The metal-driven biogeochemistry of gaseous compounds in the environment*. eds. P. M. H. Kroneck and M. Sosa Torres (Cham: Springer International Publishing AG), 279–313.

Kappler, U., Sly, L. I., and McEwan, A. G. (2005). Respiratory gene clusters of *Metallosphaera sedula* - differential expression and transcriptional organization. *Microbiology* 151, 35–43. doi: 10.1099/mic.0.27515-0

King, P. (2012). *Haemophilus influenzae* and the lung (*Haemophilus* and the lung). *Clin. Transl. Med.* 1:10. doi: 10.1186/2001-1326-1-10

Kurokawa, M., and Ying, B. W. (2017). Ying, precise, high-throughput analysis of bacterial growth. *J. Vis. Exp.*:e56197. doi: 10.3791/56197-v

Langereis, J. D., and de Jonge, M. I. (2020). Unraveling *Haemophilus influenzae* virulence mechanisms enable discovery of new targets for antimicrobials and vaccines. *Curr. Opin. Infect. Dis.* 33, 231–237. doi: 10.1097/QCO.0000000000000645

Lansbury, L., Lim, B., Baskaran, V., and Lim, W. S. (2020). Co-infections in people with COVID-19: a systematic review and meta-analysis. *J. Infect.* 81, 266–275. doi: 10.1016/j.jinf.2020.05.046

López-López, N., Gil-Campillo, C., Díez-Martínez, R., and Garmendia, J. (2021). Learning from –omics strategies applied to uncover *Haemophilus influenzae* host-pathogen interactions: current status and perspectives. *Comput. Struct. Biotechnol. J.* 19, 3042–3050. doi: 10.1016/j.csbj.2021.05.026

McNicholas, P. M., Chiang, R. C., and Gunsalus, R. P. (1998). Anaerobic regulation of the *Escherichia coli dmsABC* operon requires the molybdate-responsive regulator ModE. *Mol. Microbiol.* 27, 197–208. doi: 10.1046/j.1365-2958.1998.00675.x

Morey, P., Viadas, C., Euba, B., Hood, D. W., Barberán, M., Gil, C., et al. (2013). Relative contributions of Lipooligosaccharide inner and outer Core modifications to Nontypeable *Haemophilus influenzae* pathogenesis. *Infect. Immun.* 81, 4100–4111. doi: 10.1128/IAI.00492-13

Nasreen, M., Dhouib, R., Hosmer, J., Wijesinghe, H. G. S., Fletcher, A., Mahawar, M., et al. (2020). Peptide methionine sulfoxide reductase from *Haemophilus influenzae* is required for protection against HOCl and affects the host response to infection. *ACS Infect. Dis.* 6, 1928–1939. doi: 10.1021/acsinfecdis.0c00242

Nasreen, M., Fletcher, A., Hosmer, J., Zhong, Q., Essilfie, A.-T., McEwan, A. G., et al. (2021). The alternative sigma factor RpoE2 is involved in the stress response to hypochlorite and *in vivo* survival of *Haemophilus influenzae*. *Front. Microbiol.* 12:637213. doi: 10.3389/fmicb.2021.637213

Nasreen, M., Nair, R. P., McEwan, A. G., and Kappler, U. (2022). The peptide methionine sulfoxide reductase (MsrAB) of *Haemophilus influenzae* repairs Oxidatively damaged outer membrane and periplasmic proteins involved in nutrient acquisition and virulence. *Antioxidants* 11:1557. doi: 10.3390/antiox11081557

Othman, D. S. M. P., Schirra, H. J., McEwan, A. G., and Kappler, U. (2014). Metabolic versatility in *Haemophilus influenzae*: a metabolomic and genomic analysis. *Front. Microbiol.* 5:69. doi: 10.3389/fmicb.2014.00069

Pang, B., Hong, W., Kock, N. D., and Swords, W. E. (2012). Dps promotes survival of nontypeable *Haemophilus influenzae* in biofilm communities *in vitro* and resistance to clearance *in vivo*. *Front. Cell. Infect. Microbiol.* 2:58. doi: 10.3389/fcimb.2012.00058

Pauwels, F., Vergauwen, B., and Van Beeumen, J. J. (2004). Physiological characterization of *Haemophilus influenzae* Rd deficient in its glutathione-dependent peroxidase PGdx. *J. Biol. Chem.* 279, 12163–12170. doi: 10.1074/jbc.M312037200

Pezzulo, A. A., Starner, T. D., Scheetz, T. E., Traver, G. L., Tilley, A. E., Harvey, B.-G., et al. (2011). The air-liquid interface and use of primary cell cultures are important to recapitulate the transcriptional profile of *in vivo* airway epithelia. *Am. J. Physiol. Lung Cell. Mol. Physiol.* 300, L25–L31. doi: 10.1152/ajplung.00256.2010

Poje, G., and Redfield, R. J. (2003). "Transformation of *Haemophilus influenzae*" in *Haemophilus influenzae protocols*. eds. M. A. Herbet, D. W. Hood and E. R. Moxon (Totowa, NJ: Humana Press), 57–70.

Ruijter, J. M., Ramakers, C., Hoogaars, W. M., Karlen, Y., Bakker, O., van den Hoff, M. J., et al. (2009). Amplification efficiency: linking baseline and bias in the analysis of quantitative PCR data. *Nucleic Acids Res.* 37:e45. doi: 10.1093/nar/gkp045

Saliu, F., Rizzo, G., Bragonzi, A., Cariani, L., Cirillo, D. M., Colombo, C., et al. (2021). Chronic infection by nontypeable *Haemophilus influenzae* fuels airway inflammation. *ERJ Open Res.* 7:00614-02020. doi: 10.1183/23120541.00614-2020

Sambasivarao, D., and Weiner, J. H. (1991). Dimethyl sulfoxide reductase of *Escherichia coli*: an investigation of function and assembly by use of *in vivo* complementation. *J. Bacteriol.* 173, 5935–5943. doi: 10.1128/jb.173.19.5935-5943.1991

Schembri, M. A., and Klemm, P. (2001). Biofilm formation in a hydrodynamic environment by novel FimH variants and ramifications for virulence. *Infect. Immun.* 69, 1322–1328. doi: 10.1128/IAI.69.3.1322-1328.2001

Short, B., Carson, S., Devlin, A.-C., Reihill, J. A., Crilly, A., MacKay, W., et al. (2021). Non-typeable *Haemophilus influenzae* chronic colonization in chronic obstructive pulmonary disease (COPD). *Crit. Rev. Microbiol.* 47, 192–205. doi: 10.1080/1040841X.2020.1863330

SimalaGrant, J. L., and Weiner, J. H. (1996). Kinetic analysis and substrate specificity of *Escherichia coli* dimethyl sulfoxide reductase. *Microbiology* 142, 3231–3239. doi: 10.1099/13500872-142-11-3231

Staerck, C., Gastebois, A., Vandeputte, P., Calenda, A., Larcher, G., Gillmann, L., et al. (2017). Microbial antioxidant defense enzymes. *Microb. Pathog.* 110, 56–65. doi: 10.1016/j.micpath.2017.06.015

Struwe, M. A., Kalimuthu, P., Luo, Z., Zhong, Q., Ellis, D., Yang, J., et al. (2021). Active site architecture reveals coordination sphere flexibility and specificity determinants in a group of closely related molybdoenzymes. *J. Biol. Chem.* 296:100672. doi: 10.1016/j.jbc.2021.100672

Tatusov, R. L., Mushegian, A. R., Bork, P., Brown, N. P., Hayes, W. S., Borodovsky, M., et al. (1996). Metabolism and evolution of *Haemophilus influenzae* deduced from a whole-genome comparison with *Escherichia coli*. *Curr. Biol.* 6, 279–291. doi: 10.1016/S0960-9822(02)00478-5

Tufvesson, E., Bjermer, L., and Ekberg, M. (2015). Patients with chronic obstructive pulmonary disease and chronically colonized with *Haemophilus influenzae* during stable disease phase have increased airway inflammation. *Int. J. Chron. Obstruct. Pulmon. Dis.* 10, 881–889. doi: 10.2147/COPD.S78748

Tushinski, R. J., Oliver, I. T., Guilbert, L. J., Tynan, P. W., Warner, J. R., and Stanley, E. R. (1982). Survival of mononuclear phagocytes depends on a lineage-specific growth factor that the differentiated cells selectively destroy. *Cell* 28, 71–81. doi: 10.1016/0092-8674(82)90376-2

Ulfig, A., and Leichert, L. I. (2021). The effects of neutrophil-generated hypochlorous acid and other hypohalous acids on host and pathogens. *Cell. Mol. Life Sci.* 78, 385–414. doi: 10.1007/s00018-020-03591-y

Van Eldere, J., Slack, M. P. E., Ladhani, S., and Cripps, A. W. (2014). Non-typeable *Haemophilus influenzae*, an under-recognised pathogen. *Lancet Infect. Dis.* 14, 1281–1292. doi: 10.1016/S1473-3099(14)70734-0

Watanabe, T., and Honda, K. (1982). Measurement of the extinction coefficient of the methyl viologen cation radical and the efficiency of its formation by semiconductor photocatalysis. *J. Phys. Chem.* 86, 2617–2619. doi: 10.1021/j100211a014

Wen, S., Feng, D., Chen, D., Yang, L., and Xu, Z. (2020). Molecular epidemiology and evolution of *Haemophilus influenzae*. *Infect. Genet. Evol.* 80:104205. doi: 10.1016/j.meegid.2020.104205

Wong, S. M. S., Alugupalli, K. R., Ram, S., and Akerley, B. J. (2007). The ArcA regulon and oxidative stress resistance in *Haemophilus influenzae*. *Mol. Microbiol.* 64, 1375–1390. doi: 10.1111/j.1365-2958.2007.05747.x

Yeo, A. J., Henningham, A., Fantino, E., Galbraith, S., Krause, L., Wainwright, C. E., et al. (2019). Increased susceptibility of airway epithelial cells from ataxia-telangiectasia to *S. pneumoniae* infection due to oxidative damage and impaired innate immunity. *Sci. Rep.* 9:2627. doi: 10.1038/s41598-019-38901-3

Zhong, Q., Kobe, B., and Kappler, U. (2020). Molybdenum enzymes and how they support virulence in pathogenic bacteria. *Front. Microbiol.* 11:615860. doi: 10.3389/fmicb.2020.615860

frontiers | Frontiers in Microbiology

TYPE Original Research
PUBLISHED 18 April 2024
DOI 10.3389/fmicb.2024.1373469

OPEN ACCESS

EDITED BY
Z. Petek Cakar,
Istanbul Technical University, Türkiye

REVIEWED BY
Vineet Kumar,
The University of Texas at Austin,
United States
Hee-Soo Park,
Kyungpook National University,
Republic of Korea
István Pócsi,
University of Debrecen, Hungary
Shuji Tani,
Osaka Metropolitan University, Japan

*CORRESPONDENCE
Celso Martins
✉ celso.martins@unil.ch
Cristina Silva Pereira
✉ spereira@itqb.unl.pt

†These authors have contributed equally to this work

‡PRESENT ADDRESSES
Celso Martins,
Center for Integrative Genomics,
Faculty of Biology and Medicine,
University of Lausanne,
Lausanne, Switzerland
Diego O. Hartmann,
Sea4Us – Biotecnologia e Recursos Marinhos S.A., Porto de Pesca da Baleeira,
Armazém 8, Sagres, Portugal

RECEIVED 19 January 2024
ACCEPTED 29 March 2024
PUBLISHED 18 April 2024

CITATION
Jorge JMP, Martins C, Domingos P, Martins TM, Hartmann DO, Goldman GH and Silva Pereira C (2024) *NmrB* (*AN9181*) expression is activated under oxidative stress conditions acting as a metabolic repressor of *Aspergillus nidulans*. *Front. Microbiol.* 15:1373469. doi: 10.3389/fmicb.2024.1373469

NmrB (*AN9181*) expression is activated under oxidative stress conditions acting as a metabolic repressor of *Aspergillus nidulans*

João M. P. Jorge[1†], Celso Martins[1*†‡], Patrícia Domingos[1], Tiago M. Martins[1], Diego O. Hartmann[1‡], Gustavo H. Goldman[1,2] and Cristina Silva Pereira[1*]

[1]Instituto de Tecnologia Química e Biológica António Xavier, NOVA University Lisbon, Av. da República, Oeiras, Portugal, [2]Faculdade de Ciências Farmacêuticas de Ribeirão Preto, Universidade de São Paulo, Ribeirão Preto, Brazil

Aspergilli comprise a diversity of species that have been extensively studied due to their catabolic diversity, biotechnological and ecological value, and pathogenicity. An impressive level of structural and functional conservation has been shown for aspergilli, regardless of many (yet) cryptic genomic elements. We have hypothesized the existence of conserved genes responsive to stress in aspergilli. To test the hypothesis of such conserved stress regulators in aspergilli, a straightforward computational strategy integrating well-established bioinformatic tools was used as the starting point. Specifically, five transcriptome-based datasets on exposure to organic compounds were used, covering three distinct *Aspergillus* species. Among the identified up-regulated genes, only one gene showed the same response in all conditions, *AN9181*. This gene encodes a protein containing a phenylcoumaran benzylic ether reductase-*like* domain and a Nitrogen metabolite repressor regulator domain (NmrA). Deletion of this gene caused significant phenotypic alterations compared to that of the parental strain across diverse conditions. Specifically, the deletion of *AN9181* raised the mutant's metabolic activity in different nitrogen sources. The acquired data supports that *AN9181* acts by repressing (slowing down) *A. nidulans* growth when exposed to aromatic compounds in a concentration dependent manner. The same phenotype was observed for amphotericin B. Finally, *AN9181* underwent differential upregulation under oxidative stress conditions. Collectively, the data suggest that *AN9181*, herein assigned as *NmrB* (Nitrogen Metabolite Repression Regulator B), builds up the genetic machinery of perception of oxidative stress by negatively regulating growth under such conditions.

KEYWORDS

organic chemicals, stress responses, transcriptomics, aspergilli, phenylcoumaran benzylic ether reductase-like domain (IPR045312), NmrA-like domain (IPR008030), global regulators, oxidative stress

1 Introduction

The aspergilli comprise a diverse group of saprophytic filamentous fungi covering over 200 million years of evolution (Galagan et al., 2005; Gupta et al., 2021) that are found virtually everywhere. Aspergilli have been extensively studied mostly due to high biotechnological value, for example *Aspergillus oryzae* and *A. niger* are used for the production of sake and citric

acid, respectively (Machida et al., 2008; Behera, 2020), and *A. terreus* was the first known producer of lovastatin, a cholesterol-lowering statin (Hajjaj et al., 2001; Pearce, 2019). Aspergilli are also important human pathogens, mainly *A. fumigatus*, which is the major causative agent of aspergillosis (Steenwyk et al., 2020). Recently, this species was included in the list of priority fungal pathogens published by the World Health Organization (World Health Organization, 2022). Despite the extensive knowledge already acquired about aspergilli genomes, many gene functions remain unknown or poorly understood (Galagan et al., 2005).

Fungi show great potential to degrade and/or mineralize various aromatic compounds, including environmental pollutants, a capacity mostly attributed to their impressive catabolic capabilities (Harms et al., 2011; Varela et al., 2015, 2017; Martins et al., 2019). Regardless of efficient degradation, a great stress is imposed; this has been linked to increased pathogenic potential of a fungal community (Martins et al., 2018) and to the production of virulent airborne spores from aspergilli strains in environments polluted with aromatic compounds (Martins et al., 2023). Earlier studies on the genome's structure and evolution in aspergilli revealed an impressive level of structural and functional conservation and synteny (Galagan et al., 2005; Steenwyk et al., 2020), both in coding and non-coding regions, regardless of evident evolutionary rearrangements. Taking the catabolism of aromatic compounds as an example, in the different available Dikarya genomes, the pathway gene clusters are found often in an array with the peripheral pathway genes (Martins et al., 2019). Such high level of genomic similarity in aspergilli, underlines the hypothesis of the existence of conserved regulatory genes responsive to variable chemical stresses (Galagan et al., 2005; Martins et al., 2019). In the present study, we integrated the transcriptome signatures of different aspergilli (three species) to distinct organic compounds, gathering original and publicly available datasets. To identify genes showing the same response across the different datasets, a straightforward computational strategy that allows comparing transcriptomic-based datasets initially collected in distinct *Aspergillus* species was used. Only one gene – *AN9181*, assigned as *NmrB* (Nitrogen Metabolite Repression Regulator B), showed the same response in all the datasets. The phenotype of *A. nidulans* single deletion-mutant Δ*AN9181* was compared to that of the wild type, covering for example germination fitness, growth rate and susceptibility to distinct chemical stressors. The collected data suggest that *NmrB* negatively regulates the metabolism of *A. nidulans* in specific stress conditions.

2 Materials and methods

2.1 Chemicals

Bromoquinol (BMQ) was purchased from Alfa Aesar; 6-iodoquinoline (IDQ) and resveratrol (RVT) from TCI Europe; hydrogen peroxide (H_2O_2) from Merck; dimethyl sulfoxide from Fisher Chemical, and the remaining compounds from Sigma Aldrich, namely pentachlorophenol (PCP), triclosan (TCS), salicylate (Sal), benzo[a]pyrene (BaP), congo red, sodium benzoate, menadione sodium bisulfite (MSB), amphotericin B (Amph B), caspofungin (CSP), itraconazole (ITZ), miconazole (Mic) and 2,7-dichlorofluorescin diacetate (DCFH-DA).

2.2 Transcriptomics analysis of *Aspergillus fumigatus* upon exposure to iodoquinoline

Aspergillus fumigatus CEA17 reference strain was propagated at 37°C in solid complete medium [1% D-glucose, 0.2% Peptone, 0.1% Yeast extract, 0.1% Casamino acids, 50 mL of a 20× salt solution, 0.1% trace elements, 0.1% Vitamin solution, 2% agar, pH 6.5 with NaOH]. The composition of the trace elements, vitamins, and nitrate salts has been described previously (Kafer, 1977).

The Minimal Inhibitory Concentration (MIC) for fungal growth inhibition of IDQ, initially acquired from The Pathogen Box (www.pathogenbox.org/), was defined following the standard methodology implemented by the Clinical and Laboratory Standards Institute (CLSI, 2018). The compound's antifungal activity was analyzed by serial dilutions using MIC assay (0 to 25 μM) in MOPS buffered RPMI 1640 medium (Sigma-Aldrich), pH 7.0 in 96-wells plates. In each well, a total of 1×10^4 conidia of *A. fumigatus* wild-type strain was inoculated. Plates were incubated at 37°C without shaking for 48 h. Non-inoculated controls were done in parallel. All experiments were done in triplicate.

The preparation of total RNA samples for RNA-seq Expression Profiling was as follows. Erlenmeyer flasks (125 mL) were used to inoculate 1×10^7 spores in 30 mL of Vogel's Minimal Media (Vogel, 1956) and incubated for 16 h at 37°C, 180 rpm. The medium was then exchanged, and 0, 0.5x MIC (=0.35 μM) or 2x MIC (=1.4 μM) of IDQ was added and incubated for 4 h at 37°C, 180 rpm. Six replicates for each condition were prepared. At the end of the incubation period, the cultures were filtered and frozen immediately in liquid nitrogen. Total RNA from six mycelia per condition were extracted using RNeasy Plant Mini Kit (Qiagen), according to the manufacturer's protocol, a TissueLyser LT (Qiagen) for cell disruption, and approximately 30 mg of poly(vinylpolypyrrolidone) per sample. RNA quality (integrity) was evaluated using a Nucleic Acid QC - Fragment Analyzer.

For single-end RNA sequencing (RNA-seq), libraries were generated using the Smart-Seq2® mRNA assay (Illumina, Inc.) according to the manufacturer's instructions. Six samples were indexed and sequenced on the Illumina NextSeq550 (20 M reads per sample). Generated FastQ files were analyzed with FastQC, and any low-quality reads were trimmed with Trimmomatic (20). All libraries were aligned to the corresponding model fungus *A. fumigatus* A1163 genome assembly (ASM15014v1) with gene annotations from Ensembl Fungi v. 45 using HISAT2 v. 2.1.0 (Kim et al., 2015), and only matches with the best score were reported for each read. All RNA-seq experiments were carried out in three biological replicates. Differential expression analysis was performed using DESeq2 v. 1.24.0 (Love et al., 2014). The genes that showed more than $\log_2$ 1-fold expression changes with *p-adj value* < 0.05 were considered as significantly differentially expressed (IDQ dataset in Supplementary Dataset 1).

2.3 Selection of transcriptomics datasets

The transcriptomics datasets were selected based on the following stringent rules: only studies on aspergilli were considered (i), comprising an exposure period lower than six days (ii) to an organic compound displaying broad environmental, biotechnological or health relevance (iii) with a molar mass below 500 g·mol^{-1}.

Consequently, we selected five transcriptome-based datasets: the catabolism of the simple aromatic hydrocarbon salicylate (Sal) in *A. nidulans* (Martins et al., 2021); the mode of action of the polyphenol resveratrol (RVT) in *A. flavus* (Wang et al., 2015); the degradation of the polycyclic aromatic hydrocarbon benzo[a]pyrene (BaP) in *Aspergillus* sp. (Loss et al., 2019); the inhibitory effects of the quinoline bromoquinol (BMQ) (Ben Yaakov et al., 2017) and of 6-iodoquinoline (IDQ) in *A. fumigatus* (see above). The full gene lists (up-regulated only) used in our analysis are available in Supplementary Dataset 2.

2.4 Comprehensive co-expression analysis

The COCOA strategy uses a set of established bioinformatics tools (Figure 1A) as detailed below. First, we performed the curation and validation of the five selected datasets by reprocessing the raw data to obtain the gene counts using the HISAT2 methodology (Kim et al., 2015) and identifying the differentially expressed genes using the *DESeq2* R-based package (Love et al., 2014). Then, a full protein-translated genome orthology transformation to *A. nidulans* (the "receiver species") was performed for eight distinct aspergilli available in the FungiDB database: *A. aculeatus* ATCC16872, *A. flavus* NRRL3357, *A. fumigatus* A1163, *A. nidulans* FGSCA4, *A. niger* ATCC13496, *A. sydowii* CBS593.65, *A. terreus* NIH2624, and *A. versicolor* CBS583.65 (Stajich et al., 2012). For the orthology analyzes, we used OrthoFinder (Emms and Kelly, 2015, 2017, 2019) because of its proven excellent performance compared to other orthology tools (Emms and Kelly, 2015). The use of these additional genomes than those strictly necessary adds robustness to the construction of gene trees, resulting in better discrimination and stringency levels between orthogroups (Emms and Kelly, 2015, 2017, 2019; Martins et al., 2020). We transposed the list of the up-regulated genes in the five datasets to the corresponding *A. nidulans* orthologues. After that, the co-expressed genes were identified using the online tool InteractiVenn (Heberle et al., 2015). Finally, we performed a whole-genome protein domain analysis for the protein-translated genome of the "receiver species," aiming to obtain hints on the putative functions played by the co-expressed genes, necessary when a functional annotation is lacking.

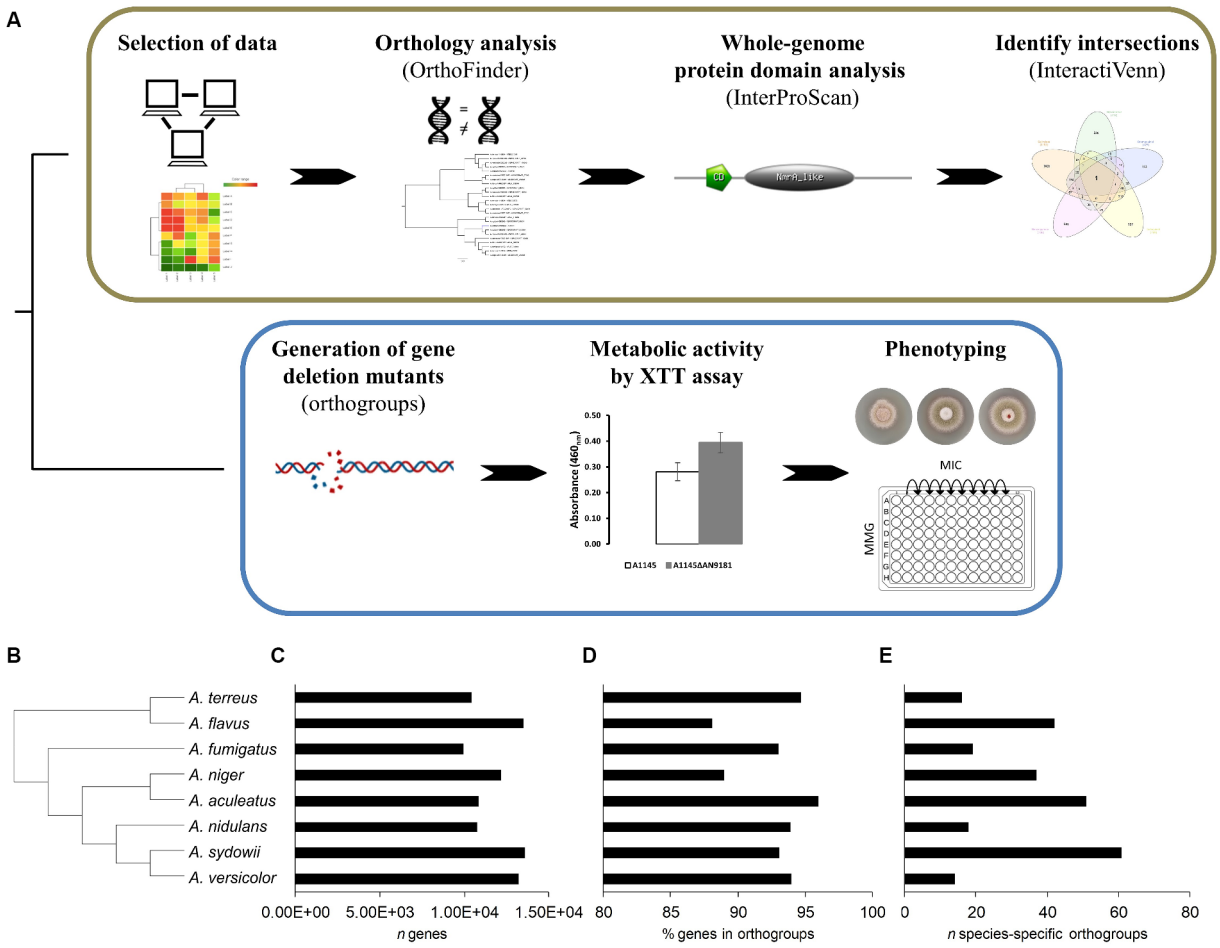

FIGURE 1
Schematic overview of the COmpregensive CO-expression Analysis (COCOA) strategy developed in this work. **(A)** – the iterative use of the well-established bioinformatics tools OrthoFinder, InterProScan and InteractiVenn upon selection of suitable and meaningful transcriptome-based datasets is displayed. Laboratory assays implemented to understand the biological relevance of the gene identified by COCOA. Results of the orthology analysis performed using the genomes of eight *Aspergillus* spp. **(B)** – the species tree, **(C)** – the number of genes of each analyzed genome, **(D)** the percentage of genes in orthogroups and **(E)** the number (*n*) of species-specific orthogroups are depicted.

2.5 *Aspergillus nidulans* culture media

If not mentioned, assays used minimal medium with glucose (10 g·L^{-1}) and nitrate (MMGN), as follows: thiamine (0.01 g·L^{-1}), 5% (v/v) nitrate salts solution [$NaNO_3$ (120.0 g·L^{-1}), KCl (10.4 g·L^{-1}), $MgSO_4$·7H2O (10.4 g·L^{-1}) and KH_2PO_4 (30.4 g·L^{-1})], 0.1% (v/v) trace elements solution [$ZnSO_4$·7H2O (22.0 g·L^{-1}); H_3BO_3 (11.0 g·L^{-1}); $MnCl_2$·4H2O (5.0 g·L^{-1}); $FeSO_4$·7H2O (5.0 g·L^{-1}); $CoCl_2$·6H_2O (1.7 g·L^{-1}); $CuSO_4$·5H_2O (1.6 g·L^{-1}); Na_2MoO_4·2H_2O (1.5 g·L^{-1}), and Na_4EDTA (50.0 g·L^{-1})], and the pH was adjusted to 6.5 with NaOH. Whenever needed, the media was jellified with 1.5% agar (solid cultivation). The MMG is similar to that described above except that sodium nitrate was removed. Most functional assays used MMG supplemented or not with a defined amount of a N source as mentioned in the results section. Moreover, in all comparative assays of mutant versus parental strain, the medium was supplemented with the essential nutrients: uracil (1.12 g·L^{-1}), uridine (1.22 g·L^{-1}), riboflavin (2.5 mg·L^{-1}) and pyridoxine (0.05 mg·L^{-1}).

2.6 Half maximal effective concentration (EC_{50})

EC_{50} levels of each organic compound were assessed on basis of hyphal radial growth rate for the strain *A. nidulans* FGSC A4 grown in petri dishes (55 mm) containing the MMGN (jellified) and supplemented with either BaP (1.0–3.5 mM); BMQ (0.1–1.0 mM); Sal (75–400 mM); IDQ (0.002–1.0 mM); RVT (0.005–1.5 mM); or sodium benzoate (25–200 mM). Controls without the organic compounds were also made. The assay was carried out by inoculating 2×10^5 conidia into the center of the plate, and incubate at 30°C for 120 h. Radial growth of mycelia (colony diameter in cm) was measured using a Vernier caliper (error ± 0.05 mm). The plates that did not displayed visible growth were visualized under microscope to confirm growth inhibition. The EC_{50} values were calculated using the XLSTAT tool (Microsoft Excel) with the Gompertz model.

2.7 *Aspergillus nidulans* submerged cultures

For the targeted gene expression analysis of the two genes of the AN9181 orthogroup, *Aspergillus nidulans* (5×10^5 spores·mL^{-1}) was pre-grown during 24 h in 12-well plates (2 mL of MMGN per well) at 30°C with gentle agitation (100 rpm), in the dark. After the pre-growth phase, the selected organic compounds were added to the cultures at a defined concentration (Time 0). The concentrations used were as follows: 0.2 mM for BaP [similar to the concentration used by Loss et al. (2019)]; 0.5 mM for BMQ (half of the minimal inhibitory concentration described by Ben Yaakov et al. (2017); 0.3 mM for PCP (concentration previously tested before by Varela et al. (2017), and 0.2 mM for TCS to match the range used for the other organic compounds. For the gene expression analysis of *AN9181* in the presence of H_2O_2, A1145 strain (1×10^6 spores·mL^{-1}) was pre-grown during 140 h in 12-well plates (2 mL of MMG per well) at 30°C with gentle agitation (100 rpm), in the dark. After the pre-growth phase, H_2O_2 was added to the cells at a defined concentration (1.0 –4.0 mM) and incubated at 30°C for 30 min. Controls without addition of H_2O_2 were grown as well. Mycelia samples were collected from the 12-well plates, and immediately frozen using liquid nitrogen until further analysis.

2.8 Real-time quantitative polymerase chain reaction

Total RNA extraction and cDNA synthesis were performed using the RNeasy Plant Mini Kit (Qiagen) and the iScript cDNA Synthesis Kit (Bio-Rad), and the RT-*q*PCR performed as previously reported (Martins et al., 2020). The oligonucleotide pairs for specific *A. nidulans* genes (Supplementary Table 1) were designed using the Primer-Blast web tool (www.ncbi.nlm.nih.gov/tools/primer-blast/), and purchased from STAB Vida Lda. (Portugal). The RT-*q*PCR analysis was performed in a CFX96 Thermal Cycler (Bio-Rad), using the SsoFast EvaGreen Supermix (Bio-Rad), 250 nM of each oligonucleotide and the cDNA template equivalent to 10 ng of total RNA, at a final volume of 10 µL per well, in at least three biological replicates. The PCR conditions were as follows: enzyme activation at 95°C for 30 s; 40 cycles of denaturation at 95°C for 5 s, and annealing/extension at 60°C for 15 s; and the melting curve obtained from 65 to 95°C, consisting of 0.5°C increments for 5 s. Data were analyzed with the CFX Manager software (Bio-Rad). In more detail, the expression of each gene was taken as the relative expression compared to the time zero (before incubation with the tested compounds) or as the relative expression compared to the no addition of the stressor. The expression of all target genes was normalized by the expression of the histone *H2B* gene (*AN3469*) (Supplementary Dataset 3), used as the internal control. Statistical analyzes used the XL-STAT (Addinsoft) software, and multiple Student's *t-tests*. Differences in gene expression with a *p-value* below 0.05 were considered statistically significant.

2.9 Generation of single-gene deletion mutants

The gene *AN9181* was replaced with *Aspergillus fumigatus pyrG* gene (*pyrG*^{Afu}) in *Aspergillus nidulans* A1145 and A1149, both auxotrophic strains (*pyrG*$^-$). Deletion cassettes combining the 5′ and 3′-flanking regions of each target gene with *pyrG*^{Afu} were obtained by fusion PCR and were used to transform *A. nidulans* A1145 or A1149 protoplasts and plated onto selective media to generate single-deletion mutant strains (Supplementary Table 2). Isolated transformants were cultivated on the selective media for three generations to assure stable mutations. In greater detail, the deletion cassettes were constructed using a fusion PCR protocol. Six primers (P1-P6) were designed, based on sequences from the *Aspergillus* Genome Database (www.aspgd.org), and analyzed using the NetPrimer web tool (www.premierbiosoft.com/NetPrimer/AnalyzePrimer.jsp) (listed in Supplementary Table 3). PCR reactions were performed in a T100 Thermal Cycler (Bio-Rad; conditions in Supplementary Table 4). *A. fumigatus pyrG* was amplified from plasmid pCDS60 (FGSC, Kansas City, MO, United States) using primers CDS164 and CDS165. Flanking fragments upstream and downstream of the gene were amplified with primer pairs P1/P3 and P4/P6, respectively, using genomic DNA from *A. nidulans* A4 as

template. The final cassette was produced by fusing the flanking regions with the *A. fumigatus pyrG* using nested primers P2 and P5 for the target gene. PCR products were cleaned with NZYGelPure kit (NZYTech). Then, to produce transformable protoplasts, *A. nidulans* mycelia grown overnight from 10^8 conidia in 50 mL MMGN with the appropriate nutritional supplements (30°C, 90 rpm), recovered by centrifugation and washed (0.6 M $MgSO_4$), were digested in 20 mL enzymatic mix (300 mg lysing enzymes from *Trichoderma harzianum*, 150 µL β-glucuronidase from bovine liver, type B-1, and 150 mg Driselase from *Basidiomycetes* sp., all from Sigma-Aldrich) in osmotic medium (1.2 M $MgSO_4 \cdot 7H_2O$ and 10 mM sodium phosphate buffer pH 6.5; final pH adjusted to 5.8 with Na_2HPO_4) for 20 h at 30°C, 90 rpm. The protoplasts suspension was overlaid (2:1) with trapping buffer (0.6 M sorbitol and 100 mM Tris–HCl pH 7.0), and then recovered by centrifugation (1,500 *g*, 4°C, 15 min, swing-bucket rotor), washed three times with 10 mL of ST10 buffer (1.2 M sorbitol and 10 mM Tris–HCl pH 7.5) and finally resuspended in 1 mL of the same buffer and incubated overnight at 4°C. In the next day, the protoplasts were collected by centrifugation (1,000 *g*, at 4°C, 2 min), and resuspended in 700 µL cold STC buffer (1.2 M sorbitol, 10 mM Tris–HCl pH 7.5 and 10 mM $CaCl_2$). The obtained protoplasts (100 µL) were then transformed by mixing with the cleaned fusion PCR product (10 µL), subsequently adding freshly filtered polyethylene glycol (PEG) solution (25% (w/v) in STC buffer; 50 µL) and kept in an ice bath for 25 min. Then, additional PEG solution was added (1 mL), gently mixed using a micropipette and placed at room temperature for 25 min. For the single mutants A1145Δ*AN9181* and A1149Δ*AN9181*, 100 µL of the transformation mix were plated onto a selective medium containing glucose (5.0 g·L^{-1}), yeast extract (5.0 g·L^{-1}), sucrose (342.3 g·L^{-1}), riboflavin (2.5 mg·L^{-1}), pyridoxin (0.05 mg·L^{-1}), 0.1% (v/v) trace elements solution (see above), and 1.5% agar. The selective plates were incubated for 3 to 4 days at 30°C. All transformants were morphologically identical to the parental strain. Two isolated A1145Δ*AN9181* transformants (randomly selected) were streaked onto complete medium plates containing glucose (10.0 g·L^{-1}), peptone (2.0 g·L^{-1}), yeast extract (1.0 g·L^{-1}), casein hydrolysate (1.0 g·L^{-1}), 5% (v/v) nitrate salts solution (see above), 0.1% (v/v) trace elements solution, riboflavin (2.5 mg·L^{-1}), pyridoxin (0.05 mg·L^{-1}), pH 6.5, and incubated at 30°C for 4 days. Three generations of each transformant were grown to assure stable mutations and then grown again in MMG without uracil and uridine to confirm the prototrophy to the compounds of the mutant strains (Supplementary Figure 1).

2.10 Confirmation of gene replacement

DNA from each transformant was extracted with Quick-DNA™ Fungal/Bacterial Microprep Kit (Zymo Research), and diagnostic PCR was performed with primers P1 and P6 for each gene. Based on amplicon size (3,222 bp for WT and 3,904 bp for A1145Δ*AN9181*, Supplementary Figure 2A), it was possible to confirm the correct gene replacement of the transformants. To obtain further confirmation, the PCR products were digested for 1 h with the restriction enzymes ApaI or KpnI selected to give differential digestion patterns for mutant and wild-type strains. Supplementary Figure 2B show the products of diagnostic PCR and restriction enzymes digestion for the A1145Δ*AN9181* selected strain.

2.11 Cellular metabolic activity measured by XTT assay

Cell viability was evaluated using the XTT assay in 96-well plates (200 µL per well) using Malt Extract medium or MMG supplemented with 10 mM N source, and an inoculum of 1×10^6 spores·mL^{-1}, and incubated at 30°C for 24 h (triplicates). After, 10 µL of a solution containing 4.6 mg·mL^{-1} of XTT and 0.104 mg·mL^{-1} of menadione was added to each well, incubated for further 2 h, and the absorbance measured (460 nm).

2.12 *Aspergillus nidulans* growth and inhibition assays

The strains' spore germination fitness, *i.e.*, number of spores that are able to form a colony, was evaluated by spreading 100 spores onto solid media, then counting the colony forming units (CFUs) daily, during five days (triplicates). The radial growth diameter of each strain (inoculum: 1 µL of a suspension of 2×10^8 spores·mL^{-1}) in solid MMG, supplemented or not with specific compounds (*viz.* congo red, H_2O_2, MSB, Amph B, CSP and ITZ) was measured after five days of incubation (30°C, dark, triplicates). The MIC of each antifungal was determined using the micro-broth dilution method (MMG, 96-well plates, 200 µL per well), testing specific concentration ranges for Amph B (250–550 mg·L^{-1}), CSP (60–120 mg·L^{-1}) and ITZ (0.2–0.5 mg·L^{-1}). An inoculum of 1×10^6 spores·mL^{-1} was used, and the plates were incubated at 30°C for 48 h. Negative controls were done in parallel. The lowest concentration that showed no growth under microscopic observation was considered the MIC.

2.13 ROS quantification

Intracellular ROS was quantified using DCFH-DA. Cultures were grown in MMG (140 h, 30°C); then 2.5 µg·mL^{-1} of DCFH-DA was added and incubated (30°C, 30 min). H_2O_2 was added to the cells at increasing concentrations, from 1 mM to 4 mM, and the incubation step repeated. The cell suspension was disrupted in a TissueLyzer LT (Qiagen) with a metal bead at a maximum speed (3 cycles of 1 min). The fluorescence intensity of the supernatant (recovered by centrifugation: 12000 *g*, 10 min) was measured using a Tecan Infinite M Nano$^+$ Microplate (Männedorf, Switzerland) as follows: excitation length 485/9; emission 528/20; optics, top; read speed, normal; gain, 89; number of flashes, 25; integration time, 40 µs. The fluorescence intensity (per mycelia dry weight) was normalized against the control (no H_2O_2 added).

3 Results and discussion

3.1 Genes comprised in the AN9181 orthogroup underwent differentially upregulation during growth in the presence of aromatic compounds

The orthology analysis (Figure 1A) revealed a total of 11,992 orthogroups among the eight analyzed *Aspergillus* spp. genomes

(Supplementary Dataset 4). Among these, only 258 were species-specific orthogroups, comprising 0.7% of the total number of genes. Figure 1B displays the phylogenetic relations computed by the orthology analysis, and Figures 1C–E provide for each species the total number of genes, the percentage of genes in orthogroups and the number of species-specific orthogroups, respectively. The number of species-specific orthogroups (Figure 1E) is not necessarily correlated with the percentage of genes in orthogroups (Figure 1D) nor the genome size (Figure 1C). For instance, *A. versicolor* possesses the third larger genome among the eight analyzed *Aspergillus* spp. yet displays one of the highest percentages of genes present in orthogroups but the lowest number of species-specific orthogroups. On the other hand, *A. sydowii*, which possesses a genome size comparable to that of *A. versicolor* and only a slightly lower percentage of genes belonging to orthogroups, is the species presenting the higher number of species-specific orthogroups. This is an indication of a higher occurrence of gene duplication events (Emms and Kelly, 2015) in *A. sydowii* compared to other aspergilli, a feature also visible in *A. aculeatus* and *A. flavus*. Finally, *A. fumigatus* and *A. nidulans* present similarly sized genomes, as well as a comparable percentage of genes included in orthogroups and number of species-specific orthogroups.

Upon transposing the differentially expressed genes (up-regulated) from the five transcriptomic datasets analyzed to the corresponding orthologues in the genome of *A. nidulans* (Supplementary Dataset 2) we analyzed the set of genes present in at least three, four or five transcriptome-based datasets on exposure to selected organic compounds. We observed that, out of the 241 genes present in at least three datasets, several are predicted to be transporters or secondary metabolism-related genes (Supplementary Dataset 5). Twenty-two genes are present in at least four datasets (Table 1), of which a single gene, *AN9181*, is present in all five datasets (Figure 2A). This gene is part of an orthogroup that contains two genes in *A. nidulans*, being the other one *AN8970*.

The AN9181 orthogroup (gene tree displayed in Figure 2B) comprises 25 genes across the eight analyzed aspergilli genomes, namely four in *A. aculeatus*, four in *A. flavus*, two in *A. fumigatus*, two in *A. nidulans* (as mentioned), two in *A. niger*, four in *A. sydowii*, three in *A. terreus*, and four in *A. versicolor*. The existence of the AN9181 orthogroup is therefore highly conserved in these aspergilli. The presence of four genes belonging to the AN9181 orthogroup in *A. sydowii*, *A. aculeatus* and *A. flavus* reinforces the indication of higher occurrence of gene duplication events in these species. This is an indication that the AN9181 orthogroup, like many other regulatory genes, is undergoing rapid evolution in *Aspergillus* sp. as a response to environmental changes and adaptive lifestyles. This plasticity is often associated with the evolution/transition to pathogenic lifestyles in aspergilli (Rokas, 2022). The 25 genes that compose the AN9181 orthogroup are largely uncharacterized with neither relevant information in FungiDB and nor predicted protein interactions. However, the orthologous gene *cip1* of *Candida albicans* is involved in oxidative stress response, being regulated by the transcription factor Cap1p (Wang et al., 2006; Znaidi et al., 2009). This past evidence raises the hypothesis that *AN9181* participates in stress responses.

Through a computational protein domain analysis (InterProScan), we observed that the *AN9181* encodes a protein containing a phenylcoumaran benzylic ether reductase-*like* domain (IPR045312) and a Nitrogen metabolite repressor regulator (NmrA)-*like* domain (IPR008030), while *AN8970* encodes a protein containing a NAD(P)-binding domain (IPR016040). A deletion mutant of *padA*, that encodes a protein also carrying a NmrA-*like* domain of *Dictyostelium discoideum*, showed to be more sensitive to ammonia than the wild-type (Núñez-Corcuera et al., 2008). Moreover, disruption of this gene resulted in phenotypic defects in development and growth, namely, the thermosensitive mutant allele *padA*$^{-}$ showed poor and null growth at permissive and restrictive temperatures, respectively. Deletion of the *NmrA* gene in *A. flavus* reduced growth in several nitrogen (N) sources, but increased conidia and sclerotia production (Han et al., 2016). This mutant strain produces less aflatoxin when cultivated in glutamine and alanine supplemented media, and shows reduced virulence and increased sensitivity in response to rapamycin and methyl methanesulfonate, but not in response to the osmotic stressors NaCl and sorbitol (Han et al., 2016).

The genes *AN9181* and *AN8970* are in separated clusters within the AN9181 orthogroup gene tree (Figure 2B). This observation is consistent with the fact that they possess distinct functional domains (Gabaldón and Koonin, 2013), and therefore, they are not paralogs. Though *AN9181* was the initial candidate, we also evaluated the gene expression of *AN8970* (same orthogroup) aiming to understand which one would be functionally relevant to regulate stress responses. Therefore, the expression profiles of either gene composing the AN9181 orthogroup (*AN9181* and *AN8970*) were evaluated after 2, 4 and 24 h of exposure to four selected organic compounds in a medium containing a poor N source. The organic compounds comprise two which were found in the selected transcriptome datasets: benzo[a] pyrene (BaP), and bromoquinol (BMQ), and two additional aromatic halogenated based compounds, namely pentachlorophenol (PCP) and triclosan (TCS), classified as persistent organic pollutant and contaminant of emergent concern, respectively (Varela et al., 2017). The last two compounds were tested due to their frequent association to soil and water contamination (Czaplicka, 2004; Morgan et al., 2015), and past studies showing that either compound increased the production of virulent aspergilli conidia within soil colonizing fungi (Martins et al., 2023). The *AN9181* revealed lower expression levels compared to *AN8970* (Figures 2C,D). However, compared to control conditions, a significant increase in the expression levels of *AN9181* was systematically noticed after 4 h of exposure to all the tested organic compounds, as well as in additional time-points, namely after 2 h to PCP, 2 and 24 h to TCS, and 24 h to BaP (Figure 2C). Recently, *AN9181* was also found to be up-regulated after fungal growth in a nitrate minimal medium supplemented with either cadmium chloride, congo red or amphotericin B (Antal et al., 2020). In contrast to *AN9181*, the expression profiles of *AN8970* were similar between the control and upon exposure to organic compounds, except for PCP at 24 h and for TCS 4 h (Figure 2D). At the experimental conditions used, the gene expression analysis did not support the idea of a concerted action of the two genes of the AN9181 orthogroup in *A. nidulans*. Based on these results, we focused the remaining analyzes on the *AN9181*.

3.2 *AN9181* does not affect germination and growth in solid media but influences metabolic activity in a N source dependent manner

To better understand the functional roles of *AN9181*, this gene was deleted and functionally analyzed in *A. nidulans*. The colony

10.3389/fmicb.2024.1373469

TABLE 1 List of genes present in at least four distinct transcriptome-based datasets out of the five analyzed using the COCOA strategy.

Gene ID	Product description	InterPro code	InterPro domain
AN0016	Putative nonribosomal peptide synthase	IPR000873 IPR001242 IPR006162 IPR009081 IPR010071 IPR020806 IPR020845 IPR023213 IPR036736 IPR042099 IPR045851	AMP-dependent synthetase/ligase domain; Condensation domain; Phosphopantetheine attachment site; Phosphopantetheine binding ACP domain; Amino acid adenylation domain; Polyketide synthase, phosphopantetheine-binding domain; AMP-binding, conserved site; Chloramphenicol acetyltransferase-like domain superfamily; ACP-like superfamily; ANL, N-terminal domain; AMP-binding enzyme; C-terminal domain superfamily
AN0029	Putative transmembrane transporter	IPR011701 IPR020846 IPR036259	Major facilitator superfamily; Major facilitator superfamily domain; MFS transporter superfamily
AN2959	Has domain(s) with a predicted role in transmembrane transport and integral component of membrane localization	IPR011701 IPR020846 IPR036259	Major facilitator superfamily; Major facilitator superfamily domain; MFS transporter superfamily
AN3225	Putative cytochrome P450	IPR002403 IPR001128 IPR036396 IPR017972	Cytochrome P450, E-class, group IV; Cytochrome P450; Cytochrome P450 superfamily; Cytochrome P450, conserved site
AN4643	Putative cytochrome P450	IPR001128 IPR002401 IPR036396 IPR017972	Cytochrome P450; Cytochrome P450, E-class, group I; Cytochrome P450 superfamily; Cytochrome P450, conserved site
AN5310	Has domain(s) with predicted FAD binding, oxidoreductase activity and role in metabolic process	IPR002938 IPR036188	FAD-binding domain; FAD/NAD(P)-binding domain superfamily
AN5553	Putative cytochrome P450	IPR001128 IPR002401 IPR036396 IPR017972	Cytochrome P450; Cytochrome P450, E-class, group I; Cytochrome P450 superfamily; Cytochrome P450, conserved site
AN6450	Tetrahydroxynaphthalene reductase	IPR002347 IPR020904 IPR036291	Short-chain dehydrogenase/reductase SDR; Short-chain dehydrogenase/reductase, conserved site; NAD(P)-binding domain superfamily
AN7154	protein of unknown function	IPR008030 IPR036291	NmrA-like domain; NAD(P)-binding domain superfamily
AN7359	Putative cytochrome P450	IPR001128 IPR002401 IPR036396 IPR017972	Cytochrome P450; Cytochrome P450, E-class, group I; Cytochrome P450 superfamily; Cytochrome P450, conserved site
AN7772	Putative cytochrome P450	IPR001128 IPR002401 IPR017972 IPR036396	Cytochrome P450; Cytochrome P450, E-class, group I; Cytochrome P450, conserved site; Cytochrome P450 superfamily
AN7969	Putative cytochrome P450	IPR001128 IPR002401 IPR036396 IPR017972	Cytochrome P450; Cytochrome P450, E-class, group I; Cytochrome P450 superfamily; Cytochrome P450, conserved site
AN7972	Has domain(s) with a predicted role in transmembrane transport and integral component of membrane localization	IPR011701 IPR020846 IPR036259	Major facilitator superfamily; Major facilitator superfamily domain; MFS transporter superfamily

(Continued)

TABLE 1 (Continued)

Gene ID	Product description	InterPro code	InterPro domain
AN8354	Has domain(s) with predicted NAD binding, oxidoreductase activity, acting on the aldehyde or oxo group of donors, NAD or NADP as acceptor activity and role in cellular amino acid metabolic process, oxidation–reduction process	IPR008030 IPR036291 IPR045312	NmrA-like domain; NAD(P)-binding domain superfamily; Phenylcoumaran benzylic ether reductase-like
AN8952	Putative cytochrome P450	IPR001128 IPR002401 IPR036396	Cytochrome P450; Cytochrome P450, E-class, group I; Cytochrome P450 superfamily
AN8970	Ortholog of *A. nidulans* FGSC A4: AN9181	IPR016040 IPR036291	NAD(P)-binding domain; NAD(P)-binding domain superfamily
AN9005	Putative polyketide synthase (PKS)	IPR001227 IPR009081 IPR011032 IPR013217 IPR013968 IPR014030 IPR014031 IPR014043 IPR016035 IPR016036 IPR016039 IPR018201 IPR020807 IPR020841 IPR020843 IPR029063 IPR032821 IPR036291 IPR036736 IPR042104 IPR049551 IPR049552	Acyl transferase domain superfamily; Phosphopantetheine binding ACP domain; GroES-like superfamily; Methyltransferase type 12; Polyketide synthase, ketoreductase domain; Beta-ketoacyl synthase, N-terminal; Beta-ketoacyl synthase, C-terminal; Acyl transferase; Acyl transferase/acyl hydrolase/lysophospholipase; Malonyl-CoA ACP transacylase, ACP-binding; Thiolase-like,Beta-ketoacyl synthase, active site; Polyketide synthase, dehydratase domain; Polyketide synthase, beta-ketoacyl synthase domain; Polyketide synthase, enoylreductase domain; S-adenosyl-L-methionine-dependent methyltransferase superfamily; Polyketide synthase, C-terminal extension; NAD(P)-binding domain superfamily; ACP-like superfamily; Polyketide synthase, dehydratase domain superfamily; Polyketide synthase, dehydratase domain, C-terminal; Polyketide synthase, dehydratase domain, N-terminal
AN9044	Has domain(s) with predicted FMN binding, catalytic activity, oxidoreductase activity and role in oxidation–reduction process	IPR001155 IPR013785 IPR044152	NADH:flavin oxidoreductase/NADH oxidase, N-terminal; Aldolase-type TIM barrel; NADPH dehydrogenase YqjM-like
AN9161	Has domain(s) with predicted FAD binding, oxidoreductase activity and role in metabolic process	IPR002938 IPR036188	FAD-binding domain; FAD/NAD(P)-binding domain superfamily
AN9181	Ortholog of *A. nidulans* FGSC A4: AN8970	IPR008030 IPR036291 IPR045312	NmrA-like domain; NAD(P)-binding domain superfamily; Phenylcoumaran benzylic ether reductase-like
AN10259	Putative cytochrome P450	IPR001128 IPR002401 IPR036396 IPR017972	Cytochrome P450; Cytochrome P450, E-class, group I; Cytochrome P450 superfamily; Cytochrome P450, conserved site
AN11681	protein of unknown function	No domain	No domain

The genes' IDs and Product Descriptions based on FungiDB annotation are available. The assigned InterPro codes and names of the predicted domains upon InterProScan analysis are also provided.

morphology of the parental strain and the A1145Δ*AN9181* mutant (hereafter referred to as Δ*AN9181*) on Malt extract agar (MEA) medium were similar (Figures 3A,B). After five days of growth, the colony diameters of either strain in MMG containing a high amount of a non-preferred (*i.e.*, poor) N source were also comparable (*i.e.*, 71 mM sodium nitrate, Supplementary Figure 3). The conidia viability

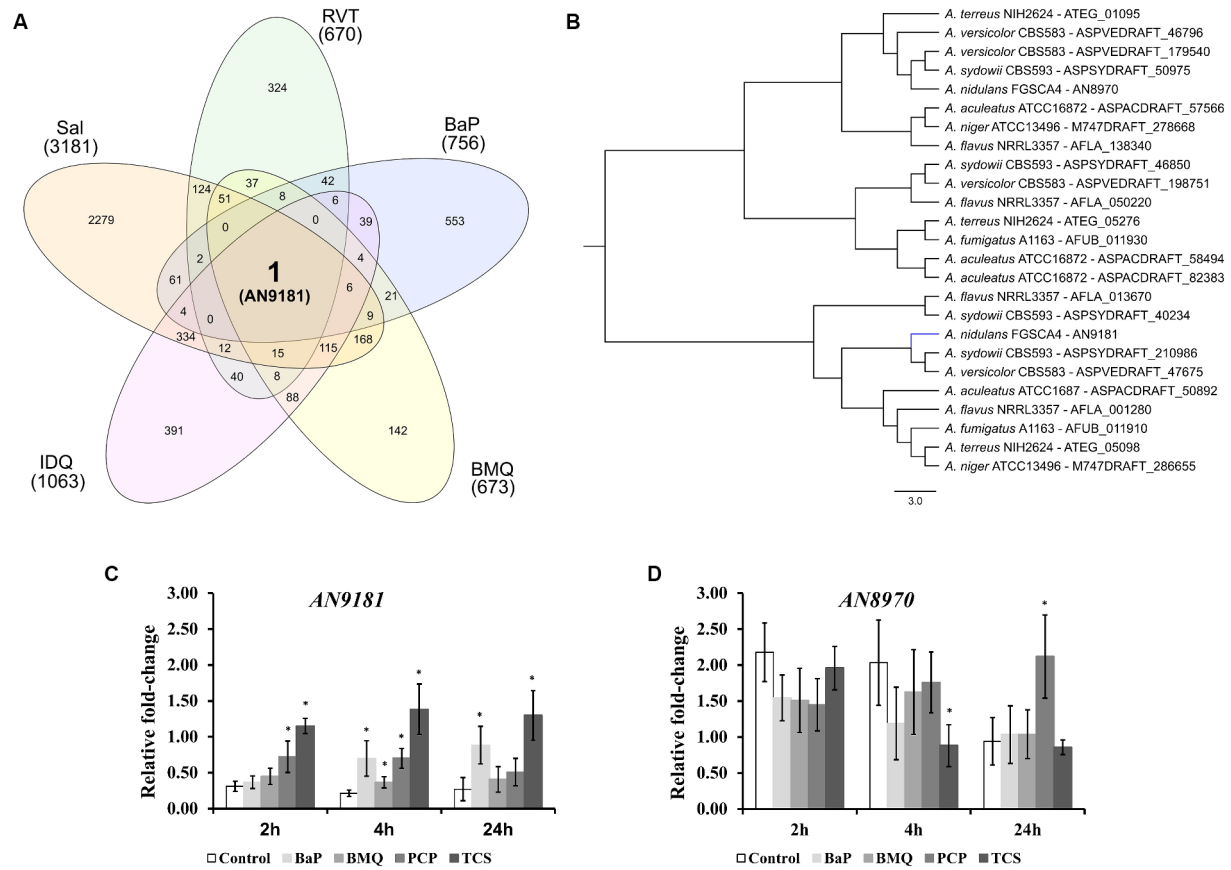

FIGURE 2
Different expressed genes in the five transcriptomic datasets. **(A)** – upon orthology transformation of the transcriptome-based datasets to the "receiver species" *Aspergillus nidulans*, *AN9181* was the only gene found consistently up-regulated in all the analyzed datasets. BaP (Benzo[a]pyrene); BMQ (Bromoquinoline); Sal (Sodium Salicylate); IDQ (6-iodoquinoline) and RVT (Resveratrol). **(B)** – the AN9181 orthogroup comprises 25 genes present in the genomes of the eight orthology-analyzed *Aspergillus* species, which are separated into two distinct clusters in the gene-tree obtained upon OrthoFinder analysis. **(C,D)** – targeted gene expression analysis (assessed by RT-*q*PCR) is displayed for AN9181 **(C)** and AN8970 **(D)**.

of either strain (*i.e.*, germination fitness) was measured directly by counting the numbers of CFUs. CFUs were similar for both strains when germinated in the rich medium MEA (Figure 3C) and MMG supplemented with either a superior (*i.e.*, rich) N source (10 mM of ammonium sulfate) (Figure 3D) or a non-preferred N source at high concentration (71 mM of sodium nitrate) (Supplementary Figure 4A). However, the Δ*AN9181* conidial viability in MMG supplemented with 10 mM sodium nitrate or no added N source were 1.7-fold and 1.5-fold higher, respectively, compared to the parental strain (Figures 3E,F). This result suggests that *AN9181* strongly influences the fitness of conidia germinating in medium having low availability of poor nitrogen sources.

The *AN9181* encodes for a protein containing a NmrA-*like* domain. NmrA is a negative transcriptional regulator of several fungi, involved in the post-translational modulation of the GATA transcription factor AreA (Hensel et al., 1998). In *A. nidulans*, *areA* regulates the activation of genes involved in the utilization of a broad range of N sources: in the presence of rich N sources, e.g., ammonium and glutamine, NmrA binds to AreA preventing nitrogen catabolic gene expression; contrarily in the presence of nitrate, NmrA and AreA dissociation occurs, hence genes involved in the utilization of alternative nitrogen sources are activated (Han et al., 2016). Based on this, we questioned if *AN9181* influences the utilization of different N sources. Specifically, we measured the cellular metabolic activity of both the Δ*AN9181* and the parental strain in distinct media. Measurements were similar in both strains grown in media having rich N sources (*i.e.*, MEA and ammonium sulfate) (Figure 3G) and a high availability of sodium nitrate (poor alternative N source) (Supplementary Figure 4B). However, the mutant showed a significant increase in metabolic activity when grown in media with a low availability of a poor N source (10 mM sodium nitrate) or no added N source (Figure 3G). Another mutant - #2Δ*AN9181*, randomly selected, was used for validation purposes. This mutant showed consistently similar metabolic activity in media having rich N sources and increased metabolic activity in media with low availability of a poor N source or no added N source (Supplementary Figure 5). In addition, the Δ*AN9181* and the parental strain were tested in MMG supplemented with 10 mM N of each of the 20 proteinogenic amino acids. Compared to the parental strain, the mutant strain showed higher metabolic activity in tryptophan (aromatic); serine, glycine and methionine (serine family); asparagine (aspartate family); and alanine and valine (pyruvate family) (Figure 3H). Collectively the results suggest that *AN9181* influences the utilization of N sources (hence also spore germination fitness) in a nitrogen type specific manner.

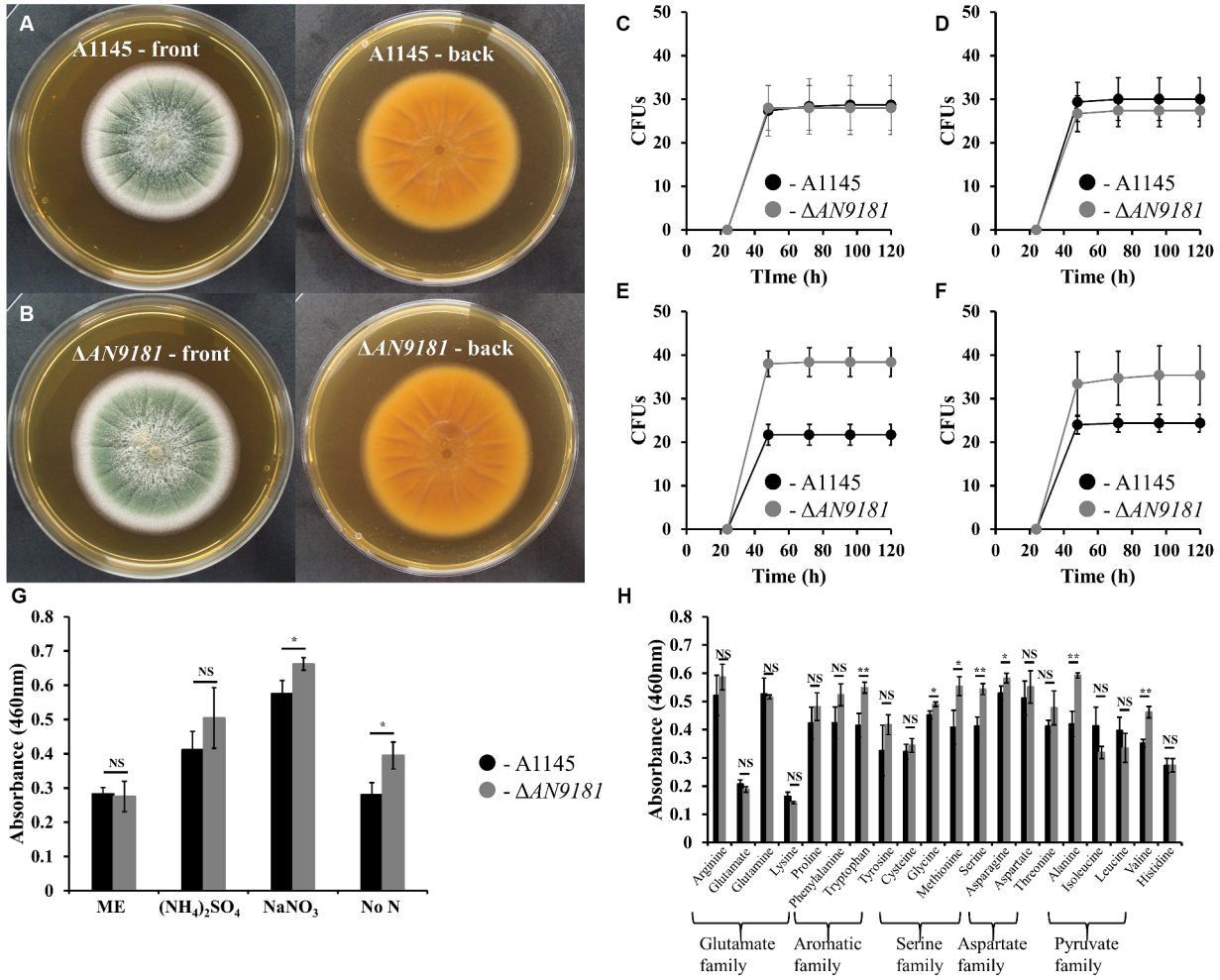

FIGURE 3
Phenotype features of A1145 and Δ*AN9181*. **(A,B)** – the morphology and pigmentation of A1145 strain **(A)** and Δ*AN9181* strain **(B)** after cultivation at 30°C for five days in Malt Extract Agar. **(C–F)** – colony forming units of A1145 (black) and Δ*AN9181* (gray) strains plated on Malt Extract Agar **(C)**; minimal medium glucose supplemented with 10 mM nitrogen from different sources $(NH_4)_2SO_4$ **(D)**; 10 mM $NaNO_3$ **(E)**; no nitrogen added **(F)**. **(G,H)** – cell viability and proliferation measured by XTT assay. A1145 (black) and Δ*AN9181* (gray) strains were grown in Malt Extract or in minimal medium glucose supplemented with 10 mM nitrogen from the different nitrogen sources **(G)** including amino acids **(H)**. Values and error bars represent the mean and the standard deviation of triplicates. Significant differences (Student's *t-test*) are marked with asterisks [*]. * $p \leq 0.05$; ** $p \leq 0.01$, and *** $p \leq 0.001$. "NS" means non-significant.

Overall, the mutant phenotype suggests that *AN9181* participates in the regulation of nitrogen catabolism in *A. nidulans*, resembling *NmrA* negative regulation of N utilization in many rich N sources. Further assays are however needed to better understand *AN9181* regulatory network in the context of nitrogen utilization.

3.3 *AN9181* regulates *Aspergillus nidulans* growth in medium supplemented with sodium salicylate and resveratrol

The growth of Δ*AN9181* strain in the presence of each organic compound initially covered in the investigated transcriptome datasets was tested. To standardize conditions, all growth assays used MMG supplemented with the compounds under test at their determined EC_{50} values (Supplementary Table 5). In the presence of BaP, BMQ and IDQ no differences in growth were observed between the parental and the mutant strain. On the contrary, in media supplemented with sodium salicylate or resveratrol, the Δ*AN9181* strain grows more than the parental strain (Figure 4A). The cultivation conditions varied from those of the initial studies, including medium composition, time and temperature, as well as the concentration of the aromatic compounds. To test if the latter was influencing the phenotype, we tested the mutant's growth in media supplemented with increasing concentrations of two selected aromatic compounds. Salicylate is degraded via the catechol branch of the 3-oxoadipate pathway in *A. nidulans* (Martins et al., 2015). The Ascomycota *Phomopsis liquidambari* degrades resveratrol into 3,5-dihydroxybenzaldehyde and 4-hydroxybenzaldehyde, which are subsequently oxidized to 3,5-dihydroxybenzoic acid and 4-hydroxybenzoic acid, respectively (Abo-Kadoum et al., 2022). The latter, is an intermediate of the protocatechuate branch of the 3-oxoadipate pathway used by *A. nidulans* to degrade benzoate. Therefore, it is possible that resveratrol and benzoate pathways are interconnected in *A. nidulans*, thus the phenotype was tested in

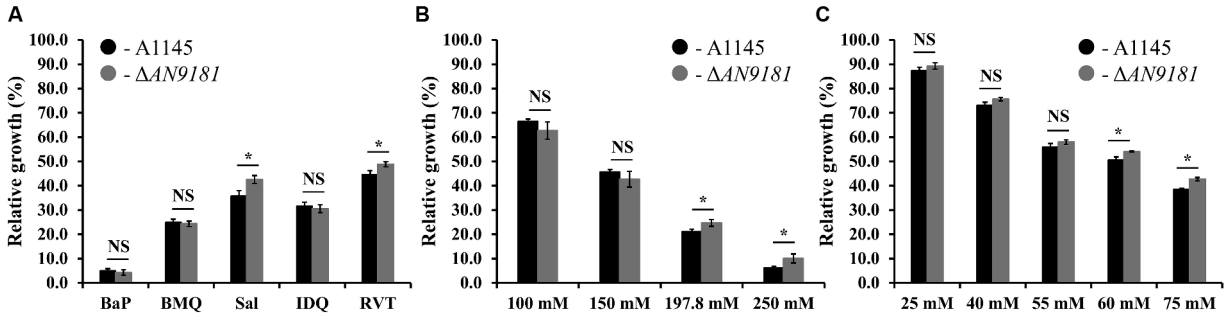

FIGURE 4
Phenotype features of A1145 and Δ*AN9181*. **(A–C)** relative growth of the A1145 (black) and Δ*AN9181* (gray) strains grown in minimal medium glucose (solid) supplemented with the EC_{50} concentrations of each organic compound compared to the control condition (no chemical addition). BaP (Benzo[a]pyrene, 1.61 mM); BMQ (5-Bromoquinoline, 0.2 mM); Sal (Sodium Salicylate, 197.8 mM); IDQ (6-iodoquinoline, 0.2 mM) and RVT (Resveratrol, 0.45 mM) **(A)**; and with increasing concentrations of sodium salicylate **(B)** or sodium benzoate **(C)**. Values and error bars represent the mean and the standard deviation of triplicates. Significant differences (Student's *t-test*) are marked with asterisks (*). *$p \leq 0.05$; **$p \leq 0.01$, and ***$p \leq 0.001$. "NS" means non-significant.

increasing concentrations of sodium salicylate and sodium benzoate (the last instead of resveratrol). The results showed that the Δ*AN9181* strain growth-phenotype is indeed concentration dependent for sodium salicylate and for sodium benzoate: a clear phenotype is noticed for concentrations >150 mM and > 55 mM, respectively (*i.e.*, concentrations equal or above the EC_{50} determined for these compounds; see Supplementary Table 5) (Figures 4B,C).

The absence of a phenotype in three (out of five) of the organic compounds herein tested (Figure 4A) is likely related to the fact that the used concentrations were below the threshold to cause major stress effect under the utilized cultivation conditions. Moreover, the response is also influenced by the regulation of nitrogen catabolism as analyzed above. The observation that the growth phenotype of the Δ*AN9181* strain is sodium salicylate and sodium benzoate concentration dependent, obvious for concentrations above the corresponding EC_{50} values, is consistent with the working hypothesis that *AN9181* regulates stress responsive metabolism.

3.4 Δ*AN9181* strain shows decreased susceptibility to amphotericin B, congo red, hydrogen peroxide, and menadione sodium bisulfite

Recently, it was reported that *AN9181* underwent up-regulation during *A. nidulans* exposure to congo red or amphotericin B grown in a nitrate minimal medium (Antal et al., 2020). This result expands the regulatory impact of *AN9181* under growth in stress conditions. We evaluated if *AN9181* deletion influences the susceptibility to congo red and to different antifungal drugs: amphotericin B (targets the cell membrane), caspofungin (targets the cell wall), and itraconazole (inhibits the synthesis of ergosterol, altering the cell membrane permeability). The results showed that Δ*AN9181* strain susceptibility to amphotericin B is lower compared to the parental strain (Figure 5A). On the contrary, compared to the parental strain, the susceptibility of the mutant strain was similar and higher to caspofungin and itraconazole, respectively (Figure 5A). Similar results were attained with the A1149Δ*AN9181*

TABLE 2 MICs of antifungals A1145 and Δ*AN9181* strains.

	MIC (mg·L^{-1})		
	Caspofungin	Amphotericin B	Itraconazole
A1145	75	350	0.5
Δ*AN9181*	75	500	0.5

compared to its corresponding parental strain (Supplementary Figure 6A), notwithstanding that the magnitude of the susceptibility decrease to amphotericin B was more obvious. The determined MICs of each antifungal for the Δ*AN9181* mutant strain and its parental strain validate these results (Table 2). Specifically, the MIC of amphotericin B for the Δ*AN9181* mutant strain increase 1.4-fold compared to that of the parental strain (Table 2). The determined MICs of itraconazole and caspofungin were similar for the mutant and the parental strains (liquid media), regardless of the mutant's higher susceptibility to itraconazole (solid media). Differences in the growth phenotypes between liquid and solid media have been reported before (Nichols et al., 2011; Martins et al., 2015). These differences can be related to changes in the drug bioavailability and also carbon availability. We also reassessed the growth phenotype of the strains in the presence of congo red (Figure 5A). A significant decrease in the susceptibility of Δ*AN9181* mutant strain compared to the parental strain was noticed. The MIC for congo red in either strain is higher than 256 mg·L^{-1}, regardless that the upper inhibitory limit could not be precisely determined due to the strong red color of the media. All tests were conducted in the same growth media, hence the observed differential responses to the antifungal compounds cannot be simply explained by the regulation of nitrogen utilization by *AN9181*.

Additionally, the growth phenotype of the strains in the presence of H_2O_2 and in the presence of the superoxide menadione sodium bisulfite was assessed. The susceptibility of the Δ*AN9181* mutant strain compared to the parental strain showed a major and minor decrease in the presence of H_2O_2 and MSB, respectively (Figure 5B). Using another mutant – #2ΔAN9181 – it was confirmed that the

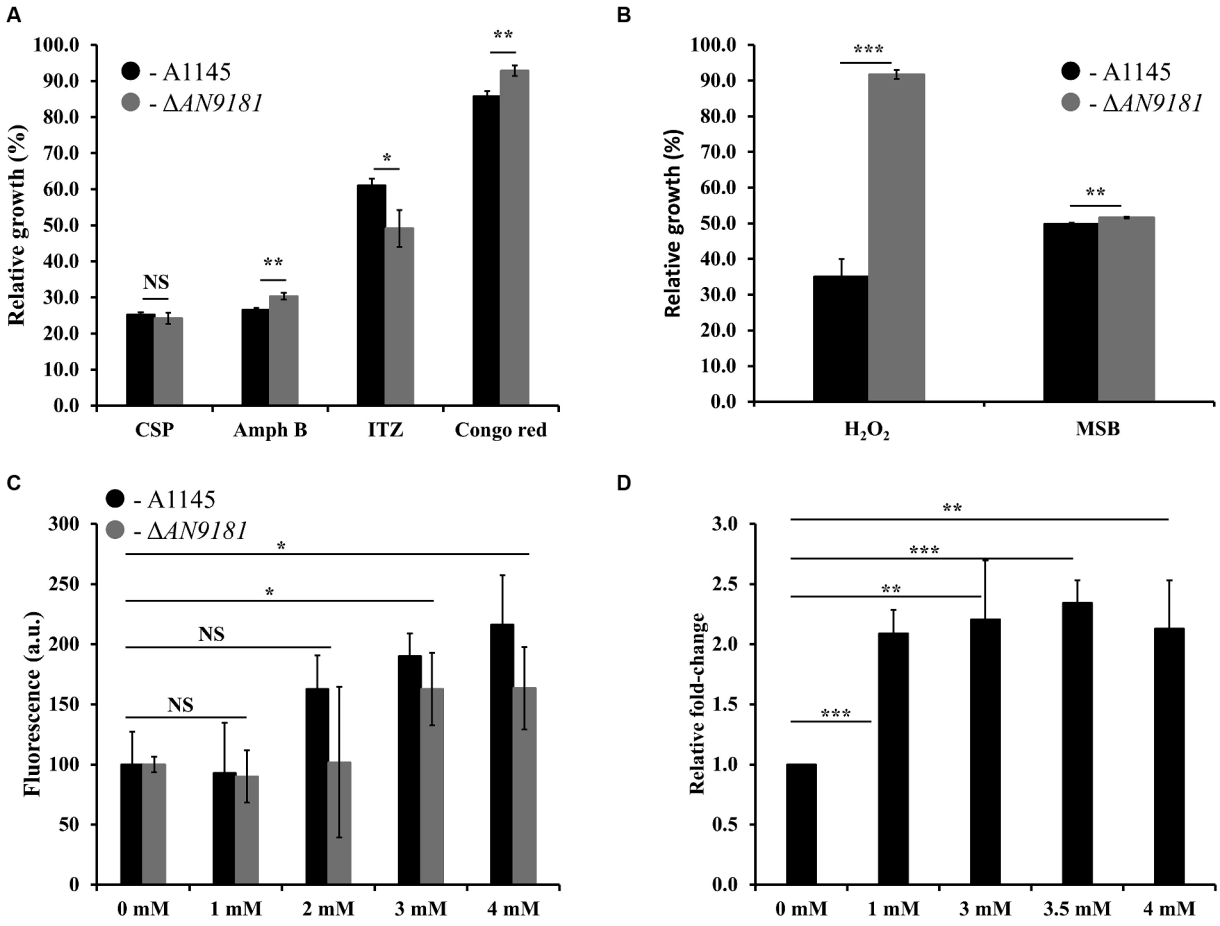

FIGURE 5
Phenotype features of A1145 and Δ*AN9181*. **(A,B)** relative growth of the A1145 (black) and Δ*AN9181* (gray) strains grown in minimal medium glucose (solid) supplemented with Caspofungin (0.5 mg·L^{-1}), Amphotericin B (150 mg·L^{-1}), Itraconazole (0.01 mg·L^{-1}), Congo Red (0.01 mM), hydrogen peroxide (3.5 mM) and menadione sodium bisulfite (0.1 mM) compared to the control condition (no chemical addition). Values and error bars represent the mean and the standard deviation of triplicates. **(C)** Intracellular ROS production, as indicated by DCFH-DA, quantified for the A1145 (black) and Δ*AN9181* (gray) strains in the presence of different concentrations of H_2O_2. The fluorescence intensity per biomass dry weight amount of the control was defined as 100. Values and error bars represent the mean and the standard deviation of at least five replicates. **(D)** targeted gene expression analysis (assessed by RT-*q*PCR) is displayed for AN9181. Fold change relative to the control (without H_2O_2 addition) and normalized to *AN3469*. Significant differences (Student's *t-test*) are marked with asterisks (*). *$p \leq 0.05$; **$p \leq 0.01$, and ***$p \leq 0.001$. "NS" means non-significant.

mutant susceptibility to H_2O_2 was indeed lower than that of the parental strain (Supplementary Figure 6B).

To complement this result, we evaluated the intracellular ROS levels of the parental and the Δ*AN9181* mutant strains after exposure to specific compounds. The ROS intracellular levels increased upon exposure of either strain to 3 mM or higher concentrations of H_2O_2 (Figure 5C). ROS levels increased when the parental strain was exposed to either Amph B or RVT at a concentration where its growth was lower than that of the mutant but slight decreased when exposed to either BMQ and ITZ at concentrations where its growth was similar or higher than that of the mutant, respectively (Supplementary Figure 7). Finally, we observed that the expression of *AN9181* in the parental strain underwent a 2-fold increase in the presence of H_2O_2 ($\geq$ 1 mM) compared to the negative control; a clear indication that the *AN9181* is upregulated under oxidative stress (Figure 5D). Collectively the results suggest that *AN9181* participates indeed in stress responses upon exposure to different chemical agents leading to oxidative stress.

4 Conclusion

In this study, we aimed to disclose aspergilli genes showing a conserved response when exposed to different organic compounds. For that, we used mostly peer-reviewed public data in combination with a straightforward computational strategy to test the strength of this scientific hypothesis. Relevant transcriptome-based datasets (Wang et al., 2015; Ben Yaakov et al., 2017; Loss et al., 2019; Martins et al., 2021) (one of which was yet unpublished), initially focusing very different biological questions were selected (five datasets in total). The computational strategy herein used allowed to pinpoint *AN9181* as the only gene that showed the same differential upregulation in all five datasets. The AN9181 orthogroup comprises only two genes in *A. nidulans*: *AN9181* and *AN8970*. These genes are located in different clusters of the AN9181 orthogroup gene tree and possess distinct functional domains. Only *AN9181* showed differential upregulation when the fungus was grown in media containing distinct chemical stressors, including two that were used

in the previous studies, and two additional toxic aromatic compounds. Therefore, subsequent experimental analyzes focused on the gene *AN9181,* specifically by studying the phenotype of the generated single-deletion mutant compared to the parental strain. This included measuring the viability of the conidia (*i.e.*, germination fitness), the metabolic profile in different nitrogen sources, the radial growth in the presence of different stress conditions and the minimal inhibitory concentration to different antifungal drugs. The acquired data showed that the deletion of the gene *AN9181* lead to higher metabolic activities in different N sources, and a decreased susceptibility to sodium salicylate, resveratrol, H_2O_2, MSB, congo red and amphotericin B (a clinically relevant antifungal drug). These opening results support the hypothesis that *AN9181* is involved in the regulation against different stress responses, including oxidative stress, in aspergilli, impacting also nitrogen utilization. This gene, *AN9181*, herein assigned as *NmrB* (Nitrogen Metabolite Repression Regulator B), deserves focused in-deep analysis, especially as it is not only conserved in aspergilli but also in several other fungi (*e. g. Candida* spp., *Fusarium* spp., or *Neurospora* spp., to name a few). The identification of the *AN9181* as a putative regulator of stress in aspergilli could not be anticipated, regardless that some of the transcriptome-based datasets used here were generated years ago. This strategy can help to identify (yet) cryptic genetic elements by reusing publicly available peer-reviewed transcriptome-based data from a diversity of scientific fields. It remains unresolved the nature of its regulation but *AN9181* apparently is able to slow down growth and metabolic activity in conditions that would be otherwise harmful for the fungus. The absence of orthologs in the human genome (according to OrthoMCL) increases the significance of this inaugural observations, especially in the context of invasive aspergillosis.

Data availability statement

The data presented in the study are deposited in the NCBI repository, accession number PRJNA1065793.

Author contributions

JJ: Formal analysis, Investigation, Methodology, Writing – original draft, Writing – review & editing. CM: Conceptualization, Investigation, Methodology, Writing – original draft, Writing – review & editing. PD: Formal analysis, Investigation, Writing – review & editing. TM: Formal analysis, Investigation, Writing – review & editing. DH: Investigation, Writing – review & editing. GG: Funding acquisition, Resources, Writing – review & editing. CS: Conceptualization, Funding acquisition, Project administration, Resources, Supervision, Writing – review & editing.

Funding

The author(s) declare that financial support was received for the research, authorship, and/or publication of this article. This work was financially supported by Fundação para a Ciência e a Tecnologia (FCT) by Project MOSTMICRO ITQB with refs UIDB/04612/2020 and UIDP/04612/2020, LS4FUTURE Associated Laboratory (LA/P/0087/2020) and Project FATE with ref. PDTC/CTA-AMB/6587/2020. JJ is grateful for the working contract PTDC/CTA-AMB/6587/2020. CM and DH are grateful for the fellowships SFRH/BD/118377/2016 and SFRH/BPD/121354/2016. TM is grateful for the working contract financed by national funds under norma transitória D.L. n.° 57/2016.

Conflict of interest

The authors declare that the research was conducted in the absence of any commercial or financial relationships that could be construed as a potential conflict of interest.

The author(s) declared that they were an editorial board member of Frontiers, at the time of submission. This had no impact on the peer review process and the final decision.

Publisher's note

Supplementary material

The Supplementary material for this article can be found online at: https://www.frontiersin.org/articles/10.3389/fmicb.2024.1373469/full#supplementary-material

References

Abo-Kadoum, M. A., Abouelela, M. E., al Mousa, A. A., Abo-Dahab, N. F., Mosa, M. A., Helmy, Y. A., et al. (2022). Resveratrol biosynthesis, optimization, induction, bio-transformation and bio-degradation in mycoendophytes. *Front. Microbiol.* 13:13. doi: 10.3389/fmicb.2022.1010332

Antal, K., Gila, B. C., Pócsi, I., and Emri, T. (2020). General stress response or adaptation to rapid growth in aspergillus nidulans? *Fungal Biol.* 124, 376–386. doi: 10.1016/j.funbio.2019.10.009

Behera, B. C. (2020). Citric acid from aspergillus Niger: a comprehensive overview. *Crit. Rev. Microbiol.* 46, 727–749. doi: 10.1080/1040841X.2020.1828815

Ben Yaakov, D., Shadkchan, Y., Albert, N., Kontoyiannis, D. P., and Osherov, N. (2017). The quinoline bromoquinol exhibits broad-spectrum antifungal activity and induces oxidative stress and apoptosis in *Aspergillus fumigatus*. *J. Antimicrob. Chemother.* 72, 2263–2272. doi: 10.1093/jac/dkx117

CLSI, *Performance standards for antimicrobial susceptibility testing: Approved 28th* (2018). Wayne, PA: CLSI.

Czaplicka, M. (2004). Sources and transformations of chlorophenols in the natural environment. *Sci. Total Environ.* 322, 21–39. doi: 10.1016/j.scitotenv.2003.09.015

Emms, D. M., and Kelly, S. (2015). OrthoFinder: solving fundamental biases in whole genome comparisons dramatically improves orthogroup inference accuracy. *Genome Biol.* 16:157. doi: 10.1186/s13059-015-0721-2

Emms, D. M., and Kelly, S. (2017). STRIDE: species tree root inference from gene duplication events. *Mol. Biol. Evol.* 34, 3267–3278. doi: 10.1093/molbev/msx259

Emms, D. M., and Kelly, S. (2019). OrthoFinder: phylogenetic orthology inference for comparative genomics. *Genome Biol.* 20:238. doi: 10.1186/s13059-019-1832-y

Gabaldón, T., and Koonin, E. V. (2013). Functional and evolutionary implications of gene orthology. *Nat. Rev. Genet.* 14, 360–366. doi: 10.1038/nrg3456

Galagan, J. E., Calvo, S. E., Cuomo, C., Ma, L. J., Wortman, J. R., Batzoglou, S., et al. (2005). Sequencing of aspergillus nidulans and comparative analysis with a. fumigatus and *A. oryzae*. *Nature* 438, 1105–1115. doi: 10.1038/nature04341

Gupta, S. K., Srivastava, M., Osmanoglu, Ö., Xu, Z., Brakhage, A. A., and Dandekar, T. (2021). *Aspergillus fumigatus* versus genus aspergillus: conservation, adaptive evolution and specific virulence genes. *Microorganisms* 9:2014. doi: 10.3390/microorganisms9102014

Hajjaj, H., Niederberger, P., and Duboc, P. (2001). Lovastatin biosynthesis by aspergillus terreus in a chemically defined medium. *Appl. Environ. Microbiol.* 67, 2596–2602. doi: 10.1128/AEM.67.6.2596-2602.2001

Han, X., Qiu, M., Wang, B., Yin, W. B., Nie, X., Qin, Q., et al. (2016). Functional analysis of the nitrogen metabolite repression regulator gene nmrA in aspergillus flavus. *Front. Microbiol.* 7:1794.

Harms, H., Schlosser, D., and Wick, L. Y. (2011). Untapped potential: exploiting fungi in bioremediation of hazardous chemicals. *Nat. Rev. Microbiol.* 9, 177–192. doi: 10.1038/nrmicro2519

Heberle, H., Meirelles, G. V., da Silva, F. R., Telles, G. P., and Minghim, R. (2015). InteractiVenn: a web-based tool for the analysis of sets through Venn diagrams. *BMC Bioinform.* 16, 1–7. doi: 10.1186/s12859-015-0611-3

Hensel, M., Arst Jr, H. N., Aufauvre-Brown, A., and Holden, D. W. (1998). The role of the *Aspergillus fumigatus* areA gene in invasive pulmonary aspergillosis. *Mol. Gen. Genet.* 258, 553–557. doi: 10.1007/s004380050767

Kafer, E. (1977). Meiotic and mitotic recombination in aspergillus and its chromosomal aberrations. *Adv. Genet.* 19, 33–131.

Kim, D., Langmead, B., and Salzberg, S. L. (2015). HISAT: a fast spliced aligner with low memory requirements. *Nat. Methods* 12, 357–360. doi: 10.1038/nmeth.3317

Loss, E. M. O., Lee, M. K., Wu, M. Y., Martien, J., Chen, W. P., Amador-Noguez, D., et al. (2019). Cytochrome P450 monooxygenase-mediated metabolic utilization of benzo[a]pyrene by aspergillus species. *MBio.* 10:e00558–197. doi: 10.1128/mBio.00558-19

Love, M. I., Huber, W., and Anders, S. (2014). Moderated estimation of fold change and dispersion for RNA-seq data with DESeq2. *Genome Biol.* 15:550. doi: 10.1186/s13059-014-0550-8

Machida, M., Yamada, O., and Gomi, K. (2008). Genomics of aspergillus oryzae: learning from the history of Koji mold and exploration of its future. *DNA Res.* 15, 173–183. doi: 10.1093/dnares/dsn020

Martins, T. M., Hartmann, D. O., Planchon, S., Martins, I., Renaut, J., and Silva Pereira, C. (2015). The old 3-oxoadipate pathway revisited: new insights in the catabolism of aromatics in the saprophytic fungus aspergillus nidulans. *Fungal Genet. Biol.* 74, 32–44. doi: 10.1016/j.fgb.2014.11.002

Martins, C., Hartmann, D. O., Varela, A., Coelho, J. A. S., Lamosa, P., Afonso, C. A. M., et al. (2020). Securing a furan-based biorefinery: disclosing the genetic basis of the degradation of hydroxymethylfurfural and its derivatives in the model fungus aspergillus nidulans. *Microb. Biotechnol.* 13, 1983–1996. doi: 10.1111/1751-7915.13649

Martins, T. M., Martins, C., Guedes, P., and Silva Pereira, C. (2021). Twists and turns in the salicylate catabolism of aspergillus terreus, revealing new roles of the 3-Hydroxyanthranilate pathway. *mSystems* 6:e00230–20. doi: 10.1128/mSystems.00230-20

Martins, T. M., Martins, C., and Silva Pereira, C. (2019). Multiple degrees of separation in the central pathways of the catabolism of aromatic compounds in fungi belonging to the Dikarya sub-kingdom. *Adv. Microb. Physiol.* 75, 177–203. doi: 10.1016/bs.ampbs.2019.07.003

Martins, C., Piontkivska, D., Mil-Homens, D., Guedes, P., Jorge, J. M. P., Brinco, J., et al. (2023). Increased production of pathogenic, airborne fungal spores upon exposure of a soil Mycobiota to chlorinated aromatic hydrocarbon pollutants. *Microbiol. Spectr.* 11:e0066723. doi: 10.1128/spectrum.00667-23

Martins, C., Varela, A., Leclercq, C. C., Núñez, O., Větrovský, T., Renaut, J., et al. (2018). Specialisation events of fungal metacommunities exposed to a persistent organic pollutant are suggestive of augmented pathogenic potential. *Microbiome* 6:208. doi: 10.1186/s40168-018-0589-y

Morgan, M., Jones, P., and Sobus, J. (2015). Short-term variability and predictors of urinary pentachlorophenol levels in Ohio preschool children. *Int. J. Environ. Res. Public Health* 12, 800–815. doi: 10.3390/ijerph120100800

Nichols, R. J., Sen, S., Choo, Y. J., Beltrao, P., Zietek, M., Chaba, R., et al. (2011). Phenotypic landscape of a bacterial cell. *Cell* 144, 143–156. doi: 10.1016/j.cell.2010.11.052

Núñez-Corcuera, B., Serafimidis, I., Arias-Palomo, E., Rivera-Calzada, A., and Suarez, T. (2008). A new protein carrying an NmrA-like domain is required for cell differentiation and development in Dictyostelium discoideum. *Dev. Biol.* 321, 331–342. doi: 10.1016/j.ydbio.2008.06.027

Pearce, C. J. (2019). Review of new and future developments in microbial biotechnology and bioengineering: aspergillus system properties and applications. *J. Nat. Prod.* 82:1051. doi: 10.1021/acs.jnatprod.9b00211

Rokas, A. (2022). Evolution of the human pathogenic lifestyle in fungi. *Nat. Microbiol.* 7, 607–619. doi: 10.1038/s41564-022-01112-0

Stajich, J. E., Harris, T., Brunk, B. P., Brestelli, J., Fischer, S., Harb, O. S., et al. (2012). FungiDB: an integrated functional genomics database for fungi. *Nucleic Acids Res.* 40, D675–D681. doi: 10.1093/nar/gkr918

Steenwyk, J. L., Mead, M. E., Knowles, S. L., Raja, H. A., Roberts, C. D., Bader, O., et al. (2020). Variation among biosynthetic gene clusters, secondary metabolite profiles, and cards of virulence across aspergillus species. *Genetics* 216, 481–497. doi: 10.1534/genetics.120.303549

Varela, A., Martins, C., Núñez, O., Martins, I., Houbraken, J. A., Martins, T. M., et al. (2015). Understanding fungal functional biodiversity during the mitigation of environmentally dispersed pentachlorophenol in cork oak forest soils. *Environ. Microbiol.* 17, 2922–2934. doi: 10.1111/1462-2920.12837

Varela, A., Martins, C., and Silva Pereira, C. (2017). A three-act play: pentachlorophenol threats to the cork oak forest soils mycobiome. *Curr. Opin. Microbiol.* 37, 142–149. doi: 10.1016/j.mib.2017.06.007

Vogel, H. J. (1956). A convenient growth medium for Neurospora (medium N). *Microb. Genet. Bull.* 13, 42–43.

Wang, Y., Cao, Y. Y., Jia, X. M., Cao, Y. B., Gao, P. H., Fu, X. P., et al. (2006). Cap1p is involved in multiple pathways of oxidative stress response in *Candida albicans*. *Free Radic. Biol. Med.* 40, 1201–1209.

Wang, H., Lei, Y., Yan, L., Cheng, K., Dai, X., Wan, L., et al. (2015). Deep sequencing analysis of transcriptomes in aspergillus flavus in response to resveratrol. *BMC Microbiol.* 15:182. doi: 10.1186/s12866-015-0513-6

World Health Organization. WHO fungal priority pathogens list to guide research, development and public health action, I. 978-92-4-006024-1, Editor. (2022).

Znaidi, S., Barker, K. S., Weber, S., Alarco, A. M., Liu, T. T., Boucher, G., et al. (2009). Identification of the *Candida albicans* Cap1p regulon. *Eukaryot. Cell* 8, 806–820. doi: 10.1128/EC.00002-09

frontiers | Frontiers in Microbiology

TYPE Original Research
PUBLISHED 27 June 2024
DOI 10.3389/fmicb.2024.1412294

OPEN ACCESS

EDITED BY
Reeta Goel,
GLA University, India

REVIEWED BY
Davide Zannoni,
University of Bologna, Italy
Piyush Pandey,
Assam University, India

*CORRESPONDENCE
Zeynep Petek Çakar
✉ cakarp@itu.edu.tr

†PRESENT ADDRESS
Mevlüt Arslan,
Department of Genetics,
Faculty of Veterinary Medicine, Van Yüzüncü Yıl University, Van, Türkiye

RECEIVED 04 April 2024
ACCEPTED 12 June 2024
PUBLISHED 27 June 2024

CITATION
Atay G, Holyavkin C, Can H, Arslan M, Topaloğlu A, Trotta M and Çakar ZP (2024) Evolutionary engineering and molecular characterization of cobalt-resistant *Rhodobacter sphaeroides*. *Front. Microbiol.* 15:1412294. doi: 10.3389/fmicb.2024.1412294

Evolutionary engineering and molecular characterization of cobalt-resistant *Rhodobacter sphaeroides*

Güneş Atay[1,2], Can Holyavkin[1,2], Hanay Can[1,2], Mevlüt Arslan[1,2†], Alican Topaloğlu[1,2], Massimo Trotta[3] and Zeynep Petek Çakar[1,2*]

[1]Department of Molecular Biology and Genetics, Faculty of Science and Letters, Istanbul Technical University, İstanbul, Türkiye, [2]Dr. Orhan Öcalgiray Molecular Biology, Biotechnology and Genetics Research Center (İTÜ-MOBGAM), Istanbul Technical University, İstanbul, Türkiye, [3]IPCF-CNR Istituto per I processi Chimico-Fisici, Consiglio Nazionale delle Ricerche, Bari, Italy

With its versatile metabolism including aerobic and anaerobic respiration, photosynthesis, photo-fermentation and nitrogen fixation, *Rhodobacter sphaeroides* can adapt to diverse environmental and nutritional conditions, including the presence of various stressors such as heavy metals. Thus, it is an important microorganism to study the molecular mechanisms of bacterial stress response and resistance, and to be used as a microbial cell factory for biotechnological applications or bioremediation. In this study, a highly cobalt-resistant and genetically stable *R. sphaeroides* strain was obtained by evolutionary engineering, also known as adaptive laboratory evolution (ALE), a powerful strategy to improve and characterize genetically complex, desired microbial phenotypes, such as stress resistance. For this purpose, successive batch selection was performed in the presence of gradually increased cobalt stress levels between 0.1–15 mM $CoCl_2$ for 64 passages and without any mutagenesis of the initial population prior to selection. The mutant individuals were randomly chosen from the last population and analyzed in detail. Among these, a highly cobalt-resistant and genetically stable evolved strain called G7 showed significant cross-resistance against various stressors such as iron, magnesium, nickel, aluminum, and NaCl. Growth profiles and flame atomic absorption spectrometry analysis results revealed that in the presence of 4 mM $CoCl_2$ that significantly inhibited growth of the reference strain, the growth of the evolved strain was unaffected, and higher levels of cobalt ions were associated with G7 cells than the reference strain. This may imply that cobalt ions accumulated in or on G7 cells, indicating the potential of G7 for cobalt bioremediation. Whole genome sequencing of the evolved strain identified 23 single nucleotide polymorphisms in various genes that are associated with transcriptional regulators, NifB family-FeMo cofactor biosynthesis, putative virulence factors, TRAP-T family transporter, sodium/proton antiporter, and also in genes with unknown functions, which may have a potential role in the cobalt resistance of *R. sphaeroides*.

KEYWORDS

adaptive laboratory evolution, cobalt resistance, evolutionary engineering, genomic analysis, *Rhodobacter sphaeroides*, stress resistance

1 Introduction

Photosynthetic purple non-sulfur bacteria are commonly used as model organisms to study bacterial photosynthesis (Allen et al., 1988; Yeates et al., 1988; Grattieri et al., 2022). They are also industrially important microorganisms because of their ability to produce hydrogen (H_2) (Gökçe et al., 2012, 2017; Vasiliadou et al., 2018; Li et al., 2024), and their potential applications in bioremediation and bio-sensing (Buscemi et al., 2022; Grattieri et al., 2022). Among photosynthetic purple non-sulfur bacteria, *Rhodobacter sphaeroides* is particularly important, as it has a high adaptation ability that allows it to grow in diverse nutritional and environmental conditions, including heavy-metal-polluted environments (Volpicella et al., 2014). The versatile metabolism of *R. sphaeroides* includes growth by aerobic and anaerobic respiration, photosynthesis under anaerobic conditions in the presence of light and photo-fermentation (Kiley and Kaplan, 1988; Martínez-Luque et al., 1991; Gupta et al., 2024). Upon decreasing oxygen levels, it can easily switch to photosynthetic growth by remodeling the intracellular membrane and producing pigments required for capturing light energy (Imam et al., 2014). *R. sphaeroides* is able to fix CO_2 and N_2, and produce H_2 and polyhydroxybutyrate (PHB) (Mackenzie et al., 2007; Imam et al., 2013). It has a significant biotechnological potential regarding bio-based production of chemicals and fuels (Zeilstra-Ryalls et al., 1998; Mackenzie et al., 2007; Burger et al., 2017; Henry et al., 2020).

Various studies have shown that *R. sphaeroides* can tolerate metal stress, sequester metal ions and reduce oxyanions (Moore and Kaplan, 1992; Bebien et al., 2001; Giotta et al., 2006), as reported previously (Volpicella et al., 2014). Giotta et al. (2006) have shown that *R. sphaeroides* is highly tolerant to Hg^{2+}, Cu^{2+}, Fe^{2+}, Ni^{2+}, Co^{2+}, MoO_4^{2-}, and CrO_4^{2-}, particularly to Co^{2+}, MoO_4^{2-} and Fe^{2+}. The EC_{50} value for Co^{2+} was 0.8 mM, and a consistent biomass yield was obtained even at high cobalt concentrations (5 mM), indicating high cobalt tolerance for *R. sphaeroides* (Giotta et al., 2006). These findings have led to more detailed investigations of the response and resistance of *R. sphaeroides* to cobalt stress.

Cobalt is an industrially important element with magnetic properties and a variety of applications, including refining of alloys, production of gas turbines, jet engines, electrochemical materials and permanent magnets. It is also used in catalysts, paints, varnishes, pigments, inks, ceramics and surgical implants (Stadler and Schweyen, 2002). Most importantly, cobalt has been increasingly used in the cathodes of lithium-ions batteries of highly demanded electric vehicles, to tackle the global warming issue (Lee and Manthiram, 2022). In line with the transition of energy system to clean energy, the global cobalt industry chain has been in focus for risk management and sustainability purposes (Shi et al., 2022).

In addition to its industrial importance, cobalt also has important biological functions. As an essential micronutrient, it is used as a cofactor of vitamin B12 (cobalamin), and in the catalysis of important enzymes in microorganisms, plants and animals (Battersby, 1994; Kobayashi and Shimizu, 1999). However, as a transition metal, cobalt is toxic to living organisms at high concentrations (Çakar et al., 2009; Pisani et al., 2009; Belviso et al., 2013). In a yeast (*Saccharomyces cerevisiae*) reference strain CEN.PK 113-7D; 2.5 mM $CoCl_2$ resulted in 50% inhibition of growth, and no growth was observed at $CoCl_2$ concentrations higher than 5 mM (Çakar et al., 2009). The bacterium *Pseudomonas aeruginosa* could tolerate Co^{2+} concentrations lower than 0.8 mM (Hassen et al., 1998). In *R. sphaeroides*, the Co^{2+} concentration required in the growth medium (M27) is about 1 μM. However, high concentrations of cobalt result in toxic effects that can decrease its growth: the effective concentration (EC_{50}) of Co^{2+} to reduce the growth rate of *R. sphaeroides* by 50% of the value observed under control conditions is 0.8 mM (Giotta et al., 2006). In various studies with *R. sphaeroides* that focused on the effects of cobalt stress, the growth medium had about 5 mM Co^{2+} concentration (Pisani et al., 2009; Losurdo et al., 2010; Belviso et al., 2013; Volpicella et al., 2014), as *R. sphaeroides* could still have a consistent biomass yield, even at about 5 mM $CoCl_2$ (Giotta et al., 2006). The high cobalt tolerance of *R. sphaeroides* has led to further investigations of the mechanisms of cobalt response and resistance in this species. Italiano et al. (2009) studied the bioadsorption and bioaccumulation of Co, Ni and Mg, using inductively coupled plasma atomic emission spectroscopy and attenuated total reflection Fourier transform infrared spectroscopy (ATR-FTIR). Their results revealed the competition of Co^{2+} with Mg^{2+} for the same carboxylate binding groups on the outer membrane of *R. sphaeroides* (Italiano et al., 2009). In addition, X-ray absorption spectroscopy results revealed extensive binding of cobalt ions to sulfolipids on the photosynthetic membrane of *R. sphaeroides* (Belviso et al., 2013). Lipidome analysis of *R. sphaeroides* in the presence of cobalt and chromate ions stress using thin-layer chromatography coupled with matrix-assisted laser desorption ionization mass spectrometry (MALDI-MS) showed that, upon Co^{2+} ion stress, a significant increase occurred in sulfoquinovosyldiacylglycerols and a decrease in phosphatidylglycerols was observed in the membrane lipids of *R. sphaeroides* (Calvano et al., 2013). The photosynthetic membrane proteome analysis of *R. sphaeroides* revealed that many proteins of the photosynthetic apparatus were differentially expressed upon exposure to cobalt stress (Italiano et al., 2011).

Despite the biotechnological importance of both *R. sphaeroides* and cobalt, there is a limited number of studies that investigated the genetic factors associated with cobalt resistance in *R. sphaeroides*: Volpicella et al. (2014) selected cobalt-sensitive mutants from a *R. sphaeroides* transposon insertion library and performed comparative transcriptomic and genomic analyses of a selected cobalt-sensitive mutant. The transcriptome profiling results showed that an ATP-binding cassette (ABC) sugar transporter was significantly downregulated in the cobalt-sensitive mutant strain which had a mutation (transposon insertion) in the RSP_7363 gene that encodes a hypothetical protein. Interestingly, the mutant strain was not significantly inhibited in the presence of high levels of cobalt stress when cultured under photosynthetic conditions. Thus, it was concluded that an additional energetic resource provided by the ABC sugar transporter may be required to overcome the cobalt stress, and the ability of the mutant strain to exploit light energy during photosynthetic conditions may compensate for the impairment of the ABC sugar transporter (Volpicella et al., 2014). More recently, using a bioinformatics approach, functional annotation of heavy metal tolerance genes of *R. sphaeroides* were analyzed and the majority of those genes (255 genes, about 63%) were encoding metal-dependent enzymes or enzymes reducing metallic compounds to elemental metals. In addition, the second largest group (127 genes, about 34%) was encoding transporters that involve metal-binding proteins and ATPase translocases, making *R. sphaeroides* a good model organism for studying heavy metal tolerance and for bioremediation applications

(Johnson et al., 2019). The exact molecular mechanisms of metal or cobalt-resistance in *R. sphaeroides* are yet to be clarified.

Evolutionary engineering or adaptive laboratory evolution (ALE) is a powerful strategy to improve industrially important microbial properties with an unknown molecular basis (Mavrommati et al., 2023; Topaloğlu et al., 2023). It exploits nature's evolutionary principles based on random mutation and systematic selection to favor a desirable phenotype (Butler et al., 1996; Sauer, 2001). In our research group, we have successfully applied evolutionary engineering to obtain cobalt-resistant (Çakar et al., 2009; Alkım et al., 2013), iron-resistant (Balaban et al., 2020), nickel-resistant (Küçükgöze et al., 2013), silver-resistant (Terzioğlu et al., 2020) and oxidative stress-resistant (Kocaefe-Özşen et al., 2022) yeast (*S. cerevisiae*) strains. In addition, we have also successfully applied evolutionary engineering to industrially important bacteria such as *Rhodobacter capsulatus* (Gökçe et al., 2012, 2017), and *Bacillus boroniphilus* (Şen et al., 2011), to improve their heat- and boron-resistance, respectively. Using comparative genomic, transcriptomic, and/or physiological analysis of the highly-resistant evolved and original/reference strains, the complex molecular basis of the desired properties, such as resistance to a particular stress type, can be identified.

The aim of this study was to obtain a cobalt-hyperresistant *R. sphaeroides* strain by using evolutionary engineering and to investigate the molecular basis of cobalt resistance in the metabolically diverse bacterium *R. sphaeroides* by comparative genomic and physiological analyses. For this purpose, *R. sphaeroides* reference strain was subjected to an evolutionary batch selection procedure at gradually increased cobalt concentrations between 0.1–15 mM $CoCl_2$ in the culture medium. Individual colonies (mutants) were randomly picked upon growing the final population of selection on solid plates. The colonies were then physiologically characterized based on their stress resistance and genetic stability, to identify an evolved strain (G7) with superior resistance properties. Whole-genome re-sequencing of the evolved strain G7 and the reference strain revealed single nucleotide polymorphisms (SNPs) that may be associated with the high cobalt-resistance of the evolved strain. The resistance tests against cobalt and other stressors, growth physiological analyses and genome sequence data showed that the growth of the evolved strain was not inhibited by 4 mM $CoCl_2$ that significantly inhibited the reference strain's growth and higher amounts of cobalt ions were accumulated in or on the evolved strain, compared to the reference strain, indicating a bioremediation potential for the evolved strain. The SNPs were observed in diverse genes of the evolved strain related to transcriptional regulation, NifB family-FeMo cofactor biosynthesis, putative virulence factors, TRAP-T family transporter, sodium/proton antiporter, and many genes with unknown function that may play a key role in the cobalt resistance of *R. sphaeroides*.

2 Materials and methods

2.1 Strain, media and growth conditions

The *Rhodobacter sphaeroides* R-26 strain (Dr. Massimo Trotta's laboratory collection) was used in this study. The original carotenoidless strain is known to have a tendency to revert (Kwa et al., 2008). In this study, it was allowed to revert to the reddish form to avoid any further stress imposed by the maintenance of the mutant. For this purpose, the chemoheterotrophically grown R-26 culture was directly placed under strict anaerobic photosynthetic conditions, as described previously (Kiley et al., 1988) which has been shown to increase the frequency of revertants in the population (Kiley et al., 1988). The reverted strain - named RR-26 - was used as the reference strain (RS) throughout this study and is now available from the laboratories. Unless otherwise stated, *R. sphaeroides* cultures in this study were grown under aerobic conditions in the dark, at 37°C and 150 rpm using Medium 27 (M27) of Deutsche Sammlung von Mikroorganismen und Zellkulturen GmbH (DSMZ). M27 consisted of 100 µg/L $ZnSO_4.7H_2O$, 30 µg/L $MnCl_2.4H_2O$, 300 µg/L H_3BO_3, 200 µg/L $CoCl_2.6H_2O$, 10 µg/L $CuCl_2.2H_2O$, 20 µg/L $NiCl_2.6H_2O$, and 30 µg/L $Na_2MoO_4.2H_2O$ as micronutrients; and 500 mg/L KH_2PO_4, 800 mg/L $MgSO_4.7H_2O$, 400 mg/L NaCl, 400 mg/L NH_4Cl, 50 mg/L $CaCl_2.2H_2O$, 1,500 mg/L D-L malic acid, 2000 mg/L yeast extract, 1 mg/L p-amino benzoic acid, and 18 mg/L iron (II) citrate as macronutrients that were dissolved in ddH_2O (Italiano et al., 2009). The pH of the medium was adjusted to 6.8 after macronutrients were dissolved in deionized water and autoclaved at 121°C for 15 min. Micronutrients were filter-sterilized using 0.22 µm pore-size filters, and then added into the sterilized M27 medium. The medium was stored at 4°C in the dark. For solid plate cultivations, Luria-Bertani (LB) medium was used. It included 10 g NaCl, 10 g tryptone, 5 g yeast extract and 20 g agar in 1 L of ddH_2O (Bertani, 1951). Growth was monitored by optical density measurements at 660 nm (OD_{660}), using a spectrophotometer (Shimadzu UV- 1700, Japan). Cultures were stored at −80°C in 2 mL M27 medium containing 30% (v/v) glycerol.

2.2 Evolutionary engineering of cobalt-resistant *Rhodobacter sphaeroides* strains

To determine the initial cobalt stress levels to be applied in evolutionary engineering experiments, overnight pre-culture of the reference strain grown aerobically in the dark in M27 medium at 37°C and 150 rpm was inoculated into 15 mL fresh M27 medium containing 0–5 mM $CoCl_2$ in 50 mL culture tubes, to an initial OD_{660} of 0.1. Cultures were then incubated aerobically at 37°C, 150 rpm in the dark for 24 h, serially diluted and spread on LB plates. Three independent values of colony-forming units (CFU) were determined by direct plate counting, upon 72-h incubation at 37°C. The survival rates under various cobalt stress conditions were calculated by dividing the CFU values under cobalt stress condition to the CFU value of the control culture. Successive batch selection was used as an evolutionary engineering strategy by gradually increasing $CoCl_2$ concentration throughout the passages or populations. For this purpose, 100 µL of the reference strain's (RS) stock culture at - 80°C were inoculated into 15 mL fresh M27 medium in a 50 mL culture tube, and incubated overnight at 37°C and 150 rpm, aerobically in the dark. This pre-culture was then inoculated into 15 mL fresh M27 medium containing 0.1 mM $CoCl_2$ in a 50 mL culture tube, and incubated overnight again aerobically at 37°C in the dark and at 150 rpm. This culture treated with 0.1 mM $CoCl_2$ stress was named as the first population of selection. This procedure was repeated for a total of 64 passages or populations, by gradually increasing the $CoCl_2$ concentration at each passage. For each population, the cultures were also incubated under control conditions in M27 medium, in the absence of $CoCl_2$.

These control cultures were used to determine the survival rates for each population, by dividing the final OD_{660} value of the stressed culture to that of the control culture. The final population of the selection was diluted by 10^6 –fold, and spread on solid LB plates to randomly pick individual mutant colonies after 4 days of incubation at 37°C.

2.3 Estimation of stress resistance

Cobalt resistance levels of selected individual mutants from the final population were quantitatively determined using the Most Probable Number (MPN) method (Russek and Colwell, 1983; Çakar et al., 2005), by applying serial dilutions in 96-well plates containing 180 µL M27 (control), and varying amounts of $CoCl_2$ in 180 µL M27 (cobalt stress condition). The MPN method was applied as five replicates. Briefly, in control plates, cultures were diluted in the range of 10^{-1} to 10^{-12}, and in plates with 2 mM, 4 mM, 6 mM, 8 mM or 15 mM $CoCl_2$ stress, cultures were diluted in the 10^{-1} to 10^{-8} range. After incubation at 37°C for 4 days, the number of surviving cells at different cobalt concentrations was estimated by using MPN tables (Lindquist, 2020).

Resistance of selected individual mutants to $CoCl_2$ and other stressors were determined using spot assay. Individual mutants and the RS were revived in M27 medium. During exponential growth phase of the cells, cultures were inoculated into 10 mL M27 in 50 mL culture tubes at a starting OD_{660} of 0.2 and incubated aerobically at 37°C, 150 rpm in the dark. When the cultures reached an OD_{660} of 1.2, 5 OD_{660} units/mL cells were collected by centrifugation at 10,000 × g for 5 min. Pellets were resuspended in 1 mL M27 and serial dilutions of the cultures were made and spotted on solid LB plates containing 1–5 mM $CoCl_2$ as cobalt stress conditions, and on an LB plate without $CoCl_2$, as the control condition. Similarly, to test for cross-resistance to other stressors, serial dilutions of the cultures were spotted on solid LB plates containing ethanol (8% v/v), NaCl (0.5 M), $AlCl_3$ (5 mM), $CuCl_2$ (0.5 mM), $NiCl_2$ (2.0–2.4 mM), $MgCl_2$ (0.5 - 1 M), H_2O_2 (1–2 mM), $FeCl_2$ (4–5 mM), $MnCl_2$ (10 mM), H_3BO_3 (30–50 mM), caffeine (20 mM), $(NH_4)_2$ Fe $(SO_4)_2$ (5 mM), and $ZnCl_2$ (1 mM). Plates were incubated at 37°C for 4 days.

2.4 Growth analyses

Growth profiles of RS and a cobalt-resistant, evolved strain were obtained spectrophotometrically at OD_{660} and by dry weight measurements. For this purpose, firstly, precultures were prepared by inoculating 100 µL of stock cultures into 10 mL fresh M27 medium in 50 mL culture tubes. After overnight incubation at 37°C and 150 rpm aerobically and in the dark, cultures were inoculated into 500 mL flasks containing 100 mL M27 (control condition) and 100 mL M27 with 4 mM CoCl2 (cobalt stress condition), to an initial OD_{660} value of 0.2, and grown again aerobically in the dark, at 37°C and 150 rpm. Samples were taken from the cultures at two-hour intervals. For cell dry weight analysis, 1.5 mL microfuge tubes were dried in an oven at 80°C for 48 h, placed in a desiccator for 3 h, and then weighed. Two mL of samples were withdrawn from the cultures, transferred to the pre-weighed microfuge tubes, and centrifuged at 15,000 g for 5 min. The culture supernatants were discarded and pellets were placed in an oven at 80°C to dry. After 48 h, the tubes were reweighed. The experiments were performed in triplicate.

2.5 Determination of cellular cobalt contents by flame atomic absorption spectrometry (FAAS)

Pre-cultures were prepared by inoculating 100 µL of the stock cultures into 10 mL fresh M27 in 50 mL culture tubes, and incubating overnight and aerobically in the dark at 37°C and 150 rpm. After overnight incubation, pre-cultures were inoculated into 10 mL fresh M27 (control condition), and M27 with 4 mM $CoCl_2$ (cobalt stress condition) in 50 mL culture tubes, to an initial OD_{660} of 0.25. Cultures were incubated under aerobic conditions in the dark at 37°C, 150 rpm for 24 h. They were then centrifuged at 5000 g for 15 min. The supernatants were discarded and the cell pellets were washed twice by using distilled water, dried at 110°C for 2 h and the cell dry weights were measured as described in the previous section. Cell pellets were then hydrolyzed at 90°C for 2 h, by using 10 M HNO_3. Cobalt contents were determined by using a Flame Atomic Absorption Spectrophotometer (FAAS), an Analytik-Jena Model AAS Vario 6 (Germany), with a hollow cathode lamp. The wavelength and slit width values were 240.7 and 0.2 nm. The experiments were performed in triplicate.

2.6 Whole genome re-sequencing

For comparative whole genome re-sequencing, 100 µL of the stock cultures of the RS and the evolved strain were inoculated into 10-mL fresh M27 medium in 50 mL culture tubes. Upon overnight incubation under aerobic conditions at 37°C, and 150 rpm in the dark, 500 µL of cultures were centrifuged at 15000 g for 5 min and DNA isolation was performed by using the MasterPure DNA Purification Kit (Epicentre) according to the manufacturer's protocol. DNA purity and concentration were determined by using a NanoDrop 2000 UV–Vis spectrophotometer (Thermo Fisher Scientific). The sequencing libraries were prepared by Ion Xpress Plus Fragment Library Kit (Thermo Fisher Scientific) and Ion 540Chip Kit, following the manufacturer's protocol. Next generation sequencing was performed on the Ion S5 Platform (Thermo Fisher Scientific), by using automated library prep platform Ion ChefTM (Thermo Fisher Scientific). The quality control of raw data was performed by using FastQC software v.0.11.9 (Babraham Bioinformatics). The Trimmomatic v.0.39 software (Bolger et al., 2014) was used to remove adapter sequences and low-quality sequences from reads. The reference genome of *R. sphaeroides* 2.4.1 was used to align the reads from the cobalt-resistant, evolved strain and the *R. sphaeroides* R-26 reference strain used in this study. Subsequently, the variations shared between the evolved strain and R-26 were identified. Once these common variations were defined, the remaining ones were determined to be specific to the evolved strain. Burrows– Wheeler aligner MEM v.0.7.1 (Li and Durbin, 2009) was used as a sequence alignment tool. Variant calling was carried out by using Genome Analysis Toolkit (GATK) v.3.8.0 (DePristo et al., 2011) and each nucleotide change was inspected with Genome Browse v2.1.2 (GoldenHelix). In-house R scripts were used to eliminate low-quality single nucleotide

polymorphisms (SNPs). Remaining SNPs were annotated by using Variant Effect Predictor v.90. Whole-genome re-sequencing data have been deposited in the NCBI Sequence Read Archive (SRA) under BioProject PRJNA1047122.

3 Results

3.1 Evolutionary engineering of cobalt-resistant *Rhodobacter sphaeroides*

Before starting with the evolutionary engineering experiments, the reference strain was cultivated in the presence of varying levels of cobalt stress (0–5 mM $CoCl_2$), and the survival rates of the cultures were determined by direct plate counting. According to the survival rate values of these cultures, 0.1 mM $CoCl_2$ was chosen as the initial, mild cobalt stress level for evolutionary selection experiments (Supplementary Figure S1). The reference strain could not grow at $CoCl_2$ concentrations higher than 10 mM (data not shown).

As the evolutionary engineering strategy, successive batch selection was used by gradually increasing $CoCl_2$ concentration from an initial level of 0.1 mM up to 15 mM for 64 passages or populations. The $CoCl_2$ concentration was increased by 0.05 mM at each population between the first and 13th populations (between 0.1 mM and 0.7 mM $CoCl_2$), and then gradually increased at varying steps, as indicated in Table 1, reaching the final cobalt stress level of 15.0 mM $CoCl_2$ at the 64th passage of selection. The 64th passage of the selection was named as the final population of selection, and was spread on LB plates. Upon incubation for 4 days, eight individual colonies were randomly picked from the final population plates as individual mutant strains to investigate their stress resistance. An evolved strain was defined as a mutant strain that has been isolated as a colony from the final (64th) population of selection.

3.2 Stress resistance properties of the evolved strains

The eight individual mutant colonies (named G1-G8) randomly picked from the final population plate had varying red pigmentation intensities: G1, G2 and G3 had pink color, G4 and G5 were red, and G6, G7 and G8 were dark red. The quantitative estimation of cobalt resistance of the evolved strains was made by using the MPN method. For this purpose, the individual mutants and RS were cultivated in 96-well plates in the absence and presence of 2–8 mM $CoCl_2$ stress. These $CoCl_2$ concentrations were chosen based on the literature information (Giotta et al., 2006; Volpicella et al., 2014) and our cobalt stress survival data for the reference strain determined by direct plate counting (Supplementary Figure S1). The stress survival rates of the individual mutants were calculated by dividing the estimated number of the individual mutant cells upon $CoCl_2$ stress exposure to that under control (no stress) condition. The stress survival rates of the individual mutants were normalized to that of the RS. The results revealed that the individual mutants showed significantly higher resistance to $CoCl_2$ stress than the RS. Among them, the mutant G7 had higher cobalt resistance levels than most of the other mutant individuals at 4–6 and 8 mM $CoCl_2$ (Figure 1).

The spot assay results of the evolved strains confirmed the $CoCl_2$ stress resistance of the evolved strains. The cobalt stress resistance levels of the evolved strains G1-G8 and the 64th population were determined by spotting serial dilutions of the cultures on LB plates containing 0–5 mM $CoCl_2$. These $CoCl_2$ concentrations were also chosen based on the literature information (Giotta et al., 2006; Volpicella et al., 2014) and our cobalt stress survival data for the reference strain determined by direct plate counting (Supplementary Figure S1). As the individual mutant G2 became contaminated, it was excluded from the spot assay and further analyses. The spot assay results revealed that the evolved strains had significantly higher resistance than the RS. At $CoCl_2$ concentrations higher than 3 mM on LB plates, the growth of the RS was completely inhibited. However, the evolved strains could grow up to higher dilution levels at these inhibitory $CoCl_2$ concentrations which indicates their high cobalt resistance (Figure 2).

TABLE 1 $CoCl_2$ stress levels that were applied during 64 successive batch populations of evolutionary engineering selection.

Population number	$CoCl_2$ stress level increase (mM) at each population	$CoCl_2$ stress level (mM) of the population
1–13	0.05	0.1–0.7
13–16	0.1	0.7–1.0
16–49	0.2	1.0–7.6
49–50	0.4	7.6–8.0
50–64	0.5	8.0–15.0

3.3 Cross-resistance of cobalt-resistant mutant individuals to other stress factors

It is known that bacterial cultures can develop cross-resistance against other stress types, when they are exposed to one stress type. This phenomenon is also known as environmental adaptation or cross-protection (Rangel, 2011). To test for the potential cross-resistance of the cobalt-resistant evolved strains against other stressors, spot assay was performed in the presence of various stressors, as described in the Materials and Methods section. The concentrations of other stressors were determined based on our previous cross-resistance studies (Çakar et al., 2009; Terzioğlu et al., 2020; Kocaefe-Özşen et al., 2022) and preliminary optimization experiments to find those stressor concentrations that can cause a clear growth difference between the reference strain and the evolved strains in spot assays. For NaCl, for example, the required amount provided in the M27 medium for the growth of *R. sphaeroides* is about 6.6 mM (400 mg/L). Although it has been reported that NaCl concentrations up to 300 mM did not cause a significant growth inhibition in *R. sphaeroides*, complete growth inhibition was observed at NaCl concentrations higher than 1 M (Labarile et al., 2021). Thus, 0.5 M NaCl was chosen as the NaCl stress condition in this study, to test for the potential halotolerance of the evolved strains. The results revealed that the evolved strain G7 was highly cross-resistant to most of the stressors tested. Among all evolved strains and the RS, it was the only strain that could grow in the presence of 20 mM caffeine, 2.2 and 2.4 mM $NiCl_2$, 0.75 and 1 M $MgCl_2$, 50 mM H_3BO_3 and 5 mM $(NH_4)_2Fe(SO_4)_2$ stress. In addition, G7 also showed significantly higher resistance than the reference

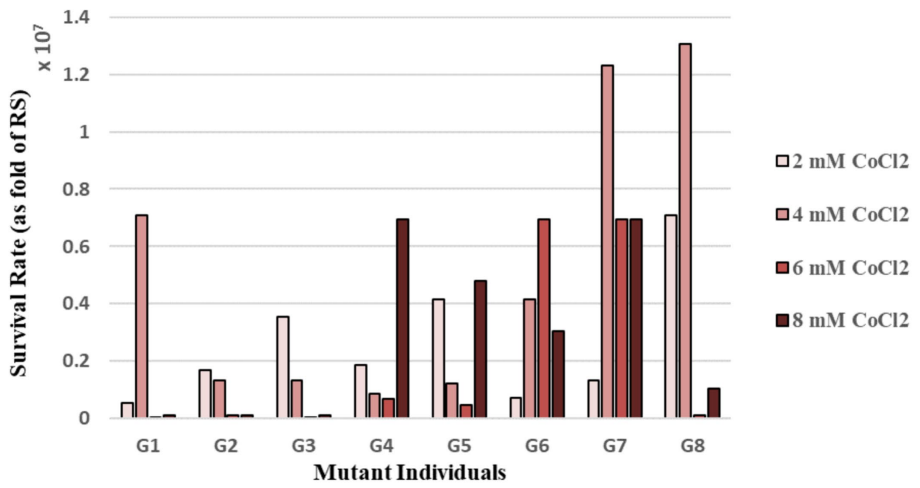

FIGURE 1
Survival rates [as fold of the reference strain (RS)] of the mutant individual colonies of the final population of selection, upon continuous exposure to varying levels of cobalt stress, as determined by the Most Probable Number (MPN) method.

strain and the other evolved strains against 0.5 M NaCl, 5 mM $AlCl_3$ and 5 mM $FeCl_2$ stresses (Figure 3).

As the evolved strain G7 was highly resistant to cobalt stress and showed high levels of cross-resistance against many other stressors, this robust strain was chosen for genetic stability test and further detailed investigations. The genetic stability test was performed by growing G7 in M27 medium in the absence of cobalt stress for 10 successive passages and testing for the cobalt resistance of each passage by growth on LB plates containing 4 mM $CoCl_2$. The results revealed that there was no loss of resistance levels upon this successive cycle (data not shown).

3.4 Growth profiles of the RS and the evolved strain G7

The growth behavior of the RS and the evolved strain G7 was investigated in M27 medium under aerobic conditions in the dark, both in the presence and absence of cobalt stress (4 mM $CoCl_2$). The results revealed that 4 mM $CoCl_2$ stress had no significant inhibitory effect on the evolved strain G7, although it significantly inhibited the growth of the RS (Figure 4).

The maximum specific growth rates of G7 in the absence and presence of 4 mM $CoCl_2$ stress were calculated as 0.19 h^{-1} and 0.13 h^{-1}, respectively. For the RS, however, the μ_{max} values in the absence and presence of 4 mM $CoCl_2$ stress were 0.23 h^{-1}, and 0.07 h^{-1}, respectively. The strong inhibitory effect of 4 mM $CoCl_2$ stress on the RS and the strong cobalt resistance of G7 were also verified by the final cell dry weights (CDW) of the cultures (Figure 5).

3.5 Cobalt contents of the RS and the evolved strain G7

The cobalt contents of the RS and the evolved strain were determined using Flame Atomic Absorption Spectrometry (FAAS). Both strains were grown aerobically, in the dark, and in the presence of 4 mM $CoCl_2$ which is the same cobalt stress level used for growth experiments, to enable comparison of growth profiles and cobalt content data under the same stress conditions. The results revealed that the cobalt-resistant, evolved strain G7 had a significantly higher cobalt content (about 13 mg/g CDW) than the RS which accumulated only about 0.6 mg cobalt/g CDW (Table 2).

3.6 Comparative whole-genome resequencing of the evolved strain G7

Whole-genome resequencing results revealed 23 mutations in the evolved strain G7 that were not found in the RS. One start-loss, 14 non-synonymous (missense) and 8 synonymous mutations were identified in the G7 genome (Table 3).

The start-loss mutation was found in the open reading frame (ORF) ID: RSP_7501 that encodes a hypothetical protein. Two missense mutations were identified in the MviN gene that codes for the putative virulence factor MviN. Other missense mutations were identified in RSP_2320 that encodes a TRAP-T family transporter, periplasmic binding protein; in the hutC gene encoding a histidine utilization repressor of the gntR family; rpoD gene that encodes the RNA polymerase sigma 70 subunit RpoD; nifB gene coding for an FeMo cofactor biosynthesis protein of the NifB family; mbfA gene that codes for a membrane-bound ferritin; nhaD gene encoding a sodium/proton antiporter of the NhaD family; RSP_2417 that codes for a transglutaminase-like enzyme, a predicted cysteine protease; RSP_3478 coding for a type VI secretion protein; RSP_3988 encoding a putative glycosyltransferase; and RSP_4277 encoding a transcriptional regulator of MerR family. Interestingly, two missense and eight synonymous mutations were observed in RSP_3791 that encodes a hypothetical protein (Table 3).

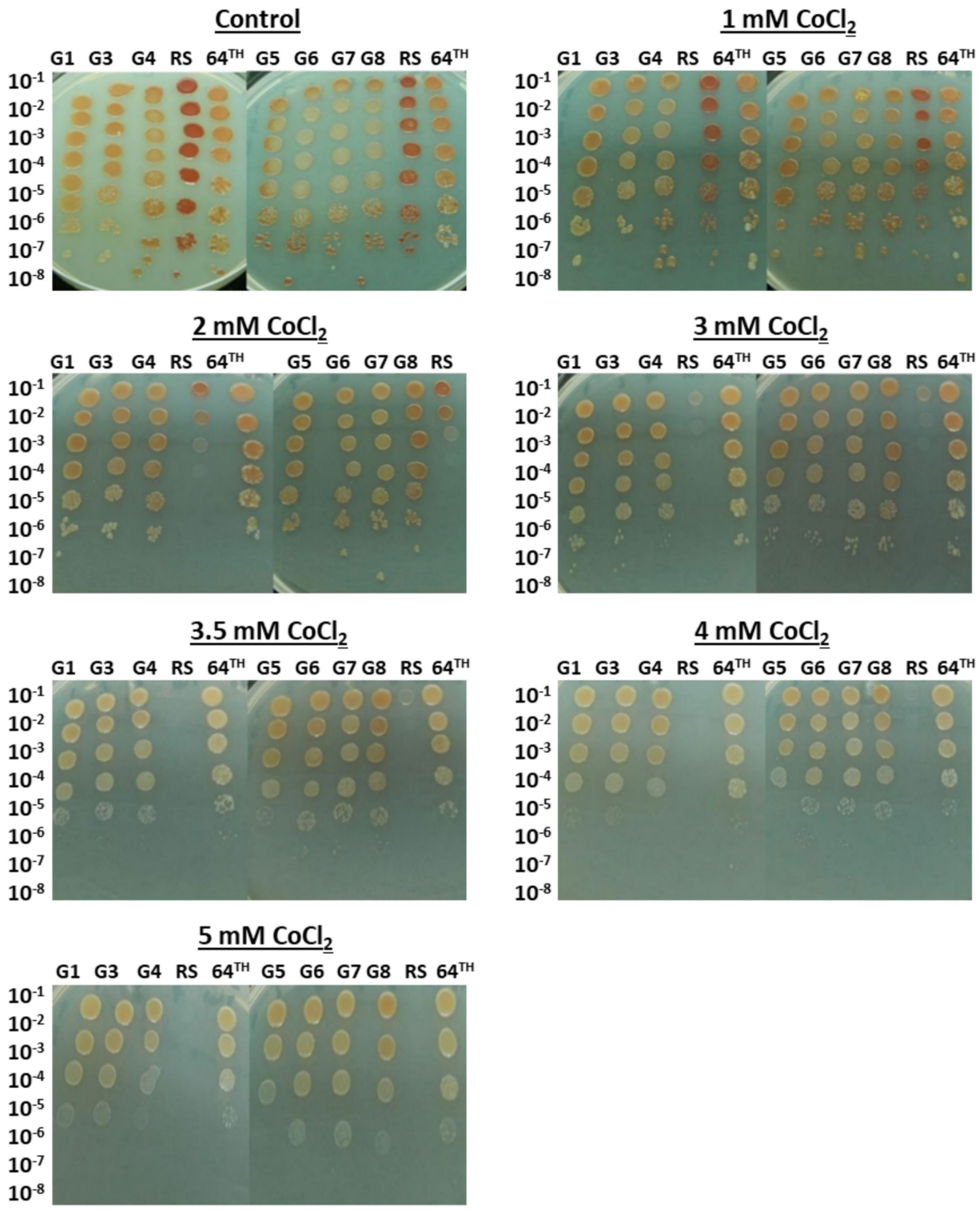

FIGURE 2
Cobalt stress resistance of the mutant individual colonies, final (64th) population of selection and the reference strain (RS), as determined by the spot assay. The cultures were spotted on LB (control condition) and 1–5 mM $CoCl_2$-containing LB (stress conditions) plates in serial dilutions, and incubated at 37°C for 4 days.

4 Discussion

In this study, we have successfully obtained a highly cobalt-resistant and genetically stable *R. sphaeroides* strain by evolutionary engineering. The evolved strain was isolated from the final (64^{th}) population of the successive batch selection in the presence of increasing levels of $CoCl_2$ stress, starting from 0.1 mM $CoCl_2$ in the first population and gradually increasing up to 15 mM in the final

10.3389/fmicb.2024.1412294

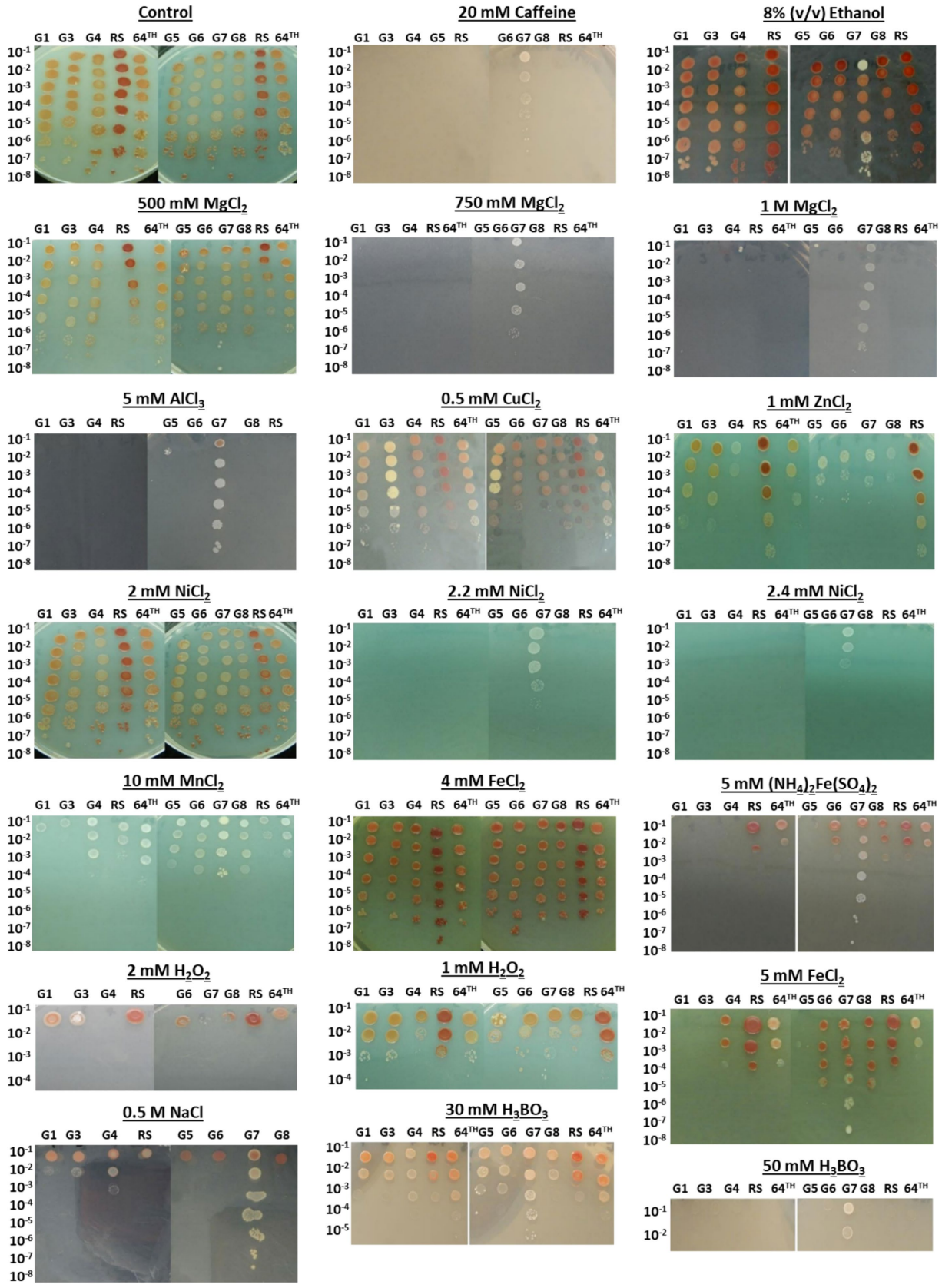

FIGURE 3
Cross- resistance of the mutant individual colonies, final (64th) population of selection and the reference strain (RS) against various stressors, as determined by the spot assay. The cultures were spotted on LB plates (control condition) and LB plates with various stressors (stress conditions) in serial dilutions, and incubated at 37°C for 4 days.

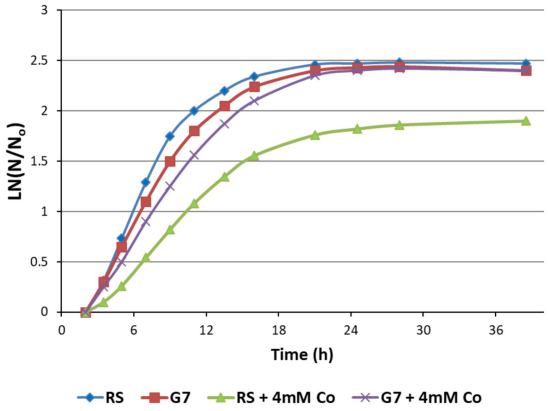

FIGURE 4
Growth curves of the reference strain (RS) and the cobalt-resistant, evolved strain G7 represented as ln (N/N_0), in the presence and absence of 4 mM $CoCl_2$. N is the number of cells and N_0 is the initial number of cells in the culture. Cultures were grown at 37°C for 38 h, using M27 medium.

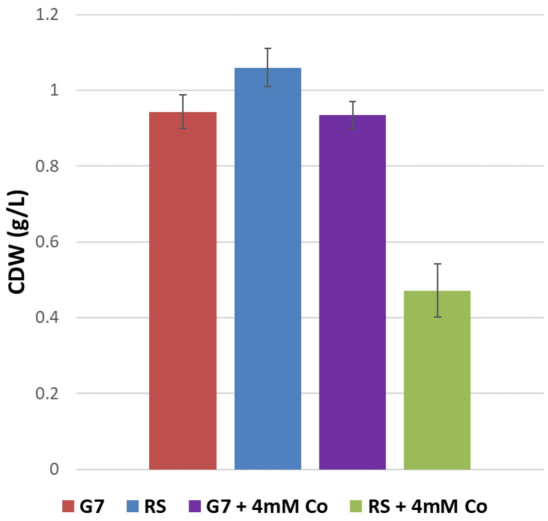

FIGURE 5
Final cell dry weights (CDW) of the reference strain (RS) and the cobalt-resistant, evolved strain G7, in the presence and absence of 4 mM $CoCl_2$. Cultures were grown in M27 medium at 37°C for 38 h.

population. To our knowledge, 15 mM $CoCl_2$ is the highest $CoCl_2$ stress level that has been reported so far, at which *R. sphaeroides* cells could survive.

Our physiological analyses of the highly cobalt-resistant, evolved strain G7 revealed that, in addition to its high level of cobalt resistance, G7 was highly cross-resistant against many other stressors. These stressors include $FeCl_2$, $(NH_4)_2Fe(SO_4)_2$, NaCl, $MgCl_2$, H_3BO_3, $AlCl_3$, $NiCl_2$, and caffeine (Figure 3). With its dark red color, the highly cobalt-resistant, evolved strain G7 had also a high pigmentation intensity. The relationship between stress conditions and carotenoid production has been reported previously for diverse organisms. The mollusc *Perna viridis* with high carotenoid content was shown to be highly resistant to environmental pollution, and the concentration of carotenoids was high when the heavy metal concentrations including cobalt were high in the tissues of *P. viridis* (Tewari et al., 2001). In the copper-tolerant yeast strain *Rhodotorula mucilaginosa* RCL-11, the presence of copper and the oxidative stress agent H_2O_2 in the culture medium increased its carotenoid pigment levels and changed the carotenoid profiles (Irazusta et al., 2013). Moreover, in photosynthetic bacteria (*Rhodopseudomonas*) that could tolerate high salinity, it was shown that salinity stress of about 50 g/L NaCl enhanced carotenoid and bacteriochlorophyll production (Wang et al., 2017). Thus, the high level of pigmentation in our evolved strain G7 may be associated with its improved tolerance against various stressors.

Iron is an essential element for living organisms, as it is involved as a cofactor in several enzymes and regulatory proteins. Studies with *Escherichia coli* and *Salmonella enterica* identified iron–sulfur [Fe-S] proteins as the primary targets of cobalt ions. It was shown that cobalt competes out iron during [Fe-S] cluster synthesis in metabolically essential proteins, and inactivates [Fe-S] enzymes. Cobalt stress resulted in oxidative stress, perturbation of iron homeostasis and decreased sulfur assimilation. Moreover, genes related to the biosynthesis of [Fe-S] gene clusters and cobalt efflux were upregulated, and genes involved in the transport of iron and nickel ions were downregulated in *E.coli* cells, when exposed to cobalt ions. This suggested that the transporters for nickel and iron were possibly used by cobalt ions to enter the cells (Ranquet et al., 2007; Barras and Fontecave, 2011). As reduced iron results in oxygen toxicity by producing hydroxyl radicals in the Fenton reaction, life under aerobic conditions requires a strictly regulated iron metabolism. Consequently, a transcriptomic study with *R. sphaeroides* showed that many genes of iron metabolism are induced upon oxidative stress (Peuser et al., 2012). Thus, the observed cross-resistance against iron stress may also provide survival and growth advantage to our evolved strain G7 under aerobic conditions. It is also important to note that *R. sphaeroides* may have increased its activities related to iron transport and metabolism, as a response and resistance mechanism against cobalt stress, considering the fact that both Co^{2+} and Fe^{2+} are divalent cations and the existing cellular mechanism for Fe^{2+} response can be used by the cells when they are exposed to a less common ion, such as Co^{2+}, as reported for *E. coli* previously (Barras and Fontecave, 2011). We have previously observed this behaviour also in a cobalt-resistant, evolved yeast (*S. cerevisiae*) strain that was cross-resistant to iron and nickel stress, and many genes implicated in iron metabolism under the control of the transcriptional activator Aft1p were found to be highly upregulated in that cobalt-resistant *S. cerevisiae* strain (Çakar et al., 2009; Alkım et al., 2013). In addition, a nickel-resistant, evolved *S. cerevisiae* strain also showed cross-resistance against cobalt and iron stress, along with the upregulation of many Aft1p-regulated genes (Küçükgöze et al., 2013), indicating that resistance against cobalt and nickel stress may be associated with the iron response and resistance mechanism in *S. cerevisiae*. The observed cross-resistance of the G7 strain against iron and nickel stress may also be related to a similar, common resistance mechanism in *R. sphaeroides* for cobalt, iron and nickel stresses. The nickel cross-resistance of G7 was also high, as it could survive 2.4 mM $NiCl_2$ stress. In a previous study with nickel-resistant bacteria isolated from industrial wastewater, the maximum tolerable nickel concentrations of some isolated species were 1 mM for *Moraxella bovis*, 2 mM for *Acinetobacter lwoffii, Providencia stuartii* and *Branhamella catarrhalis* (Alboghobeish et al., 2014), implying that our G7 strain's nickel resistance is comparable to that of the bacterial isolates from heavy metal-rich industrial

TABLE 2 Cobalt contents [in mg/g cell dry weight (CDW)] of G7 and RS in the presence of 4 mM $CoCl_2$ stress.

Stress condition	Replicate no	RS (mg/g CDW)	G7 (mg/g CDW)
	1	0.60	8.64
4 mM $CoCl_2$	2	0.69	15.84
	3	0.41	13.98
Average		**0.57 ± 0.14**	**12.82 ± 3.74**

TABLE 3 Mutations that were identified in the cobalt-resistant, evolved *R. sphaeroides* strain G7, based on comparative whole genome-resequencing of G7 and the reference strain (RS).

ORF ID	Gene name	Genomic location	Type of mutation	Amino acid change	Codon change	Description (bacteria.ensembl.org)
RSP_7501	–	1:140292	Start lost	M/T	aTg/aCg	Hypothetical protein
RSP_1810	mviN	1:397063	Missense variant	V/A	gTc/gCc	Putative virulence factor, MviN
RSP_1810	mviN	1:397064	Missense variant	V/I	Gtc/Atc	Putative virulence factor, MviN
RSP_2320	–	1:943423	Missense variant	Y/H	Tac/Cac	TRAP-T family transporter, periplasmic binding protein
RSP_2417	–	1:1049374	Missense variant	E/K	Gag/Aag	Transglutaminase-like enzyme, predicted cysteine protease
RSP_2932	hutC	1:1610205	Missense variant	V/A	gTg/gCg	Histidine utilization repressor, gntR family
RSP_0395	rpoD	1:2126519	Missense variant	C/R	Tgc/Cgc	RNA polymerase, sigma 70 subunit, RpoD
RSP_0546	nifB	1:2282436	Missense variant	A/T	Gcg/Acg	NifB family--FeMo cofactor biosynthesis protein
RSP_0850	mbfA	1:2600637	Missense variant	A/P	Gct/Cct	Membrane-bound ferritin
RSP_0998	nhaD	1:2757127	Missense variant	S/G	Agt/Ggt	Sodium/proton antiporter, NhaD family
RSP_3478	–	2:548776	Missense variant	G/D	gGc/gAc	Type VI secretion protein, EvpB/VC_A0108 family
RSP_3791	–	2:897168	Synonymous variant	A	gcC/gcG	Hypothetical protein
RSP_3791	–	2:897177	Synonymous variant	G	ggG/ggC	Hypothetical protein
RSP_3791	–	2:897225	Synonymous variant	G	ggT/ggC	Hypothetical protein
RSP_3791	–	2:897227	Missense variant	G/S	Ggt/Agt	Hypothetical protein
RSP_3791	–	2:897243	Synonymous variant	P	ccC/ccT	Hypothetical protein
RSP_3791	-	2:897264	Synonymous variant	A	gcC/gcG	Hypothetical protein
RSP_3791	-	2:897297	Synonymous variant	L	ctG/ctC	Hypothetical protein
RSP_3791	-	2:897313	Missense variant	S/F	tCc/tTc	Hypothetical protein
RSP_3791	-	2:897321	Synonymous variant	V	gtC/gtG	Hypothetical protein
RSP_3791	-	2:897329	Synonymous variant	R	Agg/Cgg	Hypothetical protein
RSP_3988	-	B:63268	Missense variant	V/A	gTg/gCg	Putative glycosyltransferase
RSP_4277	-	E:22638	Missense variant	A/V	gCg/gTg	Transcriptional regulator, MerR family

wastewater. Thus, a comparative transcriptomic analysis of our cobalt-resistant evolved strain is likely to provide differentially expressed genes related to Fe-S clusters and iron and nickel transporters, similar to the transcriptomic results with cobalt-exposed *E.coli* (Barras and Fontecave, 2011).

The observed cross-resistance of G7 against Mg^{2+} stress may possibly be associated with the competition of Co^{2+} with Mg^{2+} in ion transport (Losurdo et al., 2010), as high Mg^{2+} concentrations were shown to rescue *R. sphaeroides* from Co^{2+} toxicity. It has been previously shown that Co^{2+} interferes with the extracellular immobilization of Mg^{2+} and its transport across the membrane, implying that Co^{2+} and Mg^{2+} share binding sites on the cell envelope and ion transport systems (Italiano et al., 2009).

The cobalt-resistant, evolved strain G7 was also highly cross-resistant against 0.5 M NaCl stress. A previous study with *R. sphaeroides* strain R26 showed that the strain was halotolerant when grown under anaerobic conditions. It was also suggested that *R. sphaeroides* could be used for the bioremediation of saline and hypersaline polluted environments, as an environmentally friendly and cost-efficient strategy (Labarile et al., 2021). Our results revealed that the evolved G7 strain of *R. sphaeorides* was halotolerant under aerobic growth conditions, supporting its potential in bioremediation of saline and hypersaline environments that are polluted by various metals and/or chemicals.

Our Flame Atomic Absorption Spectrometry results revealed that the cobalt-resistant, evolved strain G7 had a significantly higher cobalt content than RS (Table 2). It has been previously reported that, when grown in the presence of 5 mM Co^{2+}, *R. sphaeroides* cells could bind cobalt ions. A previous X-ray absorption spectroscopy study showed that cobalt was bound to the carboxylate groups in the soluble portion of *R. sphaeroides* cells. Carboxylate and sulfonate moieties were shown to be involved in the binding of the bivalent ion in the case of the cell envelope fraction, where the sulfonate functional groups resulted from the sulfolipids of the *R. sphaeroides* cell envelope (Belviso et al., 2013). In the case of our evolved strain G7, it is likely that the same groups may play an active role in binding cobalt ions which remains to be investigated further by X-ray absorption spectroscopy and transmission electron microscopy (TEM) analyses to determine the final cellular destination of cobalt ions. A similar study that involved X-ray absorption spectroscopy and TEM analysis of a cobalt-resistant *Geobacter sulfurreducens* strain showed that cobalt was immobilized on the cell surface. Transcriptomic analysis of that *G. sulfurreducens* strain also revealed various changes such as upregulation of several metal efflux pumps, downregulation of non-essential proteins with metals and thiol groups that Co^{2+} preferentially targets, cell envelope modification to increase metal resistance and biofilm formation, and activation of sensory and regulatory proteins involved in detoxification (Dulay et al., 2020). Thus, it is likely that Co^{2+} may also be immobilized on the cell surface of our evolved strain, associated with the cell envelope.

The ability of the G7 strain to hold high amounts of cobalt ions, and its high resistance against cobalt and many other stressors indicate its high bioremediation potential.

Comparative whole genome re-sequencing results of the cobalt-resistant, evolved strain G7 revealed two missense mutations in the mviN gene that encodes a putative virulence factor. In *E. coli*, the mviN gene codes for an essential protein for peptidoglycan synthesis, MviN (MurJ), a kind of integral membrane protein, and it has a role as a flippase which transports lipids from the exoplasmic surface toward the cytosolic surface (Ruiz, 2008). As a kind of lipid II flippase, MviN translocates peptidoglycan precursors (lipid II) across the cytoplasmic membrane to the cytoplasm (Ruiz, 2016). Similarly, MviN was also expected to function as a flippase in *Mycobacterium tuberculosis*, as the deficiency of it resulted in the accumulation of peptidoglycan precursors in the cytoplasm (Arora et al., 2018). The two missense mutations in the mviN gene of our evolved strain might have resulted in changes in the cell membrane and/or peptidoglycan that possibly contributed to an increase in cobalt resistance and robustness of G7.

The missense mutation observed in RSP_2320 may also be important for the cobalt resistance of our evolved strain. RSP_2320 encodes a Tripartite ATP-independent periplasmic (TRAP) family transporter, periplasmic binding protein (Callister et al., 2006). TRAP transporters use ionoelectrochemical gradients to transport molecules actively across a membrane in the same direction (Rosa et al., 2018). In a previous study, comparative transcriptomic and genomic analyses of cobalt-sensitive mutant strains of *R. sphaeorides* obtained by transposon mutagenesis were performed. It was found that RSP_0097 encoding 'TRAP-type C4-dicarboxylate transport system periplasmic component' and RSP_1419 encoding 'TRAP-T family transporter small inner membrane subunit' were downregulated in a cobalt-sensitive mutant strain (Volpicella et al., 2014). Comparative photosynthetic membrane proteome analysis of *R. sphaeroides* under 5 mM cobalt stress and control conditions also identified the TRAP di-carboxylate family transporter DctP subunit as an upregulated protein (Italiano et al., 2011). More recently, the lack of the TakP transporter, a member of the TRAP family of transporters, was shown to lead to selenite-induced oxidative stress in *R. sphaeroides* (Adnan et al., 2021). Based on these findings, it can be suggested that the identified missense mutation in RSP_2320 associated with a TRAP family transporter might have increased the TRAP transporter activity of our evolved strain G7, which may have contributed to its increased resistance to cobalt and other stressors. The exact mechanism, however, is yet to be investigated.

Another missense mutation was observed in the rpoD gene encoding the RNA polymerase, sigma 70 subunit RpoD. In a previous study with cobalt-sensitive *R. sphaeroides* mutants obtained by transposon mutagenesis, it was found that the rpoH2 gene (RSP_0601) encoding a DNA-directed RNA polymerase sigma subunit was upregulated in a cobalt-sensitive mutant strain (Volpicella et al., 2014). The exact role of RNA polymerase in the cobalt resistance of *R. sphaeroides* is yet to be investigated in more detail.

The nifB gene encoding the FeMo cofactor biosynthesis protein of NifB family in *R. sphaeroides* also had a missense mutation in our evolved strain G7. Bacterial nif genes are nitrogen fixation regulatory genes and have roles in encoding the nitrogenase enzyme complex components (Dahal et al., 2021). Volpicella et al. (2014) showed that genes that code for the nitrogenase subunit NifH (ATPase), bchX (RSP_0262) and bchL (RSP_0288), and genes encoding a nitrogenase molybdenum-iron protein alpha and beta chain, bchZ (RSP_0260) and bchY (RSP_0261), were upregulated in a cobalt-sensitive *R. sphaeroides* strain obtained by transposon mutagenesis. These findings indicate that the nitrogenase enzyme complex may have a potential role in the cobalt resistance of *R. sphaeroides*.

The nhaD gene that encodes a sodium/proton antiporter protein of the NhaD family in *R. sphaeroides* also had a missense mutation in

our cobalt-resistant, evolved strain G7. In a previous study, RSP_2638 that encodes a Ca^{2+}/Na^{2+} antiporter was found to be upregulated in a cobalt-sensitive *R. sphaeroides* strain (Volpicella et al., 2014). It is known that sodium/proton-antiporters (Nha) are important in pH and Na^{+}-homeostasis (Kurz et al., 2006). Thus, the observed high NaCl cross-resistance of G7 may be related to a possibly activated NhaD antiporter and the changes in transporter activities in G7 may also be related to its resistance to cobalt and many other stressors.

Another missense mutation was observed in RSP_3988 that codes for a putative glycosyltransferase. In a previous study, proteomic characterization of the *R. sphaeroides* photosynthetic membrane was performed, and 28 proteins were identified as intracytoplasmic membrane (ICM)-associated proteins, most likely localized in the periplasm, cytoplasm or outer membrane of *R. sphaeroides* cells. ICM is an inducible membrane that has an important role in bacterial photosynthesis, harvesting light energy, separation of primary charges and electron transport. Interestingly, the product of RSP_3988 was also present among these 28 ICM-associated proteins, along with six other proteins that are periplasmic subunits of ABC or TRAP transporters (Zeng et al., 2007). The exact role of RSP_3988 in *R. sphaeroides* energy metabolism and cobalt resistance needs to be investigated in more detail.

ABC transporters are conserved from bacteria to humans, and are powered by ATP to move substrates across cellular membranes. They are strongly regulated to balance essential nutrient needs and substrate toxicity effects, and they consist of both exporters and importers. ABC transporters are necessary for the transport of various compounds such as antibiotics, lipids, and proteins. Moreover, various ABC transporters have been reported to transport diverse metals such as zinc, manganese, iron, nickel and cobalt (Tanaka et al., 2018). An ABC transporter (cntABCDF) responsible for cobalt and nickel transport was identified in the major opportunistic pathogen *Staphylococcus aureus*. It also affected urease activity and bacterial colonization in systemic and urinary tract infection models, indicating the role of this cobalt and nickel transporter in the virulence of *S. aureus* (Remy et al., 2013). Similarly, another ABC transporter (FecDE and CeuE) that contributes to nickel and cobalt acquisition was identified in the bacterial pathogen *Helicobacter mustelae,* where the *fecD* mutant had decreased cobalt levels and improved cobalt resistance (Stoof et al., 2010). As reported previously, in a cobalt-sensitive *R. sphaeroides* strain mutated in the RSP_7363 gene that encodes a hypothetical protein, an ABC sugar transporter was significantly downregulated. It was suggested that the ABC sugar transporter may provide an additional energy source that may help the mutant strain to overcome cobalt stress, as the mutant strain was not inhibited when grown under photosynthetic conditions that can provide an additional energy source instead of the impaired ABC sugar transporter (Volpicella et al., 2014). A different ABC sugar transporter of *R. sphaeroides* was found to play a role in its adaptation to high concentrations of selenite ions: a *R. sphaeroides* mutant strain deficient in *smoK* gene encoding an ABC transporter for the uptake of sugar alcohols could tolerate selenite. It was suggested that selenite uptake into *R. sphaeroides* cells may occur by a sugar alcohol transporter in *R. sphaeroides* (Bebien et al., 2001). Similarly, in the soil bacterium *Sinorhizobium meliloti* that can form N_2-fixing root nodules on its plant host alfalfa, an ABC sugar transporter was shown to play a role in the regulation of potassium transport and response to alkali stress conditions (Lin et al., 2009). It was also reported that the gene cluster *cbtJKL* encodes an ABC-type cobalt-transport system in *S. meliloti*, which was required for the growth of free-living cells at required trace element cobalt concentrations, but not required for symbiotic N_2 fixation (Cheng et al., 2011). Thus, in our cobalt-resistant *R. sphaeroides* strain, it is also likely that the observed cobalt resistance may be associated with differential expression of some ABC transporters as reported previously (Volpicella et al., 2014), which remains to be investigated by comparative transcriptomic analyses.

In our evolved strain G7, another missense mutation was detected in RSP_4277 that encodes a transcriptional regulator of MerR family. Zeller et al. (2007) investigated the regulatory functions of the OxyR protein in *R. sphaeroides*. OxyR is known as a regulatory protein of H_2O_2 response in bacteria. Comparative transcriptomic analysis results of wild-type and *OxyR* mutant *R. sphaeroides* strains in the presence and absence of 1 mM H_2O_2 stress (with 7 min exposure time) revealed that multiple genes were upregulated both in the wild-type and OxyR mutant strains, including RSP_4277. It was concluded that additional regulatory pathways other than OxyR may play a role in the oxidative stress response of *R sphaeroides*. Thus, the RSP_4277 missense mutation observed in our evolved strain may also be related to its oxidative stress response and/or cobalt resistance.

The mbfA gene (RSP_0850) codes for a membrane-bound ferritin in *R. sphaeroides*, and is associated with iron storage (Peuser et al., 2012). Thus, the missense mutation in the mbfA gene of our evolved strain G7 may also contribute to its resistance against cobalt and iron stresses.

In this study, we have identified novel mutations that may play an important role in the cobalt-resistance and robustness of *R. sphaeroides*. In a previous study with two cobalt-sensitive *R. sphaeroides* strains obtained by transposon mutagenesis, the insertion sites were identified in other genes such as RSP_7363, encoding a hypothetical protein, which are not mutated in our cobalt-resistant, evolved strain (Volpicella et al., 2014). These findings imply the multigenic and complex molecular basis of cobalt-resistance in *R. sphaeroides*. Volpicella et al. (2014) also reported that all insertions were detected outside the chromosome II, supporting a previous statement that the genes with essential roles are located in the chromosome II of *R. sphaeroides* (Choudhary et al., 1994). In our cobalt-resistant evolved strain, however, we have detected three missense mutations (two in RSP_3791 and one in RSP_3478) and multiple synonymous mutations (in RSP_3791) in chromosome II, in addition to some other mutations in chromosome I, Plasmid B (in RSP_3988) and Plasmid E (RSP_4277) (Table 3).

It is important to note that, in our cobalt-resistant evolved strain, two missense and eight synonymous mutations were identified in RSP_3791, encoding a hypothetical protein. In addition, many genes encoding hypothetical proteins were differentially regulated in a cobalt-sensitive mutant *R. sphaeroides* strain obtained by transposon mutagenesis (Volpicella et al., 2014). Thus, the hypothetical protein encoded by RSP_3791 and other hypothetical proteins may play a crucial role in the cobalt resistance of *R. sphaeroides* which is yet to be investigated.

The purpose of performing comparative whole-genome re-sequencing of the cobalt-resistant, evolved *R. sphaeroides* strain was to identify genomic variations in the evolved strain that may be potential molecular targets for cobalt resistance. Our results showed that the genomic variations identified in the evolved strain do not seem to belong to the genes that are directly related to cobalt

accumulation (Table 3). A previous study on cobalt-sensitive mutants of *R. sphaeroides* obtained by transposon mutagenesis also revealed mutations in genes that seem not to be directly related to cobalt accumulation or in genes encoding hypothetical proteins. It was, however, found that, at transcriptomic level these mutations can reduce the expression of ABC sugar transporter operon subunits, indicating that cobalt response is associated with energy metabolism (Volpicella et al., 2014). It is important to note that cobalt resistance and stress resistance, in general, are multigenic and complex traits, which usually involve multiple, seemingly unrelated molecular factors and/or pathways, as we have also observed in our previous studies with yeast (Alkım et al., 2013; Balaban et al., 2020; Terzioğlu et al., 2020). Considering that the *R. sphaeroides* strain was not exposed to random/chemical mutagenesis prior to evolutionary engineering, it is likely that many of the observed mutations in our evolved strain that occurred only under the selective pressure of cobalt stress may be related to cobalt resistance, or they may influence the expression levels of cobalt-associated genes, at the transcriptomic level.

5 Conclusion

In this study, we have obtained a highly cobalt-resistant and genetically stable *R. sphaeroides* strain by using evolutionary engineering. The evolved strain could resist as high as 15 mM $CoCl_2$ stress, which, to the best of our knowledge, has not been reported so far. In addition, the evolved strain could accumulate significantly higher amounts of cobalt than the reference strain. It was also cross-resistant to many other stressors, which indicate a high potential for its use as a robust and multi-stress resistant *R. sphaeroides* strain in bioremediation applications. Comparative genomic analyses of the evolved strain identified several unique mutations in multiple genes with diverse functions and particularly in genes encoding hypothetical proteins, such as RSP_3791, the exact role of which remains to be investigated in detail to fully understand the complex, multigenic basis of cobalt resistance in *R. sphaeroides*. To this end, comparative transcriptomic and/or proteomic analyses of the evolved strain, and reverse engineering studies to introduce the observed genetic variations into the reference strain by genome editing and testing the resulting strains for cobalt resistance are planned as future studies.

Data availability statement

The datasets presented in this study can be found in online repositories. The names of the repository/repositories and accession number(s) can be found at: https://www.ncbi.nlm.nih.gov/, BioProject PRJNA1047122.

Author contributions

GA: Project administration, Writing – review & editing, Data curation, Methodology, Writing – original draft. CH: Data curation, Methodology, Project administration, Writing – original draft, Writing – review & editing. HC: Data curation, Methodology, Writing-original draft. MA: Data curation, Methodology, Writing – original draft. AT: Data curation, Methodology, Writing – original draft, Project administration, Writing – review & editing. MT: Project administration, Writing – review & editing, Conceptualization, Funding acquisition, Supervision. ZÇ: Conceptualization, Funding acquisition, Project administration, Supervision, Writing – review & editing.

Funding

The author(s) declare that financial support was received for the research, authorship, and/or publication of this article. This research was performed as a collaborative work resulting from the COST Action CM0902, 'Molecular machineries for ion translocation across biomembranes'.

Acknowledgments

We thank Cihan Erdinç Gülsev and Nazlı Kocaefe Özşen for technical assistance with the whole genome re-sequencing experiments, and Ceren Alkım, Burcu Turanlı Yıldız, Ülkü Yılmaz, Hande Tekarslan and Özge Özmeral for initial cultivation experiments. We also thank Sema Gündüz and Prof. Dr. Süleyman Akman (Department of Chemistry, Istanbul Technical University) for F-AAS analysis.

Conflict of interest

The authors declare that the research was conducted in the absence of any commercial or financial relationships that could be construed as a potential conflict of interest.

The author(s) declared that they were an editorial board member of Frontiers, at the time of submission. This had no impact on the peer review process and the final decision.

Publisher's note

Supplementary material

The Supplementary material for this article can be found online at: https://www.frontiersin.org/articles/10.3389/fmicb.2024.1412294/full#supplementary-material

References

Adnan, F., Jalil, A., Ahmed, T., Rahman, A., Dawood, N., Haider, G., et al. (2021). TRAP transporter TakP: a key player in the resistance against selenite-induced oxidative stress in *Rhodobacter sphaeroides*. *Microbiol. Res.* 252:126828. doi: 10.1016/j.micres.2021.126828

Alboghobeish, H., Tahmourespour, A., and Doudi, M. (2014). The study of nickel resistant Bacteria (NiRB) isolated from wastewaters polluted with different industrial sources. *J. Environ. Health Sci. Eng.* 12:44. doi: 10.1186/2052-336X-12-44

Alkım, C., Benbadis, L., Yılmaz, Ü., Çakar, Z. P., and Francois, J. M. (2013). Mechanisms other than activation of the Iron regulon account for the hyper-resistance to cobalt of a *Saccharomyces cerevisiae* strain obtained by evolutionary engineering. *Metallomics* 5, 1043–1060. doi: 10.1039/c3mt00107e

Allen, J. P., Feher, G., Yeates, T. O., Komiya, H., and Rees, D. C. (1988). Structure of the reaction center from *Rhodobacter sphaeroides* R-26: protein-cofactor (quinones and Fe2+) interactions. *PNAS* 85, 8487–8491. doi: 10.1073/pnas.85.22.8487

Arora, G., Chaudhary, D., Kidwai, S., Sharma, D., and Singh, R. (2018). CitE enzymes are essential for *Mycobacterium tuberculosis* to establish infection in macrophages and Guinea pigs. *Front. Cell. Infect. Microbiol.* 8, 1–15. doi: 10.3389/fcimb.2018.00385

Balaban, G., Yılmaz, Ü., Alkım, C., Topaloglu, A., Kısakesen, H. I., Holyavkin, C., et al. (2020). Evolutionary engineering of an Iron-resistant *Saccharomyces cerevisiae* mutant and its physiological and molecular characterization. *Microorganisms* 8, 1–26. doi: 10.3390/microorganisms8010043

Barras, F., and Fontecave, M. (2011). Cobalt stress in *Escherichia coli* and *Salmonella enterica*: molecular bases for toxicity and resistance. *Metallomics* 3, 1130–1134. doi: 10.1039/c1mt00099c

Battersby, A. R. (1994). How nature builds the pigments of life: the conquest of vitamin B12. *Science* 264, 1551–1557. doi: 10.1126/science.8202709

Bebien, M., Chauvin, J.-P., Adriano, J.-M., Grosse, S., and Vermeglio, A. (2001). Effect of selenite on growth and protein synthesis in the phototrophic bacterium *Rhodobacter sphaeroides*. *Appl. Environ. Microbiol.* 67, 4440–4447. doi: 10.1128/AEM.67.10.4440-4447.2001

Belviso, B. D., Italiano, F., Caliandro, R., Carrozzini, B., Costanza, A., and Trotta, M. (2013). Cobalt binding in the photosynthetic bacterium *R. sphaeroides* by X-ray absorption spectroscopy. *Biometals* 26, 693–703. doi: 10.1007/s10534-013-9641-3

Bertani, G. (1951). Studies on Lysogenesis. *J. Bacteriol.* 62, 293–300. doi: 10.1128/jb.62.3.293-300.1951

Bolger, A. M., Lohse, M., and Usadel, B. (2014). Trimmomatic: a flexible trimmer for Illumina sequence data. *Bioinformatics* 30, 2114–2120. doi: 10.1093/bioinformatics/btu170

Burger, B. T., Imam, S., Scarborough, M. J., Noguera, D. R., and Donohue, T. J. (2017). Combining genome-scale experimental and computational methods to identify essential genes in *Rhodobacter sphaeroides*. *mSystems* 2, e00015–e00017. doi: 10.1128/msystems.00015-17

Buscemi, G., Vona, D., Stufano, P., Labarile, R., Cosma, P., Agostiano, A., et al. (2022). Bio-inspired redox-adhesive Polydopamine matrix for intact Bacteria biohybrid Photoanodes. *ACS Appl. Mater. Interfaces* 14, 26631–26641. doi: 10.1021/acsami.2c02410

Butler, P. R., Brown, M., and Oliver, S. G. (1996). Improvement of antibiotic titers from *Streptomyces bacteria* by interactive continuous selection. *Biotechnol. Bioeng.* 49, 185–196. doi: 10.1002/(SICI)1097-0290(19960120)49:2<185::AID-BIT7>3.0.CO;2-M

Çakar, Z. P., Alkım, C., Turanlı, B., Tokman, N., Akman, S., Sarıkaya, M., et al. (2009). Isolation of cobalt hyper-resistant mutants of *Saccharomyces cerevisiae* by in vivo evolutionary engineering approach. *J. Biotech.* 143, 130–138. doi: 10.1016/j.jbiotec.2009.06.024

Çakar, Z. P., Seker, U. O. S., Tamerler, C., Sonderegger, M., and Sauer, U. (2005). Evolutionary engineering of multiple-stress resistant *Saccharomyces cerevisiae*. *FEMS Yeast Res.* 5, 569–578. doi: 10.1016/j.femsyr.2004.10.010

Callister, S. J., Nicora, C. D., Zeng, X., Roh, J. H., Dominguez, M. A., Tavano, C. L., et al. (2006). Comparison of aerobic and photosynthetic *Rhodobacter sphaeroides* 2.4.1 proteomes. *J. Microbiol. Methods* 67, 424–436. doi: 10.1016/j.mimet.2006.04.021

Calvano, C. D., Italiano, F., Catucci, L., Agostiano, A., Cataldi, T. R. I., Palmisano, F., et al. (2013). The lipidome of the photosynthetic bacterium *Rhodobacter sphaeroides* R26 is affected by cobalt and chromate ions stress. *Biometals* 27, 65–73. doi: 10.1007/s10534-013-9687-2

Cheng, J., Poduska, B., Morton, R. A., and Finan, T. M. (2011). An ABC-type cobalt transport system is essential for growth of *Sinorhizobium meliloti* at trace metal concentrations. *J. Bacteriol.* 193, 4405–4416. doi: 10.1128/JB.05045-11

Choudhary, M., Mackenzie, C., Nereng, K. S., Sodergren, E., Weinstock, G. M., and Kaplan, S. (1994). Multiple chromosomes in bacteria: structure and function of chromosome II of *Rhodobacter sphaeroides* 2.4.1T. *J. Bacteriol.* 176, 7694–7702. doi: 10.1128/jb.176.24.7694-7702.1994

Dahal, R. H., Chaudhary, D. K., Kim, D. U., and Kim, J. (2021). Azohydromonas caseinilytica sp. nov., a nitrogen-fixing bacterium isolated from Forest soil by using optimized culture method. *Front. Microbiol.* 12, 1–10. doi: 10.3389/fmicb.2021.647132

DePristo, M. A., Banks, E., Poplin, R., Garimella, K. V., Maguire, J. R., Hartl, C., et al. (2011). A framework for variation discovery and genotyping using next-generation DNA sequencing data. *Nat. Genet.* 43, 491–498. doi: 10.1038/ng.806

Dulay, H., Tabares, M., Kashefi, K., and Reguera, G. (2020). Cobalt resistance via detoxification and mineralization in the Iron-reducing bacterium *Geobacter sulfurreducens*. *Front. Microbiol.* 11:600463. doi: 10.3389/fmicb.2020.600463

Giotta, L., Agostiano, A., Italiano, F., Milano, F., and Trotta, M. (2006). Heavy metal ion influence on the photosynthetic growth of *Rhodobacter sphaeroides*. *Chemosphere* 62, 1490–1499. doi: 10.1016/j.chemosphere.2005.06.014

Gökçe, A., Öztürk, Y., and Çakar, Z. P. (2017). Comparative genomic analysis of two heat-resistant *Rhodobacter capsulatus* mutants with different hydrogen production levels reveals mutations related to hydrogen production. *Int. J. Hydrog. Energy* 42, 20529–20539. doi: 10.1016/j.ijhydene.2017.07.005

Gökçe, A., Öztürk, Y., Çakar, Z. P., and Yücel, M. (2012). Temperature resistant mutants of *Rhodobacter capsulatus* generated by a directed evolution approach and effects of temperature resistance on hydrogen production. *Int. J. Hydrog. Energy* 37, 16466–16472. doi: 10.1016/j.ijhydene.2012.02.169

Grattieri, M., Labarile, R., Buscemi, G., and Trotta, M. (2022). The periodic table of photosynthetic purple non-sulfur bacteria: intact cell-metal ions interactions. *Photochem. Photobiol. Sci.* 21, 101–111. doi: 10.1007/s43630-021-00116-9

Gupta, S., Fernandes, A., Lopes, A., Grasa, L., and Salafranca, J. (2024). Photo-fermentative bacteria used for hydrogen production. *Appl. Sci.* 14:1191. doi: 10.3390/app14031191

Hassen, A., Saidi, N., Cherif, M., and Boudabous, A. (1998). Resistance of environmental bacteria to heavy metals. *Bioresour. Technol.* 64, 7–15. doi: 10.1016/S0960-8524(97)00161-2

Henry, K. K., Ross, W., Myersb, K. S., Lemmer, K. C., Vera, J. M., Landick, R., et al. (2020). A majority of *Rhodobacter sphaeroides* promoters lack a crucial RNA polymerase recognition feature, enabling coordinated transcription activation. *PNAS* 117, 29658–29668. doi: 10.1073/pnas.2010087117

Imam, S., Noguera, D. R., and Donohue, T. J. (2013). Global insights into energetic and metabolic networks in *Rhodobacter sphaeroides*. *BMC Syst. Biol.* 7:89. doi: 10.1186/1752-0509-7-89

Imam, S., Noguera, D. R., and Donohue, T. J. (2014). Global analysis of photosynthesis transcriptional regulatory networks. *PLoS Genet.* 10:e1004837. doi: 10.1371/journal.pgen.1004837

Irazusta, V., Nieto-Peñalver, C. G., Cabral, M. E., Amoroso, M. J., and de Figueroa, L. I. C. (2013). Relationship among carotenoid production, copper bioremediation and oxidative stress in *Rhodotorula mucilaginosa* RCL-11. *Process Biochem.* 48, 803–809. doi: 10.1016/j.procbio.2013.04.006

Italiano, F., Buccolieri, A., Giotta, L., Agostiano, A., Valli, L., Milano, F., et al. (2009). Response of the carotenoidless mutant *Rhodobacter sphaeroides* growing cells to cobalt and nickel exposure. *Int. Biodeterior. Biodegrad.* 63, 948–957. doi: 10.1016/j.ibiod.2009.05.001

Italiano, F., D'Amici, G. M., Rinalducci, S., De Leo, F., Zolla, L., Gallerani, R., et al. (2011). The photosynthetic membrane proteome of *Rhodobacter sphaeroides* R-26.1 exposed to cobalt. *Res. Microbiol.* 162, 520–527. doi: 10.1016/j.resmic.2011.04.008

Johnson, H., Cho, H., and Choudhary, M. (2019). Bacterial heavy metal resistance genes and bioremediation potential. *CMB* 9, 1–12. doi: 10.4236/cmb.2019.91001

Kiley, P. J., and Kaplan, S. (1988). Molecular genetics of photosynthetic membrane biosynthesis in *Rhodobacter sphaeroides*. *Microbiol. Rev.* 52, 50–69. doi: 10.1128/mr.52.1.50-69.1988

Kiley, P. J., Varga, A., and Kaplan, S. (1988). Physiological and structural analysis of light-harvesting mutants of *Rhodobacter sphaeroides*. *J. Bacteriol.* 170, 1103–1115. doi: 10.1128/jb.170.3.1103-1115.1988

Kobayashi, M., and Shimizu, S. (1999). Cobalt proteins. *Eur. J. Biochem.* 261, 1–9. doi: 10.1046/j.1432-1327.1999.00186.x

Kocaefe-Özşen, N., Yilmaz, B., Alkım, C., Arslan, M., Topaloğlu, A., Kısakesen, H. I., et al. (2022). Physiological and molecular characterization of an oxidative stress-resistant *Saccharomyces cerevisiae* strain obtained by evolutionary engineering. *Front. Microbiol.* 13:822864. doi: 10.3389/fmicb.2022.822864

Küçükgöze, G., Alkım, C., Yılmaz, Ü., Kısakesen, H. I., Gündüz, S., Akman, S., et al. (2013). Evolutionary engineering and transcriptomic analysis of nickel-resistant *Saccharomyces cerevisiae*. *FEMS Yeast Res.* 13, 731–746. doi: 10.1111/1567-1364.12073

Kurz, M., Brünig, A. N. S., and Galinski, E. A. (2006). NhaD type sodium/proton-antiporter of *Halomonas elongata*: a salt stress response mechanism in marine habitats. *Saline Syst.* 2, 1–12. doi: 10.1186/1746-1448-2-10

Kwa, L. G., Wegmann, D., Brügger, B., Wieland, F. T., Wanner, G., and Braun, P. (2008). Mutation of a single residue, beta-glutamate-20, alters protein-lipid interactions of light harvesting complex II. *Mol. Microbiol.* 67, 63–77. doi: 10.1111/j.1365-2958.2007.06017.x

Labarile, R., Farinola, G. M., Varsalona, M., Italiano, F., Buscemi, G., Trotta, M., et al. (2021). Halotolerance of *Rhodobacter sphaeroides* for saline and hypersaline wastewater bioremediation. 2021 international workshop on metrology for the sea; learning to measure sea health parameters (MetroSea) Italy, pp. 37–42.

Lee, S., and Manthiram, A. (2022). Can cobalt be eliminated from Lithium-ion batteries? *ACS Energy Lett.* 7, 3058–3063. doi: 10.1021/acsenergylett.2c01553

Li, H., and Durbin, R. (2009). Fast and accurate short read alignment with burrows-wheeler transform. *Bioinformatics* 25, 1754–1760. doi: 10.1093/bioinformatics/btp324

Li, S., Tabatabaei, M., Li, F., and Ho, S.-H. (2024). A review of green biohydrogen production using anoxygenic photosynthetic bacteria for hydrogen economy: challenges and opportunities. *Int. J. Hydrog. Energy* 54, 218–238. doi: 10.1016/j.ijhydene.2022.11.014

Lin, D. X., Tang, H., Wang, E. T., and Chen, W. X. (2009). An ABC transporter is required for alkaline stress and potassium transport regulation in *Sinorhizobium meliloti*. *FEMS Microbiol. Lett.* 293, 35–41. doi: 10.1111/j.1574-6968.2009.01500.x

Lindquist, J. (2020). The most probable number method. Available at: https://www.jlindquist.com/generalmicro/102dil3a.html (Accessed January 17, 2020).

Losurdo, L., Italiano, F., Trotta, M., Gallerani, R., Ceci, L. R., and De Leo, F. (2010). Assessment of an internal reference gene in *Rhodobacter sphaeroides* grown under cobalt exposure. *J. Basic Microbiol.* 50, 302–305. doi: 10.1002/jobm.200900340

Mackenzie, C., Eraso, J. M., Choudhary, M., Roh, J. H., Zeng, X., Bruscella, P., et al. (2007). Postgenomic adventures with *Rhodobacter sphaeroides*. *Ann. Rev. Microbiol.* 61, 283–307. doi: 10.1146/annurev.micro.61.080706.093402

Martínez-Luque, M., Dobao, M. M., and Castillo, F. (1991). Characterization of the assimilatory and dissimilatory nitrate-reducing systems in Rhodobacter: a comparative study. *FEMS Microbiol. Lett.* 83, 329–333. doi: 10.1016/0378-1097(91)90497-X

Mavrommati, M., Papanikolaou, S., and Aggelis, G. (2023). Improving ethanol tolerance of *Saccharomyces cerevisiae* through adaptive laboratory evolution using high ethanol concentrations as a selective pressure. *Process Biochem.* 124, 280–289. doi: 10.1016/j.procbio.2022.11.027

Moore, M. D., and Kaplan, S. (1992). Identification of intrinsic high-level resistance to rare-earth oxides and oxyanions in members of the class proteobacteria: characterization of tellurite, selenite, and rhodium sesquioxide reduction in *Rhodobacter sphaeroides*. *J. Bacteriol.* 174, 1505–1514. doi: 10.1128/jb.174.5.1505-1514.1992

Peuser, V., Remes, B., and Klug, G. (2012). Role of the Irr protein in the regulation of Iron metabolism in *Rhodobacter sphaeroides*. *PLoS One* 7:e42231. doi: 10.1371/journal.pone.0042231

Pisani, F., Italiano, F., Leo, de, F., Gallerani, R., Rinalducci, S., Zolla, L., et al. (2009). Soluble proteome investigation of cobalt effect on the Carotenoidless mutant of *Rhodobacter sphaeroides*. *J. Appl. Microbiol.* 106, 338–349. doi: 10.1111/j.1365-2672.2008.04007.x

Rangel, D. E. N. (2011). Stress induced cross-protection against environmental challenges on prokaryotic and eukaryotic microbes. *World J. Microbiol. Biotechnol.* 27, 1281–1296. doi: 10.1007/s11274-010-0584-3

Ranquet, C., Ollagnier-de-Choudens, S., Loiseau, L., Barras, F., and Fontecave, M. (2007). Cobalt stress in *Escherichia coli*. The effect on the iron-sulfur proteins. *J. Biol. Chem.* 282, 30442–30451. doi: 10.1074/jbc.M702519200

Remy, L., Carrière, M., Derré-Bobillot, A., Martini, C., Sanguinetti, M., and Borezée-Durant, E. (2013). The *Staphylococcus aureus* Opp1 ABC transporter imports nickel and cobalt in zinc-depleted conditions and contributes to virulence. *Mol. Microbiol.* 87, 730–743. doi: 10.1111/mmi.12126

Rosa, L. T., Bianconi, M. E., Thomas, G. H., and Kelly, D. J. (2018). Tripartite ATP-independent periplasmic (TRAP) transporters and tripartite Tricarboxylate transporters (TTT): from uptake to pathogenicity. *Front. Cell. Infect. Microbiol.* 8:33. doi: 10.3389/fcimb.2018.00033

Ruiz, N. (2008). Bioinformatics identification of MurJ (MviN) as the peptidoglycan lipid II Flippase in *Escherichia coli*. *PNAS* 105, 15553–15557. doi: 10.1073/pnas.0808352105

Ruiz, N. (2016). Lipid Flippases for bacterial peptidoglycan biosynthesis. *Lipid Insights* 8, 21–32. doi: 10.4137/LPI.S31783

Russek, E., and Colwell, R. R. (1983). Computation of most probable numbers. *Appl. Environ. Microbiol.* 45, 1646–1650. doi: 10.1128/aem.45.5.1646-1650.1983

Sauer, U. (2001). Evolutionary engineering of industrially important microbial phenotypes. *Adv. Biochem. Eng. Biotechnol.* 73, 130–166. doi: 10.1007/3-540-45300-8_7

Şen, M., Yılmaz, Ü., Baysal, A., Akman, S., and Çakar, Z. P. (2011). In vivo evolutionary engineering of a boron-resistant bacterium: *Bacillus boroniphilus*. *Antonie Van Leeuwenhoek* 99, 825–835. doi: 10.1007/s10482-011-9557-2

Shi, Q., Sun, X., Xu, M., and Wang, M. (2022). The multiplex network structure of global cobalt industry chain. *Resour. Policy* 76:102555. doi: 10.1016/j.resourpol.2022.102555

Stadler, J. A., and Schweyen, R. J. (2002). The yeast Iron regulon is induced upon cobalt stress and crucial for cobalt tolerance. *JBC* 277, 39649–39654. doi: 10.1074/jbc.M203924200

Stoof, J., Kuipers, E. J., Klaver, G., and van Vliet, A. H. (2010). An ABC transporter and a TonB ortholog contribute to *Helicobacter mustelae* nickel and cobalt acquisition. *Infect. Immun.* 78, 4261–4267. doi: 10.1128/IAI.00365-10

Tanaka, K. J., Song, S., Mason, K., and Pinkett, H. W. (2018). Selective substrate uptake: the role of ATP-binding cassette (ABC) importers in pathogenesis. *Biochim. Biophys. Acta Biomembr.* 1860, 868–877. doi: 10.1016/j.bbamem.2017.08.011

Terzioğlu, E., Alkım, C., Arslan, M., Balaban, B. G., Holyavkin, C., Kısakesen, H. I., et al. (2020). Genomic, transcriptomic and physiological analyses of silver-resistant *Saccharomyces cerevisiae* obtained by evolutionary engineering. *Yeast* 37, 413–426. doi: 10.1002/yea.3514

Tewari, A., Joshi, H. V., Raghunathan, C., Kumar, V. G. S., and Khambhaty, Y. (2001). Effect of heavy metal pollution on growth, carotenoid content and bacterial flora in the gut of *Perna viridis* (L.) in *in situ* condition. *Curr. Sci.* 81, 819–828.

Topaloğlu, A., Esen, Ö., Turanlı-Yıldız, B., Arslan, M., and Çakar, Z. P. (2023). From *Saccharomyces cerevisiae* to ethanol: unlocking the power of evolutionary engineering in metabolic engineering applications. *J. Fungi* 9:984. doi: 10.3390/jof9100984

Vasiliadou, I. A., Berná, A., Manchon, C., Melero, J. A., Martinez, F., Esteve-Nuñez, A., et al. (2018). Biological and bioelectrochemical Systems for Hydrogen Production and Carbon Fixation Using Purple Phototrophic Bacteria. *Front. Energy Res.* 6:107. doi: 10.3389/fenrg.2018.00107

Volpicella, M., Costanza, A., Palumbo, O., Italiano, F., Leoni, C., Placido, A., et al. (2014). *Rhodobacter sphaeroides* adaptation to high concentrations of cobalt ions requires energetic metabolism changes. *FEMS Microbiol. Ecol.* 88, 345–357. doi: 10.1111/1574-6941.12303

Wang, H., Yang, A., Zhang, G., Ma, B., Meng, F., Peng, M., et al. (2017). Enhancement of carotenoid and bacteriochlorophyll by high salinity stress in photosynthetic bacteria. *Int. Biodeterior. Biodegradation* 121, 91–96. doi: 10.1016/j.ibiod.2017.03.028

Yeates, T. O., Komiya, H., Chirino, A., Rees, D. C., Allen, J. P., and Feher, G. (1988). Structure of the reaction center from *Rhodobacter sphaeroides* R-26 and 2.4.1: protein-cofactor (bacteriochlorophyll, bacteriopheophytin, and carotenoid) interactions. *PNAS* 85, 7993–7997. doi: 10.1073/pnas.85.21.7993

Zeilstra-Ryalls, J. H., Gomelsky, M., Yeliseev, A. A., Eraso, J. M., and Kaplan, S. (1998). Transcriptional regulation of photosynthesis operons in *Rhodobacter sphaeroides* 2.4.1. *Methods Enzymol.* 297, 151–166. doi: 10.1016/S0076-6879(98)97012-4

Zeller, T., Mraheil, M. A., Moskvin, O. V., Li, K., Gomelsky, M., and Klug, G. (2007). Regulation of hydrogen peroxide-dependent gene expression in *Rhodobacter sphaeroides*: regulatory functions of OxyR. *J. Bacteriol.* 189, 3784–3792. doi: 10.1128/JB.01795-06

Zeng, X., Roh, J. H., Callister, S. J., Tavano, C. L., Donohue, T. J., Lipton, M. S., et al. (2007). Proteomic characterization of the *Rhodobacter sphaeroides* 2.4.1 photosynthetic membrane: identification of new proteins. *J. Bacteriol.* 189, 7464–7474. doi: 10.1128/JB.00946-07

frontiers | Frontiers in Microbiology

TYPE Original Research
PUBLISHED 05 July 2024
DOI 10.3389/fmicb.2024.1423995

OPEN ACCESS

EDITED BY
Haike Antelmann,
Free University of Berlin, Germany

REVIEWED BY
Johid Malik,
University of Nebraska Medical Center, United States
Vineet Kumar,
The University of Texas at Austin, United States

*CORRESPONDENCE
Jose Echenique
✉ jechenique@unc.edu.ar

†PRESENT ADDRESS
Nicolas M. Reinoso-Vizcaino,
Department of Molecular Genetics and Microbiology, Duke Center for Virology, Duke University School of Medicine, Durham, NC, United States

RECEIVED 26 April 2024
ACCEPTED 18 June 2024
PUBLISHED 05 July 2024

CITATION
Hernandez-Morfa M, Reinoso-Vizcaino NM, Zappia VE, Olivero NB, Cortes PR, Stempin CC, Perez DR and Echenique J (2024) Intracellular *Streptococcus pneumoniae* develops enhanced fluoroquinolone persistence during influenza A coinfection.
Front. Microbiol. 15:1423995.
doi: 10.3389/fmicb.2024.1423995

Intracellular *Streptococcus pneumoniae* develops enhanced fluoroquinolone persistence during influenza A coinfection

Mirelys Hernandez-Morfa[1,2], Nicolas M. Reinoso-Vizcaino[1,2†], Victoria E. Zappia[1,2], Nadia B. Olivero[1,2], Paulo R. Cortes[1,2], Cinthia C. Stempin[1,2], Daniel R. Perez[3] and Jose Echenique[1,2*]

[1]Centro de Investigaciones en Bioquímica Clínica e Inmunología (CIBICI)-Consejo Nacional de Investigaciones Científicas y Técnicas (CONICET), Córdoba, Argentina, [2]Departamento de Bioquímica Clínica, Facultad de Ciencias Químicas, Universidad Nacional de Córdoba, Córdoba, Argentina, [3]Department of Population Health, College of Veterinary Medicine, University of Georgia, Athens, GA, United States

Streptococcus pneumoniae is a major pathogen responsible for severe complications in patients with prior influenza A virus (IAV) infection. We have previously demonstrated that *S. pneumoniae* exhibits increased intracellular survival within IAV-infected cells. Fluoroquinolones (FQs) are widely used to treat pneumococcal infections. However, our prior work has shown that *S. pneumoniae* can develop intracellular FQ persistence, a phenomenon triggered by oxidative stress within host cells. This persistence allows the bacteria to withstand high FQ concentrations. In this study, we show that IAV infection enhances pneumococcal FQ persistence during intracellular survival within pneumocytes, macrophages, and neutrophils. This enhancement is partly due to increased oxidative stress induced by the viral infection. We find that this phenotype is particularly pronounced in autophagy-proficient host cells, potentially resulting from IAV-induced blockage of autophagosome-lysosome fusion. Moreover, we identified several *S. pneumoniae* genes involved in oxidative stress response that contribute to FQ persistence, including *sodA* (superoxide dismutase), *clpL* (chaperone), *nrdH* (glutaredoxin), and *psaB* (Mn^{+2} transporter component). Our findings reveal a novel mechanism of antibiotic persistence promoted by viral infection within host cells. This underscores the importance of considering this phenomenon when using FQs to treat pneumococcal infections, especially in patients with concurrent influenza A infection.

KEYWORDS

***Streptococcus pneumoniae*, influenza A, oxidative stress, stress response, intracellular survival, persistence, fluoroquinolones, autophagy**

Introduction

Streptococcus pneumoniae (pneumococcus), a bacterium colonizing the human nasopharynx, is a major cause of diverse infections, ranging from mild otitis media (ear infection) and sinusitis (sinus infection) to life-threatening meningitis and community-acquired pneumonia (CAP) (Anderson and Feldman, 2023). These severe pneumococcal

infections significantly impact global health, causing over 1 million deaths annually (Walker et al., 2013; Wahl et al., 2018).

It is known that pneumococcal infections may result in severe pneumonia in patients previously infected with respiratory viruses such as influenza A, rhinovirus, adenovirus, metapneumovirus, respiratory syncytial virus, and SARS-CoV-2 (Westblade et al., 2021; Wada et al., 2024). These viral infections alter the immune response and allow secondary bacterial infections that are related to worse patient outcomes, particularly in those with comorbidities such as chronic respiratory and cardiovascular diseases, and diabetes mellitus (Cilloniz et al., 2022). We focused our study on the synergism that exists between *S. pneumoniae* and influenza A, the best viral/bacterial interaction described so far. *S. pneumoniae* is a notorious culprit in bacterial coinfections following influenza infection (Sender et al., 2021). Historical evidence from influenza outbreaks underscores how influenza significantly increases vulnerability to secondary bacterial infections (Smith and McCullers, 2014). Notably, coinfections involving both influenza virus and bacteria are far more severe and deadly than bacterial pneumonia alone (Joseph et al., 2013). Indeed, estimates suggest that secondary bacterial infections caused by *S. pneumoniae* may have been responsible for the majority of the 40–50 million deaths during the devastating 1918 Spanish influenza pandemic (Morens et al., 2008).

Influenza A virus (IAV) infection paves the way for secondary bacterial infections through a multi-pronged attack on the host's defenses (McCullers, 2014). Firstly, the virus's reliance on host cell machinery leads to widespread cellular dysfunction. IAV damages the lung's epithelial lining, impairing mucociliary clearance, the body's primary mechanism for expelling bacteria-laden mucus (McCullers, 2006). Additionally, viral neuraminidase alters the composition of mucus, creating a more hospitable environment for bacterial adhesion (McCullers, 2014). Secondly, IAV infection directly compromises immune cells, hindering their ability to engulf and destroy bacteria (McNamee and Harmsen, 2006). Finally, the virus triggers oxidative stress, overwhelming the delicate antioxidant balance within host cells. This imbalance weakens cellular defenses, creating an ideal environment for opportunistic bacteria to thrive.

During the infection process, *S. pneumoniae* employs a multifaceted strategy involving reactive oxygen species (ROS). This bacterium can produce ROS to gain a competitive advantage over resident microbiota in the respiratory tract, inflict damage on host cells (Ercoli et al., 2018), and disrupt inflammasome-dependent innate immune responses (Ogawa et al., 2018). Paradoxically, ROS are also critical components of the host's defense mechanisms, posing a challenge that *S. pneumoniae* must overcome to thrive within host cells (Hernandez-Morfa et al., 2023). Intriguingly, research demonstrates that *S. pneumoniae* can survive within diverse host cell types, including pneumocytes (Cortes et al., 2015; Pinas et al., 2018; Reinoso-Vizcaino et al., 2020), macrophages (Cortes et al., 2015; Ercoli et al., 2018), and neutrophils (Martner et al., 2008; Barbuti et al., 2010), all of which generate varying levels of ROS. This remarkable intracellular persistence is facilitated by the bacterium's ability to mount its own oxidative stress response, allowing it to tolerate both the ROS it produces and those released by the host's immune cells (Yesilkaya et al., 2013; Li et al., 2015; Hernandez-Morfa et al., 2022, 2023). Our previous research demonstrated that *S. pneumoniae* can persist for extended periods within A549 pneumocytes, a process dependent on the bacteria's oxidative stress response mechanisms (Pinas et al., 2018). Intriguingly, coinfection with IAV significantly enhances bacterial survival within these host cells. This synergistic effect is mediated by the pneumococcal SirRH two-component system, which regulates genes involved in both acid and oxidative stress tolerance (Reinoso-Vizcaino et al., 2020).

The global spread of antibiotic-resistant *S. pneumoniae* strains severely complicates treatment of invasive diseases like meningitis, a challenge worsened by IAV coinfection (MacIntyre et al., 2018; Feldman and Anderson, 2020). Fluoroquinolones (FQs) are critical for treating these infections, but their effectiveness is threatened by the emergence of FQ-resistant strains (Kim L. et al., 2016). Beyond resistance, bacteria such as *S. pneumoniae* employ adaptive mechanisms, including tolerance and persistence, to endure the presence of antibiotics. Unlike antibiotic resistance, tolerance and persistence are not genetically inherited traits, enabling bacteria to withstand lethal antibiotic levels without undergoing replication. While tolerance impacts the entire bacterial population, persistence is observed in only a specific subset (Balaban et al., 2019). Our work shows that oxidative stress encountered during host cell infection triggers FQ persistence in *S. pneumoniae*, affecting macrophages, neutrophils, and pneumocytes. This classifies it as a triggered persistence mechanism (Balaban et al., 2019). Furthermore, we have demonstrated that oxidative stress and growth arrest act synergistically to induce this FQ persistence in *S. pneumoniae* (Hernandez-Morfa et al., 2022, 2023).

This study investigates how IAV infection synergistically enhances FQ persistence in *S. pneumoniae* during intracellular survival in host cells. Our results demonstrate that expression of oxidative stress response genes in *S. pneumoniae* contributes to this influenza-induced persistence enhancement. By elucidating the interplay between IAV and pneumococcal oxidative stress mechanisms, we provide new insights into FQ persistence. This heightened persistence has potential clinical implications, suggesting that fluoroquinolone treatment of pneumococcal infections might be less effective in patients with concurrent influenza A infection.

Results

Influenza A coinfection increases *Streptococcus pneumoniae* survival in pneumocytes, but not in macrophages or neutrophils

In a previous work, we have demonstrated that IAV coinfection increases *S. pneumoniae* survival within host cells by two main reasons. Firstly, the fusion between lysosomes and autophagosomes, where *S. pneumoniae* resides, is inhibited by the viral infection. In consequence, pneumococci are not killed by lysosomal enzymes and survive longer in autophagosomes. Secondly, in response to the heightened ROS production induced by IAV in host cells, pneumococci are compelled to upregulate the expression of various antioxidant proteins (such as SodA, TpxD, among others)(Reinoso-Vizcaino et al., 2020). In addition, we have reported that host cell oxidative stress induces pneumococcal FQ persistence (Hernandez-Morfa et al., 2022). We sought to determine whether IAV coinfection also enhances FQ persistence in human cell lines: A549 pneumocytes, THP-1 macrophages, and PLB-985 neutrophils. Building on our

earlier findings in A549 cells (Reinoso-Vizcaino et al., 2020), we investigated this viral/bacterial synergy in THP-1 and PLB-985 cells using established infection protocols (Hernandez-Morfa et al., 2023). The *S. pneumoniae* R801 strain was incubated at a multiplicity of infection (MOI) of 30 for 3 h in A549 and THP-1 cells and for 1 h in PLB-985 cells. In viral/bacterial coinfections, host cells were first inoculated with the PR8 strain of IAV at a MOI of 10 for 24 h prior to bacterial inoculation, and the viral percentage (96–99%) was determined by flow cytometry (Supplementary Figure S1). Interestingly, while IAV coinfection reduced *S. pneumoniae* survival slightly in PLB-985 cells and showed no effect in THP-1 cells, it significantly increased bacterial survival within A549 pneumocytes (Figure 1). This cell-type specificity aligns with previous observations in 16HBE14o- bronchial cells (Reinoso-Vizcaino et al., 2020), and suggests a crucial difference in how pulmonary epithelial cells and immune cells handle IAV/pneumococcal coinfection. Our findings indicated that coinfection with influenza A enhances the survival of *S. pneumoniae* in pneumocytes, while no significant impact was observed in macrophages or neutrophils. Naturally, the robust antimicrobial mechanisms of immune cells likely explain their ability to better control intracellular pneumococcal survival compared to pulmonary cells.

Studies have shown that this viral infection increases ROS production in A549 pneumocytes (Komaravelli and Casola, 2014; Pyo et al., 2014). In our hands, the IAV infection of A549 pneumocytes augmented 33% ROS after 24 h (Reinoso-Vizcaino et al., 2020). To investigate the role of host cell oxidative stress in viral/bacterial synergy, we treated coinfected cells with N-acetylcysteine (NAC), a known inhibitor of ROS production. We used 5 mM NAC for A549 cells and 10 mM NAC for THP-1 and PLB-985 cells, applying the treatment starting 1 h before and during bacterial infection. Reducing ROS levels by the NAC treatment enhanced intracellular *S. pneumoniae* survival in both A549 and THP-1 cells (Figure 1), consistent with previous observations (Pinas et al., 2018). In contrast, PLB-985 cells exhibited reduced bacterial viability, potentially attributed to other ROS-independent NAC effect that improve phagocytic functions, as previously outlined (Oddera et al., 1994).

These results further support the critical role of ROS in regulating pneumococcal survival within host cells, consistent with our previous findings (Reinoso-Vizcaino et al., 2020). These results enable us to suggest that the induction of intracellular survival of *S. pneumoniae* is contingent upon the specific human cell line used in the coinfection assays.

IAV boosts *Streptococcus pneumoniae* fluoroquinolone persistence

Building upon the observed IAV-induced increase in *S. pneumoniae* intracellular survival in A549 pneumocytes, we investigated whether the virus also influences pneumococcal FQ persistence within host cells. Using our coinfection model, we exposed infected A549 cells, THP-1 macrophages, and PLB-985 neutrophils to levofloxacin (6 μg/mL). Intriguingly, we observed a significant increase in the proportion of levofloxacin persisters, hereafter, referred as levo-persisters (Figure 2A; Supplementary Figure S2). This indicates that viral infection promotes FQ persistence in *S. pneumoniae* across a range of cell types.

Host cell oxidative stress induced by IAV infection promotes *Streptococcus pneumoniae* FQ persistence

We have previously shown that oxidative stress within host cells induces FQ persistence in *S. pneumoniae* (Hernandez-Morfa et al.,

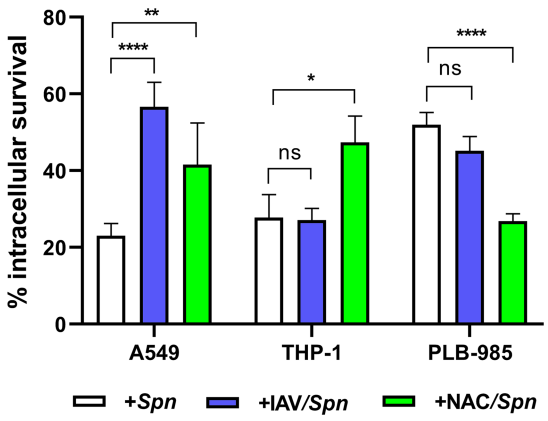

FIGURE 1
Synergistic increase in bacterial survival after IAV infection is specific to pneumocytes. A549 (lung epithelial), THP-1 (macrophages) and PLB-985 (neutrophils) cells were infected with IAV at a multiplicity of infection (MOI) of 10:1 for 24 h, followed by *S. pneumoniae* strain R801 (MOI 30:1). A549 cells were pre-treated (1 h) and co-treated (during bacterial infection) with 5 mM NAC, while PLB-985 and THP-1 cells received 10 mM NAC using the same regimen. The A549 and THP-1 cells were infected with pneumococci at a multiplicity of infection (MOI) of 30 for 3 h, and PLB-985 cells with the same MOI for 1 h. Bacterial survival was assessed using a gentamicin protection assay. In these assays, the 100% value of intracellular survival corresponds to the colony-forming units (CFUs) obtained after the gentamicin treatment, which was used to eliminate extracellular bacteria. Samples were collected at designated time points, lysed, diluted, and plated on BHI blood agar for CFU enumeration. Percentage survival represents the mean ± SEM of at least three replicates with statistically significant differences determined by a two-tailed test (**$p < 0.01$; ***$p < 0.001$; ****$p < 0.0001$). NS indicates non-significant. Data are representative of at least three independent experiments.

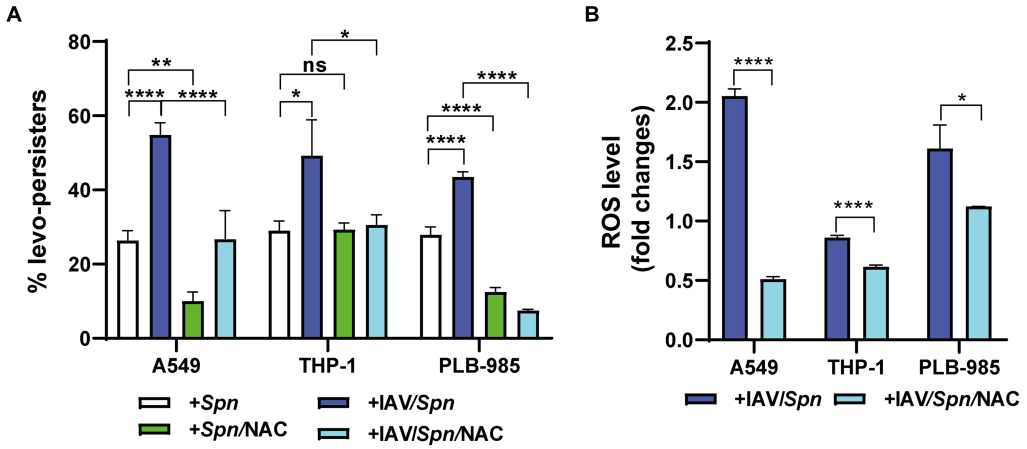

FIGURE 2
Influenza A Virus (IAV)-induced oxidative stress in host cells enhances levofloxacin persistence of *S. pneumoniae*. **(A)** Determination of Levofloxacin Persistence in Host Cells. A549, THP-1, and PLB-985 cells were infected with IAV at a MOI of 10:1 for 24 h. Subsequently, these cells were infected with pneumococci at a MOI of 30:1 using the same infection scheme shown in Figure 1. To assess the impact of ROS production, NAC treatment was performed as described in the Figure 1 legend. Bacterial survival was evaluated using a standard gentamicin protection assay. The percentage of levofloxacin-persisting bacteria was calculated relative to the total number of internalized bacteria. After the gentamycin treatment, which was used to eliminate extracellular bacteria, 6 μg/mL levofloxacin was added, and samples were collected at various time points depending on the cell type. Finally, the cells were lysed via centrifugation. Diluted samples in brain heart infusion (BHI) were plated on BHI blood agar and incubated for 16 h at 37°C. **(B)** Determination of ROS levels by flow cytometry. Intracellular ROS levels were quantified using the peroxide-sensitive fluorescent probe 2′,7′-dichlorodihydrofluorescein diacetate (H_2DCFDA) as detailed in the Materials and Methods section. Fold changes represent the ratio of fluorescence intensity in IAV-infected cells compared to non-infected cells, with or without NAC treatment (as described in Figure 1 legend). Error bars represent the standard deviation of at least three replicates. Statistical significance was determined using a two-tailed t-test. Data are representative of at least three independent experiments, with statistically significant differences indicated as $*p < 0.01$, $**p < 0.001$, $***p < 0.0001$.

2022) and that IAV infection elevates intracellular ROS levels, aligning with other studies (Gennaris and Collet, 2013; Komaravelli and Casola, 2014). To directly test the link between ROS and FQ persistence, we treated cells with NAC for 1 h at either 5 mM (A549 cells) or 10 mM (THP-1 and PLB-985 cells), prior to bacterial challenge and followed by levofloxacin (6 μg/mL) treatment during bacterial infection. We observed a significant decrease in FQ persistence in *S. pneumoniae*-infected A549 and PLB-985 cells treated with NAC, confirming our previous findings (Hernandez-Morfa et al., 2022; Figure 2A). Importantly, in IAV-infected cells across all three cell types, NAC treatment similarly reduced *S. pneumoniae* FQ persistence (Figure 2A). This strengthens the connection between oxidative stress and FQ persistence and demonstrates that this mechanism remains relevant even during IAV coinfection.

Previous studies, including our own, have shown that IAV infection increases ROS production in A549 pneumocytes (Pyo et al., 2014; Reinoso-Vizcaino et al., 2020). Even during coinfection with IAV/*S. pneumoniae*, we confirmed this effect in A549, THP-1, and PLB-985 cells, demonstrating a significant fold-change increase in intracellular ROS levels upon IAV infection (Figure 2B). Importantly, pre-treating these IAV-infected cells with NAC (5 mM for A549, 10 mM for PLB-985 and THP-1 cells) for 1 h prior to bacterial challenge reduced both ROS levels and FQ persistence when measuring these phenotypes simultaneously (Figure 2B). This finding directly links IAV-induced oxidative stress to the heightened FQ persistence in *S. pneumoniae*. Despite this complexity, our data collectively indicates a strong association between IAV-induced oxidative stress in host cells and the heightened FQ persistence observed in *S. pneumoniae*.

Streptococcus pneumoniae oxidative stress genes linked to FQ persistence during coinfection

From our previous work demonstrating the crucial role of SirRH in promoting *S. pneumoniae* survival during coinfection with IAV (Reinoso-Vizcaino et al., 2020), we sought to elucidate the underlying mechanisms. Transcriptomic and proteomic analyses revealed a link between SirRH and the expression of *clpL*, *nrdH*, and *psaB* genes under acidic conditions, which mimics the environment found within autophagosomes where *S. pneumoniae* resides during coinfection (Reinoso-Vizcaino et al., 2020). Interestingly, these genes are also potentially involved in the pneumococcal response to oxidative stress, as previously described for *psaB* that encodes a subunit of the Mn^{2+} transporter (McAllister et al., 2004; McCluskey et al., 2004) and *sodA* that encodes a superoxide dismutase (not regulated by SirR) (Eijkelkamp et al., 2014). We hypothesized that this network contributes to the complex phenomenon of fluoroquinolone (FQ) persistence.

To investigate this hypothesis, we systematically generated *S. pneumoniae* mutants lacking each of these genes (*clpL, nrdH, psaB*, and *sodA*) (Supplementary Table S1). As anticipated, all mutants showed increased susceptibility to H_2O_2-induced oxidative stress (Supplementary Figure S3), confirming their importance in combating oxidative damage. And following exposure to H_2O_2 (20 mM) and subsequent treatment with levofloxacin (6 μg/mL), a significant decrease in FQ persistence was observed for all mutants compared to wild-type pneumococci (Figure 3A; Supplementary Figure S4). This suggests these genes contribute to an intrinsic stress tolerance mechanism in

S. pneumoniae, one that likely helps pneumococci withstand antibiotic pressure even in the absence of host cell interactions.

In IAV-infected A549 pneumocytes, THP-1 macrophages, and PLB-985 neutrophils, mutants generally displayed decreased FQ persistence across all cell lines compared to the wild-type strain (Figures 3B–D; Supplementary Figures S5–S7). This highlights the intriguing possibility that IAV infection promotes FQ persistence in *S. pneumoniae* by activating pathways that inadvertently increase antibiotic tolerance. We speculate that this might occur through IAV-triggered, SirRH-mediated pneumococcal stress response pathways involving these genes.

However, this relationship becomes more nuanced when we compare mutant behavior between different cell types (Figure 3). The unique behavior of the *ΔclpL* mutant in THP-1 cells (no effect on FQ persistence, Figure 3C) underscores that cell-type specific factors likely modulate FQ persistence during coinfection. Similarly, despite exhibiting reduced FQ persistence in single-infection models, IAV coinfection generally increased FQ persistence in most mutants across A549 and THP-1 cells, with notable exceptions: *ΔpsaB* in A549 (Figure 3B) and *ΔnrdH* & *ΔclpL* in THP-1 (Figure 3C). Conversely, most mutants in coinfected PLB-985 cells showed decreased FQ persistence, except *ΔsodA* and *ΔclpL* (Figure 3D). These findings paint a complex picture. While IAV infection seems to generally promote FQ persistence through oxidative stress pathways in *S. pneumoniae*, the specific genes involved, and the magnitude of the effect appear to be highly dependent on the oxidative environment and unique defense mechanisms of different host cell types.

Autophagy in host cells is essential for IAV-induced FQ persistence in *Streptococcus pneumoniae*

We had established that influenza A virus (IAV) promotes *S. pneumoniae* intracellular survival via a mechanism dependent on host cell autophagy (Reinoso-Vizcaino et al., 2020). To delve deeper

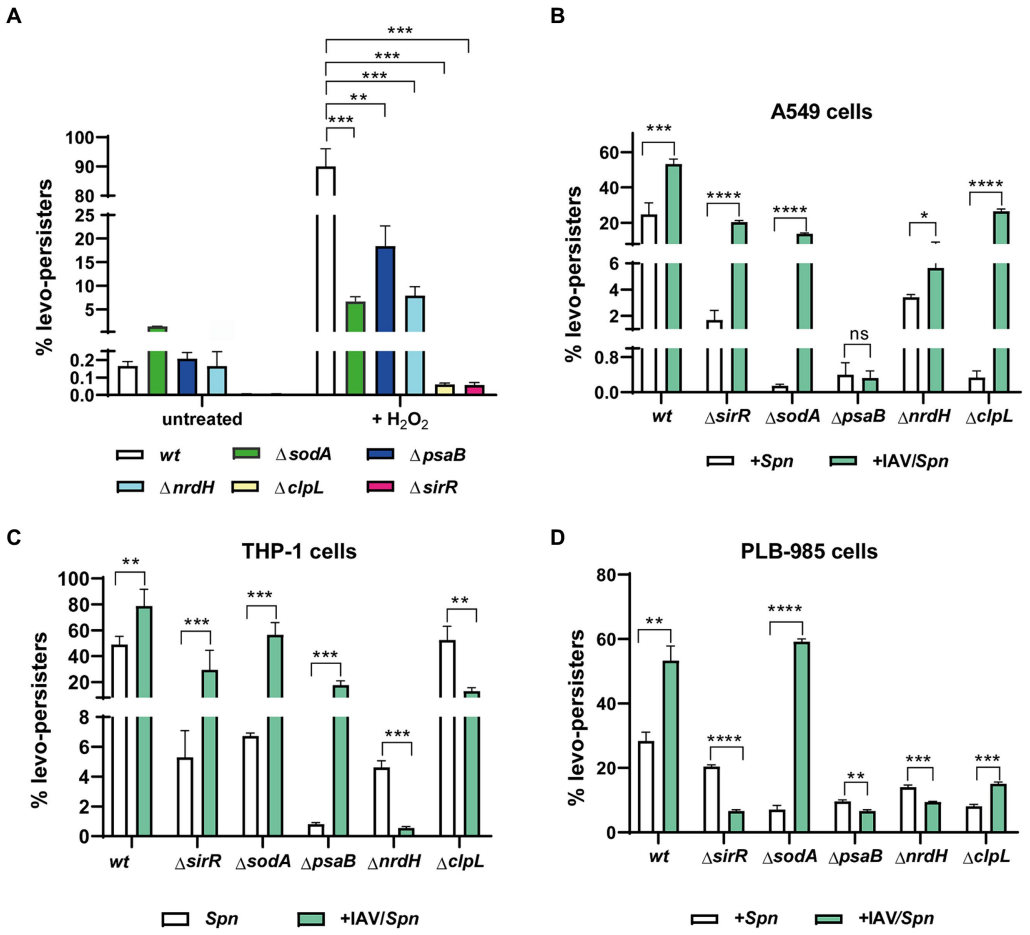

FIGURE 3
Involvement of *clpL, sodA, psaB, nrdH,* and *sirR* genes in levofloxacin persistence during *S. pneumoniae* infection in host cells. **(A)** Decreased FQ persistence of *ΔclpL, ΔsodA, ΔpsaB, ΔnrdH,* and *ΔsirR* mutants in culture media. *S. pneumoniae* strains (*wt* and indicated mutants) were grown to mid-exponential phase (OD_{600nm} 0.3) and exposed to oxidative stress (20 mM H_2O_2 for 30 min) or left untreated. Following stress/no-stress treatment, cultures were exposed to 6 μg/mL levofloxacin, and FQ persistence was evaluated as described previously. **(B–D)** Influence of IAV infection on FQ persistence in *ΔclpL, ΔsodA, ΔpsaB, ΔnrdH,* and *ΔsirR* mutants within A549, THP-1, and PLB-985 cells. FQ persistence of each pneumococcal mutant was analyzed in both IAV-infected and non-infected cells of the indicated host cell line. Experimental details for infection and FQ persistence assays are provided in the Materials and Methods section and Figure 2. Error bars represent the standard deviation of at least three replicates. Statistical significance was determined using a two-tailed *t*-test, indicated as $*p < 0.01$, $**p < 0.001$, or $****p < 0.0001$.

into the relationship between autophagy and IAV-induced FQ persistence, we utilized a coinfection model with mouse embryonic fibroblasts (MEFs). Specifically, we compared autophagy-deficient MEF *ATG5-KO* cells (which lack the crucial Atg5 protein) to their autophagy-proficient wildtype counterparts (MEF-*wt*) (Kuma et al., 2004; Nishida et al., 2009; Zhou et al., 2009; Don Wai Luu et al., 2022). Confirming our earlier findings, IAV coinfection failed to enhance *S. pneumoniae* survival in MEF *ATG5-KO* cells (Figure 4; Supplementary Figure S8), underscoring the importance of autophagy in this process (Reinoso-Vizcaino et al., 2020).

Next, we investigated levofloxacin persistence. Intriguingly, we observed the expected IAV-induced increase in FQ persistence only within the autophagy-proficient MEF-*wt* cells (Figure 4; Supplementary Figure S8), paralleling our observations in human cell lines. Critically, in MEF *ATG5-KO* cells, where autophagy is impaired, FQ persistence actually decreased regardless of IAV infection. These results provide compelling evidence that IAV-induced FQ persistence in *S. pneumoniae* is directly linked to functional autophagy pathways within host cells. This exciting finding opens avenues for further investigation into the precise mechanisms by which autophagy contributes to this antibiotic persistence phenomenon.

Based on previous data showing that IAV M2 protein blocks autophagosome-lysosome fusion (Gannage et al., 2009), and that IAV promotes *S. pneumoniae* survival within autophagosomes (Reinoso-Vizcaino et al., 2020), we hypothesized that M2 could independently drive both intracellular survival and FQ persistence. To test this, we expressed M2 protein in A549 pneumocytes using a vector that also produces a green fluorescent protein (GFP) marker (pIRES-M2). Transfection efficiency was confirmed by flow cytometry (37%, Figure 5A; Supplementary Table S1). Western blot analysis verified M2 protein expression only in pIRES-M2 transfected cells and not in control cells transfected with an empty vector (Figure 5B). Critically, A549 cells expressing M2 displayed increased *S. pneumoniae* survival and FQ persistence, mirroring the effects observed in IAV-infected cells (Figure 5C). Conversely, control cells transfected with the empty vector showed survival rates like non-infected cells. These findings strongly suggest that the influenza A M2 protein alone is sufficient to recapitulate the IAV-mediated enhancement of both *S. pneumoniae* intracellular survival and FQ persistence within A549 pneumocytes.

Discussion

Streptococcus pneumoniae and IAV are major human pathogens (McCullers, 2014). *S. pneumoniae* causes invasive disease with high mortality (55% in children with pneumonia) in low-and middle-income countries, contributing to over 1.5 million deaths globally (GBD-LRI, 2017). IAV infections result in roughly 1 billion cases, 3–5 million severe illnesses, and 300,000–500,000 deaths worldwide annually (Klein et al., 2016). Influenza A infections frequently become more severe due to secondary bacterial infections, especially those caused by *S. pneumoniae*. This co-infection worsens respiratory problems and significantly increases illness and death rates (Joseph et al., 2013; Smith and McCullers, 2014; Cilloniz et al., 2022; Okahashi et al., 2022). Estimates suggest a substantial portion of the 40–50 million deaths during the 1918 Spanish influenza pandemic stemmed from secondary pneumococcal infections (Brundage and Shanks, 2008; Morens et al., 2008). Similarly, around 34% of fatalities attributed to the 2009 influenza A pandemic involved subsequent bacterial infections, with *S. pneumoniae* being the most common culprit (Dawood et al., 2012; Chertow and Memoli, 2013). Recent studies have shown that in controlled environments, 11–35% of confirmed influenza cases were linked to secondary pneumococcal infections (Klein et al., 2016). This situation presents a substantial treatment challenge, as it raises the risk of ineffective initial antibiotic therapy and poorer patient outcomes. The growing problem of antimicrobial resistance makes managing *S. pneumoniae* infections with antibiotics increasingly

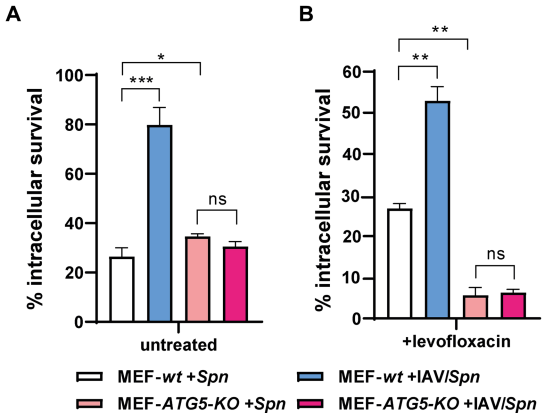

FIGURE 4
Autophagy-proficient MEFs exhibit Levofloxacin persistence. Wild-type MEFs (MEF *wt*) and autophagy-deficient MEFs lacking ATG5 (MEF *ATG5-KO*) were infected with IAV at a MOI of 10:1. After 24 h, the cells were co-infected with *S. pneumoniae* for 3 h. Intracellular pneumococcal survival was assessed with standard gentamicin protection assay. The percentage of surviving *S. pneumoniae* was determined relative to the total internalized bacteria after 30 min of gentamicin treatment (considered 100%). To quantify levofloxacin-persistent bacteria (levo-persisters), cells were exposed to 6 μg/mL levofloxacin immediately after gentamicin treatment, followed by lysis and plating on BHI blood agar plates after 3 h. The data represent the mean with standard deviation from three independent samples. Error bars represent the standard deviation of at least three replicates. Statistical significance was determined using a two-tailed t-test. Data are representative of at least three independent experiments, with statistically significant differences indicated as $*p < 0.01$, $**p < 0.001$, $***p < 0.0001$.

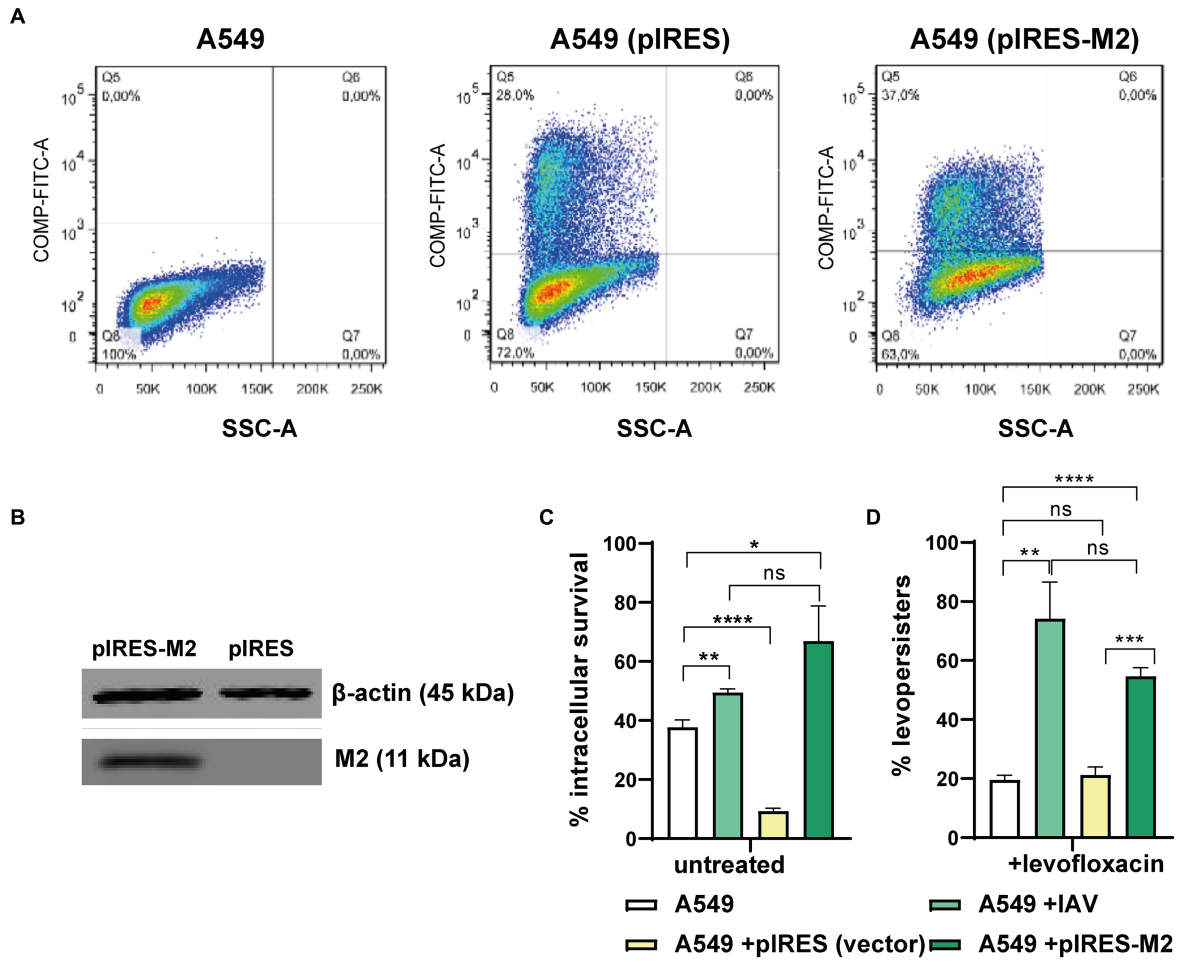

FIGURE 5
Viral M2 protein and levo-persistence. **(A)** Transfection Efficiency: A549 cells were transfected with pIRES (empty vector) or pIRES-M2 plasmids. Transfection efficacy was evaluated using GFP expression (a fluorescent marker within the pIRES vector) by flow cytometry. Green fluorescence intensity (FITC-A channel) is shown for non-transfected, pIRES-transfected, and pIRES-M2-transfected cells. The percentage of transfected cells is displayed in the Q5 quadrant of each graph. **(B)** M2 Protein Expression: Western blot analysis confirmed M2 protein expression in A549 cells transfected with pIRES-M2 compared to control (pIRES). β-actin served as a loading control. **(C)** Levo-persistence and M2: *S. pneumoniae* persistence was assessed in A549 cells transfected with pIRES or pIRES-M2, followed by bacterial infection. For comparison, A549 cells were infected with IAV before bacterial infection to mimic M2 expression during viral infection. Intracellular bacterial survival was measured using a gentamicin protection assay. Levo-persistence was determined following levofloxacin treatment as described in Figure 3. Data represent at least three independent experiments. Statistical significance is indicated: $*p < 0.01$, $**p < 0.001$, $****p < 0.0001$.

difficult (Reinert, 2009; Feldman and Anderson, 2020; Zahari et al., 2023). In recognition of this, the World Health Organization's Global Antimicrobial Resistance Surveillance System (GLASS) has identified *S. pneumoniae* as a priority pathogen for antibiotic-resistant surveillance (GLASS, 2015).

Fluoroquinolones (FQs) are widely used to treat invasive pneumococcal disease. However, the emergence of FQ-resistant strains compromises their effectiveness (Kim T. et al., 2016). Beyond resistance, bacterial persistence poses an additional challenge. Persisters are a phenotypic subpopulation that can tolerate high, typically lethal antibiotic concentrations without altering the minimum inhibitory concentration (Gefen and Balaban, 2009; Kester and Fortune, 2014).

Our group previously identified the first antibiotic persistence mechanism in *S. pneumoniae* triggered by oxidative stress during intracellular survival within host cells. This mechanism allows the bacteria to tolerate lethal FQ concentrations (Hernandez-Morfa et al., 2022, 2023). In this study, we demonstrate that coinfection of host cells with IAV and *S. pneumoniae* increases bacterial FQ persistence. This phenomenon is observed across human pneumocytes, macrophages, and neutrophils, suggesting a cell-type independent mechanism (Hernandez-Morfa et al., 2022, 2023).

Initially, we proposed two hypotheses to explain this response to viral coinfection and that impact on FQ persistence. The first one posits that IAV infection enhances intracellular survival of pneumococci into pneumocytes, thereby increasing FQ persistence.

S. pneumoniae's ability to persist within splenic macrophages suggests a potential reservoir for septicemia (Ercoli et al., 2018). Moreover, evidence demonstrates pneumococci residing in autophagic vesicles during early infection stages in human nasopharyngeal epithelial cells and mouse embryonic fibroblasts (Ogawa et al., 2018). Our research further indicates that *S. pneumoniae*'s stress response

mechanisms promote its survival within A549 pneumocytes (Cortes et al., 2015; Pinas et al., 2018). This synergistic effect requires functional autophagy pathways and correlates with pneumococcal survival inside autophagosomes (Reinoso-Vizcaino et al., 2020). IAV infection blocks lysosomal fusion via its M2 protein, leading to autophagosome accumulation (Gannage et al., 2009). We therefore hypothesized that M2 contributes to the observed increase in intracellular *S. pneumoniae* survival during co-infection (Reinoso-Vizcaino et al., 2020). Accordingly, in this work we found that expressing the M2 protein in pneumococci infected A549 pneumocytes significantly increased *S. pneumoniae* intracellular survival, similar to the effect observed during IAV infection. Furthermore, M2 expression augmented FQ persistence. Given our previous findings that *S. pneumoniae* accumulates within autophagosomes in IAV-infected A549 cells (Reinoso-Vizcaino et al., 2020) and that FQ persistence is induced within autophagy-proficient cells, we propose that FQ persistence of *S. pneumoniae* in A549 and MEF cells infected by IAV is a consequence of bacterial survival within autophagosomes.

Apparently, the first hypothesis regarding the FQ persistence mechanism *of S. pneumoniae* in host cells coinfected with IAV, which involves an increased intracellular survival, is valid for pulmonary cells. However, this phenotype was not detected in macrophages, indicating the existence of another IAV-induced mechanism that increases FQ persistence in host cells. An alternative hypothesis to explain FQ persistence emphasizes the intracellular oxidative environment within host cells, particularly during pneumococcal-IAV coinfection. Prior studies indicate IAV infection increases host cell ROS production (Pyo et al., 2014). We propose this IAV-induced oxidative stress may trigger FQ persistence in *S. pneumoniae*. This hypothesis is supported by our observation that the antioxidant N-acetylcysteine (NAC) significantly reduced FQ persistence in all coinfected cell lines. Further, we detected elevated intracellular ROS during coinfection of A549 pneumocytes, THP-1 macrophages and PLB-985 neutrophils with influenza A. This confirms the relevance of the oxidative stress response on the induction of FQ persistence in host cells.

Our previous work identified *S. pneumoniae* oxidative stress genes (e.g., *spxB*, *sodA*, *tpxD*) involved in host cell ROS-induced FQ persistence. These genes, regulated by StkP-ComE signaling (Pinas et al., 2018), exhibited reduced FQ persistence upon mutation in A549, Raw 264.7, and PLB-985 infection models (Hernandez-Morfa et al., 2022). We further established the SirRH two-component system's critical role in the cooperative effect of IAV infection on intracellular *S. pneumoniae* survival (Reinoso-Vizcaino et al., 2020). Comparative transcriptomic analysis revealed that the SirR response regulator governs the expression of oxidative stress genes, including *clpL* (encoding a chaperone), *psaB* (encoding an Mn^{+2} transporter), and *nrdH* (encoding a glutaredoxin-like protein) (Reinoso-Vizcaino et al., 2020). Mutations in *sirR*, *clpL*, *psaB*, and *nrdH* significantly reduced FQ persistence within host cells and diminished the response to oxidative stress compared to the wild-type strain (Reinoso-Vizcaino et al., 2020). Notably, the *ΔnrdH* mutant displayed a similar phenotype, highlighting a novel role for this gene in bacterial persistence. These findings corroborate our previous work demonstrating the importance of other oxidative stress genes like *spxB*, *tpxD*, and *sodA* (used as a control here) in FQ persistence (Hernandez-Morfa et al., 2022).

Here, we report the first characterization of a bacterial defense mechanism against antibiotics enhanced by intracellular survival within host cells due to a viral coinfection. The impact of mutations in genes associated with oxidative stress response (*sirR, sodA, clpL, psaB,* and *nrdH*) on FQ persistence was assessed. Coinfected A549 and THP-1 cells displayed enhanced FQ persistence in most mutants compared to pneumococci-only infections. However, this effect was less pronounced in PLB-985 cells, suggesting the influence of cell-type specific responses. This highlights the functional diversity of oxidative stress genes in *S. pneumoniae*, with distinct enzymes potentially playing varying roles in different host cell environments. These findings underscore the importance of a robust oxidative stress response for *S. pneumoniae* survival and FQ persistence within host cells. Furthermore, our data indicate that the synergistic effect of IAV coinfection on FQ persistence extends beyond just the oxidative stress response. Mechanisms such as M2-mediated blockage of autophagosome-lysosome fusion, previously reported to enhance intracellular survival (Gannage et al., 2009), likely also contribute.

Previously, we proposed that the induction of FQ persistence within host cells could impact the effectiveness of antibiotic treatment in patients with pneumococcal infections (Hernandez-Morfa et al., 2022). Importantly, persistence to beta-lactams and FQs have been reported in clinical strains of *S. pneumoniae* (Geerts et al., 2022). In this study, we particularized on the exacerbation of this phenomenon due to influenza A virus (IAV) infection, speculating that the use of FQs in coinfected individuals may complicate antimicrobial therapy. Furthermore, we posit that prolonged exposure to these antibiotics could facilitate the development of FQ resistance. This resistance is acquired through a gradual accumulation of genetic mutations in the quinolone resistance-determining regions (QRDRs) of the *parC* gene (encoding topoisomerase IV) and/or the *gyrA* gene (encoding DNA gyrase) (Kim L. et al., 2016).

In conclusion, this study shows that enhanced antibiotic persistence due to IAV co-infection could make treatment of *S. pneumoniae* infections more difficult. Prolonged antibiotic exposure of FQ persisters could potentially contribute to the development of full-fledged FQ resistance in *S. pneumoniae*. Thus, further research is needed to evaluate the emergence of FQ resistance among FQ persisters in *S. pneumoniae*.

Materials and methods

Bacterial strains, growth conditions, and primers

Bacterial strains, plasmids, and oligonucleotides used in this study are described in Supplementary Table S1. Oligonucleotide synthesis and DNA sequencing services were performed by Macrogen Inc. (Seoul, South Korea). The mutagenesis procedure (Echenique and Trombe, 2001), DNA transformation procedures (Cortes et al., 2008a), growth conditions (Cortes et al., 2008b), and stock preparation of the pneumococcal strains (Albarracin Orio et al., 2008) have been previously reported.

Antibiotic survival assay

Pneumococcal strains were cultured in Brain Heart Infusion (BHI) media at 37°C until an optical density of 0.3 at 600 nm (OD_{600nm}) was reached. To induce persister formation, cultures were exposed to

20 mM H_2O_2 for 30 min. Bacterial cells were then centrifuged, washed with PBS, and resuspended in fresh culture media. Following H_2O_2 treatment, cultures were exposed to 6 μg/mL levofloxacin for 5 h, in accordance with an established protocol (Hernandez-Morfa et al., 2022). Samples were collected after the 5-h incubation, serially diluted, and plated on blood agar plates for quantification. Surviving colonies were counted and reported as colony-forming units per milliliter (CFU/mL), representing FQ persisters. Minimum inhibitory concentrations (MICs) were determined using the broth microdilution method as recommended by the Clinical and Laboratory Standards Institute (CLSI) (CLSI, 2021).

Preparation of influenza A virus stock

The influenza A/Puerto Rico/8/34 (H1N1) strain (PR8) was used for this study (Francis and Magill, 1937). Viral stocks were propagated in 9-day-old specific pathogen-free (SPF) embryonated chicken eggs (sourced from Avico, Argentina). Each egg was inoculated via the amniotic cavity with 200 μL of diluted viral sample. The dilutions were prepared in phosphate-buffered saline (PBS) supplemented with gentamicin to prevent bacterial contamination. Eggs were incubated for 72 h at 37°C. Following incubation, the allantoic fluid was harvested, aliquoted, and stored at −80°C. Madin-Darby canine kidney cells (MDCK; ATCC CCL-34) were used to determine the titer of the propagated viral stock (Chockalingam et al., 2012; Reinoso-Vizcaino et al., 2020).

Cell lines and culture conditions

A549 cells (ATCC CCL-185, from human lung epithelial carcinoma) were cultured in DMEM (4.5 g/L glucose, 10% heat-inactivated FBS; Gibco BRL, Gaithersburg, MD) at 37°C, 5% CO_2. Cells were passaged every 2–3 days using trypsin/EDTA (25 μg/mL, 0.5 mM) and seeded into 75 cm^2 flasks (Greiner Bio-one) before transfection (Reinoso-Vizcaino et al., 2020). Transfections with pIRES2-EGFP and/or pIRES2-M2 used JetPRIME (Polyplus-transfection, Illkirch, France) in serum-free DMEM with 5% FBS (Reinoso-Vizcaino et al., 2020). Mouse Embryonic Fibroblast (MEF) and autophagy-deficient MEF *ATG5-KO* cell lines (Kuma et al., 2004) were generously provided by Dr. Noboru Mizushima (The University of Tokyo, Japan) and cultured under the same conditions as described for A549 cells. The human monomyelocytic PLB-985 and PLB-985 *gp91^{phox}* KO (PLB-985-*KO*) cell lines (provided by Prof. Mary C. Dinauer, Indiana University, USA) (Zhen et al., 1993; Panday et al., 2015) were cultured in RPMI 1640 (1% penicillin/streptomycin, 10% heat-inactivated FBS) at 37°C, 5% CO_2, with density maintained below 1.5 × 106 cells/mL (Zhen et al., 1993). The *gp91^{phox}* gene (also known as CYBB or nox2) encodes the cytochrome β-245, β-chain NADPH oxidase 2 (gp91^{phox} or Nox2), the catalytic subunit of NADPH oxidase, a major source of cellular reactive oxygen species (ROS). THP-1 cells were grown in RPMI 1640 supplemented with 1% non-essential amino acids, 50 μM β-mercaptoethanol, 10% FBS (Sigma-Aldrich Co), and 1% penicillin/streptomycin. Macrophage differentiation used 500,000 cells/well with 50 ng/mL PMA for 24 h. All cell lines were routinely tested for *Mycoplasma, Acholeplasma*, and *Ureaplasma* (Shahhosseiny et al., 2010).

Neutrophil differentiation by DMSO treatment

Neutrophil differentiation in PLB-985 and PLB-985-KO cells was induced as described previously (Hernandez-Morfa et al., 2022). Cells were seeded at 1×10^5 cells/mL in RPMI 1640 supplemented with 5% FBS, 1% penicillin/streptomycin, and 1.3% DMSO (Sigma-Aldrich Co.) for 5 days to mimic neutrophil development (Rincon et al., 2018). Cell density was adjusted to 1×10^6 cells/mL on day 3 and maintained throughout differentiation. Undifferentiated PLB-985 cells were cultured without DMSO as controls. Flow cytometry analysis of CD11b surface expression confirmed successful differentiation, as reported previously (Pedruzzi et al., 2002).

Influenza A infection of host cells

After cells were infected with IAV (MOI 10) for 24 h at 37°C, the viral infection was confirmed by targeting the HA protein of IAV. Cells were incubated with the anti-HA primary antibody (rabbit) for 1 h, as HA is a protein specific to IAV, followed by incubation with the secondary antibody labelled with Alexa Fluor 633 (goat, anti-rabbit, Invitrogen) for 30 min, using the protocol suggested by the manufacturer (Invitrogen). Finally, the samples were analyzed using the FACS Canto cytometer to detect the Alexa Fluor 633 signal and to quantify the percentage of IAV-infected cells.

Determination of intracellular survival and FQ persistence in IAV/pneumococci coinfected cells

Intracellular pneumococcal survival assays followed established protocols (Hernandez-Morfa et al., 2022). A549, MEF, MEF-*ATG5-KO*, PLB-985, PLB-985-*KO* or THP-1 cells (1.5×10^5/well) were seeded in 12-well plates (Greiner Bio-One) and incubated for 24 h in DMEM or RPMI (5% FBS) with cell line-specific supplements. Cells were then infected with IAV (MOI 10) for 24 h at 37°C. Antioxidant treatment used NAC (Sigma): 5 mM for A549, 10 mM for THP-1, MEF, MEF-ATG5-KO, and PLB-985 cells, applied 1 h before and during bacterial infection. The *ΔsodA, ΔpsaB, ΔsirR, ΔclpL, ΔnrdH*, and *wt S. pneumoniae* strains were grown in BHI to OD_{600nm} 0.3, then resuspended in cell-specific media (DMEM/RPMI, 5% FBS). Cells were infected at a bacterial MOI of 30 for 3 h (A549) or 1 h (THP-1, MEF, MEF-*ATG5-KO*). After washing with PBS, fresh media with 200 μg/mL gentamicin sulfate (US Biological) was added to eliminate extracellular bacteria. Optimization confirmed 30 min gentamicin exposure was sufficient (Cortes et al., 2015). Bacterial counts at this point were designated 100% survival for subsequent normalization. To assess FQ-persistence, infected A549, THP-1, MEF, or MEF-*ATG5-KO* cells were cultured in DMEM (1% FBS, 6 μg/mL levofloxacin) (Hernandez-Morfa et al., 2022). For suspension-grown PLB-985 cells, low-speed centrifugation (1,000 g) was used before 30 min gentamicin treatment. Cells were then cultured in RPMI (1.3% DMSO, 6 μg/mL levofloxacin) (Hernandez-Morfa et al., 2022). Intracellular bacteria were released by centrifugation (15,000 g, 5 min), resuspended in BHI, and plated on BHI-agar-blood for CFU counting. IAV and IAV/pneumococcus-induced apoptosis/necrosis was determined by flow cytometry (Annexin V/propidium iodide kit, Invitrogen).

Quantification of ROS in host cells

Intracellular ROS accumulation in host cells was measured using the peroxide-sensitive fluorescent probe 2′,7′ dichloro-dihydrofluorescein diacetate (H_2DCFDA; Sigma) (Satoh et al., 1996). A549, PLB-985, THP-1, and MEF cells were collected at designated time points and centrifuged (1,800 g). Cell pellets were PBS-washed and resuspended in PBS (GIBCO) with 10 μM dihydrofluorescein diacetate. After 30 min of dark incubation at 37°C, cells were centrifuged again and resuspended in PBS containing 50 μg/mL propidium iodide for dead cell detection. Flow cytometry (Beckton Dickinson FACSCanto II) analyzed DCF fluorescence distribution (excitation: 488 nm, emission: 535 nm). Mitochondrial ROS measurement followed a similar procedure, with the addition of a 10 μM dihydrofluorescein diacetate exposure step to assess total ROS after initial centrifugation. FlowJo™ v 7.6.2 Software (BD Life Sciences) was used for data analysis.

Protein expression analysis by western blot

Western blot analysis was performed as described (Reinoso-Vizcaino et al., 2020). Briefly, A549 cells transfected with pIRES or pIRES-M2 were lysed with Laemmli solution (5% β-mercaptoethanol) and heated (90°C, 5 min). Supernatants were collected, and 40 μg of each sample was separated on 15% SDS-PAGE gels in Tris-Glycine-SDS running buffer (100 V cm-1). Proteins were transferred to PVDF membranes (wet transfer) and blocked with 5% BSA-PBS (1 h, room temperature). Membranes were incubated overnight at 4°C with primary antibodies against Influenza A M2 protein (ab5416, Abcam; 1:1000 dilution in 5% BSA-PBS) and β-actin (ab8226, Abcam; 1:2000 dilution). After washing (0.5% Tween-TBS), membranes were incubated with Alexa-conjugated secondary antibodies (1:1000 dilution, 1 h, room temperature). Fluorescence was detected using the Odyssey CLx Imaging System (LI-COR).

Data availability statement

The original contributions presented in the study are included in the article/Supplementary material, further inquiries can be directed to the corresponding author.

Ethics statement

Ethical approval was not required for the studies on humans and animals in accordance with the local legislation and institutional requirements because only commercially available established cell lines were used.

Author contributions

MH-M: Conceptualization, Data curation, Formal analysis, Investigation, Methodology, Software, Writing – review & editing. NR-V: Formal analysis, Methodology, Supervision, Validation, Writing – review & editing. VZ: Formal analysis, Methodology, Writing – review & editing. NO: Investigation, Methodology, Writing – review & editing. PC: Investigation, Writing – review & editing. CS: Methodology, Writing – review & editing. DP: Funding acquisition, Writing – review & editing. JE: Conceptualization, Formal analysis, Funding acquisition, Investigation, Project administration, Resources, Supervision, Visualization, Writing – original draft, Writing – review & editing.

Funding

The author(s) declare that financial support was received for the research, authorship, and/or publication of this article. This work was supported by NIAID-CEIRS (HHSN272201400008C, Options 20E and 15B, to DP and JE), ANPCYT (IP-COVID-19 240, FONCYT-PICT-2016-#0805, FONCYT-PICT 2018-#2046-Prestamo BID, to JE), and the National University of Cordoba (SECYT-UNC, to JE).

Acknowledgments

We thank Mary Dinauer (Indiana University, US) for providing the PLB-985 cells, and Noboru Mizushima (The University of Tokyo, Japan) for providing the MEF and MEF ATG5-KO cell lines. We are grateful to Gabriela Furlan, Noelia Maldonado, Luciana Reyna, Laura Gatica, Paula Abadie, Pilar Crespo, and Alejandra Romero (CIBICI-CONICET) for their technical assistance.

Conflict of interest

JE and CS are Research Career members at CONICET. MH-M, NR-V, and NO hold CONICET Ph.D. fellowships, and VZ holds an ANPCYT Ph.D. fellowship.

The remaining authors declare that the research was conducted in the absence of any commercial or financial relationships that could be construed as a potential conflict of interest.

The author(s) declared that they were an editorial board member of Frontiers, at the time of submission. This had no impact on the peer review process and the final decision.

Publisher's note

Supplementary material

The Supplementary material for this article can be found online at: https://www.frontiersin.org/articles/10.3389/fmicb.2024.1423995/full#supplementary-material

References

Albarracin Orio, A. G., Cortes, P. R., Tregnaghi, M., Pinas, G. E., and Echenique, J. R. (2008). A new serotype 14 variant of the pneumococcal Spain9V-3 international clone detected in the central region of Argentina. *J. Med. Microbiol.* 57, 992–999. doi: 10.1099/jmm.0.2008/000505-0

Anderson, R., and Feldman, C. (2023). The global burden of community-acquired pneumonia in adults, encompassing invasive pneumococcal disease and the prevalence of its associated cardiovascular events, with a focus on Pneumolysin and macrolide antibiotics in pathogenesis and therapy. *Int. J. Mol. Sci.* 24:1038. doi: 10.3390/ijms241311038

Balaban, N. Q., Helaine, S., Lewis, K., Ackermann, M., Aldridge, B., Andersson, D. I., et al. (2019). Definitions and guidelines for research on antibiotic persistence. *Nat. Rev. Microbiol.* 17, 441–448. doi: 10.1038/s41579-019-0196-3

Barbuti, G., Moschioni, M., Fumarulo, R., Censini, S., and Montemurro, P. (2010). *Streptococcus pneumoniae* modulates the respiratory burst response in human neutrophils. *FEMS Immunol. Med. Microbiol.* 60, 57–62. doi: 10.1111/j.1574-695X.2010.00716.x

Brundage, J. F., and Shanks, G. D. (2008). Deaths from bacterial pneumonia during 1918-19 influenza pandemic. *Emerg. Infect. Dis.* 14, 1193–1199. doi: 10.3201/eid1408.071313

Chertow, D. S., and Memoli, M. J. (2013). Bacterial coinfection in influenza: a grand rounds review. *JAMA* 309, 275–282. doi: 10.1001/jama.2012.194139

Chockalingam, A. K., Hickman, D., Pena, L., Ye, J., Ferrero, A., Echenique, J. R., et al. (2012). Deletions in the neuraminidase stalk region of H2N2 and H9N2 avian influenza virus subtypes do not affect postinfluenza secondary bacterial pneumonia. *J. Virol.* 86, 3564–3573. doi: 10.1128/JVI.05809-11

Cilloniz, C., Pericas, J. M., Rojas, J. R., and Torres, A. (2022). Severe infections due to respiratory viruses. *Semin. Respir. Crit. Care Med.* 43, 060–074. doi: 10.1055/s-0041-1740982

CLSI (2021). Performance standards for antimicrobial susceptibility testing, M100. Wayne, PA: Clinical and Laboratory Standards Institute.

Cortes, P. R., Orio, A. G., Regueira, M., Pinas, G. E., and Echenique, J. (2008a). Characterization of in vitro-generated and clinical optochin-resistant strains of *Streptococcus pneumoniae* isolated from Argentina. *J. Clin. Microbiol.* 46, 1930–1934. doi: 10.1128/JCM.02318-07

Cortes, P. R., Pinas, G. E., Albarracin Orio, A. G., and Echenique, J. R. (2008b). Subinhibitory concentrations of penicillin increase the mutation rate to optochin resistance in *Streptococcus pneumoniae*. *J. Antimicrob. Chemother.* 62, 973–977. doi: 10.1093/jac/dkn322

Cortes, P. R., Pinas, G. E., Cian, M. B., Yandar, N., and Echenique, J. (2015). Stress-triggered signaling affecting survival or suicide of *Streptococcus pneumoniae*. *Int. J. Med. Microbiol.* 305, 157–169. doi: 10.1016/j.ijmm.2014.12.002

Dawood, F. S., Iuliano, A. D., Reed, C., Meltzer, M. I., Shay, D. K., Cheng, P. Y., et al. (2012). Estimated global mortality associated with the first 12 months of 2009 pandemic influenza A H1N1 virus circulation: a modelling study. *Lancet Infect. Dis.* 12, 687–695. doi: 10.1016/S1473-3099(12)70121-4

Don Wai Luu, L., Kaakoush, N. O., and Castano-Rodriguez, N. (2022). The role of ATG16L2 in autophagy and disease. *Autophagy* 18, 2537–2546. doi: 10.1080/15548627.2022.2042783

Echenique, J. R., and Trombe, M. C. (2001). Competence modulation by the NADH oxidase of *Streptococcus pneumoniae* involves signal transduction. *J. Bacteriol.* 183, 768–772. doi: 10.1128/JB.183.2.768-772.2001

Eijkelkamp, B. A., Morey, J. R., Ween, M. P., Ong, C. L., McEwan, A. G., Paton, J. C., et al. (2014). Extracellular zinc competitively inhibits manganese uptake and compromises oxidative stress management in *Streptococcus pneumoniae*. *PLoS One* 9:e89427. doi: 10.1371/journal.pone.0089427

Ercoli, G., Fernandes, V. E., Chung, W. Y., Wanford, J. J., Thomson, S., Bayliss, C. D., et al. (2018). Intracellular replication of *Streptococcus pneumoniae* inside splenic macrophages serves as a reservoir for septicaemia. *Nat. Microbiol.* 3, 600–610. doi: 10.1038/s41564-018-0147-1

Feldman, C., and Anderson, R. (2020). Pneumococcal virulence factors in community-acquired pneumonia. *Curr. Opin. Pulm. Med.* 26, 222–231. doi: 10.1097/MCP.0000000000000674

Francis, T., and Magill, T. P. (1937). The antibody response of human subjects vaccinated with the virus of human influenza. *J. Exp. Med.* 65, 251–259. doi: 10.1084/jem.65.2.251

Gannage, M., Dormann, D., Albrecht, R., Dengjel, J., Torossi, T., Ramer, P. C., et al. (2009). Matrix protein 2 of influenza A virus blocks autophagosome fusion with lysosomes. *Cell Host Microbe* 6, 367–380. doi: 10.1016/j.chom.2009.09.005

GBD-LRI (2017). Estimates of the global, regional, and national morbidity, mortality, and aetiologies of lower respiratory tract infections in 195 countries: a systematic analysis for the global burden of disease study 2015. *Lancet Infect. Dis.* 17, 1133–1161. doi: 10.1016/S1473-3099(17)30396-1

Geerts, N., De Vooght, L., Passaris, I., Delputte, P., Van den Bergh, B., and Cos, P. (2022). Antibiotic tolerance indicative of persistence is pervasive among clinical *Streptococcus pneumoniae* isolates and shows strong condition dependence. *Microbiol Spectr* 10:e0270122. doi: 10.1128/spectrum.02701-22

Gefen, O., and Balaban, N. Q. (2009). The importance of being persistent: heterogeneity of bacterial populations under antibiotic stress. *FEMS Microbiol. Rev.* 33, 704–717. doi: 10.1111/j.1574-6976.2008.00156.x

Gennaris, A., and Collet, J. F. (2013). The 'captain of the men of death', *Streptococcus pneumoniae*, fights oxidative stress outside the 'city wall'. *EMBO Mol. Med.* 5, 1798–1800. doi: 10.1002/emmm.201303482

GLASS (2015). Manual for early implementation. Geneva: World Health Organization (WHO).

Hernandez-Morfa, M., Olivero, N. B., Zappia, V. E., Pinas, G. E., Reinoso-Vizcaino, N. M., Cian, M. B., et al. (2023). The oxidative stress response of *Streptococcus pneumoniae*: its contribution to both extracellular and intracellular survival. *Front. Microbiol.* 14:1269843. doi: 10.3389/fmicb.2023.1269843

Hernandez-Morfa, M., Reinoso-Vizcaino, N. M., Olivero, N. B., Zappia, V. E., Cortes, P. R., Jaime, A., et al. (2022). Host cell oxidative stress promotes intracellular fluoroquinolone Persisters of *Streptococcus pneumoniae*. *Microbiol Spectr* 10:e0436422. doi: 10.1128/spectrum.04364-22

Joseph, C., Togawa, Y., and Shindo, N. (2013). Bacterial and viral infections associated with influenza. *Influenza Other Respir. Viruses* 7, 105–113. doi: 10.1111/irv.12089

Kester, J. C., and Fortune, S. M. (2014). Persisters and beyond: mechanisms of phenotypic drug resistance and drug tolerance in bacteria. *Crit. Rev. Biochem. Mol. Biol.* 49, 91–101. doi: 10.3109/10409238.2013.869543

Kim, L., McGee, L., Tomczyk, S., and Beall, B. (2016). Biological and epidemiological features of antibiotic-resistant *Streptococcus pneumoniae* in pre-and post-conjugate vaccine eras: a United States perspective. *Clin. Microbiol. Rev.* 29, 525–552. doi: 10.1128/CMR.00058-15

Kim, T., Park, S. J., Chong, Y. P., Park, K. H., Lee, Y. M., Hong, H. L., et al. (2016). Fluoroquinolone resistance of *Streptococcus pneumoniae* isolates causing invasive disease: special focus on zabofloxacin. *Diagn. Microbiol. Infect. Dis.* 86, 181–183. doi: 10.1016/j.diagmicrobio.2016.07.019

Klein, E. Y., Monteforte, B., Gupta, A., Jiang, W., May, L., Hsieh, Y. H., et al. (2016). The frequency of influenza and bacterial coinfection: a systematic review and meta-analysis. *Influenza Other Respir. Viruses* 10, 394–403. doi: 10.1111/irv.12398

Komaravelli, N., and Casola, A. (2014). Respiratory viral infections and subversion of cellular antioxidant defenses. *J Pharmacogenomics Pharmacoproteomics* 5:1000141. doi: 10.4172/2153-0645.1000141

Kuma, A., Hatano, M., Matsui, M., Yamamoto, A., Nakaya, H., Yoshimori, T., et al. (2004). The role of autophagy during the early neonatal starvation period. *Nature* 432, 1032–1036. doi: 10.1038/nature03029

Li, P., Shi, J., He, Q., Hu, Q., Wang, Y. Y., Zhang, L. J., et al. (2015). *Streptococcus pneumoniae* induces autophagy through the inhibition of the PI3K-I/Akt/mTOR pathway and ROS hypergeneration in A549 cells. *PLoS One* 10:e0122753. doi: 10.1371/journal.pone.0122753

MacIntyre, C. R., Chughtai, A. A., Barnes, M., Ridda, I., Seale, H., Toms, R., et al. (2018). The role of pneumonia and secondary bacterial infection in fatal and serious outcomes of pandemic influenza a(H1N1)pdm09. *BMC Infect. Dis.* 18:637. doi: 10.1186/s12879-018-3548-0

Martner, A., Dahlgren, C., Paton, J. C., and Wold, A. E. (2008). Pneumolysin released during *Streptococcus pneumoniae* autolysis is a potent activator of intracellular oxygen radical production in neutrophils. *Infect. Immun.* 76, 4079–4087. doi: 10.1128/IAI.01747-07

McAllister, L. J., Tseng, H. J., Ogunniyi, A. D., Jennings, M. P., McEwan, A. G., and Paton, J. C. (2004). Molecular analysis of the PSA permease complex of *Streptococcus pneumoniae*. *Mol. Microbiol.* 53, 889–901. doi: 10.1111/j.1365-2958.2004.04164.x

McCluskey, J., Hinds, J., Husain, S., Witney, A., and Mitchell, T. J. (2004). A two-component system that controls the expression of pneumococcal surface antigen a (PsaA) and regulates virulence and resistance to oxidative stress in *Streptococcus pneumoniae*. *Mol. Microbiol.* 51, 1661–1675. doi: 10.1111/j.1365-2958.2003.03917.x

McCullers, J. A. (2006). Insights into the interaction between influenza virus and pneumococcus. *Clin. Microbiol. Rev.* 19, 571–582. doi: 10.1128/CMR.00058-05

McCullers, J. A. (2014). The co-pathogenesis of influenza viruses with bacteria in the lung. *Nat. Rev. Microbiol.* 12, 252–262. doi: 10.1038/nrmicro3231

McNamee, L. A., and Harmsen, A. G. (2006). Both influenza-induced neutrophil dysfunction and neutrophil-independent mechanisms contribute to increased susceptibility to a secondary *Streptococcus pneumoniae* infection. *Infect. Immun.* 74, 6707–6721. doi: 10.1128/IAI.00789-06

Morens, D. M., Taubenberger, J. K., and Fauci, A. S. (2008). Predominant role of bacterial pneumonia as a cause of death in pandemic influenza: implications for pandemic influenza preparedness. *J. Infect. Dis.* 198, 962–970. doi: 10.1086/591708

Nishida, Y., Arakawa, S., Fujitani, K., Yamaguchi, H., Mizuta, T., Kanaseki, T., et al. (2009). Discovery of Atg5/Atg7-independent alternative macroautophagy. *Nature* 461, 654–658. doi: 10.1038/nature08455

Oddera, S., Silvestri, M., Sacco, O., Eftimiadi, C., and Rossi, G. A. (1994). N-acetylcysteine enhances in vitro the intracellular killing of *Staphylococcus aureus* by human alveolar macrophages and blood polymorphonuclear leukocytes and partially protects phagocytes from self-killing. *J. Lab. Clin. Med.* 124, 293–301.

Ogawa, M., Matsuda, R., Takada, N., Tomokiyo, M., Yamamoto, S., Shizukuishi, S., et al. (2018). Molecular mechanisms of *Streptococcus pneumoniae*-targeted autophagy via pneumolysin, Golgi-resident Rab41, and Nedd4-1-mediated K63-linked ubiquitination. *Cell. Microbiol.* 20:e12846. doi: 10.1111/cmi.12846

Okahashi, N., Sumitomo, T., Nakata, M., and Kawabata, S. (2022). Secondary streptococcal infection following influenza. *Microbiol. Immunol.* 66, 253–263. doi: 10.1111/1348-0421.12965

Panday, A., Sahoo, M. K., Osorio, D., and Batra, S. (2015). NADPH oxidases: an overview from structure to innate immunity-associated pathologies. *Cell. Mol. Immunol.* 12, 5–23. doi: 10.1038/cmi.2014.89

Pedruzzi, E., Fay, M., Elbim, C., Gaudry, M., and Gougerot-Pocidalo, M. A. (2002). Differentiation of PLB-985 myeloid cells into mature neutrophils, shown by degranulation of terminally differentiated compartments in response to N-formyl peptide and priming of superoxide anion production by granulocyte-macrophage colony-stimulating factor. *Br. J. Haematol.* 117, 719–726. doi: 10.1046/j.1365-2141.2002.03521.x

Pinas, G. E., Reinoso-Vizcaino, N. M., Yandar Barahona, N. Y., Cortes, P. R., Duran, R., Badapanda, C., et al. (2018). Crosstalk between the serine/threonine kinase StkP and the response regulator ComE controls the stress response and intracellular survival of *Streptococcus pneumoniae*. *PLoS Pathog.* 14:e1007118. doi: 10.1371/journal.ppat.1007118

Pyo, C. W., Shin, N., Jung, K. I., Choi, J. H., and Choi, S. Y. (2014). Alteration of copper-zinc superoxide dismutase 1 expression by influenza A virus is correlated with virus replication. *Biochem. Biophys. Res. Commun.* 450, 711–716. doi: 10.1016/j.bbrc.2014.06.037

Reinert, R. R. (2009). The antimicrobial resistance profile of *Streptococcus pneumoniae*. *Clin. Microbiol. Infect.* 15, 7–11. doi: 10.1111/j.1469-0691.2009.02724.x

Reinoso-Vizcaino, N. M., Cian, M. B., Cortes, P. R., Olivero, N. B., Hernandez-Morfa, M., Pinas, G. E., et al. (2020). The pneumococcal two-component system SirRH is linked to enhanced intracellular survival of *Streptococcus pneumoniae* in influenza-infected pulmonary cells. *PLoS Pathog.* 16:e1008761. doi: 10.1371/journal.ppat.1008761

Rincon, E., Rocha-Gregg, B. L., and Collins, S. R. (2018). A map of gene expression in neutrophil-like cell lines. *BMC Genomics* 19:573. doi: 10.1186/s12864-018-4957-6

Satoh, T., Sakai, N., Enokido, Y., Uchiyama, Y., and Hatanaka, H. (1996). Survival factor-insensitive generation of reactive oxygen species induced by serum deprivation in neuronal cells. *Brain Res.* 733, 9–14. doi: 10.1016/0006-8993(96)00527-6

Sender, V., Hentrich, K., and Henriques-Normark, B. (2021). Virus-induced changes of the respiratory tract environment promote secondary infections with *Streptococcus pneumoniae*. *Front. Cell. Infect. Microbiol.* 11:643326. doi: 10.3389/fcimb.2021.643326

Shahhosseiny, M. H., Hosseiny, Z., Khoramkhorshid, H. R., Azari, S., and Shokrgozar, M. A. (2010). Rapid and sensitive detection of Mollicutes in cell culture by polymerase chain reaction. *J. Basic Microbiol.* 50, 171–178. doi: 10.1002/jobm.200800174

Smith, A. M., and McCullers, J. A. (2014). Secondary bacterial infections in influenza virus infection pathogenesis. *Curr. Top. Microbiol. Immunol.* 385, 327–356. doi: 10.1007/82_2014_394

Wada, F. W., Desta, A. F., Gebre, M., Mihret, W., Seyoum, T., Melaku, K., et al. (2024). Pneumococcal colonization and coinfecting respiratory viruses in children under 5 years in Addis Ababa, Ethiopia: a prospective case-control study. *Sci. Rep.* 14:4174. doi: 10.1038/s41598-024-54256-w

Wahl, B., O'Brien, K. L., Greenbaum, A., Majumder, A., Liu, L., Chu, Y., et al. (2018). Burden of *Streptococcus pneumoniae* and *Haemophilus influenzae* type b disease in children in the era of conjugate vaccines: global, regional, and national estimates for 2000-15. *Lancet Glob. Health* 6, e744–e757. doi: 10.1016/S2214-109X(18)30247-X

Walker, C. L. F., Rudan, I., Liu, L., Nair, H., Theodoratou, E., Bhutta, Z. A., et al. (2013). Global burden of childhood pneumonia and diarrhoea. *Lancet* 381, 1405–1416. doi: 10.1016/S0140-6736(13)60222-6

Westblade, L. F., Simon, M. S., and Satlin, M. J. (2021). Bacterial coinfections in coronavirus disease 2019. *Trends Microbiol.* 29, 930–941. doi: 10.1016/j.tim.2021.03.018

Yesilkaya, H., Andisi, V. F., Andrew, P. W., and Bijlsma, J. J. (2013). Streptococcus pneumoniae and reactive oxygen species: an unusual approach to living with radicals. *Trends Microbiol.* 21, 187–195. doi: 10.1016/j.tim.2013.01.004

Zahari, N. I. N., Engku Abd Rahman, E. N. S., Irekeola, A. A., Ahmed, N., Rabaan, A. A., Alotaibi, J., et al. (2023). A review of the resistance mechanisms for beta-lactams, macrolides and fluoroquinolones among *Streptococcus pneumoniae*. *Medicina (Kaunas)* 59:1927. doi: 10.3390/medicina59111927

Zhen, L., King, A. A., Xiao, Y., Chanock, S. J., Orkin, S. H., and Dinauer, M. C. (1993). Gene targeting of X chromosome-linked chronic granulomatous disease locus in a human myeloid leukemia cell line and rescue by expression of recombinant gp91phox. *Proc. Natl. Acad. Sci. USA* 90, 9832–9836. doi: 10.1073/pnas.90.21.9832

Zhou, Z., Jiang, X., Liu, D., Fan, Z., Hu, X., Yan, J., et al. (2009). Autophagy is involved in influenza A virus replication. *Autophagy* 5, 321–328. doi: 10.4161/auto.5.3.7406

frontiers | Frontiers in Microbiology

TYPE Original Research
PUBLISHED 09 July 2024
DOI 10.3389/fmicb.2024.1430038

OPEN ACCESS

EDITED BY
Jose Echenique,
National University of Córdoba, Argentina

REVIEWED BY
Vineet Kumar,
The University of Texas at Austin, United States
Mayumi Nakanishi-Matsui,
Iwate Medical University, Japan

*CORRESPONDENCE
Chengwang Zhang
✉ zhangchengwangzcw@126.com
Songquan Wu
✉ lswsq163@163.com

RECEIVED 09 May 2024
ACCEPTED 28 June 2024
PUBLISHED 09 July 2024

CITATION
Zhang C, Liu J, Liu X, Xu Y, Gan Q, Cheng Q, Liu W, Gao X and Wu S (2024) Glutamine enhances pneumococcal growth under methionine semi-starvation by elevating intracellular pH.
Front. Microbiol. 15:1430038.
doi: 10.3389/fmicb.2024.1430038

Glutamine enhances pneumococcal growth under methionine semi-starvation by elevating intracellular pH

Chengwang Zhang[1]*, Juncheng Liu[1], Xiaohui Liu[2,3], Yueyu Xu[1], Qingxiu Gan[1], Qinqian Cheng[1], Weiping Liu[1], Xiangmin Gao[1] and Songquan Wu[1]*

[1]Department of Basic Medical Science, School of Medicine, Lishui University, Lishui, Zhejiang, China, [2]National Protein Science Facility, Tsinghua University, Beijing, China, [3]School of Life Sciences, Tsinghua University, Beijing, China

Introduction: Bacteria frequently encounter nutrient limitation in nature. The ability of living in this nutrient shortage environment is vital for bacteria to preserve their population and important for some pathogenic bacteria to cause infectious diseases. Usually, we study how bacteria survive after nutrient depletion, a total starvation condition when bacteria almost cease growth and try to survive. However, nutrient limitation may not always lead to total starvation.

Methods: Bacterial adaptation to nutrient shortage was studied by determining bacterial growth curves, intracellular pH, intracellular amino acid contents, gene transcription, protein expression, enzyme activity, and translation and replication activities.

Results: No exogenous supply of methionine results in growth attenuation of Streptococcus pneumoniae, a human pathogen. In this paper, we refer to this inhibited growth state between ceased growth under total starvation and full-speed growth with full nutrients as semi-starvation. Similar to total starvation, methionine semi-starvation also leads to intracellular acidification. Surprisingly, it is intracellular acidification but not insufficient methionine synthesis that causes growth attenuation under methionine semi-starvation. With excessive glutamine supply in the medium, intracellular methionine level was not changed, while bacterial intracellular pH was elevated to ~ 7.6 (the optimal intracellular pH for pneumococcal growth) by glutamine deamination, and bacterial growth under semi-starvation was restored fully. Our data suggest that intracellular acidification decreases translation level and glutamine supply increases intracellular pH to restore translation level, thus restoring bacterial growth.

Discussion: This growth with intracellular pH adjustment by glutamine is a novel strategy we found for bacterial adaptation to nutrient shortage, which may provide new drug targets to inhibit growth of pathogenic bacteria under semi-starvation.

KEYWORDS

***Streptococcus pneumoniae*, methionine, semi-starvation, glutamine, growth, intracellular pH**

Introduction

In nature, nutrient starvation is a common condition that bacteria encounter in their whole lives. Usually, we describe nutrient starvation as depletion of certain nutrient(s), in which state bacteria grow extremely slowly (Gray et al., 2019). However, between the nearly stopped growth

under total starvation and full growth with sufficient nutrients, there exists an intermediate state that bacteria have an obvious growth but its growth is inhibited. Growth of *Streptococcus pneumoniae* in chemically defined medium (CDM) without methionine supply is a good example to exhibit this intermediate state. *S. pneumoniae* is an opportunistic human pathogen that colonizes in the nasopharynx of human as a commensal but causing pneumococcal diseases opportunistically, such as pneumonia, bacteremia, meningitis, and otitis media (Bogaert et al., 2004; Weiser et al., 2018). As an important amino acid, except for direct use for protein translation, methionine is the precursor of formyl methionine, the first building block for bacterial protein translation (Hondorp and Matthews, 2013) and *S*-adenosylmethionine (SAM), the methyl donor for the synthesis of DNA, RNA and proteins (Sperandio et al., 2007). Our previous studies show that the deletion of methionine synthesis gene *metE* plus limited methionine supply (1 μg/mL) in CDM causes total starvation in *S. pneumoniae* (Zhang et al., 2021, 2023). In this condition, methionine acquisition only comes from uptake by methionine transporter(s). When the limited methionine is exhausted, bacteria enter into methionine total starvation.

Although methionine is not an essential amino acid for pneumococcal growth, no methionine supply attenuates pneumococcal growth in CDM (Haertel et al., 2012). The work by Haertel et al. (2012) reveals that in the 20 amino acids, 8 amino acids are essential for pneumococcal growth in CDM. They are arginine, cysteine, histidine, glycine, glutamine, isoleucine, leucine and valine (Haertel et al., 2012). However, no supply of some of the remaining 12 amino acids (not essential) attenuates pneumococcal growth, especially for glutamate, proline or methionine (Haertel et al., 2012). Without exogenous supply, bacteria only rely on the precursors to synthesize the demanded amino acids. Similar phenomena were also found in Group B Streptococci. The absence of a certain amino acid in the media caused growth attenuation in some strains of Group B Streptococci (Milligan et al., 1978). Even for *Escherichia coli*, the removal of serine from medium reduced 22% of specific growth rate (Maser et al., 2020).

This intermediate growth state is characterized by no supply of a certain nutrient and synthesis of this nutrient by bacteria, and the growth yield is less than the full growth. We name this intermediate growth state semi-starvation. How bacteria adapt to semi-starvation is a fascinating question. In total starvation of amino acids, the alarmones guanosine 5′-monophosphate 3′-diphosphate (pGpp), guanosine tetraphosphate (ppGpp) and guanosine pentaphosphate (pppGpp), collectively referred to as (pp)pGpp (Cashel and Gallant, 1969; Haseltine and Block, 1973; Atkinson et al., 2011) are involved in DNA replication repression and rRNA synthesis inhibition (Potrykus and Cashel, 2008). In total starvation, bacteria try to survive, but not continue to grow. However, in semi-starvation, bacteria still try to grow. Our recent study shows that in methionine total starvation, pneumococcal cytoplasm is acidified and intracellularly accumulated glutamine balances intracellular pH to a mildly acidified level to enhance bacterial survival (Zhang et al., 2023). Glutamine can be deaminated to release ammonia that can neutralize protons (Lu et al., 2013). Whether intracellular pH homeostasis plays a role in pneumococcal growth under semi-starvation needs to be studied.

Intracellular pH is typically homeostatic in bacteria due to its important role in influencing enzyme activity, nucleic acid structure, redox potential, and secretion system activity (Veine et al., 1998; Slonczewski et al., 2009; Kenney, 2019). Unlike acidophiles and alkaliphiles that have an acidic and alkaline intracellular pH, respectively, (Matin et al., 1982; Sturr et al., 1994), neutralophiles usually keep their intracellular acidity closer to neutrality. For example, *E. coli* maintains the intracellular pH at 7.4–7.8 when it is cultured in pH 5–9 (Slonczewski et al., 2009). Intracellular pH homeostasis is important for bacterial growth (Slonczewski et al., 2009). However, at least two questions still remain to be answered. One is that to maintain a full growth, to what extent bacteria can withstand the fluctuation of intracellular pH. Another is that why this homeostasis is important for bacterial growth. In other words, unbalanced intracellular pH influence what to attenuate bacterial growth.

In this paper, we found that methionine semi-starvation did lead to intracellular acidification of *S. pneumoniae*. The optimal intracellular pH (~7.6) is extremely important for pneumococcal full-speed growth. Even a tiny change of intracellular pH caused growth attenuation. In total starvation, glutamine balances intracellular pH to a moderately acidified level (~7.2) to enhance bacterial survival but not growth (Zhang et al., 2023). In semi-starvation, glutamine elevates intracellular pH to enhance pneumococcal growth. With excessive glutamine, pneumococcal intracellular pH was increased to the optimal level (~7.6) and bacteria had a full growth even without methionine supply. We try to reveal how glutamine functions in methionine semi-starvation and how intracellular pH influences pneumococcal growth. Pneumococcal growth in blood is critical for the septicemia elicited by it (Yuste et al., 2005). In human blood, methionine is limited while glutamine is abundant (Bergstrom et al., 1974). *S. pneumoniae* may utilize this strategy of enhanced growth by glutamine in blood, which provides us new drug targets to treat pneumococcal disease.

Results

Intracellular acidification occurs under semi-starvation of methionine

Our previous work shows that deletion of methionine synthesis gene *metE* plus limited methionine supply (1 μg/mL) resulted in significant attenuation of pneumococcal growth (Zhang et al., 2023). In this culture, methionine acquisition only comes from exogenous supply. Metabolomics data show that after 6 h' culture, intracellular methionine level of *metE* mutant is only 3% of that in Wild-type (WT) strain (Zhang et al., 2023), indicating the exhaustion of methionine. Besides this total starvation, bacteria could encounter another condition when methionine is not supplemented, while methionine synthesis functions well. In this condition, methionine acquisition only comes from synthesis.

To determine how *S. pneumoniae* grows in this culture without methionine supply, *S. pneumoniae* D39 WT strain (D39) was cultured in CDM with no methionine or 200 μg/mL methionine (standard concentration). Bacterial growth with no methionine was attenuated significantly than growth with sufficient methionine (Figure 1A). Each point of growth curves represents the mean OD_{620} value of three replicates at each time point. The error bars of the growth curves were too short to be exhibited (also for other growth data in this paper). After 6 h' culture, the OD_{620} values of bacteria cultured with no or 200 μg/mL methionine were 0.485 and 0.595, respectively. We name this weakened growth semi-starvation. Previously, we found that methionine total starvation induces intracellular acidification (Zhang

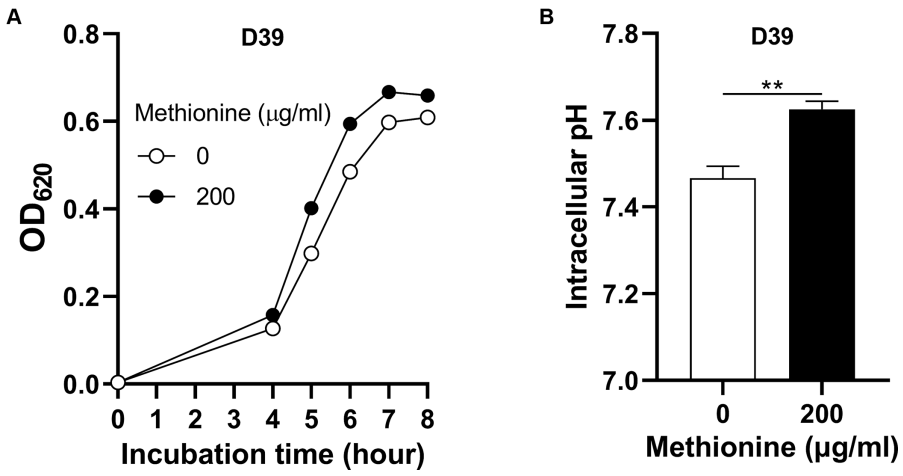

FIGURE 1
Intracellular acidification under methionine semi-starvation. **(A)** Growth attenuation of *S. pneumoniae* D39 under methionine semi-starvation. D39 growth in CDM with no or 200 μg/mL methionine was assessed by optical density at 620 nm (OD_{620}) at various time points after inoculation. **(B)** Intracellular acidification of D39 under methionine semi-starvation. Intracellular pH of D39 cultured in CDM with no or 200 μg/mL methionine was determined at 6 h post inoculation. ** means *P* value < 0.01.

et al., 2023). However, it is still unknown whether it happens under semi-starvation. Intracellular pH of bacteria cultured with no or 200 μg/mL methionine was 7.47 and 7.62, respectively, at 6 h post inoculation (Figure 1B). Obviously, intracellular acidification happened under methionine semi-starvation. Glutamine was previously found to be extremely important for pH balance under total starvation, in which massive intracellular glutamine accumulation was observed. Despite lower level, glutamine accumulation was also observed under semi-starvation (Zhang et al., 2023), indicating the function of glutamine for pneumococcal growth under semi-starvation. We next examined whether glutamine is important for pneumococcal growth under semi-starvation.

Glutamine enhances pneumococcal growth and elevates intracellular pH under methionine semi-starvation

To know whether glutamine is important for pneumococcal growth under methionine semi-starvation, we firstly determined bacterial demand for glutamine in the culture with no methionine or sufficient methionine (200 μg/mL). The standard concentration of glutamine in CDM is 100 μg/mL. With no methionine, D39 was cultured with different concentrations of glutamine. After 8 h' culture, the OD_{620} values of bacteria cultured with 1, 5, and 10 μg/mL glutamine were 0.344, 0.453 and 0.449 respectively, which are 56.2, 73.8, and 73.2% of the culture with 100 μg/mL glutamine (0.613) (Figure 2A). With 200 μg/mL methionine, the OD_{620} values of bacteria cultured with 1, 5, or 10 μg/mL glutamine were 0.485, 0.613, and 0.642, respectively, at 8 h post inoculation, which are 75.9, 95.8, and 100.5% of the culture with 100 μg/mL glutamine (0.639) (Figure 2B). These data show that with sufficient methionine, bacterial demand for glutamine decreased. With sufficient methionine, 10 μg/mL glutamine was enough for pneumococcal full growth. Further decrease of glutamine concentration in CDM with 200 μg/mL methionine also caused less attenuation of growth than culture with no methionine. Based on these data, we noticed that more glutamine is demanded for pneumococcal growth when methionine is not supplied, which means a growth enhancement function of glutamine under methionine semi-starvation.

How glutamine enhances pneumococcal growth under methionine semi-starvation is the key question we need to answer in this work. Glutamine is able to increase intracellular pH, we therefore gave our key hypothesis that intracellular acidification caused by semi-starvation impaired bacterial growth and glutamine elevate intracellular pH to enhance bacterial growth. To verify this hypothesis, we firstly determined whether glutamine can elevate intracellular pH under methionine semi-starvation. With no methionine supply, intracellular pH of D39 cultured in CDM with 10 or 100 μg/mL glutamine was 7.28 and 7.47, respectively, (Figure 2C). Decreased supply of glutamine did decrease intracellular pH significantly under methionine semi-starvation. However, with 200 μg/mL methionine, there was no significant difference of intracellular pH between the culture with 10 and 100 μg/mL glutamine (Figure 2D). Obviously, glutamine specifically increases intracellular pH under semi-starvation. If glutamine increases intracellular pH to enhance growth, then intracellular pH homeostasis must be essential for pneumococcal full growth. We next determined the importance of this homeostasis for bacterial growth.

Intracellular pH 7.6 is essential for full-speed growth of *Streptococcus pneumoniae*

Although intracellular pH homeostasis was important for bacterial growth (Slonczewski et al., 2009), which range of this homeostasis has not been investigated. To determine if there exists an optimal intracellular pH for pneumococcal growth, D39 were cultured in CDM with full nutrients and supplemented with different concentrations of sodium lactate. Lactate is a weak organic acid, which can release H^+ in the cytoplasm to cause intracellular acidification

10.3389/fmicb.2024.1430038

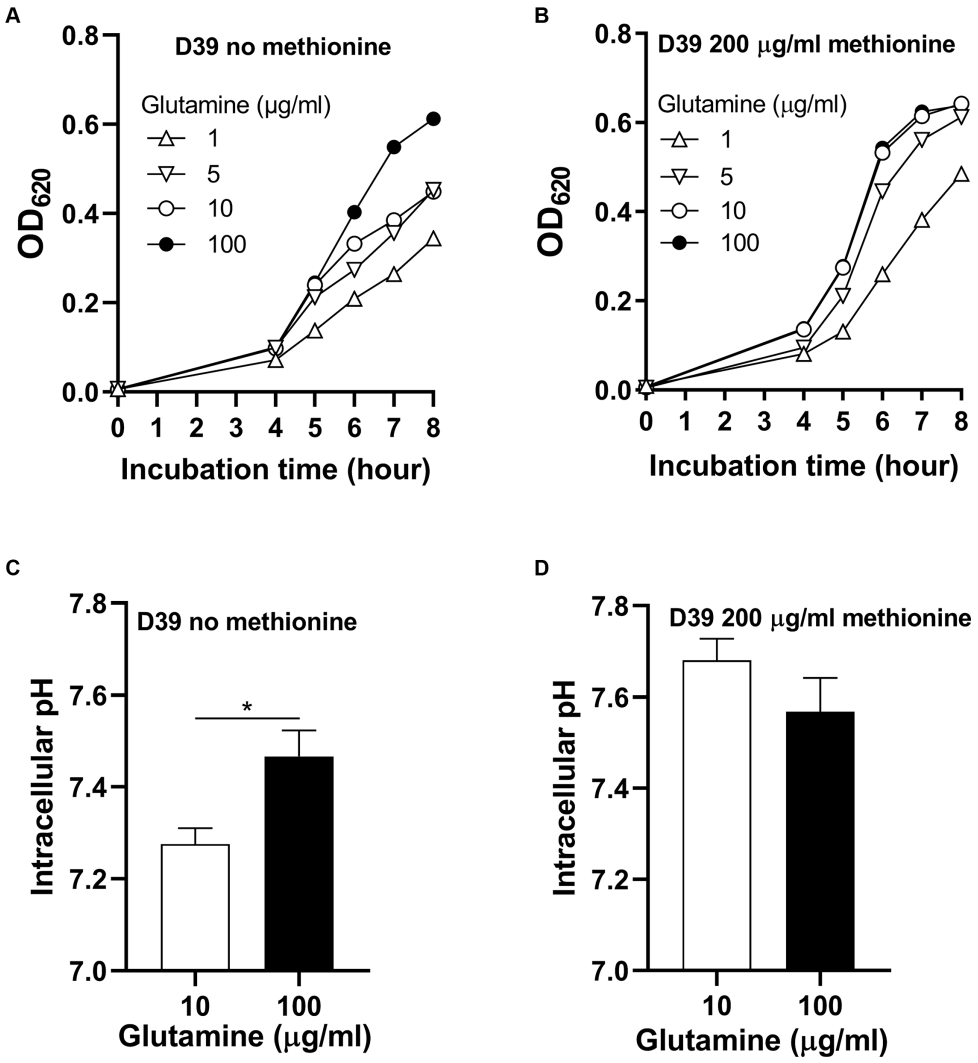

FIGURE 2
Growth enhancement and intracellular pH elevation by glutamine under methionine semi-starvation. **(A)** Growth enhancement of D39 under methionine semi-starvation by glutamine supply. D39 growth in CDM with no methionine and 1, 5, 10, or 100 μg/mL glutamine was determined by OD_{620} value at various time points. **(B)** Growth of D39 with sufficient methionine and different concentrations of glutamine. D39 growth in CDM with 200 μg/mL methionine and 1, 5, 10, or 100 μg/mL glutamine was determined by OD_{620} value at various time points. **(C)** Intracellular pH elevation by glutamine under methionine semi-starvation. Intracellular pH of D39 cultured with no methionine and 10 or 100 μg/mL glutamine was determined at 6 h post inoculation. **(D)** Intracellular pH of D39 cultured with sufficient methionine and different concentrations of glutamine. Intracellular pH of D39 cultured with 200 μg/mL methionine and 10 or 100 μg/mL glutamine was determined at 6 h post inoculation. *means *p* value < 0.05.

(Russell and DiezGonzalez, 1998). With no sodium lactate, the intracellular pH of D39 is 7.60 (Figure 3A). Supplement of 1.5 mM and 2 mM sodium lactate led to the decrease of intracellular pH to 7.50 and 7.36, respectively, (Figure 3A). This intracellular acidification impaired bacterial growth significantly. After 6 h' culture with 0-, 1.5-, or 2-mM sodium lactate, the OD_{620} values of bacteria were 0.671, 0.207, and 0.073, respectively, (Figure 3B). Even a 0.1 drop of intracellular pH caused severe growth attenuation.

We also determined the impact of intracellular pH increment on bacterial growth by adding $NH_3.H_2O$. Supplement of 0.05% $NH_3.H_2O$ increased intracellular pH from 7.62 to 7.76 (Figure 3C). This increase of intracellular pH also attenuated pneumococcal growth. After 5 h' culture with no or 0.05% $NH_3.H_2O$, the OD_{620} values of bacteria were 0.483 and 0.366, respectively, (Figure 3D). Interestingly, this increase of intracellular pH caused less growth attenuation than growth with decreased intracellular pH. At 8 h post inoculation, the OD_{620} value of bacterial culture with supply of $NH_3.H_2O$ was even higher than without $NH_3.H_2O$ supply and there was no significant difference between their intracellular pH (Supplementary Figure S1). After 6 h' cultivation, the nitrogen source might become limited and NH_3 might be utilized by bacteria as a nitrogen source for growth. Therefore, intracellular pH was not elevated and bacteria grew better by $NH_3.H_2O$ supply at 6 to 8 h post inoculation.

Taken together, these data show that even tiny disturbance of intracellular pH impairs bacterial growth, which emphasizes the importance of intracellular pH homeostasis for pneumococcal full growth. We can also conclude that intracellular pH ~ 7.6 is essential for pneumococcal full growth. In other words, this homeostasis range is very narrow. Currently, we know that semi-starvation induces intracellular acidification that impairs pneumococcal growth and glutamine elevates intracellular pH to enhance bacterial growth. The further question is how glutamine works to elevate intracellular

10.3389/fmicb.2024.1430038

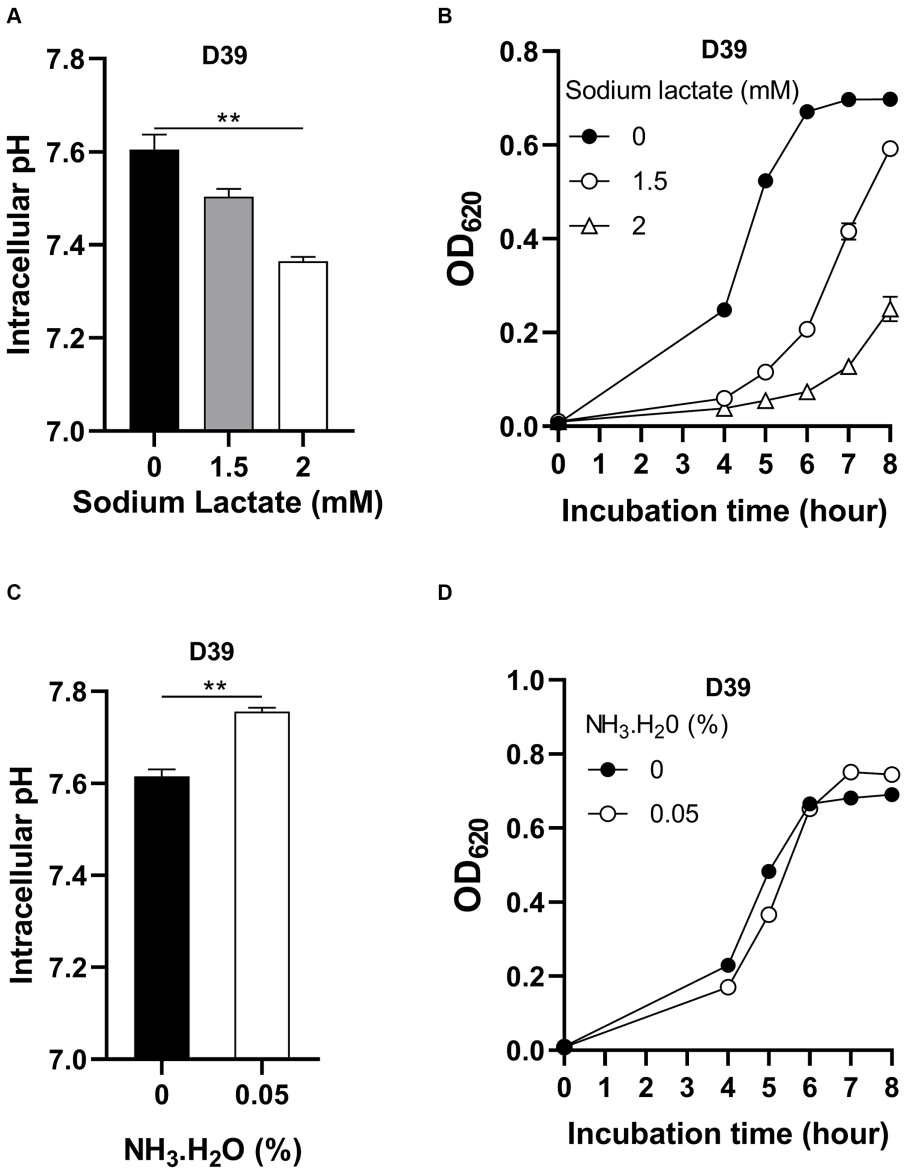

FIGURE 3
Impact of intracellular pH on pneumococcal growth. **(A)** Intracellular acidification by sodium lactate supply. Intracellular pH of D39 cultured in CDM with full nutrients and supplied with 0-, 1.5-, or 2-mM sodium lactate was determined at 6 h post inoculation. **(B)** Growth of D39 under intracellular acidification. Growth of D39 in CDM with supply of 0-, 1.5-, or 2-mM sodium lactate was determined by OD_{620} value at various time points. **(C)** Intracellular pH elevation by $NH_3.H_2O$. Intracellular pH of D39 cultured in CDM with full nutrients and supplied with no or 0.05% $NH_3.H_2O$ was determined at 6 h post inoculation. **(D)** Growth of D39 under intracellular basification. Growth of D39 in CDM with supply of no or 0.05% $NH_3.H_2O$ was determined by OD_{620} value at various time points. ** means *P* value < 0.01.

pH. Glutamine can be deaminated to release NH_3, which can neutralize proton (Lu et al., 2013). Therefore, to find the glutamine deaminase is the key to solve this question.

Glutamine deamination elevates intracellular pH under methionine semi-starvation to enhance pneumococcal growth

The deamination of glutamine is illustrated in Figure 4A. With one molecule H_2O, the terminal NH_2- of glutamine is replaced by -OH and NH_3 is released. This reaction catalyzed by glutamine deaminase converts glutamine to glutamate. Four putative glutamine deaminases were identified. They are SPD0974, SPD1296, SPD1417, and SPD1899 (Zhang et al., 2023). To determine which deaminase contributes to the deamination of glutamine under methionine semi-starvation, the transcription levels of the four genes were compared in different cultures, no methionine and 10 μg/mL glutamine (M0Q10), no methionine and 100 μg/mL glutamine (M0Q100), and 200 μg/mL methionine and 100 μg/mL glutamine (CDM). Compared to CDM, transcription of SPD1296 and SPD1899 in M0Q100 was up-regulated (>1.5-fold), 1.6- and 2.2-fold, respectively, (Figure 4B). Each bar for qRT-PCR data represents the mean value of three technically repeated samples and each qRT-PCR experiment was repeated once (same for other

10.3389/fmicb.2024.1430038

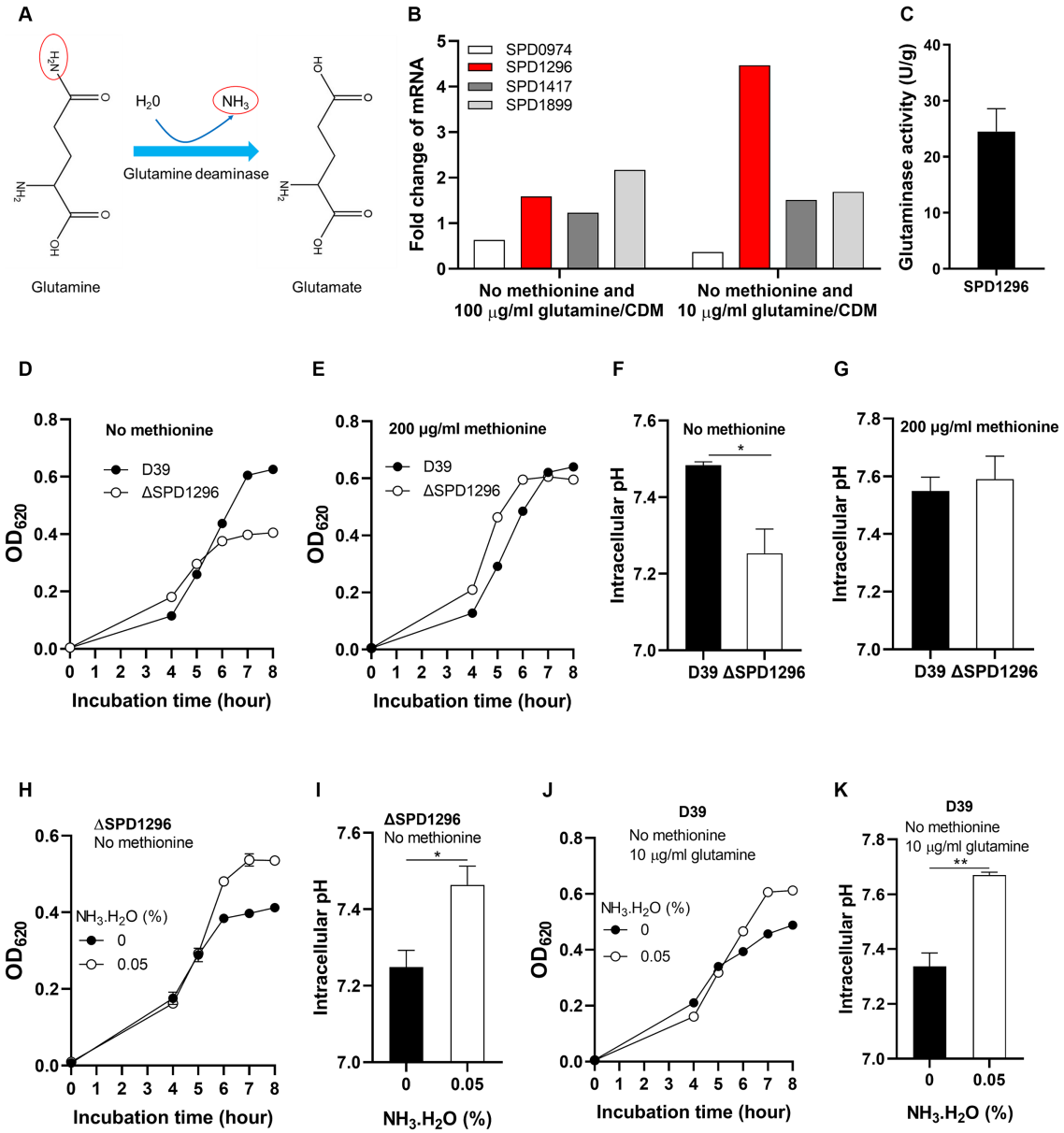

FIGURE 4
Enhanced growth under methionine semi-starvation by glutamine deamination. **(A)** Diagram of glutamine deamination. In the presence of glutamine deaminase and H_2O, the NH_2- at the C-terminus of glutamine is released to form NH_3 and glutamine is converted to glutamate. **(B)** Transcription change of glutamine deaminase genes under methionine semi-starvation. mRNA levels of SPD0974, SPD1296, SPD1417, and SPD1899 were compared between the culture of D39 in CDM with no methionine and with full nutrients or no methionine plus 10 μg/mL glutamine and full nutrients. **(C)** Glutaminase activity (U/g protein) of SPD1296. **(D)** Importance of SPD1296 for pneumococcal growth under methionine semi-starvation. Growth of D39 and SPD1296 deletion mutant (ΔSPD1296) in CDM with no methionine was determined by OD_{620} value at various time points. **(E)** Dispensable role of SPD1296 for pneumococcal growth in full nutrients. Growth of D39 and SPD1296 deletion mutant in CDM with full nutrients was determined by OD_{620} value at various time points. **(F)** Intracellular acidification of SPD1296 mutant under methionine semi-starvation. Intracellular pH of D39 and SPD1296 mutant cultured in CDM with no methionine was determined at 6 h post inoculation. **(G)** Intracellular pH of D39 and SPD1296 mutant cultured in CDM with full nutrients. Intracellular pH was determined at 6 h post inoculation. **(H)** Enhanced growth of SPD1296 mutant under methionine semi-starvation by $NH_3.H_2O$ supplement. Growth of SPD1296 mutant in CDM with no methionine and supplied with no or 0.05% $NH_3.H_2O$ was determined by OD_{620} value at various time points. **(I)** Intracellular pH elevation of SPD1296 mutant under methionine semi-starvation by NH_3 supplement. Intracellular pH of SPD1296 mutant cultured in CDM with no or 0.05% $NH_3.H_2O$ was determined at 6 h post inoculation. **(J)** Enhanced growth of D39 under methionine semi-starvation by $NH_3.H_2O$ supplement. Growth of D39 in CDM with no methionine and 10 μg/mL glutamine and supplied with no or 0.05% $NH_3.H_2O$ was determined by OD_{620} value at various time points. **(K)** Intracellular pH elevation of D39 under methionine semi-starvation by $NH_3.H_2O$ supplement. Intracellular pH of D39 cultured in M0Q10 with no or 0.05% $NH_3.H_2O$ was determined at 6 h post inoculation. *means p value < 0.05. ** means p value < 0.01.

qRT-PCR data in this paper). Further decrease of glutamine concentration (M0Q10) up-regulates the transcription of SPD1296 further (4.5-fold of that in CDM, Figure 4B). However, transcription of other 3 genes was not up-regulated further. These data indicate the important role of SPD1296 for pneumococcal growth under methionine semi-starvation.

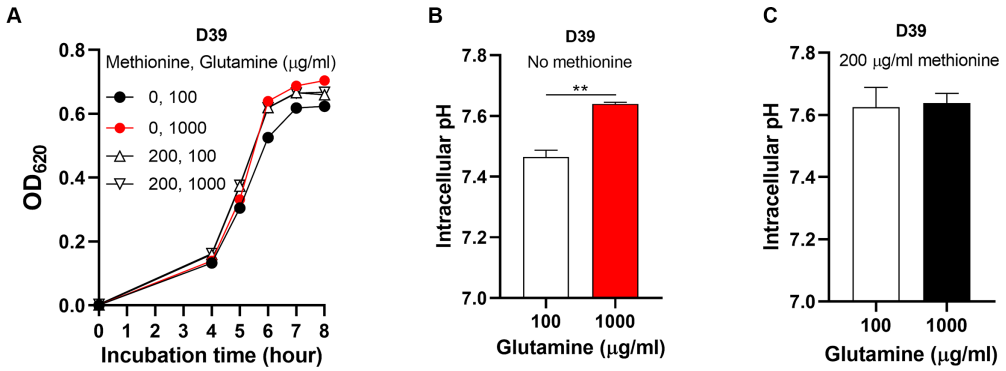

FIGURE 5
Abolished semi-starvation by excessive glutamine supply. **(A)** Recovered growth of D39 under methionine semi-starvation by excessive glutamine supply. Growth of D39 cultured in CDM with no methionine and 100 μg/mL glutamine, no methionine and 1,000 μg/mL glutamine, 200 μg/mL methionine and 100 μg/mL glutamine or 200 μg/mL methionine and 1,000 μg/mL glutamine was determined by OD_{620} value at various time points. **(B)** Restored intracellular pH under methionine semi-starvation by excessive glutamine supply. Intracellular pH of D39 cultured in CDM with no methionine and 100 μg/mL glutamine or no methionine and 1,000 μg/mL glutamine was determined at 6 h post inoculation. **(C)** Intracellular pH of D39 cultured in CDM with 200 μg/mL methionine and 100 μg/mL glutamine or 200 μg/mL methionine and 1,000 μg/mL glutamine. Intracellular pH was determined at 6 h post inoculation. ** means *P* value < 0.01.

The function of SPD1296 as glutamine deaminase was verified by *in vitro* deamination reaction assay. Purified SPD1296 with N-terminal 6×His tag was shown in the sodium dodecyl sulfate (SDS)-polyacrylamide gel stained by Coomassie blue (Supplementary Figure S2). The reaction system contained glutamine, buffer and crude enzyme. The product (glutamate) was detected by HPLC–MS. Successful detection of glutamate from the reaction showed the glutamine deaminase activity of SPD1296. The specific activity of SPD1296 as a glutamine deaminase was 24.5 U/g (Figure 4C). By comparing the growth of D39 and SPD1296 deletion mutant (ΔSPD1296) with no or 200 μg/mL methionine, we observed that deletion of SPD1296 impaired bacterial growth severely when no methionine was supplied (Figure 4D). However, with sufficient methionine, SPD1296 mutant grew even better than D39 (Figure 4E). These growth data confirmed the importance of SPD1296 for pneumococcal growth under methionine semi-starvation. Deletion of SPD1296 decreased intracellular pH from 7.48 to 7.25 under semi-starvation (Figure 4F). However, it did not lead to intracellular acidification when methionine was sufficient (Figure 4G). These results show that SPD1296, as a glutamine deaminase, contributes to bacterial growth under methionine semi-starvation by increasing intracellular pH.

To confirm the function of SPD1296 as glutamine deaminase to increase intracellular pH, $NH_3.H_2O$ was added into the culture of SPD1296 mutant. Supply of 0.05% $NH_3.H_2O$ enhanced the growth of SPD1296 mutant without methionine. After 8 h' culture, the OD_{620} value of SPD1296 mutant cultured with no or 0.05% $NH_3.H_2O$ was 0.412 and 0.535, respectively, (Figure 4H). Supply of $NH_3.H_2O$ increased intracellular pH of SPD1296 mutant from 7.25 to 7.46 (Figure 4I). These data indicated that deletion of SPD1296 reduced intracellular NH_3 level and supply of $NH_3.H_2O$ replenished the diminished NH_3 to increase intracellular pH. Similarly, supply of $NH_3.H_2O$ restored the growth of D39 cultured with no methionine and 10 μg/mL glutamine (Figure 4J). This supply of NH_3 increased intracellular pH from 7.34 to 7.67 (Figure 4K).

By far, these results illustrate that glutamine increases intracellular pH by deamination to enhance pneumococcal growth under semi-starvation. However, we raised another question that why 100 μg/mL glutamine (standard concentration in CDM) did not rescue bacterial growth with no methionine to the level of growth with full nutrients. We speculated that 100 μg/mL glutamine is not enough to fully rescue bacterial growth. In other words, with sufficient glutamine, semi-starvation would not occur. We next tried to verify this.

Insufficient glutamine supply results in methionine semi-starvation

The intracellular pH of D39 cultured with no methionine and 100 μg/mL glutamine is still lower than D39 cultured with full nutrients. Supply of more glutamine (over 100 μg/mL) may further enhance bacterial growth and elevate its intracellular pH. To verify this, we firstly compared the growth of D39 with no methionine and 100 μg/mL glutamine (M0Q100), no methionine and 1,000 μg/mL glutamine (M0Q1000), 200 μg/mL methionine and 100 μg/mL glutamine (M200Q100), and 200 μg/mL methionine and 1,000 μg/mL glutamine (M200Q1000). After 6 h' culture, the OD_{620} values of M0Q100, M0Q1000, and M200Q100 were 0.526, 0.640, and 0.620, respectively, (Figure 5A). Supply of more glutamine (M0Q1000) did further enhance the growth of D39 with no methionine (M0Q100) to the level of growth with full nutrients (M200Q100). With this excessive glutamine (1,000 μg/mL) supply, growth attenuation in methionine semi-starvation disappeared. Interestingly, with sufficient methionine (200 μg/mL), supply of more glutamine (M200Q1000) did not enhance its growth. After 6 h' culture, the OD_{620} value of M200Q1000 was 0.619 (Figure 5A). These data show that 100 μg/mL glutamine is enough for pneumococcal growth with 200 μg/mL methionine, but not enough for growth with no methionine. Growth enhancement by glutamine only works when methionine is not supplied.

After 6 h' culture, the intracellular pH of M0Q1000 was 7.64, significantly higher than M0Q100 (pH 7.46) (Figure 5B). This shows that insufficient glutamine supply caused the intracellular acidification

in semi-starvation, thus attenuating bacterial growth. Interestingly, this increase of intracellular pH did not happen in the culture with sufficient methionine. The intracellular pH of M200Q100 and M200Q1000 was 7.62 and 7.64, respectively, (Figure 5C). This shows that although glutamine elevates intracellular pH, it will not elevate intracellular pH over the optimal level (~7.6). Taken together, these results show that it is the intracellular acidification that causes semi-starvation. Excessive glutamine (1,000 μg/mL) elevated intracellular pH to the optimal level to eliminate the growth attenuation under methionine semi-starvation. Currently, we know that glutamine elevates intracellular pH to enhance pneumococcal growth with no methionine. Obviously, intracellular acidification attenuates pneumococcal growth under methionine semi-starvation. The question is that which cellular process is influenced by cytoplasmic acidification.

Glutamine elevates translation level to enhance pneumococcal growth under semi-starvation

Although glutamine elevates intracellular pH to enhance bacterial growth, we still do not know which cellular process is rescued by glutamine. Under methionine semi-starvation, methionine acquisition only comes from synthesis. We hypothesized that intracellular acidification down-regulates the transcription of methionine synthesis gene *metE* and the growth attenuation is caused by insufficient methionine synthesis. To test this hypothesis, we compared the transcription of *metE* in the culture of M0Q10, M0Q100, M0Q1000, and M200Q100. The transcription of *metE* in M0Q1000 was 16.7-fold of *metE* in M200Q100 (Figure 6A). In our hypothesis, with the decreased concentrations of glutamine, the transcription level of *metE* decreased. Surprisingly, decreased supply of glutamine up-regulated the transcription of *metE*. The transcription of *metE* in M0Q100 and M0Q10 was 46.5-fold and 71.5-fold of that in M200Q100, respectively, (Figure 6A). To determine whether more mRNA of *metE* produces more MetE protein, MetE protein (with 6×His tag) from 1 optical density (OD) bacteria cultured in M0Q10, MOQ100, M0Q1000, or M200Q100 was determined at 6 h post inoculation by western blot. MetE protein was not detected in bacteria cultured in M200Q100 (Figure 6B), which shows the dispensable role of MetE when sufficient methionine is supplied. When methionine was not supplied, with the decreasing concentration of glutamine (from 1,000 to 10 μg/mL), MetE protein level decreased. The gray scales of MetE protein in M0Q1000, M0Q100, and M0Q10 are 66,091, 58,849 and 41,933, respectively. More *metE* mRNA did not produce more MetE protein, but conversely, less MetE protein (Figure 6B). These data show that the translation of MetE was enhanced by glutamine supply in the culture with no methionine.

To determine whether intracellular methionine level was reduced due to the shortage of glutamine under methionine semi-starvation, intracellular methionine quantification was determined by Liquid Chromatography Tandem-mass Spectrometry (LC–MS/MS). Interestingly, there is no significant difference of intracellular methionine amount among the cultures of M0Q10, M0Q100, and M0Q1000 (Figure 6C). Besides, intracellular methionine levels in these cultures were significantly lower than that in M200Q100 (Figure 6C). These results provide us with several important information. Firstly, methionine synthesis ability is limited. Even with excessive glutamine and optimal intracellular pH (~7.6), intracellular methionine level of M0Q1000 could not reach (still lower than) the level of M200Q100. Secondly, since the growth of M0Q1000 was as well as M200Q100, less intracellular methionine in M0Q1000 does not mean worse growth. It is not the less intracellular methionine but intracellular acidification that causes growth attenuation in methionine semi-starvation. Thirdly, supplement of glutamine elevates intracellular pH but did not enhance methionine synthesis ability under methionine semi-starvation.

Based on the above data, it seems that translation inhibition contributes to growth attenuation under methionine semi-starvation. Chloramphenicol inhibits the translation of bacteria. If the translation of *S. pneumoniae* was inhibited, then the inhibition function of chloramphenicol (chl) would be weakened. After incubation for 6, 7, and 8 h, the OD_{620} values of M200Q100 with no chloramphenicol were 0.596, 0.729 and 0.741, respectively, (Figure 6D). At the same time, the OD_{620} values of M200Q100 with 4 μg/mL chloramphenicol were 0.313, 0.418, and 0.514, respectively. The percentages of OD_{620} values (chl/no chl) were 52.5, 57.3, and 69.3%, respectively, at 6, 7, and 8 h post inoculation, respectively. The growth of D39 in M200Q100 was weakened significantly by chloramphenicol addition (Figure 6D). However, the growth of D39 in M0Q10 was not weakened by addition of chloramphenicol (Figure 6E). After incubation for 6, 7, or 8 h, the percentages of OD_{620} values (chl/no chl) at 6, 7, and 8 h were 77.4, 92.3, and 95.1%, respectively. However, for M0Q100, the percentages of OD_{620} values (chl/no chl) at 6, 7, and 8 h were 69.5, 72.1, and 81.6%, respectively, (Figure 6F). For M0Q1000, the percentages of OD_{620} values (chl/no chl) at 6, 7, and 8 h were 62.9, 67.4, and 79.2%, respectively, (Figure 6G). These data show that with the increasing supply of glutamine in the culture of no methionine, the growth inhibition effect by chloramphenicol increased, which strongly suggest that glutamine supply increased translation level under methionine semi-starvation.

Whether intracellular acidification under methionine semi-starvation caused translation inhibition needs to be verified. Sodium lactate addition decreases intracellular pH (Figure 3A). Supplement of 1.5- or 2-mM sodium lactate in CDM increased the transcription of *metE* by 0.7- and 1.1-fold, respectively, (Figure 6H). We also tested another gene *spxB* that encodes a pyruvate oxidase catalyzing pyruvate, phosphate and O_2 to acetyl phosphate, CO_2 and H_2O_2 (Lisher et al., 2017). The transcription of *spxB* in M0Q1000, M0Q100, and M0Q10 was 1.2-, 1.8-, and 2.1-fold of that in M200Q100, respectively, (Figure 6I). Supply of 1.5- or 2-mM sodium lactate increased the transcription of *spxB* by 3.1-fold and 5.7-fold, respectively, (Figure 6J). These results indicate the attenuated translation by intracellular acidification. Glutamine may elevate intracellular pH to enhance translation.

In order to determine the impact of intracellular acidification on translation activity, we used L-Azidohomoalanine (AHA) click labeling assay to determine the newly synthesized global proteins. The mechanism of this method is the click reaction of azide and alkyne. AHA containing an azide moiety is a methionine analog that can be used as substrate for protein synthesis (incorporation). After incorporation of AHA into the newly synthesized proteins, biotin-alkyne was added. AHA and biotin-alkyne was connected by azide-alkyne cycloaddition. Then AHA could be detected by western blot using HRP-conjugated streptavidin that detects biotin. D39 was

10.3389/fmicb.2024.1430038

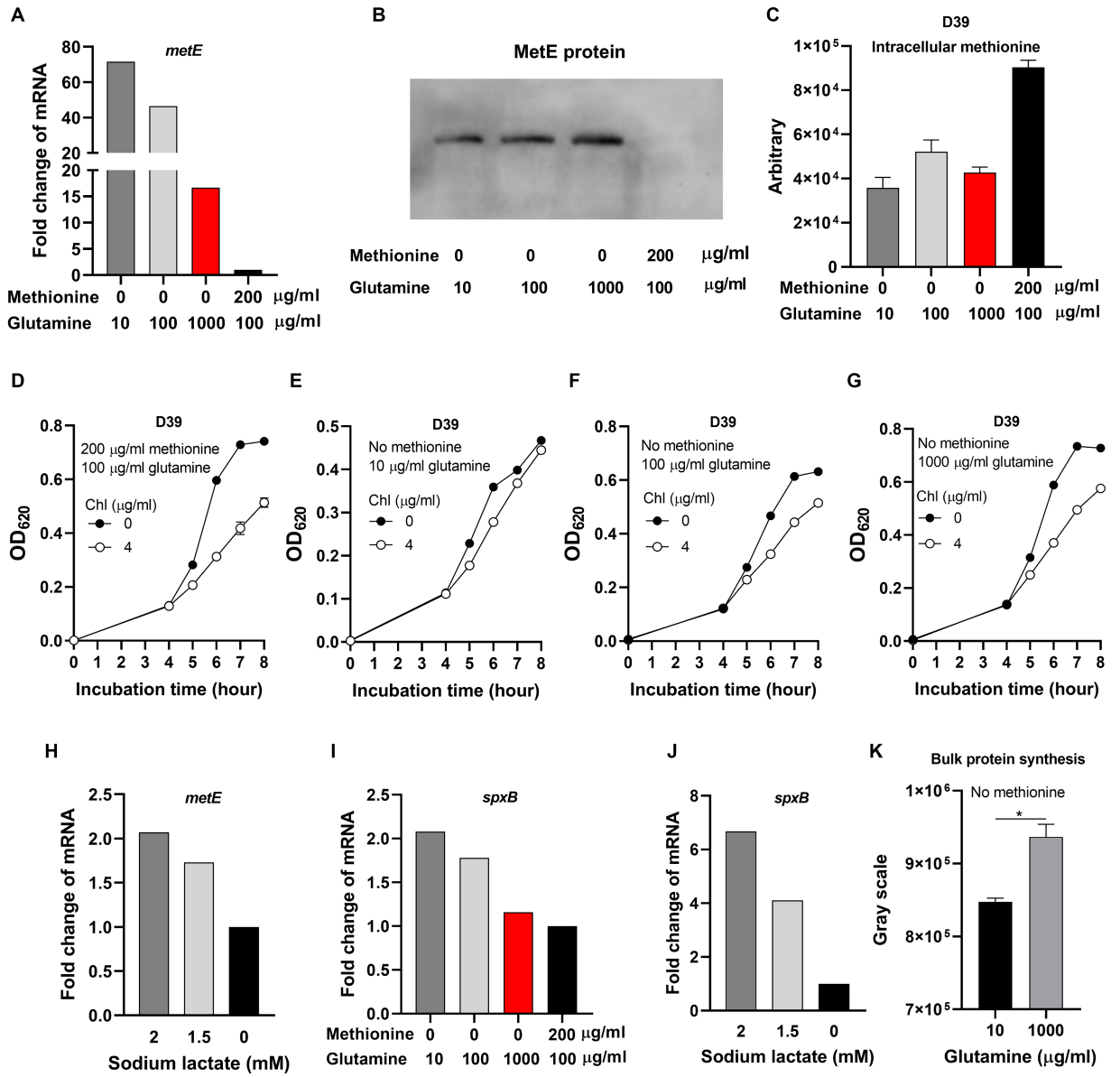

FIGURE 6
Inhibited translation under methionine semi-starvation. **(A)** Comparison of *metE* transcription level in D39 cultured with different concentrations of methionine and glutamine. mRNA levels of *metE* were compared among the cultures with no methionine and 10 μg/mL glutamine, no methionine and 100 μg/mL glutamine, no methionine and 1,000 μg/mL glutamine, and 200 μg/mL methionine and 100 μg/mL glutamine, respectively. mRNA of *metE* in 200 μg/mL methionine and 100 μg/mL glutamine was set as 1. **(B)** Comparison of MetE protein levels in the cultures in **(A)**. One OD bacteria were collected at 6 h post inoculation. MetE protein with 6 × His tag was detected by western blot. **(C)** Intracellular methionine amount of D39 cultured as in **(A)**. Intracellular methionine of bacteria cultured at 6 h post inoculation was quantified by Liquid Chromatography Tandem-mass Spectrometry (LC–MS/MS). **(D–G)** Reduced sensitivity to chloramphenicol under methionine semi-starvation. Growth of D39 cultured in 200 μg/mL methionine and 100 μg/mL glutamine with no or 4 μg/mL chloramphenicol (chl) **(D)**, no methionine and 10 μg/mL glutamine with no or 4 μg/mL chloramphenicol (chl) **(E)**, no methionine and 100 μg/mL glutamine with no or 4 μg/mL chloramphenicol (chl) **(F)**, and no methionine and 1,000 μg/mL glutamine with no or 4 μg/mL chloramphenicol (chl) **(G)** respectively was determined by OD_{620} value at various time points. **(H)** Comparison of *metE* transcription level in D39 cultured with full nutrients (CDM) and supply of different concentration of sodium lactate. mRNA levels of *metE* were compared among the cultures supplied with 0-, 1.5-, and 2-mM sodium lactate. mRNA of *metE* in 0 mM sodium lactate was set as 1. **(I)** Comparison of *spxB* transcription level in D39 cultured with different concentrations of methionine and glutamine. mRNA levels of *spxB* in D39 were compared among the cultures in **(A)**. mRNA of *spxB* in 200 μg/mL methionine and 100 μg/mL glutamine was set as 1. **(J)** Comparison of *spxB* transcription level in D39 cultured with full nutrients (CDM) and supply of different concentration of sodium lactate. mRNA levels of *spxB* were compared among the cultures with 0-, 1.5-, and 2-mM sodium lactate. mRNA of *spxB* in 0 mM sodium lactate was set as 1. **(K)** Enhanced translation by glutamine supply under methionine semi-starvation. At 6 h post inoculation, newly synthesized proteins in 2 optical density (OD) D39 cultured with no methionine and 10 μg/mL glutamine or no methionine and 1,000 μg/mL glutamine were detected by L-Azidohomoalanine (AHA) click labeling assay. The gray scales of total proteins detected were calculated by ImageJ_v1.8.0. *means *p* value < 0.05.

cultured in CDM with no methionine and 10 or 1,000 μg/mL glutamine. At 6 h post inoculation, the same amount of bacteria (2 OD) were collected for AHA click labeling assay. Most of the newly synthesized proteins (Supplementary Figure S3) are more abundant in bacteria cultured with no methionine and excessive (1,000 μg/mL) glutamine, compared with bacteria cultured with no methionine and 10 μg/mL glutamine. The bulk protein synthesis (shown by gray scale detected by western blot) of bacteria cultured with no methionine and 1,000 μg/mL glutamine is significantly more abundant than that of bacteria cultured with no methionine and 10 μg/mL glutamine (Figure 6K). These data show the increased translation activity by excessive glutamine supply. Since bacteria cultured with no methionine and 1,000 μg/mL glutamine has a higher intracellular pH, it suggests that intracellular acidification attenuates bacterial translation.

Low intracellular pH may decrease DNA replication. In order to determine the impact of intracellular acidification on replication activity, we used BeyoClick™ EdU (5-ethynyl-2′-deoxyuridine) cell proliferation kit (Beyotime Biotechnology, China) to determine the newly synthesized DNA. This method used the click reaction of azide labeled by a fluorescent probe and alkyne moiety contained in Edu. Edu is an analog of thymidine, which can be incorporated in to the newly synthesized DNA. D39 were cultured in CDM with no methionine and 10 or 1,000 μg/mL glutamine. At 6 h post inoculation, 1 OD bacteria were collected for Edu assay. Interestingly, the fluorescence was stronger in bacteria cultured with 10 μg/mL glutamine, compared with 1,000 μg/mL glutamine (Supplementary Figure S4). This indicates that low intracellular pH increases DNA replication. We speculated that this enhanced replication is also a way for compensating attenuated translation.

Taken together, we raised a model. In the culture of no methionine, bacterial cytoplasm acidified. This intracellular acidification down-regulates translation efficiency. To compensate for impaired translation, bacteria up-regulates the replication activity and the transcription of some genes (producing more mRNA). More mRNA means more protein. However, even more mRNA produces still less protein, which means the failure of this rescue. More glutamine supply increases intracellular pH to increase translation efficiency, thus diminishing the need for mRNA. Finally, this enhanced translation by glutamine supply rescued bacterial growth under methionine semi-starvation.

Discussion

There are plenty of studies about nutrient starvation in bacteria. Most of these studies are about total starvation. For example, bacteria enter into stationary phase after exhausting nutrients in exponential phase (Llorens et al., 2010). Increased level of alternative sigma factor RpoS during stationary phase regulates the transcription of up to 10% genes to enhance the adaptation of *E. coli* to stresses (Weber et al., 2005). The stringent response is induced under amino acid starvation. The accumulated ppGpp down-regulates DNA replication and rRNA synthesis and promotes amino acid synthesis (Magnusson et al., 2005). However, the intermediate state between the fast-growing state and starvation state was ignored. In this work, the growth of *S. pneumoniae* in CDM without methionine supply was attenuated. Under this condition, bacteria still had an exponential growth phase but its growth yield was less than full growth with all nutrients supplied. We refer to this intermediate state between ceased growth and fast growth as semi-starvation. In semi-starvation, nutrient acquisition only comes from synthesis.

We hold the view that as long as the approach for getting the nutrient exists, bacteria will try to utilize this approach to increase the scale of their population. A big population may be extremely important for avoiding the clearance of this population under various environmental stresses. In total starvation, bacteria almost cease growth and pay their attention to how to survive for a longer time as a population. However, in semi-starvation, bacteria still try to grow. In methionine semi-starvation of *S. pneumoniae*, methionine synthesis still works. Synthesis of methionine needs cysteine as the precursor (Ferla and Patrick, 2014). However, without methionine supply, even with 413 μg/mL (the standard concentration in CDM) cysteine, bacteria grew worse than the full growth. The amount of intracellular methionine of bacteria in M0Q100 is 57.7% of that in M200Q100. It seems that insufficient methionine synthesis contributes to growth attenuation. Surprisingly, it is intracellular acidification but not insufficient methionine synthesis that causes growth attenuation. Previously, we found that methionine starvation causes intracellular acidification. In methionine semi-starvation, intracellular acidification also occurs, which indicates that as long as intracellular methionine amount is lower than methionine level in the culture supplied with sufficient methionine, bacterial cytoplasm will be acidified. Glutamine promotes bacterial growth by elevating intracellular pH. Excessive glutamine supply fully restored bacterial growth under methionine semi-starvation but did not increase intracellular methionine level. Therefore, it needs to be emphasized that this lower level of intracellular methionine is still able to support bacterial full growth. The prerequisite is that bacterial cytoplasm is not acidified.

Although glutamine functions by deamination to increase intracellular pH, the extents of this intracellular pH adjustment are quite different in total starvation and semi-starvation. Cytoplasmic acidification is more severe under methionine total starvation than under methionine semi-starvation. Glutamine prevents the over-acidification of cytoplasm and intracellular pH maintains at a moderately acidified level under methionine total starvation. Maintaining a moderately acidified cytoplasm may reduce the production of harmful compounds that contributes to bacterial death, thus enhancing bacterial survival. Therefore, the optimal intracellular pH for pneumococcal survival under total starvation is below 7.6. By suppling sodium lactate to decrease intracellular pH and $NH_3.H_2O$ to increase intracellular pH, we observed that the optimal intracellular pH for pneumococcal growth is stringently confined to ~7.6. Even a tiny change of intracellular pH (0.1) significantly impaired bacterial growth. Under methionine semi-starvation, glutamine tries to elevate intracellular pH to ~7.6 to meet the demand for full-speed growth. The reason why semi-starvation occurs is that glutamine is not supplied sufficiently. The standard concentration of glutamine in CDM is 100 μg/mL. Normally, this concentration is high enough to support bacterial full-speed growth. Actually, when methionine is sufficient (200 μg/mL), only 10 μg/mL glutamine is enough for pneumococcal full-speed growth. However, when methionine was removed, 100 μg/mL glutamine was not enough to support full-speed growth of bacteria. In methionine semi-starvation, 100 μg/mL glutamine cannot elevate intracellular pH to 7.6. By adding excessive glutamine (1,000 μg/mL), intracellular pH increased to 7.6 and growth attenuation disappeared. Interestingly, when methionine was sufficient, 1,000 μg/mL glutamine in CDM did not further elevate

intracellular pH and intracellular pH still remained at 7.6. The extra glutamine seems not to be utilized in this condition. This again emphasized the importance of the optimal intracellular pH (7.6) for pneumococcal full growth.

Our previous work has demonstrated that glutamine cannot be converted to methionine by isotope tracing (Zhang et al., 2023). In this paper, glutamine supply did not increase intracellular methionine level. The way of suppling excessive glutamine to recover bacterial growth under methionine semi-starvation is an interesting phenomenon. Actually, the increased population size means the exhaustion of methionine precursor cysteine. Is this an artificial phenomenon, or it can happen in the nature? In natural environment, the increasing concentration of glutamine may mean the possible source of other nutrients. In this condition, bacteria need to prepare to utilize the upcoming nutrients. Nutrients acquisition time may be very short. Only the immediate response to the nutrients makes bacteria grow as soon as possible. In semi-starvation, intracellular acidification prevents the immediate response of bacteria to nutrients. Excessive glutamine increases intracellular pH to the optimal level for growth and makes bacteria utilize the upcoming nutrients immediately and efficiently.

How intracellular pH influences bacterial growth is not well studied. The work by Zilberstein et al. (1984) shows that in a mutant of *E. coli* that is defective in pH homeostasis, the protein synthesis rate decreased to 50% after the shift of extracellular pH from 7.2 to 8.8 for 100 min and the DNA synthesis rate decreased to 60% after 3–5 min (Zilberstein et al., 1984). These results indicate the relationship between intracellular pH and translation or replication. In this study, the data suggested that pneumococcal overall transcription level increased and the overall translation rate decreased under methionine semi-starvation. These indicate that maintaining protein synthesis rate is an important function of intracellular pH homeostasis. In other words, protein synthesis is sensitive to cytoplasmic acidity. Disturbance of the homeostasis of intracellular pH decreases protein translation rate, thus attenuating bacterial growth. The up-regulation of transcription may be a try to enhance the production of protein by providing more mRNA. However, this try failed. In addition, the massive production of mRNA may consume too much energy, thus causing burden to bacterial growth.

The functions of glutamine for enhanced pneumococcal survival under total starvation and enhanced pneumococcal growth under methionine semi-starvation were summarized in Figure 7. When

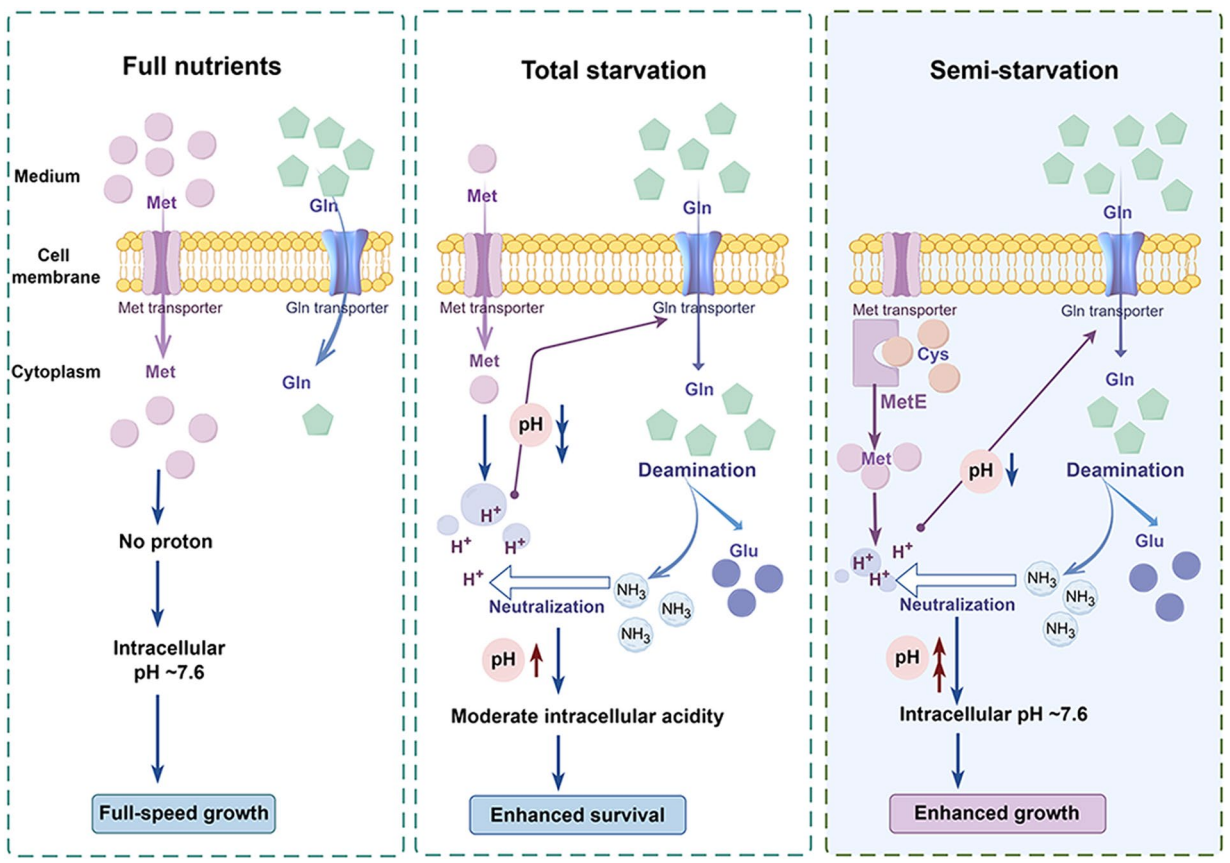

FIGURE 7
Model of enhanced bacterial survival under methionine total starvation and enhanced bacterial growth under methionine semi-starvation by glutamine. (By Figdraw.). When methionine (met) supply is sufficient, intracellular methionine level is high and bacterial cytoplasm is not acidified. Therefore, bacteria grow with full speed. When methionine is extremely limited and methionine synthesis does not work, intracellular methionine level becomes very low after a short time of culture. In this total starvation condition, bacterial cytoplasm is acidified severely and bacteria almost cease growth. This intracellular acidification induces the uptake of glutamine (gln), which elevates intracellular pH by deamination to a moderate acidity level that is most beneficial for bacterial survival. When no methionine is supplied and methionine synthase MetE works, intracellular methionine level is still lower than the full nutrients condition. Under this semi-starvation, the acidification of cytoplasm also occurs, which attenuates bacterial growth. With excessive glutamine supply, intracellular pH is elevated to ~7.6, which recovers bacterial growth fully.

methionine is sufficient, bacteria acquire methionine by methionine transporter. In this condition, intracellular methionine level is high and intracellular acidification will not be induced. Therefore, intracellular pH maintains at ~7.6, the optimal value for growth. This normal intracellular pH will not up-regulate the transport of glutamine. Therefore, intracellular glutamine level is not high. When methionine is limited and meanwhile methionine synthesis cannot work, methionine acquisition comes from uptake. However, when the limited methionine is depleted, bacteria enter into total starvation. In total starvation, intracellular proton level increases, leading to severe drop of intracellular pH. This cytoplasmic acidification causes massive glutamine uptake. The accumulated glutamine is deaminated to release ammonia that neutralize protons to increase intracellular pH. Interestingly, intracellular pH is not elevated to ~7.6, but stays at a moderate acidity level, which enhances bacterial survival under total starvation. An intermediate state between full-speed growth and total starvation is the semi-starvation. In semi-starvation, methionine acquisition only comes from synthesis. In this condition, intracellular methionine level is lower than that with sufficient methionine supply, therefore intracellular acidification is still induced, just with a lighter degree. This intracellular acidification also induces the uptake of glutamine. With excessive glutamine supply, intracellular glutamine is deaminated to elevate intracellular pH. Particularly, intracellular pH can be elevated to ~7.6, thus recovering bacterial growth under semi-starvation to the growth with full nutrients.

Among the 20 amino acids, glutamine concentration is highest in human plasma and skeletal muscles (Bergstrom et al., 1974; Lacey and Wilmore, 1990; Kim, 2011). Glutamine concentration is 0.57 ± 0.088 mmol/L (~83 μg/mL) in human plasma. However, methionine concentration is 0.02 ± 0.005 mmol/L (~3 μg/mL) in human plasma, only 3.5% of glutamine. This makes methionine become the least abundant amino acid in human plasma (Bergstrom et al., 1974). In addition, methionine is the one of the 8 essential amino acids for human (Rose, 1949). *S. pneumoniae* can cause septicemia (Yuste et al., 2005). Growth of *S. pneumoniae* in the blood is important for causing septicemia. The low concentration of methionine in blood may cause semi-starvation to *S. pneumoniae*. Cysteine concentration in human plasma is 0.11 ± 0.086 mmol/L (~13 μg/mL), which can provide the substrate for pneumococcal methionine synthesis. The much higher concentration of glutamine in blood can enhance bacterial growth under this semi-starvation. To block the growth enhancement by glutamine, we can develop the drug that targets glutamine transport and deamination in *S. pneumoniae*. This will be a novel strategy to treat pneumococcal disease.

Materials and methods

Bacterial cultivation and reagents

The parental strain used in this study is *S. pneumoniae* serotype 2 (D39) (Lanie et al., 2007). Pneumococci were cultured in Todd-Hewitt broth supplemented with 0.5% yeast extract (THY), chemically defined medium (CDM) or tryptic soy agar (TSA) plates with sheep blood (3%) at 37°C, 5% CO_2 as previously described (Lu et al., 2006). CDM was prepared according to the previous study (Willett and Morse, 1966). Appropriate antibiotics were supplemented to the media when necessary as described (Lu et al., 2006). All chemicals and enzymes for molecular biology were brought from Sigma (Beijing, China) and New England BioLabs (Beijing, China), respectively. All strains used in this study are described in Supplementary Table S1.

Mutant construction

All gene deletions were operated in strain TH4306, a streptomycin-resistant derivative of strain D39, by natural transformation using Janus cassette (JC)-based counter selection as previously described (Sung et al., 2001; Li et al., 2016). Briefly, the up- and down-stream sequences of target genes and JC were individually amplified. The amplicons were linked by enzymatic digestion and ligation. For natural transformation, the gene was replaced by JC, which contains the kanamycin resistance *kan* gene for selection and *rpsL* for counter-selection. The transformants were selected by kanamycin resistance. For counter-selection, the flanking regions of the target genes were amplified. The amplicons were digested with BsaI and fused as described (Li et al., 2016). The primers used in this work are listed in Supplementary Table S2. The specific setup for construction of each mutant is described in Supplementary Table S3.

Characterization of bacterial growth and survival

Growth of pneumococci was characterized as previously described (Shelver et al., 2003). Briefly, bacteria were grown in THY to an optical density at 620 nm (OD_{620}) of 0.5. Then bacteria were washed twice with Ringer's solution by centrifugation and resuspension. Bacterial pellets were resuspended in Ringer's solution to OD_{620} 0.5, and diluted at a 1:100 ratio in standard CDM (Willett and Morse, 1966) or CDM with various modifications in amino acid content. Bacterial growth was measured by determining the value of OD_{620}.

Intracellular pH determination

Intracellular pH was determined using a pH-sensitive green fluorescent protein (pH-GFP) as previously described (Wang et al., 2019; Zhang et al., 2023). Briefly, plasmid pIB166 harboring the pH-GFP gene was transformed into pneumococci by natural transformation. Strains with pH-GFP plasmid were cultured in THY till mid-log phase, then washed and diluted into CDM as in bacterial growth determination. At the time for pH detection, 0.6 OD_{620} bacteria were collected and washed twice by colorless CDM, which excludes glutamine, glutamate, methionine, cysteine, cystine, lysine, $Fe_2SO_4.7H_2O$, $MnSO_4.4H_2O$ and vitamins (Eguchi et al., 2018). Bacterial pellets were resuspended in 1200 μL colorless CDM and dispensed into black 96-well plates (200 μL/well) (Corning Incorporated, United States). Fluorescence was determined at Reading1 (excitation 395 at nm, emission at 510 nm) and Reading2 (excitation at 475 nm, emission at 510 nm) by a microplate reader (BioTek Synergy H1, Agilent, United States). The ratio of "Reading1-Blank1" to "Reading2-Blank2 (X) was used to determining the value of intracellular pH (Y) with an equation: $Y = 2.1868 \times \ln(X) + 7.0626$.

qRT-PCR

Quantitative real-time reverse transcriptase PCR (qRT-PCR) was performed as described (Liu et al., 2017). Briefly, D39 (TH4306) was diluted in duplicate of 7 mL CDM supplemented with various concentrations of methionine and glutamine. At 6 h post inoculation, bacteria were collected and processed for extraction of total RNA using RNAprep Kit (Tiangen, Beijing). Extracted RNA was used to construct cDNA pools with iScript™ cDNA Synthesis Kit (Bio-Rad, United States). The following primer pairs were used to amplify the target genes: Pr15131/Pr15132 (*metE*), Pr17523/Pr17524 (SPD0974), Pr17525/Pr17526 (SPD1296), Pr17527/Pr17628 (SPD1417), Pr17529/Pr17530 (SPD1899), and Pr0023/Pr0024 (*spxB*). SPD0857 (*era*, amplified by Pr7932/Pr7933) was used as a reference gene for normalization of gene expression. The primer sequences are listed in Supplementary Table S2. Each gene was tested using triplicate samples for the first time, and subsequently retested once.

Protein expression and purification

Expression of glutamine deaminase SPD1296 in *E. coli* BL21(DE3) was achieved using pET28a vector. Briefly, SPD1296 was amplified by Pr18930/Pr18931. Then the amplicon was cloned into BamHI/HindIII site of pET28a and transformed to *E. coli* BL21(DE3). The N-terminal 6 × His tag was added in the construct. *E. coli* BL21(DE3) expressing target proteins was cultured in Luria Broth medium supplemented with 50 μg/mL kanamycin at 37°C. The cells (OD_{600} of 0.5) were induced with 0.2 mM isopropyl-beta-D-thiogalactopyranoside (IPTG) overnight at 16°C before being harvested by centrifugation at 8,000 rpm for 10 min at 4°C and washed once with lysis buffer (50 mM Tris–HCl pH 8.0, 300 mM NaCl and 10 mM imidazole).

For purification, the cells were resuspended in lysis buffer containing 10 μg/mL RNase, 5 μg/mL DNase, 1 mg/mL lysosome and 1 mM phenylmethanesulfonyl fluoride (PMSF) and broken by a French pressure cell at 4°C. The cell debris was removed by centrifugation at 11,000 rpm for 1 h at 4°C. The supernatant was loaded onto a 1 mL Nickel-Sepharose resin column and washed with 30 column volumes (CV) of washing buffer (50 mM Tris–HCl pH 8.0, 300 mM NaCl and 20 mM imidazole). The bound protein was eluted by elution buffer (50 mM Tris–HCl pH 8.0, 300 mM NaCl and 250 mM imidazole) and loaded onto a Superdex 75 gel filtration column equilibrated with ITC buffer (20 mM Na-Mes pH 5.5 and 150 mM NaCl).

Enzyme activity determination

Glutamine deaminase activity was determined as previously described (Zhang et al., 2019). One mL reaction mixture containing 440 μL glutamine (100 mM), 440 μL Tris–HCl (100 mM, pH 7.5), and 20 μL crude glutaminase was incubated at 37°C for 2 min. Reaction was terminated by adding 100 μL trichloroacetic acid [15% (w/v)]. 200 μL of the reaction mixture was mixed with 800 μL 100% methyl alcohol for protein precipitation. After centrifuged at 12000 rpm, 4°C for 20 min, the supernatant was analyzed by HPLC–MS. Absolute quantification was used to determine the concentration of glutamate. One unit of glutamine deaminase was defined as the amount of enzyme that produces 1 μmol glutamate per minute under the reaction condition. Bradford method with bovine serum albumin was used to determine protein concentration.

Amino acid quantification

Quantification of intracellular methionine was accomplished by liquid chromatography and mass spectrometry. At 6 h post inoculation in CDM, 0.5 OD_{620} bacteria were collected and washed twice by ice-cold Ringer's solution by centrifugation at 4°C, 12,000 rpm for 3 min and resuspension. After being frozen by liquid nitrogen, bacterial pellets were resuspended in 1 mL 80% methanol stored at −80°C. The solution was transferred into a 2-ml grinding tube containing 1 g of glass beads (0.4–0.6 mm, BE6098-100 g, EASYBIO, China) and ground by high-throughput tissuelyser (SCIENTZ-48, SCIENTZ, China) with high speed for 10 times (1 min for each time). Between each grinding, there was 1 min for sample cooling in ice water. Ground samples were stored at −80°C for 1 h and then centrifuged at 4°C, 12,000 rpm in a 1.5 mL centrifuge tube for 20 min. The supernatants were collected and dried for methionine quantitation in a vacuum dryer. A 6,500 plus QTrap mass spectrometer (AB SCIEX, United States) coupled with ACQUITY UPLC H-Class system (Waters, United States) was used for metabolite quantitation. Chromatographic separation was achieved using an ACQUITY UPLC BEH Amide column (2.1 × 100 mm, 1.7 μm; Waters). Mobile phase A contained HPLC-grade H_2O-ACN 5/95 (v/v) with 7.5 mM ammonium formate, and mobile B was H_2O-ACN 50/50 (v/v) with 7.5 mM ammonium formate. Data were acquired in multiple reaction monitoring (MRM) mode in positive mode. The ion transitions were optimized using chemical standards. The nebulizer gas (Gas1), heater gas (Gas2), and curtain gas were set at 55, 55, and 30 psi, respectively. The ion spray voltage was 5,500 v for positive ion mode. The optimal probe temperature was determined to be 550°C, and the column oven temperature was set at 45°C. SCIEX OS 1.6 software (AB SCIEX, United States) was applied for metabolite identification and peak integration.

Western blot

Western blot was carried out as previous described (Lu et al., 2008; Liu et al., 2019). Briefly, 1 optical density (OD) D39 bacteria cultured in CDM with different concentrations of methionine and glutamine were washed once with Ringer's solution by centrifugation and resuspension. Then each bacterial pellet was resuspended in 21 μL lysis buffer (phosphate-buffered saline, 100 mM of dithiothreitol, 25 mM of $MgCl_2$, 0.1% Triton-X-100), mixed with 3 μL 100 mM PMSF and 6 μL 5× sodium dodecyl sulfate (SDS)-polyacrylamide gel loading buffer. After boiling for 10 min, 10 μL sample was loaded into the each well of 12% Tris-Glycine SDS-polyacrylamide gel. Proteins were electro-transferred to polyvinylidene difluoride membrane (Shenggong, China). The expression of His_6-tagged proteins was detected with a mouse anti-His monoclonal antibody (Beyotime Biotechnology, China) at the dilution of 1:1000 and horseradish

peroxidase-conjugated goat anti-mouse IgG antibody (Proteintech Group, China) at the dilution of 1:2000. The gray scales of MetE protein were calculated by ImageJ_v1.8.0.

L-azidohomoalanine (AHA) click labeling

The AHA click labeling assay was carried out as previously described with minor modification (Imami and Yasuda, 2019; Rong et al., 2020). D39 was cultured in CDM with no methionine and 10 or 1,000 μg/mL glutamine. At 6 h post inoculation, 2 OD bacteria were collected and washed twice by Ringer's solution. Then bacteria were resuspended in 1 mL CDM with no methionine and 100 μg/mL glutamine, which contains 2 mM AHA.HCl. After incubation at 37°C for 30 min, bacteria were washed twice by Ringer's solution and then resuspended in 50 μL lysis buffer containing 0.5 μL 100× protease cocktail, 100 μM Biotin-Alkyne, 1 mM TCEP, 100 μM THPTA, and 1 mM $CuSO_4$. After incubation for 30 min at room temperature, 12.5 μL 5 × SDS loading was added. Samples were then boiled for 10 min. 20 μL sample was loaded into each well of SDS-polyacrylamide gel. The newly synthesized proteins were detected by western blot using HRP-conjugated streptavidin (Proteintech Group, China) at the dilution of 1:2000.

DNA replication activity determination

DNA replication activity was determined by BeyoClick™ EdU (5-ethynyl-2′-deoxyuridine) cell proliferation kit (Beyotime Biotechnology, China) as previously described with minor modification (Ma et al., 2019). D39 were cultured in CDM with no methionine and 10 or 1,000 μg/mL glutamine. At 6 h post inoculation, 1 OD bacteria were collected and washed twice by Ringer's solution. Then bacteria were resuspended in 1 mL CDM with 200 μg/mL methionine and 100 μg/mL glutamine, which contains 10 μM Edu. After incubation for 30 min at 37°C, bacteria were treated by fixing solution and permeabilization solution. Then bacterial pellets were incubated with the click reaction solution containing click reaction buffer, $CuSO_4$, Azide 488 and click additive solution. After incubation for 30 min at room temperature without light, bacteria were washed and resuspended in Ringer's solution. After transferring samples into a black 96-well plate (200 μL/well) (Corning Incorporated, United States), fluorescence was determined by a microplate reader (BioTek Synergy H1, Agilent, United States).

Statistical analysis

All experiments reported in this work were conducted in triplicate samples and repeated at least once. The relevant data are presented as mean ± SEM (standard error of mean), and analyzed by two-tailed unpaired Student's *t*-test in Graphpad Prism 8. Significant differences are defined by *p*-values of <0.05 (*), <0.01 (**), <0.001 (***), and <0.0001 (****).

Data availability statement

The original contributions presented in the study are included in the article/Supplementary material, further inquiries can be directed to the corresponding authors.

Author contributions

CZ: Conceptualization, Data curation, Formal analysis, Investigation, Methodology, Project administration, Resources, Software, Supervision, Validation, Visualization, Writing – original draft, Writing – review & editing. JL: Methodology, Validation, Writing – original draft. XL: Conceptualization, Methodology, Resources, Writing – original draft. YX: Validation, Writing – original draft. QG: Validation, Writing – original draft. QC: Validation, Writing – original draft. WL: Validation, Writing – original draft. XG: Validation, Writing – original draft. SW: Funding acquisition, Writing – original draft.

Funding

The author(s) declare that financial support was received for the research, authorship, and/or publication of this article. This work was supported by grant from National Natural Science Foundation of China (81570013).

Acknowledgments

We thank the Center of Metabolomics and Lipidomics in the National Protein Science Technology Center in Tsinghua University for LC–MS/MS experiments.

Conflict of interest

The authors declare that the research was conducted in the absence of any commercial or financial relationships that could be construed as a potential conflict of interest.

Publisher's note

Supplementary material

The Supplementary material for this article can be found online at: https://www.frontiersin.org/articles/10.3389/fmicb.2024.1430038/full#supplementary-material

References

Atkinson, G. C., Tenson, T., and Hauryliuk, V. (2011). The RelA/SpoT homolog (RSH) superfamily: distribution and functional evolution of ppGpp synthetases and hydrolases across the tree of life. *PLoS One* 6:e23479. doi: 10.1371/journal.pone.0023479

Bergstrom, J., Furst, P., Noree, L. O., and Vinnars, E. (1974). Intracellular free amino acid concentration in human muscle tissue. *J. Appl. Physiol.* 36, 693–697. doi: 10.1152/jappl.1974.36.6.693

Bogaert, D., de Groot, R., and Hermans, P. W. M. (2004). *Streptococcus pneumoniae* colonisation: the key to pneumococcal disease. *Lancet Infect. Dis.* 4, 144–154. doi: 10.1016/S1473-3099(04)00938-7

Cashel, M., and Gallant, J. (1969). Two compounds implicated in the function of the RC gene of *Escherichia coli*. *Nature* 221, 838–841. doi: 10.1038/221838a0

Eguchi, Y., Fukumori, Y., and Taoka, A. (2018). Measuring magnetosomal pH of the magnetotactic bacterium *Magnetospirillum magneticum* AMB-1 using pH-sensitive fluorescent proteins. *Biosci. Biotechnol. Biochem.* 82, 1243–1251. doi: 10.1080/09168451.2018.1451739

Ferla, M. P., and Patrick, W. M. (2014). Bacterial methionine biosynthesis. *Microbiology* 160, 1571–1584. doi: 10.1099/mic.0.077826-0

Gray, D. A., Dugar, G., Gamba, P., Strahl, H., Jonker, M. J., and Hamoen, L. W. (2019). Extreme slow growth as alternative strategy to survive deep starvation in bacteria. *Nat. Commun.* 10:890. doi: 10.1038/s41467-019-08719-8

Haertel, T., Eylert, E., Schulz, C., Petruschka, L., Gierok, P., Grubmueller, S., et al. (2012). Characterization of central carbon metabolism of *Streptococcus pneumoniae* by Isotopologue profiling. *J. Biol. Chem.* 287, 4260–4274. doi: 10.1074/jbc.M111.304311

Haseltine, W. A., and Block, R. (1973). Synthesis of guanosine tetra- and pentaphosphate requires the presence of a codon-specific, uncharged transfer ribonucleic acid in the acceptor site of ribosomes. *Proc. Natl. Acad. Sci. USA* 70, 1564–1568. doi: 10.1073/pnas.70.5.1564

Hondorp, E. R., and Matthews, R. G. (2013). Methionine. *EcoSal Plus* 2, 1–36. doi: 10.1128/ecosalplus.3.6.1.7

Imami, K., and Yasuda, T. (2019). Measuring protein synthesis during cell cycle by azidohomoalanine (AHA) labeling and flow cytometric analysis. *Bio Protoc* 9:e3215. doi: 10.21769/BioProtoc.3215

Kenney, L. J. (2019). The role of acid stress in Salmonella pathogenesis. *Curr. Opin. Microbiol.* 47, 45–51. doi: 10.1016/j.mib.2018.11.006

Kim, H. (2011). Glutamine as an immunonutrient. *Yonsei Med. J.* 52, 892–897. doi: 10.3349/ymj.2011.52.6.892

Lacey, J. M., and Wilmore, D. W. (1990). Is glutamine a conditionally essential amino acid? *Nutr. Rev.* 48, 297–309. doi: 10.1111/j.1753-4887.1990.tb02967.x

Lanie, J. A., Ng, W. L., Kazmierczak, K. M., Andrzejewski, T. M., Davidsen, T. M., Wayne, K. J., et al. (2007). Genome sequence of Avery's virulent serotype 2 strain D39 of *Streptococcus pneumoniae* and comparison with that of unencapsulated laboratory strain R6. *J. Bacteriol.* 189, 38–51. doi: 10.1128/JB.01148-06

Li, J., Li, J. W., Feng, Z., Wang, J., An, H., Liu, Y., et al. (2016). Epigenetic switch driven by DNA inversions dictates phase variation in *Streptococcus pneumoniae*. *PLoS Pathog.* 12:e1005762. doi: 10.1371/journal.ppat.1005762

Lisher, J. P., Tsui, H. C. T., Ramos-Montañez, S., Hentchel, K. L., Martin, J. E., Trinidad, J. C., et al. (2017). Biological and chemical adaptation to endogenous hydrogen peroxide production in *Streptococcus pneumoniae* D39. *msphere* 2:e00291-16. doi: 10.1128/mSphere.00291-16

Liu, X., Li, J. W., Feng, Z. X., Luo, Y. F., Veening, J. W., and Zhang, J. R. (2017). Transcriptional repressor PtvR regulates phenotypic tolerance to vancomycin in *Streptococcus pneumoniae*. *J. Bacteriol.* 199:19. doi: 10.1128/JB.00054-17

Liu, Y., Zeng, Y., Huang, Y., Gu, L., Wang, S., Li, C., et al. (2019). HtrA-mediated selective degradation of DNA uptake apparatus accelerates termination of pneumococcal transformation. *Mol. Microbiol.* 112, 1308–1325. doi: 10.1111/mmi.14364

Llorens, J. M. N., Tormo, A., and Martínez-García, E. (2010). Stationary phase in gram-negative bacteria. *FEMS Microbiol. Rev.* 34, 476–495. doi: 10.1111/j.1574-6976.2010.00213.x

Lu, P., Ma, D., Chen, Y., Guo, Y., Chen, G.-Q., Deng, H., et al. (2013). L-glutamine provides acid resistance for *Escherichia coli* through enzymatic release of ammonia. *Cell Res.* 23, 635–644. doi: 10.1038/cr.2013.13

Lu, L., Ma, Z., Jokiranta, T. S., Whitney, A. R., DeLeo, F. R., and Zhang, J. R. (2008). Species-specific interaction of *Streptococcus pneumoniae* with human complement factor H. *J. Immunol.* 181, 7138–7146. doi: 10.4049/jimmunol.181.10.7138

Lu, L., Ma, Y., and Zhang, J. R. (2006). *Streptococcus pneumoniae* recruits complement factor H through the amino terminus of CbpA. *J. Biol. Chem.* 281, 15464–15474. doi: 10.1074/jbc.M602404200

Ma, J., Hu, X., Liao, C., Xiao, H., Zhu, Q., Li, Y., et al. (2019). Gypenoside L inhibits proliferation of liver and esophageal Cancer cells by inducing senescence. *Molecules* 24:1054. doi: 10.3390/molecules24061054

Magnusson, L. U., Farewell, A., and Nyström, T. (2005). ppGpp: a global regulator in *Escherichia coli*. *Trends Microbiol.* 13, 236–242. doi: 10.1016/j.tim.2005.03.008

Maser, A., Peebo, K., Vilu, R., and Nahku, R. (2020). Amino acids are key substrates to *Escherichia coli* BW25113 for achieving high specific growth rate. *Res. Microbiol.* 171, 185–193. doi: 10.1016/j.resmic.2020.02.001

Matin, A., Wilson, B., Zychlinsky, E., and Matin, M. (1982). Proton motive force and the physiological basis of delta pH maintenance in *Thiobacillus acidophilus*. *J. Bacteriol.* 150, 582–591. doi: 10.1128/jb.150.2.582-591.1982

Milligan, T. W., Doran, T. I., Straus, D. C., and Mattingly, S. J. (1978). Growth and amino acid requirements of various strains of group B streptococci. *J. Clin. Microbiol.* 7, 28–33. doi: 10.1128/jcm.7.1.28-33.1978

Potrykus, K., and Cashel, M. (2008). (p)ppGpp: still magical? *Ann. Rev. Microbiol.* 62, 35–51. doi: 10.1146/annurev.micro.62.081307.162903

Rong, B., Zhang, Q., Wan, J., Xing, S., Dai, R., Li, Y., et al. (2020). Ribosome 18S m^6A methyltransferase METTL5 promotes translation initiation and breast Cancer cell growth. *Cell Rep.* 33:108544. doi: 10.1016/j.celrep.2020.108544

Rose, W. C. (1949). Amino acid requirements of man. *Fed. Proc.* 8, 546–552.

Russell, J. B., and DiezGonzalez, F. (1998). The effects of fermentation acids on bacterial growth. *Adv. Microb. Physiol.* 39, 205–234.

Shelver, D., Rajagopal, L.Harris TO, and Rubens, C. E. (2003). MtaR, a regulator of methionine transport, is critical for survival of group B streptococcus in vivo. *J. Bacteriol.* 185, 6592–6599. doi: 10.1128/JB.185.22.6592-6599.2003

Slonczewski, J. L., Fujisawa, M., Dopson, M., and Krulwich, T. A. (2009). Cytoplasmic pH measurement and homeostasis in Bacteria and Archaea. *Adv. Microb. Physiol.* 55, 1–79. doi: 10.1016/S0065-2911(09)05501-5

Sperandio, B., Gautier, C., McGovern, S., Ehrlich, D. S., Renault, P., Martin-Verstraete, I., et al. (2007). Control of methionine synthesis and uptake by MetR and homocysteine in *Streptococcus mutans*. *J. Bacteriol.* 189, 7032–7044. doi: 10.1128/JB.00703-07

Sturr, M. G., Guffanti, A. A., and Krulwich, T. A. (1994). Growth and bioenergetics of alkaliphilic *Bacillus firmus* OF4 in continuous culture at high pH. *J. Bacteriol.* 176, 3111–3116. doi: 10.1128/jb.176.11.3111-3116.1994

Sung, C. K., Li, H., Claverys, J. P., and Morrison, D. A. (2001). An rpsL cassette, janus, for gene replacement through negative selection in *Streptococcus pneumoniae*. *Appl. Environ. Microbiol.* 67, 5190–5196. doi: 10.1128/AEM.67.11.5190-5196.2001

Veine, D. M., Arscott, L. D., and Williams, C. H. (1998). Redox potentials for yeast, *Escherichia coli* and human glutathione reductase relative to the NAD^+/NADH redox couple: enzyme forms active in catalysis. *Biochemistry* 37, 15575–15582. doi: 10.1021/bi9811314

Wang, X., Zeng, Y., Sheng, L., Larson, P., Liu, X., Zou, X., et al. (2019). A Cinchona alkaloid antibiotic that appears to target ATP synthase in *Streptococcus pneumoniae*. *J. Med. Chem.* 62, 2305–2332. doi: 10.1021/acs.jmedchem.8b01353

Weber, H., Polen, T., Heuveling, J., Wendisch, V. F., and Hengge, R. (2005). Genome-wide analysis of the general stress response network in *Escherichia coli*: sigmaS-dependent genes, promoters, and sigma factor selectivity. *J. Bacteriol.* 187, 1591–1603. doi: 10.1128/JB.187.5.1591-1603.2005

Weiser, J. N., Ferreira, D. M., and Paton, J. C. (2018). *Streptococcus pneumoniae*: transmission, colonization and invasion. *Nat. Rev. Microbiol.* 16, 355–367. doi: 10.1038/s41579-018-0001-8

Willett, N. P., and Morse, G. E. (1966). Long-chain fatty acid inhibition of growth of *Streptococcus agalactiae* in a chemically defined medium. *J. Bacteriol.* 91, 2245–2250. doi: 10.1128/jb.91.6.2245-2250.1966

Yuste, J., Botto, M., Paton, J. C., Holden, D. W., and Brown, J. S. (2005). Additive inhibition of complement deposition by pneumolysin and PspA facilitates *Streptococcus pneumoniae* septicemia. *J. Immunol.* 175, 1813–1819. doi: 10.4049/jimmunol.175.3.1813

Zhang, C., An, H., Hu, J., Li, J., Zhang, W., Lan, X., et al. (2021). MetR is a molecular adaptor for pneumococcal carriage in the healthy upper airway. *Mol. Microbiol.* 116, 438–458. doi: 10.1111/mmi.14724

Zhang, C., Liu, Y., An, H., Wang, X., Xu, L., Deng, H., et al. (2023). Amino acid starvation-induced glutamine accumulation enhances pneumococcal survival. *mSphere* 8:e0062522. doi: 10.1128/msphere.00625-22

Zhang, X., Xu, Z. Y., Liu, S., Qian, K., Xu, M. J., Yang, T. W., et al. (2019). Improving the production of salt-tolerant Glutaminase by integrating multiple copies of *Mglu* into the protease and *16S rDNA* genes of *Bacillus subtilis* 168. *Molecules* 24:592. doi: 10.3390/molecules24030592

Zilberstein, D., Agmon, V., Schuldiner, S., and Padan, E. (1984). *Escherichia coli* intracellular pH, membrane potential, and cell growth. *J. Bacteriol.* 158, 246–252. doi: 10.1128/jb.158.1.246-252.1984

Frontiers in Microbiology

Explores the habitable world and the potential of microbial life

The largest and most cited microbiology journal which advances our understanding of the role microbes play in addressing global challenges such as healthcare, food security, and climate change.

Discover the latest Research Topics

See more →

Frontiers

Avenue du Tribunal-Fédéral 34
1005 Lausanne, Switzerland
frontiersin.org

Contact us

+41 (0)21 510 17 00
frontiersin.org/about/contact